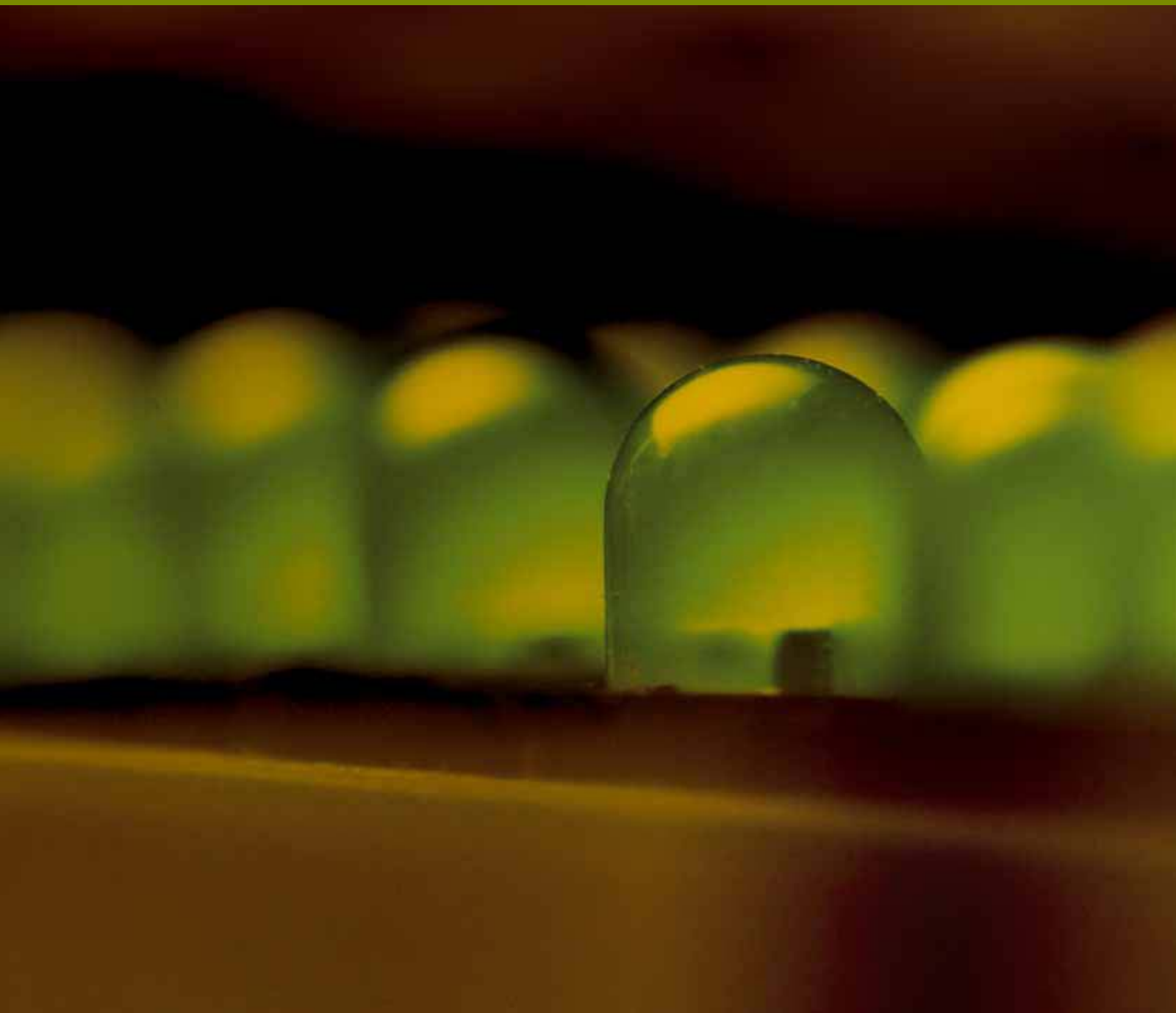


# Modern Trends in Metamaterial Applications

Guest Editors: Ivan D. Rukhlenko, Pavel A. Belov,  
Natalia M. Litchinitser, and Alexandra Boltasseva





---

# **Modern Trends in Metamaterial Applications**

Advances in OptoElectronics

---

## **Modern Trends in Metamaterial Applications**

Guest Editors: Ivan D. Rukhlenko, Pavel A. Belov,  
Natalia M. Litchinitser, and Alexandra Boltasseva



---

Copyright © 2012 Hindawi Publishing Corporation. All rights reserved.

This is a special issue published in “Advances in OptoElectronics.” All articles are open access articles distributed under the Creative Commons Attribution License, which permits unrestricted use, distribution, and reproduction in any medium, provided the original work is properly cited.

## Editorial Board

Armin G. Aberle, Singapore  
Ralf Bergmann, Germany  
Xian An Cao, USA  
Wen-Chang Chen, Taiwan  
Philippe Goldner, France  
Jung Y. Huang, Taiwan  
Anthony J. Kenyon, UK  
Yaomin Lin, USA

Wenning Liu, USA  
Yalin Lu, USA  
Alfred Margaryan, USA  
Samir K. Mondal, India  
Michele Norgia, Italy  
Satishchandra B. Ogale, India  
Adrian Podoleanu, UK  
Richard Rizk, France

Lucimara Stolz Roman, Brazil  
Jayanta K. Sahu, UK  
Somenath N. Sarkar, India  
Vasily Spirin, Mexico  
Chang Q. Sun, Singapore  
Yuqin Zong, USA

# Contents

**Modern Trends in Metamaterial Applications**, Ivan D. Rukhlenko, Pavel A. Belov, Natalia M. Litchinitser, and Alexandra Boltasseva

Volume 2012, Article ID 514270, 2 pages

**Applications of Hyperbolic Metamaterial Substrates**, Yu Guo, Ward Newman, Cristian L. Cortes, and Zubin Jacob

Volume 2012, Article ID 452502, 9 pages

**Extension of the Multipole Approach to Random Metamaterials**, A. Chipouline, S. Sugavanam, J. Petschulat, and T. Pertsch

Volume 2012, Article ID 161402, 16 pages

**Rolled-Up Metamaterials**, Stephan Schwaiger, Andreas Rottler, and Stefan Mendach

Volume 2012, Article ID 782864, 10 pages

**Conditions of Perfect Imaging in Negative Refraction Materials with Gain**, Haowen Liang, Yifeng Shao, Jianying Zhou, Boris A. Malomed, and Gershon Kurizki

Volume 2012, Article ID 347875, 5 pages

**Plasmonic Nanostructure for Enhanced Light Absorption in Ultrathin Silicon Solar Cells**, Jinna He, Chunzhen Fan, Junqiao Wang, Yongguang Cheng, Pei Ding, and Erjun Liang

Volume 2012, Article ID 592754, 8 pages

**Field Enhancement in a Grounded Dielectric Slab by Using a Single Superstrate Layer**,

Constantinos A. Valagiannopoulos and Nikolaos L. Tsitsas

Volume 2012, Article ID 439147, 9 pages

**Realization of Radar Illusion Using Active Devices**, B. Z. Cao, L. Sun, and Z. L. Mei

Volume 2012, Article ID 736876, 9 pages

**Dirac Dispersion in Two-Dimensional Photonic Crystals**, C. T. Chan, Zhi Hong Hang, and Xueqin Huang

Volume 2012, Article ID 313984, 11 pages

**Recent Advances in Multiband Printed Antennas Based on Metamaterial Loading**, F. Paredes, G. Zamora, S. Zufanelli, F. J. Herraiz-Martínez, J. Bonache, and F. Martín

Volume 2012, Article ID 968780, 12 pages

**Nanocouplers for Infrared and Visible Light**, A. Andryieuski and A. V. Lavrinenko

Volume 2012, Article ID 839747, 17 pages

**Metaoptics with Nonrelativistic Matter Waves**, T. Taillandier-Loize, J. Baudon, M. Hamamda, G. Dutier, V. Bocvarski, M. Boustimi, F. Perales, and M. Ducloy

Volume 2012, Article ID 734306, 8 pages

**Homogeneous Hyperbolic Systems for Terahertz and Far-Infrared Frequencies**, Leonid V. Alekseyev, Viktor A. Podolskiy, and Evgenii E. Narimanov

Volume 2012, Article ID 267564, 6 pages

**The Performance of Active Coated Nanoparticles Based on Quantum-Dot Gain Media,**

Sawyer D. Campbell and Richard W. Ziolkowski

Volume 2012, Article ID 368786, 6 pages

**Nonlinear Scattering by Anisotropic Dielectric Periodic Structures,**

O. V. Shramkova and A. G. Schuchinsky

Volume 2012, Article ID 154847, 11 pages

**Laser Writing of Multiscale Chiral Polymer Metamaterials,** E. P. Furlani, H. S. Jee, H. S. Oh, A. Baev,  
and P. N. Prasad

Volume 2012, Article ID 861569, 7 pages

**3D Photonic Nanostructures via Diffusion-Assisted Direct fs Laser Writing,** Gabija Bickauskaite,  
Maria Manousidaki, Konstantina Terzaki, Elmina Kambouraki, Ioanna Sakellari, Nikos Vasilantonakis,  
David Gray, Costas M. Soukoulis, Costas Fotakis, Maria Vamvakaki, Maria Kafesaki, Maria Farsari,  
Alexander Pikulin, and Nikita Bityurin

Volume 2012, Article ID 927931, 6 pages

**Design of Matched Absorbing Layers for Surface Plasmon-Polaritons,** Sergio de la Cruz,

Eugenio R. Méndez, and Alexei A. Maradudin

Volume 2012, Article ID 598213, 7 pages

**Optical Manipulation with Plasmonic Beam Shaping Antenna Structures,** Young Chul Jun and Igal Brener

Volume 2012, Article ID 595646, 6 pages

**Plasmonic Modes of Metamaterial-Based Slot Waveguides,** Ivan D. Rukhlenko, Malin Premaratne,  
and Govind P. Agrawal

Volume 2012, Article ID 907183, 5 pages

**Magnetic Plasmon Sensing in Twisted Split-Ring Resonators,** J. X. Cao, H. Liu, S. M. Wang, Y. J. Zheng,  
C. Zhu, Y. Wang, and S. N. Zhu

Volume 2012, Article ID 609691, 5 pages

## Editorial

# Modern Trends in Metamaterial Applications

**Ivan D. Rukhlenko,<sup>1</sup> Pavel A. Belov,<sup>2,3</sup> Natalia M. Litchinitser,<sup>4</sup> and Alexandra Boltasseva<sup>5</sup>**

<sup>1</sup> *Advanced Computing and Simulation Laboratory (AxL), Department of Electrical and Computer Systems Engineering, Monash University, Clayton, VIC 3800, Australia*

<sup>2</sup> *Photonics and Optical Information Theory Department, National Research University of Information Technologies, Mechanics and Optics, Kronversky pr. 49, St. Petersburg 197101, Russia*

<sup>3</sup> *Queen Mary, University of London, Mile End Road, London E1 4NS, UK*

<sup>4</sup> *Department of Electrical Engineering, The State University of New York at Buffalo, 230L Davis Hall, Buffalo, NY 14260, USA*

<sup>5</sup> *Birk Nanotechnology Center and School of Electrical and Computer Engineering, Purdue University, 1205 West State Street, West Lafayette, IN 47907, USA*

Correspondence should be addressed to Ivan D. Rukhlenko, [ivan.rukhlenko@monash.edu](mailto:ivan.rukhlenko@monash.edu)

Received 8 November 2012; Accepted 8 November 2012

Copyright © 2012 Ivan D. Rukhlenko et al. This is an open access article distributed under the Creative Commons Attribution License, which permits unrestricted use, distribution, and reproduction in any medium, provided the original work is properly cited.

The concept of metamaterials, which has been enunciated in the pivotal works of V. G. Veselago and J. B. Pendry, has drastically altered our way of thinking about light-matter interactions and greatly enriched the fields of classical and quantum electrodynamics. It has become apparent over the last decade that the propagation of electromagnetic waves can be manipulated almost at will using artificially fabricated structures with prescribed electromagnetic properties, the diversity of which is limited only by the ingenuity of the researchers and the sophistication of the fabrication techniques. This new understanding has revolutionized the design paradigm of photonic devices and quickly resulted in the experimental demonstration of several counterintuitive effects with far-reaching breakthrough applications. In particular, it was shown that not only could negative-index metamaterials be fabricated practically, but they can also be used to create super- and hyperlenses with subwavelength optical resolution. Likewise, it is possible to fabricate metamaterials designed using the transformation optics approach and apply them in real invisibility cloaks. Today, scientists and engineers all over the world are combating the fundamental and technological challenges that deter the wide commercial use of these and other exciting functionalities offered by metamaterials.

As is customary with great ideas, the reality of unusual metamaterial properties has been the subject of much controversy. Even now, some experts in optics and electromagnetism argue over this reality in regards to phase advance

in evanescent waves, as well as over the existence of a negative refractive index, thus showing that the physics behind these phenomena is more complicated than it may appear at first glance. Interestingly, the analysis of metamaterial critiques may be quite instructive, as it helps one to appreciate the subtleties of the field and gain a deeper insight into it. While leaving such an analysis for future textbooks, we wish to note here that disproving the objections against any metamaterial phenomenon requires the careful consideration of several fundamental principles, including the causality requirement, which makes metamaterials essentially dispersive.

Despite all the differences between the electromagnetic behaviour of ordinary materials and metamaterials, they are both governed by the same set of Maxwell equations. Therefore, it is the new functionalities and design guidelines enabled by the metamaterial paradigm—rather than new physics—that have aroused a relentless interest in metamaterials. This interest remains equally strong from both the physics and engineering communities since the field of metamaterials mediates science and technology. It is therefore not surprising that in recent years we have witnessed a rapidly escalating number of publications on the physics, design, and applications of various types of metamaterials. The focus of theoretical studies shifts from negative-index materials to hyperbolic, tuneable, nonlinear, and nonlocal metamaterials, as well as to media with extreme material parameters. The modern trends in metamaterial applications include superresolution imaging and optical



sensing, the advancement of photonic circuitry with meta-tronics, all-optical and electrooptical dynamic control of light, electromagnetic cloaking, and light harvesting for improved solar-cell technology. This special issue focuses on the advances along these research avenues and on the new photonic devices associated with them.

## **Acknowledgment**

The editors would like to thank the authors for their high-quality research and review articles. Their thanks also go out to the referees for their hard work in revising the submissions. They are also grateful to the editorial staff of Advances in OptoElectronics, especially Mr. Mohamed Abdel Razek, for their valuable assistance in preparing the special issue. They hope that the many physicists and engineers in the field of metamaterials will find the special issue interesting and useful for their future work.

*Ivan D. Rukhlenko*  
*Pavel A. Belov*  
*Natalia M. Litchinitser*  
*Alexandra Boltasseva*

## Review Article

# Applications of Hyperbolic Metamaterial Substrates

**Yu Guo, Ward Newman, Cristian L. Cortes, and Zubin Jacob**

*Department of Electrical and Computer Engineering, University of Alberta, Edmonton, AB, Canada T6G 2V4*

Correspondence should be addressed to Zubin Jacob, zjacob@ualberta.ca

Received 28 August 2012; Accepted 31 October 2012

Academic Editor: Pavel A. Belov

Copyright © 2012 Yu Guo et al. This is an open access article distributed under the Creative Commons Attribution License, which permits unrestricted use, distribution, and reproduction in any medium, provided the original work is properly cited.

We review the properties of hyperbolic metamaterials and show that they are promising candidates as substrates for nanoimaging, nanosensing, fluorescence engineering, and controlling thermal emission. Hyperbolic metamaterials can support unique bulk modes, tunable surface plasmon polaritons, and surface hyperbolic states (Dyakonov plasmons) that can be used for a variety of applications. We compare the effective medium predictions with practical realizations of hyperbolic metamaterials to show their potential for radiative decay engineering, bioimaging, subsurface sensing, metaplasmonics, and super-Planckian thermal emission.

## 1. Introduction

Metamaterial technologies have matured over the past decade for a variety of applications such as superresolution imaging [1, 2], cloaking [3], and perfect absorption [4]. Various classes of metamaterials have emerged that show exotic electromagnetic properties like negative index [5], optical magnetism [6], giant chirality [7–9], epsilon-near-zero [10], bianisotropy [11], and spatial dispersion [12] among many others. The central guiding principle in all the metamaterials consists of fabricating a medium composed of unit cells far below the size of the wavelength. The unique resonances of the unit cell based on its structure and material composition as well as coupling between the cells lead to a designed macroscopic electromagnetic response.

One class of artificial media which received a lot of attention are hyperbolic metamaterials [13–15]. They derive their name from the unique form of the isofrequency curve which is hyperbolic instead of circular as in conventional dielectrics. The reason for their widespread interest is due to the relative ease of nanofabrication, broadband nonresonant response, wavelength tunability, bulk three-dimensional response, and high figure of merit [16]. Hyperbolic metamaterials (HMMs) can be used for a variety of applications from negative index waveguides [13] and subdiffraction photonic funnels [17] to nanoscale resonators [18]. In the visible and near-infrared wavelength regions, HMMs are the most promising artificial media for practical applications [19].

In this paper, we describe the potential of hyperbolic metamaterial substrates for five distinct applications: (1) fluorescence engineering [20–22], (2) nanoimaging [23–25], (3) subsurface sensing [26], (4) dyakonov plasmons [27, 28], and (5) super-Planckian thermal emission [29, 30]. Our work presents a unified view for these distinct applications and elucidates many key design principles useful to experimentalists and theorists. We focus on the physical origin of hyperbolic behavior in various practical realizations and compare the device performances to theoretical idealizations. We expect this work to provide an overview and starting point for varied practical applications of hyperbolic metamaterials.

## 2. Hyperbolic Metamaterials

HMMs can be considered as uniaxial metacrystals with an extremely anisotropic dielectric tensor,  $\vec{\epsilon} = \text{diag}[\epsilon_{xx}, \epsilon_{yy}, \epsilon_{zz}]$  such that  $\epsilon_{xx} = \epsilon_{yy}$  and  $\epsilon_{zz} \cdot \epsilon_{xx} < 0$ . The properties of HMMs are best understood by studying the isofrequency surface of extraordinary waves in this medium:

$$\frac{(k_x^2 + k_y^2)}{\epsilon_{zz}} + \frac{k_z^2}{\epsilon_{xx}} = \left(\frac{\omega}{c}\right)^2. \quad (1)$$

The above equation represents a hyperboloid when  $\epsilon_{zz} \cdot \epsilon_{xx} < 0$  which is an open surface in stark contrast to the closed spherical dispersion in an isotropic medium. The

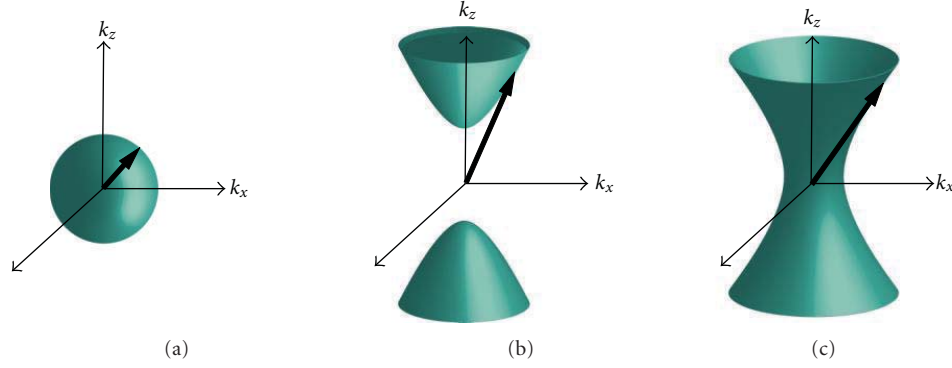


FIGURE 1:  $k$ -Space topology. (a) The isofrequency contour for an isotropic dielectric is a sphere. For extraordinary waves in an extremely anisotropic uniaxial medium, the isofrequency contour becomes a hyperboloid which supports waves with unbounded wavevectors, in stark contrast to an isotropic medium. (b) A type 1 HMM has one component of the dielectric tensor negative ( $\epsilon_{xx} = \epsilon_{yy} > 0$  and  $\epsilon_{zz} < 0$ ) and supports low- $k$  and high- $k$  waves. (c) A type 2 HMM has two components of the dielectric tensor negative ( $\epsilon_{xx} = \epsilon_{yy} < 0$  and  $\epsilon_{zz} > 0$ ) and only supports high- $k$  waves.

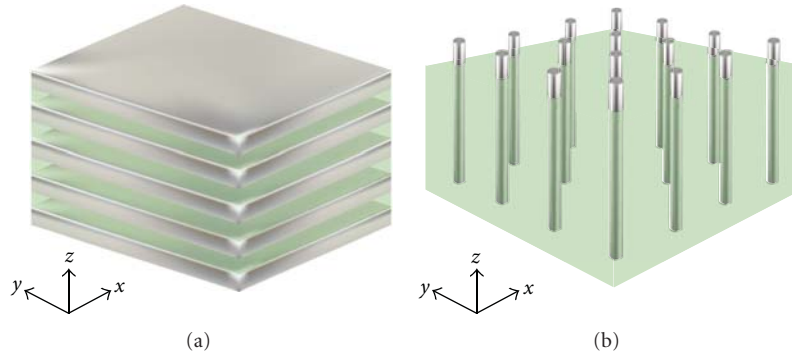


FIGURE 2: (a) Multilayer realization of hyperbolic metamaterials consisting of alternating subwavelength layers of metal and dielectric (b) metal nanorod realization in a dielectric host matrix.

immediate physical consequence of this dispersion relation is the existence of propagating waves with large wavevectors known as high- $k$  waves which are evanescent in conventional media. Multiple device applications and physical phenomena in hyperbolic metamaterials are related to the properties of these high- $k$  waves. It was recently proposed that these states cause a broadband divergence in the photonic density of states, the physical quantity governing various phenomena such as spontaneous and thermal emission [20, 31–33]. This prediction led to multiple experimental [21, 34] and computational efforts [35, 36] to verify the predictions and explore applications of this phenomenon.

We now introduce nomenclature to classify the two types of hyperbolic metamaterials based on the number of components of the dielectric tensor which are negative [19]. Note that if all three components are negative, we have an effective metal, and propagating waves are not allowed in such a medium.

Type I: if there is only one negative component, that is,  $\epsilon_{zz} < 0$  in the tensor, then we term such metamaterials as type I HMMs. They have low loss because of their predominantly dielectric nature but are difficult to achieve in practice.

Type II: if there are two components in the dielectric tensor which are negative, that is,  $\epsilon_{xx} = \epsilon_{yy} < 0$ , we term them as type II HMMs. They have higher loss and high-impedance mismatch with vacuum due to their predominantly metallic nature.

Figure 1 shows the isofrequency surfaces for an isotropic dielectric (i.e., glass) and for a type 1 and type 2 HMMs.

### 3. 1D and 2D Realizations

There are two prominent methods to engineer practical hyperbolic media. The first consists of alternating layers of metal and dielectric with the layer thicknesses far below the size of the wavelength. The second approach consists of metal nanorods in a dielectric host such as porous anodic alumina (AAO). Figure 2 is a schematic illustration of these two approaches. Both these approaches achieve the desired extremely anisotropic response according to Maxwell-Garnett effective medium theory [16, 37–40]. It is important to note that effective medium theory predicts the desired response in a broad spectral bandwidth because of its nonresonant nature. This is crucial since absorption

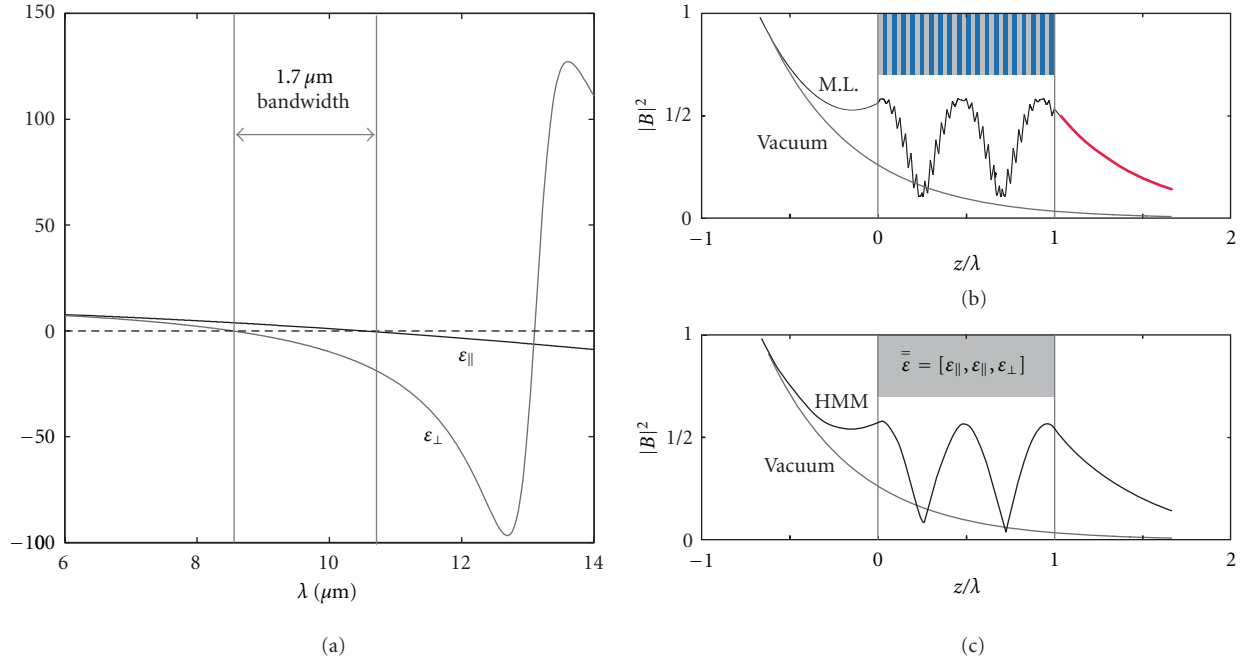


FIGURE 3: (a) Dispersion of the dielectric constants in a practical multilayer semiconductor realization of the HMM. Note the broadband region in which type I HMM response is achieved. (b) Exact numerical calculation (neglecting loss) in the multilayer structure showing the Bloch high- $k$  mode and coupled surface plasmons at the interfaces. (c) Evanescent wave incident on an effective medium slab couples to the high- $k$  mode and is transmitted. In contrast, the evanescent wave decays away in vacuum.

in resonant metamaterials is a major detriment to practical applications.

**3.1. Material Systems.** The response of the hyperbolic metamaterial can be tuned by the choice of constituent metal and dielectric and their relative volume ratios.

- (i) UV and visible: silver is the ideal choice of metal due to its low losses. Alumina ( $\text{Al}_2\text{O}_3$ ) is a compatible dielectric in the UV range, but at higher wavelengths, the large negative real part of the metallic dielectric constant requires a shift to high-index dielectrics. Titanium dioxide is an excellent candidate due to its large index, opening the possibility of impedance matching with vacuum [41].
- (ii) Near-IR: none of the conventional plasmonic metals such as gold or silver are good candidates for hyperbolic metamaterials at near-IR wavelengths. This is because far below the plasma frequency, metals are extremely reflective and lead to high-impedance mismatch with surrounding media. The recently developed alternative plasmonic metals based on oxides and nitrides are ideal for applications in hyperbolic metamaterials since their plasma frequency can be tuned to lie in the near-IR [42].
- (iii) Mid-IR: at midinfrared wavelengths, doped semiconductors can act as the metallic building block for hyperbolic metamaterials [16]. Another option is the use of phonon-polaritonic metals such as silicon

carbide which have their Reststrahlen band in the mid-IR range [43].

**3.2. What Is the Origin of the High- $k$  Modes?** We now analyze the physical origin of the high- $k$  modes in a practical realization of hyperbolic metamaterials. Due to the metallic building block needed to achieve a negative dielectric constant in one direction, HMMs support bulk plasmon-polaritonic or phonon-polaritonic modes. Thus, high- $k$  modes of HMM can be considered as engineered bulk polaritonic modes which owe their large momentum to light-matter coupling. In Figure 3, we contrast an incident evanescent wave on a conventional dielectric as opposed to a hyperbolic metamaterial. We take negligible losses to clarify the origin of the high- $k$  states. The evanescent wave decays in a simple dielectric but couples to a high- $k$  propagating wave in the hyperbolic metamaterial. We consider a practical multilayer semiconductor realization of the hyperbolic metamaterial [16]. The high- $k$  mode is seen to arise due to the coupling between the surface plasmon polaritons on each of the interfaces. Thus, the high- $k$  modes are in fact the Bloch modes due to the coupled surface plasmon polaritons on the metal-dielectric multilayer superlattice [12].

**3.3. Validity of Effective Medium Theory.** We now consider the transmission of evanescent waves through a practical multilayer structure to determine the largest wavevector that can be transmitted/supported by the hyperbolic metamaterial. In the effective medium limit, waves with infinitely large

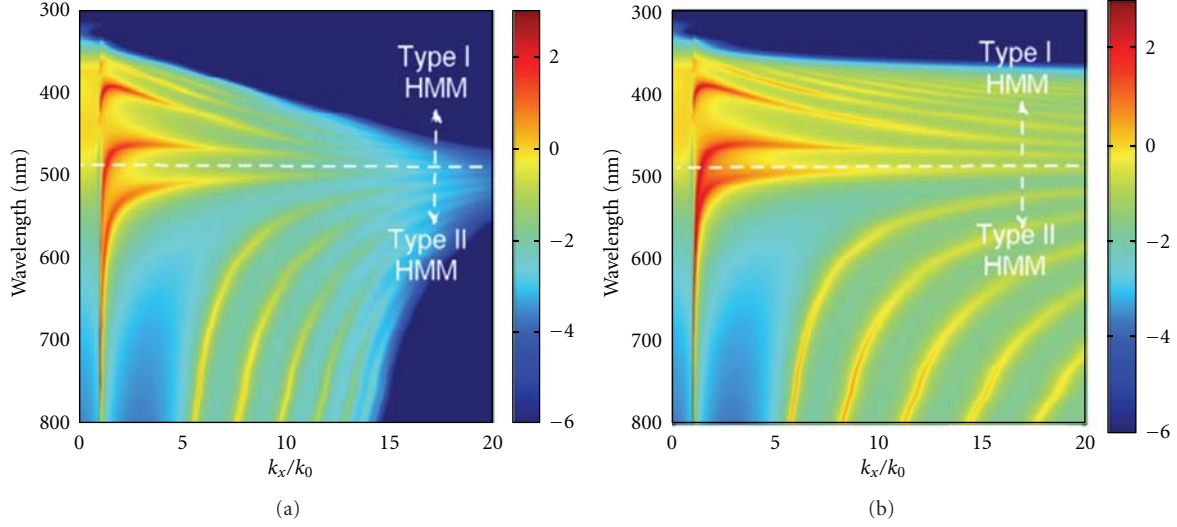


FIGURE 4: (a) Transmission of waves through a multilayer realization consisting of silver-tio2 layers each of 10 nm thickness (total 16 layers) including loss and dispersion. The high- $k$  modes are seen to tunnel across the layers. (b) In the effective medium limit, there are infinitely many high- $k$  waves in the type I and type II HMM. Notice that there is no upper cutoff in the effective medium limit, but in the multilayer realization, the size of the unit cell imposes a strict upper limit to tunneling ( $k_0$  is the free space wavevector).

wavevectors can be transmitted in the entire bandwidth of hyperbolic dispersion. However, this is never true in reality since the size of the unit cell places an upper cutoff to the largest wavevector that can be transmitted through the structure. Waves with wavevectors comparable to the inverse unit cell size lie at the edge of the Brillouin zone of the periodic lattice. They do not perceive the metamaterial in the effective medium limit but in fact start Bragg scattering. This is evident in the comparison shown in Figure 4 which considers an Ag/TiO<sub>2</sub> multilayer HMM stack both in the effective medium limit and a practical multilayer realization. Our transfer matrix simulations take into account the absorption, dispersion, and the size of the unit cell. It is seen that high- $k$  waves are transmitted through the multilayer structure in excellent agreement with the effective medium theory prediction. The practical realization however has a cutoff to the largest wavevector that can be transmitted which is related to the unit cell size of the HMM.

## 4. Applications

**4.1. Fluorescence Engineering.** The presence of high- $k$  waves opens a new route into which quantum emitters can decay when placed on an HMM substrate. In the near field of any medium, there are in general three routes of decay corresponding to the types of electromagnetic modes supported by the structure (Figure 5). A quantum emitter or fluorophore can emit into propagating waves of vacuum or bound modes (such as waveguide modes or surface plasmon polaritons), and if the body is absorptive ( $\text{Im}(\epsilon) \neq 0$ ), the third nonradiative route for relaxation is opened up. Fluorescence can be completely quenched due to near-field absorption.

The physical origin for quenching can be understood by considering the size of the fluorescent dye molecule (point

dipole like) which is far below the size of the wavelength. This implies that waves with large wavevectors are necessarily emitted by the emitter which do not normally carry energy to the far field. However, these waves can be completely absorbed in the near field by lossy structures. In stark contrast to quenching, the HMM couples to these waves with large wavevectors leading to radiative relaxation in the near field. The signature of this coupling is the enhanced decay rate of dye molecules placed on hyperbolic metamaterial substrates. The coupling to high- $k$  states opens the possibility of high-contrast fluorescence imaging as well as sensitive-phase measurements [20, 21, 44]. The decay rate in the near field at a distance “ $d$ ” from the HMM is dominated by high- $k$  waves and for type I HMM is given by

$$\Gamma_{\text{high-}k} \approx \frac{\mu_{\perp}^2}{8\hbar d^3} \frac{2\sqrt{|\epsilon_{xx}||\epsilon_{zz}|}}{1 + |\epsilon_{xx}||\epsilon_{zz}|}, \quad (2)$$

where  $\mu_{\perp}$  is the dipole moment of a perpendicularly oriented dipole. The decay rate into the high- $k$  modes of the HMM can exceed the rate of emission into vacuum by factors of 10 even without any subwavelength confinement of the emitters.

The validity of the effective medium theory and point dipole approximation for spontaneous emission has been studied in detail [19, 35, 36, 45].

**4.2. Super-Planckian Thermal Emission.** The above-mentioned high- $k$  states which lead to decrease in radiative spontaneous emission lifetime can also play a key role in thermal conductivity [32] and thermal emission [30]. This was initially pointed out in multiple references as [19–21, 31, 32] as well as [46, 47]. Figure 6 shows that due to the enhanced density of states, a hyperbolic metamaterial in equilibrium at temperature  $T$  emits super-Planckian thermal radiation [30]. This can lead to near-field thermal energy

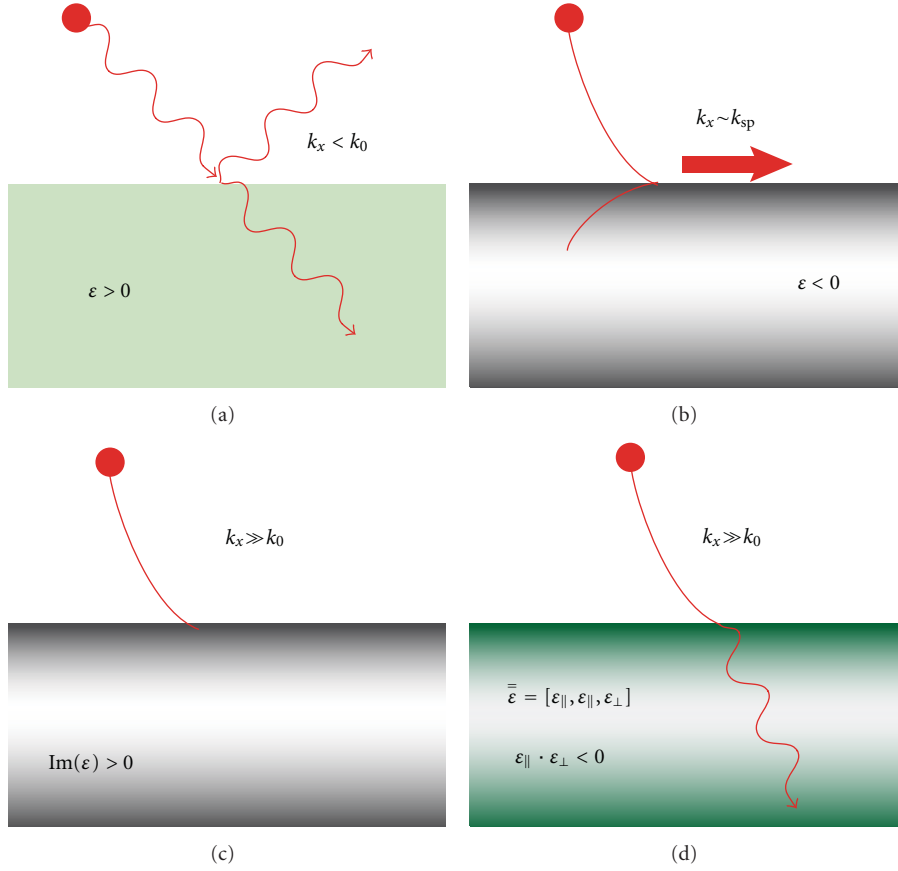


FIGURE 5: A subwavelength emitter such as quantum dot emits light with all spatial frequencies (i.e., wavevectors). (a) The light can couple to propagating waves in vacuum which are reflected and transmitted by a slab (e.g., dielectric) placed in the vicinity of the emitter. (b) If the slab is metallic, another route opens up which corresponds to the coupling of light to surface plasmons. The wavevector of light that couples to the surface plasmon polariton is  $k_{sp} > k_0$ . (c) The light with large wavevectors emanating from the emitter cannot propagate in vacuum. If the slab is lossy (metal or dielectric), these high- $k$  waves are simply absorbed. This is the phenomenon of quenching occurring in the near field of any lossy object. (d) A slab of hyperbolic metamaterial allows the propagation of these high- $k$  waves. In the near field, the subwavelength emitter couples most efficiently to the HMM states as compared to plasmons or propagating waves in vacuum. This is due to the availability of a large number of these HMM states.

transfer beyond the black body limit. The main property that sets it apart from other resonant methods of super-planckian thermal emission is the broad bandwidth and also presence of topological transitions [30].

In the effective medium limit, the thermal energy density in the near field of the hyperbolic metamaterial is given by

$$u(z, \omega, T)^{z \ll \lambda} \approx \frac{U_{BB}(\omega, T)}{8} \left[ \frac{2\sqrt{|\epsilon_{xx}\epsilon_{zz}|}}{(k_0 z)^3 (1 + |\epsilon_{xx}\epsilon_{zz}|)} - \epsilon'' \frac{2(\epsilon_{xx} + \epsilon_{zz})}{(k_0 z)^3 (1 + |\epsilon_{xx}\epsilon_{zz}|)^2} \right], \quad (3)$$

where  $u(z, \omega, T)$  is the energy density at a distance  $z$  and frequency  $\omega$ , while  $T$  denotes the temperature.  $k_p = \sqrt{k_x^2 + k_y^2}$ ,  $k_0 = \omega/c$ ,  $\epsilon_{||} = \epsilon_{xx} + i\epsilon''$ ,  $\epsilon_{\perp} = \epsilon_{zz} + i\epsilon''$ , and  $\epsilon_{xy} \cdot \epsilon_{zz} < 0$  and  $U_{BB}(\omega, T)$  is the black body emission spectrum at temperature  $T$ . These results were recently presented [30], where the fluctuational electrodynamics of

hyperbolic metamaterials was developed. This has many implications for thermal engineering using metamaterials, and experiments are currently underway using phonon-polaritonic HMMs [43] to measure this unique effect using topological transitions [30, 44].

**4.3. Nano-Imaging.** The hyperlens is an imaging device made of hyperbolic metamaterials which can break the far-field diffraction limit [23, 25]. The subwavelength resolution in the far field arises from the cylindrical (or spherical) nature of the HMM. The device can be fabricated by the same multilayer design principles presented earlier. In the future, integrating the hyperlens with microfluidic channels can make a significant impact for real-time bioimaging.

The functioning of the device can be understood by noting that the diffraction limit arises since waves with large spatial frequencies which carry subwavelength information are evanescent in vacuum. This leads to a loss of information in the far-field image. Near the HMM, these high- $k$  waves are



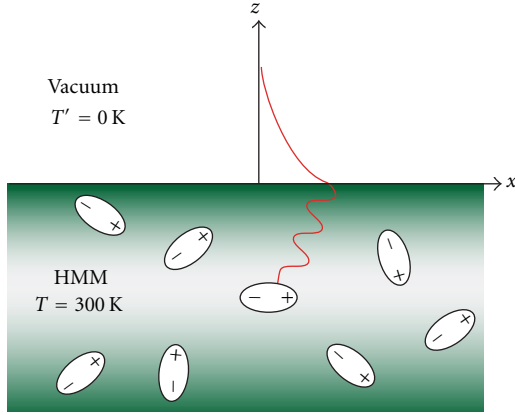


FIGURE 6: Recently, a fluctuational electrodynamics of hyperbolic metamaterials was developed, and super-planckian thermal emission from these media was predicted [30]. In the nearfield, a heated HMM can emit and thus transfer thermal radiation beyond the black body limit. This paves the way for near-field thermal engineering using metamaterials.

captured and turned into propagating waves, and the information is carried within the HMM. Conservation of angular momentum ( $m \sim k_{\theta}r$ ) ensures that at the outer surface of the hyperlens, the tangential momentum is reduced, and the waves can escape to the far field. Another interpretation of far-field imaging is based on the realization that hyperbolic media only allow waves to propagate along subwavelength resonance cones in the radial direction [48, 49]. Thus, points on the inner surface are mapped one to one to points on the outer surface. Thus, the spacing between diffraction-limited points on the inner radius can be much larger than the wavelength on the outer surface, if the outer radius is chosen to be big enough [49]. These well-separated points can be viewed by a conventional microscope even if the original points cannot. Figure 7 shows a conceptualized hyperlens-based device capable of providing real-time and truly nano-scale resolution of biological material being transported in a microfluidic channel.

**4.4. Subsurface Sensing.** A doped semiconductor-based HMM can be used for noninvasive subsurface sensing [26] and subdiffraction imaging in the IR. The semiconductor InGaAs can be doped to have its metallic properties tuned across the IR. Therefore, a multilayer structure consisting of InGaAs/AlInAs layers can be constructed to have a broadband ( $\Delta\lambda \sim 2\mu\text{m}$ ) type 1 HMM behavior across the IR [16]. AlInAs act as the dielectric. Potential applications and device geometries are described below.

Subsurface sensing and imaging are especially important for IR fingerprinting. Combining IR spectroscopy with subdiffraction imaging may allow for chemical identification on a truly molecular scale. Another application is quality control in integrated circuits (ICs) or microelectromechanical devices (MEMs) since silicon is transparent to IR wavelengths. Therefore, cracks or defects in ICs or MEMs can be detected through the scattering and diffraction of IR light

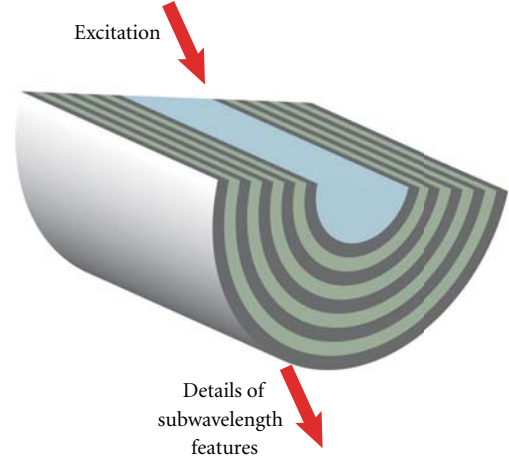


FIGURE 7: Integrating microfluidic channels with the hyperlens can lead to real-time superresolution imaging for biological applications. The schematic shows the optofluidic channel and the cylindrical multilayer hyperlens.

at these defects. The main problem with the conventional technique is the diffraction limit: cracks and defects smaller than the illuminating wavelength cannot be imaged noninvasively. In terms of IR, this corresponds to imperfections of the size  $\sim 2\text{--}3\mu\text{m}$ . By using an HMM, subdiffraction resolution may be obtained so that defects with deep subwavelength dimensions may be observed noninvasively.

The applications described above are conceptualized in Figure 8. Refractive index changes may be detected noninvasively through HMM slab. The emission power densities are overlaid to demonstrate the capability of sub-surface sensing. The power densities are calculated using the Green's function approach for an effective medium HMM slab.

**4.5. Dyakonov Plasmons.** Hyperbolic isofrequency curves can also be obtained for two-dimensional surface states. This is schematically shown in Figure 9. The isofrequency curve for in-plane surface plasmon polaritons on a gold substrate is circular. As opposed to this, when a uniaxial crystal is placed on top of the metal film with different indices along the principle axes, there exists the possibility that plasmons are allowed to propagate in one direction but not in the perpendicular direction. This gives rise to in-plane hyperbolic isofrequency curves for the surface plasmon polaritons. They are a mixed state consisting of both TE and TM polarized light and are called Dyakonov plasmons [28].

The above example is that of interface states on a metallic substrate with a uniaxial dielectric on top. Hyperbolic metamaterials can support surface states with similar unconventional properties [28]. If the principle axis of the hyperbolic metamaterial ( $z$ -axis) lies in the interface plane with vacuum, then Dyakonov plasmon solutions with hyperbolic isofrequency curves are allowed. Dyakonov plasmons show all the properties of bulk hyperbolic states such as subdiffraction imaging and directional resonance cone beaming [27, 28, 50].

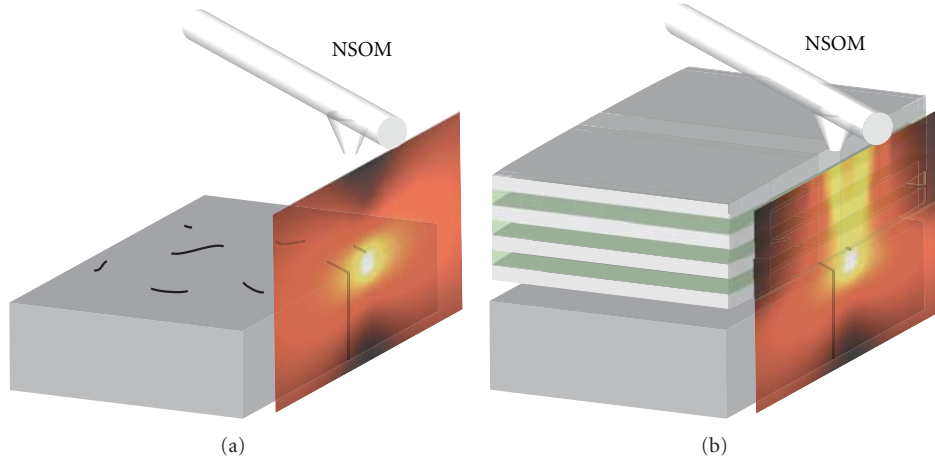


FIGURE 8: Subsurface sensing: illumination of a Si wafer from below by  $\lambda \sim 9.8 \mu\text{m}$ . The incident light scatters through cracks in the wafer. (a) A subwavelength dimension crack in a Si wafer can be detected by a near-field scanning optical microscope (NSOM) only if the detector is brought very close to the crack ( $< \lambda/6$ ). (b) If an AlInAs/InGaAs HMM is placed above the wafer, then the NSOM can detect the crack up to  $2\text{--}3 \times \lambda$  from the wafer. The HMM allows high spatial frequencies to propagate and enhances their intensity in the image.

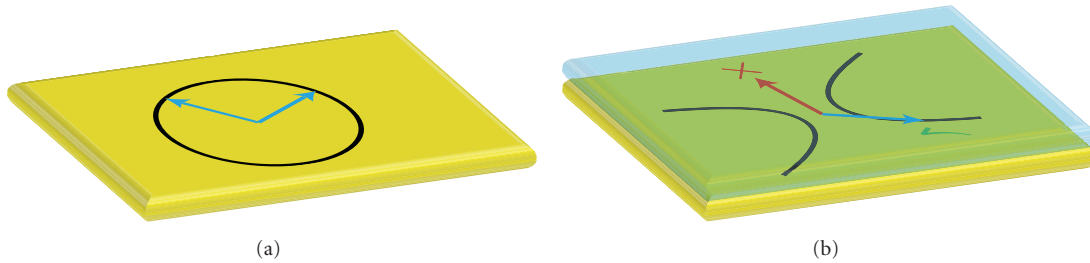


FIGURE 9: Dyakonov plasmonics: schematic showing (a) isofrequency curve of conventional plasmons on an isotropic gold film. The circular isofrequency curve corresponds to the fact that plasmons can propagate in all directions (blue arrows). (b) Isofrequency curve becomes hyperbolic when an anisotropic slab is placed on top of the gold film. This occurs in the range of frequencies when conventional plasmons which occur along the high-symmetry directions are allowed in one direction (blue arrow) but are not allowed in the perpendicular direction (red arrow).

Note that the above-mentioned states are fundamentally different from conventional surface-plasmon polariton (SPP) solutions allowed in type II metamaterials when the interface plane permittivity is negative and the principle axis ( $z$ -axis), normal to the plane, has positive dielectric permittivity. All modes of hyperbolic media (high- $k$ , SPP, and Dyakonov plasmons) are tunable since the optical constants governing them depend on the metallic fill fraction.

## 5. Future and Conclusion

The last decade has seen tremendous progress in the physics and nanofabrication of various classes of metamaterials. The next decade is set for metamaterial applications in different fields. For devices in the visible and near-IR wavelength ranges, hyperbolic metamaterials are expected to lead the way due to their varied properties and applicability. One major direction of application will be quantum nanophotonics [51, 52]. We have shown here the potential of HMMs for nanoimaging, subsurface sensing, Dyakonov plasmonics, fluorescence engineering, and thermal emission control. This

paper should help experimentalists gather a unified view of the multiple applications of hyperbolic metamaterials for designing devices.

## Acknowledgments

Z. Jacob wishes to acknowledge E. E. Narimanov and S. Pramanik for fruitful discussions. This work was partially supported by the National Science and Engineering Research Council of Canada, Canadian School of Energy and Environment, Alberta Nanobridge, and Alberta Innovates.

## References

- [1] J. B. Pendry, "Negative refraction makes a perfect lens," *Physical Review Letters*, vol. 85, no. 18, pp. 3966–3969, 2000.
- [2] N. Fang, H. Lee, C. Sun, and X. Zhang, "Sub-diffraction-limited optical imaging with a silver superlens," *Science*, vol. 308, no. 5721, pp. 534–537, 2005.
- [3] J. B. Pendry, D. Schurig, and D. R. Smith, "Controlling electromagnetic fields," *Science*, vol. 312, no. 5781, pp. 1780–1782, 2006.



- [4] N. I. Landy, S. Sajuyigbe, J. J. Mock, D. R. Smith, and W. J. Padilla, "Perfect metamaterial absorber," *Physical Review Letters*, vol. 100, no. 20, Article ID 207402, 2008.
- [5] W. Cai and V. Shalaev, *Optical Metamaterials: Fundamentals and Applications*, Springer, 2009.
- [6] W. Cai, U. K. Chettiar, H. K. Yuan et al., "Metamagnetics with rainbow colors," *Optics Express*, vol. 15, no. 6, pp. 3333–3341, 2007.
- [7] N. Liu, H. Liu, S. Zhu, and H. Giessen, "Stereometamaterials," *Nature Photonics*, vol. 3, no. 3, pp. 157–162, 2009.
- [8] E. Plum, X. X. Liu, V. A. Fedotov, Y. Chen, D. P. Tsai, and N. I. Zheludev, "Metamaterials: optical activity without chirality," *Physical Review Letters*, vol. 102, no. 11, Article ID 113902, 2009.
- [9] E. Plum, V. A. Fedotov, A. S. Schwanecke, N. I. Zheludev, and Y. Chen, "Giant optical gyrotropy due to electromagnetic coupling," *Applied Physics Letters*, vol. 90, no. 22, Article ID 223113, 2007.
- [10] A. Alù, M. G. Silveirinha, A. Salandrino, and N. Engheta, "Epsilon-near-zero metamaterials and electromagnetic sources: tailoring the radiation phase pattern," *Physical Review B*, vol. 75, no. 15, Article ID 155410, 2007.
- [11] X. Chen, B. I. Wu, J. A. Kong, and T. M. Grzegorzczak, "Retrieval of the effective constitutive parameters of bianisotropic metamaterials," *Physical Review E*, vol. 71, Article ID 046610, 2005.
- [12] J. Elser, V. A. Podolskiy, I. Salakhutdinov, and I. Avrutsky, "Nonlocal effects in effective-medium response of nanolayered metamaterials," *Applied Physics Letters*, vol. 90, no. 19, Article ID 191109, 2007.
- [13] V. A. Podolskiy and E. E. Narimanov, "Strongly anisotropic waveguide as a nonmagnetic left-handed system," *Physical Review B*, vol. 71, no. 20, pp. 1–4, 2005.
- [14] D. R. Smith, P. Kolinko, and D. Schurig, "Negative refraction in indefinite media," *Journal of the Optical Society of America B*, vol. 21, no. 5, pp. 1032–1043, 2004.
- [15] P. A. Belov and Y. Hao, "Subwavelength imaging at optical frequencies using a transmission device formed by a periodic layered metal-dielectric structure operating in the canalization regime," *Physical Review B*, vol. 73, no. 11, Article ID 113110, 4 pages, 2006.
- [16] A. J. Hoffman, L. Alekseyev, S. S. Howard et al., "Negative refraction in semiconductor metamaterials," *Nature Materials*, vol. 6, no. 12, pp. 946–950, 2007.
- [17] A. A. Govyadinov and V. A. Podolskiy, "Metamaterial photonic funnels for subdiffraction light compression and propagation," *Physical Review B*, vol. 73, no. 15, Article ID 155108, pp. 1–5, 2006.
- [18] J. Yao, X. Yang, X. Yin, G. Bartal, and X. Zhang, "Three-dimensional nanometer-scale optical cavities of indefinite medium," *Proceedings of the National Academy of Sciences of the United States of America*, vol. 108, no. 28, pp. 11327–11331, 2011.
- [19] C. L. Cortes, W. Newman, S. Molesky, and Z. Jacob, "Quantum nanophotonics using hyperbolic metamaterials," *Journal of Optics*, vol. 14, no. 6, Article ID 063001, 2012.
- [20] Z. Jacob, I. I. Smolyaninov, and E. E. Narimanov, "Broadband purcell effect: radiative decay engineering with metamaterials," *Applied Physics Letters*, vol. 100, Article ID 181105, 4 pages, 2012.
- [21] Z. Jacob, J. Kim, G. Naik, A. Boltasseva, E. Narimanov, and V. Shalaev, "Engineering photonic density of states using metamaterials," *Applied Physics B*, vol. 100, no. 1, pp. 215–218, 2010.
- [22] J. R. Lakowicz, "Radiative decay engineering 3. Surface plasmon-coupled directional emission," *Analytical Biochemistry*, vol. 324, no. 2, pp. 153–169, 2004.
- [23] Z. Jacob, L. V. Alekseyev, and E. Narimanov, "Optical hyperlens: far-field imaging beyond the diffraction limit," *Optics Express*, vol. 14, no. 18, pp. 8247–8256, 2006.
- [24] Z. Liu, H. Lee, Y. Xiong, C. Sun, and X. Zhang, "Far-field optical hyperlens magnifying sub-diffraction-limited objects," *Science*, vol. 315, no. 5819, p. 1686, 2007.
- [25] A. Salandrino and N. Engheta, "Far-field subdiffraction optical microscopy using metamaterial crystals: theory and simulations," *Physical Review B*, vol. 74, no. 7, Article ID 075103, 2006.
- [26] T. Taubner, D. Korobkin, Y. Urzhumov, G. Shvets, and R. Hillenbrand, "Near-field microscopy through a SiC superlens," *Science*, vol. 313, no. 5793, p. 1595, 2006.
- [27] D. Artigas and L. Torner, "Dyakov surface waves in photonic metamaterials," *Physical Review Letters*, vol. 94, no. 1, Article ID 013901, 2005.
- [28] Z. Jacob and E. E. Narimanov, "Optical hyperspace for plasmons: dyakov states in metamaterials," *Applied Physics Letters*, vol. 93, no. 22, Article ID 221109, 2008.
- [29] A. V. Shchegrov, K. Joulain, R. Carminati, and J. J. Greffet, "Near-field spectral effects due to electromagnetic surface excitations," *Physical Review Letters*, vol. 85, no. 7, pp. 1548–1551, 2000.
- [30] Y. Guo, C. L. Cortes, S. Molesky, and Z. Jacob, "Broadband super-Planckian thermal emission from hyperbolic metamaterials," *Applied Physics Letters*, vol. 101, no. 13, Article ID 131106, 5 pages, 2012.
- [31] Z. Jacob, *Classical and quantum optics of hyperbolic metamaterials [Ph.D dissertation]*, Purdue University, 2010.
- [32] E. E. Narimanov and I. I. Smolyaninov, "Beyond stefan-boltzmann law: thermal hyper-conductivity," <http://arxiv.org/abs/1109.5444>.
- [33] I. I. Smolyaninov and E. E. Narimanov, "Metric signature transitions in optical metamaterials," *Physical Review Letters*, vol. 105, no. 6, Article ID 067402, 2010.
- [34] M. A. Noginov, H. Li, Y. A. Barnakov et al., "Controlling spontaneous emission with metamaterials," *Optics Letters*, vol. 35, no. 11, pp. 1863–1865, 2010.
- [35] O. Kidwai, S. V. Zhukovsky, and J. E. Sipe, "Dipole radiation near hyperbolic metamaterials: applicability of effective-medium approximation," *Optics Letters*, vol. 36, no. 13, pp. 2530–2532, 2011.
- [36] A. N. Poddubny, P. A. Belov, and Y. S. Kivshar, "Spontaneous radiation of a finite-size dipole emitter in hyperbolic media," *Physical Review A*, vol. 84, no. 2, Article ID 023807, 6 pages, 2011.
- [37] M. A. Noginov, Y. A. Barnakov, G. Zhu, T. Tumkur, H. Li, and E. E. Narimanov, "Bulk photonic metamaterial with hyperbolic dispersion," *Applied Physics Letters*, vol. 94, no. 15, Article ID 151105, 2009.
- [38] P. A. Belov, C. R. Simovski, and P. Ikonen, "Canalization of subwavelength images by electromagnetic crystals," *Physical Review B*, vol. 71, no. 19, 2005.
- [39] W. Dickson, G. A. Wurtz, P. Evans et al., "Dielectric-loaded plasmonic nanoantenna arrays: a metamaterial with tuneable optical properties," *Physical Review B*, vol. 76, no. 11, Article ID 115411, 2007.
- [40] J. Yao, Z. Liu, Y. Liu et al., "Optical negative refraction in bulk metamaterials of nanowires," *Science*, vol. 321, no. 5891, p. 930, 2008.

- [41] Y. Xiong, Z. Liu, C. Sun, and X. Zhang, "Two-dimensional imaging by far-field superlens at visible wavelengths," *Nano Letters*, vol. 7, no. 11, pp. 3360–3365, 2007.
- [42] G. V. Naik, J. Kim, and A. Boltasseva, "Oxides and nitrides as alternative plasmonic materials in the optical range," *Optical Materials Express*, vol. 1, no. 6, pp. 1090–1099, 2011.
- [43] D. Korobkin, B. Neuner III, C. Fietz, N. Jegenyess, G. Ferro, and G. Shvets, "Measurements of the negative refractive index of sub-diffraction waves propagating in an indefinite permittivity medium," *Optics Express*, vol. 18, no. 22, pp. 22734–22746, 2010.
- [44] H. N. S. Krishnamoorthy, Z. Jacob, E. Narimanov, I. Kretzschmar, and V. M. Menon, "Topological transitions in metamaterials," *Science*, vol. 336, no. 6078, pp. 205–209, 2012.
- [45] I. Iorsh, A. Poddubny, A. Orlov, P. Belov, and Y. Kivshar, "Spontaneous emission enhancement in metal-dielectric metamaterials," *Physics Letters A*, vol. 376, pp. 185–187, 2012.
- [46] S. A. Biehs, P. Ben-Abdallah, F. S. S. Rosa, K. Joulain, and J. J. Greffet, "Nanoscale heat flux between nanoporous materials," *Optics Express*, vol. 19, no. S5, pp. A1088–A1103, 2011.
- [47] S. A. Biehs, M. Tschikin, and P. Ben-Abdallah, "Hyperbolic metamaterials as an analog of a blackbody in the near field," *Physical Review Letters*, vol. 109, no. 10, Article ID 104301, 5 pages, 2012.
- [48] L. B. Felsen and N. Marcuvitz, *Radiation and Scattering of Waves*, Wiley-IEEE Press, 1994.
- [49] Z. Jacob, L. V. Alekseyev, and E. Narimanov, "Semiclassical theory of the hyperlens," *Journal of the Optical Society of America A*, vol. 24, no. 10, pp. A52–A59, 2007.
- [50] I. I. Smolyaninov, Y. J. Hung, and C. C. Davis, "Magnifying superlens in the visible frequency range," *Science*, vol. 315, no. 5819, pp. 1699–1701, 2007.
- [51] Z. Jacob and V. M. Shalaev, "Plasmonics goes quantum," *Science*, vol. 334, no. 6055, pp. 463–464, 2011.
- [52] Z. Jacob, "Quantum plasmonics," *MRS Bulletin*, vol. 37, no. 8, pp. 761–767, 2012.

## Research Article

# Extension of the Multipole Approach to Random Metamaterials

**A. Chipouline, S. Sugavanam, J. Petschulat, and T. Pertsch**

*Institut für Angewandte Physik, Friedrich-Schiller-Universität Jena, Max Wien Platz 1, 07743 Jena, Germany*

Correspondence should be addressed to A. Chipouline, arkadi.chipouline@uni-jena.de

Received 1 July 2012; Accepted 11 September 2012

Academic Editor: Natalia M. Litchinitser

Copyright © 2012 A. Chipouline et al. This is an open access article distributed under the Creative Commons Attribution License, which permits unrestricted use, distribution, and reproduction in any medium, provided the original work is properly cited.

Influence of the short-range lateral disorder in the meta-atoms positioning on the effective parameters of the metamaterials is investigated theoretically using the multipole approach. Random variation of the near field quasi-static interaction between metaatoms in form of double wires is shown to be the reason for the effective permittivity and permeability changes. The obtained analytical results are compared with the known experimental ones.

## 1. Introduction

Metamaterials are artificial media that allow tailoring the macroscopic properties of the light propagation by a careful choice of a design for the microscopic unit cell (called the meta-atom). By controlling the geometrical shape and the material dispersion of the meta-atom, novel effects such as negative refraction [1–3], optical cloaking [4–9], as well as series of optical analogues to phenomena known from different disciplines in physics could be observed [10–14]. Despite the possibility to rely on rigorous computations for describing the light propagation on the microscopic level, an enduring problem in metamaterial research is the question on how the effective material tensor looks like for a certain metamaterial. A simple and versatile analytical model describing propagation of electromagnetic waves in metamaterials has been recently developed following classical approach of Maxwell equation averaging procedure [15]. This transition from the microscopic to macroscopic system of Maxwell equations takes into account all peculiarities of carriers dynamics under the action of the resulted electromagnetic field through the introduction of multipole moments which are supposed to be represented as the functions of the macroscopic electric and magnetic fields [16]. One of the great advantages of this model is the ability to evaluate straightforwardly influence of the charge dynamics of the meta-atoms on the effective properties of the metamaterials. In fact, the multipole moments are calculated through the averaged charge dynamics in the

meta-atoms. Any factors influencing the charge dynamics (e.g., interaction between the meta-atoms, extra coupling of the meta-atoms with the other objects, etc.) cause the changes in the multipole expressions, which in turn change the effective parameters. It is important for the analysis presented here that the interaction between the meta-atoms and hence its influence on the effective permittivity and permeability can be straightforwardly taken into account [17].

The interaction between the small particles, both dielectric and metallic, and propagation of an optical excitation in a regular chain of such particles have been intensively investigated [18–23]. Interest to the chains of metallic nanoparticles is stipulated mainly by the request for subwavelength guiding structures for a new generation of the optoelectronic components for communication and information processing. Nevertheless, theoretical tools for the modeling of these chains (irrespective to the nature and sizes) remain invariant: the electromagnetic excitation in the particles are supposed to be described by taking into account all possible eigen modes [18, 20] and interaction between all particles in a chain. There are several approximations which are typically accepted in this kind of problems. First, depending on the size of the particles, the model can be restricted by consideration of dipole moment only (for metallic nanoparticles) [19, 23]; the higher moments can be taken into consideration as well in the case of investigation of magnetic response [22, 24]. Usually, for the problem of electromagnetic excitation propagation along the chain,

the dipole approximation is enough [25], provided distance between particles is not less than about three times their sizes. Second, the interaction between the particles in a chain can be considered in the frame of the quasi-static approximation, where no retardation between particles is retained; otherwise, interaction between dipoles contains terms proportional to the  $1/r$  and  $1/r^2$  in addition to the quasi-static term  $1/r^3$  ( $r$  is the distance between dipoles). The problem possesses an exact solution for the infinite chain in the quasistatic case, while taking into consideration the retardation leads to known math difficulties and requires continuation into the lower half frequency plane [19]. Consideration of the finite chain is free from these excessive math problems but can be treated only numerically; the respective solutions for both longitudinal and transverse modes are presented in [19, 26].

Natural expansion of the developed models of the electromagnetic excitation transport on a chain of particles with randomly varying parameters revealed several interesting peculiarities. The problem of wave propagation through disordered systems attracts great attention in both quantum and classical physics [27]. In disordered chains of different dimensions, destructive interference between scattered waves gives rise to an existence of the localized modes, exponentially decaying in space—this effect has been originally found in solid state physics and is known as Anderson localization [28]. The existence of delocalized modes that can extend over the sample via multiple resonances and have a transmission close to 1 was found in [29, 30] and experimentally confirmed in [31, 32]. Disorder-induced change of the guiding properties in a chain of plasmonic nanoparticles under small random uncontrollable disorder was considered in [26], and analogy of the Anderson localization in a chain of such particles was theoretically investigated in [33]. In the present analysis, the effect of Anderson localization is not considered; nevertheless, it is believed, that the developed analytical tool in this paper turns out to be suitable for the treatment of the similar effect in metamaterials with different types of disorder.

An influence of various types of disorder on the effective properties of the metamaterials was intensively investigated as well. Light propagation and Anderson localization in superlattices were theoretically considered in [34, 35] using the model of multilayered system with phenomenological permittivity and permeability (positive and negative) in each of the layers. The effect of the statistical distribution of the sizes of the meta-atoms on the increase of losses in the operation frequency band was considered in [36] using generalized Clausius-Mossotti relation. A significant influence of a small (10%) deviation of the parameters of the microscopic resonances on the propagation wave in a wide frequency range was found in [37] using quasistatic expressions for the effective parameters. Averaging of the Lorenz-type expressions for the effective permittivity and permeability using a phenomenological probability distribution function showed that passband and negative refraction are still present under small positional disorder [38]; the results were proven experimentally as well. Interaction in a chain of magnetic particles and its influence on the effective permeability

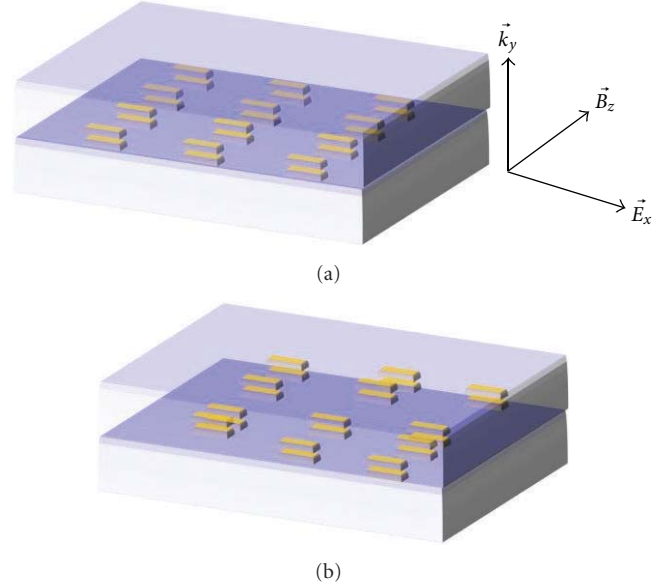


FIGURE 1: (a) Regular and (b) laterally (along  $z$  direction) random positioning of the meta-atoms in a metamaterial. Plane wave propagation is in  $y$  direction, and electric field polarization coincides with the  $x$  axis and with the elongation of the nano wires. Note that only one layer, which the metamaterial consists of, is shown in the figure.

were investigated in [24]. Using the introduced concept of “coherent” and “incoherent” metamaterials, authors of [39] showed that the influence of disorder on long-range correlated metamaterials is significantly more pronounced in comparison with the same effect in short-range ordered metamaterials. Random variation of interaction between meta-atoms was shown to be a main reason for the disappearance of the long-range correlation and consequently of the “coherent” state [39].

In the presented work, attention is primarily devoted to the extension of the multipole approach to describe in-plane disorder in metamaterials, which means the randomness in positioning of the meta-atoms in the plane of the substrate; see Figure 1. In [26], it was shown that the variations of the electromagnetic properties of the inclusions are less important than the disorder in their positions. Metamaterials formed by a self-organization display exactly this kind of disorder [40–43]. Results of control experiments with the 2D metamaterials exhibiting such in-plane disorder [44] are used as a test of the model. The most notable discovery is the fact that although disorder has a deterrent effect on the permittivity, the permeability seems to remain practically unaffected. A theoretical model for such a class of random metamaterials should reproduce these observations.

The qualitative explanation of the influence of the spatial disorder on the effective parameters is in following. The positional disorder creates different conditions for the charged dynamics in the meta-atoms due to the interaction between them [21, 22]. This in turn leads to the changes of the averaged dipole, quadrupole, and magnetic dipole moments of the media and results in the changes of



the effective parameters, which are expressed through these averaged multipole moments [15, 45].

This qualitative hypothesis requires further development of the existing theoretical multipole model; in particular, the interaction between the meta-atoms [17] has to be incorporated and adopted to the random character of this interaction. Let us assume that the charge dynamics in the microscopic multipole moments of the meta-atoms depends on the distance  $\delta_k$  between them (see Figure 2). Following the approach of [15], it is necessary to average the resulted charge dynamics in the multipole moments over all possible representations; in other words, the microscopic multipole moments have to be additionally averaged over all possible distances between the meta-atoms, which mathematically is expressed as an integral over a probability distribution function  $\text{PDF}(\delta_k)$ ; namely,

$$\chi_{\text{macro}} = \int \chi_{\text{micro}}(\delta_k) \text{PDF}(\delta_k) d\delta_k, \quad (1)$$

Here,  $\chi_{\text{micro}}(\delta)$  is the microscopic multipole moment of the meta-atoms, and  $\text{PDF}(\delta_k)$  governs the distribution over all possible interseparation distances  $\delta_k$  in a randomly arranged ensemble of the meta-atoms. In case of regular spatial distribution, each metaatom is affected by the same fields,  $\text{PDF}(\delta_k)$  is reduced to the delta function, and averaging (1) restores the microscopic multipole moments.

The quest to obtain such  $\text{PDF}(\rho_k)$  and the effort to incorporate the effect of disorder into the existing multipole model are discussed in details here. The paper is organized as follows. First, the probability model used to incorporate positional disorder into the multipole theory is described. As a test of principle and in order to create a systematic model, the approach is then applied to the simple case of randomly arranged dipoles. Then the treatment is extended to the case of randomly arranged quadrupoles. The probabilistic approach is applied to the specific case of randomly positioned meta-atoms, and the obtained results are compared with the experimental observations [44]; the mathematical procedures used to account for the other forms of disorder are highlighted.

The main difference of the approach here in comparison with the previous ones in the use of the multipole model is that the charge dynamics in meta-atoms is primarily considered and calculated taking into account the interaction between meta-atoms, which is expressed as a function of distance between them. Finally, averaging over all possible realization of the inter-metaatom distance gives the expression for the effective parameters. This paper is primarily devoted to the elaboration of the model and to the effective parameters calculation; further applications of the presented approach (disorder in propagation direction, transition “coherent-incoherent” states, influence of the Anderson localization on the effective parameters, etc.) will be done elsewhere. Interaction between meta-atoms is taken into account using a simplest way of dipole-dipole near field interaction in quasi-static limit; extrapolation of the model on the dynamic case is left for the future work. The interaction between quadrupoles is treated the same way, which makes the presented approach suitable for consideration of

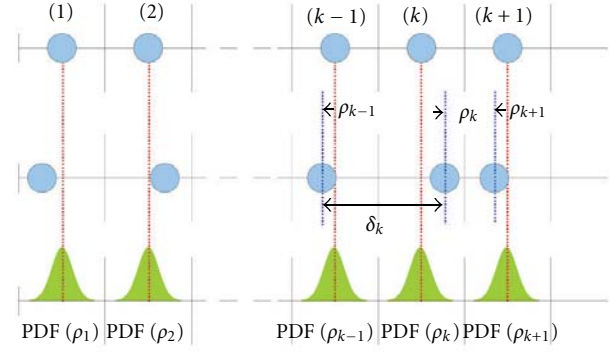


FIGURE 2: Geometry for the probability function elaboration, the spheres show meta-atoms. The first row shows a regular arrangement of the meta-atoms, where each meta-atom occupies the center of a slot of length equal to the mean period. The second row depicts an arrangement of the meta-atoms exhibiting random uncorrelated positional disorder (denoted by  $\rho_k$ ), the extent of the disorder being governed by the  $\text{PDF}(\rho_k)$  as shown in the last row. The interseparation  $\delta_k$  between the two subsequent meta-atoms is a function of the random variables  $\rho_k$  and  $\rho_{k-1}$ , and the analytic form of the  $\text{PDF}(\delta_k)$  can be obtained by the use of the statistical methods if the analytic form of the  $\text{PDF}(\rho_k)$  is given.

the magnetic properties of the metamaterials. In spite of the excessive simplification of the interaction, the presented model treats the effective parameters (especially magnetic response) in much more correct way than it was done before by just introduction of permeability and/or magnetic susceptibility, and is believed to provide a suitable platform for analytical or semianalytical treatment of the problems, appearing in the case of disordered metamaterials.

## 2. Modeling of Positional Disorder

The problem of the positional disorder modeling can be tackled in several ways. The most general formulation of the problem requires a Markovian treatment. As an illustration, the one-dimensional equivalent of the problem is considered here. Supposing that the meta-atoms are introduced one by one on a line of given length, the probability that a particle will take up a certain position on the line, and hence the probability of a particular inter separation distance, depends not only on the last particle, but also on the history and existing configuration. This is the essence of the Markovian approach. Standard techniques exist for tackling such problems, formulating a rigorous treatment. Nevertheless, due to its complex nature, an alternative simpler math treatment is developed in the present paper.

The math treatment accepted in the presented work is stipulated by the real technological chains for the producing of the nanostructure. When performing control experiments, masks for random metamaterials are manufactured by e-beam lithography methods. The writing algorithms are modified so that instead of a periodic grid a randomized one is generated by the scanner. The extent of randomness can be specifically controlled, and statistically relevant parameters

such as the mean period and the variance can be assigned to each mask. Translating the above approach to mathematics, one assumes that the meta-atoms are initially placed in well-defined slots of equal length (see Figure 1) and then are perturbed from their mean positions. The perturbation is described by  $\text{PDF}(\rho_k)$ . This PDF describes the extent of the perturbation and also ensures that the displacement is not beyond a certain space slot. However,  $\text{PDF}(\rho_k)$  is the *positional* disorder distribution function not the PDF for the metaatom interseparation  $\text{PDF}(\delta_k)$ ; the latter has to be found based on given  $\text{PDF}(\rho_k)$ , and  $\text{PDF}(\delta_k)$  can then be used in averaging procedure (1) to obtain the required material parameters. In this work, interseparation  $\text{PDF}(\delta_k)$  is obtained by employing a characteristic function approach. The characteristic function  $Q_\rho(\omega)$  is given by a Fourier transformation of given  $\text{PDF}(\rho_k)$ :

$$Q_{\rho,k}(\omega) = \int_{-\infty}^{\infty} \text{PDF}(\rho_k) e^{i\omega t} d\rho_k, \quad (2)$$

where  $\text{PDF}(\rho_k)$  satisfies the normalization condition:

$$\int_{-\infty}^{\infty} \text{PDF}(\rho_k) d\rho_k = 1. \quad (3)$$

Alternatively, the characteristic function can be considered as an expectation value of function  $e^{i\omega t}$ :

$$Q_{\rho,k}(\omega) = \langle e^{i\omega t} \rangle_{\text{PDF}(\rho_k)}. \quad (4)$$

The one-dimensional equivalent of the problem is formulated as follows. A periodic arrangement of  $N$  meta-atoms on a given length  $L$  is considered (see Figure 1). The spacing period for the slots is given by  $z_0 = L/N$ , and the location of the  $k$ th metaatom can thus be given as  $z_k = (z_0/2)(2k + 1)$ . Now, the perturbation of the  $k$ th metaatom from its mean position can be given using a random function  $\rho_k$ , such that.

$$z_k = \frac{z_0}{2}(2k + 1) + \rho_k, \quad -\frac{z_k}{2} < \rho_k < \frac{z_k}{2}. \quad (5)$$

So, the spacing between the meta-atoms is given by.

$$\Delta_k = z_{k+1} - z_k = z_0 + (\rho_{k+1} - \rho_k) = z_0 + \delta_k. \quad (6)$$

The random functions  $\rho_k$  and  $\rho_{k+1}$  are completely independent from each other. For the present problem, the random function of interest is

$$\delta_k = \rho_{k+1} - \rho_k. \quad (7)$$

The mathematical form of  $\text{PDF}(\delta_k)$  has to be found. The form of the above probability function can be obtained by using characteristic functions. The characteristic function formed by a sum or difference of two or more PDFs is nothing but the product of the characteristic functions of the ingredient PDFs. That is, if one is interested in a probability distribution function for variable  $z$ , given by

$$z = y_1 + y_2 + \dots + y_n, \quad (8)$$

where  $y_1, y_2$  and so forth are independent random functions and  $Q_i(\omega)$  are their mutually independent characteristic functions, then the characteristic function of  $z$  will be given by

$$Q_Z(\omega) = Q_1(\omega)Q_2(\omega) \cdots Q_N(\omega). \quad (9)$$

So, the form of  $z$  can be simply obtained by an inverse Fourier transformation on the product of the characteristic functions.

Define the characteristic functions for  $\rho_k$  and  $\rho_{k+1}$  as

$$\begin{aligned} Q_{\rho_k}(\omega) &= \int_{-\infty}^{\infty} \text{PDF}(\rho_k) e^{i\rho_k \omega} d\rho_k, \\ Q_{-\rho_{k+1}}(\omega) &= Q_{\rho_{k+1}}^*(\omega) = \int_{-\infty}^{\infty} \text{PDF}(\rho_{k+1}) e^{-i\rho_{k+1} \omega} d\rho_{k+1}. \end{aligned} \quad (10)$$

Then making use of the above-stated method, the characteristic function  $Q_\delta(\omega)$  of the required  $\text{PDF}(\delta_k)$  is.

$$Q_{\delta,k}(\omega) = Q_{\rho_{k+1}}(\omega) Q_{\rho_k}^*(\omega). \quad (11)$$

Then, required  $\text{PDF}(\delta_k)$  can be obtained by simply using the convolution theorem:

$$\begin{aligned} \text{PDF}(\delta_k) &= \text{FT}^{-1} [Q_{\rho_{k+1}}(\omega) Q_{\rho_k}^*(\omega)] \\ &= \int_{-\infty}^{\infty} \text{PDF}(\rho_k) \text{PDF}^*(\delta_k - \rho_k) d\rho_k \\ &= \int_{-\infty}^{\infty} \text{PDF}(\rho_k) \text{PDF}(\delta_k - \rho_k) d\rho_k. \end{aligned} \quad (12)$$

Hence, required  $\text{PDF}(\rho_k)$  is the autocorrelation function of the positional disorder  $\text{PDF}(\rho_k)$ . The integral is taken over the displacement of the metaatom from its mean position and limited by the finite values of the slot length. The strength of the method is the fact that no explicit assumption has been made regarding the form of  $\text{PDF}(\rho_k)$  describing the positional disorder.

The mathematical procedure has to ensure that the perturbation does not become so large that the meta-atoms overlap each other. In the analysis, the particles are assumed to be placed in average in the center of the slots of a length equal to the mean spacing period. The particles can randomly move within their own slot, and the extent of the displacement from the center of the slot is given by  $\text{PDF}(\rho_k)$ . A consequence of such a restraint is that  $\text{PDF}(\rho_k)$  has to be restricted and normalized within this slot. Figure 5 shows how the autocorrelation function approaches a triangular function from its initial Gaussian form, as the position of the particle within the slot becomes completely random (i.e.,  $\text{PDF}(\rho_k)$  takes a rectangular form). A simple algebraic form of the probability distribution function cannot be obtained due to this truncation. Hence, the following approach was adopted: the normalized versions of  $\text{PDF}(\delta_k)$  for the inter separation were obtained using numerical code, and they were subsequently used for numerical integration (according to (1)) for obtaining the effective material parameters.

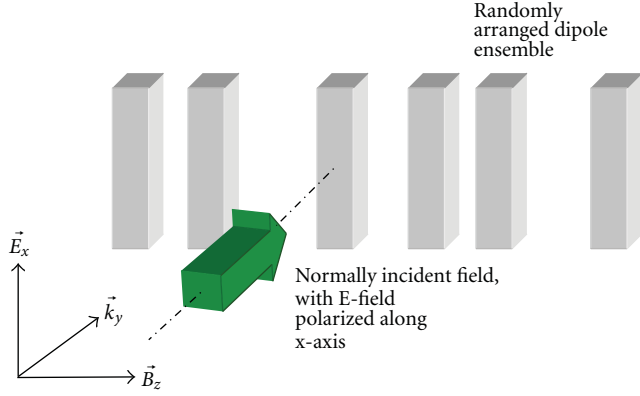


FIGURE 3: Geometry of propagation for randomly arranged dipole ensemble.

### 3. Case of Randomly Positioned Dipoles

In this section, using the above mentioned principles, the effect of disorder in a chain of periodically placed dipoles is investigated. The geometry is given in Figure 3. The bold arrow shows the direction of propagation of the electromagnetic wave.

The system can be mathematically modeled as follows. Considering the coupling dynamics between two equal adjacent oscillators, one can write the equation describing their dynamics as

$$\begin{aligned} \frac{\partial^2 x_1}{\partial t^2} + \gamma \frac{\partial x_1}{\partial t} + \omega_0^2 x_1 + \sigma x_2 &= \frac{q}{m} E_x, \\ \frac{\partial^2 x_2}{\partial t^2} + \gamma \frac{\partial x_2}{\partial t} + \omega_0^2 x_2 + \sigma x_1 &= \frac{q}{m} E_x. \end{aligned} \quad (13)$$

The term on the right side is the same for both oscillators, and as the same field impinges on both of them. By substituting the time ansatz  $x_i(t) = x_i(\omega) \exp(-i\omega t)$ , the system can be easily solved for  $x_1(\omega)$  and  $x_2(\omega)$  as follows:

$$\begin{bmatrix} R & \sigma \\ \sigma & R \end{bmatrix} \begin{bmatrix} x_1(\omega) \\ x_2(\omega) \end{bmatrix} = \frac{q}{m} \begin{bmatrix} E_x(\omega) \\ E_x(\omega) \end{bmatrix}, \quad (14)$$

$$R = \omega_0^2 - \omega - i\gamma\omega.$$

Thus,

$$\begin{aligned} x_1(\omega) = x_2(\omega) &= \frac{q/m}{\omega_0^2 - \omega - i\gamma\omega + \sigma} E_x(\omega), \\ \sigma &= \sigma(z) = \sigma_0 \frac{a_0^3}{z^3}. \end{aligned} \quad (15)$$

Here,  $\sigma_0$  and  $a_0$  are the coupling constant and the distance between the oscillator. It is assumed that the interaction between the oscillators is the near field one between the dipoles that stipulates the inverse cubic distance dependence in the second equation in (15).

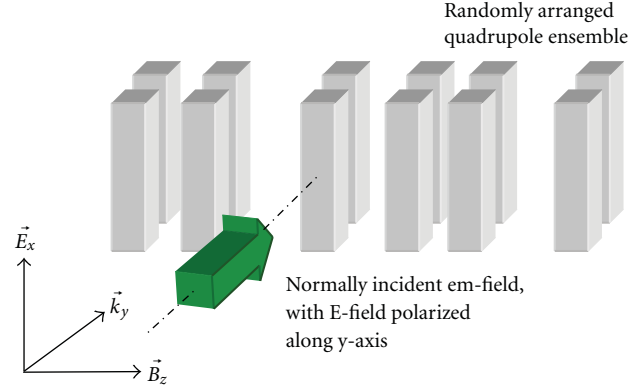


FIGURE 4: Geometry of propagation for randomly arranged quadrupole ensemble.

The response of the system can thus be obtained by monitoring the susceptibility of the medium. The polarization of the system can be written as

$$P_x(z, \omega) = \frac{2q^2\eta}{m} \frac{1}{\omega_0^2 - \omega - i\gamma\omega + \sigma(z)} E_x(\omega), \quad (16)$$

so that the effective susceptibility is

$$\chi_x(z, \omega) = \frac{2q^2\eta}{m} \frac{1}{\omega_0^2 - \omega - i\gamma\omega + \sigma(z)}. \quad (17)$$

To incorporate the effect of disorder, following (1), the averaged form of the above susceptibility can be obtained as

$$\langle \chi(z_0, \omega) \rangle_z = \int_{-\infty}^{\infty} \text{PDF}(\delta, D) \chi(z_0, \delta, \omega) d\delta \quad (18)$$

or

$$\begin{aligned} \langle \chi(z_0, \omega) \rangle_z &= \frac{2q^2\eta}{m} \int_{-\infty}^{\infty} \text{PDF}(\delta, D) \frac{(z_0 + \delta)^3}{(\omega_0^2 - \omega - i\gamma\omega)(z_0 + \delta)^3 + \sigma_0 a_0^3} d\delta, \end{aligned} \quad (19)$$

where  $\text{PDF}(\delta, D)$  is the inter separation PDF and  $D$  here quantizes the amount of disorder presented in the system.

### 4. Case of Randomly Positioned Quadrupoles

The extension of the above model to metamaterials (i.e., taking into account the magnetic response) firstly requires that the interaction between the adjacent meta-atoms is taken into consideration. The system is taken to be similar as the one shown in Figure 3, but the dipoles are now replaced by quadrupoles (Figure 4). The long axis of the cut wires is oriented along the  $x$ -axis. The cut wires forming the quadrupole are separated along the  $y$  direction. The meta-atoms are arranged randomly (in terms of above described random positioning in the respective slots) along the  $z$  direction.

Assuming that a plane electromagnetic wave now propagates through the ensemble along the  $y$  direction, while its electric vector is polarized along the  $x$  direction, the coupled dynamics of two meta-atoms can be modeled via four coupled oscillator equations:

$$\begin{aligned} \frac{\partial^2 x_1}{\partial t^2} + \gamma \frac{\partial x_1}{\partial t} + \omega_0^2 x_1 + ax_2 + bx_3 + cx_4 &= \frac{q}{m} E_{x,1}, \\ \frac{\partial^2 x_2}{\partial t^2} + \gamma \frac{\partial x_2}{\partial t} + \omega_0^2 x_2 + ax_1 + bx_3 + cx_4 &= \frac{q}{m} E_{x,2}, \\ \frac{\partial^2 x_3}{\partial t^2} + \gamma \frac{\partial x_3}{\partial t} + \omega_0^2 x_3 + ax_4 + bx_1 + cx_2 &= \frac{q}{m} E_{x,3}, \\ \frac{\partial^2 x_4}{\partial t^2} + \gamma \frac{\partial x_4}{\partial t} + \omega_0^2 x_4 + ax_3 + bx_2 + cx_1 &= \frac{q}{m} E_{x,4}, \end{aligned} \quad (20)$$

where

$$a = \sigma_0, \quad b = \sigma_0 \frac{y_0^3}{z^3}, \quad c = \sigma_0 \frac{y_0^3}{(y_0^2 + z^2)^{3/2}}, \quad (21)$$

and  $\sigma_0$  is the value of the coupling constant measured for the interseparation  $y_0$ . The magnitude of the coupling constant varies inversely as the cube of the distance, and so its value can be obtained for other interseparations—here  $z$  and the diagonal distance  $(y_0^2 + z^2)^{1/2}$ . The exponential phase factors in the right side take into account the retardation effect. It is clear that a change in the excitation conditions will affect the form of the right hand side of the above equations, while a change in the configuration of the meta-atoms can be accounted by a change in the form of the coupling coefficients. The procedure of determining the response of the medium then remains the same—one seeks to determine effective susceptibilities (corresponding to the symmetric and antisymmetric modes of oscillation), average them over all possible coupling configurations, and then use these values for ascertaining the effective material parameters.

The first step is to find the solution of the above set of equations. They can be transferred to the Fourier domain by using ansatz  $x_i(t) = x_i(\omega) \exp(-i\omega t)$ ,  $i = 1, 2, 3, 4$ , so that the system can be rewritten in a matrix form:

$$\begin{bmatrix} R & a & b & c \\ a & R & c & b \\ b & c & R & a \\ c & b & a & R \end{bmatrix} \begin{bmatrix} x_1(\omega) \\ x_2(\omega) \\ x_3(\omega) \\ x_4(\omega) \end{bmatrix} = \frac{q}{m} \begin{bmatrix} E_x(\omega) \exp(iky_1) \\ E_x(\omega) \exp(-iky_1) \\ E_x(\omega) \exp(iky_1) \\ E_x(\omega) \exp(-iky_1) \end{bmatrix}, \quad (22)$$

$$R = \omega_0^2 - \omega - i\gamma\omega.$$

The modes of oscillation of interest are given by  $x_1(t) \pm x_2(\omega)$ . The system can be solved to obtain the values of  $x_1(t)$  and  $x_2(\omega)$ , and the modes of the system can be written as.

$$\begin{aligned} x_1(t) + x_2(\omega) &= \frac{qE_x}{m} \frac{2 \cos(ky_1)}{\omega_0^2 - \omega - i\gamma\omega + (a + b + c)}, \\ x_1(t) - x_2(\omega) &= \frac{qE_x}{m} \frac{2 \cos(ky_1)}{\omega_0^2 - \omega - i\gamma\omega - (a - b + c)}, \end{aligned} \quad (23)$$

and hence one can define the effective susceptibilities:

$$\chi^\pm(z_0, \delta, \omega) = \frac{qE_x}{m} \frac{2 \cos(ky_1)}{\omega_0^2 - \omega - i\gamma\omega \pm (a \pm b + c)}, \quad (24)$$

where the  $z_0$  and  $\delta$  dependences are due to  $a$ ,  $b$ , and  $c$ . Due to this form of definition, the functional forms of the polarization, quadrupole moment, and magnetization remain the same:

$$\begin{aligned} P &= 2q\eta y_1 \begin{pmatrix} 2\chi^+(\omega) \cos(ky_1) \\ 0 \\ 0 \end{pmatrix} E_x(y, \omega), \\ Q &= q\eta y_1 \begin{pmatrix} 0 & 2i\chi^-(\omega) \sin(ky_1) & 0 \\ 2i\chi^-(\omega) \sin(ky_1) & 0 & 0 \\ 0 & 0 & 0 \end{pmatrix} \times E_x(y, \omega), \\ M &= q\eta y_1 \begin{pmatrix} 0 \\ 0 \\ 2i\chi^-(\omega) \sin(ky_1) \end{pmatrix} E_x(y, \omega). \end{aligned} \quad (25)$$

The effect of disorder can then be taken into account by carrying out the extra averaging integration (1):

$$\langle \chi^\pm(z_0, \omega, D) \rangle = \int_{-\infty}^{\infty} \text{PDF}(\delta, D) \chi^\pm(z_0, \delta, \omega) d\delta, \quad (26)$$

or, more explicitly:

$$\langle \chi^\pm(z_0, \omega, D) \rangle = \int_{-\infty}^{\infty} \text{PDF}(\delta, D) \frac{1}{(\omega_0^2 - \omega - i\gamma\omega) \pm \sigma_0 \left( 1 \pm \left( y_0^3 / (z_0 + \delta)^3 \right) + \left( y_0^3 / (y_0^2 + (z_0 + \delta)^2) \right)^{3/2} \right)} d\delta, \quad (27)$$

where  $z_0$  is the mean period. The limits of the integration indicate that the autocorrelation procedure for  $\text{PDF}(\delta, D)$

has been already carried out. This integral can be solved numerically for a given value of frequency.



With the effective susceptibility as defined above, one may now consider a planar metamaterial, which is formed by the identical rows of the randomly positioned meta-atoms. The effect of randomness is taken into account by the

averaging procedure, and hence the dispersion relation and the effective material parameters can be written in analogy to [16]. Adhering to the same conditions of geometry and excitation, the following expressions can be utilized:

$$\begin{aligned}
 k_y^2(\omega) &= \frac{\omega^2}{c^2} \frac{1 + A \langle \chi^+(z_0, \omega, D) \rangle}{1 + (\omega^2/c^2) A y_1^2 \left( (1/2) \langle \chi^+(z_0, \omega, D) \rangle - \langle \chi^-(z_0, \omega, D) \rangle \right)}, \\
 \epsilon_{\text{eff}} &= 1 + A \langle \chi^+(z_0, \omega, D) \rangle \\
 &\quad - A \frac{k_y^2 y_1^2}{2} \left( \frac{1}{2} \langle \chi^+(z_0, \omega, D) \rangle - \langle \chi^-(z_0, \omega, D) \rangle \right), \\
 \mu_{\text{eff}} &= \frac{1}{1 - (\omega^2/c^2) A y_1^2 \langle \chi^-(z_0, \omega, D) \rangle}.
 \end{aligned} \tag{28}$$

The previous expressions can be easily carried over to a numerical code to obtain the material parameters of interest. The following section presents the results and compares them with the experimental observations.

## 5. Method of Numerical Implementation

For convenience, the integrations and other expressions have been converted to their normalized versions. The frequencies

are normalized with respect to the resonant frequency  $\omega_0$  of the independent cut wire, while the distances are normalized with respect to the cut-wire spacing  $a_0$ . Specifically, the susceptibilities for the case of dipoles and quadrupoles are

$$\begin{aligned}
 \langle \chi^\pm(z_0, \omega) \rangle_z &= \int_{-\infty}^{\infty} \text{PDF}(\delta_n, D_n) \frac{(1 + \delta_n)^3}{(1 - \omega_n^2 - i(\omega_n/Q)) (1 + \delta_n) + \sigma_0/\omega_0^2} d\delta_n, \\
 \langle \chi^\pm(z_0, \omega) \rangle_z &= \int_{-\infty}^{\infty} \frac{\text{PDF}(\delta_n, D_n)}{(1 - \omega_n^2 - i(\omega_n/Q)) \pm \sigma_0 \left( 1 \pm 1/((z_0)_n + \delta_n)^3 + 1/(1 + ((z_0)_n + \delta_n)^2)^{3/2} \right)} d\delta_n,
 \end{aligned} \tag{29}$$

where

$$\delta_n = \frac{\delta}{a_0}, \quad D_n = \frac{D}{a_0}, \quad \omega_n = \frac{\omega}{\omega_0} \tag{30}$$

PDF( $\rho_k, D$ ) is assumed to be Gaussian:

$$\begin{aligned}
 \text{PDF}(\rho_k, D) &= \frac{1}{\sqrt{2D}} \exp\left(-\frac{\rho_k^2}{2D^2}\right), \quad -\frac{a_0}{2} < \rho_k < \frac{a_0}{2}, \\
 \text{PDF}(\rho_k, D) &= 0, \quad -\frac{a_0}{2} < \rho_k, \rho_k > \frac{a_0}{2}.
 \end{aligned} \tag{31}$$

The excursion of the dipoles around their mean positions had to be limited within the interval  $[-a_0/2, a_0/2]$ ; recalculation PDF( $\rho_k, D$ ) into PDF( $\delta_k, D$ ) is given by (12). The integrals cannot be taken analytically and was done using the mathematical software MATLAB. Truncation of the positional PDF was achieved by coding. To obtain the autocorrelation of the PDF, a standard subroutine was used. The results of the operations are shown in Figure 5.

All the constants used in the analysis were taken from [16]. The spacing between the cut wires  $a_0$  was taken to be 65 nm, and the resonant frequency of an isolated cut wire was taken as  $\omega_0 = 1.39 \times 10^{15} \text{ rad s}^{-1}$ . The damping coefficient was taken to be  $\gamma = 9.42 \times 10^{13} \text{ rad s}^{-1}$ . The mean periodic spacing  $z_0 = 1.8$  (the mean spacing between the meta-atoms was taken to be 1.8 times the cut wire spacing  $y_0$ ).

To verify the correct functioning of the code, the results for a very small disorder were compared with the result for a perfectly ordered system (with neighboring meta-atoms interacting with each other); see Figure 6.

## 6. Results

The results of the analysis for dipoles are presented in Figure 7, and the results of the analysis for quadrupoles are presented in Figures 8 and 9.

The analysis was carried out for two values of the spacing period  $z_n$ , namely,  $z_n = 1.2$  (Figure 8) and  $z_n = 1.8$  (Figure 9). The positional PDF was taken for the four

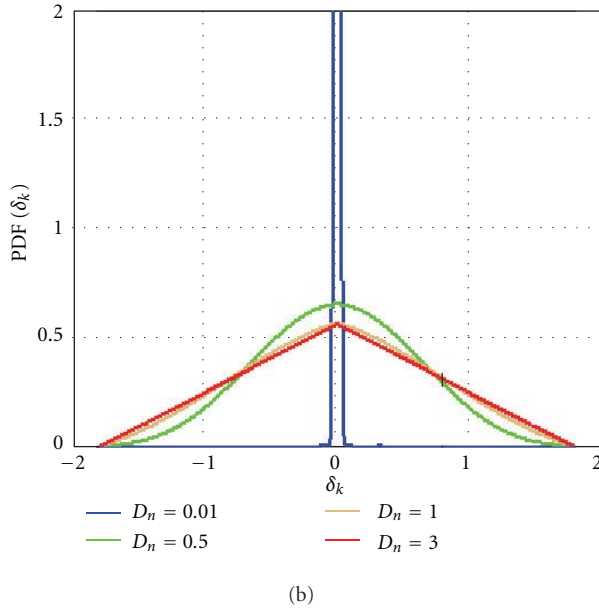
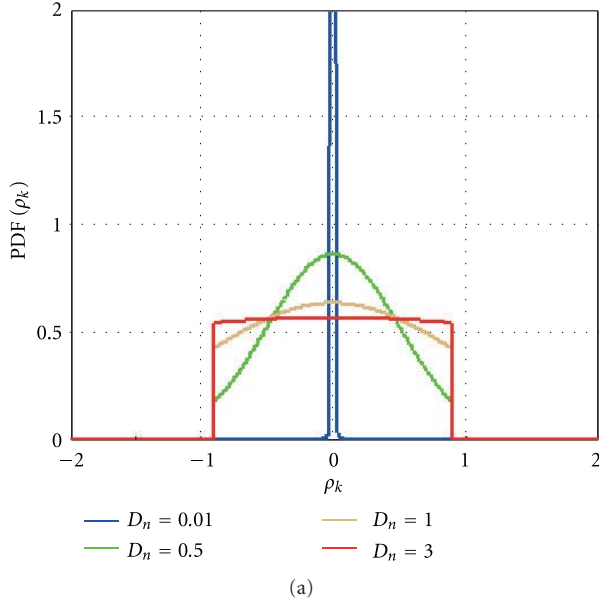


FIGURE 5: Relationship between the positional disorder function (a) and the interseparation probability distribution function (b). As the positional PDF (b) deviates from the Gaussian form for higher values of disorder (due to restrained excursion), the interseparation PDF approaches a triangular form.

different values of the standard deviation  $D$ , and consequently the inter separation PDF( $\delta_n, D$ ) was obtained using numerical coding in MATLAB. The effective susceptibilities were calculated by numerical implementation of the integration (29) and (31), and then the effective material parameters (28) were calculated.

The following features are clearly noted.

- (i) For the disordered dipole ensemble, the fall in the permittivity with increasing disorder is clearly visible (Figures 7(e), 7(f), 7(g), and 7(h)). The  $\text{Im}(\epsilon)$  curve

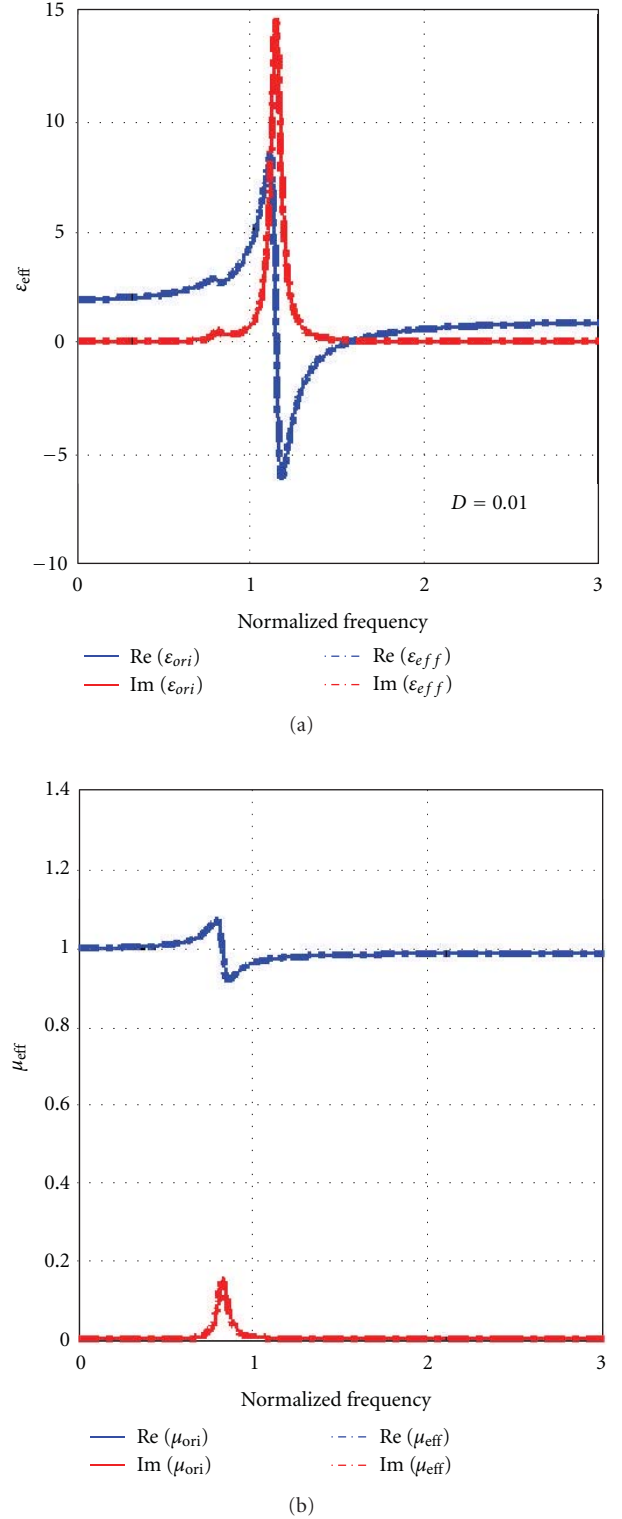


FIGURE 6: Verification of the code—typical values from [16] were used in the computer code written for the calculation of the effective material parameters for metamaterials with positional disorder having a very small amount of disorder ( $D = 0.01$ ). The results obtained match with those in [16]—this is expected as the nature of coupling considered in the present theory should have negligible influence upon the material parameters for very large spatial periods ( $z_n > 3$ ).

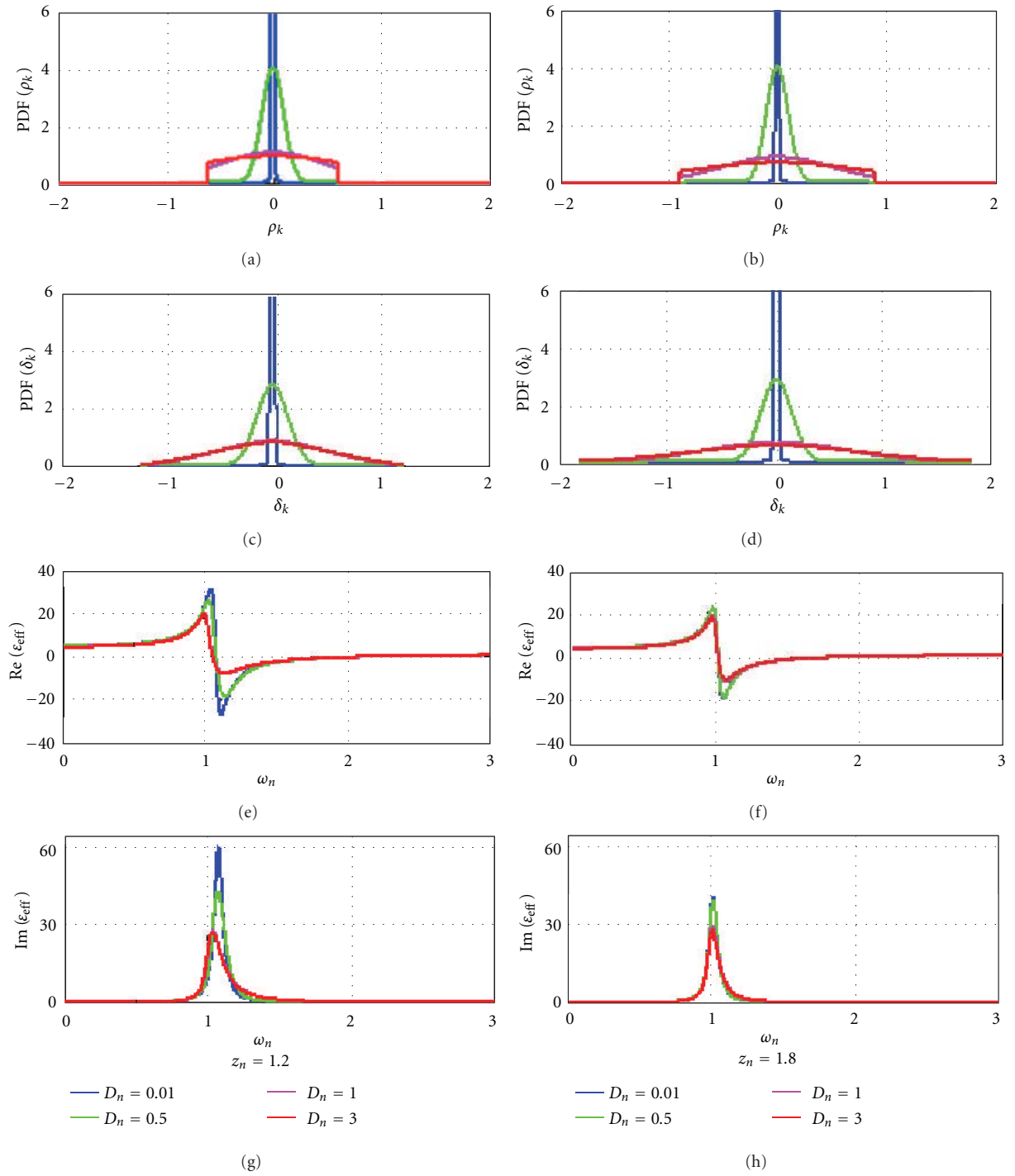


FIGURE 7: Effective material parameter curves for dipole ensembles exhibiting positional disorder. The effective permittivity and permeability curves for disordered dipole ensembles are presented for different values of disorder. The first column pertains to values obtained for a mean period of  $z_n = 1.2$ , while the second column pertains to those obtained for a mean period of  $z_n = 1.8$ . For the respective periodicities: (a) and (b) the positional disorder function; (c) and (d) the respective interseparation PDFs; (e) and (f) scaled real part of the permittivity; (g) and (h) scaled imaginary parts of the permittivity. Clearly, increase in disorder brings about a fall in the maximums of the response of the system.

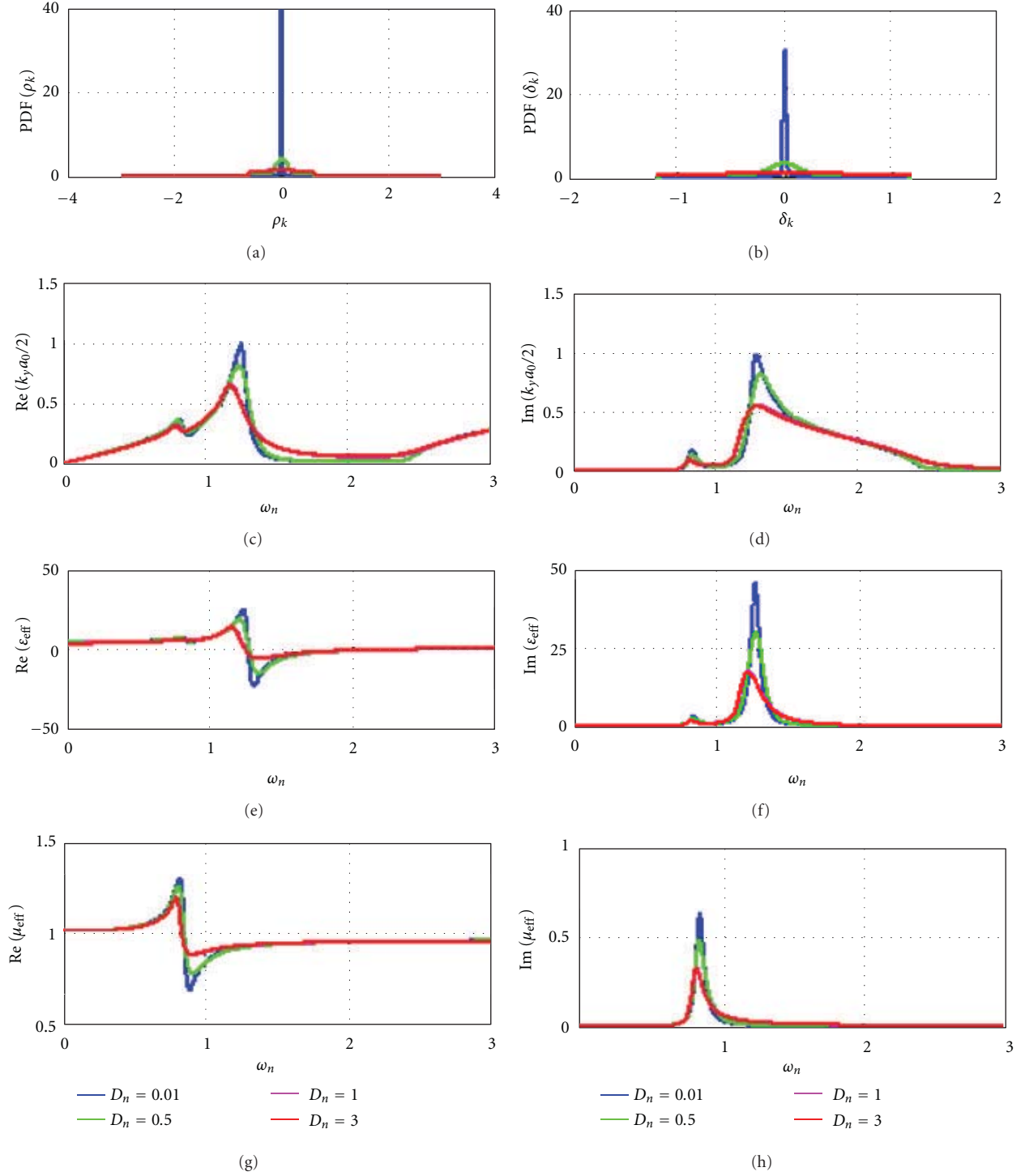


FIGURE 8: Dispersion and effective material parameter curves for quadrupole ensemble with  $z_n = 1.2$ : (a) positional disorder function PDF; (b) interseparation PDF; (c) and (d) real and imaginary part of  $k$ -vector (in normalized units of cut-wire separation distance  $a_0/2$ ); (e) and (f) real and imaginary parts of effective permittivity; (g) and (h) real and imaginary parts of effective permeability.

is symmetric for very small values of the variance (here,  $D = 0.01$ ). But as the disorder increases, the peak shifts towards lower frequencies, and the curves become broadened and asymmetric. The reason for these observed effects can be explained as follows. A

disordered system can be thought to be made up of several different periodic systems. The resonant frequency for each periodic ensemble depends inversely on its spatial period. If the response of the disordered system is approximated by the sum of the responses

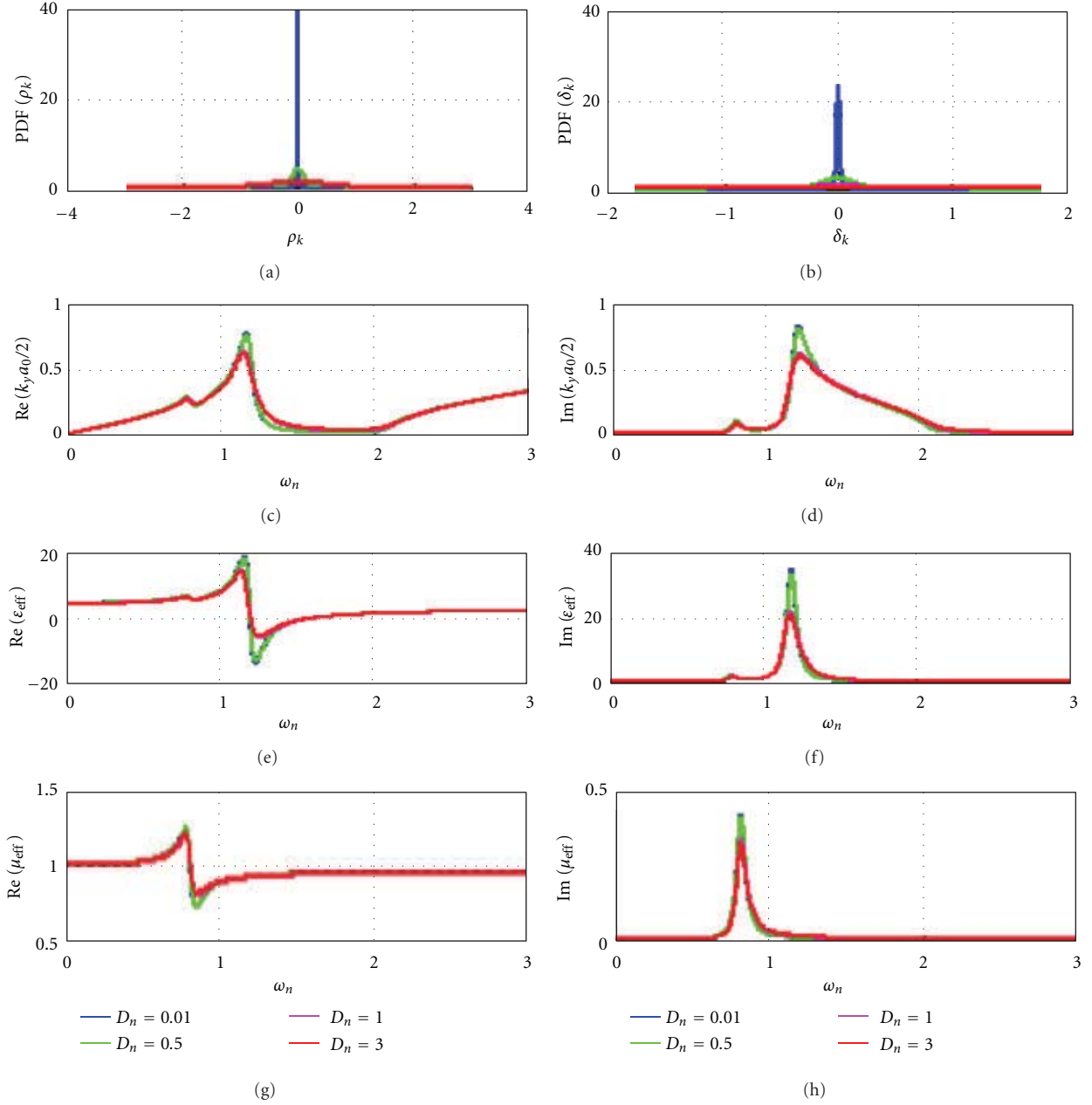


FIGURE 9: Dispersion and effective material parameter curves for quadrupole ensemble with  $z_n = 1.8$ : (a) positional disorder function; (b) interseparation PDF; (c) and (d) real and imaginary part of  $k$ -vector (normalized with the cut-wire separation distance  $a_0/2$ ) (e) and (f) real and imaginary parts of effective permittivity; (g) and (h) real and imaginary parts of effective permeability.

of its constituent periodic systems, it becomes evident that the final curve will develop a tail approaching the blue end of the spectrum. The asymmetry can thus be attributed to an inverse power relationship between resonance frequency and interseparation. The effect of broadening is a consequence of particle conservation. On the other hand, the lowest frequency/largest wavelength of response is not a function of the periodicity, but is actually limited by the eigenfrequency of the independent oscillator. In fact, the resonance frequency approaches the eigenfrequency for a periodic assembly of dipoles,

when the spatial period becomes large. Hence, as the disorder in the system increases, the curves become broadened and asymmetric, and the peak response shifts towards the eigenfrequency of the independent oscillator.

- (ii) In the case of the quadrupole ensemble, a decrease in the value of the electric permittivity is observed as  $D$  is increased. This is in agreement with the experimental results. However, there is also a decrease in the value of the magnetic permeability. This decrease is more pronounced for  $z_n = 1.2$  as

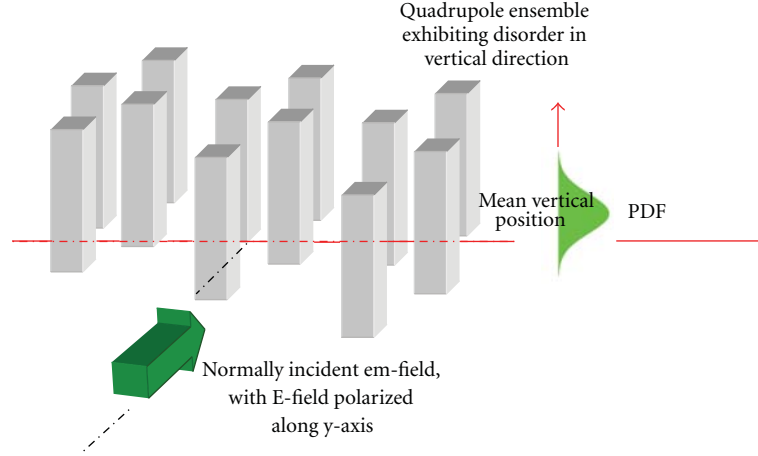


FIGURE 10: Disorder along the cut-wire axis direction—the figure shows a one-dimensional disorder arrangement of meta-atoms. The extent of disorder can be quantified in terms of the angle, the total range of variation being limited to  $(-\pi/2, \pi/2)$ .

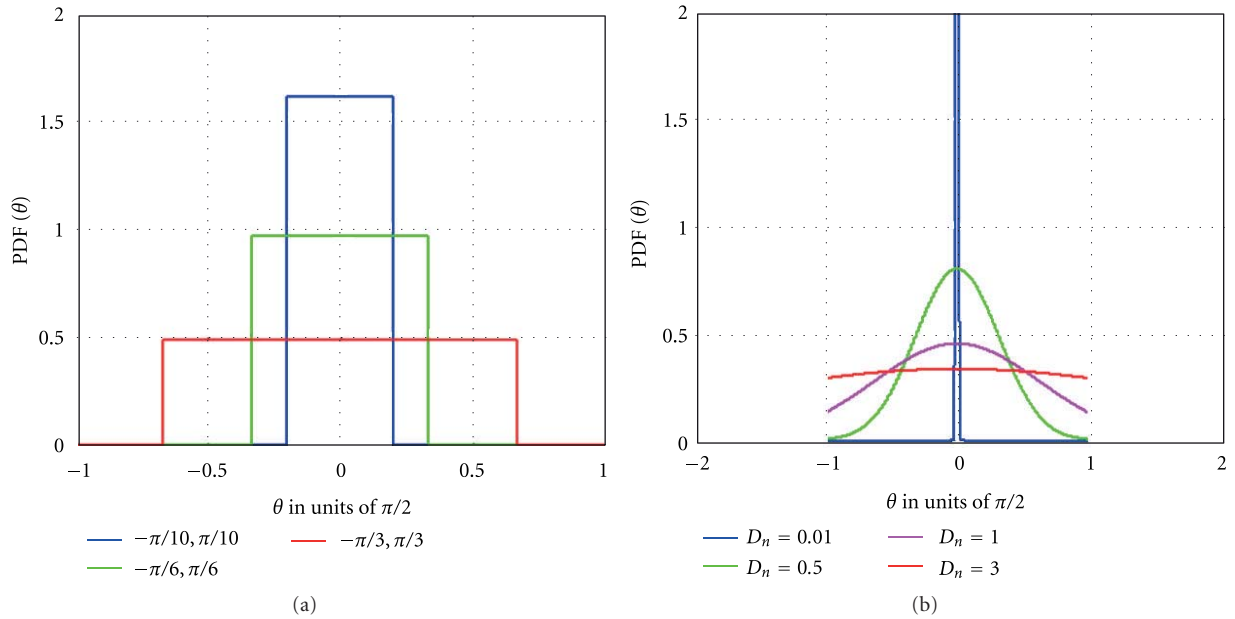


FIGURE 11: (a) Rectangular and (b) Gaussian forms of distribution function used for governing the positional disorder of the metamaterials along the lateral direction. The positional disorder is expressed in terms of the relative angle between two neighboring meta-atoms. The effective material parameters of the ensemble are derived and presented in Figure 12 for three different values of disorder.

compared to  $z_n = 1.8$ . This is an unexpected result, as the magnetic response should remain almost unaffected. The reason for this discrepancy could lie in the simple form of the probabilistic model chosen to describe the randomness.

- (iii) Generally speaking, the final expressions for the permittivity and the permeability were derived under several approximations, associated with (1). The observed discrepancy could also be attributed to these approximations. Above all, the fundamental limitations of the multipole theory itself could affect the final results as well. These possibilities have to be investigated further.

In the light of the above arguments, it is concluded that as the observed positions of the resonances and the relative magnitudes of the parameters are within the limits of approximation, the analysis is valid and can be used to roughly predict the properties of metamaterials with incorporated randomness.

## 7. Other Forms of Disorder

In the preceding analysis, the effect of positional disorder (arising due to aperiodicity) on the averaged material parameters was considered. In a random metamaterial other

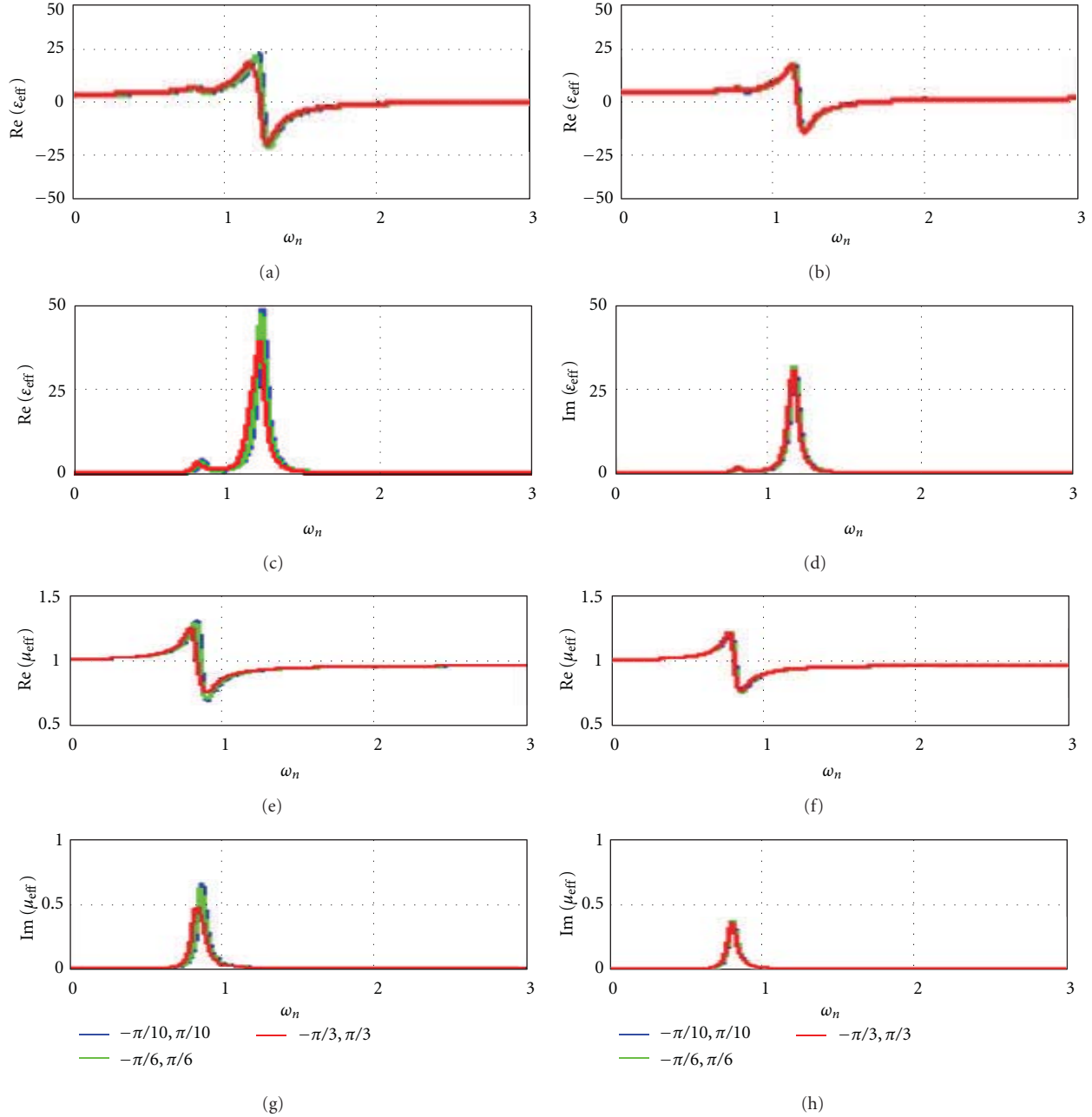


FIGURE 12: Effective material parameters for metamaterials exhibiting positional disorder along the lateral direction ( $y$  direction) governed by the rectangular distribution function (Figure 11(a)). The first column gives the material parameters for a metamaterial ensemble having a mean period of  $z_n = 1.2$ , while the second column is for metamaterials having a mean period of  $z_n = 1.8$ .

forms of disorder can exist as well. A particular case of interest is positional disorder along the cut-wire axis; see Figure 10.

If this form of positional disorder is taken into consideration along with the aperiodicity, the model would then be a step closer to emulate a true self-organized random metamaterial [46]. In the multipole model, the individual cut wires are replaced by dipoles. In case the quadrupoles are disarrayed, the coupling between them will also be

a function of their relative angular positioning. This angular dependence can be introduced into the coupling terms of the dynamic equations. More specifically, the coupling constants  $b$  and  $c$  in the differential equations will include the angular dependence. All other mathematics remaining the same, the averaging procedure can now be carried out between angles  $(-\pi/2, \pi/2)$ .

The curves in Figures 12 and 13 summarize the results obtained by using the multipole approach.

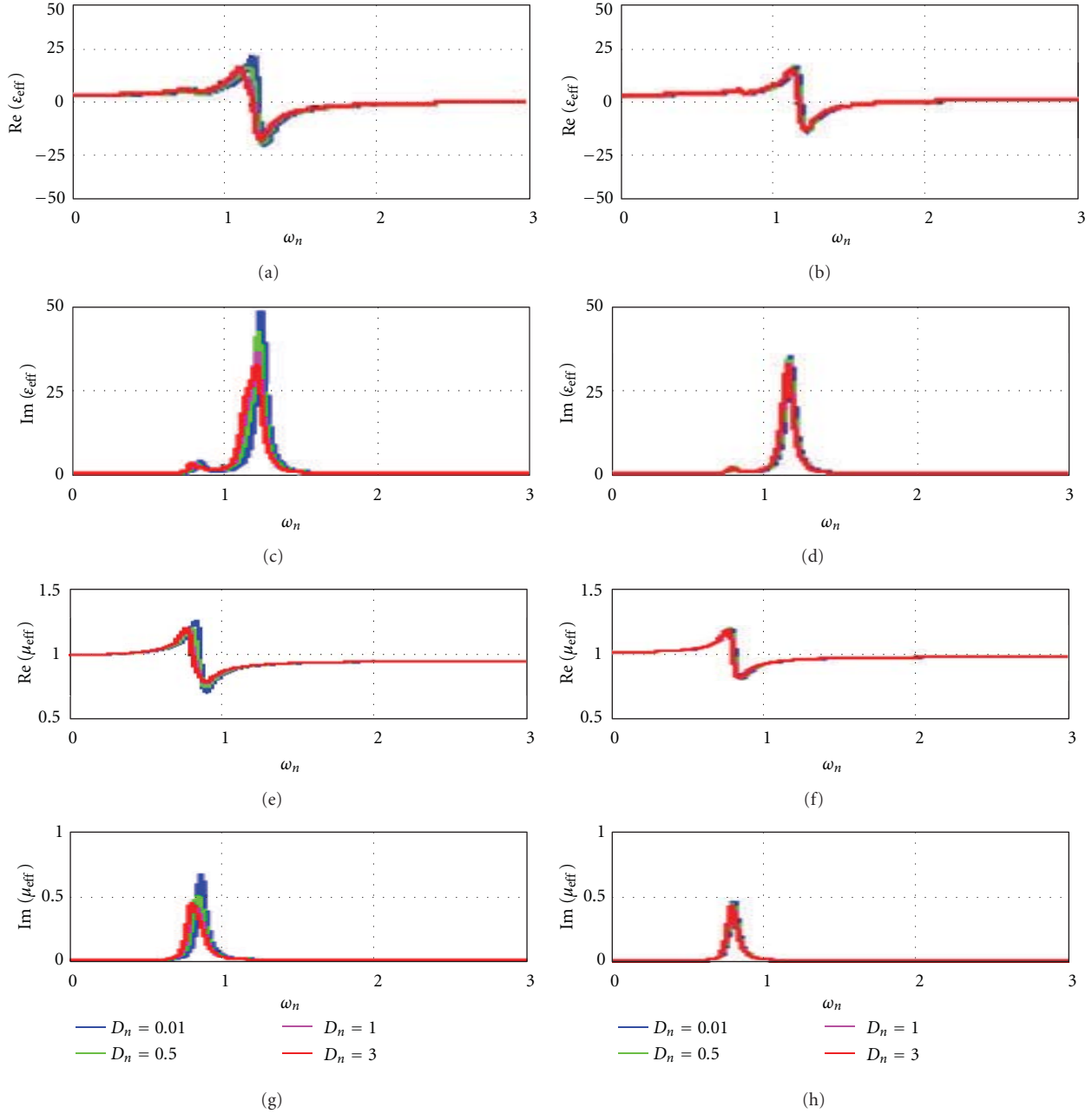


FIGURE 13: Effective material parameters for metamaterials exhibiting positional disorder along the lateral direction ( $x$ -direction) governed by the Gaussian distribution function (Figure 11(b)). The first column gives the material parameters for a metamaterial ensemble having a mean period of  $z_n = 1.2$ , while the second column is for metamaterials having a mean period of  $z_n = 1.8$ .

Two forms of the distribution function were used in the analysis (Figure 11). The extent of disorder is correlated to the relative angular position of the dipoles. The first form of the angular PDF distribution function used was a rectangular function (see Figure 11(a)). The second form used was a Gaussian distribution (Figure 11(b)), the random variable being the relative angular position. The function is centered about 0 degrees, the extent of disorder being quantified by the standard deviation  $D$ ;  $b$  and  $c$  are multiplied by the term  $\cos(\theta)$  to incorporate the angular dependence. Clearly

then, when  $\theta = \pi/2$ , there is no interaction between the cut wires. The Riemannian integration is limited between the values  $(-\pi/2, \pi/2)$ . The constants were again taken from the original reference [22], and the mean periodicity was taken to be  $z_n = 1.8$ . The results (Figures 12 and 13) show that both the effective permittivity and permeability are clearly affected by the angular disorder. In a similar fashion, in-plane and out-of-plane skew disorders of meta-atoms can also be accounted by the model, by making appropriate changes to the coupling terms.



## 8. Conclusions

In extending the multipole approach [16] to the case of random metamaterials, the effect of spatial distribution of the meta-atoms was taken into account by considering the near field coupling between neighboring meta-atoms. The effective susceptibility was expressed as a function of the inter-separation between meta-atoms, the ensemble averaged susceptibility was then obtained as an expectation value, weighed by the probability distribution function of all possible inter-separations. In the present work, the disorder was considered only along one direction (in-plane, perpendicular to cut-wire long axis), assuming that adjacent rows of meta-atoms do not interact with each other. Results obtained by the numerical implementation of the equations indeed confirm the experimental finding that increasing disorder has a more pronounced effect on the effective electrical permittivity than on the effective magnetic permeability. For smaller periodicities, however, the electrical permittivity and magnetic permeability are affected equally. This conflicting result could be caused by a coupling of the quadrupole moments of neighboring meta-atoms. This has not been explicitly considered in the present version of the model. Also, other factors such as the effect of incident polarization, or the coupling between adjacent rows, have not been considered in the present theory. The understanding gained from the study of this simple case can now be used to account for the above specific and more involved cases.

## References

- [1] U. K. Chettiar, A. V. Kildishev, H. K. Yuan et al., "Dual-band negative index metamaterial: double negative at 813 nm and single negative at 772 nm," *Optics Letters*, vol. 32, no. 12, pp. 1671–1673, 2007.
- [2] G. Dolling, M. Wegener, C. M. Soukoulis, and S. Linden, "Negative-index metamaterial at 780 nm wavelength," *Optics Letters*, vol. 32, no. 1, pp. 53–55, 2007.
- [3] J. Valentine, S. Zhang, T. Zentgraf et al., "Three-dimensional optical metamaterial with a negative refractive index," *Nature*, vol. 455, no. 7211, pp. 376–379, 2008.
- [4] J. Valentine, J. Li, T. Zentgraf, G. Bartal, and X. Zhang, "An optical cloak made of dielectrics," *Nature Materials*, vol. 8, no. 7, pp. 568–571, 2009.
- [5] A. Alu and N. Engheta, "Cloaking a sensor," *Physical Review Letters*, vol. 102, 2009.
- [6] Y. Lai, J. Ng, H. Chen et al., "Illusion optics: the optical transformation of an object into another object," *Physical Review Letters*, vol. 102, 2009.
- [7] M. Farhat, S. Guenneau, and S. Enoch, "Ultrabroadband elastic cloaking in thin plates," *Physical Review Letters*, vol. 103, 2009.
- [8] D. Schurig, J. J. Mock, B. J. Justice et al., "Metamaterial electromagnetic cloak at microwave frequencies," *Science*, vol. 314, no. 5801, pp. 977–980, 2006.
- [9] U. Leonhardt, "Optical conformal mapping," *Science*, vol. 312, no. 5781, pp. 1777–1780, 2006.
- [10] E. E. Narimanov and A. V. Kildishev, "Optical black hole: broadband omnidirectional light absorber," *Applied Physics Letters*, vol. 95, Article ID 041106, 2009.
- [11] S. M. Vukovic, I. V. Shadrivov, and Y. S. Kivshar, "Surface Bloch waves in metamaterial and metal-dielectric superlattices," *Applied Physics Letters*, vol. 95, Article ID 041902, 2009.
- [12] D. Ö. Gönüney and D. A. Meyer, "Negative refraction gives rise to the Klein paradox," *Physical Review A*, vol. 79, p. 1, 2009.
- [13] N. Papasimakis, V. Fedotov, and N. Zheludev, "Metamaterial analog of electromagnetically induced transparency," *Physical Review Letters*, vol. 101, Article ID 253903, 2008.
- [14] N. Liu, L. Langguth, T. Weiss et al., "Plasmonic analogue of electromagnetically induced transparency at the Drude damping limit," *Nature Materials*, vol. 8, no. 9, pp. 758–762, 2009.
- [15] P. Mazur and B. R. A. Nijboer, "On the statistical mechanics of matter in an electromagnetic field—I. Derivation of the Maxwell equations from electron theory," *Physica*, vol. 19, no. 1–12, pp. 971–986, 1953.
- [16] A. Chipouline, J. Petschulat, A. Tuennermann et al., "Multipole approach in electrodynamics of metamaterials," *Applied Physics A*, vol. 103, no. 3, pp. 899–904, 2011.
- [17] A. Chipouline, S. Sugavanam, J. Petschulat, and T. Pertsch, "Metamaterials with interacting Metaatoms," <http://arxiv.org/abs/1205.6839>.
- [18] C. S. Deng, H. Xu, and L. Deych, "Optical transport and statistics of radiative losses in disordered chains of microspheres," *Physical Review A*, vol. 82, no. 4, Article ID 041803, 2010.
- [19] W. H. Weber and G. W. Ford, "Propagation of optical excitations by dipolar interactions in metal nanoparticle chains," *Physical Review B*, vol. 70, no. 12, Article ID 125429, 8 pages, 2004.
- [20] M. Quinten, A. Leitner, J. R. Krenn, and F. R. Aussenegg, "Electromagnetic energy transport via linear chains of silver nanoparticles," *Optics Letters*, vol. 23, no. 17, pp. 1331–1333, 1998.
- [21] N. A. Gippius, T. Weiss, S. G. Tikhodeev, and H. Giessen, "Resonant mode coupling of optical resonances in stacked nanostructures," *Optics Express*, vol. 18, no. 7, pp. 7569–7574, 2010.
- [22] N. Feth, M. König, M. Husnik et al., "Electromagnetic interaction of split-ring resonators: the role of separation and relative orientation," *Optics Express*, vol. 18, no. 7, pp. 6545–6554, 2010.
- [23] A. Alù and N. Engheta, "Theory of linear chains of metamaterial/plasmonic particles as subdiffraction optical nanotransmission lines," *Physical Review B*, vol. 74, no. 20, Article ID 205436, 2006.
- [24] J. M. Rico-García, J. M. López-Alonso, and A. Aradian, "Toy model to describe the effect of positional blocklike disorder in metamaterials composites," *Journal of the Optical Society of America B*, vol. 29, p. 53, 2012.
- [25] S. A. Maier, P. G. Kik, and H. A. Atwater, "Optical pulse propagation in metal nanoparticle chain waveguides," *Physical Review B*, vol. 67, no. 20, Article ID 205402, pp. 2054021–2054025, 2003.
- [26] A. Alù and N. Engheta, "Effect of small random disorders and imperfections on the performance of arrays of plasmonic nanoparticles," *New Journal of Physics*, vol. 12, Article ID 013015, 2010.
- [27] J. B. Pendry, "Light finds a way through maze," *Physics*, vol. 1, p. 20, 2008.
- [28] P. W. Anderson, "Absence of diffusion in certain random lattices," *Physical Review*, vol. 109, no. 5, pp. 1492–1505, 1958.
- [29] J. B. Pendry, "Quasi-extended electron states in strongly disordered systems," *Journal of Physics C*, vol. 20, no. 5, p. 733, 1987.

- [30] A. V. Tartakovskii, M. V. Fistul, M. E. Raikh, and I. M. Ruzin, "Hopping conductivity of metal-semiconductor-metal contacts," *Soviet Physics*, vol. 21, p. 370, 1987.
- [31] J. Bertolotti, S. Gottardo, D. S. Wiersma, M. Ghulinyan, and L. Pavesi, "Optical necklace states in anderson localized 1D systems," *Physical Review Letters*, vol. 94, no. 11, Article ID 113903, 2005.
- [32] K. Y. Bliokh, Y. P. Bliokh, V. Freilikher, A. Z. Genack, B. Hu, and P. Sebbah, "Localized modes in open one-dimensional dissipative random systems," *Physical Review Letters*, vol. 97, no. 24, Article ID 243904, 2006.
- [33] F. Rütting, "Plasmons in disordered nanoparticle chains: localization and transport," *Physical Review B*, vol. 83, no. 11, Article ID 115447, 2011.
- [34] D. Mogilevtsev, F. A. Pinheiro, R. R. Dos Santos, S. B. Cavalcanti, and L. E. Oliveira, "Suppression of Anderson localization of light and Brewster anomalies in disordered superlattices containing a dispersive metamaterial," *Physical Review B*, vol. 82, no. 8, Article ID 081105, 2010.
- [35] W. Tan, Y. Sun, Z. G. Wang, H. Chen, and H. Q. Lin, "Transparency induced by coupled resonances in disordered metamaterials," *Optics Express*, vol. 17, no. 26, pp. 24371–24376, 2009.
- [36] L. Jylhä, I. Kolmakov, S. Maslovski, and S. Tretyakov, "Modeling of isotropic backward-wave materials composed of resonant spheres," *Journal of Applied Physics*, vol. 99, no. 4, Article ID 043102, 2006.
- [37] M. V. Gorkunov, S. A. Gredeskul, I. V. Shadrivov, and Y. S. Kivshar, "Effect of microscopic disorder on magnetic properties of metamaterials," *Physical Review E*, vol. 73, no. 5, Article ID 056605, 2006.
- [38] X. Zhou, X. P. Zhao, and Y. Liu, "Disorder effects of left-handed metamaterials with unitary dendritic structure cell," *Optics Express*, vol. 16, no. 11, pp. 7674–7679, 2008.
- [39] N. Papasimakis, V. A. Fedotov, Y. H. Fu, D. P. Tsai, and N. I. Zheludev, "Coherent and incoherent metamaterials and order-disorder transitions," *Physical Review B*, vol. 80, no. 4, Article ID 041102, 2009.
- [40] A. Boltasseva and V. M. Shalaev, "Fabrication of optical negative-index metamaterials: recent advances and outlook," *Metamaterials*, vol. 2, no. 1, pp. 1–17, 2008.
- [41] J. P. Wright, O. Worsfold, C. Whitehouse, and M. Himmelhaus, "Ultraflat ternary nanopatterns fabricated using colloidal lithography," *Advanced Materials*, vol. 18, no. 4, pp. 421–426, 2006.
- [42] P. Hanarp, D. Sutherland, J. Gold, and B. Kasemo, "Nanos-structured model biomaterial surfaces prepared by colloidal lithography," *Nanostructured Materials*, vol. 12, no. 1, pp. 429–432, 1999.
- [43] R. Glass, M. Möller, and J. P. Spatz, "Block copolymer micelle nanolithography," *Nanotechnology*, vol. 14, no. 10, pp. 1153–1160, 2003.
- [44] C. Helgert, C. Rockstuhl, C. Etrich et al., "Effective properties of amorphous metamaterials," *Physical Review B*, vol. 79, Article ID 233107, 2009.
- [45] J. Petschulat, C. Menzel, A. Chipouline et al., "Multipole approach to metamaterials," *Physical Review A*, vol. 78, no. 4, Article ID 043811, 2008.
- [46] D. A. Pawlak, S. Turczynski, M. Gajc et al., "How far are we from making metamaterials by self-organization? the microstructure of highly anisotropic particles with an SRR-like geometry," *Advanced Functional Materials*, vol. 20, no. 7, pp. 1116–1124, 2010.

## Review Article

# Rolled-Up Metamaterials

**Stephan Schwaiger, Andreas Rottler, and Stefan Mendach**

*Institut für Angewandte Physik und Zentrum für Mikrostrukturforschung, Universität Hamburg, Jungiusstrasse 11, 20355 Hamburg, Germany*

Correspondence should be addressed to Stefan Mendach, smendach@physnet.uni-hamburg.de

Received 18 August 2012; Accepted 25 September 2012

Academic Editor: Ivan D. Rukhlenko

Copyright © 2012 Stephan Schwaiger et al. This is an open access article distributed under the Creative Commons Attribution License, which permits unrestricted use, distribution, and reproduction in any medium, provided the original work is properly cited.

In this paper we review metamaterials fabricated from self-rolling strained metal-semiconductor layer systems. These systems relax their strain upon release from the substrate by rolling up into microtubes with a cross-section similar to a rolled-up carpet. We show that the walls of these microtubes represent three-dimensional optical metamaterials which so far could be used, for example, for the realization of broadband hyperlenses, fishnet metamaterials, or optically active three-dimensional metamaterials utilizing the unique possibility to stack optically active semiconductor heterostructures and metallic nanostructures. Furthermore, we discuss THz metamaterials based on arrays of rolled-up metal semiconductor microtubes and helices.

## 1. Introduction

While the concept of metamaterials, that is, tailoring the optical properties of a material to desired values by cleverly designing its subwavelength composites, is in principle scalable in frequency, the realization of three-dimensional metamaterials for optical frequencies remains one of the current challenges in the research area of metamaterials [1, 2]. Compared to the fabrication used in the pioneering works on metamaterials operating in the microwave regime [3–6], which were composed of millimeter-sized metallic structures produced with well-established printed circuit board techniques, the deliberate structuring on the nanoscale in three dimensions for the production of three-dimensional optical metamaterials is much more elaborate. Possible routes are, for example, stacking of single-layered metamaterials by repeating planar lithographic processing steps [7], focused ion beam milling of multilayers [8], multilayer deposition on patterned substrates [9, 10], galvanization in combination with three-dimensional laser interference lithography [11], or galvanization in combination with anodic oxidation [12]. Here we discuss three-dimensional metamaterials prepared by rolling up a single-layered metamaterial with multiple rotations into a radial stack, similar to rolling up a bilayer of biscuit and cream into a Swiss-roll cake. One possibility

to follow this route is actively rolling up the layer system as demonstrated by Gibbons and colleagues, who rolled up a gold-polymer bilayer around a millimeter-sized glass rod and obtained a high quality radial multilayer system [13]. Another possibility is utilizing the concept of strain induced self-rolling of nanolayers which was pioneered by Prinz and coworkers for the InGaAlAs semiconductor system [14, 15] and since then adopted to various kinds of material systems including metals, semiconductors, isolators, and hybrids thereof [16–22]. Smith and coworkers pointed out in theoretical works that rolled-up metal-isolator systems might be promising candidates for the realization of metamaterial waveguides [23] and hyperlenses [24, 25]. Particularly interesting are hybrid systems of semiconductors and metals, since they open up the unique possibility to stack electrically or optically active semiconductor layers and metallic components in order to obtain active metamaterials. In the following we review our work in this direction utilizing self-rolling strained InGaAlAs/metal layers for the realization of three-dimensional optical metamaterials including hyperlenses [26–28], fishnet metamaterials [29], and optically active metamaterials [30–32]. In addition we discuss the possibility to use arrays of rolled-up InGaAs/metal structures to realize metamaterials for far infrared frequencies [33, 34].

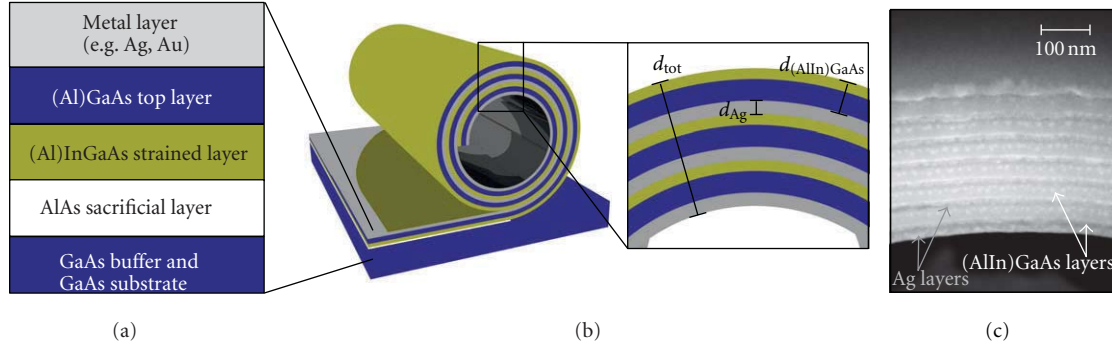


FIGURE 1: (a) layer sequence for producing a rolled-up metamaterial, (b) rolled-up multilayer of silver and (In)GaAs. Inset: the wall of the resulting tube represents a three-dimensional metamaterial. (c) Scanning electron microscopic cross-section image of a realized metamaterial consisting of 6 lattice cells with  $d_{Ag} = 22$  nm and  $d_{In} = 34$  nm.

## 2. Preparation of Rolled-Up Metamaterials

Figure 1(a) shows a typical layer sequence, as used, for example, for the preparation of the rolled-up hyperlens shown in Figure 1(c) and discussed in Section 3. Molecular beam epitaxy (MBE) is used to grow a typically 40 nm thick AlAs sacrificial layer followed by a strained (Al)InGaAs layer and an (Al)GaAs layer, each a few nanometers thick, on top of a GaAs substrate. On top of this strained semiconductor heterostructure a few nanometers thick metal film is deposited by thermal evaporation. After the selective etching of the AlAs sacrificial layer with buffered hydrofluoric acid, the strained layer system is detached from the substrate and rolls up into a tube as sketched in Figure 1(b). The walls of these tubes are the basic structure used for the optical three-dimensional metal-semiconductor metamaterials discussed in the following. Due to the fact that the entire structure comes from the same layer, rolled-up metamaterials exhibit a perfect uniformity and give the unique opportunity to stack identical MBE-grown semiconductor heterostructures with metallic structures. The tube diameter of the devices discussed here typically amounts to a few microns and can be controlled by the layer thicknesses and composition; the number of revolutions  $N$  is adjustable by the etching time. The passive rolled-up hyperlens structure consisting of nonfunctionalized semiconductor layers and planar metal films, as shown in Figure 1, is discussed in Section 3. Patterning the rolled-up structures shown in Figure 1 after the rolling-up process results in fishnet metamaterials as discussed in Section 4. In Sections 5 and 6 we demonstrate that quantum wells can be integrated into the semiconductor component of the rolled-up structures to realize optically active metamaterials. Optionally, the metal films can be replaced by plasmonic nanostructures, which are prepared onto the strained semiconductor prior to rolling up, as demonstrated in Section 6. A different ansatz using the same preparation technique but considering the whole tube as one cell of a metamaterial for the THz regime is addressed in Section 7.

## 3. Rolled-Up Hyperlens

Multistacks of thin metal layers and thin dielectric layers might be approximated as an effective medium with an anisotropic permittivity tensor as described, for example, in [35]. This permittivity tensor has on the major axis  $\epsilon_{||} = (\epsilon_M + \eta\epsilon_D)/(1 + \eta)$  for the two directions in the plane of the layers and  $\epsilon_{\perp} = (1 + \eta)/(1/\epsilon_M + \eta/\epsilon_D)$  for the direction perpendicular to the layers and zeros otherwise. In this case,  $\epsilon_D$  is the permittivity of the dielectric layer,  $\epsilon_M$  is the permittivity of the metal layer, and  $\eta$  is the layer thickness ratio of dielectric and metal layer. Due to the special ellipsoidal and hyperbolic shapes of their Fresnel surfaces, that is, their isofrequency surfaces in  $k$  space, one can use such media for subwavelength imaging under certain conditions [35–37]. For  $0 < \epsilon_{||} \ll |\epsilon_{\perp}|$  one obtains flat extended iso-frequency surfaces in  $k$  space, which leads to the propagation of very high  $k$  components with a common group velocity perpendicular to the multilayers. This directed imaging of very fine details is called hyperlensing and, when using curved instead of flat multilayers, can be used to magnify subwavelength details with a magnification given by the ratio of outer and inner radius of the multilayer structure [38]. Cylindrical hyperlenses working in the ultraviolet [10] as well as spherical hyperlenses operating in the blue [9] could be realized in the group of Xiang Zhang by sequential deposition of layers of silver and dielectric on patterned substrates.

Rolled-up metamaterials made of silver-InGaAs multilayers are promising candidates for hyperlensing at near infrared and visible frequencies. Due to the significantly higher permittivity of the semiconductor compared to dielectrics like, for example, Aluminum Oxide or Titanium Oxide, the operation range, where the condition  $0 < \epsilon_{||} \ll |\epsilon_{\perp}|$  is satisfied in silver-InGaAs multilayers, can easily be shifted over the visible and near infrared regime by choosing the respective layer ratio  $\eta$ . Experimentally, the zero crossing of  $\epsilon_{||}$  and thus the lower cutoff frequency for hyperlensing operation can be obtained from transmission and reflection measurements. At normal incidence one expects  $\epsilon_{||} < 0$  for



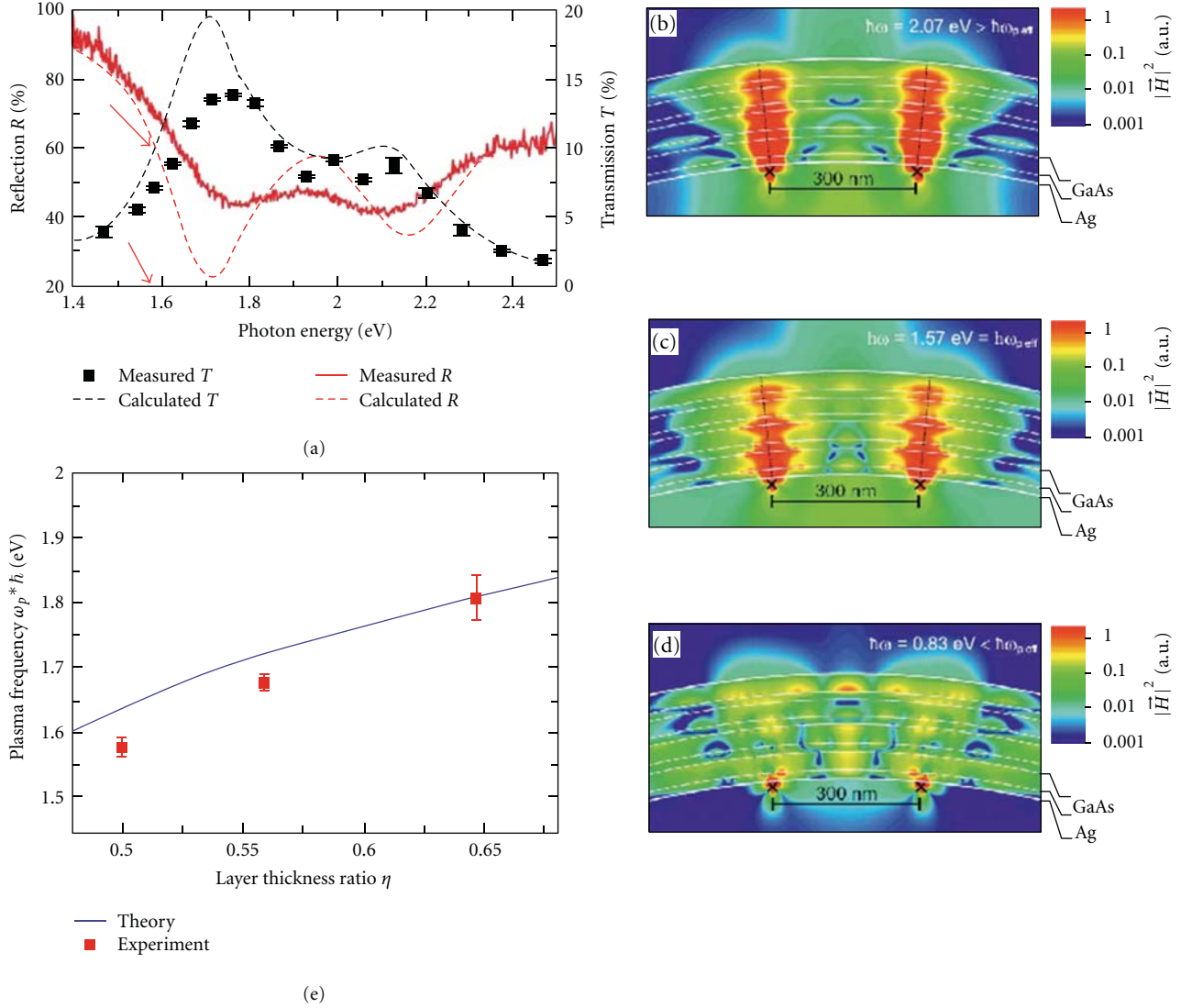


FIGURE 2: (a) Experimental reflectance and transmittance of a rolled-up hyperlens together with corresponding theoretical curves from transfer matrix calculations. (b), (c) Simulation of the imaging of two dipoles from the inside of the hyperlens to the outer perimeter for two frequencies above the plasma edge, (d) Corresponding simulation for a frequency below the plasma edge. (e) Experimentally observed frequency of the plasma edge as a function of layer thickness ratio of silver and InGaAs.

metallic reflection and  $\varepsilon_{||} > 0$  for dielectric transmission; that is,  $\varepsilon_{||} = 0$  marks the plasma edge of the effective material.

While the measurement of reflection from a rolled-up metamaterial can be performed with slight modifications of conventional reflection setups, the measurement of transmission through the rolled-up metamaterials is challenging since it requires a transmission light source inside the rolled-up structure. As sketched in Figure 4(a) in Section 5 we realize such a transmission source with a metal coated fiber which we manipulate into the rolled-up metamaterial by means of piezo actuators. Light scattered from a nanohole with typically a few 100 nm diameter, which is prepared into the metallization of the fiber tip by focused ion beams, is transmitted through the rolled-up metamaterial and collected with a microscope objective. As a reference

we measure the emission from the nanohole with the fiber tip outside of the rolled-up metamaterial. Figure 2(a) shows transmission measurements (black squares) and reflection measurements (red curve) of a rolled-up silver-InGaAs hyperlens ( $\eta = 0.5$ ,  $d_{\text{Ag}} = 17 \text{ nm}$ ,  $d_{\text{InGaAs}} = 34 \text{ nm}$ ,  $N = 4$ ), together with corresponding transfer matrix calculations. The red arrows indicate the plasma edge. At frequencies above the plasma edge distinct resonances appear. In [28] we could show that these resonances are due to Fabry-Perot interferences corresponding to the total layer thickness and can be used to enhance the transmission through a rolled-up hyperlens at desired frequencies. Towards high frequencies, the transmission decreases again due to the high absorption in the semiconductor component. As Figure 2(e) illustrates, we have experimentally demonstrated that the plasma edge

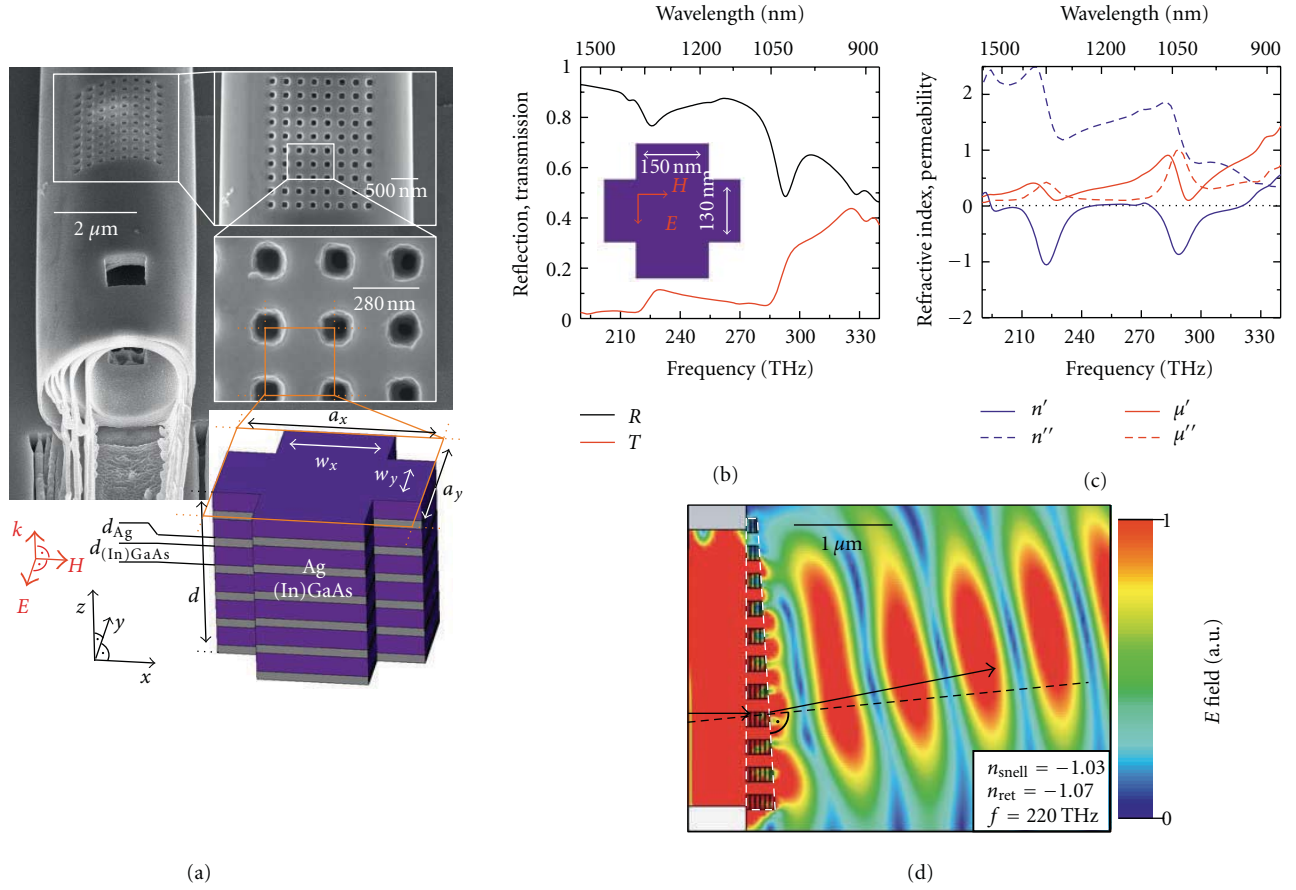


FIGURE 3: (a) Microroll with six alternating layers of metal and semiconductor with a fishnet pattern obtained by focused ion beam milling. As visible, the end of the tube exhibits noncompact layer stacking. Nevertheless, in the area of the fishnet pattern the layer stacking is compact. The sketch shows the unit cell of the fishnet pattern. The electromagnetic wave is incident in  $z$  direction. (b) Calculated reflection and transmission through the structure in (a). (c) The permeability ( $\mu = \mu' + i\mu''$ ) and refractive index ( $n = n' + in''$ ), calculated by a parameter retrieval method, reveal that  $n'$  becomes negative at certain frequencies. (d) A wave impinging from the left ( $f = 220$  THz) gets negatively refracted by a prism that is cut into the fishnet structure. The prism is depicted by the white, dashed lines, with the structure infinitely extended in the direction perpendicular to the image plane. Figure reprinted from [29] with slight modifications.

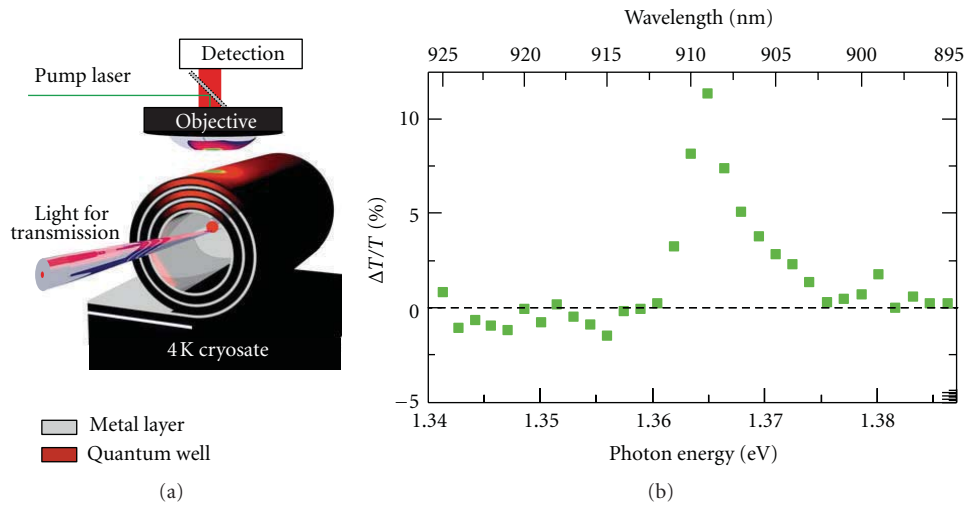


FIGURE 4: (a) Sketch of the setup for measurements of the transmission through an active rolled-up metamaterial. The setup allows to optically excite active layers, for example, InGaAs quantum wells, inside the metamaterial to enhance the light transmission. (b) The transmission enhancement of an active rolled-up metamaterial is plotted against the photon energy showing a pronounced maximum of  $\Delta T/T = 10\%$  at a photon energy of  $E = 1.36$  eV. Images taken from [30].

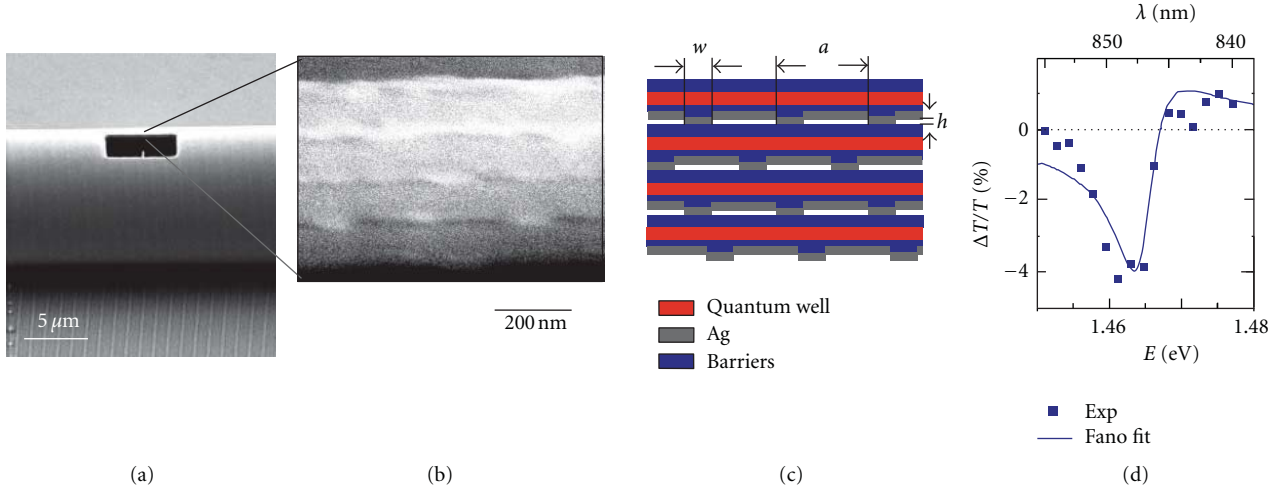


FIGURE 5: (a)-(b) Scanning electron micrographs of a rolled-up metamaterial consisting of a three-dimensional silver lattice interleaved with quantum wells. (c) Schematic of the metamaterial according to the cross-section shown in (b). (d) Pump-induced change in transmission through the metamaterial (blue squares), together with a Fano fit (blue line).

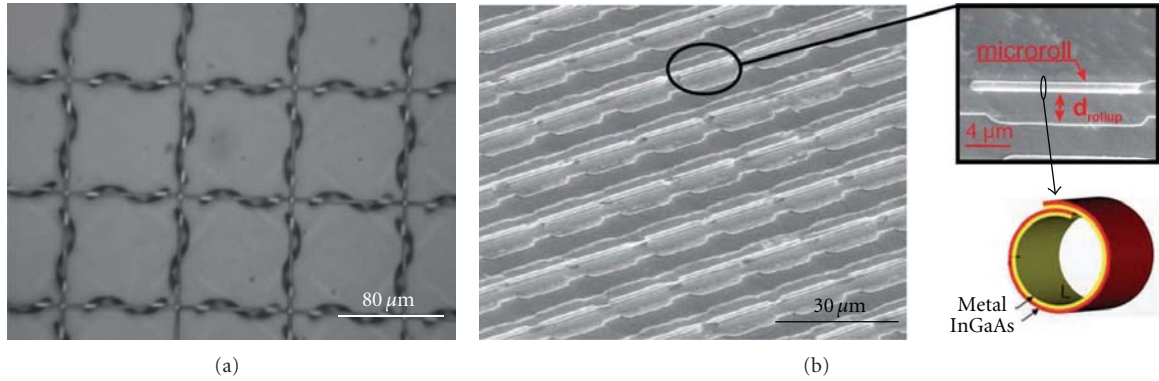


FIGURE 6: (a) Chiral metamaterial made of an array of rolled-up InGaAs/GaAs/Ti/Au microhelices realized by Prinz and coworkers. The material exhibits circular dichroism and linear polarization rotation in the operation frequency range around 2 THz. The image is taken from [34]. (b) Metamaterial made of an array of rolled-up InGaAs/GaAs/Cr microtubes. The zoom-in shows a single microtube. As sketched in the bottom right, the microtubes exhibit slightly more than one rotation resembling the concept of a split ring resonator [3]. We showed by means of finite difference time domain simulations that these structures might be used to obtain a magnetic response at THz frequencies.

can be shifted over the visible and near infrared regime by changing the layer thickness ratio  $\eta$ . Figures 2(b)–2(d) show finite difference time domain simulations (Lumerical FDTD Solutions) for light propagation in the hyperlens with a plasma edge at 1.57 eV (cf. Figure 2(a)). On the inner surface of the hyperlens two dipoles are placed at a distance of 300 nm. In fact, for frequencies at and above the plasma edge we observe hyperlensing, that is, radially directed imaging of the dipoles onto the outer hyperlens surface (Figures 2(b) and 2(c)). In contrast to this, no hyperlensing occurs for frequencies below the plasma edge (Figure 2(d)). A particularly interesting aspect of these simulations is the fact that hyperlensing occurs also for relatively thick individual layers as used in our structures, which exceed the individual layer thickness limit of approximately 5 nm for the

applicability of effective medium retrieval methods to our structures [27].

#### 4. Three-Dimensional Fishnet Metamaterial with Negative Refractive Index at 1000 nm Wavelength

Figure 3(a) shows a rolled-up metamaterial similar to the one presented in Figure 1 with six windings, where an array of holes with diameters smaller than 100 nm has been cut into its wall using focused ion beam milling after the rolling-up process. In [29] we showed by means of finite difference time domain simulation that a negative index of refraction in the near-infrared regime is expected in

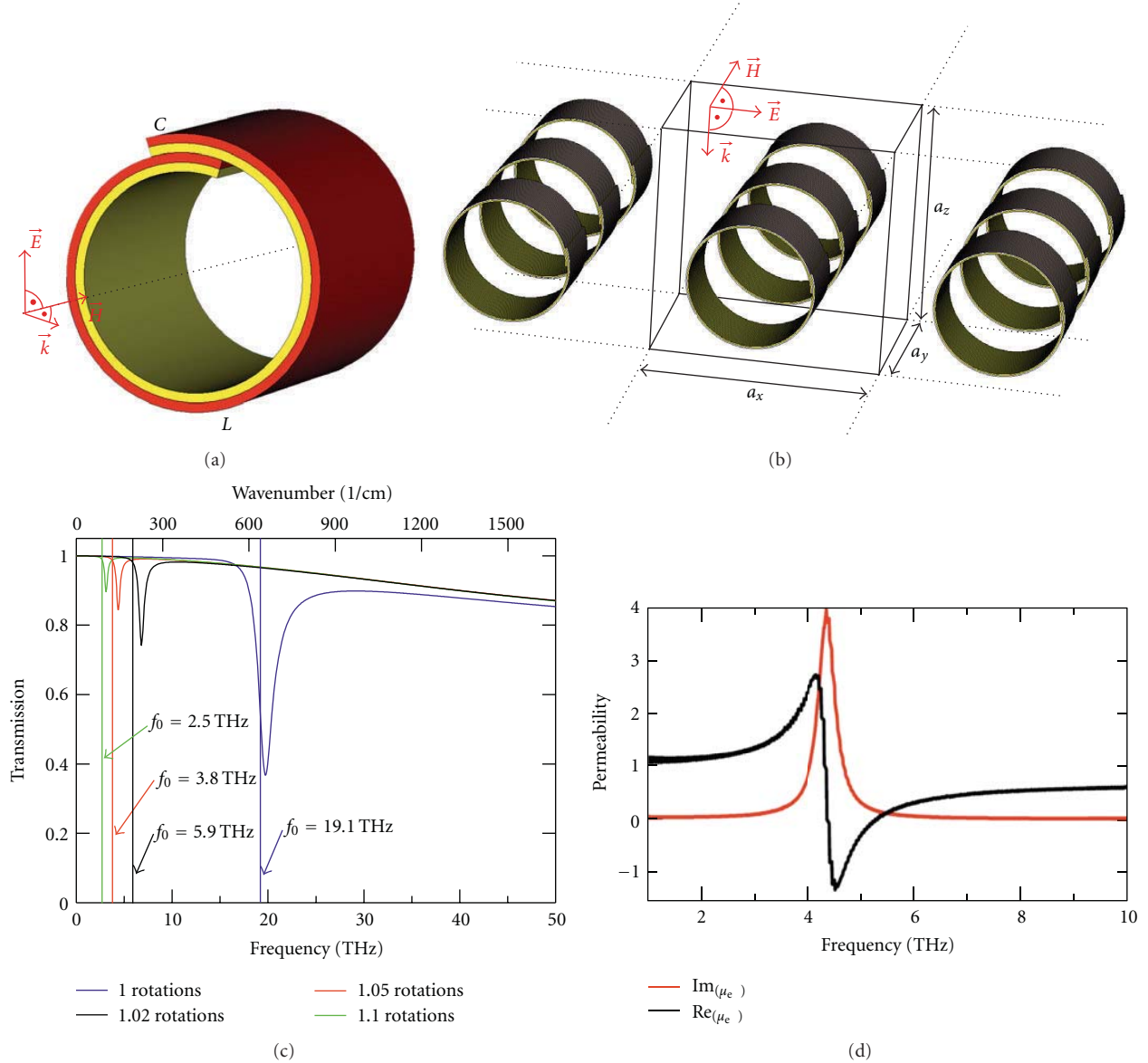


FIGURE 7: (a) Sketch of a microroll consisting of an (In)GaAs (red) and a gold layer (yellow). (b) Simulation setup: black lines indicate the simulation volume with periodic boundary conditions in the  $x$  and  $y$  direction. A plane wave is incident in  $z$  direction with the magnetic field vector pointing along the tube axis; that means in the  $y$  direction. (c) Simulated transmission spectra of microroll arrays with varying winding numbers  $n$  and the calculated resonance frequencies  $f_0$ . (d) Retrieved complex permeability  $\mu_{\text{eff}}$  of a microroll array for a winding number of  $n = 1.05$ . Figure reprinted from [33] with slight modifications.

such a three-dimensional fishnet metamaterial. Figure 3(b) depicts the simulated reflection and transmission through the structure. Retrieving the effective refractive index reveals that the real part ( $n'$ ) is negative at the resonance positions in the reflectivity. At the positions where the real part is negative, the effective permeability shows a Lorentzian-shaped resonance (see Figure 3(c)). In Figure 3(d) a prism has been cut into the multilayer stack. As depicted by the black arrows it can be clearly seen that a wave impinging from the left side gets negatively refracted. Calculating the real part

of the refractive index via Snell's law for a frequency of  $f = 220$  THz leads to a refractive index of  $n' = -1.03$ . This is in very good agreement with the refractive index of  $n' = -1.07$  calculated from the simulated spectra with the parameter retrieval method by Smith et al. [39]. Apart from the high uniformity and possibility to activate the semiconductor component as discussed above in the fabrication section, our rolled-up fishnet metamaterials have the advantage that they need much thinner functional layers due to the high refractive index of the semiconductor component in



comparison to the commonly discussed fishnet structures based on sequential deposition of metal and materials like  $\text{MgF}_2$  or hydrogen silsesquioxane ( $n' \approx 1.5$ ).

## 5. Optically Active Rolled-Up Metamaterials

The integration of quantum emitters into metamaterials opens up the exciting opportunity to study quantum emitters in tailorable dielectric environments. For hyperbolic metamaterials an enhanced spontaneous emission is expected [40–42]. Furthermore, metamaterials can be optically activated by the integration of quantum emitters, for example, to compensate for the typically very high ohmic losses given by the metallic component of metamaterials or to investigate coupling effects with the metallic components of the metamaterials. A major challenge is the realization of such metamaterials with embedded quantum emitters. Monolayered metamaterials with integrated quantum emitters have been realized as fishnet metamaterials with embedded rhodamine dye molecules [43], slit-ring resonator arrays covered with colloidal quantum dots [44, 45], and slit-ring resonator arrays prepared on top of an InGaAs quantum well heterostructure [46, 47]. Reference [41] is one of the few examples in literature for three-dimensional metamaterials containing quantum emitters. In their work Tumkur et al. sequentially deposited metal layers and polymer layers doped with dye molecules.

As discussed in the fabrication section, three-dimensional rolled-up metamaterials fabricated from semiconductor systems intrinsically offer the possibility to embed high quality quantum structures. In [30] we showed that optically active quantum wells embedded in a hyperlens structure can be used to actively modify the transmission and reduce losses via optical pumping. The investigated structure was based on a semiconductor heterostructure grown by MBE on a GaAs substrate. The functional semiconductor heterostructure consists of a strained  $\text{In}_{13}\text{Al}_{20}\text{Ga}_{67}\text{As}$  barrier layer (23 nm), a strained  $\text{In}_{16}\text{Ga}_{84}\text{As}$  quantum well (7 nm), and an unstrained  $\text{Al}_{23}\text{Ga}_{77}\text{As}$  barrier layer (21 nm). After MBE growth the structure was metalized with an Ag layer (13 nm) and rolled up into a microtube with several rotations. Like the hyperlens structure presented in Section 3, the wall of the rolled-up microtube represents a metamaterial consisting of alternating layers of Ag and semiconductor, but in contrast to the passive hyperlens, it represents an optically active rolled-up metamaterial.

In order to investigate the influence of optical pumping of the embedded quantum well, the transmission enhancement was measured. For that purpose a low-temperature transmission measurement setup operating at liquid helium temperatures was used as sketched in Figure 4(a). In this setup a light emitting fiber tip was inserted into the hollow core of the microtube to illuminate the rolled-up metamaterial from the inside. The light transmitted through the metamaterial was collected by a microscope objective and detected with a single photon counting diode. A pump laser was simultaneously focused onto the outer perimeter of the metamaterial to optically pump the embedded quantum

well. With this setup the transmission enhancement of the metamaterial  $\Delta T/T$  was obtained from the transmitted light intensity  $I_{\text{TPL}}$  under optical excitation of the quantum well, the photoluminescence intensity  $I_{\text{PL}}$ , when no light is transmitted through the metamaterial, the transmitted intensity  $I_{\text{T}}$  without pumping of the quantum well, and the dark count intensity  $I_{\text{D}}$ , as follows:  $\Delta T/T = (I_{\text{TPL}} - I_{\text{PL}})/(I_{\text{T}} - I_{\text{D}})$ . In Figure 4(b) the transmission enhancement  $\Delta T/T$  (squares) of the active rolled-up metamaterial is plotted against the photon energy of the transmitted light. The transmission enhancement has a maximum at a photon energy of  $E = 1.36$  eV with a value of  $\Delta T/T = 10\%$ .

## 6. Fano Resonance in Optically Active Rolled-Up Plasmonic Metamaterials

After the first observation of optical gain by quantum emitters in a three-dimensional rolled-up metamaterial as discussed above, we in the next step realized rolled-up metamaterials with integrated quantum emitters and plasmonic nanostructures and detected a characteristic Fano resonance caused by the coupling between the quantum emitters and the plasmon polaritons in the plasmonic structures [31]. As a quantum emitter we used a GaAs quantum well (17 nm) embedded between an  $\text{In}_{20}\text{Al}_{30}\text{Ga}_{50}\text{As}$  barrier (17 nm) and an  $\text{Al}_{20}\text{Ga}_{80}\text{As}$  barrier (17 nm). Before the rolling-up process the upper  $\text{Al}_{20}\text{Ga}_{80}\text{As}$  barrier was modulated with a wire profile with a height of  $h = 10$  nm, a wire width of  $w = 100$  nm and a period of  $a = 500$  nm using laser interference lithography and wet chemical etching. Subsequently, a 13 nm thick silver film was deposited onto the modulated surface. Rolling-up this structure along the wire profiles (Figure 5(a)) results in a three-dimensional metamaterial consisting of alternating layers of a quantum well heterostructure and silver wires as sketched in Figure 5(c). Figure 5(b) shows the corresponding scanning electron micrographs of a realized metamaterial. To make the stacked wire structure visible, a hole was cut into the rolled-up metamaterial using focused ion beams. As visible in Figure 5(b) and the corresponding sketch in Figure 5(c) the wires are not perfectly stacked but laterally displaced by  $\Delta$  due to the finite angle  $\gamma$  between wire direction and rolling direction. For compactly rolled-up systems one obtains  $\Delta = \pi(d + 2tN)\tan(\gamma)$ , where  $d$  is the diameter of the rolled-up metamaterial,  $t$  is the single layer thickness, and  $N$  is the index of the respective rotation position. We have investigated such stacked lattice structures using finite difference time domain simulations and rigorous coupled wave analysis and found plasmon polariton resonances with a spectral position, which strongly depends on the lattice parameters  $h$ ,  $w$ ,  $a$ , and  $\Delta$ . We modeled the embedded quantum well as a Lorentz resonance in the permittivity of the semiconductor component and examined the coupling of the quantum well with the plasmon polaritons. Depending on their spectral overlap and the gain assumed for the quantum well, we predicted characteristic Fano resonances in the pumpinduced transmission change. For spectral coincidence and moderate quantum well gain we expect a pumping-induced reduction of transmission and for

very strong quantum well gain we expect a net gain through the metamaterial [32].

In measurements of the pump-induced transmission change  $\Delta T/T$  through rolled-up metamaterials as shown in Figure 5 we indeed found characteristic Fano resonances, as depicted in Figure 5(d) [31]. The transmission enhancement  $\Delta T/T$  (squares) is plotted against the photon energy of the transmitted light. The measured data can be fitted by applying a Fano resonance model (solid lines) assuming a Fano type resonance interaction between the quantum well resonance and the surface plasmon polariton resonance mediated via the embedded grating. The pumping-induced reduction in the transmission reflects the moderate gain of the GaAs quantum well used in these structures. In the next step it is a very interesting question, if optimization of the coupling and maximization of the quantum well gain might enable net gain through these structures.

## 7. Rolled-Up Metamaterials for the Terahertz Regime

Instead of using the walls of rolled-up structures as metamaterials for optical frequencies, as discussed above, an alternative approach is to use the entire rolled-up structures as a unit cell of a metamaterial. Prinz and coworkers showed that rolled-up nanostructures also allow the experimental realization of metamaterials with strong chiral properties in the Terahertz regime [34]. An array of (In)GaAs/GaAs/Ti/Au microhelices of 11  $\mu\text{m}$  diameter and 52–53 degree helix angle is shown in Figure 6(a). For the preparation of such helices with well defined helix angle, Prinz and coworkers utilized the strong preferential rolling direction of self-rolling layers in the InGaAs system. A strained mesa, which is aligned to one of the  $\langle 100 \rangle$  rolling directions, rolls up into a tube while a strained mesa, which is canted with respect to the rolling direction, rolls up into a helix with helix angle given by the canting angle of the mesa. In polarization resolved transmission measurements Prinz and coworkers found circular dichroism and polarization rotation around 2 THz for the chiral metamaterial shown in Figure 6(a) in agreement with analytical modeling [34]. Figure 6(b) shows a THz metamaterial, which was developed in our group and is based on an array of rolled-up InGaAs/GaAs/Cr microtubes. As schematically illustrated at the bottom right, these structures exhibit slightly more than one rotation and resemble an LC circuit in analogy to the concept of a split ring resonator [3]. In [33] we investigated this type of metamaterial theoretically and found magnetic responses, which can be tuned from a few THz to a few ten THz depending on the number of rotations. Figures 7(a) and 7(b) illustrate the simulation setup. We could show that arrays of gold/(In)GaAs microrolls with slightly more than one winding (see Figure 7(a)) exhibit a negative permeability in the Terahertz regime. Figure 7(c) depicts the transmission spectra of arrays of microrolls with varying winding numbers of  $n = 1.00, 1.02, 1.05$ , and  $1.10$ . Well pronounced resonances are found with frequencies in the Terahertz regime that can be tailored by the winding number. The resonance frequency can be well modeled with

a simple Lorentz-oscillator model. The (In)GaAs in the overlap area is sandwiched between two metal layers that form a capacitance  $C$ . The inductivity  $L$  of the microroll can be approximated by the inductivity of a ring coil with a single winding. The resonance frequency  $f_0 = 1/\sqrt{LC}$  can then be calculated in good agreement with the simulation results (cf. vertical lines in Figure 7(c)). Retrieving the real and imaginary parts of the effective permeability of the array with the parameter retrieval method by Smith et al. [39] reveals that its real part becomes negative near the resonance. This is exemplarily shown for the array with the winding number  $n = 1.05$  (Figure 7(d)).

## 8. Conclusion

In conclusion we reviewed pioneering works for the fabrication and utilization of metamaterials based on self-rolling strained layers including three-dimensional optical metamaterials like broadband rolled-up hyperlenses, rolled-up fishnet metamaterials, and optically active devices containing semiconductor quantum wells as well as THz metamaterials exhibiting circular dichroism and negative permeability. These works demonstrate that the concept of rolled-up metamaterials is a powerful and unique tool to produce three-dimensional metamaterials, optionally with integrated semiconductor quantum emitters, from two-dimensional metamaterial layers. Such robust three-dimensional systems are interesting, for example, for the investigation of the Purcell effect in hyperbolic media [40–42], for gain experiments on stacked plasmonic elements interleaved with quantum emitters [48], or for the realization of polarizers based on stacks of plasmonic structures [49].

## Acknowledgments

The authors thank Markus Bröll and Detlef Heitmann for many fruitful discussions on rolled-up metamaterials. They also thank David Sonnenberg, Andrea Stemmann, Christian Heyn, and Wolfgang Hansen for the growth of the molecular beam epitaxy samples and Yulia Stark, Daniel Stickler, and Hans-Peter Oepen for focused ion beam preparation. The authors acknowledge financial support by the Deutsche Forschungsgemeinschaft via SFB508, SFB668, GK1286 and financial support by the city of Hamburg via LExI “Nanospintronics”.

## References

- [1] H. O. Moser and C. Rockstuhl, “3D THz metamaterials from micro/nanomanufacturing,” *Laser and Photonics Reviews*, vol. 6, no. 2, pp. 219–244, 2012.
- [2] C. M. Soukoulis and M. Wegener, “Past achievements and future challenges in the development of three-dimensional photonic metamaterials,” *Nature Photonics*, vol. 5, article 523, 2011.
- [3] J. B. Pendry, A. J. Holden, D. J. Robbins, and W. J. Stewart, “Magnetism from conductors and enhanced nonlinear phenomena,” *IEEE Transactions on Microwave Theory and Techniques*, vol. 47, no. 11, pp. 2075–2084, 1999.

- [4] R. A. Shelby, D. R. Smith, and S. Schultz, "Experimental verification of a negative index of refraction," *Science*, vol. 292, no. 5514, pp. 77–79, 2001.
- [5] A. A. Houck, J. B. Brock, and I. L. Chuang, "Experimental observations of a left-handed material that obeys Snell's law," *Physical Review Letters*, vol. 90, no. 13, Article ID 137401, 4 pages, 2003.
- [6] D. Schurig, J. J. Mock, B. J. Justice et al., "Metamaterial electromagnetic cloak at microwave frequencies," *Science*, vol. 314, no. 5801, pp. 977–980, 2006.
- [7] N. Liu, H. Guo, L. Fu, S. Kaiser, H. Schweizer, and H. Giessen, "Three-dimensional photonic metamaterials at optical frequencies," *Nature Materials*, vol. 7, no. 1, pp. 31–37, 2008.
- [8] J. Valentine, S. Zhang, T. Zentgraf et al., "Three-dimensional optical metamaterial with a negative refractive index," *Nature*, vol. 455, no. 7211, pp. 376–379, 2008.
- [9] J. Rho, Z. Ye, Y. Xiong et al., "Spherical hyperlens for two-dimensional sub-diffractional imaging at visible frequencies," *Nature Communications*, vol. 1, no. 9, article 143, 2010.
- [10] Z. Liu, H. Lee, Y. Xiong, C. Sun, and X. Zhang, "Far-field optical hyperlens magnifying sub-diffraction-limited objects," *Science*, vol. 315, no. 5819, p. 1686, 2007.
- [11] J. K. Gansel, M. Thiel, M. S. Rill et al., "Gold helix photonic metamaterial as broadband circular polarizer," *Science*, vol. 325, no. 5947, pp. 1513–1515, 2009.
- [12] J. Yao, Z. Liu, Y. Liu et al., "Optical negative refraction in bulk metamaterials of nanowires," *Science*, vol. 321, no. 5891, p. 930, 2008.
- [13] N. Gibbons, J. J. Baumberg, C. L. Bower, M. Kolle, and U. Steiner, "Scalable cylindrical metallodielectric metamaterials," *Advanced Materials*, vol. 21, no. 38-39, pp. 3933–3936, 2009.
- [14] V. Ya Prinz, V. A. Seleznev, and A. K. Gutakovskiy, "Self-formed InGaAs/GaAs Nanotubes: Concept, Fabrication, Properties," in *Proceedings of the 25th International Conference on the Physics of Semiconductors*, Jerusalem, Israel, 1998.
- [15] V. Y. Prinz, V. A. Seleznev, A. K. Gutakovskiy et al., "Free-standing and overgrown InGaAs/GaAs nanotubes, nano-helices and their arrays," *Physica E*, vol. 6, no. 1, pp. 828–831, 2000.
- [16] S. V. Golod, V. Y. Prinz, V. I. Mashanov, and A. K. Gutakovskiy, "Fabrication of conducting GeSi/Si micro- and nanotubes and helical microcoils," *Semiconductor Science and Technology*, vol. 16, no. 3, pp. 181–185, 2001.
- [17] O. Schumacher, S. Mendach, H. Welsch, A. Schramm, C. Heyn, and W. Hansen, "Lithographically defined metal-semiconductor-hybrid nanoscrolls," *Applied Physics Letters*, vol. 86, no. 14, Article ID 143109, 3 pages, 2005.
- [18] C. Deneke, W. Sigle, U. Eigenthaler, P. A. Van Aken, G. Schütz, and O. G. Schmidt, "Interfaces in semiconductor/metal radial superlattices," *Applied Physics Letters*, vol. 90, no. 26, Article ID 263107, 3 pages, 2007.
- [19] Y. Mei, G. Huang, A. A. Solovov et al., "Versatile approach for integrative and functionalized tubes by strain engineering of nanomembranes on polymers," *Advanced Materials*, vol. 20, no. 21, pp. 4085–4090, 2008.
- [20] F. Balhorn, S. Mansfeld, A. Krohn et al., "Spin-wave interference in three-dimensional rolled-up ferromagnetic microtubes," *Physical Review Letters*, vol. 104, no. 3, Article ID 037205, 4 pages, 2010.
- [21] F. M. Huang, J. K. Sinha, N. Gibbons, P. N. Bartlett, and J. J. Baumberg, "Direct assembly of three-dimensional mesh plasmonic rolls," *Applied Physics Letters*, vol. 100, no. 19, Article ID 193107, 4 pages, 2012.
- [22] O. G. Schmidt and K. Eberl, "Thin solid films roll up into nanotubes," *Nature*, vol. 410, article 168, 2001.
- [23] E. J. Smith, Z. Liu, Y. Mei, and O. G. Schmidt, "Combined surface plasmon and classical waveguiding through metamaterial fiber design," *Nano Letters*, vol. 10, no. 1, pp. 1–5, 2010.
- [24] E. J. Smith, Z. Liu, Y. F. Mei, and O. G. Schmidt, "System investigation of a rolled-up metamaterial optical hyperlens structure," *Applied Physics Letters*, vol. 95, no. 8, Article ID 083104, 3 pages, 2009.
- [25] E. J. Smith, Z. Liu, Y. F. Mei, and O. G. Schmidt, "Erratum: 'System investigation of a rolled-up metamaterial optical hyperlens structure' [ Appl. Phys. Lett. 95, 083104 (2009) ]," *Applied Physics Letters*, vol. 96, no. 1, Article ID 019902, 2 pages, 2010.
- [26] S. Schwaiger, M. Bröll, A. Krohn et al., "Rolled-up three-dimensional metamaterials with a tunable plasma frequency in the visible regime," *Physical Review Letters*, vol. 102, no. 16, Article ID 163903, 4 pages, 2009.
- [27] S. Schwaiger, A. Rottler, M. Bröll et al., "Broadband operation of rolled-up hyperlenses," *Physical Review B*, vol. 85, no. 23, Article ID 235309, 9 pages, 2012.
- [28] J. Kerbst, S. Schwaiger, A. Rottler et al., "Enhanced transmission in rolled-up hyperlenses utilizing Fabry-Pérot resonances," *Applied Physics Letters*, vol. 99, no. 19, Article ID 191905, 3 pages, 2011.
- [29] A. Rottler, M. Harland, M. Bröll et al., "Rolled-up nanotechnology for the fabrication of three-dimensional fishnet-type GaAs-metal metamaterials with negative refractive index at near-infrared frequencies," *Applied Physics Letters*, vol. 100, no. 15, Article ID 151104, 4 pages, 2012.
- [30] S. Schwaiger, M. Klingbeil, J. Kerbst et al., "Gain in three-dimensional metamaterials utilizing semiconductor quantum structures," *Physical Review B*, vol. 84, no. 15, Article ID 155325, 5 pages, 2011.
- [31] S. Schwaiger, A. Koitmäe, L. S. Fohrmann et al., "Fano resonances in optically active rolled-up three dimensional metamaterials," unpublished.
- [32] A. Rottler, S. Schwaiger, A. Koitmäe, D. Heitmann, and S. Mendach, "Transmission enhancement in three-dimensional rolled-up plasmonic metamaterials containing optically active quantum wells," *Journal of the Optical Society of America B*, vol. 28, no. 10, pp. 2402–2407, 2011.
- [33] A. Rottler, M. Bröll, N. Gerken, D. Heitmann, and S. Mendach, "Terahertz metamaterials based on arrays of rolled-up gold/(In)GaAs tubes," *Optics Letters*, vol. 36, no. 24, pp. 4797–4799, 2011.
- [34] I. V. Semchenko, S. A. Khakhomov, E. V. Naumova, V. Y. Prinz, S. V. Golod, and V. V. Kubarev, "Study of the properties of artificial anisotropic structures with high chirality," *Crystallography Reports*, vol. 56, no. 3, pp. 366–373, 2011.
- [35] B. Wood, J. B. Pendry, and D. P. Tsai, "Directed subwavelength imaging using a layered metal-dielectric system," *Physical Review B*, vol. 74, no. 11, Article ID 115116, 8 pages, 2006.
- [36] S. A. Ramakrishna and J. B. Pendry, "Removal of absorption and increase in resolution in a near-field lens via optical gain," *Physical Review B*, vol. 67, no. 20, Article ID 201101, 4 pages, 2003.
- [37] D. R. Smith, D. Schurig, M. Rosenbluth, S. Schultz, S. A. Ramakrishna, and J. B. Pendry, "Limitations on subdiffraction imaging with a negative refractive index slab," *Applied Physics Letters*, vol. 82, no. 10, pp. 1506–1508, 2003.

- [38] Z. Jacob, L. V. Alekseyev, and E. Narimanov, "Optical hyperlens: far-field imaging beyond the diffraction limit," *Optics Express*, vol. 14, no. 18, pp. 8247–8256, 2006.
- [39] D. R. Smith, D. C. Vier, T. Koschny, and C. M. Soukoulis, "Electromagnetic parameter retrieval from inhomogeneous metamaterials," *Physical Review E*, vol. 71, no. 3, Article ID 036617, 11 pages, 2005.
- [40] M. A. Noginov, H. Li, Y. A. Barnakov et al., "Controlling spontaneous emission with metamaterials," *Optics Letters*, vol. 35, no. 11, pp. 1863–1865, 2010.
- [41] T. Tumkur, G. Zhu, P. Black, Y. A. Barnakov, C. E. Bonner, and M. A. Noginov, "Control of spontaneous emission in a volume of functionalized hyperbolic metamaterial," *Applied Physics Letters*, vol. 99, no. 15, Article ID 151115, 3 pages, 2011.
- [42] H. N. S. Krishnamoorthy, Z. Jacob, E. Narimanov, I. Kretzschmar, and V. M. Menon, "Topological transitions in metamaterials," *Science*, vol. 336, no. 6078, pp. 205–209, 2012.
- [43] S. Xiao, V. P. Drachev, A. V. Kildishev et al., "Loss-free and active optical negative-index metamaterials," *Nature*, vol. 466, no. 7307, pp. 735–738, 2010.
- [44] E. Plum, V. A. Fedotov, P. Kuo, D. P. Tsai, and N. I. Zheludev, "Towards the lasing spaser: controlling metamaterial optical response with semiconductor quantum dots," *Optics Express*, vol. 17, no. 10, pp. 8548–8551, 2009.
- [45] K. Tanaka, E. Plum, J. Y. Ou, T. Uchino, and N. I. Zheludev, "Multifold enhancement of quantum dot luminescence in plasmonic metamaterials," *Physical Review Letters*, vol. 105, no. 22, Article ID 227403, 4 pages, 2010.
- [46] N. Meinzer, M. Ruther, S. Linden et al., "Arrays of Ag split-ring resonators coupled to InGaAs single-quantum-well gain," *Optics Express*, vol. 18, no. 23, pp. 24140–24151, 2010.
- [47] N. Meinzer, M. König, M. Ruther et al., "Distance-dependence of the coupling between split-ring resonators and single-quantum-well gain," *Applied Physics Letters*, vol. 99, no. 11, Article ID 111104, 3 pages, 2011.
- [48] D. J. Bergman and M. I. Stockman, "Surface plasmon amplification by stimulated emission of radiation: quantum generation of coherent surface plasmons in nanosystems," *Physical Review Letters*, vol. 90, no. 2, Article ID 027402, 4 pages, 2003.
- [49] Y. Zhao, M. A. Belkin, and A. Alù, "Twisted optical metamaterials for planarized ultrathin broadband circular polarizers," *Nature Communications*, vol. 3, article 870, 2012.



## Research Article

# Conditions of Perfect Imaging in Negative Refraction Materials with Gain

Haowen Liang,<sup>1</sup> Yifeng Shao,<sup>1</sup> Jianying Zhou,<sup>1</sup> Boris A. Malomed,<sup>2</sup> and Gershon Kurizki<sup>3</sup>

<sup>1</sup> State Key Laboratory of Optoelectronic Materials and Technologies, Sun Yat-sen University, Guangzhou 510275, China

<sup>2</sup> Department of Physical Electronics, School of Electrical Engineering, Faculty of Engineering, Tel Aviv University, 69978 Tel Aviv, Israel

<sup>3</sup> Chemical Physics Department, Weizmann Institute of Science, 76100 Rehovot, Israel

Correspondence should be addressed to Gershon Kurizki, gershon.kurizki@weizmann.ac.il

Received 29 June 2012; Accepted 3 October 2012

Academic Editor: Alexandra E. Boltasseva

Copyright © 2012 Haowen Liang et al. This is an open access article distributed under the Creative Commons Attribution License, which permits unrestricted use, distribution, and reproduction in any medium, provided the original work is properly cited.

Light propagation is analyzed in a negative refraction material (NRM) with gain achieved by pumping. An inherent spatial “walk-off” between the directions of phase propagation and energy transfer is known to exist in lossy NRMs. Here, the analysis is extended to the case where the NRM acts as an active material under various pumping conditions. It is shown that the condition for perfect imaging is only possible for specific wavelengths under special excitation conditions. Under excessive gain, the optical imaging can no longer be perfect.

## 1. Introduction

Negative refraction is known to offer a wide range of potential applications [1–4]. However, losses, which are an inherent feature of the negative refraction, present a major impediment to the performance of NRMs [5–9]. To overcome these problems, NRMs with gain were proposed to compensate the losses, even to turn the materials into amplified systems. Nevertheless, it is often stated that the gain will destroy the negative refraction due to causality considerations [10], although the statement was disputed by a theory demonstrating that negative refraction may be preserved in a limited spectral region [11, 12].

Common methods to introduce gain in NRMs include optical parametric amplification (OPA) [13] and externally pumped gain materials [14–18]. Optical imaging needs to collect both propagating and evanescent waves. However, only within a limited range may the wave vectors receive gain from OPA because of the strict phase-matching condition, the application of OPA to achieve perfect imaging in NRMs is not possible.

In this paper, we demonstrate that, under the action of the pumping gain, lossless and amplified light propagation may occur in a special spectral window of the NRM.

The propagation behavior is shown to be closely related to the dispersion and pumping configuration. Propagation in NRMs is also examined in different pumping configurations.

**1.1. Spatial “Walk-Off” in Lossy NRMs.** Light incidents from free space onto a homogeneous, isotropic, lossy NRM, of permittivity  $\epsilon_r(\omega) = \epsilon' + i\epsilon''$  and permeability  $\mu_r(\omega) = \mu' + i\mu''$ , were studied in detail [8]. The complex effective refractive index is then defined as  $n^2(\omega) = \epsilon_r(\omega)\mu_r(\omega)$  or  $n(\omega) = n' + in''$ . In free space, the incident wave vector  $\vec{k}$  is real, while in the lossy NRM, the wave vector  $\vec{q} = q_x\hat{x} + (q'_z + iq''_z)\hat{z}$  is complex. At a given optical frequency  $\omega$ , this implies that  $\vec{q}^2 = n^2(\omega)k^2$  for both the propagating wave ( $|q_x| < |n(\omega)k|$ ) and the evanescent one ( $|q_x| > |n(\omega)k|$ ).

To analyze light propagation in the NRM, the phase and group velocities are expressed as  $\vec{v}_p = (\omega/|\vec{q}|^2)\vec{q}$  and  $\vec{v}_g = \nabla\omega(\vec{q}) = ((A - iB)/(A^2 + B^2))\vec{q}$ , where  $A = d[\text{Re}(n^2(\omega))k^2]/d\omega$  and  $B = d[\text{Im}(n^2(\omega))k^2]/d\omega$  are determined by the NRM dispersion. The energy propagation is approximately determined by the group velocity under the assumption of low losses [19–21]. The Poynting vector can also be used to define the energy propagation.

For complex vectors  $\vec{v}_p$  and  $\vec{v}_g$ , the direction of the phase propagation and energy transfer in the wave packet are determined by their real parts [22]:

$$\vec{v}_p = \frac{\omega}{|\vec{q}|^2} (q_x \hat{x} + q_z' \hat{z}), \quad (1)$$

$$\vec{v}_g = \frac{A}{A^2 + B^2} (q_x \hat{x} + q_z' \hat{z}) + \frac{B}{A^2 + B^2} q_z'' \hat{z}. \quad (2)$$

In an ideal NRM, where the refractive index is negative without losses, the phase velocity and group velocity are strictly antiparallel [1, 19]. However, (1) and (2) show that the group velocity is no longer antiparallel because of the contribution of the last term in (2). This *spatial “walk-off”*, that is, the noncollinearity between the phase propagation and the energy transfer, becomes obvious in a homogenous, isotropic, lossy NRM. The angle between the phase velocity and the group velocity is

$$\delta = \theta_p + \theta_g, \quad (3)$$

with the “walk-off” angle defined as  $180^\circ - \delta$ .

The propagation behavior is discussed here for both propagating and evanescent waves. The dispersive curve is described as the Lorentz model, with  $\epsilon_{r\text{host}}(\omega) = 1 + \omega_p^2/(\omega_p^2 - \omega^2 - i\gamma_1\omega)$ ,  $\mu_{r\text{host}}(\omega) = 1 + \omega_p^2/(\omega_p^2 - \omega^2 - i\gamma_2\omega)$ , and  $\omega_p = 100 \times 10^{12} \text{ s}^{-1}$ ,  $\gamma_1 = 3 \times 10^{12} \text{ s}^{-1}$ ,  $\gamma_2 = 5 \times 10^{12} \text{ s}^{-1}$  in Figure 1(a) for the real and imaginary parts of the refractive index. For a typical propagating wave with  $|q_x| < |q|$ , the size of the “walk-off” is numerically simulated as shown in Figure 1(b). The analysis of the “walk-off” can be extended to evanescent waves with  $|q_x| > |q|$ , where it is found that the “walk-off” dramatically increases with  $|q_x|$ , also shown in Figure 1(b).

For perfect focusing, the “walk-off” appearing at different  $|q_x|$  should be suppressed. It was shown that this goal can be achieved by a pumping gain scheme [18]. Here, we show, in a pumped four-level model of signal amplification, that the realization of perfect imaging is possible only for a specific wavelength under strict pumping condition.

## 2. NRMs with Pumping Gain

Four-level systems represent conventional gain media. The intensity of light in a chosen spectral interval can be amplified in NRMs by introducing an extra term in the electrical field susceptibility [14, 17, 23]. It is assumed here that the gain medium is pumped in the linear regime, and no gain saturation arises. Accordingly, the population of the ground level  $N_1$  (which can be considered as the population of the gain medium) is much larger than in the other three levels as per the usual pumping condition. With the definition of polarization  $\vec{P} = \chi_{\text{ex}} \epsilon_0 \vec{E}$ , the permittivity, with the extra term in the susceptibility, is given by

$$\begin{aligned} \epsilon_r(\omega) &= \epsilon_{r\text{host}} + \chi_{\text{ex}} \\ &= 1 + \frac{\omega_p^2}{\omega_p^2 - \omega^2 - i\gamma_1\omega} - \frac{\sigma\Gamma_{\text{pump}}N_1\tau_{32}/\epsilon_0}{\omega_x^2 - \omega^2 - i\gamma_{\text{ex}}\omega}. \end{aligned} \quad (4)$$

As shown below, the last term of (4) is crucial to the performance of the gain-compensated NRMs. The components of the effective refractive index,  $n'$  and  $n''$ , are shown in Figure 2.

Whereas the optical losses in the NRM can be effectively compensated by pumping, as shown in Figure 2(b), an amplification of the input signal is achievable; the elimination of the “walk-off” depends on both the real and imaginary parts of the refractive index. The ideal case is the one with  $n' = -1$  and  $n'' = 0$ , giving rise to perfect imaging [1, 6]. However, as shown in Figure 2, this condition holds only at the optimal frequency where  $\omega = 121.28 \times 10^{12} \text{ s}^{-1}$  under appropriate pumping conditions.

Optical imaging with resolution above or below the diffraction limit depends on the system’s ability to recover the wavevector’s component for either propagating or evanescent waves. Figure 3(b) shows the size of the “walk-off” for different  $|q_x|$  with the appropriate pumping rate of  $0.21 \times 10^9 \text{ s}^{-1}$ . The propagating waves correspond to  $|q_x| < |q|$ , while the evanescent ones correspond to  $|q_x| > |q|$ . After introducing the pumping gain, a red shift is observed in the  $n'$  curve. At the optimal frequency ( $\omega = 121.28 \times 10^{12} \text{ s}^{-1}$ ) where  $n' = -1$ , the angles between the group and phase velocities are strictly antiparallel for all  $|q_x|$ . Because of the antiparallel directions of the energy transfer and phase propagation, the spatial “walk-off” is suppressed, so that the ability of directional transmission (for the propagating waves) and perfect focusing (for evanescent waves in the near-field) will be preserved. Thus, the pumping can effectively cancel the losses only in a limited spectral region, under appropriate pumping conditions. This conclusion is in agreement with those reported in [11, 12].

By contrast, the propagation in an active NRM under excessive pumping exhibits a peculiar behavior. Figure 3(c) shows the “walk-off” angles at different  $|q_x|$  for excessive pumping rate (here  $\Gamma_{\text{pump}} = 0.48 \times 10^9 \text{ s}^{-1}$ ) at the frequency where  $n' = -1$  (here  $\omega = 121.44 \times 10^{12} \text{ s}^{-1}$ ). The  $\delta$  angles are then larger than  $180^\circ$ , indicating that the “walk-off” reappears, with the respective angles  $180^\circ + \delta$ . The “walk-off” becomes more significant at larger  $|q_x|$ . It also shows that  $\delta$  increases dramatically with the increase of  $|q_x|$  for the evanescent wave with  $|q_x| > |q|$ . Hence, the perfect focus for the near-field component is impossible under excessive pumping. Notice that because of the red shift in  $n'(\omega)$ , the “walk-off” is suppressed at the frequency of  $121.20 \times 10^{12} \text{ s}^{-1}$ , where  $n'(\omega) \approx -1.3$  (the red arrow in Figure 3(c)). However, perfect lensing requires  $n'(\omega) = -1$  [1, 6], hence the perfect focus cannot be obtained under excessive pumping.

In order to achieve perfect focusing, the pumping rates should be reduced and the pumping central frequencies should be blue-shifted, as shown in Figure 3(c). Light with all values of  $|q_x|$  can then perfectly focus through the slab.

## 3. Conclusions

To conclude, we have analyzed the effect of gain on the negative refraction in NRMs. In a lossy NRM, even though it is isotropic and homogeneous, the group and phase velocities

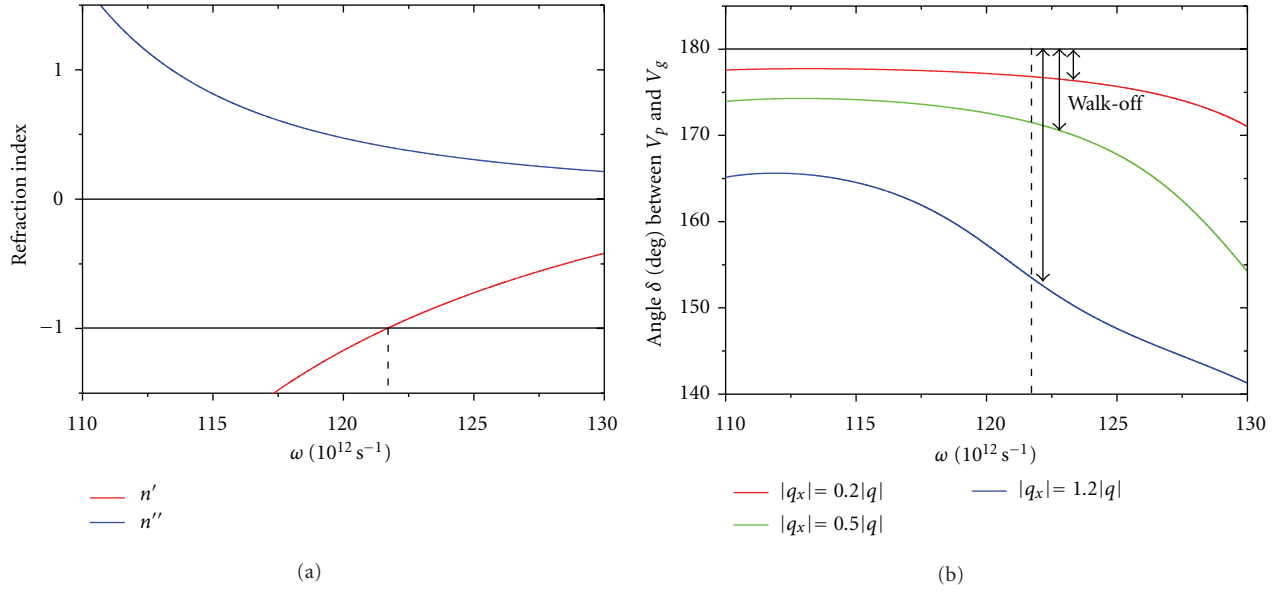


FIGURE 1: (a) The refractive index of the NRM slab. The red and blue lines show the real and imaginary parts of the refractive index  $n(\omega)$ , respectively. The frequency is  $\omega = 121.67 \times 10^{12} \text{ s}^{-1}$ , where  $\epsilon_r(\omega) \approx \mu_r(\omega) \approx -1$  [15]. (b)  $\vec{v}_p$  and  $\vec{v}_g$  are not strictly antiparallel ( $\delta < 180^\circ$ ) in the lossy NRM slab, featuring the “walk-off” angle about  $3.2^\circ$  at  $|q_x| = 0.2|q|$ ,  $8.5^\circ$  at  $|q_x| = 0.5|q|$ , and  $26.4^\circ$  at  $|q_x| = 1.2|q|$ . The carrier frequency is  $\omega = 121.67 \times 10^{12} \text{ s}^{-1}$ .

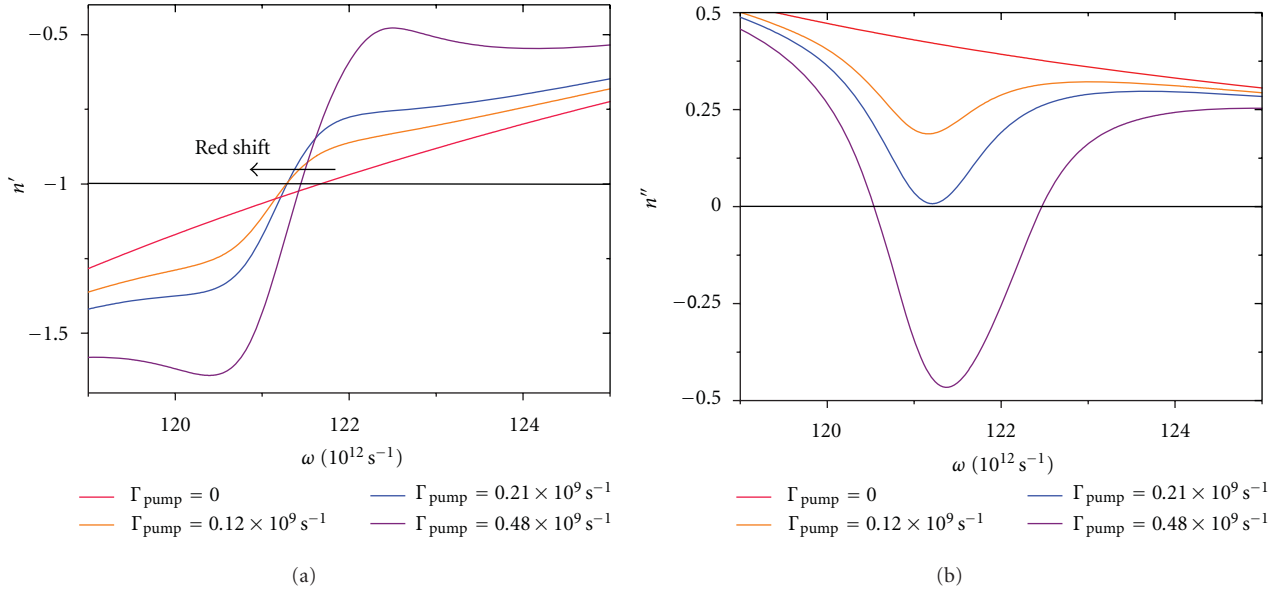


FIGURE 2: The parameters for the four-level system are chosen as  $\sigma = 10^{-4} \text{ C}^2/\text{kg}$  (C stands for Coulomb), which is the strength of the coupling between the gain material and the host NRM,  $\gamma_{\text{ex}} = 0.76 \times 10^{12} \text{ s}^{-1}$  is related to the linewidth of the gain medium,  $\omega_x = 121.6 \times 10^{12} \text{ s}^{-1}$  is the central pumping frequency, determined by the frequency difference between state 3 and state 2, at which  $n'(\omega) \approx -1$  is satisfied without the gain (see Figure 1(a)), and the decay time of the gain level 2 is  $\tau_{32} = 5 \times 10^{-12} \text{ s}$ . The value of the occupation density is set to be  $N_1 = 5 \times 10^{23} \text{ m}^{-3}$ . The pumping rates  $\Gamma_{\text{pump}}$  are assumed to be  $0.12 \times 10^9 \text{ s}^{-1}$  for insufficient pumping,  $0.21 \times 10^9 \text{ s}^{-1}$  for the appropriate pumping (to be discussed below), and  $0.48 \times 10^9 \text{ s}^{-1}$  for the excessive pumping, respectively. (a) The real part of the refractive index for different pumping amplitudes. A red shift of the frequency is observed at  $n' = -1$ . (b) The imaginary part of the refractive index for different pumping amplitudes. Loss-free windows (intervals of amplification) are revealed by the  $n''$  curves. Increasing the pumping rate may compensate the losses, or even turn the material into an active medium.



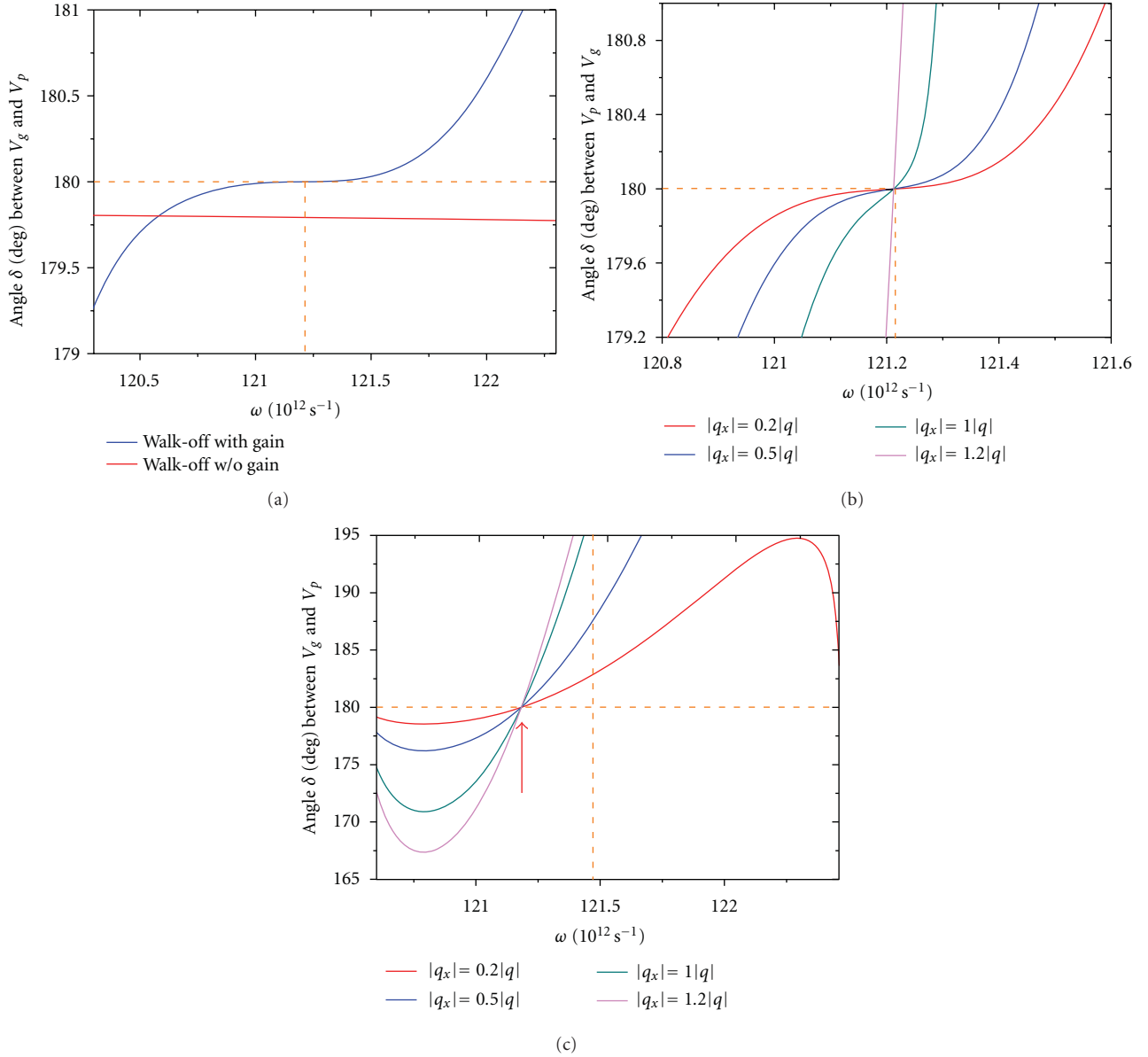


FIGURE 3: The “walk-off” angles as function of frequency  $\omega$  in an active (pumped) NRM. The dashed line in all the plots shows the frequencies at which  $n'(\omega) = -1$ . (a) The blue line is the spatial “walk-off” angle with the pumping rate of  $\Gamma_{\text{pump}} = 0.21 \times 10^9 \text{ s}^{-1}$  at  $|q_x| = 0.01|q|$ . Both losses and the “walk-off” within the gain window are precisely canceled. (b) The  $\delta$  angles obtained at the pumping rate of  $\Gamma_{\text{pump}} = 0.21 \times 10^9 \text{ s}^{-1}$ . The group velocities and phase velocities are strictly antiparallel in this case ( $\delta = 180^\circ$ ) at different  $|q_x|$  when  $n'(\omega) = -1$  (at  $\omega = 121.28 \times 10^{12} \text{ s}^{-1}$ ). (c) The  $\delta$  angles obtained at the pumping rate of  $\Gamma_{\text{pump}} = 0.48 \times 10^9 \text{ s}^{-1}$ . Even though at this pumping rate the NRM is turned into a light-amplifying medium, the spatial “walk-off” reappears and depends on the value of  $|q_x|$  when  $n'(\omega) = -1$ , which may lead to degradation of the optical performance of an NRM.

are not strictly antiparallel, yielding a spatial “walk-off”, which may restrict the applications of NRMs in a variety of fields. By introducing gain, losses can be effectively reduced, and light amplification can be realized within a narrow spectral range. Appropriately setting the gain to strictly cancel the losses, the “walk-off” for both propagating and evanescent waves can be effectively eliminated for all values of  $|q_x|$ , leading to an ideal NRM. However, for excessively pumped NRMs, the spatial “walk-off” reappears. Thus, the use of optical pumping to realize perfect imaging is restricted to a very narrow spectral region, under precisely defined

pumping conditions. An alternative method of overcoming NRM losses without signal distortion may involve self-induced transparency (SIT) solitons, which were predicted in metamaterials [24], in analogy with SIT in other resonantly absorbing structures [25, 26].

## Acknowledgments

This work is supported by The National Key Basic Research Special Foundation (G2012CB921904) and by the Chinese National Natural Science Foundation (10934011).

## References

- [1] J. B. Pendry, "Negative refraction makes a perfect lens," *Physical Review Letters*, vol. 85, no. 18, pp. 3966–3969, 2000.
- [2] R. A. Shelby, D. R. Smith, and S. Schultz, "Experimental verification of a negative index of refraction," *Science*, vol. 292, no. 5514, pp. 77–79, 2001.
- [3] K. L. Tsakmakidis, A. D. Boardman, and O. Hess, "'Trapped rainbow' storage of light in metamaterials," *Nature*, vol. 450, no. 7168, pp. 397–401, 2007.
- [4] H. G. Chen, C. T. Chan, and P. Sheng, "Transformation optics and metamaterials," *Nature Materials*, vol. 9, no. 5, pp. 387–396, 2010.
- [5] R. W. Ziolkowski and E. Heyman, "Wave propagation in media having negative permittivity and permeability," *Physical Review E*, vol. 64, no. 5, Article ID 056625, 2001.
- [6] D. R. Smith, D. Schurig, M. Rosenbluth, S. Schultz, S. A. Ramakrishna, and J. B. Pendry, "Limitations on subdiffraction imaging with a negative refractive index slab," *Applied Physics Letters*, vol. 82, no. 10, pp. 1506–1508, 2003.
- [7] A. G. Ramm, "Does negative refraction make a perfect lens?" *Physics Letters A*, vol. 372, no. 43, pp. 6518–6520, 2008.
- [8] Y.-J. Jen, A. Lakhtakia, C.-W. Yu, and C.-T. Lin, "Negative refraction in a uniaxial absorbent dielectric material," *European Journal of Physics*, vol. 30, no. 6, pp. 1381–1390, 2009.
- [9] W. H. Wee and J. B. Pendry, "Looking beyond the perfect lens," *New Journal of Physics*, vol. 12, Article ID 053018, 2010.
- [10] M. I. Stockman, "Criterion for negative refraction with low optical losses from a fundamental principle of causality," *Physical Review Letters*, vol. 98, no. 17, Article ID 177404, 2007.
- [11] P. Kinsler and M. W. McCall, "Causality-based criteria for a negative refractive index must be used with care," *Physical Review Letters*, vol. 101, no. 16, Article ID 167401, 2008.
- [12] K. J. Webb and L. Thylén, "Perfect-lens-material condition from adjacent absorptive and gain resonances," *Optics Letters*, vol. 33, no. 7, pp. 747–749, 2008.
- [13] A. K. Popov and V. M. Shalaev, "Compensating losses in negative-index metamaterials by optical parametric amplification," *Optics Letters*, vol. 31, no. 14, pp. 2169–2171, 2006.
- [14] P. P. Orth, J. Evers, and C. H. Keitel, "Lossless negative refraction in an active dense gas of atoms," 2007, <http://arxiv.org/abs/0711.0303>.
- [15] A. Fang, T. Koschny, M. Wegener, and C. M. Soukoulis, "Self-consistent calculation of metamaterials with gain," *Physical Review B*, vol. 79, no. 24, Article ID 241104, 2009.
- [16] Y. Sivan, S. Xiao, U. K. Chettiar, A. V. Kildishev, and V. M. Shalaev, "Frequency-domain simulations of a negative-index material with embedded gain," *Optics Express*, vol. 17, no. 26, pp. 24060–24074, 2009.
- [17] S. Wuestner, A. Pusch, K. L. Tsakmakidis, J. M. Hamm, and O. Hess, "Overcoming losses with gain in a negative refractive index metamaterial," *Physical Review Letters*, vol. 105, no. 12, Article ID 127401, 2010.
- [18] S. Xiao, V. P. Drachev, A. V. Kildishev et al., "Loss-free and active optical negative-index metamaterials," *Nature*, vol. 466, no. 7307, pp. 735–738, 2010.
- [19] M. W. McCall, "What is negative refraction?" *Journal of Modern Optics*, vol. 56, no. 16, pp. 1727–1740, 2009.
- [20] V. Gerasik and M. Stastna, "Complex group velocity and energy transport in absorbing media," *Physical Review E*, vol. 81, no. 5, Article ID 056602, 2010.
- [21] L. Muschietti and C. T. Dum, "Real group velocity in a medium with dissipation," *Physics of Fluids B*, vol. 5, no. 5, pp. 1383–1397, 1993.
- [22] M. Born and E. Wolf, *Principals of Optics*, Cambridge University Press, 7th edition, 1999.
- [23] A. A. Goyadinov, V. A. Podolskiy, and M. A. Noginov, "Active metamaterials: sign of refractive index and gain-assisted dispersion management," *Applied Physics Letters*, vol. 91, no. 19, Article ID 191103, 2007.
- [24] J. Zeng, J. Zhou, G. Kurizki, and T. Opatrny, "Backward self-induced transparency in metamaterials," *Physical Review A*, vol. 80, no. 6, Article ID 061806, 2009.
- [25] M. Blaauboer, B. A. Malomed, and G. Kurizki, "Spatiotemporally localized multidimensional solitons in self-induced transparency media," *Physical Review Letters*, vol. 84, no. 9, pp. 1906–1909, 2000.
- [26] T. Opatrny, B. A. Malomed, and G. Kurizki, "Dark and bright solitons in resonantly absorbing gratings," *Physical Review E*, vol. 60, no. 5, pp. 6137–6149, 1999.

## Research Article

# Plasmonic Nanostructure for Enhanced Light Absorption in Ultrathin Silicon Solar Cells

Jinna He,<sup>1,2</sup> Chunzhen Fan,<sup>1</sup> Junqiao Wang,<sup>1</sup> Yongguang Cheng,<sup>1</sup> Pei Ding,<sup>3</sup> and Erjun Liang<sup>1</sup>

<sup>1</sup> School of Physical Science and Engineering and Key Laboratory of Material Physics of The Ministry of Education of China, Zhengzhou University, Zhengzhou 450052, China

<sup>2</sup> Electric and information Engineering College, Pingdingshan University, Henan Province, Pingdingshan 467000, China

<sup>3</sup> Department of Mathematics and Physics, Zhengzhou Institute of Aeronautical Industry Management, Zhengzhou 450015, China

Correspondence should be addressed to Erjun Liang, ejliang@zzu.edu.cn

Received 9 July 2012; Revised 18 September 2012; Accepted 24 September 2012

Academic Editor: Pavel A. Belov

Copyright © 2012 Jinna He et al. This is an open access article distributed under the Creative Commons Attribution License, which permits unrestricted use, distribution, and reproduction in any medium, provided the original work is properly cited.

The performances of thin film solar cells are considerably limited by the low light absorption. Plasmonic nanostructures have been introduced in the thin film solar cells as a possible solution around this issue in recent years. Here, we propose a solar cell design, in which an ultrathin Si film covered by a periodic array of Ag strips is placed on a metallic nanograting substrate. The simulation results demonstrate that the designed structure gives rise to 170% light absorption enhancement over the full solar spectrum with respect to the bare Si thin film. The excited multiple resonant modes, including optical waveguide modes within the Si layer, localized surface plasmon resonance (LSPR) of Ag stripes, and surface plasmon polaritons (SPP) arising from the bottom grating, and the coupling effect between LSPR and SPP modes through an optimization of the array periods are considered to contribute to the significant absorption enhancement. This plasmonic solar cell design paves a promising way to increase light absorption for thin film solar cell applications.

## 1. Introduction

The low conversion efficiencies and high production costs have been the major difficulties facing photovoltaic technology. For solar cells based on bulk crystalline silicon, around 40% of a solar cell module's price comes from the silicon (Si) materials and its processing costs. To reduce the costs, thin film solar cells with an active layer thickness of about 1 to 2  $\mu\text{m}$  are desired. Thin film solar cells with the thickness of material film smaller than the carrier diffusion length can also reduce carrier recombination and improve carrier collection efficiency in bulk recombination-dominated semiconductors. In addition, a significant reduction of the active materials enables some scarce semiconductor materials such as Te and In to be used in a large scale. However, the performance of all thin film solar cells is limited by the poor light absorption due to the reduced absorber thickness. For example, the indirect band gap semiconductor Si material has poor absorption to near-band gap light, where the absorption length is larger than 300  $\mu\text{m}$ . Therefore, light

trapping schemes are essential for the design of ultrathin solar cells with improved absorption.

In the past years, many light trapping techniques have been investigated for solar cell applications. A typical example is the use of micron-size pyramidal surface textures [1]. However, such textures are not suitable for thin film solar cells due to large texturing size with respect to the film thickness. Recently, the concept of plasmonic solar cells, that is, the combination of plasmonics and photovoltaic fields, has been proposed to improve light absorption [2–4]. Metallic nanostructures engineered within the solar cell geometry enable concentrating and folding light into the ultrathin active layer, and thereby increase light absorption. For example, Au or Ag nanoparticles placed on the top surface of solar cells can act as scattering elements to couple light into the absorber layer through effectively increasing the optical path length [5–8]. Over 30% enhancement in photocurrent has been demonstrated experimentally in a 1.25  $\mu\text{m}$  thick silicon-on-insulator by utilizing this approach [8]. The dependences of incoupling efficiency on

nanoparticle shape and size have also been discussed in detail [9]. Furthermore, the strong near fields resulting from the LSPRs excitations of metallic strips on the top of the active layer can effectively trap light into the absorber layer and lead to an enhancement of about 43% in short circuit currents [10]. More recently, a kind of novel thin film solar cell design of introducing several metallic patterned back contacts has been investigated widely [11–15]. These patterned back contacts can couple the sunlight into SPP mode propagating along the metal/semiconductor interface and waveguide mode within the absorber layer, leading to about 30% broadband absorption enhancement over the solar spectrum when compared to the bared thin film cells [11].

Since the excitation of plasmon resonances can capture and trap the sunlight into the active layer and increase absorption strength, multiple plasmon resonances are desired for the thin film solar cell with superior performance. Previous designs of plasmonic solar cells are mostly based on placing one- or two-dimensional metallic nanoparticle arrays on the top or buried inside the active layer [5–8, 16–18], or introducing several metallic nanogratings, such as the nanohole, hexagonal or triangular structures [12, 19, 20] at the bottom of active layer as the patterned back contacts for improving light absorption. The common disadvantages associated with those efforts are that LSPR or SPP modes are excited individually only by utilizing the metallic nanoparticles or nanograting structures. In this work, we propose an ultrathin solar cell design, which consists of a periodic array of Ag strips on a silica-coated Si film supported by a metallic grating substrate, as shown in Figure 1. This design not only takes advantage of LSPR excited in metal strips on the top, but also can couple sunlight to multiple SPP modes at metal/semiconductor interface by the coupling of the bottom nanograting. Furthermore, the coupling effects between the LSPR and SPP modes can be achieved by tuning the array periods for further increasing light absorption inside the active layer. A remarkable absorption enhancement of about 170% with a broad period range is obtained over the full solar spectrum when compared with the case of metallic nanostructures absence (i.e., the bared thin film cells). Such an absorption enhancement is much higher than those reported previously for ultrathin Si solar cells based on metal nanostructures placed on the top or at the bottom [10, 11, 14, 16–20] where either LSPR modes or SPP modes are excited alternatively. Additionally, the proposed design with the ultrathin absorber layer can reduce the usage of the active materials significantly and decrease the production costs of solar cells. Moreover, the metallic stripes on the top surface can also act as surface electrodes, eliminating the involvement of common surface electrodes (e.g., ITO). Finally, the fabrication of such metal-semiconductor-metal nanograting structures is technically feasible by using some advance nanofabrication methods [21, 22].

## 2. Structure Design and Simulation Method

The proposed structure with the defined structural parameters is illustrated in Figures 1(a) and 1(b), which consists

from the top surface to the bottom of a periodic array of Ag strips, a dielectric spacer layer of SiO<sub>2</sub>, an absorber layer of Si, and an Ag nanograting substrate. The grooves of nanograting are filled with SiO<sub>2</sub>. The dielectric spacer layer can avoid the strong damping of LSPR in Ag stripes, which is responsible for enhanced light absorption inside absorber layer. Since a large spacer is very detrimental for high near-fields enhancement inside the active layer, a suitable thickness of 5 nm was selected here. In all our calculations, the thickness of Ag strips and the depth of nanograting are set to  $t = s = 40$  nm; the widths of the Ag strips and the grooves in nanograting are chosen to be  $w = 50$  nm and  $g = 150$  nm; the thickness of Si layer and the height of Ag nanograting are fixed at  $h_1 = 80$  nm and  $h_2 = 100$  nm, and the period is set to  $p = 300$  nm, respectively.

Numerical electromagnetic simulations were performed by the commercial finite element software of COMSOL Multiphysics 3.5. The periodic boundaries were employed to a unit cell for simulating an infinite array. Perfectly matched layers (PML) were applied in the propagation direction to eliminate the nonphysical reflections at domain boundaries. The whole structure was illuminated from the top surface at normal incidence with E-field along the metal stripes (TE wave) or H-field along the metal stripes (TM wave). The absorption inside the absorber layer for an incidence monochrome plane wave with certain wavelength was calculated by using

$$\text{Absorption} = \oint_s \vec{S}(\vec{r}, \lambda) \cdot d\vec{a}, \quad (1)$$

where  $\vec{S}(\vec{r}, \lambda)$  is the Poynting vector and  $s$  is the boundary of the analyzed active layer [11].

The absorption enhancement function ( $\Pi(\lambda)$ ) is defined as the ratio of the absorption inside the absorber layer combined with metal nanostructures to that without the metal nanostructures. The absorption efficiency for the thin film solar cell was obtained by calculating the ratio of light absorption power inside the Si layer to the incident light power. In our simulations, the absorber material is crystalline silicon and the dispersive optical properties (refractive index, absorption) of silver and crystalline silicon materials are from the experimentally obtained data [23, 24]. The SiO<sub>2</sub> permittivity is chosen to be 3.24 and the external dielectric environment is considered to be air. In addition, to match the solar spectrum to Si absorption, a wavelength range from 400 nm to 1000 nm was considered.

## 3. Results and Discussions

**3.1. Excitations of Multiple Absorption Enhancement Bands.** Figures 2(a) and 2(b) show the absorption efficiency spectra for the thin film solar cells with and without metal nanostructures, respectively. For the case of the bared Si film (Figure 2(a)), two absorption peaks are exhibited in the considered spectrum range. The enhanced magnetic fields inside the Si layer associated with the two absorption resonances reveal them originating from the Fabry-Perot (FP) cavity resonance [25], as the insets shown in Figure 2(a).

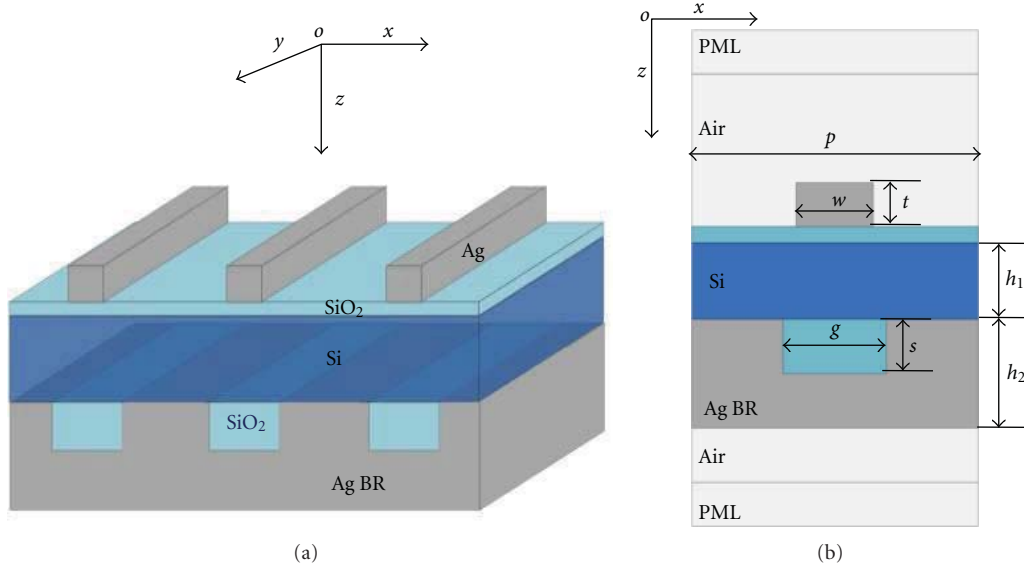


FIGURE 1: (a) Schematic diagram of the proposed thin film Si solar cell structure. (b) Side view of the unit cell, where the structural parameters are defined.

The FP resonance occurs generally when both the layer thickness and the incidence wavelengths satisfy the resonance condition, and thereby are sensitively dependent on the thickness of the Si layer. As the layer thickness increases, the FP cavity resonances shift to red and its higher-order modes will appear at the short wavelengths. When combining the Si film with the metal nanostructures, multiple absorption peaks appear in the absorption spectrum (Figure 2(b)). For comparison, the absorption enhancement spectrum ( $\Pi(\lambda)$ ) is also calculated as shown in the insets of Figure 2(b). It can be seen clearly that the introduction of metal structures leads to multiple strong enhanced absorption bands. Furthermore, it is also indicated that generating the large absorption enhancements at the longer wavelengths where the Si film is weakly absorbing is relatively easy compared to the short wavelengths where the Si film exhibits strong absorption.

**3.2. Absorption Enhancement Mechanisms.** To explore the mechanisms of absorption enhancement and improve the light absorption capability of the proposed structure for solar cell applications, the absorption enhancement map ( $\Pi(\lambda)$ ) versus the period of unit cells and the normalized magnetic field distributions ( $|H_y/H_0|$ ) across the Si layer at the wavelengths of the absorption enhancement peaks are investigated, as shown in Figures 3 and 4, respectively. Inside those maps of Figure 3, each point represents the full-field simulation result with the corresponding wavelengths and periods. The field distributions ( $|H_y/H_0|$ ) in Figure 4 correspond to illuminations with TM polarized plane wave (H-field along the metal strips and E-field in this plane normal to the metal strips). Four possible enhancement mechanisms, including the slab waveguide modes, the high near field enhancement associated with LSPR modes of metal strips, and the SPP modes at the metal/silicon interface as

well as the coupling effects between LSPR and SPP modes will be discussed in detail in the following.

Figure 3(a) shows that the proposed structure exhibits multiple strong absorption enhancement bands at different values of periods. For the structure with a period of 320 nm (as the vertical white dashed line shown in Figure 3(a)), three obvious absorption enhancement peaks are observed, which are marked as “a,” “b,” and “c” in the map and the corresponding field distributions ( $|H_y/H_0|$ ) are plotted in Figures 4(a), 4(b), and 4(c), respectively. In Figure 3(a), the wavelength of the absorption peak “a” is always located around 550 nm when the period changes (the horizontal red dashed line). Moreover, the corresponding magnetic field distributions in Figure 4(a) exhibit a modal profile of the slab waveguide modes of finite thickness planar dielectric films, which have been given in various situations including with and without the metal back contacts [12, 26]. The wavelength of the slab waveguide mode depends on the absorber thickness. The induced electromagnetic fields for the slab waveguide mode are mostly confined inside the absorber layer and decay sharply into the surrounding air or metal slab, contributing to the absorption enhancement.

In Figure 3(a), the absorption enhancement peak “b” is always located around 700 nm (the black dashed line) while the absorption enhancement peak “c” depends quite sensitively on the array periods (the green dashed line of “2”), suggesting different physical origins of the two absorption enhancement bands. Since the peak “b” does not shift with changing the periods and the corresponding field distributions in Figure 4(b) carry a clear feature of localized surface plasmon mode with the enhanced magnetic fields still confined in the Si layer but mostly surrounding the metal strips, it can be attributed to LSPR mode of the metal strips. The resonant wavelength of the LSPR mode depends



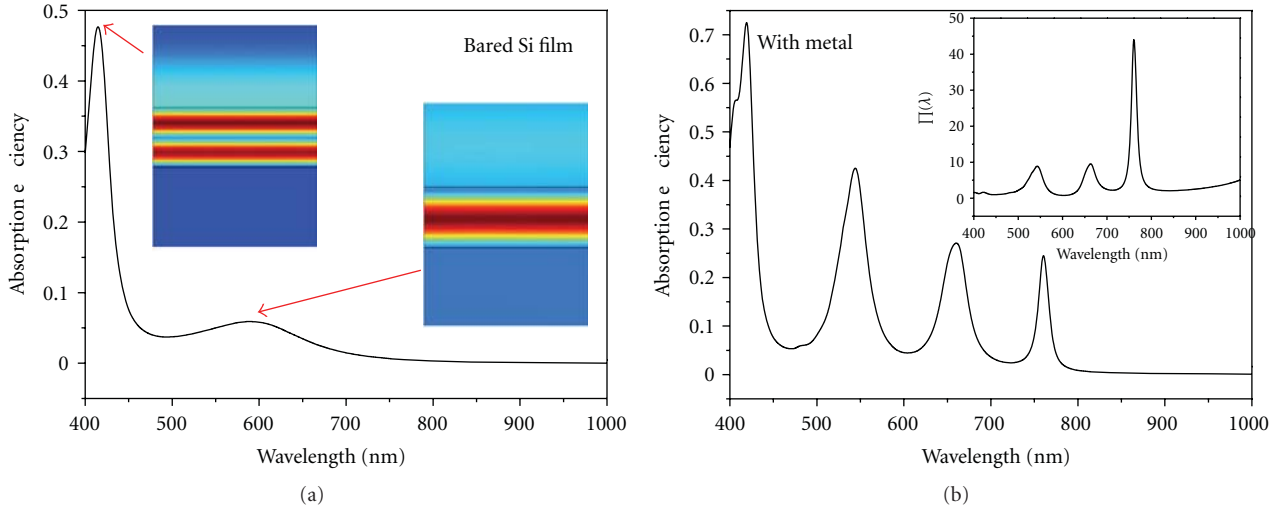


FIGURE 2: (a) Absorption spectrum of the bared Si film. The insets show the normalized stimulated magnetic field distributions ( $|H_y/H_0|$ ) at wavelengths of 420 nm and 600 nm, respectively. (b) Absorption spectrum for the proposed solar cell structure under TM polarized plane wave incidences. The absorption enhancement spectrum ( $\Pi(\lambda)$ ) is shown in the insets.

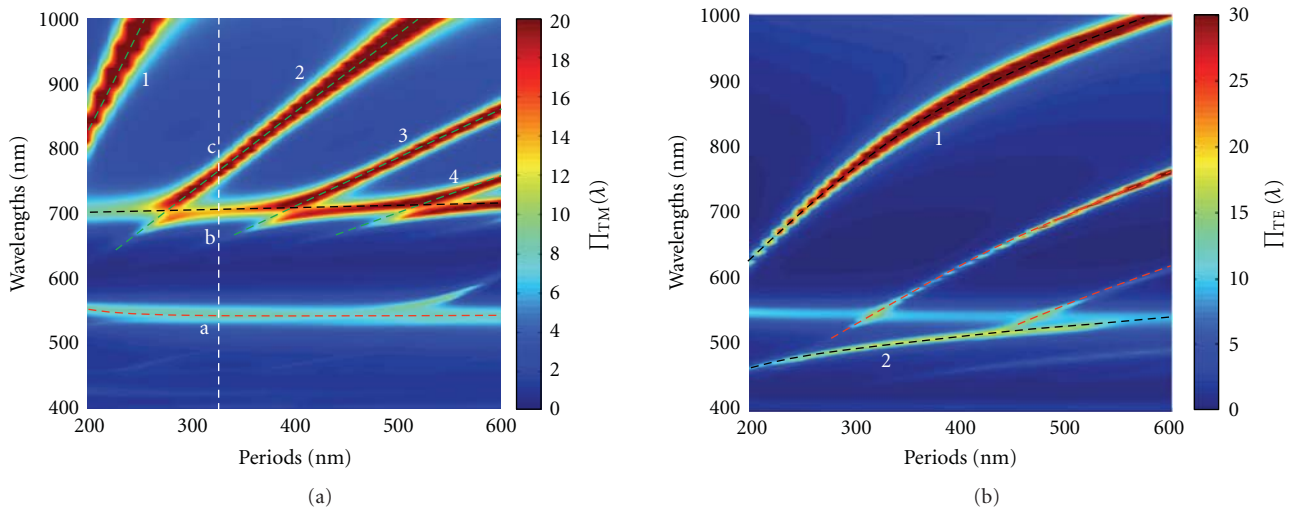


FIGURE 3: Map of the absorption enhancement ( $\Pi(\lambda)$ ) spectra for the proposed structure with 80 nm thick Si layer versus the periods of unit cell under (a) TM and (b) TE polarized plane wave incidence, respectively.

sensitively on the structural parameters of metal strips. The width  $w$  and thickness  $t$  of metal strips have been carefully chosen through optimization because small nanoparticles scatter very weakly, whereas large nanoparticles behave like a mirror to reflect a large fraction of incident light back into free space and are not beneficial for light absorption inside the absorber layer. The peak “c” shifts to red with increasing the periods and the changing trend (the green dashed line of “2”) presents a dispersive behavior of a SPP mode propagating at the metal/semiconductor interface according to the grating coupling theory [27, 28]. Moreover, the corresponding field distribution in Figure 4(c) exhibits the characteristic of surface wave with the maximum field intensity near the metal/silicon interface but decay quickly

apart from the interface. Thus, the peak “c” can be attributed to SPP mode excited by the bottom grating. Since the attenuation rate of the field intensity in the metal is much larger than that in the silicon layer due to higher loss of metal materials, the view of coupled light energies mostly confined into the semiconductor layer give a suggestion of absorption enhancement mechanism.

Figure 3(a) shows that as the period is increased from the initial value of 200 nm, the wavelength of the SPP mode redshifts to approach that of the LSPR mode and a behavior of anticrossing is observed around  $p = 280$  nm, suggesting a strong interaction of the localized and propagating surface plasmons [29, 30]. The absorption enhancement bands of LSPR and SPP modes become stronger and broader in



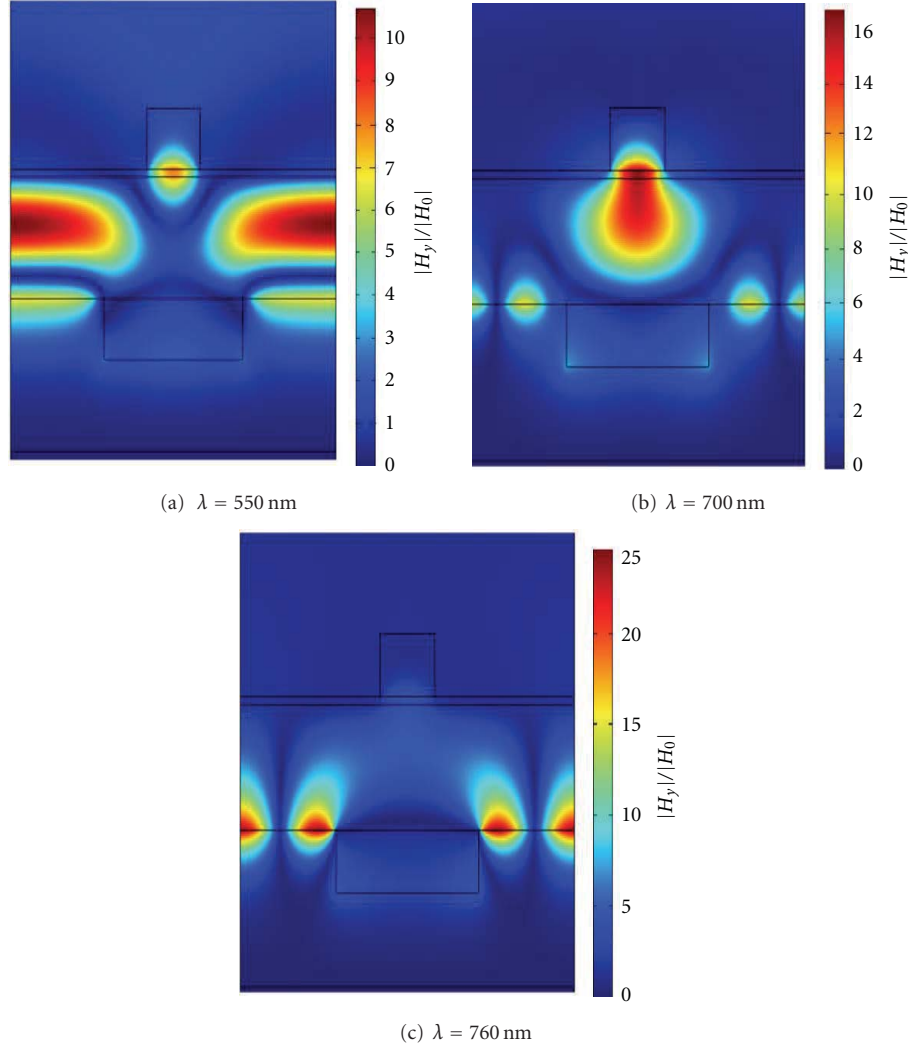


FIGURE 4: The normalized magnetic field distribution ( $|H_y/H_0|$ ) in the cross-section for TM polarized plane wave incidence at the wavelengths of (a) 545 nm, (b) 670 nm, and (c) 760 nm, corresponding to the three absorption enhancement peaks “a,” “b,” and “c” displayed in Figure 2(b), respectively.

the regions of coupling and light absorption is increased further by coupling effects. When the period continues to increase, multiple absorption enhancement bands appear and the anticrossing behavior is observed when the wavelengths of these absorption peaks overlap with that of LSPR mode. The changing trend of other three enhanced absorption bands with the periods are highlighted by the green dashed lines of “1,” “3,” and “4,” respectively, which present a similar dispersive behavior as that of the SPP mode marked by “2,” implying a SPP-related absorption enhancement mechanism. Obviously, as the period increases, the SPP mode redshifts and more higher-order SPP modes appear, leading to multiple absorption enhancement bands at longer wavelengths.

Unlike TM polarizations, the SPP and LSPR modes are absent under TE plane wave incidence (E-field along the metal strips and H-field in this plane normal to the metal strips). Only the enhanced absorption related to the TE

waveguide modes are observed in Figure 4(b), where the two enhanced absorption bands marked as the black dashed line of “1” and “2” are expected to attribute to the  $TE_0$  and  $TE_1$  waveguide modes. It can be seen that the absorption enhancement factor related to the TE waveguide modes is very high, but the width of absorption enhancement bands is very narrow. As the period become large, the absorption enhancement increases and some higher-order modes of  $TE_0$  waveguide appear (the red dashed line), contributing to the overall absorption enhancement under TE plane wave incidence.

**3.3. Total Absorption Enhancement under the Solar Illuminations.** To perform a full evaluation on the performance of the proposed design, the total absorption enhancement under solar illuminations must be considered. Generally, the short circuit current in a solar cell is proportional to the number of absorbed photons if assuming unity internal

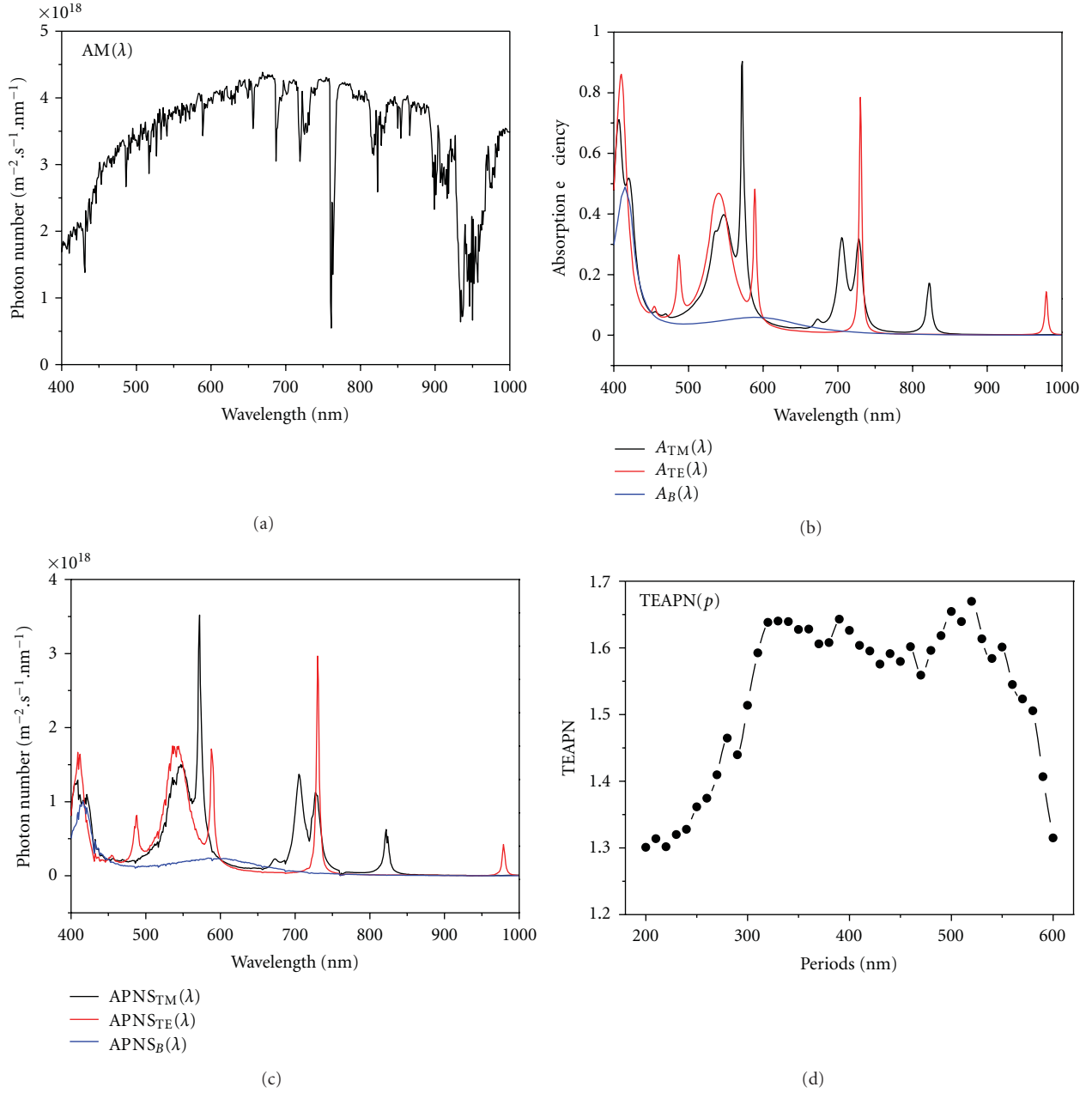


FIGURE 5: (a) Photon number spectrum of the AM1.5 solar irradiations ( $AM(\lambda)$ ). (b) Absorption efficiency spectrum ( $A(\lambda)$ ). (c) Absorbed photon number spectrum (APNS). (d) Total enhancement of absorbed photon number (TEAPN) inside the Si layer over the entire solar spectrum versus the different array periods. The subscripts “TE” and “TM” in (a) and (b) represent different polarizations for the proposed solar cells with a period of 550 nm. The subscript “B” corresponds to the bared Si film with a thickness of 80 nm.

quantum efficiency (every photoexcited electron-hole pair is collected). Therefore, the total absorption enhancement must be evaluated based on the number of photons being absorbed. Figure 5(a) presents the photon number spectrum of the standard AM1.5 solar irradiation ( $AM(\lambda)$ ). The absorbed photon number spectrum (APNS) inside the active layer under solar illuminations can be obtained by using the following equation [31]:

$$APNS(\lambda) = A(\lambda) \times AM(\lambda), \quad (2)$$

where the absorption efficiency spectrum  $A(\lambda)$  represents the absorbed power inside the Si layer with unity incident light power, as shown in Figure 5(b) for TM or TE polarized light incidence. Figure 5(c) displays the APNS for the proposed solar cells at two polarizations and that for an 80 nm thick bared Si film, respectively. Compared to the bared Si film, the introduction of metal structures in thin film solar cells leads to an obvious increase of the absorbed photon numbers inside the Si layer.

Considering the equal contributions from TE and TM polarized light, the APNS of the proposed solar cells under randomly polarized sunlight can be described as

$$\text{APNS}(\lambda) = \frac{1}{2}(\text{APNS}_{\text{TE}}(\lambda) + \text{APNS}_{\text{TM}}(\lambda)), \quad (3)$$

where the subscript represent the case of TE or TM polarizations. The total enhancement of absorbed photon number (TEAPN) inside the Si layer is defined as

$$\text{TEAPN} = \frac{\int \text{APNS}(\lambda)_{\text{with\_metal-structures}} d\lambda - \int \text{APNS}(\lambda)_{\text{without\_metal-structures}} d\lambda}{\int \text{APNS}(\lambda)_{\text{without\_metal-structures}} d\lambda}. \quad (4)$$

The wavelength range for integrating is selected from 400 nm to 1000 nm. Figure 5(d) shows the simulation results of the total enhancement (TEAPN) versus different array periods. Obviously, a very large enhancement up to 170% can be achieved in our designed structures when compared with the case of a bared Si layer. Furthermore, the high enhancement of about 170% is broadband for the array period with a large range from about 300 nm to 550 nm, thus providing a very good fabrication tolerance for practical devices. Such results are impressive and superior to those of some previous designs of plasmonic thin film solar cells. In addition, it should be pointed that although the thickness of 80 nm employed in our simulations was used in certain devices, the active layer thickness for the ultrathin Si solar cells is typically 200–600 nm in the practical device applications. In this case, more optical waveguide modes would be excited to play important roles in absorption enhancement [11, 12]. Therefore, for the proposed structure with thicker active layer, multiple plasmon resonance modes associated with the introduction of metal structures together with these optical modes are predicated to contribute to the overall absorption enhancement. Since the configuration of metallic materials rather than the discussed crystalline silicon materials is responsible for the absorption enhancement in our proposed design, similar performances are also expected by extending the similar design into other active solar materials such as CdTe and organics. Therefore, our proposed design has the potential to become a solar cell platform for various thin film solar cell systems.

#### 4. Conclusion

In conclusion, the light absorption properties of a novel ultrathin film Si solar cell structure were discussed in detail by using the finite element method. As compared to a bared Si thin film, the total absorption enhancement of absorbed photon number can reach to 170% within a broad period range by introducing Ag strips on top and Ag nanograting as the back contacts in the solar cell structure. The absorption enhancement mechanisms are revealed by analyzing the enhanced field distributions and investigating the absorption enhancement spectra as a function of periods. These results pave a promising way for the realization of high efficiency thin-film solar cells.

#### Acknowledgments

This work is supported by the National Science Foundation of China (no. 10974183 and 11104252), the Ministry of Education of China (no. 20114101110003), the Aeronautical Science Foundation of China (no. 2011ZF55015), and the Basic and Frontier Technology Research Program of Henan Province (no. 122300410162 and 112300410264).

#### References

- [1] M. A. Green, "Lambertian light trapping in textured solar cells and light-emitting diodes: analytical solutions," *Progress in Photovoltaics*, vol. 10, no. 4, pp. 235–241, 2002.
- [2] H. A. Atwater and A. Polman, "Plasmonics for improved photovoltaic devices," *Nature Materials*, vol. 9, no. 3, pp. 205–213, 2010.
- [3] K. R. Catchpole and A. Polman, "Plasmonic solar cells," *Optics Express*, vol. 16, no. 26, pp. 21793–21800, 2008.
- [4] P. Spinelli, V. Ferry, J. van de Groep et al., "Plasmonic light trapping in thin-film Si solar cells," *Journal of Optics*, vol. 14, no. 2, Article ID 024002, 11 pages, 2012.
- [5] D. M. Schaad, B. Feng, and E. T. Yu, "Enhanced semiconductor optical absorption via surface plasmon excitation in metal nanoparticles," *Applied Physics Letters*, vol. 86, no. 6, Article ID 063106, 3 pages, 2005.
- [6] D. Qu, F. Liu, Y. Huang, W. Xie, and Q. Xu, "Mechanism of optical absorption enhancement in thin film organic solar cells with plasmonic metal nanoparticles," *Optics Express*, vol. 19, no. 24, pp. 24795–24803, 2011.
- [7] C. Hägglund, M. Zäch, G. Petersson, and B. Kasemo, "Electromagnetic coupling of light into a silicon solar cell by nanodisk plasmons," *Applied Physics Letters*, vol. 92, no. 5, Article ID 053110, 3 pages, 2008.
- [8] S. Pillai, K. R. Catchpole, T. Trupke, and M. A. Green, "Surface plasmon enhanced silicon solar cells," *Journal of Applied Physics*, vol. 101, no. 9, Article ID 093105, 8 pages, 2007.
- [9] K. R. Catchpole and A. Polman, "Design principles for particle plasmon enhanced solar cells," *Applied Physics Letters*, vol. 93, no. 19, Article ID 191113, 3 pages, 2008.
- [10] R. A. Pala, J. White, E. Barnard, J. Liu, and M. L. Brongersma, "Design of plasmonic thin-film solar cells with broadband absorption enhancements," *Advanced Materials*, vol. 21, no. 34, pp. 3504–3509, 2009.
- [11] W. Wang, S. Wu, K. Reinhardt, Y. Lu, and S. Chen, "Broadband light absorption enhancement in thin-film silicon solar cells," *Nano Letters*, vol. 10, no. 6, pp. 2012–2018, 2010.
- [12] V. E. Ferry, L. A. Sweatlock, D. Pacifici, and H. A. Atwater, "Plasmonic nanostructure design for efficient light coupling

- into solar cells,” *Nano Letters*, vol. 8, no. 12, pp. 4391–4397, 2008.
- [13] R. Biswas and D. Zhou, “Simulation and modelling of photonic and plasmonic crystal back reflectors for efficient light trapping,” *Physica Status Solidi A*, vol. 207, no. 3, pp. 667–670, 2010.
  - [14] R. B. Dunbar, T. Pfadler, and L. Schmidt-Mende, “Highly absorbing solar cells—a survey of plasmonic nanostructures,” *Optics Express*, vol. 20, no. 2, pp. A177–A189, 2012.
  - [15] W. Wang, S. Wu, R. J. Knize, K. Reinhardt, Y. Lu, and S. Chen, “Enhanced photon absorption and carrier generation in nanowire solar cells,” *Optics Express*, vol. 20, no. 4, pp. 3733–3743, 2012.
  - [16] C. Rockstuhl, S. Fahr, and F. Lederer, “Absorption enhancement in solar cells by localized plasmon polaritons,” *Journal of Applied Physics*, vol. 104, no. 12, Article ID 123102, 7 pages, 2008.
  - [17] Y. A. Akimov, W. S. Koh, and K. Ostrikov, “Enhancement of optical absorption in thin-film solar cells through the excitation of higher-order nanoparticle plasmon modes,” *Optics Express*, vol. 17, no. 12, pp. 10195–10205, 2009.
  - [18] H. Shen, P. Bienstman, and B. Maes, “Plasmonic absorption enhancement in organic solar cells with thin active layers,” *Journal of Applied Physics*, vol. 106, no. 7, Article ID 073109, 5 pages, 2009.
  - [19] W. Bai, Q. Gan, G. Song, L. Chen, Z. Kafafi, and F. Bartoli, “Broadband short-range surface plasmon structures for absorption enhancement in organic photovoltaics,” *Optics Express*, vol. 18, no. 4, pp. A620–A630, 2010.
  - [20] E. Battal, T. A. Yogurt, L. E. Aygun, and A. K. Okyay, “Triangular metallic gratings for large absorption enhancement in thin film Si solar cells,” *Optics Express*, vol. 20, no. 9, pp. 9548–9464, 2009.
  - [21] L. J. Guo, “Nanoimprint lithography: methods and material requirements,” *Advanced Materials*, vol. 19, no. 4, pp. 495–513, 2007.
  - [22] J. Y. Chen and K. W. Sun, “Enhancement of the light conversion efficiency of silicon solar cells by using nanoimprint anti-reflection layer,” *Solar Energy Materials and Solar Cells*, vol. 94, no. 3, pp. 629–633, 2010.
  - [23] P. B. Johnson and R. W. Christy, “Optical constants of the noble metals,” *Physical Review B*, vol. 6, no. 12, pp. 4370–4379, 1972.
  - [24] E. D. Palik, *Handbook of Optical Constants of Solids*, Academic Press, 1985.
  - [25] A. W. Snyder and J. D. Love, *Optical Waveguide Theory*, Springer, 1983.
  - [26] V. E. Ferry, J. N. Munday, and H. A. Atwater, “Design considerations for plasmonic photovoltaics,” *Advanced Materials*, vol. 22, no. 43, pp. 4794–4808, 2010.
  - [27] H. Raether, *Surface Plasmons on Smooth and Rough Surfaces and on Gratings*, Springer, Berlin, Germany, 1988.
  - [28] N. Papanikolaou, “Optical properties of metallic nanoparticle arrays on a thin metallic film,” *Physical Review B*, vol. 75, no. 23, Article ID 235426, 7 pages, 2007.
  - [29] J. N. He, G. W. Cai, P. Ding, C. Z. Fan, and E. J. Liang, “Surface plasmons coupling for local field enhancement in nanoring arrays on a metallic film,” *Physics Express*, vol. 2, no. 10, 2012.
  - [30] P. Ding, E. J. Liang, G. W. Cai, W. Q. Hu, C. Z. Fan, and Q. Z. Xue, “Dual-band perfect absorption and field enhancement by interaction between localized and propagating surface plasmons in optical metamaterials,” *Journal of Optics*, vol. 13, no. 7, Article ID 075005, 7 pages, 2011.
  - [31] Y. A. Akimov and W. S. Koh, “Design of plasmonic nanoparticles for efficient subwavelength light trapping in thin-film solar cells,” *Plasmonics*, vol. 6, no. 1, pp. 155–161, 2011.

## Research Article

# Field Enhancement in a Grounded Dielectric Slab by Using a Single Superstrate Layer

Constantinos A. Valagiannopoulos<sup>1</sup> and Nikolaos L. Tsitsas<sup>2</sup>

<sup>1</sup>Department of Radio Science and Engineering, School of Electrical Engineering, Aalto University, Otakaari 5A Street, 02150 Espoo, Finland

<sup>2</sup>Department of Informatics, Aristotle University of Thessaloniki, 54124 Thessaloniki, Greece

Correspondence should be addressed to Nikolaos L. Tsitsas, ntsitsas@csd.auth.gr

Received 19 June 2012; Revised 22 September 2012; Accepted 24 September 2012

Academic Editor: Natalia M. Litchinitser

Copyright © 2012 C. A. Valagiannopoulos and N. L. Tsitsas. This is an open access article distributed under the Creative Commons Attribution License, which permits unrestricted use, distribution, and reproduction in any medium, provided the original work is properly cited.

The addition of a dielectric layer on a slab configuration is frequently utilized in various electromagnetic devices in order to give them certain desired operational characteristics. In this work, we consider a grounded dielectric film-slab, which is externally excited by a normally-incident Gaussian beam. On top of the film-slab, we use an additional suitably selected single isotropic superstrate layer in order to increase the field concentration inside the slab and hence achieve optimal power transfer from the external source to the internal region. We define a quantity of interest, called “enhancement factor,” expressing the increase of the field concentration in the film-slab when the superstrate is present compared to the case that it is absent. It is shown that large enhancement factor values may be achieved by choosing properly the permittivity, the permeability, and the thickness of the superstrate. In particular, it is demonstrated that the field in the film-slab is significantly enhanced when the slab is composed by an  $\epsilon$ -near-zero (ENZ) or low-index metamaterial.

## 1. Introduction

Increased field intensity in a localized area is required in a variety of applications from simple traditional implementations to complex state-of-the-art experiments. Indicatively, a resonance plasmon mode, characterized by a substantial local electric field enhancement, has been reported to be formed between a gold nanorod and an infinite slab in infrared range [1]. In addition, the optical trapping force on a spherical dielectric particle for an arbitrarily positioned focused beam has been demonstrated in [2], by using the generalized vector diffraction theory. Moreover, when considering a simple, analytically solvable cylindrical configuration, it has been shown that optical vortices appear which can be used to stably trap particles of particular sizes and index contrasts with the background [3]. Field enhancement of incident near-infrared light has been also investigated in [4], by using the exhibited surface plasmon polariton from erbium ions in a golden film.

On the other hand, layered, dielectric slab configurations are commonly used in electromagnetic (EM) devices since they possess certain functional advantages such as conformability and ease of fabrication. In particular, dielectric layers, with carefully selected physical and geometrical parameters, are extensively employed to lend particular beneficial characteristics to the considered devices. In [5], a multi-layered dielectric coating has been used in semiconductor laser diode optical amplifiers to reduce the reflection coefficient. Furthermore, a discontinuous parallel-plate waveguide acquiring highly selective frequency features through a narrow rectangular layer, filled with axially anisotropic media, has been proposed in [6]. The effect of a metal cladding on the band structure with a two-dimensional photonic crystal slab has been also analyzed in [7]; several types of claddings were used and the way that each cladding changes the background crystal has been identified. The fact that a single isotropic (idealized) cloaking layer may successfully suppress the dominant scattering coefficients of moderately



thin elongated objects, even for finite lengths comparable with the incident wavelength, has been pointed out in [8]. Finally, in [9], an additional cloaking dielectric layer has been exploited in a microstrip receiving antenna in order to render it as low profile as possible and also mitigate its EM response.

In this work, we combine the two aforementioned concepts, namely, the potential field enhancement by the addition of extra layers, in order to examine possible improvements offered in a relatively simple scattering configuration. More precisely, we consider the basic structure of a perfect electric conducting (PEC) grounded dielectric film-slab, which is frequently employed in several EM devices, see for example, [10, 11]. The slab structure is externally excited by a normally incident Gaussian beam; such an incident wave is commonly considered in similar configurations [12]. On the top of the dielectric film-slab, we use an additional superstrate layer, with controllable permittivity and permeability, in order to increase the induced field concentration inside the original film-slab. In this way, we seek to achieve an optimal transfer of the EM power from the external source to the internal region, where enhanced intensity is required. We solve semi-analytically the related boundary-value problem, and then define a basic quantity of interest expressing how large is the field concentration in the film-slab when the superstrate layer is present compared to the case when it is absent; this quantity is called “enhancement factor.” The variations of the enhancement factor with respect to the operating frequency and to the physical and geometrical characteristics of the structure are depicted. It is shown that it is possible to achieve large enhancement factor values by choosing properly the permittivity, the permeability, and the thickness of the superstrate layer. Particularly, it is demonstrated that the film-slab’s field is significantly enhanced when the slab is composed by an  $\epsilon$ -near-zero (ENZ) or low-index metamaterial.

## 2. Geometrical Configuration and Incident Field

The under consideration two-dimensional (2D) configuration, as well as the respective Cartesian  $(x, y, z)$  coordinate system, are depicted in Figure 1. The configuration is comprised of a perfect electric conductor (PEC) plane at  $y = L + w_1$  covered by a dielectric film-slab occupying the area  $L < y < L + w_1$  (region 1). The film-slab is filled by a magnetically inert material with complex relative dielectric permittivity  $\epsilon_{r1}$ . The structure of the PEC plane and the film-slab is additionally covered by a slab superstrate (region 2) of thickness  $w_2 < L$  and relative intrinsic physical parameters  $\epsilon_{r2}$  and  $\mu_{r2}$ . The infinite plane region  $y < L - w_2$  (vacuum region 0) above the superstrate is characterized by permittivity  $\epsilon_0$  and permeability  $\mu_0$ . The entire structure is assumed uniform along the direction  $\hat{z}$ .

The adopted time dependence is of the form  $\exp(j\omega t)$ , with  $\omega = 2\pi f$  being the angular frequency, and is being suppressed throughout hereinafter. Under this consideration, the imaginary part of the permittivity  $\epsilon_{r1}$  is negative

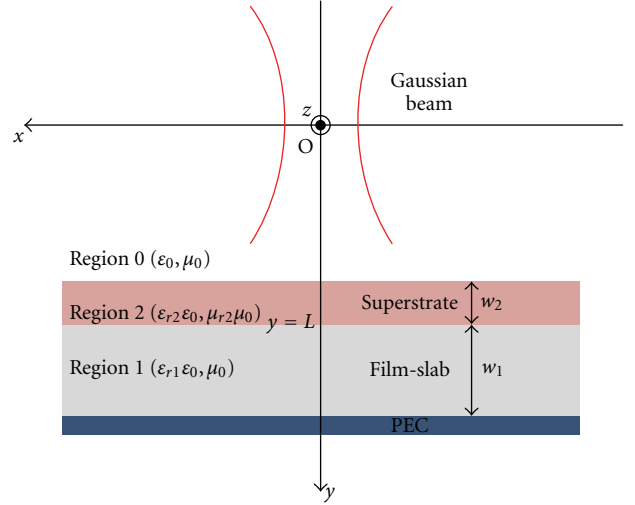


FIGURE 1: Geometrical configuration of the 2D structure under investigation composed of a planar dielectric film-slab, lying between a PEC plane and a superstrate. The structure is excited externally by a Gaussian beam.

(corresponding to passive materials). The remaining relative material parameters  $\epsilon_{r2}$  and  $\mu_{r2}$  are real.

A Gaussian beam, with its source at the origin  $O$  of the Cartesian coordinate system, illuminates normally the above described planar configuration. This incident Gaussian electric field is  $z$ -polarized and propagates along the  $y$ -axis (as will be analyzed below in details). Hence, due to the 2D nature of the configuration, all reflected and refracted electric fields in regions 0, 1, and 2 will also be  $z$ -polarized.

The aim of this work is to select suitable geometrical and physical parameters of the superstrate layer ( $w_2, \epsilon_{r2}, \mu_{r2}$ ) in order to enhance the intensity of the field induced in the film-slab region 1 by the external Gaussian beam excitation. More precisely, we require the EM field concentration in region 1 to become as large as possible in order to make it feasible for this “trapped” EM energy to be processed efficiently and be subsequently utilized for relevant applications, like for example, the ones pointed out above in the Introduction; see [1–9]. It is worth to note that we are interested only in the potential enhancement of the induced EM energy in the film-slab and not in the investigation of surface guided waves that may propagate in the infinite slab. For this reason, we consider that the slab is composed of a lossy material, characterized by a complex permittivity  $\epsilon_{r1}$ , hence constituting waves in the film-slab to become evanescent.

## 3. Analysis of the Incident Gaussian Beam

**3.1. Approximate Expression of the Beam’s Envelope.** The electric field of an incident Gaussian beam propagating in vacuum along the  $+y$ -axis is expressed as follows:

$$E_{0,\text{inc}}(x, y) = \hat{z} \Pi(x, y) \exp(-jk_0 y), \quad y > 0, \quad (1)$$

where  $k_0 = \omega \sqrt{\epsilon_0 \mu_0}$  is the free space wavenumber, while  $\Pi(x, y)$  is the envelope of the beam. It is reasonable to



consider that  $\Pi(x, y)$  is described by an exponential function involving the product of a complex function  $\beta(y)$  with a  $-x^2$  factor; the latter assures the Gaussian nature of the beam. Hence, we conclude to the expression

$$\Pi(x, y) = A(y) \exp[-\beta(y)x^2], \quad (2)$$

where  $A(y)$  is a complex amplitude function, while  $\Re[\beta(y)] \geq 0$ .

Next, in order to determine, by analytical means, approximate expressions for  $A(y)$  and  $\beta(y)$ , we substitute expression (1) of  $\mathbf{E}_{0,\text{inc}}(x, y)$  into the vector Helmholtz equation for vacuum region 0 and assume that the term proportional to  $\partial^2 \Pi / \partial y^2$  is negligible, since the main contribution with respect to  $y$  in the electric field is contained in the term  $\exp(-jk_0 y)$ . In this way, we result to two first-order coupled nonlinear ordinary differential equations, which are solved exactly yielding [13, 14]

$$\beta'(y) + \frac{2}{jk_0} \beta^2(y) = 0 \Rightarrow \beta(y) = -\frac{k_0}{k_0 S + 2jy}, \quad (3)$$

$$A'(y) + \frac{\beta(y)}{jk_0} A(y) = 0 \Rightarrow A(y) = \frac{1}{\sqrt{k_0 S + 2jy}}, \quad (4)$$

where  $S$  is an arbitrary coefficient measured in area units. We consider that  $S = -2\chi/k_0$ , where the parameter  $\chi > 0$  has length units. By combining (2)–(4) and separating the real and imaginary parts, we find that the envelope function is given by

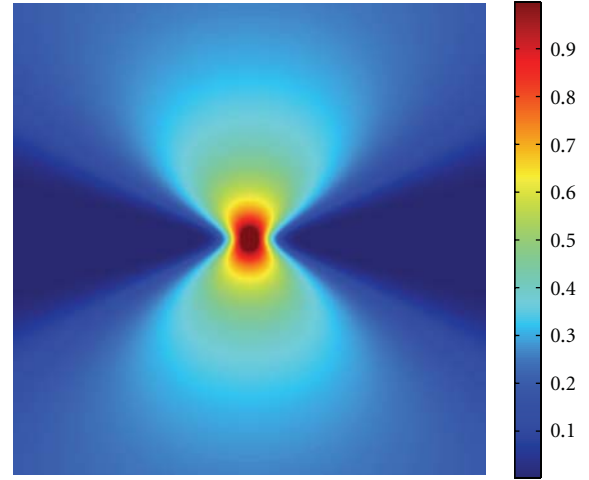
$$\begin{aligned} \Pi(x, y) = & \sqrt[4]{\frac{4\chi}{R(\chi, y)}} \exp\left[\frac{j}{2} \arctan\left(\frac{y}{\chi}\right)\right] \\ & \times \exp\left[-x^2 \frac{k_0}{R(\chi, y)}\right] \exp\left[-jx^2 \frac{k_0}{R(y, \chi)}\right], \end{aligned} \quad (5)$$

where

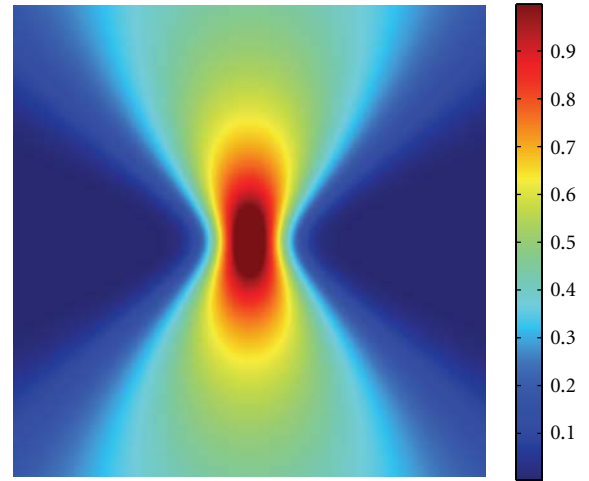
$$R(y, \chi) = 2y \left[ 1 + \left( \frac{\chi}{y} \right)^2 \right]. \quad (6)$$

The parameter  $\chi$  characterizes the Gaussian beam and will be hereinafter called “concentration length,” since it is inversely related to the local power concentration at the source (origin  $O$ ). In other words, a large concentration length indicates a slowly decaying behavior of the envelope, as  $|x|$  and  $|y|$  increase. Representative visualizations of the absolute value of the Gaussian beam’s electric field for  $\chi = 0.1, 0.3$ , and  $0.9$  are depicted in Figures 2(a)–2(c), respectively.

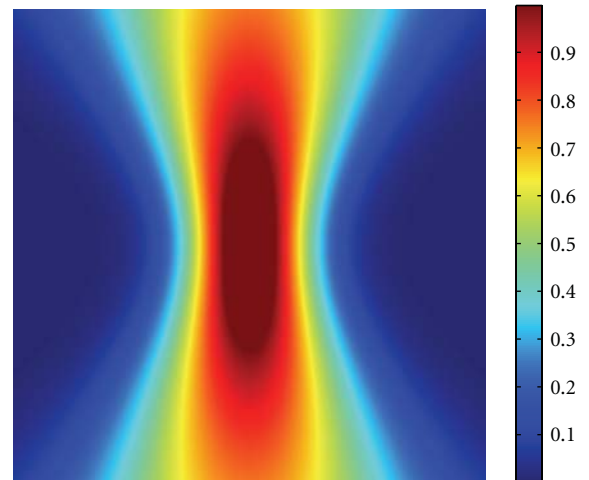
**3.2. Fourier Integral Expression of the Beam.** Let  $\mathbf{v}(x, y) = \hat{\mathbf{z}}v(x, y)$  be a vector function satisfying the Helmholtz equation. We consider the 1D Fourier transform pair of



(a)



(b)



(c)

FIGURE 2: Contour plots of the absolute value of the Gaussian beam’s field given by (1) and (5), for  $k_0 = 2\pi$  and  $\chi = 0.1, 0.3$ , and  $0.9$ , respectively; both axes correspond to arbitrary length units.

$v(x, 0)$  (namely of the restriction of  $v(x, y)$  on  $y = 0$ ) as follows:

$$v(x, 0) = \frac{1}{2\pi} \int_{-\infty}^{+\infty} V(\alpha) \exp(j\alpha x) d\alpha, \quad (7)$$

$$V(\alpha) = \int_{-\infty}^{+\infty} v(x, 0) \exp(-j\alpha x) dx. \quad (8)$$

Equation (7) expresses a complex function  $v(x, 0)$  as a weighted integral of the exponential factors  $\exp(j\alpha x)$ .

Moreover, if a function  $\mathbf{w}(x, y) = \hat{\mathbf{z}} \exp(j\alpha x) w(y)$  satisfies the Helmholtz equation, then it is readily obtained that  $w(y) = \exp(\pm y\sqrt{\alpha^2 - k_0^2})$ . Therefore, by taking into account [13]

$$\int_{-\infty}^{+\infty} \Pi(x, 0) \exp(-j\alpha x) dx = \sqrt[4]{2} \sqrt{\frac{2\pi\chi}{k_0}} \exp\left(-\frac{\chi\alpha^2}{2k_0}\right), \quad (9)$$

where the envelope  $\Pi$  is given by (5), and considering that the incident field  $\mathbf{E}_{0,\text{inc}}$ , expressed by (1) and (5), approximately satisfies the vector Helmholtz equation, we result to (see also the discussions in [14])

$$\begin{aligned} \mathbf{E}_{0,\text{inc}}(x, y) &= \hat{\mathbf{z}} \sqrt[4]{2} \sqrt{\frac{\chi}{2\pi k_0}} \int_{-\infty}^{+\infty} \exp\left(-\frac{\chi\alpha^2}{2k_0}\right) \\ &\times \exp\left(j\alpha x - y\sqrt{\alpha^2 - k_0^2}\right) d\alpha, \quad y > 0. \end{aligned} \quad (10)$$

The square root is evaluated with a positive imaginary part (in case  $|\alpha| < k_0$ ). We emphasize that (10) is not equivalent to the expression (1) of  $\mathbf{E}_{0,\text{inc}}$  (with  $\Pi$  given by (5)), since the latter expression satisfies only approximately the Helmholtz equation (the term  $\partial^2 \Pi / \partial y^2$  was assumed negligible).

Now, we assume that an arbitrary 2D layered configuration is excited at  $y > 0$  with a plane wave of the form:

$$\mathbf{e}_{\text{inc}}(x, y, \alpha) = \hat{\mathbf{z}} \exp\left(j\alpha x - y\sqrt{\alpha^2 - k_0^2}\right), \quad (11)$$

(which is propagating for  $|\alpha| < k_0$  and evanescent for  $|\alpha| > k_0$ ), and we determine the generated scattered field  $\mathbf{e}_{\text{scat}}(x, y, \alpha)$  in each of the layers. Then, the corresponding scattered field due to a Gaussian incident beam is computed by acting with the following operator:

$$\mathcal{J}\{\mathbf{f}\} \equiv \sqrt[4]{2} \sqrt{\frac{\chi}{2\pi k_0}} \int_{-\infty}^{+\infty} \exp\left(-\frac{\chi\alpha^2}{2k_0}\right) \mathbf{f} d\alpha, \quad (12)$$

on the vector  $\mathbf{f} = \mathbf{e}_{\text{scat}}(x, y, \alpha)$ . This conclusion is due to the fundamental principle of superposition and the linearity of the Maxwell's equations. The factor  $\exp(-\chi\alpha^2/2k_0)$ , appearing in (12), guarantees the convergence of the integral for  $|\alpha| \rightarrow +\infty$  (recall that  $\chi > 0$ ).

## 4. Solution of the Scattering Problem

**4.1. Auxiliary Problem: Plane Wave Excitation.** First, we analyze the auxiliary scattering problem, corresponding to

plane wave excitation. To this end, we consider that the layered configuration of Figure 1 is excited by the plane wave

$$\mathbf{e}_{0,\text{inc}}(x, y; \alpha) = \hat{\mathbf{z}} \exp[j\alpha x - \gamma_0(\alpha)y], \quad (13)$$

where the real parameter  $\alpha$  determines the direction of propagation;  $\alpha = 0$  corresponds to normal incidence on the layered structure. The radiation functions  $\gamma$  are defined by

$$\gamma_u(\alpha) = \sqrt{\alpha^2 - k_0^2 \epsilon_{ru} \mu_{ru}}, \quad u = 0, 1, 2, \quad (14)$$

with  $\epsilon_{r0} = \mu_{r0} = 1$ .

The electric field in the film-slab region 1 is given by

$$\mathbf{e}_1(x, y; \alpha) = \hat{\mathbf{z}} C_1(\alpha) \sinh[\gamma_1(\alpha)(y - L - w_1)] \exp(j\alpha x), \quad (15)$$

where  $C_1(\alpha)$  is a complex function of  $\alpha$ . By imposing the related boundary conditions, namely, continuity of the tangential electric and magnetic field components on  $y = L$ , and the PEC boundary condition on  $y = L + w_1$ , we obtain the following explicit form:

$$\begin{aligned} C_1(\alpha) &= 4e^{\gamma_0(\alpha)(w_2-L)} \mu_{r2} \gamma_0(\alpha) \gamma_2(\alpha) \\ &\times \left\{ \begin{aligned} &e^{-\gamma_2(\alpha)w_2} (\mu_{r2} \gamma_0(\alpha) - \gamma_2(\alpha)) \\ &\times [\mu_{r2} \cosh(\gamma_1(\alpha)w_1) \gamma_1(\alpha) \\ &- \sinh(\gamma_1(\alpha)w_1) \gamma_2(\alpha)] \\ &- e^{\gamma_2(\alpha)w_2} (\mu_{r2} \gamma_0(\alpha) + \gamma_2(\alpha)) \\ &\times [\mu_{r2} \cosh(\gamma_1(\alpha)w_1) \gamma_1(\alpha) \\ &+ \sinh(\gamma_1(\alpha)w_1) \gamma_2(\alpha)] \end{aligned} \right\}^{-1}. \end{aligned} \quad (16)$$

Equations (15) and (16) constitute the solution of the scattering problem due to the plane incident wave (13).

Moreover, we are also interested in the case where the superstrate is absent, namely,  $\epsilon_{r2} = \mu_{r2} = 1$  and hence  $\gamma_2(\alpha) = \gamma_0(\alpha)$ . For this case the electric field in the film-slab region 1 is given by

$$\tilde{\mathbf{e}}_1(x, y; \alpha) = \hat{\mathbf{z}} \tilde{C}_1(\alpha) \sinh[\gamma_1(\alpha)(y - L - w_1)] \exp(j\alpha x), \quad (17)$$

where function  $\tilde{C}_1(\alpha)$  takes now the following simplified form:

$$\tilde{C}_1(\alpha) = -\frac{2e^{-\gamma_0(\alpha)L} \gamma_0(\alpha)}{\cosh(\gamma_1(\alpha)w_1) \gamma_1(\alpha) + \sinh(\gamma_1(\alpha)w_1) \gamma_0(\alpha)}. \quad (18)$$

Equations (17) and (18) provide the solution of the scattering problem due to the plane incident wave (13) impinging on the corresponding configuration of Figure 1 where the superstrate layer is absent.

**4.2. Enhancement Factor.** Once the plane wave incidence electric field has been determined by means of (15) or (17), the total field induced in region 1, due to the Gaussian beam

incidence, is computed by using of the operator defined in (12) as follows:

$$\begin{aligned} \mathbf{E}_1(x, y) &= \mathcal{F}\{\mathbf{e}_1(x, y; \alpha)\} \\ &= \sqrt[4]{2} \sqrt{\frac{\chi}{2\pi k_0}} \int_{-\infty}^{+\infty} \exp\left(-\frac{\chi\alpha^2}{2k_0}\right) \mathbf{e}_1(x, y; \alpha) d\alpha, \end{aligned} \quad (19)$$

$$\begin{aligned} \tilde{\mathbf{E}}_1(x, y) &= \mathcal{F}\{\tilde{\mathbf{e}}_1(x, y; \alpha)\} \\ &= \sqrt[4]{2} \sqrt{\frac{\chi}{2\pi k_0}} \int_{-\infty}^{+\infty} \exp\left(-\frac{\chi\alpha^2}{2k_0}\right) \tilde{\mathbf{e}}_1(x, y; \alpha) d\alpha. \end{aligned} \quad (20)$$

The first and second of the above equations correspond, respectively, to the case with and without the superstrate. Moreover, we remind that the parameter  $\chi$  (concentration length) is the only degree of freedom characterizing and describing the incident Gaussian beam.

The integrations in (19) and (20) are carried out by using conventional numerical integration techniques. In particular, in order to exploit the MATLAB matrix-oriented architecture, we use the embedded `trapz(x, Y)` function for ordinary trapezoidal integrations which can accept multidimensional arguments. To be more specific, in compiled languages (like C++), the loop bodies are transformed into machine code only once at compile time. On the other hand, in interpreted languages (like MATLAB), the loop body is interpreted each time a loop is executed. Therefore, it is preferable to perform vectorized operations in MATLAB for repeated integrations. This is feasible only with `trapz(x, Y)`, where  $Y$  can be a multidimensional matrix, contrary to adaptive MATLAB routines such as `quad(f, a, b)` where a function  $f$  is integrated from  $a$  to  $b$ .

Moreover, we point out that the integrands in (19) and (20) have singularities corresponding to the eigenmode solutions of the slab waveguides formed by the grounded film-slab and the superstrate layer in isolation. However, these singularities are complex since the film-slab has been assumed to be composed of a lossy dielectric material (in order not to deal with possible surface guided waves; see Section 2 above). Hence, they do not contribute to the evaluation of the associated integrals where the integrations are performed on the real axis of the  $\alpha$ -plane.

Now, in order to estimate the effect of the superstrate layer (region 2) on the total EM power concentrated in region 1, we introduce the following “enhancement factor”:

$$\mathcal{EF} = \frac{\int_L^{L+w_1} \int_{-\infty}^{+\infty} |\hat{\mathbf{z}} \cdot \mathbf{E}_1(x, y)|^2 dx dy}{\int_L^{L+w_1} \int_{-\infty}^{+\infty} |\hat{\mathbf{z}} \cdot \tilde{\mathbf{E}}_1(x, y)|^2 dx dy}. \quad (21)$$

This factor represents the ratio of the total field’s power induced in the film-slab when the superstrate is present over the corresponding power when the superstrate is absent. The beneficial influence of the superstrate layer, leading to an enhanced power concentration, is demonstrated when  $\mathcal{EF} > 1$ .

## 5. Numerical Results

In this Section, we depict and discuss the variations of the enhancement factor  $\mathcal{EF}$  versus the superstrate’s characteristics  $w_2$ ,  $\epsilon_{r2}$ , and  $\mu_{r2}$  as well as versus the operating frequency  $f$ . In the following numerical simulations, we choose the material parameters composing the grounded layered slab configuration under consideration according to typical values encountered in similar configurations; see for example, indicatively [3, 4, 15]. In particular, the following parameters remain constant hereinafter (unless stated otherwise): operating frequency  $f_0 = 300$  THz with corresponding fixed wavelength  $\lambda_0$ , film-slab’s thickness  $w_1 = \lambda_0$ , distance between the source and the film-slab  $L = 0.5\lambda_0$ , and beam’s concentration length  $\chi = 0.1\lambda_0$ .

Figures 3(a) and 3(b) show the enhancement factor  $\mathcal{EF}$  contour plots with respect to the superstrate’s relative dielectric permittivity  $\epsilon_{r2}$  and relative magnetic permeability  $\mu_{r2}$  for  $\epsilon_{r1} = 50 - 5j$  with (a)  $w_2 = 0.1\lambda_0$  and (b)  $w_2 = 0.4\lambda_0$ . The purpose of examining such contour graphs is to find “operation points” with respect to  $\epsilon_{r2}$  and  $\mu_{r2}$  for which the electric field induced in the film-slab region 1 is considerably enhanced. From Figures 3(a) and 3(b), we observe that such points indeed exist equalling, for example, approximately  $(\epsilon_{r2}, \mu_{r2}) = (18, 3)$  for  $w_2 = 0.1\lambda_0$  and  $(\epsilon_{r2}, \mu_{r2}) = (8, 1.2)$  for  $w_2 = 0.4\lambda_0$ . At these two operating points, the  $\mathcal{EF}$  values are increased to nearly 250%, meaning that the power induced in region 1 of the layered configuration of Figure 1 is nearly 2.5 times the power induced in the corresponding superstrate-free configuration. We conclude that several choices exist for operating points with large values of  $\mathcal{EF}$ ; in particular, by comparing Figures 3(a) and 3(b), we see that the number of potential operating points increases with the thickness  $w_2$  of the superstrate. The fact that  $\mathcal{EF}$  may take large values for several choices of  $\epsilon_{r2}$ ,  $\mu_{r2}$ , and  $w_2$  offers flexibility in designing the structure and choosing appropriate and realizable material values with respect to the applications under consideration.

Moreover, Figures 4(a) and 4(b) depict  $\mathcal{EF}$  as function of the superstrate’s relative thickness  $w_2/L$  for  $\epsilon_{r1} = 50 - 5j$ ,  $\epsilon_{r2} = 9$ ,  $\mu_{r2} = 1$  with (a)  $L = 0.5\lambda_0$ , and  $\chi/\lambda_0 = 0.01, 0.05, 0.5$ , and (b)  $\chi/\lambda_0 = 0.1$ , and  $L/\lambda_0 = 0.1, 0.2, 0.3, 1$ . Figure 4(a) shows that  $\mathcal{EF}$  attains certain maxima with respect to  $w_2$  and the values of these maxima increase with  $w_2$ . Also,  $\mathcal{EF}$  generally decreases with increasing  $\chi$ , namely, as the incident Gaussian beam becomes less concentrated in the vicinity of the origin  $O$ . Even for initially very concentrated beams (small  $\chi$ ) there exist certain thicknesses  $w_2$  for which  $\mathcal{EF}$  takes large values. On the other hand, from Figure 4(b) we see that large values of  $\mathcal{EF}$  may be achieved even for small distances  $L$  between the source and the film-slab. This fact could be exploited appropriately, particularly for lasing applications.

Figures 5(a) and 5(b) represent  $\mathcal{EF}$  as function of the normalized operating frequency  $f/f_0$  for  $f_0 = 300$  THz,  $\epsilon_{r1} = 50 - 5j$ ,  $w_2 = 0.25\lambda_0$  with (a)  $\mu_{r2} = 1$ , and  $\epsilon_{r2} = 2, 5, 10, 15$ , and (b)  $\epsilon_{r2} = 5$ , and  $\mu_{r2} = 1, 2, 3, 4$ . In the entire examined frequency band, the values of  $\mathcal{EF}$  are larger than 1. Moreover,  $\mathcal{EF}$  is oscillatory with  $f$  with the period of the

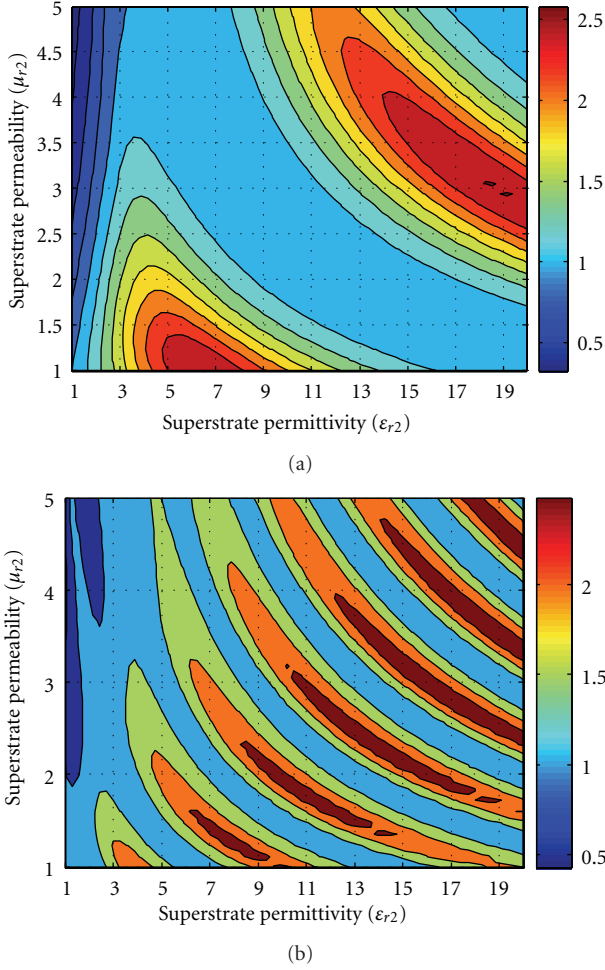


FIGURE 3: Enhancement factor contour plots as functions of the superstrate's relative dielectric permittivity  $\epsilon_{r2}$  and relative magnetic permeability  $\mu_{r2}$  for  $f_0 = 300$  THz,  $w_1 = \lambda_0$ ,  $L = 0.5\lambda_0$ ,  $\epsilon_{r1} = 50 - 5j$ ,  $\chi = 0.1\lambda_0$  with (a)  $w_2 = 0.1\lambda_0$  and (b)  $w_2 = 0.4\lambda_0$ .

oscillations decreasing for increasing  $\epsilon_{r2}(\mu_{r2})$  with constant  $\mu_{r2}(\epsilon_{r2})$ .

Also, we point out that additional numerical simulations (not reported here) have demonstrated that the values of  $\epsilon_{r2}$  and  $\mu_{r2}$  giving local maxima of  $\mathcal{EF}$  are independent of the film-slab's permittivity  $\epsilon_{r1}$ . Besides, the related maximum values of  $\mathcal{EF}$  increase with  $\epsilon_{r1}$ .

Now, we turn our attention to the investigation of the associated EM field concentration phenomena encountered in representative optical applications. To this end, we select realizable material parameter values in the optical region, according to those reported in [16–18]. Figures 6(a) and 6(b) depict the  $\mathcal{EF}$  versus the superstrate's relative (a) permittivity  $\epsilon_{r2}$  for  $\mu_{r2} = 1$ , and (b) permeability  $\mu_{r2}$  for  $\epsilon_{r2} = 2$ , with  $w_2 = 0.25\lambda_0$ ,  $\Re[\epsilon_{r1}] = -5, -2, -0.1, 2, 5$ , and  $\Im[\epsilon_{r1}] = -0.1|\Re[\epsilon_{r1}]|$ . As shown in Figure 6(a), when  $\epsilon_{r1} < 0$ , that is, the film-slab is composed of a material with negative permittivity, the  $\mathcal{EF}$  attains large values at certain distinct locations of the superstrate's permittivity in the region  $1 < \epsilon_{r2} < 5$ . In particular,  $\mathcal{EF}$  exhibits some sharp resonances

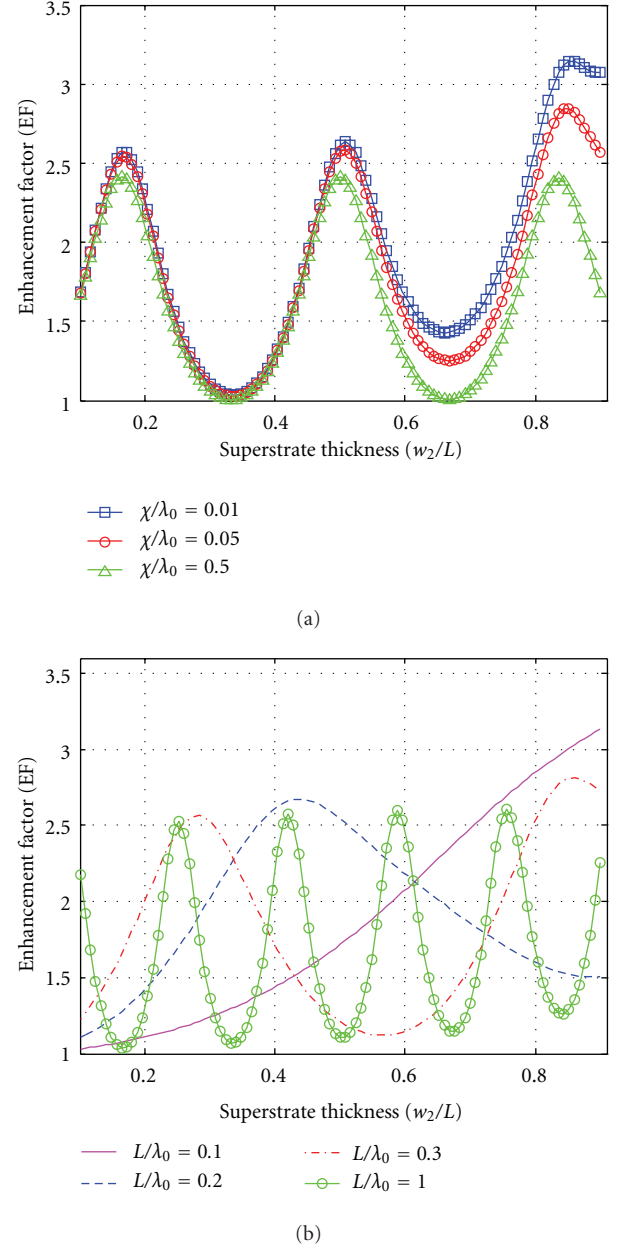


FIGURE 4: Enhancement factor as function of the superstrate's relative thickness  $w_2/L$  for  $\epsilon_{r1} = 50 - 5j$ ,  $\epsilon_{r2} = 9$ ,  $\mu_{r2} = 1$  with (a)  $L = 0.5\lambda_0$  and  $\chi/\lambda_0 = 0.01, 0.05, 0.5$  and (b)  $\chi/\lambda_0 = 0.1$  and  $L/\lambda_0 = 0.1, 0.2, 0.3, 1$ .

for a film-slab permittivity corresponding to an  $\epsilon$ -near-zero (ENZ) material [19, 20] or a low-index metamaterial (LIM) [21, 22]. Such materials are known to possess also other remarkable EM properties, including controlling the radiation pattern, and tunneling of electromagnetic energy [19, 20]. On the other hand, Figure 6(b) shows that sharp  $\mathcal{EF}$  resonances with significantly large values occur for distinct negative values of the superstrate's permeability  $\mu_{r2}$  and for a film-slab with both positive as well as negative permittivity  $\epsilon_{r1}$ . It is important to point out that  $\mathcal{EF}$  may take a value of the order of 50 for an ENZ film-slab, namely,

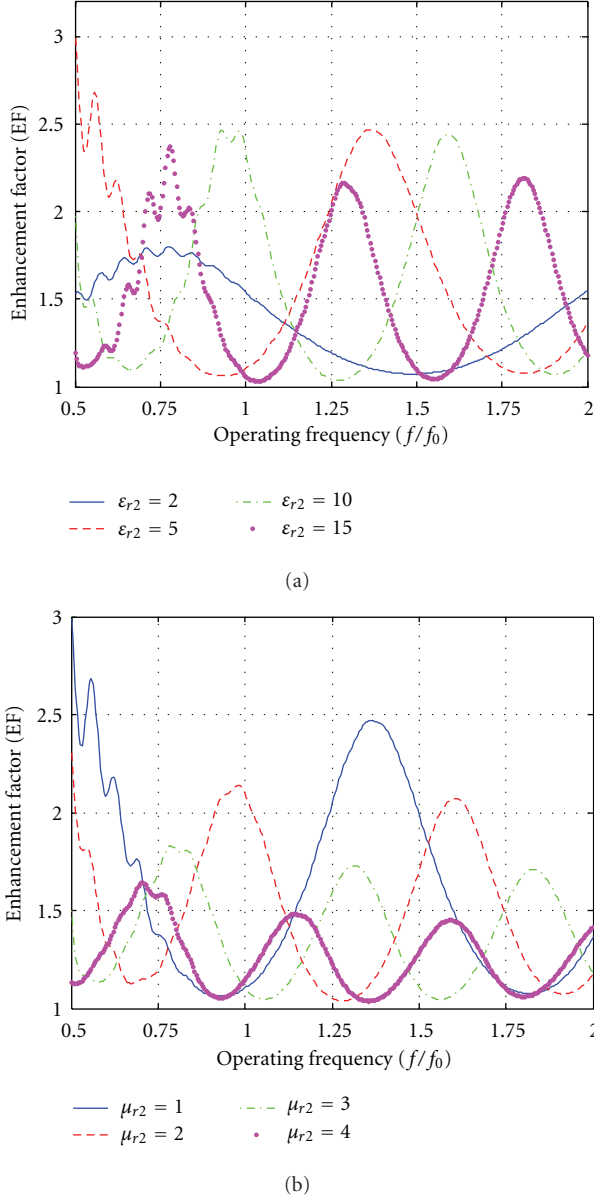


FIGURE 5: Enhancement factor as function of the structure's normalized operating frequency  $f/f_0$  for  $f_0 = 300$  THz,  $\epsilon_{r1} = 50 - 5j$ ,  $w_2 = 0.25\lambda_0$  with (a)  $\mu_{r2} = 1$  and  $\epsilon_{r2} = 2, 5, 10, 15$  and (b)  $\epsilon_{r2} = 5$  and  $\mu_{r2} = 1, 2, 3, 4$ .

meaning that the induced total field inside an ENZ film-slab, covered by the specific superstrate, becomes 50 times the corresponding field in the same slab when the superstrate is absent.

Next, we depict in Figures 7(a) and 7(b), the visualization of the total electric field induced inside the film-slab when the superstrate is absent and present, respectively. It is evident that the electric field in the slab is considerably enhanced when it is covered by a suitable superstrate. This fact also verifies that the enhancement factor  $\mathcal{EF}$ , defined according to (21), is an adequate measure in order to describe properly the induced field enhancement.

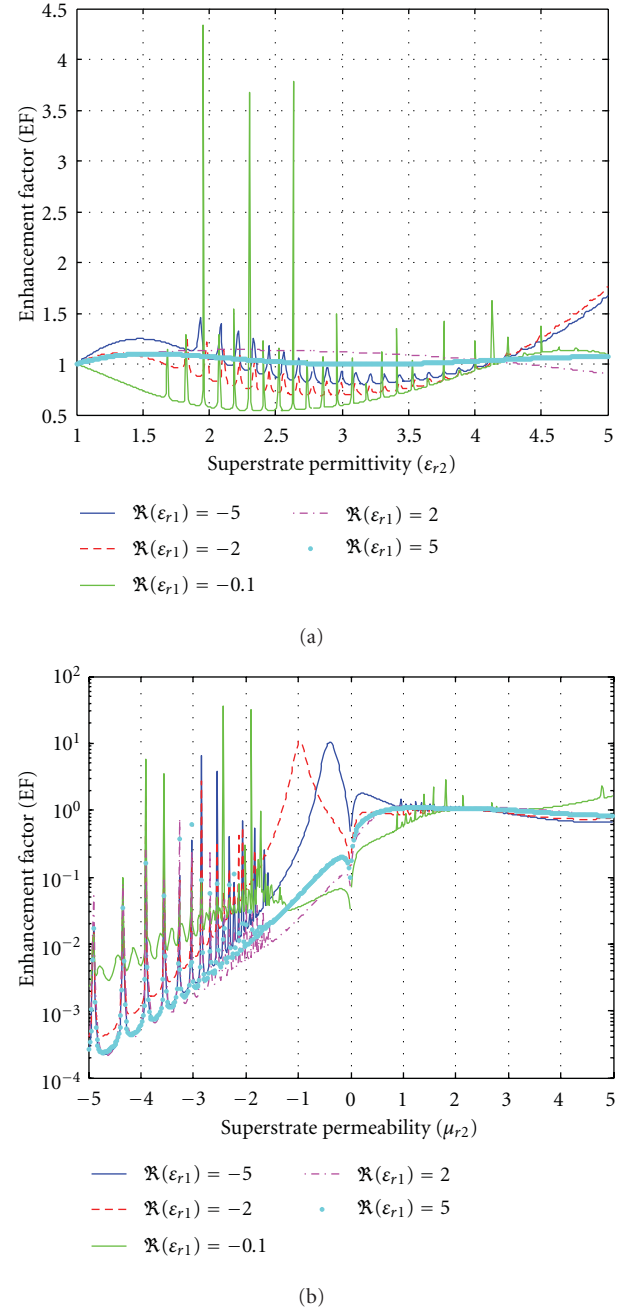


FIGURE 6: Enhancement factor as function of the superstrate's (a) relative permittivity  $\epsilon_{r2}$  for constant  $\mu_{r2} = 1$  and (b) relative permeability  $\mu_{r2}$  for constant  $\epsilon_{r2} = 2$ , with  $w_2 = 0.25\lambda_0$ ,  $\Re[\epsilon_{r1}] = -5, -2, -0.1, 2, 5$  and  $\Im[\epsilon_{r1}] = -0.1|\Re[\epsilon_{r1}]|$ .

Finally, we address the key issue concerning the physical mechanism of the achieved field enhancement. To this end, Figures 8(a) and 8(b) show the visualization of the total electric field induced in the region  $x \in \mathbb{R}, L - w_2 < y < L$  when (a) no superstrate is present, and (b) the region is occupied by the specific superstrate, considered in Figure 7. Clearly, the field in the region under consideration is significantly reduced when the superstrate is present compared to when it is absent. This fact is directly related with the corresponding



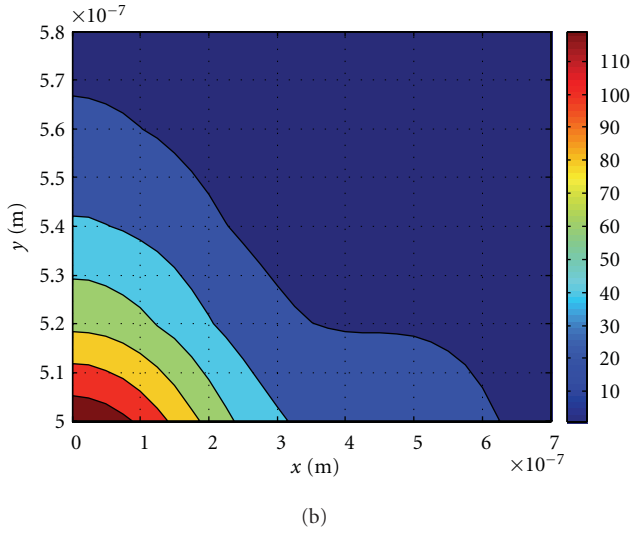
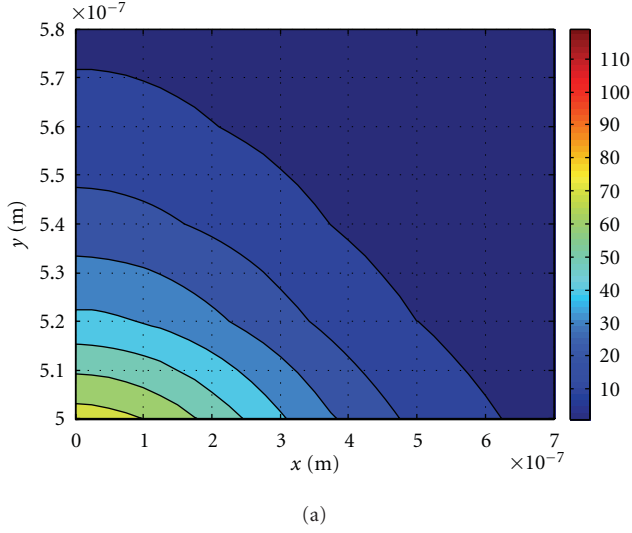


FIGURE 7: Contour plots of the total electric field induced inside the film-slab for  $\epsilon_{r1} = -5(1 + 0.1i)$  and for (a) no superstrate and (b) superstrate with  $\epsilon_{r2} = 1.94$ ,  $\mu_{r2} = 1$ ,  $w_2 = 0.25\lambda_0$ .

significant field enhancement observed inside the film-slab region when a suitable superstrate covers the slab, as depicted and discussed in Figure 7. Hence, the field is redistributed between the superstrate and film-slab regions in the sense that

- (1) when no superstrate is present, then the total field
  - (i) in the region  $x \in \mathbb{R}, L - w_2 < y < L$  attains large values since this region is close to the beam's source and no intermediate layer exists causing reflections;
  - (ii) in the film-slab attains moderate values;
- (2) when a suitable superstrate is present, then the total field

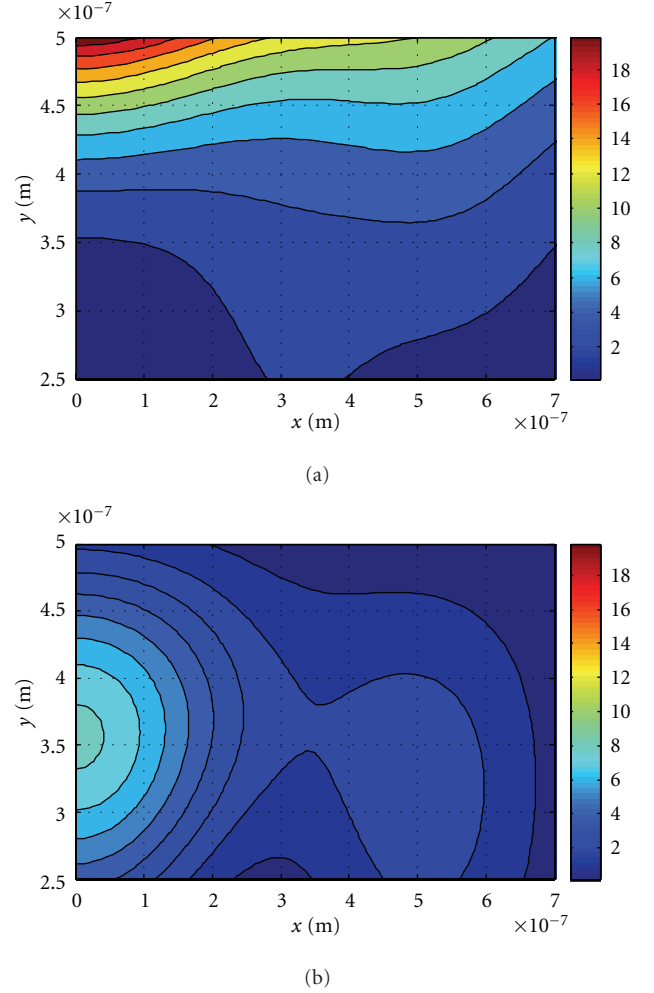


FIGURE 8: Contour plots of the total electric field induced in the region  $x \in \mathbb{R}, L - w_2 < y < L$  for the same set of constant parameters with Figure 7, when (a) no superstrate is present, and (b) the region is occupied by a superstrate with  $\epsilon_{r2} = 1.94$ ,  $\mu_{r2} = 1$ ,  $w_2 = 0.25\lambda_0$ .

- (i) in the film-slab is significantly enhanced precisely due to the presence of the specific superstrate;
- (ii) in the region  $x \in \mathbb{R}, L - w_2 < y < L$  is considerably reduced compared to case 1 where the superstrate is absent.

## 6. Conclusions

We analyzed the Gaussian beam external excitation of a grounded dielectric slab configuration. The related boundary value problem was solved by analytical techniques. The main focus was given at the investigation of the device's potential application as an electromagnetic power concentrator by suitably altering the physical and geometrical parameters of an additional superstrate layer, lying on top of the device. We defined the "enhancement factor" representing the ratio of the total field's power induced in the film-slab when the superstrate is present over the corresponding power



when the superstrate is absent. Numerical simulations were presented concerning the achieved enhancement factor of the slab configuration. It was demonstrated that it is possible to achieve large enhancement factor values by choosing properly the permittivity, the permeability, and the thickness of the superstrate layer. In particular, it was exhibited that the film-slab's field is significantly enhanced when the slab is composed by an  $\epsilon$ -near-zero or low-index metamaterial.

Interesting future work directions concern the conduction of a systematic investigation of the optimization of the superstrate's parameters in order to achieve the largest possible enhancement factor values for a given grounded slab configuration.

## References

- [1] Y. J. Zheng, H. Liu, S. M. Wang et al., "Selective optical trapping based on strong plasmonic coupling between gold nanorods and slab," *Applied Physics Letters*, vol. 98, no. 8, Article ID 083117, 2011.
- [2] A. A. R. Neves, A. Fontes, L. Y. De Pozzo et al., "Electromagnetic forces for an arbitrary optical trapping of a spherical dielectric," *Optics Express*, vol. 14, no. 26, pp. 13101–13106, 2006.
- [3] T. M. Grzegorzczuk and J. A. Kong, "Analytical prediction of stable optical trapping in optical vortices created by three TE or TM plane waves," *Optics Express*, vol. 15, no. 13, pp. 8010–8020, 2007.
- [4] E. Verhagen, L. Kuipers, and A. Polman, "Field enhancement in metallic subwavelength aperture arrays probed by erbium upconversion luminescence," *Optics Express*, vol. 17, no. 17, pp. 14586–14598, 2009.
- [5] C. Vassallo, "Theory and practical calculation of antireflection coatings on semiconductor laser diode optical amplifiers," *IEEE Proceedings*, vol. 137, no. 4, pp. 193–202, 1990.
- [6] C. A. Valagiannopoulos, "High selectivity and controllability of a parallel-plate component with a filled rectangular ridge," *Progress In Electromagnetics Research*, vol. 119, pp. 497–511, 2011.
- [7] J.-H. Choe, Q. H. Park, and H. Jeon, "Effect of metallic slab cladding on photonic crystal band structures," *Journal of the Korean Physical Society*, vol. 53, no. 5, pp. 2591–2595, 2008.
- [8] A. Alù, D. Rainwater, and A. Kerkhoff, "Plasmonic cloaking of cylinders: finite length, oblique illumination and cross-polarization coupling," *New Journal of Physics*, vol. 12, Article ID 103028, 2010.
- [9] C. A. Valagiannopoulos and N. L. Tsitsas, "Integral equation analysis of a low-profile receiving planar microstrip antenna with a cloaking superstrate," *Radio Science*, vol. 47, Article ID RS2022, 2012.
- [10] C. A. Valagiannopoulos, "Electromagnetic scattering of the field of a metamaterial slab antenna by an arbitrarily positioned cluster of metallic cylinders," *Progress in Electromagnetics Research*, vol. 114, pp. 51–66, 2011.
- [11] F. Yang, A. Aminian, and Y. Rahmat-Samii, "A novel surface-wave antenna design using a thin periodically loaded ground plane," *Microwave and Optical Technology Letters*, vol. 47, no. 3, pp. 240–245, 2005.
- [12] G. D. Landry and T. A. Maldonado, "Gaussian beam transmission and reflection from a general anisotropic multilayer structure," *Applied Optics*, vol. 35, no. 30, pp. 5870–5879, 1996.
- [13] E. E. Kriezis, P. K. Pandelakis, and A. G. Papagiannakis, "Diffraction of a Gaussian beam from a periodic planar screen," *Journal of the Optical Society of America A*, vol. 11, no. 2, pp. 630–636, 1994.
- [14] J. Yang, L.-W. Li, K. Yasumoto, and C. H. Liang, "Two-dimensional scattering of a gaussian beam by a periodic array of circular cylinders," *IEEE Transactions on Geoscience and Remote Sensing*, vol. 43, no. 2, pp. 280–285, 2005.
- [15] P. H. Bolivar, M. Brucherseifer, J. G. Rivas et al., "Measurement of the dielectric constant and loss tangent of high dielectric-constant materials at terahertz frequencies," *IEEE Transactions on Microwave Theory and Techniques*, vol. 51, no. 4, pp. 1062–1066, 2003.
- [16] A. Alù, A. Salandrino, and N. Engheta, "Negative effective permeability and left-handed materials at optical frequencies," *Optics Express*, vol. 14, no. 4, pp. 1557–1567, 2006.
- [17] B. García-Cámara, F. Moreno, F. González, J. M. Saiz, and G. Videen, "Light scattering resonances in small particles with electric and magnetic properties," *Journal of the Optical Society of America A*, vol. 25, no. 2, pp. 327–334, 2008.
- [18] P.-Y. Chen, M. Farhat, and A. Alù, "Bistable and self-tunable negative-index metamaterial at optical frequencies," *Physical Review Letters*, vol. 106, no. 10, Article ID 105503, 2011.
- [19] M. Silveirinha and N. Engheta, "Tunneling of electromagnetic energy through subwavelength channels and bends using  $\epsilon$ -near-zero materials," *Physical Review Letters*, vol. 97, no. 15, Article ID 157403, 2006.
- [20] A. Alù, M. G. Silveirinha, A. Salandrino, and N. Engheta, "Epsilon-near-zero metamaterials and electromagnetic sources: Tailoring the radiation phase pattern," *Physical Review B*, vol. 75, no. 15, Article ID 155410, 2007.
- [21] G. Lovat, P. Burghignoli, F. Capolino, D. R. Jackson, and D. R. Wilton, "Analysis of directive radiation from a line source in a metamaterial slab with low permittivity," *IEEE Transactions on Antennas and Propagation*, vol. 54, no. 3, pp. 1017–1030, 2006.
- [22] C. A. Valagiannopoulos, "Effect of cylindrical scatterer with arbitrary curvature on the features of a metamaterial slab antenna," *Progress in Electromagnetics Research*, vol. 71, pp. 59–83, 2007.

## Research Article

# Realization of Radar Illusion Using Active Devices

**B. Z. Cao,<sup>1,2</sup> L. Sun,<sup>1</sup> and Z. L. Mei<sup>1,2</sup>**

<sup>1</sup> School of Information Science and Engineering, Lanzhou University, Lanzhou 730000, China

<sup>2</sup> State Key Laboratory of Millimeter Waves, Southeast University, Nanjing 210096, China

Correspondence should be addressed to Z. L. Mei, meizl@lzu.edu.cn

Received 2 July 2012; Revised 10 September 2012; Accepted 19 September 2012

Academic Editor: Alexandra E. Boltasseva

Copyright © 2012 B. Z. Cao et al. This is an open access article distributed under the Creative Commons Attribution License, which permits unrestricted use, distribution, and reproduction in any medium, provided the original work is properly cited.

A new method is proposed for realizing radar illusion of an electromagnetic target by using active devices. The devices are installed around the target but may closely cover the target or not, leading to closed or open configurations. The amplitudes and phases of the active devices are determined by using T-matrix method. The numerical computation is calculated using MATLAB, and the results show that this method is convenient, flexible, and efficient, which has important significances for implementation of novel electromagnetic devices.

## 1. Introduction

Since invisible cloaking using metamaterials was theoretically proposed and experimentally demonstrated in 2006 [1, 2], various methods have been put forward for realizing this fabulous electromagnetic (EM) phenomenon [1–8]. Generally speaking, EM invisibility, or illusion in general, can be roughly divided into four categories: (1) rendering the object transparent or invisible by controlling the parameters of metamaterials based on the scattering cancellation theory [7, 9]; (2) making the object invisible or illusory by exploiting the abnormal EM properties and the special ability to control EM waves of metamaterials based on the transformation optics theory [10, 11]; (3) invisibility using anomalous localized resonance method [12, 13]; (4) realizing invisibility or illusion using the surface integral equation of the EM field based on active devices [14–18]. So far, realization of radar illusion for an EM target is mainly based on the method of transformation optics [19–26]. Compared with the transformation optics method, active devices can be designed to work at a broadband of frequencies and do not need materials with extreme parameters. However, only a few works on radar illusion have been reported for an object by using active devices [17, 18], to the best of our knowledge.

In this paper, we use two kinds of active devices to realize the radar illusion of an object. One is called the closed configuration, where the active devices are set around and

closely wrap the object. The other is called open configuration, where the active devices are deployed around the object but do not cover it. The drawback of the former one is that signals from outside have been blocked, leading to poor communication for the target, while the latter does not affect the information transmission. Compared to the previous works [14–18], our scheme can not only make an object invisible to the outsider but also mimic a totally different object at a different place. It is thus a direct extension of the original work. In the next section, the two kinds of active devices are designed and simulated, and errors are analyzed. Though only rotation and virtual shift effects are studied in the paper, other illusion effects can be realized using the same method, including superscattering, geometry change, and parameter transformation [22–25]. Hence the method has important applications in military sectors. We remark that the method has its weakness, and a serious drawback is that the probing wave must be known in advance [14–16].

## 2. Theory Analysis

For simplicity, we only consider problems in the two-dimensional (2D) situation. The schematic diagrams of active devices to realize virtual rotation and shift are shown in Figure 1. In Figure 1(a), the real object (a green-colored hexagon) is put at the bottom side, and it will appear at

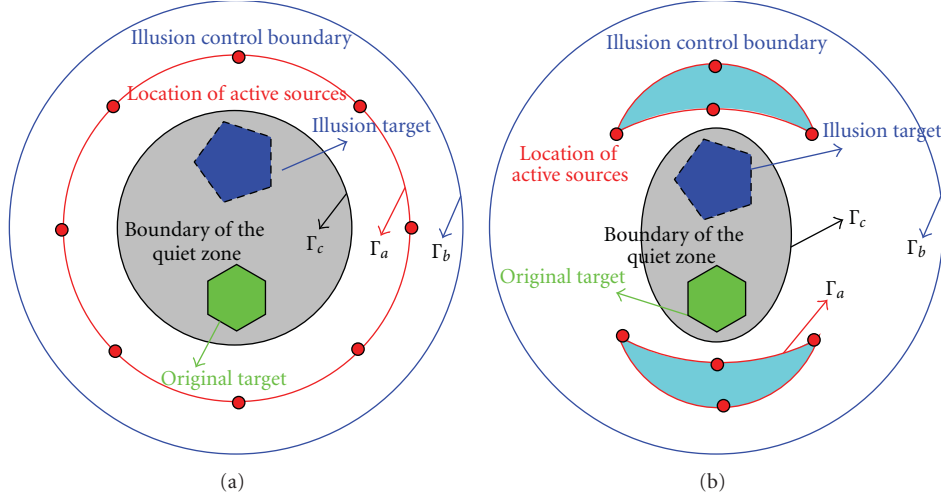


FIGURE 1: Schematic diagrams of the proposed active device to realize radar illusion. (a) Closed configuration; (b) open configuration.

the top side by using closed devices which are set along its periphery ( $\Gamma_a$  in the figure). The position of the active device, the boundary of the controlling illusion, and that of the quiet zone are expressed as  $\Gamma_a$ ,  $\Gamma_b$ , and  $\Gamma_c$ , respectively. Figure 1(b) depicts the radar illusion using an open configuration. In this case, the active device is deployed near the device but does not cover it, which is important for practical applications. The shift of the object can also be realized by using the active devices which are deployed on the boundary  $\Gamma_a$ . In both cases, an outsider will see a virtually shifted pentagon instead of the hexagon, that is, radar illusion.

Suppose the probing wave works at  $\omega$ , then the wave function  $u(\mathbf{r}, t)$  satisfies Helmholtz's equation

$$\nabla^2 u + k^2 u = 0, \quad (1)$$

where  $k = 2\pi/\lambda$  is the wave number,  $\lambda = 2\pi c/\omega$  is the wavelength, and  $c$  is the velocity of light.

For an arbitrary incident wave  $u_{\text{inc}}$ , the cancellation field generated by the active devices on  $\Gamma_c$  is required to assure a zero total field in the “quiet zone,” as its name suggests. So any object in this region has no scattering at all. At the same time, the active devices will generate a properly designed scattering field on  $\Gamma_b$  so that an external observer will see a different object at a different location and probably with different EM “fingerprint,” that is, radar illusion. When that specific field is set to zero, it means the object is totally shielded from the outsider. However, if the scattered field on  $\Gamma_b$  is consistent with what is generated by another object at another place without active devices, it means the virtual shifting effect is realized. Other illusions can be implemented using the same methodology.

Since the active devices can be considered as a series of line sources with certain distribution, the total fields radiated can be expressed by using the Fourier-Bessel series:

$$u_d(\boldsymbol{\rho}) = \sum_{m=1}^M \sum_{n=-N}^N a_{mn} H_n^{(1)}(k|\boldsymbol{\rho} - \boldsymbol{\rho}_m|) e^{jn\theta_m}, \quad (2)$$

where  $H_n^{(1)}(x)$  is Hankel function of the first kind with order  $n$ ,  $\boldsymbol{\rho}$  represents an arbitrary position vector,  $\boldsymbol{\rho}_m$  represents the position vector on  $\Gamma_a$ , and the angle  $\theta_m = \arg(\boldsymbol{\rho} - \boldsymbol{\rho}_m)$  shows direction angle between the vector  $\boldsymbol{\rho} - \boldsymbol{\rho}_m$  and the horizontal direction.

To realize virtual shift of an object, the boundary condition should be set to

$$u_d(\boldsymbol{\rho}) = \begin{cases} -u_{\text{inc}}(\boldsymbol{\rho}) & \forall \boldsymbol{\rho} \in \Gamma_c, \\ u_{\text{shift}}(\boldsymbol{\rho}) & \forall \boldsymbol{\rho} \in \Gamma_b, \end{cases} \quad (3)$$

where  $u_{\text{shift}}(\boldsymbol{\rho})$  denotes the scattered field produced by a shifted object on  $\Gamma_b$ .

During numerical calculation, one must divide the boundaries into discrete points. In our design, we set number of points to  $M$  on  $\Gamma_a$ ,  $M_b$  on  $\Gamma_b$ , and  $M_c$  on  $\Gamma_c$ , respectively. According to (3), the field on  $\Gamma_b$  and  $\Gamma_c$  can be expressed as

$$\begin{aligned} u_d(\boldsymbol{\rho}_i^b) &= \sum_{m=1}^M \sum_{n=-N}^N a_{mn} H_n^{(1)}(k|\boldsymbol{\rho}_i^b - \boldsymbol{\rho}_m|) e^{jn\theta_m} \quad \forall \boldsymbol{\rho}_i^b \in \Gamma_b, \\ u_d(\boldsymbol{\rho}_j^c) &= \sum_{m=1}^M \sum_{n=-N}^N a_{mn} H_n^{(1)}(k|\boldsymbol{\rho}_j^c - \boldsymbol{\rho}_m|) e^{jn\theta_m} \quad \forall \boldsymbol{\rho}_j^c \in \Gamma_c. \end{aligned} \quad (4)$$

The coefficients  $a_{mn}$  can be found numerically by enforcing (3) on points  $\boldsymbol{\rho}_1^b, \boldsymbol{\rho}_2^b, \dots, \boldsymbol{\rho}_{M_b}^b$ , and  $\boldsymbol{\rho}_1^c, \boldsymbol{\rho}_2^c, \dots, \boldsymbol{\rho}_{M_c}^c$  for boundary  $\Gamma_b$  and  $\Gamma_c$ , respectively. From (2), (3), and (4), the following linear equations can be obtained:

$$\begin{bmatrix} \mathbf{H}_b \\ \mathbf{H}_c \end{bmatrix} \begin{bmatrix} \mathbf{B} \\ \mathbf{C} \end{bmatrix} = \begin{bmatrix} \mathbf{U}_{\text{shift}} \\ -\mathbf{U}_{\text{inc}} \end{bmatrix}, \quad (5)$$

where  $\mathbf{B} = [a_{1n}, a_{2n}, \dots, a_{M_b n}]$ ,  $\mathbf{C} = [a_{1n}, a_{2n}, \dots, a_{M_c n}]$ ,  $[\mathbf{H}_b] = H_n^{(1)}(k|\boldsymbol{\rho}^b - \boldsymbol{\rho}_m|) e^{jn\theta_m}$ ,  $n \in [-N, N]$ , and  $[\mathbf{H}_c] = H_n^{(1)}(k|\boldsymbol{\rho}^c - \boldsymbol{\rho}_m|) e^{jn\theta_m}$ . The equation  $M(2N+1) = M_b + M_c$  must be maintained to ensure  $\mathbf{H}$  as a square matrix.

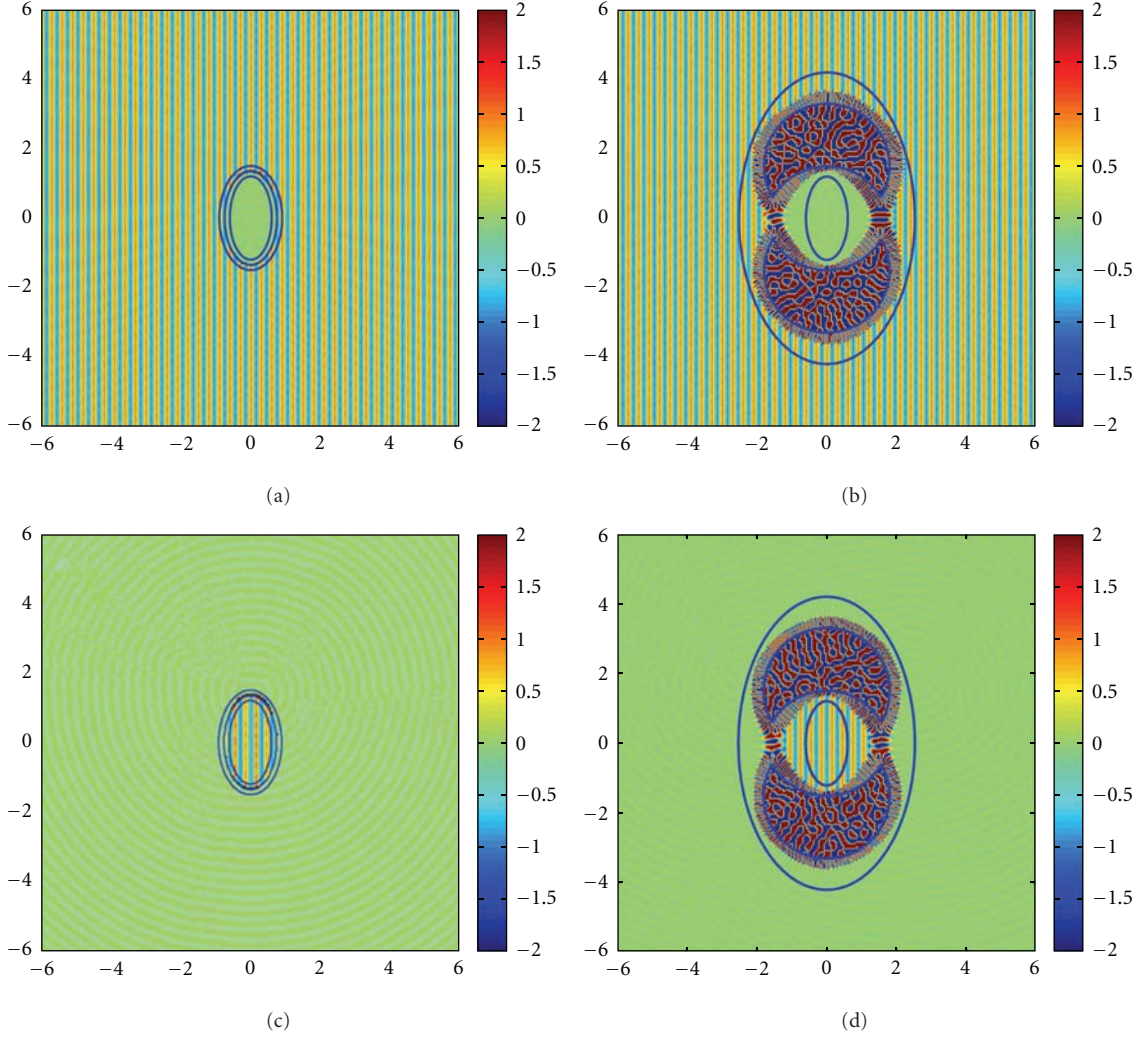


FIGURE 2: Numerical results for the active cloaking device. (a)-(b) Total fields for the closed and open configuration; (c)-(d) scattered fields for the closed and open configuration.

### 3. Numerical Calculation and Simulation for a Special Case

We first give the numerical calculation for a very special case, that is, invisibility cloaking using active devices. In this case, it is very clear that external and internal cloaking can be achieved by setting  $u_{\text{shift}} = 0$  in (3). In the simulation, a rightward propagating plane wave  $u_{\text{inc}} = e^{-jk_0x}$  is used as a probing wave just for its simplicity, but other forms of incident waves are applicable too. The total fields and the scattered fields for the two kinds of cloaking devices are shown in Figure 2, where Figures 2(a) and 2(b) show the total fields and Figures 2(c) and 2(d) show the scattered fields. In the left panels, where the closed configuration is demonstrated, active devices are uniformly placed on an elliptical curve, whose major axis is 1.35 m and the minor axis is 0.75 m. For the controlling boundary  $\Gamma_b$ , we set the major axis as 1.5 m and the minor axis as 0.9 m. While for  $\Gamma_c$ , the major axis is 1.2 m and the minor axis is 0.6 m. In

the right panels, we show the open configuration in which the active devices are placed on two separated crescents. The major and minor axes for the controlling boundary  $\Gamma_b$  are 4.2 m and 2.52 m, respectively and those for  $\Gamma_c$  are 1.2 m and 0.6 m, respectively. In both cases, the following parameters are chosen, wavelength  $\lambda = 0.3$  m,  $M(2N + 1) = 630$ ,  $M_c = 300$ , and  $M_b = 330$ . Employing the scheme described in the preceding section, we can achieve an approximate solution numerically. We can see from Figure 2 that the field inside the quiet zone is essentially zero with no scattering.

In order to quantify the overall quality of the solution, we consider the following error functions on the boundary  $\Gamma_b$  and  $\Gamma_c$ :

$$\begin{aligned} \text{Err}(\Gamma_b) &= \sum_{m=1}^{M_b} \frac{|u_d(\rho) - u_{\text{shift}}(\rho)|}{|u_{\text{shift}}(\rho)|}, \quad \rho \in \Gamma_b, \\ \text{Err}(\Gamma_c) &= \sum_{m=1}^{M_c} \frac{|u_d(\rho) + u_i(\rho)|}{|u_i(\rho)|}, \quad \rho \in \Gamma_c. \end{aligned} \quad (6)$$



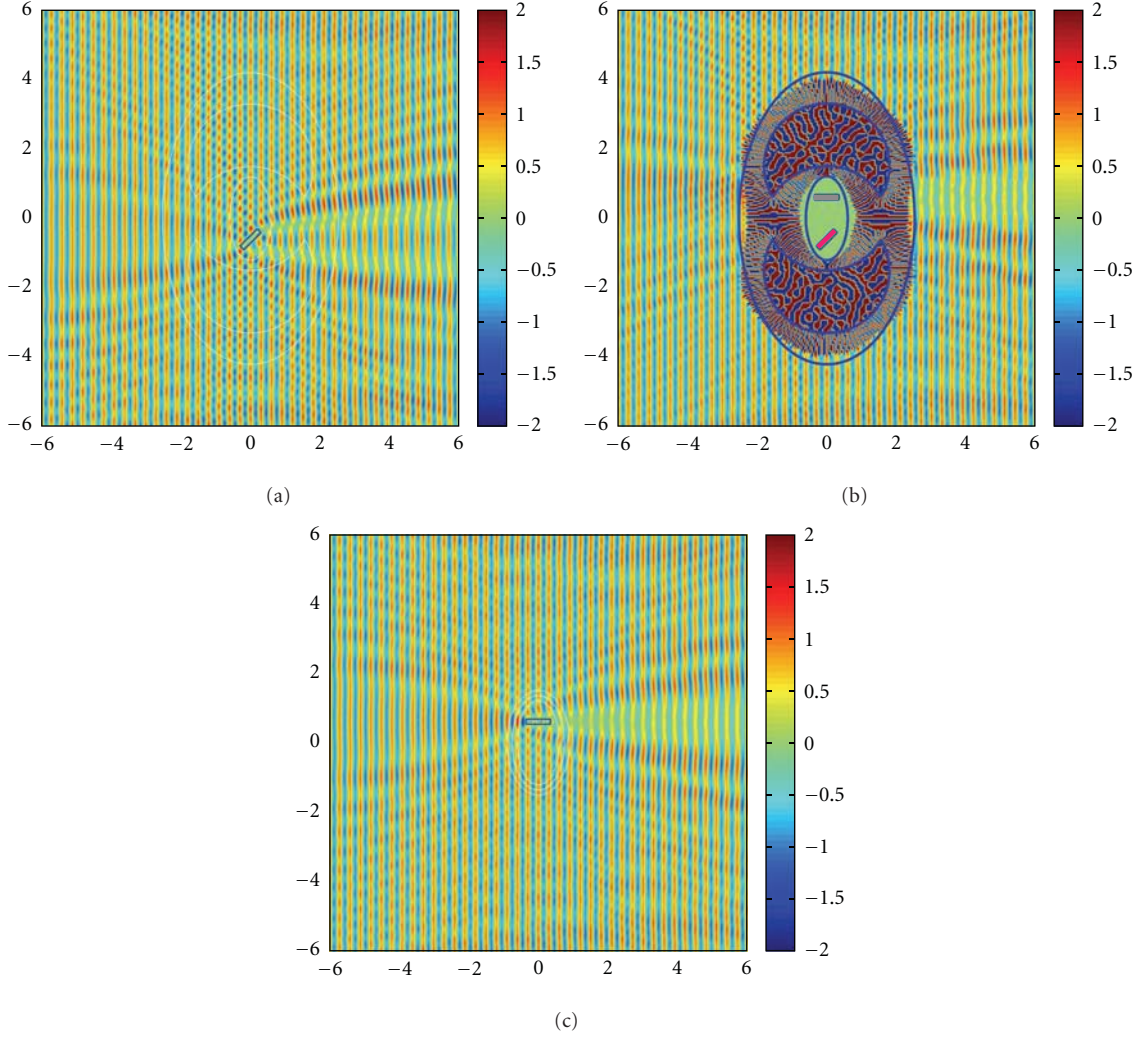


FIGURE 3: The virtual shift of a rectangular column using the open configuration. (a) Total fields distribution when the column is placed at  $(0, -0.6 \text{ m})$  with 45 degree to the horizon; (b) similar to (a) but the active device is turned on. (c) Total fields distribution when the column is placed at  $(0, 0.6 \text{ m})$  with zero degree to the horizon.

TABLE 1: The relationship between the errors on the boundary  $\Gamma_b$ ,  $\Gamma_c$  and the values of  $N$ ,  $M_b$ , and  $M_c$  for the cloak shown in Figure 2(a) ( $M = 60$ ).

$N$	1	2	3	4	5	6	7	8	9	10	11	12
$M_b$	120	200	250	320	400	450	500	550	600	700	760	820
$M_c$	60	100	170	220	260	330	400	470	540	560	620	680
$\text{Err}(\Gamma_c)$	2.5728 $e-005$	9.3572 $e-006$	1.3964 $e-005$	1.0182 $e-007$	4.6384 $e-007$	1.7500 $e-009$	1.1827 $e-008$	2.4238 $e-009$	8.3650 $e-012$	2.8560 $e-013$	1.5247 $e-012$	3.0913 $e-013$
$\text{Err}(\Gamma_b)$	3.1699 $e-005$	1.1729 $e-005$	1.7795 $e-005$	1.2499 $e-007$	6.4917 $e-007$	2.4167 $e-009$	2.6140 $e-008$	4.7026 $e-009$	9.8610 $e-012$	3.7850 $e-013$	2.1948 $e-012$	4.0417 $e-013$

The calculated errors on  $\Gamma_b$  and  $\Gamma_c$  are given in Tables 1 and 2 for the two configurations mentioned above, where Table 1 shows the errors for the internal cloak in Figure 2(a), and Table 2 shows the errors for the external cloak shown in Figure 2(b). From these two tables, it can be seen that the error decreases as we increase  $N$ . In other words, we are

able to achieve better cloaking effects if we can control the boundary fields more precisely. At the same time, it can be seen that the errors depend on the choice of  $M$ ,  $M_b$ , and  $M_c$  for a given working frequency, and the accuracy of the calculation is quite high. The results show that this method is convenient and flexible.

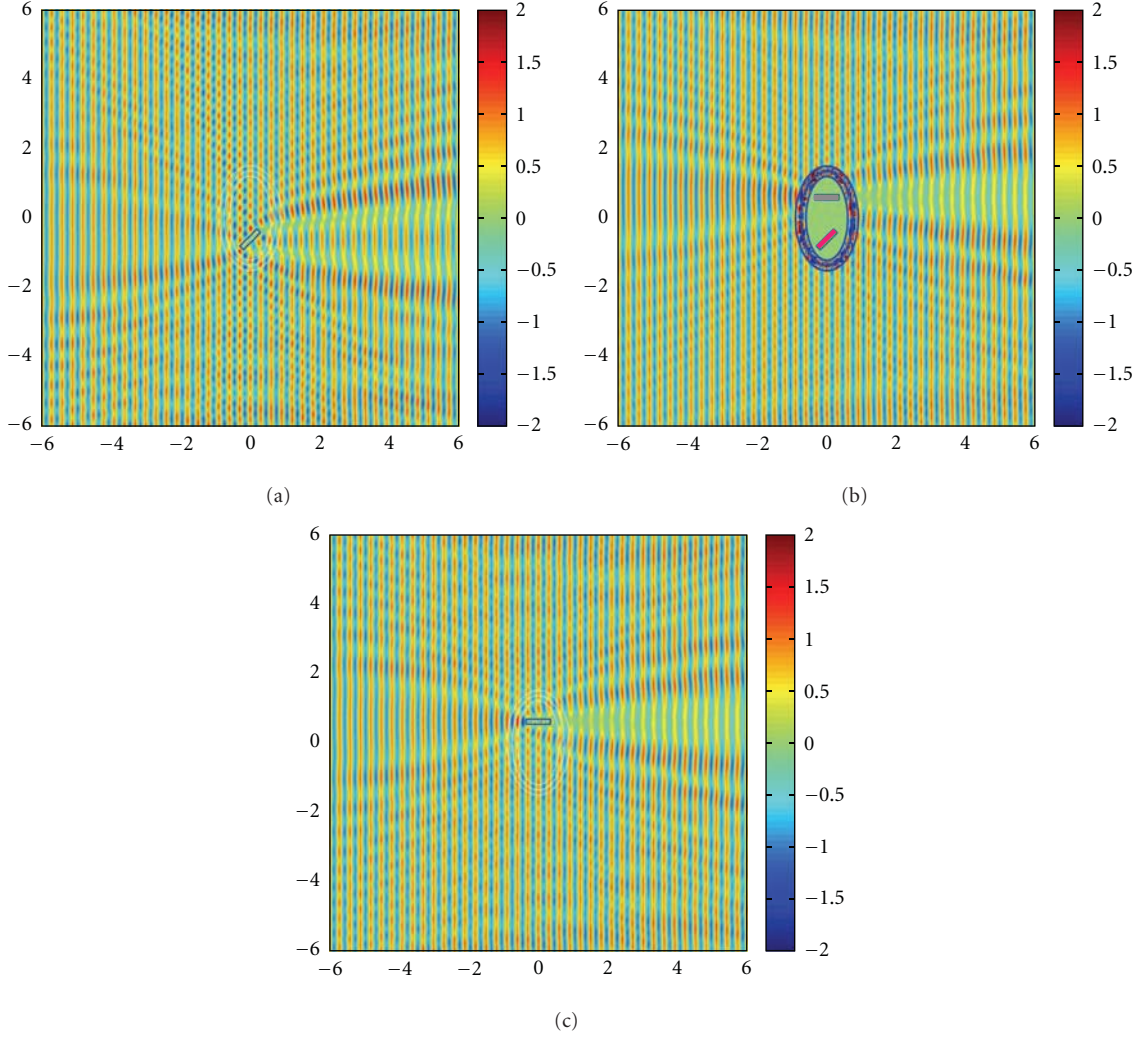


FIGURE 4: The virtual shift of a rectangular column using the closed configuration. (a) Total fields distribution when the column is placed at  $(0, -0.6 \text{ m})$  with 45 degree to the horizon; (b) similar to (a) but the active device is turned on. (c) Total fields distribution when the column is placed at  $(0, 0.6 \text{ m})$  with zero degree to the horizon.

TABLE 2: The relationship between the errors on the boundary  $\Gamma_b$ ,  $\Gamma_c$  and the values of  $N$ ,  $M_b$ , and  $M_c$  for the cloak shown in Figure 2(b) ( $M = 60$ ).

$N$	1	2	3	4	5	6	7	8	9	10	11	12
$M_b$	120	200	250	320	400	450	500	550	600	700	760	820
$M_c$	60	100	170	220	260	330	400	470	540	560	620	680
$\text{Err}(\Gamma_c)$	1.2086	9.7481 $e-005$	2.5488 $e-008$	2.8345 $e-008$	2.4315 $e-008$	1.8331 $e-008$	6.6296 $e-009$	1.8940 $e-009$	4.9820 $e-010$	8.9760 $e-011$	1.3725 $e-011$	4.6240 $e-012$
$\text{Err}(\Gamma_b)$	1.4135	7.8877 $e-005$	2.3319 $e-008$	2.6458 $e-008$	2.5146 $e-008$	1.9514 $e-008$	8.9207 $e-009$	2.4907 $e-009$	7.2545 $e-010$	1.3302 $e-010$	1.9367 $e-011$	5.5004 $e-012$

#### 4. Numerical Calculation and Simulation for Illusion of an Object

Next, we demonstrate the illusion effect where an object placed somewhere inside the quiet zone will appear at a different place. As an example, we choose a rectangular column with a cross-section of about  $0.7 \times 0.15 \text{ m}^2$  and

$\epsilon_r = 10$ ,  $\mu_r = 1$ . The wavelength of the incoming plane wave is  $\lambda = 0.3 \text{ m}$ . And other parameters are  $M(2N + 1) = 630$ ,  $M_c = 300$ , and  $M_b = 330$ , respectively. Figure 3(a) shows the total fields when the rectangular column is located at  $(0, -0.6 \text{ m})$  with 45 degree to the horizon under the plane wave illumination, while Figure 3(c) gives similar results but the rectangular column is located at  $(0, 0.6 \text{ m})$



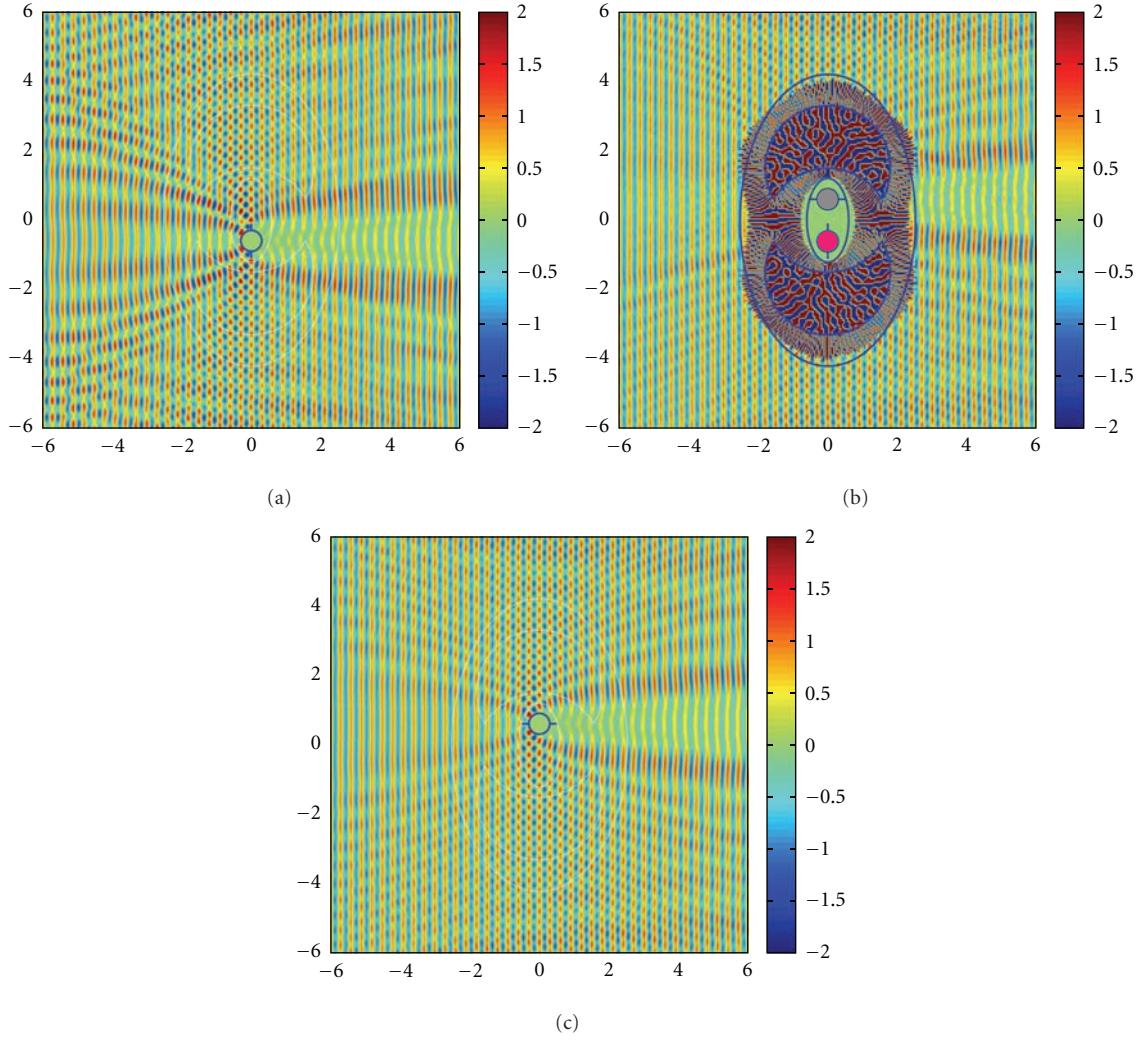


FIGURE 5: The virtual shift of a copper cylinder with a pair of metallic wings using the open configuration. (a) Total fields distribution when the column is placed at  $(0, -0.6 \text{ m})$  with 90 degree to the horizon; (b) similar to (a) but the active device is turned on. (c) Total fields distribution when the column is placed at  $(0, 0.6 \text{ m})$  with zero degree to the horizon.

with zero degree to the horizon; that is, it parallels to the horizontal line. In Figure 3(b), we show the total field of this rectangular column when the proposed active device shown in Figure 1(b) is turned on. Comparing Figure 3(b) with Figure 3(c) for the total fields outside the controlling boundary, we can see that they are very similar with each other. Therefore, the shift of the object is clearly realized together with a rotation. Figure 4 demonstrates similar results; however the closed configuration in Figure 1(a) is adopted.

Figures 5 and 6 show the virtual shift of a copper cylinder with a pair of metallic wings. The radius of the metal cylinder is about one wavelength. Other parameters are the same as those mentioned above. Figure 5(a) shows the total fields of this metal cylinder located at  $(0, -0.6 \text{ m})$  with the wings vertical to the horizon under the illumination of the plane wave. Figure 5(c) shows the total fields of the metal cylinder which is located at  $(0, 0.6 \text{ m})$  with the wings parallel to the horizon. And Figure 5(b) shows the total fields of this

metal cylinder with the active devices shown in Figure 1(b) switched on. Careful comparison between Figure 5(b) with Figure 5(c) shows that the distribution of the EM wave is exactly the same for the two figures out of the controlling boundary, which is another proof of the shift and rotation effect using this method. Figure 6 shows the similar results using active devices depicted in Figure 1(a).

To quantitatively validate the performance of the active illusion device, we also calculate the normalized scattering width for different cases, and the results are shown in Figure 7. The detailed calculation process can be found in [26]. In Figure 7(a), we give the scattering width for the open configuration, whose near fields are demonstrated in Figure 5. A careful examination shows that the normalized scattering pattern for the vertically placed metallic cylinder, represented by the blue dotted line, differs greatly from the horizontally placed one at a different position (green solid line). However, when active sources are deployed around the former one, we obtain a very similar scattering pattern,

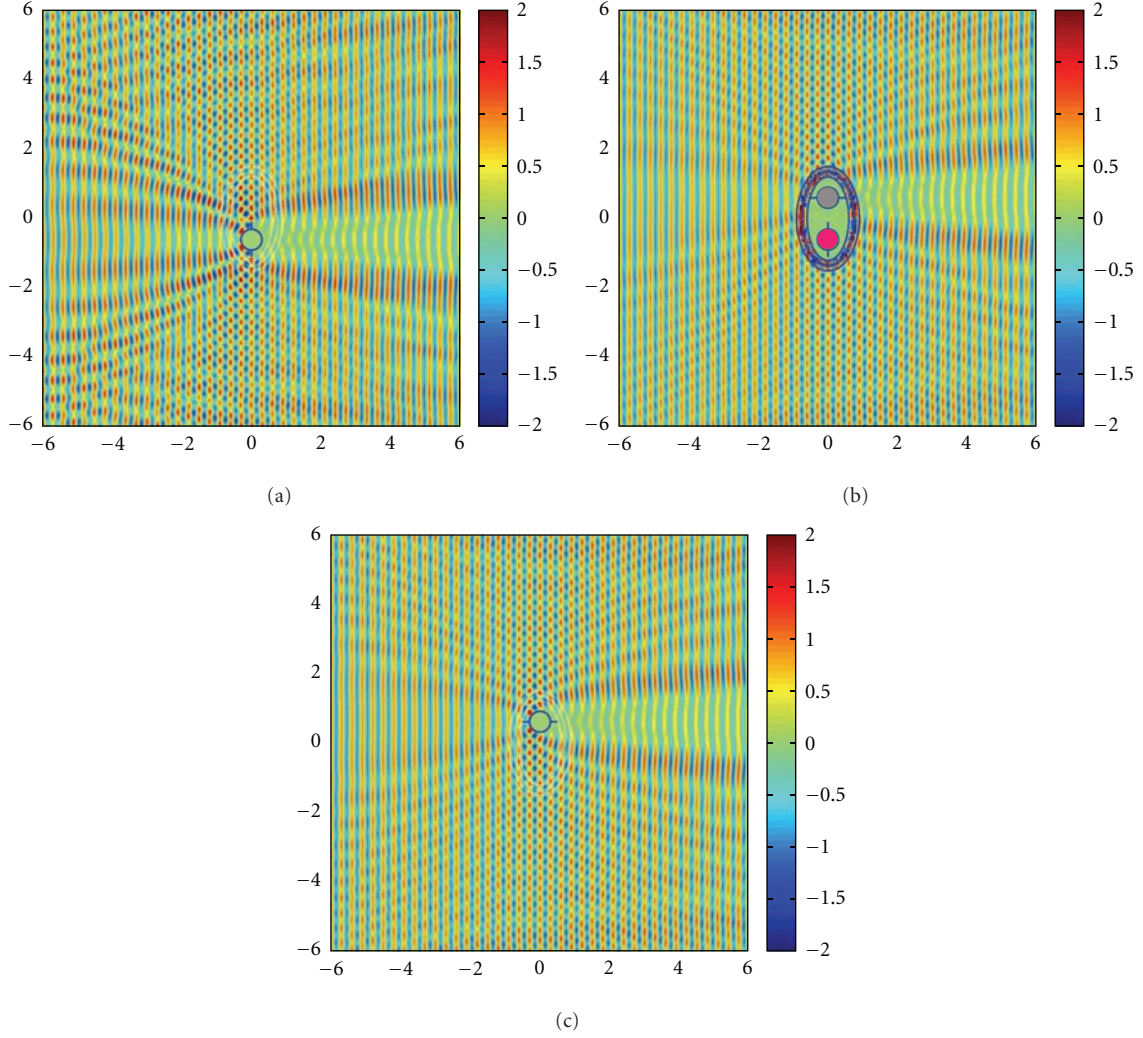


FIGURE 6: The virtual shift of a copper cylinder with a pair of metallic wings using the closed configuration. (a) Total fields distribution when the column is placed at  $(0, -0.6 \text{ m})$  with 90 degree to the horizon; (b) similar to (a) but the active device is turned on. (c) Total fields distribution when the column is placed at  $(0, 0.6 \text{ m})$  with zero degree to the horizon.

denoted by the red dash-dotted line. The differences mainly come from the following approximations: (1) limited terms used for Hankel's function,  $N = 3$  in our case; (2) limited points on the control boundary, that is,  $\Gamma_b$  and  $\Gamma_c$ , which are 330 and 300 in our calculation; (3) limited sources on  $\Gamma_a$ , which we set to 90. As mentioned in the previous section, larger numbers can lead to better performances. Figure 7(b) shows similar result for the closed structure, whose field distributions are demonstrated in Figure 6. In this case, better performances are obtained using the same parameter. This observation may be explained by a more uniform source distribution around the vertically placed metallic cylinder, which is clearly shown in Figure 1.

## 5. Summary

This paper presents a new method for realizing radar illusion for an arbitrary object by using active devices. The numerical

calculation and simulation in the 2D case are studied, which include both closed and open configurations, and the results firmly support our design. The method is convenient, flexible, efficient, and accurate. The work can be extended to three dimensions and to include other illusion effects [22–25]. The limitation of this type of radar illusion is that it requires the prior knowledge of the probing wave. However, with the development of modern digital signal processing technology, the result in this paper may have practical significance for realizing novel EM devices.

## Acknowledgments

The authors are grateful for the financial support from the State Key Laboratory of Millimeter Waves under Grant no. K201115, Natural Science Foundation of Gansu Province (no. 1107RJZA181), the Chunhui Project (no. Z2010081),

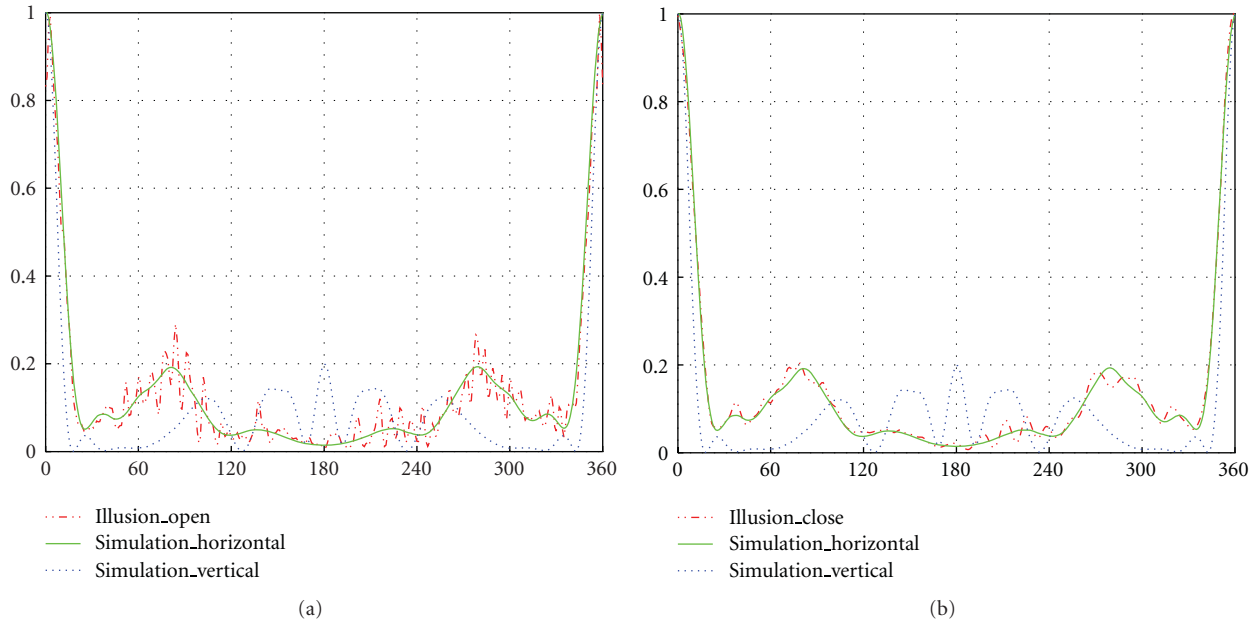


FIGURE 7: Normalized scattering width for different configurations. In the figure,  $x$ -axis represents the scanning angle (degree), and  $y$ -axis denotes the normalized scattering width. (a) The open configuration shown in Figure 5; (b) the closed configuration given in Figure 6.

and the Fundamental Research Funds for the Central Universities (no. LZUJBKY-2012-49).

## References

- [1] J. B. Pendry, D. Schurig, and D. R. Smith, "Controlling electromagnetic fields," *Science*, vol. 312, no. 5781, pp. 1780–1782, 2006.
- [2] D. Schurig, J. J. Mock, B. J. Justice et al., "Metamaterial electromagnetic cloak at microwave frequencies," *Science*, vol. 314, no. 5801, pp. 977–980, 2006.
- [3] B. Zhang, Y. Luo, X. Liu, and G. Barbastathis, "Macroscopic invisibility cloak for visible light," *Physical Review Letters*, vol. 106, no. 3, Article ID 033901, 2011.
- [4] X. Chen, Y. Luo, J. Zhang, K. Jiang, J. B. Pendry, and S. Zhang, "Macroscopic invisibility cloaking of visible light," *Nature Communications*, vol. 2, article 176, 2011.
- [5] G. W. Milton, M. Briane, and J. R. Willis, "On cloaking for elasticity and physical equations with a transformation invariant form," *New Journal of Physics*, vol. 8, no. 10, p. 248, 2006.
- [6] H. F. Ma and T. J. Cui, "Three-dimensional broadband ground-plane cloak made of metamaterials," *Nature Communications*, vol. 1, article 21, 2010.
- [7] A. Alu and N. Engheta, "Achieving transparency with plasmonic and metamaterial coatings," *Physical Review E*, vol. 72, no. 1, pp. 1–9, 2005.
- [8] H. Chen, C. T. Chan, and P. Sheng, "Transformation optics and metamaterials," *Nature Materials*, vol. 9, no. 5, pp. 387–396, 2010.
- [9] L. Sun and K. W. Yu, "Broadband electromagnetic transparency by graded metamaterials: scattering cancellation scheme," *Journal of the Optical Society of America B*, vol. 28, no. 5, pp. 994–1001, 2011.
- [10] W. Yan, M. Yan, Z. Ruan, and M. Qiu, "Coordinate transformations make perfect invisibility cloaks with arbitrary shape," *New Journal of Physics*, vol. 10, no. 4, pp. 1–13, 2008.
- [11] Y. You, G. W. Kattawar, P. W. Zhai, and P. Yang, "Invisibility cloaks for irregular particles using coordinate transformations," *Optics Express*, vol. 16, no. 9, pp. 6134–6145, 2008.
- [12] G. W. Milton and N. A. P. Nicorovici, "On the cloaking effects associated with anomalous localized resonance," *Proceedings of the Royal Society A*, vol. 462, no. 2074, pp. 3027–3059, 2006.
- [13] N. A. P. Nicorovici, G. W. Milton, R. C. McPhedran, and L. C. Botten, "Quasistatic cloaking of two-dimensional polarizable discrete systems by anomalous resonance," *Optics Express*, vol. 15, no. 10, pp. 6314–6323, 2007.
- [14] D. A. B. Miller, "On perfect cloaking," *Optics Express*, vol. 14, no. 25, pp. 12457–12466, 2006.
- [15] F. G. Vasquez, G. W. Milton, and D. Onofrei, "Broadband exterior cloaking," *Optics Express*, vol. 17, no. 17, pp. 14800–14805, 2009.
- [16] F. G. Vasquez, G. W. Milton, and D. Onofrei, "Active exterior cloaking for the 2D Laplace and Helmholtz equations," *Physical Review Letters*, vol. 103, no. 7, Article ID 073901, 2009.
- [17] H. H. Zheng, J. J. Xiao, Y. Lai, and C. T. Chan, "Exterior optical cloaking and illusions by using active sources: a boundary element perspective," *Physical Review B*, vol. 81, no. 19, pp. 1–10, 2010.
- [18] B. Z. Cao and L. Sun, "A new method for realizing illusion and shift of electromagnetic target based on active devices," in *Proceedings of the International Conference of Microwave and Millimeter Wave Technology (ICMMT '12)*, vol. 3, pp. 1–4, 2012.
- [19] Y. Lai, J. Ng, H. Chen et al., "Illusion optics: the optical transformation of an object into another object," *Physical Review Letters*, vol. 102, no. 25, pp. 1–4, 2009.
- [20] W. X. Jiang and T. J. Cui, "Moving targets virtually via composite optical transformation," *Optics Express*, vol. 18, no. 5, pp. 5161–5167, 2010.
- [21] W. X. Jiang, H. F. Ma, Q. Cheng, and T. J. Cui, "Illusion media: generating virtual objects using realizable metamaterials," *Applied Physics Letters*, vol. 96, no. 12, Article ID 121910, 2010.

- [22] T. Yang, H. Chen, X. Luo, and H. Ma, "Superscatterer: enhancement of scattering with complementary media," *Optics Express*, vol. 16, no. 22, pp. 18545–18550, 2008.
- [23] W. X. Jiang, H. F. Ma, Q. Cheng, and T. J. Cui, "Virtual conversion from metal object to dielectric object using metamaterials," *Optics Express*, vol. 18, no. 11, pp. 11276–11281, 2010.
- [24] W. X. Jiang and T. J. Cui, "Radar illusion via metamaterials," *Physical Review E*, vol. 83, no. 2, Article ID 026601, 2011.
- [25] W. X. Jiang, T. J. Cui, X. M. Yang, H. F. Ma, and Q. Cheng, "Shrinking an arbitrary object as one desires using metamaterials," *Applied Physics Letters*, vol. 98, no. 20, Article ID 204101, 2011.
- [26] C. Li and F. Li, "Two-dimensional electromagnetic cloaks with arbitrary geometries," *Optics Express*, vol. 16, no. 17, pp. 13414–13420, 2008.



## Review Article

# Dirac Dispersion in Two-Dimensional Photonic Crystals

**C. T. Chan, Zhi Hong Hang, and Xueqin Huang**

*Department of Physics, Hong Kong University of Science and Technology, Clear Water Bay, Kowloon, Hong Kong*

Correspondence should be addressed to C. T. Chan, phchan@ust.hk

Received 6 July 2012; Accepted 6 September 2012

Academic Editor: Pavel A. Belov

Copyright © 2012 C. T. Chan et al. This is an open access article distributed under the Creative Commons Attribution License, which permits unrestricted use, distribution, and reproduction in any medium, provided the original work is properly cited.

We show how one may obtain conical (Dirac) dispersions in photonic crystals, and in some cases, such conical dispersions can be used to create a metamaterial with an effective zero refractive index. We show specifically that in two-dimensional photonic crystals with  $C_{4v}$  symmetry, we can adjust the system parameters to obtain accidental triple degeneracy at  $\Gamma$  point, whose band dispersion comprises two linear bands that generate conical dispersion surfaces and an additional flat band crossing the Dirac-like point. If this triply degenerate state is formed by monopole and dipole excitations, the system can be mapped to an effective medium with permittivity and permeability equal to zero simultaneously, and this system can transport wave as if the refractive index is effectively zero. However, not all the triply degenerate states can be described by monopole and dipole excitations and in those cases, the conical dispersion may not be related to an effective zero refractive index. Using multiple scattering theory, we calculate the Berry phase of the eigenmodes in the Dirac-like cone to be equal to zero for modes in the Dirac-like cone at the zone center, in contrast with the Berry phase of  $\pi$  for Dirac cones at the zone boundary.

## 1. Introduction

The Dirac equation is the wave equation formulated to describe relativistic spin 1/2 particles [1]. In the special case where the effective mass of the spin 1/2 particle is zero, and the solution to Dirac equation has a linear dispersion in the sense that the energy  $E$  is linearly proportional to the wave vector  $k$ . The electric band structure of graphene near the Fermi level can be described by the massless Dirac equation and hence exhibit the Dirac dispersion [2–15]. The electronic band dispersion is linear near the six corners of the two-dimensional (2D) hexagonal Brillouin zone at the  $K$  and  $K'$  points, and the dispersion close to the Fermi energy at each of these corner  $k$ -points can be visualized as two cones meeting at the Fermi level at one point called the Dirac point, and the conical dispersion near the Dirac point is usually referred to as Dirac cones. This rather singular electronic band structure of graphene near the Fermi level gives rise to many unusual transport properties [2–15], including quantum hall effect [4–6], Zitterbewegung [7–11], and Klein paradox [12]. Dirac cone dispersions are not limited to graphene but can also be found in classical wave periodic systems such as photonic crystals [16–24]. In fact, linear dispersions at the Brillouin zone boundary for 2D

triangular photonic crystals appeared in the photonic band gap literature a long time ago [16] except that the attention at that time was focused on the creation of band gaps [25–27] and as Dirac points are by definition gapless, their existence was largely ignored. The special properties of such conical dispersions at the zone boundary of triangular photonic crystals were not explicitly noted until much later [21, 22]. It was noted that if an external magnetic field is used to break time reversal symmetry, unidirectional and backscattering immune electromagnetic wave propagation, analogous to quantum hall edge states, can be realized, and such ideas were indeed demonstrated subsequently using photonic crystals constructed with gyromagnetic materials [21–24, 28–32]. In 2D, the acoustic wave equation has the same form as the Maxwell equation for one polarization, and it follows immediately that Dirac cone dispersions can also be realized in acoustic wave crystals [33]. In fact, some intriguing wave transport phenomena such as Zitterbewegung is the consequence of the Dirac dispersion and hence can be realized in 2D photonic [20] and phononic crystal [33], and such effects were indeed numerically demonstrated [20] and experimentally verified [33]. With much longer wavelength compared to electrons, and without the complication of electron-electron interaction, photonic, and phononic

crystals have become an ideal platform to study various interesting wave propagation properties related to Dirac dispersion.

It turns out that the Dirac dispersion has interesting relationship with metamaterials, which are artificial composite materials that have novel wave manipulation capabilities. Since the theoretical proposal of materials with negative refractive indices proposed by Veselago in 1968 [34] and the first demonstration of a material with both effective permittivity ( $\epsilon_{\text{eff}}$ ) and effective permeability ( $\mu_{\text{eff}}$ ) less than zero in 2001 [35], metamaterials with all kinds of effective permittivity ( $\epsilon_{\text{eff}}$ ) and effective permeability ( $\mu_{\text{eff}}$ ) not found in nature have been designed and realized [35–48]. With the help of these metamaterials, many interesting waveguiding properties, some seemingly fictional, have been achieved including negative refraction [35–39], superlens [40, 41], cloaking [42–44], field concentrators [45], superscatterer [46], field rotators [47], and illusion optics [48]. While previous attention may have been focused on realizing metamaterials with negative refractive indices, materials that have zero refractive indices are equally interesting. As  $n^2 = \epsilon\mu$ , a zero-refractive-index material can have either single zero ( $\epsilon_{\text{eff}} = 0$  or  $\mu_{\text{eff}} = 0$ ) or double zero ( $\epsilon_{\text{eff}} = \mu_{\text{eff}} = 0$ ) [49–64]. There is no phase variance in the wave transport process inside a zero-index material. This leads to many peculiar properties such as the tunneling of electromagnetic waves through subwavelength channels and bends [49–57], the tailoring of the radiation phase pattern of arbitrary sources [58–60], and the cloaking of objects inside a channel with specific boundary conditions [61–64]. The tunneling phenomenon has been demonstrated experimentally using complementary split ring resonators at the microwave frequency [55]. However, the impedance mismatch is typically huge for single-zero materials, and the incident wave may encounter reflection when the aperture of the waveguide is larger than wavelength [60, 64]. This problem can be mitigated if we use double-zero material ( $\epsilon_{\text{eff}} = 0$  and  $\mu_{\text{eff}} = 0$  at the same frequency).

While Dirac cone dispersion and zero-index materials may seem unrelated, there is a subtle relationship between them. If we have a homogeneous material with isotropic dispersive permittivity  $\epsilon(\omega)$  and permeability  $\mu(\omega)$  at a particular frequency  $\omega_0$  and  $\epsilon(\omega_0) = \mu(\omega_0) = 0$ , the dispersion near  $\omega_0$  will have a linear dispersion,  $\omega = \omega_0 + v_g k$ , where  $k$  is the wave vector and  $v_g$  is the corresponding group velocity [65]. This linear dispersion and the associated conical dispersion are different from the Dirac dispersion found in graphene [2–15] or hexagonal photonic/phononic crystals [16–24, 31–33] as the Dirac point is not at the Brillouin zone boundary but at the zone center. This relationship opened a new window to the physics related to Dirac cones but the question is whether we can construct a metamaterial with  $\epsilon(\omega_D) = \mu(\omega_D) = 0$  at a particular frequency  $\omega_D$  using a conical dispersion at  $k = 0$  close to this frequency. Another important issue is that a homogenous  $\epsilon(\omega_0) = \mu(\omega_0) = 0$  implies a Dirac cone dispersion but the converse may not be true for the simple reason that an effective medium description may or may not be applicable to the composite material with a Dirac cone dispersion. We will show by

examples that there are indeed systems which have Dirac-like cone at  $k = 0$ , and we will examine the conditions for effective medium theory to be applicable [66].

We will show that if a 2D photonic crystal has  $C_{4v}$  symmetry, we can obtain accidental degeneracy of a twofold degenerate state and a nondegenerate state at  $\Gamma$  point by tuning the parameters of the structure, and that two of the states of the triply degenerate state have linear dispersions near  $\Gamma$ , and they can generate conical dispersions. We will further demonstrate that if the triply degenerate state is derived from monopole and dipole excitations, we can use effective medium theory to map this photonic crystal to a zero-index material with both permittivity and permeability equal to zero simultaneously [66]. We will also give examples that conical dispersions at the zone center can be obtained for situations in which the bands are not derived from monopole and dipole excitations, and in these cases, we will demonstrate that these Dirac-like cone systems cannot be related to an effective medium with a zero refractive index. In this paper, we will also examine the Berry phase [67] associated with the Dirac-like cone at  $k = 0$  which is the phase acquired by the eigenvector over a cyclic evolution in  $k$  space about the Dirac point. It is known that the Berry phase associated with the Dirac cone is  $\pi$  in electronic graphene and has very subtle implications in wave function transport properties [4–6]. We will show that the Berry phase associated with the Dirac-like cone at  $\Gamma$  point is different from that of graphene because of the existence of an additional quasi-longitudinal mode. The paper is organized as follows. In Section 2, we introduce the Dirac-like point at  $\Gamma$  point and M point in 2D photonic crystal with  $C_{4v}$  symmetry and examine the possibility and consequences of effective medium descriptions. In Section 3, we calculate the Berry phase of the triply degenerate state formed by Dirac-like point. We will then give a summary.

## 2. Dirac-Like Point at $\Gamma$ Point and M Point in $C_{4v}$ Symmetry

Let us first consider an example of a 2D photonic crystal that exhibits a Dirac-like cone in the zone center and in this specific structure, effective medium theory can be used to relate the system to an effectively zero-refractive-index system [66]. The photonic crystal is a square array of alumina cylinders with relative permittivity  $\epsilon = 8.8$  in air and the polarization is transverse-magnetic (TM) polarization, with electric field parallel to the cylinder axis. The radii of the cylinders are  $0.221a$ , where  $a$  is the lattice constant. There is a triply degenerate state at a frequency  $\omega_D$  at the  $\Gamma$  point. We note that the triple degeneracy is not a consequence of lattice symmetry in the sense that if we choose other system parameters (e.g., a different cylinder radius), the triple degenerate state will split into a doublet and a singlet. The field patterns of these three states are shown in Figures 1(d)–1(f). We see that electromagnetic field is mostly confined inside the high refractive index rod and two of the eigenmodes (panels (e) and (f)) have a strong dipolar character, with the wave vector perpendicular/parallel to



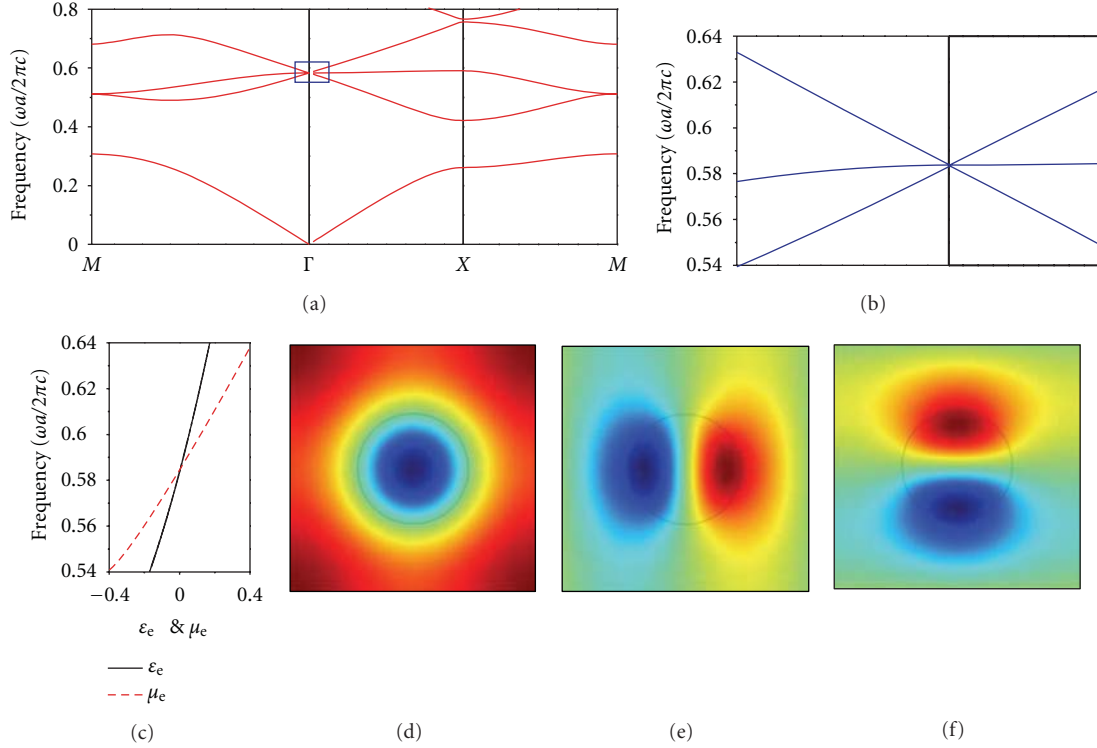


FIGURE 1: (a) The band structure of a two-dimensional photonic crystal composing of alumina cylinders arranged in a square lattice for the TM polarization. The radii of the cylinders are  $0.221a$ . The relative permittivity of the cylinders is 8.8. At the  $\Gamma$  point, a triply degenerate state is formed, and the linear dispersion near the zone center is highlighted in (b). (c) The effective permittivity  $\epsilon_{\text{eff}}$  (black solid line) and permeability  $\mu_{\text{eff}}$  (red dash line) of this alumina photonic crystal. Note that  $\epsilon_{\text{eff}} = \mu_{\text{eff}} = 0$  at the Dirac-like point. (d)–(f) The field patterns of the three eigenmodes near the Dirac-like point with a very small  $k$  along  $\Gamma X$  direction.

the dipole moment (transverse/longitudinal dipole mode), and the other eigenmode has a monopole character. By examining carefully the band diagram near  $\omega_D$  (Figure 1(b)) corresponding to the solid blue region in Figure 1(a), we found that the two linear bands generate a conical dispersion with the upper and lower cones touching at a Dirac-like point at  $\omega_D$ . The equifrequency contours are circular near  $\omega_D$  and eigenmodes in the cones are linear combinations of transverse dipole and monopole modes. There is an extra flat band intersecting the Dirac-like cones at  $\omega_D$ . The modes in this flat sheet of states are quasi-longitudinal such that the magnetic field is mostly parallel to the  $k$ -vector. It can be shown [68] that if the band dispersions in a 2D photonic crystal can be described by monopole and dipole interactions, an effective medium theory [68] can be applied to extract effective constitutive parameters and when these parameters of the photonic crystal are retrieved, we find that  $\epsilon_{\text{eff}}(\omega_D) = \mu_{\text{eff}}(\omega_D) = 0$  at the Dirac frequency  $\omega_D$  (Figure 1(c)). The sheet of quasi-longitudinal modes cutting through the Dirac-like point corresponds to the longitudinal solution to the Maxwell equation when  $\mu_x = \mu_y = 0$  for TM polarization (or  $\epsilon_x = \epsilon_y = 0$  for TE polarization). For a homogenous isotropic medium with  $\epsilon = \mu = 0$ , this longitudinal mode has exactly zero group velocity but in a composite system, this mode has a quadratic dispersion far away from the zone center because of spatial dispersion.

In order to demonstrate that the photonic crystal with a band dispersion shown in Figure 1 does have  $\epsilon_{\text{eff}}(\omega_D) = \mu_{\text{eff}}(\omega_D) = 0$  at the Dirac frequency, numerical simulations, and microwave experiments were carried out [66]. Both the focusing effect through a concave lens and the waveguiding and cloaking effect through a waveguide filled with  $\epsilon_{\text{eff}} = \mu_{\text{eff}} = 0$  photonic crystal were demonstrated. The  $\epsilon_{\text{eff}} = \mu_{\text{eff}} = 0$  photonic crystal was demonstrated to have nearly the same field distributions as a homogenous  $\epsilon = \mu = 0$  medium in wave transport simulations. For example, as there is no phase change during the propagation through a zero-index material, the zero-index material can serve as a wavefront transformer [58–60]. Here, we numerically demonstrate another wavefront transformer phenomenon, the transformation of a Gaussian beam to a plane wave. In Figure 2(a), an  $18a \times 18a$  block of a hypothetical homogeneous  $\epsilon = \mu = 0$  medium is put inside a waveguide and is illuminated with a tightly focused Gaussian beam whose waist is equal to  $3a$ , where  $a$  is the lattice constant of the photonic crystal shown in Figure 1. As the only allowed propagation mode through a homogeneous  $\epsilon = \mu = 0$  medium is a plane wave with zero parallel wavevector and as the exit surface is flat, the wave leaving the exit surface should be a plane wave with equal phase at the exit surface as demonstrated numerically in Figure 2(a). The field inside the homogeneous  $\epsilon = \mu = 0$  medium is constant. In Figure 2(b), we replace the

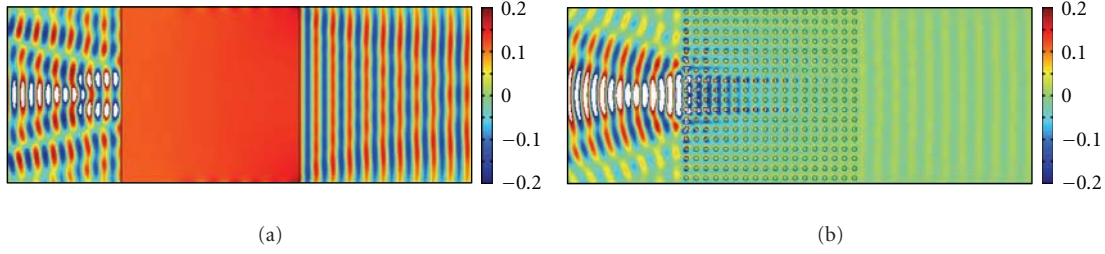


FIGURE 2: Numerical simulation that demonstrates the  $\epsilon_{\text{eff}} = \mu_{\text{eff}} = 0$  property of the alumina photonic crystal with Dirac-like cone dispersion at the Brillouin zone center. (a) An  $18a \times 18a$  block of a hypothetical homogeneous  $\epsilon = \mu = 0$  medium is placed inside a waveguide with a tightly focused (waist equal to  $3a$ ) Gaussian beam incident at the surface of the homogeneous  $\epsilon = \mu = 0$  medium. As the  $\epsilon = \mu = 0$  medium only allows plane wave with  $k_{\parallel} = 0$  to propagate, we expect only plane wave can exit, which can be clearly seen. The Gaussian wave front is transformed to a plane wave. (b) By replacing the homogeneous  $\epsilon = \mu = 0$  medium with the  $\epsilon_{\text{eff}} = \mu_{\text{eff}} = 0$  alumina photonic crystal, very similar wavefront transformation can be observed. Here,  $a$  is the lattice constant of the photonic crystal.

homogeneous  $\epsilon = \mu = 0$  medium with the photonic crystal consisting of alumina cylinders, and we observe a similar transformation of a Gaussian wave to a plane wave. The field distributions inside the photonic crystal are slightly different from the homogeneous  $\epsilon = \mu = 0$  medium shown in Figure 2(a) due to the excitation of the quasi-longitudinal mode in the photonic crystal.

The realization of  $\epsilon_{\text{eff}} = \mu_{\text{eff}} = 0$  using dielectric photonic crystals may enable us to achieve various waveguiding applications specific to zero-refractive-index medium in the near future. There are multiple ways to realize a zero refractive index. For example,  $\epsilon_{\text{eff}} = 0$  or  $\mu_{\text{eff}} = 0$  or  $\epsilon_{\text{eff}} = \mu_{\text{eff}} = 0$  metamaterial can be designed and fabricated using metallic resonant structures [55]. However, metallic resonant structure is always lossy, and the loss will become more severe when at higher frequencies. On the other hand, as the photonic crystals with Dirac-like cone at  $k = 0$  are made with dielectric, the system can function as  $\epsilon_{\text{eff}} = \mu_{\text{eff}} = 0$  system with small material loss all the way up to optical frequencies and the fabrication of nanoscale dielectric pillar structure is feasible with modern silicon nanofabrication technology [69]. We also remark that the Dirac-like cone at  $k = 0$  gives us  $\epsilon_{\text{eff}} = 0$  and  $\mu_{\text{eff}} = 0$  simultaneously (“double zero”) which has the advantage of a finite group velocity and favorable impedance matching as compared to a “single zero” material ( $\epsilon_{\text{eff}} = 0$  or  $\mu_{\text{eff}} = 0$  but not both) which has a zero group velocity and poor impedance matching. The double-zero condition is difficult to satisfy if we use metallic resonators to obtain  $\epsilon_{\text{eff}} = 0$  and  $\mu_{\text{eff}} = 0$  at the same frequency.

As the necessary (but not sufficient) condition to get an  $\epsilon_{\text{eff}} = \mu_{\text{eff}} = 0$  photonic crystal is a Dirac-like cone at  $k = 0$  and the condition to get a Dirac-like cone at the zone center is accidental degeneracy, we will discuss here how to obtain accidental degeneracy, and we limit our discussion here to square lattice systems. The point group symmetry of a photonic crystal of square array of cylinders belongs to the  $C_{4v}$  group [70]. The irreducible representations of  $C_{4v}$  point group are  $A_1$ ,  $B_1$ ,  $A_2$ ,  $B_2$ , and  $E$ , where  $A_1$ ,  $B_1$ ,  $A_2$ ,  $B_2$  are nondegenerate representations, and  $E$  is a doubly degenerate representation. The eigenstates at  $k = 0$  of a square lattice photonic crystal should have

symmetries related to these irreducible representations. At a finite frequency, the dispersion of a nondegenerate band at Brillouin zone center has to be parabolic as required by time reversal symmetry [71–73]. However, we need linear bands to generate Dirac-like cones. Linear dispersion at the Brillouin zone center ( $\Gamma$  point) can emerge as a consequence of accidental degeneracy of states which are not required by lattice symmetry to be equal in frequency and such accidental degeneracy can be obtained by tuning the dielectric constant or the radii of the cylinders in 2D photonic crystals.

For a periodic structure with a permittivity distribution  $\epsilon(\vec{r})$ , the Bloch eigenfunction  $\psi_k(\vec{r})$  should satisfy the equation

$$\nabla \times \left[ \frac{1}{\epsilon(\vec{r})} \nabla \times \psi_k(\vec{r}) \right] = \frac{\omega_k^2}{c^2} \psi_k(\vec{r}), \quad (1)$$

where  $\psi_k(\vec{r})$  is the eigenmode of the magnetic field and  $\omega_k$  is the corresponding eigenvalue. The Bloch eigenfunction can be chosen to a linear combination of the localized states (e.g., Wannier-type function) of  $A_1$ ,  $B_1$ ,  $A_2$ ,  $B_2$ ,  $E$  representations of the  $C_{4v}$  point group [72–75] centered on the cylinders. It can be written as

$$\psi_k(\vec{r}) = \frac{1}{V} \sum_{l,m} e^{i\vec{k} \cdot \vec{r}_{lm}} \sum_i A_i M^{(i)}(\vec{r} - \vec{r}_{lm}), \quad (2)$$

where  $\vec{r}_{lm} = la\hat{x} + ma\hat{y}$ ,  $a$  is the lattice constant.  $V$  is the volume of the unit cell.  $M^{(i)}(\vec{r})$  are localized functions of  $A_1$ ,  $B_1$ ,  $A_2$ ,  $B_2$ ,  $E$  representations, where  $i$  labels the irreducible representation. These basis functions are chosen to be orthogonal

$$\int_V d\vec{r} M^{(i)*}(\vec{r}) \cdot M^{(j)}(\vec{r}) = V \delta_{ij}. \quad (3)$$

The integral is over the whole unit cell  $V$ .

These basis functions have different symmetry properties. For instance, modes of the  $A_1$  representation invariant for all symmetry operation and if a band is derived from the

monopole excitations of the cylinders, it should be expanded by  $M^{A_1}(\vec{r})$ . As modes of  $E$  representations have mirror symmetry about the  $x$ - and  $y$ -axis, respectively,  $M_{1,2}^E(\vec{r})$  can be used to expand bands that derived from dipole excitations of the cylinders in the photonic crystals. We can obtain a “double-zero” photonic crystal if we design the system to have accidental degeneracy so that the monopole and dipole derived bands become degenerate at the zone center. In that case, the eigenmodes near the zone center should be expressed as a linear combination of  $M^{A_1}(\vec{r})$  and  $M_{1,2}^E(\vec{r})$  states. Generally speaking, if there is accidental degeneracy at the zone center, the eigenmodes will be a combination of two irreducible states, either a mix of three states (for the case of  $E$  state degenerate with any nondegenerate state) or a mix of two states (the degeneracy of two nondegenerate states). For simplicity, we only consider the accidental degeneracy of  $E$  state and  $A_1$  state. If we only consider the nearest neighbor interaction,  $l, m = 0, \pm 1$ , multiply  $M^{(i)*}(\vec{r})$  on both side of (1), integrate over the unit cell  $V$ , and use orthogonal condition of (3), we can transfer (1) into a secular equation

$$\left| \vec{S} - \frac{\omega_D^2}{c^2} \vec{I} \right| = 0. \quad (4)$$

$\vec{S}$  is a  $3 \times 3$  matrix with  $S_{ij} = \sum_{lm} e^{ia(lk_x + mk_y)} L_{lm}^{ij}$ , where  $L_{lm}^{ij} \equiv (1/V) \int_V d\vec{r} M^{(i)*}(\vec{r}) \cdot \nabla \times [(1/\epsilon(\vec{r})) \nabla \times M^{(j)}(\vec{r}) - \vec{r}_{lm}]$  is a transfer integral.  $\omega_D$  is the accidental degeneracy frequency.  $M^{(i/j)}$  can be either  $M^{A_1}$  or  $M_{1,2}^E$ . By solving (4) close to the  $\Gamma$  point, with tiny  $k_x$  and  $k_y$ , the dispersion near  $\omega_D$  can be found consisting of two linear bands with a finite group velocity along with a quadratic band which is very flat near the  $\Gamma$  point. The linear bands will generate conical dispersion (Dirac cone) close to the degeneracy frequency  $\omega_D$  near the  $\Gamma$  point. The degenerate frequency  $\omega_D$  is the Dirac-like point frequency we are looking for. We note that the emergence of linear bands as a consequence of accidental degeneracy at  $k = 0$  can also be obtained using multiple scattering theory [66] or  $k \cdot p$  perturbation [76, 77]. Conical dispersions will also emerge from the accidental degeneracy of  $E$  states and the other three nondegeneracy states  $B_1$ ,  $A_2$ ,  $B_2$ . The linear bands giving rise to conical dispersion will always be accompanied by a quadratic band if the accidental degeneracy is threefold.

We now have a recipe to create Dirac dispersion at a finite frequency at  $k = 0$  for the lattice with  $C_{4v}$  point group symmetry. However, we should emphasize that Dirac dispersion is a necessary but not sufficient condition to obtain  $\epsilon_{\text{eff}} = \mu_{\text{eff}} = 0$ . As we are always dealing with composite materials with at least two components, an effective medium theory must be applied to extract the effective constitutive parameters from the optical properties of the discrete system. For photonic applications, we prefer to use “local” effective parameters which depend only on the frequency but not the wave vector. The Dirac cones that are discussed in the literature are located at the Brillouin zone boundary [16–24] and at such a large wave vector, no effective medium

theory can be applied reliably. Even at the  $\Gamma$  point, effective medium theory can be applicable only if certain conditions are satisfied. It can be shown that in 2D photonic crystals, effective medium theory can be applied to extract  $\epsilon_{\text{eff}}$  and  $\mu_{\text{eff}}$  if the bands are derived from the monopole and dipole scattering of the building blocks [68], and this condition is indeed satisfied by the photonic crystal system shown in Figures 1 and 2. This condition can typically be satisfied in photonic crystals comprising dielectric cylinders in air in which the low-lying bands are formed by the scattering of monopole and dipole excitations of the individual dielectric cylinders, and the field distributions of the eigenmodes tend to be confined in the cylinders. If the eigenmodes have projections on higher multipoles, the effective medium description will not be good. This can happen if the dielectric constant of the cylinders is small so that Dirac-like cone appears at high frequencies. Also, if we have an inverted structure, such as photonic crystals with cylindrical holes drilled in high dielectric background medium, the effective medium will naturally fail as the eigenmodes in those situations typically have large projections on high multipoles centered on the holes.

From symmetry considerations, we know that as long as there is an accidental degeneracy of a doubly degenerate state with a nondegenerate state, the Dirac-like point can be formed. And we have already shown in Figure 1 that Dirac-like cones can be formed when there is accidental degeneracy of monopole and dipole modes that are described by  $E$  and  $A_1$  representations, and the photonic crystal behaves like a zero-index material near the Dirac-like point. Here, we give an example of a photonic crystal which has a Dirac-like point that is formed by the accidental degeneracy of eigenmodes of  $E$  and  $B_1$  representations. The system consists of core-shell cylinders arranged in a square lattice and the band structure for the TE polarization with the magnetic field along the cylinder axis is shown in Figure 3(a). The radii of the shell and core are  $R_{\text{shell}} = 0.4a$  and  $R_{\text{core}} = 0.181a$  respectively. Here,  $a$  is the lattice constant. The relative permittivity of the shell and core  $\epsilon_{\text{shell}} = 11.75$  and  $\epsilon_{\text{core}} = 1$ . There is a Dirac-like point at the  $\Gamma$  point at the location highlighted by the blue box, comprising of two linear bands and a flat band cross intersecting at the same frequency (Figure 3(a)). The enlarged band structure near the Dirac-like point is shown in the inset. In order to understand the underlying physics, we plot the eigenmodes of this triply degenerate state in Figures 3(b) to 3(d). Figures 3(b) and 3(c) show that the eigenmode has strong dipole character, and Figure 3(d) shows a quadrupole excitation. Symmetry analysis shows that the dipole excitations belong to the  $E$  representation, while the quadrupole excitation belongs to the  $B_1$  representation. As effective medium theory [68] is not expected to work when the bands have a strong quadrupole character, we expect that the system should not behave like a zero-index medium even though it has a conical dispersion. To see the wave transport properties of this system near the Dirac frequency, a Gaussian beam is illuminated to this photonic crystal as shown in Figure 3(e), with the same parameters as in Figure 2(b). There are phase changes inside the photonic crystal, and the field distributions outside are

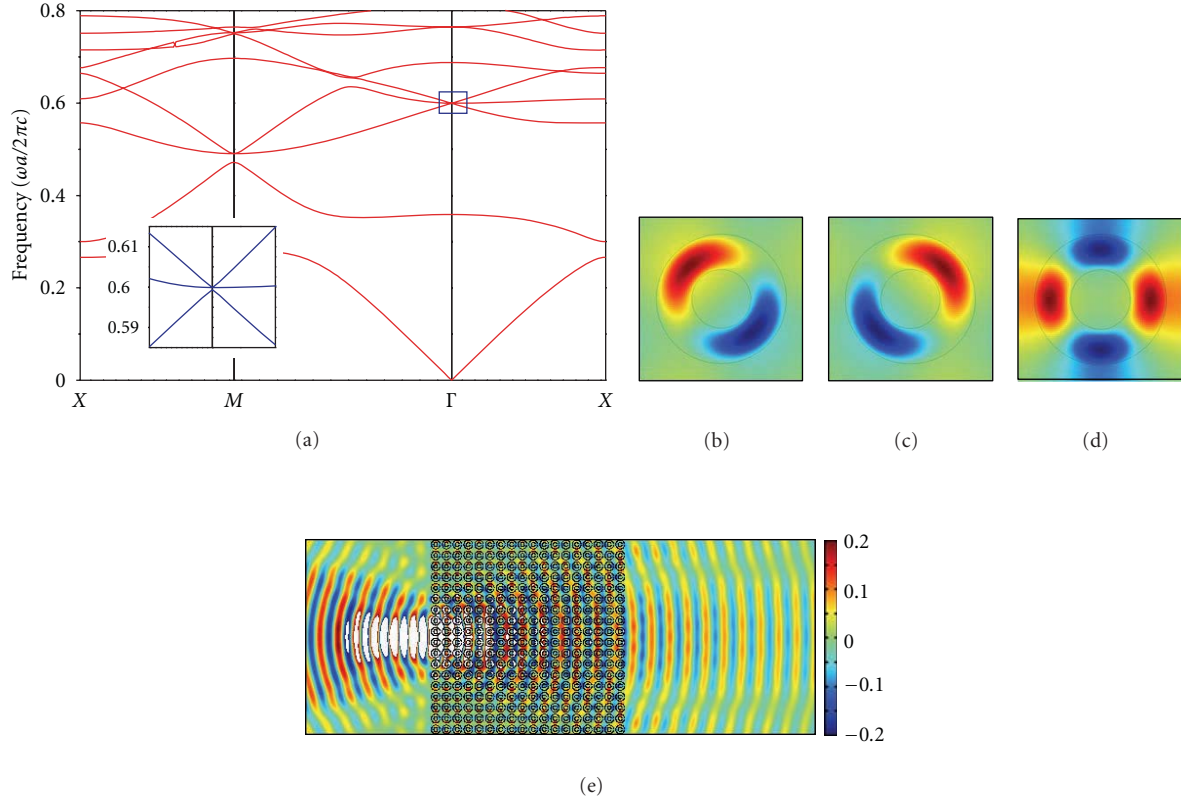


FIGURE 3: (a) The band structure of a core-shell photonic crystal arranged in square lattice for the TE polarization. The radii of the shell and core are  $R_{\text{shell}} = 0.4a$  and  $R_{\text{core}} = 0.181a$ . The relative permittivity of the shell and core are  $\epsilon_{\text{shell}} = 11.75$  and  $\epsilon_{\text{core}} = 1$ . Near the  $\Gamma$  point, there is a Dirac-like cone dispersion. The inset is the enlarged part near the Dirac-like point shown by blue solid region. (b)–(d) The eigenmodes of the photonic crystal at the  $\Gamma$  point. (b) and (c) dipole excitations, (d) quadrupole excitation. (e) As effective medium theory cannot be applied here, the crystal cannot be mapped to a  $\epsilon_{\text{eff}} = \mu_{\text{eff}} = 0$  system and hence the field distributions for an incident Gaussian beam deviate from what is expected for homogeneous  $\epsilon = \mu = 0$  medium (Figure 2(a)).

not a plane wave front. The wave transport behavior deviates from what is expected from an  $\epsilon = \mu = 0$  medium.

For completeness, we also show the properties of photonic crystals consisting of low dielectric cylinders and we examine whether such systems can be used to mimic a  $\epsilon_{\text{eff}} = \mu_{\text{eff}} = 0$  material. We use a low dielectric constant material, PMMA with  $\epsilon = 2.6$  for the cylinders. We can adjust the structural parameters to obtain accidental degeneracy and Dirac-like cone dispersion can be achieved as shown in Figure 4(a). A Dirac-like cone is obtained when the radii of the cylinders are  $0.3035a$ . The band structure is shown for the TM polarization in Figure 4(a). When we repeat the same simulation as in Figure 2(b) for this PMMA photonic crystal, the wavefront transformation effect (Figure 4(b)) is also different to what is expected from homogeneous  $\epsilon = \mu = 0$  medium. In this low dielectric contrast system, the low-lying bands are better described by a plane wave basis rather than the coupling of localized modes centered on a cylinder. Alternatively, one may say that the Dirac-like cone will be found at high frequencies if the dielectric cylinders have a low refractive index and effective medium theory has to fail at high frequencies. In fact, calculations show that

the effective medium description gets better and better if the cylinders have progressively higher dielectric constants with the corresponding Dirac-like cone moving to lower frequencies.

Some remarks are in order here. We note that the band dispersion is not just linear in one direction, but it is isotropic and linear in all directions of  $k$ -vectors and as such, the isotropic linear dispersion generates two cones that touch at one point commonly referred to a Dirac point. The Dirac cone dispersion in graphene is generated by two degrees of freedom, frequently formulated as two components of a pseudospin. These two degrees of freedom are actually the amplitude of the  $p_z$  wave functions on sites A and B of the carbon atoms within the unit cell of graphene. In the  $\Gamma$  point Dirac cone in photonic crystals, we actually have three degrees of freedom, two from the dipolar excitations and one from the monopolar excitation. These three freedoms generate a conical dispersion plus a flat band. We also remark that not all linear dispersions form Dirac cone/Dirac point. For example, most classical wave systems have linear dispersions in the limit of  $\omega \rightarrow 0$ , but this is not a Dirac cone as the negative frequency solution has no physical meaning.



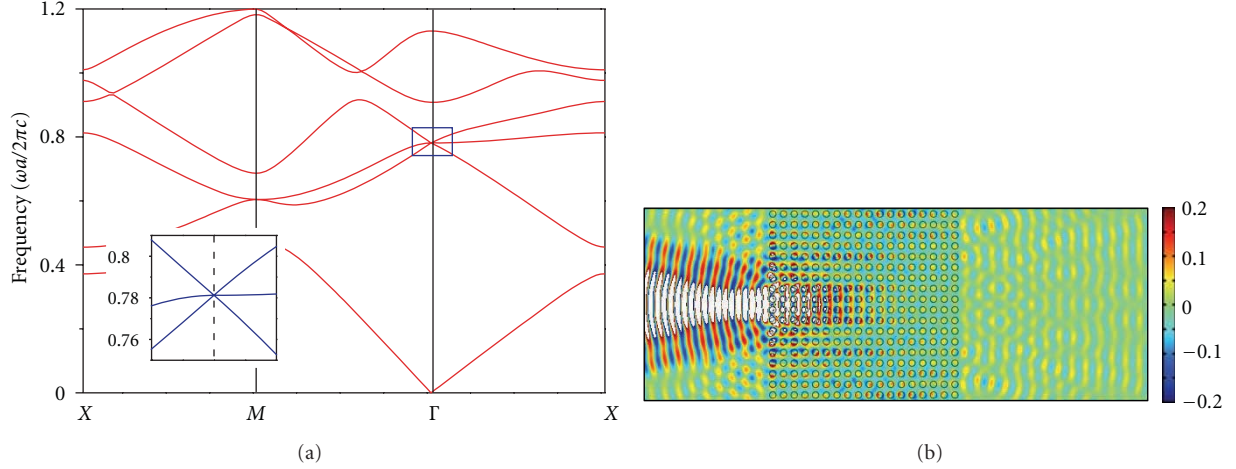


FIGURE 4: (a) The band structure of PMMA photonic crystal arranged in a square lattice for the TM polarization. The radii of the cylinders are  $0.3035a$ . The relative permittivity of the PMMA is 2.6. Near the  $\Gamma$  point, there is also a Dirac-like cone dispersion. The inset is the enlarge part near the Dirac-like point shown by blue solid region. (b) The field distributions for a Gaussian beam illumination. The Gaussian beam parameters are the same as in Figure 2.

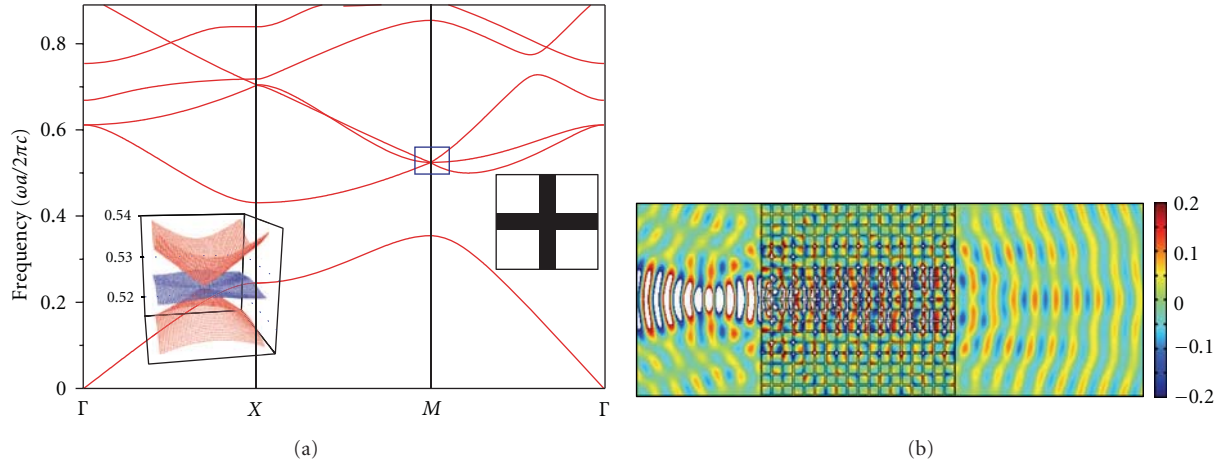


FIGURE 5: (a) The band structure of an alumina vein structure for the TE polarization, with the thickness of the vein equal to  $0.176a$ . At the  $M$  point, a conical dispersion intersects with an extra sheet. A closeup of the band diagram contour of the blue solid region is shown in the inset. (b) The field distributions for a Gaussian beam incidence deviate from what is expected for homogeneous  $\epsilon = \mu = 0$  medium (Figure 2(a)).

We also remark that linear bands cutting at one point can be found in one-dimensional photonic crystals but it takes a two-dimensional system to define a cone in  $k$ -space.

The square lattice has the special property that the group of the  $M$  point ( $\vec{k}_M = (\pi/a)\hat{x} + (\pi/a)\hat{y}$ ) is the same as that of  $\Gamma$  point and they both are  $C_{4v}$ . Triply degenerate state can again be constructed by arranging for the accidental degeneracy of the two fold degenerate state and one nondegenerate state at the  $M$  point. Symmetry analysis shows that we can get a conical dispersion close to the  $M$  point, whose dispersion can be written as  $\omega(\vec{k}) = \omega_M + v_g |\vec{k} - \vec{k}_M|$  to the first order where  $\omega_M$  is the frequency of the triply degenerate

state,  $v_g$  is the group velocity of the linear band. Along with the conical dispersion, an extra band intersects the conical dispersion at  $\omega_M$ . As we show in Figure 5(a), linear dispersion can indeed be constructed at the  $M$  point if there is accidental degeneracy while the dispersion is quadratic if the degeneracy comes from lattice symmetry [71]. To illustrate this point, the dispersion of photonic crystal with an alumina vein structure for the TE polarization is shown in Figure 5(a). As the Dirac-like cone appears at a zone boundary point  $M$ , we should not expect effective medium theory to be applicable, and the wave guiding property (Figure 5(b)) is indeed different from what is expected from a homogeneous  $\epsilon = \mu = 0$  medium. In addition, we can also

use vein-like structures to achieve Dirac-like cone dispersion at  $\Gamma$  point, which corresponds to a large square hole drill inside background medium. Again, the low-lying bands of that type of structures cannot be described by monopole and dipole excitations and the system cannot be mapped to a homogeneous  $\varepsilon = \mu = 0$  medium even if there is conical dispersion.

The above discussions show that Dirac-like cone dispersion at the  $\Gamma$  point is a necessary condition to obtain  $\varepsilon = \mu = 0$  but it is not a sufficient condition. The  $\varepsilon_{\text{eff}} = \mu_{\text{eff}} = 0$  property is a special property of some (but not all) photonic crystals with conical dispersion. We note that other intriguing wave transport properties such as pseudo-diffusive transmission [17, 18] and Zitterbewegung [20, 33] are properties of the conical dispersion and can be observed as long as there is a cone, irrespective of whether effective parameters are retrievable or not.

### 3. The Berry Phase of Dirac-Like Point with Triply Degenerate State

In the above discussion, we considered the relationship between Dirac-like point and zero-index material. The zero-index property is related to a triply degenerate state, with a flat band of a quasi-longitudinal mode crossing the Dirac-like point formed by cones generated by two linear bands. At a first glance, the longitudinal flat band with a zero group velocity in homogeneous material has no role in the Dirac-like point physics and in the literature, there are indeed calculations that ignored the longitudinal mode at all [65]. Even though the longitudinal mode inside the zero-index material cannot be excited by incident plane waves and hence do not participate in the wave transport for some cases, its existence does have some subtle effects. For example, if this longitudinal mode is ignored, the modes near the Dirac-like point can be described by a  $2 \times 2$  Hamiltonian which can be mapped to the Hamiltonian of a spinor, and such systems can potentially carry a nonzero Berry phase [78, 79]. On the other hand, the triple degenerate state is similar to the spin 1 system [78, 79] and the Berry phase should be zero. Therefore, the existence of the longitudinal state changes the Berry phase of the Dirac-like point which bears implication when we consider effects such as coherent backscattering of

light [80] when disordered is introduced. Since our zero-index materials correspond to the accidental degeneracy of the monopole and dipole, it is convenient to use the multiple scattering theory (MST) to calculate the Berry phase, as will be sketched below.

The MST equation can be written as [66]

$$\begin{pmatrix} S_0 - \frac{1}{D_{-1}} & -S_1 & S_2 \\ -S_{-1} & S_0 - \frac{1}{D_0} & -S_1 \\ S_{-2} & -S_{-1} & S_0 - \frac{1}{D_1} \end{pmatrix} \begin{pmatrix} b_{-1} \\ b_0 \\ b_1 \end{pmatrix} = 0, \quad (5)$$

where  $D_m$  and  $b_m$  are the  $T$ -matrix and Mie scattering coefficients of the angular momentum number  $m$ , respectively, and  $S_m$  denotes the lattice sum in MST. The mathematical details of the MST method can be found in [66]. We can do a small  $k$  expansion for the eigenmodes near the  $\Gamma$  point. As  $\delta k \rightarrow 0$ ,  $S_0 - 1/D_0$ ,  $S_0 - 1/D_{\pm 1}$ ,  $S_1$  and  $S_2$  can be written as

$$\begin{aligned} S_0 - \frac{1}{D_0} &\approx i(A_0(\omega) + B(\omega)\delta k^2), \\ S_0 - \frac{1}{D_{\pm 1}} &\approx i(A_{\pm 1}(\omega) + B(\omega)\delta k^2), \\ S_1 &\approx C_1(\omega)\delta k e^{i\phi_k}, \\ S_2 &\approx C_2(\omega, \phi_k)\delta k^2, \end{aligned} \quad (6)$$

where  $A_0(\omega)$ ,  $A_1(\omega)$ ,  $B(\omega)$ , and  $C_1(\omega)$  are all real functions of  $\omega$  only, and  $C_2(\omega, \phi_k)$  is a function of  $\omega$  and  $\phi_k \cdot \phi_k$  is the angle of  $\vec{\delta k}$  in the polar coordinate. If there is accidental degeneracy, such that  $\omega_m = \omega_d = \omega^*$  (here  $\omega_m$  and  $\omega_d$  are the eigen frequencies of the monopole and dipole excitations, resp.), we can do a small  $\omega$  expansion near  $\omega^*$  and obtain  $S_0 - 1/D_0 \approx i(A'_0(\omega^*)(\omega - \omega^*) + B(\omega)\delta k^2)$ , where  $A'_0(\omega) = \partial A_0(\omega)/\partial \omega$ , and  $S_0 - 1/D_{\pm 1} \approx i(A'_{\pm 1}(\omega^*)(\omega - \omega^*) + B(\omega)\delta k^2)$ , where  $A'_{\pm 1}(\omega) = \partial A_{\pm 1}(\omega)/\partial \omega$ . By substituting them into (5), we can obtain

$$\begin{pmatrix} i(A'_1(\omega - \omega^*) + B\delta k^2) & -C_1\delta k e^{i\phi_k} & C_2\delta k^2 \\ C_1\delta k e^{-i\phi_k} & i(A'_0(\omega - \omega^*) + B\delta k^2) & -C_1\delta k e^{i\phi_k} \\ -C_2^*\delta k^2 & C_1\delta k e^{-i\phi_k} & i(A'_1(\omega - \omega^*) + B\delta k^2) \end{pmatrix} \cdot \begin{pmatrix} b_{-1} \\ b_0 \\ b_1 \end{pmatrix} = 0. \quad (7)$$

The secular equation of (7) is a cubic equation of  $\delta\omega$ :

$$\begin{aligned} &-(A'_1\delta\omega + B\delta k^2)^2(A'_0\delta\omega + B\delta k^2) \\ &+ 2(A'_1\delta\omega + B\delta k^2)C_1^2\delta k^2 + (A'_0\delta\omega + B\delta k^2)|C_2|^2\delta k^4 \\ &- 2\text{Im}(C_2^* e^{2i\phi_k})C_1^2\delta k^4 = 0, \end{aligned} \quad (8)$$

where  $\delta\omega = \omega - \omega^*$ . By solving this secular equation, we find three solutions: one is  $\omega_1 - \omega^* = 0 + O(\delta k^2)$ , which corresponds to a band of quadratic dispersion. The other two solutions are  $\omega_{2,3} - \omega^* = \pm v_g \delta k + O(\delta k^2)$ , where  $v_g = \sqrt{2}|C_1|/\sqrt{A'_1 A'_0}$ , which corresponds to two bands with linear dispersions that generate a Dirac cone.



Neglecting the  $\delta k^2$  term, and substitute  $\delta\omega = (\sqrt{2}|C_1|/\sqrt{A'_1 A'_0})\delta k = v_g \delta k$  into (7) for the accidental degenerate monopole and dipoles, (7) can be written as

$$\begin{pmatrix} iA'_1 v_g \delta k & -C_1 \delta k e^{i\phi_k} & 0 \\ C_1 \delta k e^{-i\phi_k} & iA'_0 v_g \delta k & -C_1 \delta k e^{i\phi_k} \\ 0 & C_1 \delta k e^{-i\phi_k} & iA'_1 v_g \delta k \end{pmatrix} \begin{pmatrix} b_{-1} \\ b_0 \\ b_1 \end{pmatrix} = 0. \quad (9)$$

Solving (9), we can obtain the relationships between  $b_{-1}$ ,  $b_1$  with  $b_0$ ,

$$b_{-1} = -i \frac{C_1 e^{i\phi_k}}{A'_1 v_g} b_0, \quad b_1 = i \frac{C_1 e^{-i\phi_k}}{A'_1 v_g} b_0. \quad (10)$$

The eigenvector of (9) is:

$$|\Phi_k\rangle = \begin{pmatrix} -i \frac{C_1 e^{i\phi_k}}{A'_1 v_g} \\ 1 \\ i \frac{C_1 e^{-i\phi_k}}{A'_1 v_g} \end{pmatrix}. \quad (11)$$

Therefore, the Berry phase of the eigenstate  $|\Phi_k\rangle$  is

$$\begin{aligned} \oint i \langle \Phi_k | \nabla_{\vec{k}} \Phi_k \rangle \cdot d\vec{k} &= \oint i \left( i \frac{C_1 e^{-i\phi_k}}{A'_1 v_g} \quad 1 \quad -i \frac{C_1 e^{i\phi_k}}{A'_1 v_g} \right) \nabla_{\vec{k}} \begin{pmatrix} -i \frac{C_1 e^{i\phi_k}}{A'_1 v_g} \\ 1 \\ i \frac{C_1 e^{-i\phi_k}}{A'_1 v_g} \end{pmatrix} \cdot d\vec{k} \\ &= \oint i \left( i \frac{C_1 e^{-i\phi_k}}{A'_1 v_g} \quad 1 \quad -i \frac{C_1 e^{i\phi_k}}{A'_1 v_g} \right) \begin{pmatrix} \frac{C_1 e^{i\phi_k}}{A'_1 v_g} \\ 0 \\ \frac{C_1 e^{-i\phi_k}}{A'_1 v_g} \end{pmatrix} \nabla_{\vec{k}} \phi_k \cdot d\vec{k} = 0. \end{aligned} \quad (12)$$

From the above analysis, we can see that the Berry phase is equal to zero, which is caused by the existence of the longitudinal flat band. This result is consistent with the discussion shown in [77].

#### 4. Conclusion

In summary, we show that a Dirac-like point formed by a triply degenerate state can exist at the  $k$ -points  $\Gamma$  and  $M$  in photonic crystals with  $C_{4v}$  symmetry. Such triply degenerate states are consequences of accidental degeneracy, which can be achieved by tuning system parameters. Such systems have linear bands crossing the degeneracy point and these linear bands generate Dirac-like cone dispersions. These conical dispersions are generally accompanied by additional parabolic bands that are very flat at the Dirac-like point. For the special case in which the triply degenerate state is derived from monopole and dipole excitations, the system can be mapped to  $\epsilon_{\text{eff}} = \mu_{\text{eff}} = 0$  material through effective medium theory. For other cases in which the bands near the Dirac-like point are not derived from monopole and dipole excitations, effective medium theory does not apply. Using the multiple scattering theory, we calculate the Berry phase of eigenmodes in the Dirac-like cone when there is accidental degeneracy and the phase is found to be zero. Similarly, we can extend Dirac dispersion and effective medium theory to three dimensions [81, 82].

#### Acknowledgment

This work is supported by Hong Kong RGC GRF Grant 600311.

#### References

- [1] P. A. M. Dirac, "The quantum theory of the electron," *Proceedings of the Royal Society A*, vol. 117, p. 610, 1928.
- [2] K. S. Novoselov, A. K. Geim, S. V. Morozov et al., "Electric field in atomically thin carbon films," *Science*, vol. 306, no. 5696, pp. 666–669, 2004.
- [3] K. S. Novoselov, A. K. Geim, S. V. Morozov et al., "Two-dimensional gas of massless Dirac fermions in graphene," *Nature*, vol. 438, no. 7065, pp. 197–200, 2005.
- [4] Y. Zhang, Y. W. Tan, H. L. Stormer, and P. Kim, "Experimental observation of the quantum Hall effect and Berry's phase in graphene," *Nature*, vol. 438, no. 7065, pp. 201–204, 2005.
- [5] V. P. Gusynin and S. G. Sharapov, "Unconventional integer quantum hall effect in graphene," *Physical Review Letters*, vol. 95, no. 14, Article ID 146801, 2005.
- [6] K. S. Novoselov, Z. Jiang, Y. Zhang et al., "Room-temperature quantum hall effect in graphene," *Science*, vol. 315, no. 5817, p. 1379, 2007.
- [7] M. I. Katsnelson, "Zitterbewegung, chirality, and minimal conductivity in graphene," *The European Physical Journal B*, vol. 51, no. 2, pp. 157–160, 2006.
- [8] J. Cserti and G. David, "Unified description of Zitterbewegung for spintronic, graphene, and superconducting systems," *Physical Review B*, vol. 74, no. 17, Article ID 172305, 2006.

- [9] T. M. Rusin and W. Zawadzki, "Transient Zitterbewegung of charge carriers in mono and bilayer graphene, and carbon nanotubes," *Physical Review B*, vol. 76, Article ID 195439, 2007.
- [10] G. David and J. Cserti, "General theory of the Zitterbewegung," *Physical Review B*, vol. 81, Article ID 121417, 2010.
- [11] A. H. Castro Neto, F. Guinea, N. M. R. Peres, K. S. Novoselov, and A. K. Geim, "The electronic properties of graphene," *Reviews of Modern Physics*, vol. 81, no. 1, pp. 109–162, 2009.
- [12] M. I. Katsnelson, K. S. Novoselov, and A. K. Geim, "Chiral tunnelling and the Klein paradox in graphene," *Nature Physics*, vol. 2, no. 9, pp. 620–625, 2006.
- [13] S. V. Morozov, K. S. Novoselov, M. I. Katsnelson et al., "Strong suppression of weak localization in graphene," *Physical Review Letters*, vol. 97, no. 1, Article ID 016801, 2006.
- [14] A. K. Geim and A. H. MacDonald, "Graphene: exploring carbon flatland," *Physics Today*, vol. 60, no. 8, pp. 35–41, 2007.
- [15] A. K. Geim and K. S. Novoselov, "The rise of graphene," *Nature Materials*, vol. 6, no. 3, pp. 183–191, 2007.
- [16] M. Plihal and A. A. Maradudin, "Photonic band structure of two-dimensional systems: the triangular lattice," *Physical Review B*, vol. 44, no. 16, pp. 8565–8571, 1991.
- [17] R. A. Sepkhanov, Y. B. Bazaliy, and C. W. J. Beenakker, "Extremal transmission at the Dirac point of a photonic band structure," *Physical Review A*, vol. 75, no. 6, Article ID 063813, 2007.
- [18] M. Diema, T. Koschny, and C. M. Soukoulis, "Transmission in the vicinity of the Dirac point in hexagonal photonic crystals," *Physica B*, vol. 405, no. 14, pp. 2990–2995, 2010.
- [19] R. A. Sepkhanov, J. Nilsson, and C. W. J. Beenakker, "How to detect the pseudospin-1/2 Berry phase in a photonic crystal with a Dirac spectrum," *Physical Review B*, vol. 78, Article ID 045122, 2008.
- [20] X. Zhang, "Observing Zitterbewegung for photons near the Dirac point of a two-dimensional photonic crystal," *Physical Review Letters*, vol. 100, no. 11, p. 113903, 2008.
- [21] S. Raghu and F. D. M. Haldane, "Analogues of quantum Hall effect edge states in photonic crystals," *Physical Review A*, vol. 78, Article ID 033834, 2008.
- [22] F. D. M. Haldane and S. Raghu, "Possible realization of directional optical waveguides in photonic crystals with broken time-reversal symmetry," *Physical Review Letters*, vol. 100, Article ID 013904, 2008.
- [23] T. Ochiai and M. Onoda, "Photonic analog of graphene model and its extension: Dirac cone, symmetry, and edge states," *Physical Review B*, vol. 80, no. 15, p. 155103, 2009.
- [24] T. Ochiai, "Topological properties of bulk and edge states in honeycomb lattice photonic crystals: the case of TE polarization," *Journal of Physics*, vol. 22, no. 22, p. 225502, 2010.
- [25] E. Yablonovitch, "Inhibited spontaneous emission in solid-state physics and electronics," *Physical Review Letters*, vol. 58, no. 20, pp. 2059–2062, 1987.
- [26] S. John, "Strong localization of photons in certain disordered dielectric superlattices," *Physical Review Letters*, vol. 58, no. 23, pp. 2486–2489, 1987.
- [27] K. M. Ho, C. T. Chan, and C. M. Soukoulis, "Existence of a photonic gap in periodic dielectric structures," *Physical Review Letters*, vol. 65, no. 25, pp. 3152–3155, 1990.
- [28] Z. Wang, Y. D. Chong, J. D. Joannopoulos, and M. Soljačić, "Reflection-free one-way edge modes in a gyromagnetic photonic crystal," *Physical Review Letters*, vol. 100, no. 1, p. 013905, 2008.
- [29] Z. Yu, G. s Veronis, Z. Wang, and S. Fan, "One-way electromagnetic waveguide formed at the interface between a plasmonic metal under a static magnetic field and a photonic crystal," *Physical Review Letters*, vol. 100, no. 2, p. 023902, 2008.
- [30] Z. Wang, Y. Chong, J. D. Joannopoulos, and M. Soljačić, "Observation of unidirectional backscattering-immune topological electromagnetic states," *Nature*, vol. 461, no. 7265, pp. 772–775, 2009.
- [31] X. Ao, Z. Lin, and C. T. Chan, "One-way edge mode in a magneto-optical honeycomb photonic crystal," *Physical Review B*, vol. 80, no. 3, p. 033105, 2009.
- [32] Y. Poo, R. X. Wu, Z. Lin, Y. Yang, and C. T. Chan, "Experimental realization of self-guiding unidirectional electromagnetic edge states," *Physical Review Letters*, vol. 106, no. 9, p. 093903, 2011.
- [33] X. Zhang and Z. Liu, "Extremal transmission and beating effect of acoustic waves in two-dimensional sonic crystals," *Physical Review Letters*, vol. 101, no. 26, p. 264303, 2008.
- [34] V. G. Veselago, "The electrodynamics of substances with simultaneously negative values of  $\epsilon$  and  $\mu$ ," *Soviet Physics Uspekhi*, vol. 10, no. 4, p. 509, 1968.
- [35] R. A. Shelby, D. R. Smith, and S. Schultz, "Experimental verification of a negative index of refraction," *Science*, vol. 292, no. 5514, pp. 77–79, 2001.
- [36] D. R. Smith, W. J. Padilla, D. C. Vier, S. C. Nemat-Nasser, and S. Schultz, "Composite medium with simultaneously negative permeability and permittivity," *Physical Review Letters*, vol. 84, no. 18, pp. 4184–4187, 2000.
- [37] S. Zhang, W. Fan, N. C. Panoiu, K. J. Malloy, R. M. Osgood, and S. R. J. Brueck, "Experimental demonstration of near-infrared negative-index metamaterials," *Physical Review Letters*, vol. 95, no. 13, p. 137404, 2005.
- [38] V. M. Shalaev, W. Cai, U. K. Chettiar et al., "Negative index of refraction in optical metamaterials," *Optics Letters*, vol. 30, no. 24, pp. 3356–3358, 2005.
- [39] G. Dolling, M. Wegener, C. M. Soukoulis, and S. Linden, "Negative-index metamaterial at 780 nm wavelength," *Optics Letters*, vol. 32, no. 1, pp. 53–55, 2007.
- [40] J. B. Pendry, "Negative refraction makes a perfect lens," *Physical Review Letters*, vol. 85, no. 18, pp. 3966–3969, 2000.
- [41] N. Fang, H. Lee, C. Sun, and X. Zhang, "Sub-diffraction-limited optical imaging with a silver superlens," *Science*, vol. 308, no. 5721, pp. 534–537, 2005.
- [42] J. B. Pendry, D. Schurig, and D. R. Smith, "Controlling electromagnetic fields," *Science*, vol. 312, no. 5781, pp. 1780–1782, 2006.
- [43] U. Leonhardt, "Optical conformal mapping," *Science*, vol. 312, no. 5781, pp. 1777–1780, 2006.
- [44] D. Schurig, J. J. Mock, B. J. Justice et al., "Metamaterial electromagnetic cloak at microwave frequencies," *Science*, vol. 314, no. 5801, pp. 977–980, 2006.
- [45] M. Rahm, D. Schurig, D. A. Roberts, S. A. Cummer, D. R. Smith, and J. B. Pendry, "Design of electromagnetic cloaks and concentrators using form-invariant coordinate transformations of Maxwell's equations," *Photonics and Nanostructures*, vol. 6, no. 1, pp. 87–95, 2008.
- [46] T. Yang, H. Chen, X. Luo, and H. Ma, "Superscatterer: enhancement of scattering with complementary media," *Optics Express*, vol. 16, no. 22, pp. 18545–18550, 2008.
- [47] H. Y. Chen and C. T. Chan, "Transformation media that rotate electromagnetic fields," *Applied Physics Letters*, vol. 90, no. 24, p. 241105, 2007.
- [48] Y. Lai, J. Ng, H. Y. Chen et al., "Illusion optics: the optical transformation of an object into another object," *Physical Review Letters*, vol. 102, no. 25, p. 253902, 2009.

- [49] M. Silveirinha and N. Engheta, "Tunneling of electromagnetic energy through subwavelength channels and bends using  $\epsilon$ -near-zero materials," *Physical Review Letters*, vol. 97, no. 15, p. 157403, 2006.
- [50] M. Silveirinha and N. Engheta, "Design of matched zero-index metamaterials using nonmagnetic inclusions in  $\epsilon$ -near-zero media," *Physical Review B*, vol. 75, no. 7, p. 075119, 2007.
- [51] M. G. Silveirinha and N. Engheta, "Theory of supercoupling, squeezing wave energy, and field confinement in narrow channels and tight bends using  $\epsilon$  near-zero metamaterials," *Physical Review B*, vol. 76, no. 24, p. 245109, 2007.
- [52] A. Alu and N. Engheta, "Dielectric sensing in  $\epsilon$ -near-zero narrow waveguide channels," *Physical Review B*, vol. 78, p. 045102, 2008.
- [53] A. Alu, M. G. Silveirinha, and N. Engheta, "Transmission-line analysis of  $\epsilon$ -near-zero-filled narrow channels," *Physical Review E*, vol. 78, no. 1, p. 016604, 2008.
- [54] B. Edwards, A. Alu, M. G. Silveirinha, and N. Engheta, "Reflectionless sharp bends and corners in waveguides using  $\epsilon$ -near-zero effects," *Journal of Applied Physics*, vol. 105, no. 4, p. 044905, 2009.
- [55] R. Liu, Q. Cheng, T. Hand et al., "Experimental demonstration of electromagnetic tunneling through an  $\epsilon$ -near-zero metamaterial at microwave frequencies," *Physical Review Letters*, vol. 100, no. 2, p. 023903, 2008.
- [56] B. Edwards, A. Alu, M. E. Young, M. Silveirinha, and N. Engheta, "Experimental verification of  $\epsilon$ -near-zero metamaterial coupling and energy squeezing using a microwave waveguide," *Physical Review Letters*, vol. 100, no. 3, p. 033903, 2008.
- [57] K. Halterman and S. Feng, "Resonant transmission of electromagnetic fields through subwavelength zero- $\epsilon$  slits," *Physical Review A*, vol. 78, no. 2, p. 021805, 2008.
- [58] R. W. Ziolkowski, "Propagation in and scattering from a matched metamaterial having a zero index of refraction," *Physical Review E*, vol. 70, no. 4, p. 046608, 2004.
- [59] S. Enoch, G. Tayeb, P. Sabouroux, N. Guerin, and P. Vincent, "A metamaterial for directive emission," *Physical Review Letters*, vol. 89, no. 21, p. 213902, 2002.
- [60] A. Alu, M. G. Silveirinha, A. Salandrino, and N. Engheta, " $\epsilon$ -near-zero metamaterials and electromagnetic sources: tailoring the radiation phase pattern," *Physical Review B*, vol. 75, no. 15, p. 155410, 2007.
- [61] J. Hao, W. Yan, and M. Qiu, "Super-reflection and cloaking based on zero index metamaterial," *Applied Physics Letters*, vol. 96, no. 10, p. 101109, 2010.
- [62] Y. Jin and S. He, "Enhancing and suppressing radiation with some permeability-near-zero structures," *Optics Express*, vol. 18, no. 16, pp. 16587–16593, 2010.
- [63] V. C. Nguyen, L. Chen, and K. Halterman, "Total transmission and total reflection by zero index metamaterials with defects," *Physical Review Letters*, vol. 105, no. 23, p. 233908, 2010.
- [64] Y. Xu and H. Chen, "Total reflection and transmission by  $\epsilon$ -near-zero metamaterials with defects," *Applied Physics Letters*, vol. 98, no. 11, p. 113501, 2011.
- [65] L. G. Wang, Z. G. Wang, J. X. Zhang, and S. Y. Zhu, "Realization of Dirac point with double cones in optics," *Optics Letters*, vol. 34, no. 10, p. 1510, 2009.
- [66] X. Huang, Y. Lai, Z. H. Hang, H. Zheng, and C. T. Chan, "Dirac cones induced by accidental degeneracy in photonic crystals and zero-refractive-index materials," *Nature Materials*, vol. 10, no. 8, pp. 582–586, 2011.
- [67] M. V. Berry, "Quantal phase factors accompanying adiabatic changes," *Proceedings of the Royal Society of London A*, vol. 392, no. 1802, pp. 45–57, 1984.
- [68] Y. Wu, J. Li, Z. Q. Zhang, and C. T. Chan, "Effective medium theory for magnetodielectric composites: beyond the long-wavelength limit," *Physical Review B*, vol. 74, no. 8, p. 085111, 2006.
- [69] L. H. Gabrielli, J. Cardenas, C. B. Poitras, and M. Lipson, "Silicon nanostructure cloak operating at optical frequencies," *Nature Photonics*, vol. 3, no. 8, pp. 461–463, 2009.
- [70] K. Sakoda, *Optical Properties of Photonic Crystals*, Springer-Verlag, Berlin, Germany, 2nd edition, 2004.
- [71] Y. D. Chong, X. G. Wen, and M. Soljacic, "Effective theory of quadratic degeneracies," *Physical Review B*, vol. 77, no. 23, p. 235125, 2008.
- [72] K. Sakoda and H. Zhou, "Role of structural electromagnetic resonances in a steerable left-handed antenna," *Optics Express*, vol. 18, no. 26, pp. 27371–27386, 2010.
- [73] K. Sakoda and H. Zhou, "Analytical study of two-dimensional degenerate metamaterial antennas," *Optics Express*, vol. 19, no. 15, pp. 13899–13921, 2011.
- [74] K. Sakoda, "Dirac cone in two- and three-dimensional metamaterials," *Optics Express*, vol. 20, no. 4, pp. 3898–3917, 2012.
- [75] K. Sakoda, "Double Dirac cones in triangular-lattice metamaterials," *Optics Express*, vol. 20, no. 9, pp. 9925–9939, 2012.
- [76] T. Inui, Y. Tanabe, and Y. Onodera, *Group Theory and Its Applications in Physics*, Springer, Berlin, Germany, 1990.
- [77] J. Mei, Y. Wu, C. T. Chan, and Z. Q. Zhang, "Do linear dispersions of classical waves mean Dirac cones?" *Physical Review B*, vol. 86, p. 035141, 2012.
- [78] Z. Lan, N. Goldman, A. Bermudez, W. Lu, and P. Ohberg, "Dirac-Weyl fermions with arbitrary spin in two-dimensional optical superlattices," *Physical Review B*, vol. 84, no. 16, p. 165115, 2011.
- [79] B. Dora, J. Kailasvuori, and R. Moessner, "Lattice generalization of the Dirac equation to general spin and the role of the flat band," *Physical Review B*, vol. 84, no. 19, p. 195422, 2011.
- [80] E. Akkermans, P. E. Wolf, and R. Maynard, "Coherent backscattering of light by disordered media: analysis of the peak line shape," *Physical Review Letters*, vol. 56, no. 14, pp. 1471–1474, 1986.
- [81] J. T. Costa and M. G. Silveirinha, "Mimicking the Veselago-Pendry lens with broadband matched double-negative metamaterials," *Physical Review B*, vol. 84, no. 15, p. 155131, 2011.
- [82] C. T. Chan, X. Huang, F. Liu, and Z. H. Hang, "Dirac dispersion and zero-index in two dimensional and three dimensional photonic and phononic systems," *Progress In Electromagnetics Research B*, vol. 44, pp. 163–190, 2012.

## Research Article

# Recent Advances in Multiband Printed Antennas Based on Metamaterial Loading

**F. Paredes,<sup>1</sup> G. Zamora,<sup>1</sup> S. Zufanelli,<sup>1</sup> F. J. Herraiz-Martínez,<sup>2</sup> J. Bonache,<sup>1</sup> and F. Martín<sup>1</sup>**

<sup>1</sup> GEMMA/CIMITEC, Departament d'Enginyeria Electrònica, Universitat Autònoma de Barcelona, 08193 Barcelona, Spain

<sup>2</sup> Departamento de Teoría de la Señal y Comunicaciones, Universidad Carlos III, 28911 Madrid, Spain

Correspondence should be addressed to F. Martín, ferran.martin@uab.es

Received 16 May 2012; Accepted 9 July 2012

Academic Editor: Ivan D. Rukhlenko

Copyright © 2012 F. Paredes et al. This is an open access article distributed under the Creative Commons Attribution License, which permits unrestricted use, distribution, and reproduction in any medium, provided the original work is properly cited.

It is shown that printed antennas loaded with metamaterial resonators can be designed to exhibit multiband functionality. Two different antenna types and metamaterial loading are considered: (i) printed dipoles or monopoles loaded with open complementary split ring resonators (OCSRRs) and (ii) meander line or folded dipole antennas loaded with split ring resonators (SRRs) or spiral resonators (SRs). In the first case, multiband operation is achieved by series connecting one or more OCSRRs within the dipole/monopole. Such resonators force opens at their positions, and by locating them at a quarter wavelength (at the required operating frequencies) from the feeding point, it is possible to achieve multiple radiation bands. In the second case, dual-band functionality is achieved through the perturbation of the antenna characteristics caused by the presence of the metamaterial resonators. This latter strategy is specially suited to achieve conjugate matching between the antenna and the chip in radiofrequency identification (RFID) tags at two of the regulated UHF-RFID bands.

## 1. Introduction

Metamaterials are effective media made of periodic (or quasiperiodic) inclusions of conventional materials (typically metals and dielectrics) with controllable acoustic, electromagnetic, or optical properties. Indeed, by properly structuring these artificial materials, it is possible to achieve unique and exotic properties, such as negative refraction or subwavelength focusing, among others, and it is potentially possible to implement acoustic and optical cloaks. There has been an intensive research activity in this field since 2000 [1–10], when the first metamaterial structure by Smith and co-workers was reported [11]. Key to the success of this research field was the synthesis of negative effective permeability media by means of split ring resonators (SRRs) [12]. These particles are electrically small resonators that can be excited by means of an axial magnetic field. Hence, if an array of SRRs is illuminated by means of an electromagnetic radiation with the magnetic field axial to the SRRs, the structure behaves as an effective medium with negative permeability in a narrow band above SRR resonance. By combining SRRs with metallic posts (exhibiting a negative

effective permittivity up to the so-called plasma frequency), the first structure simultaneously exhibiting negative permittivity and permeability was synthesized [11]. These structures are called left-handed, or double negative, materials, and the main relevant feature of such media, derived from the negative sign of the constitutive parameters, is the antiparallelism between the phase and group velocities [13].

The metamaterial concept and some metamaterial properties were soon transferred to the microwave engineering field, since it was demonstrated that by loading a transmission line with series capacitances and shunt inductances, left-handed wave propagation (i.e., backward waves) is achieved [14–16]. These artificial lines loaded with series capacitances and shunt inductances and exhibiting some metamaterial properties are called metamaterial transmission lines. In 2003, it was demonstrated that metamaterial transmission lines can also be implemented by means SRRs [17]. Specifically, by properly combining SRRs and shunt strips in a coplanar waveguide (CPW) transmission line, backward wave propagation in a narrow band arises, and by merely loading the CPW with SRRs, the structure exhibits a stop-band behavior that has been interpreted as due to the

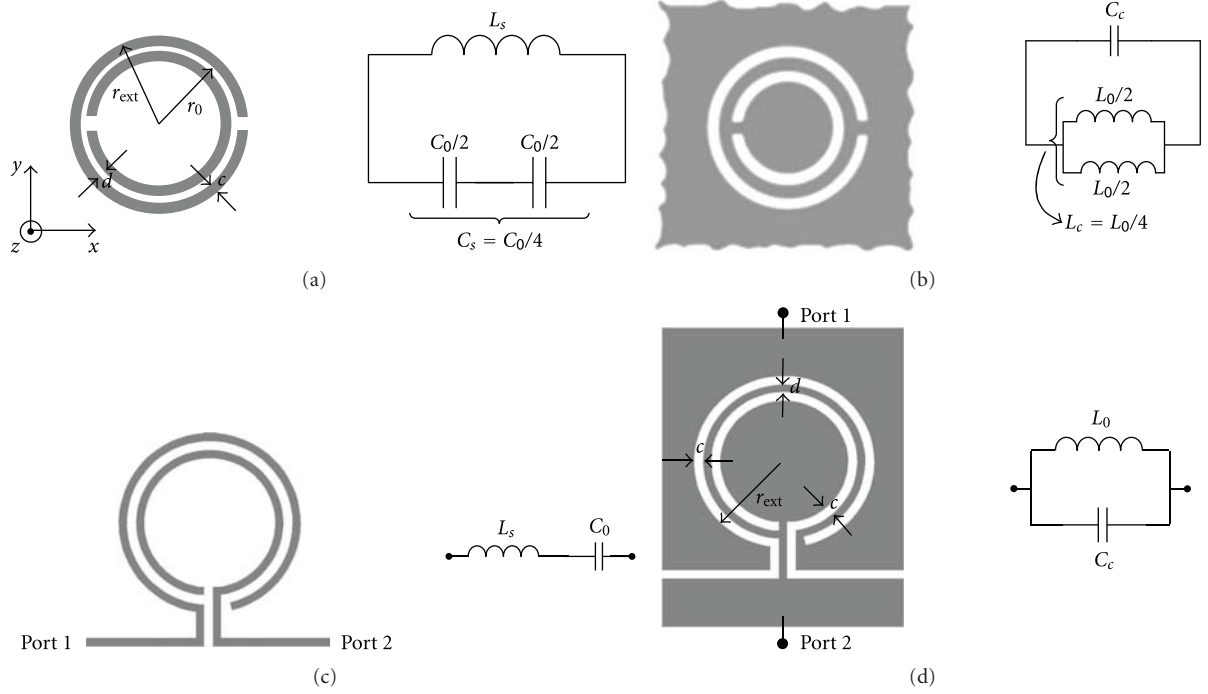


FIGURE 1: Typical topology and lumped element equivalent circuit model of the (a) SRR, (b) CSRR, (c) OSRR, and (d) OCSR.

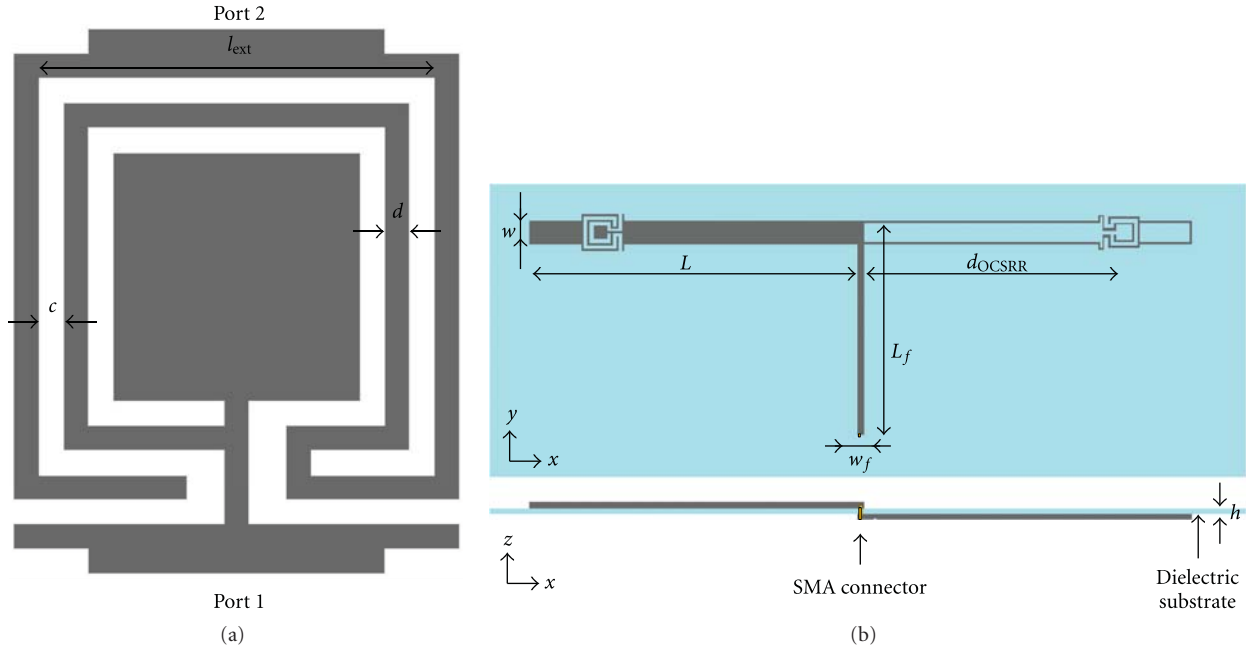


FIGURE 2: Sketch of the antipodal dipole antenna. (a) Topology of the square-shaped OCSR. (b) Top and cross-sectional views of the dipole antenna loaded with OCSRs.

negative value of the effective permeability in the stop band [18]. It is important to mention that even though effective permeability and permittivity in metamaterial transmission lines can be defined [1, 2, 4], the relevant parameters in transmission lines (fundamental for design purposes) are the phase constant and the characteristic impedance. Thanks to

the presence of reactive elements (inductances, capacitances, or electrically small resonators) in metamaterial transmission lines, it is possible to tailor these parameters to some extent in these artificial lines. Therefore, the key advantage of metamaterial transmission lines over conventional lines is the controllability of the phase constant and characteristic



impedance [19]. In many applications few (or even a single) unit cells suffice to achieve the required line specifications. Hence, periodicity and homogeneity (necessary for the implementation of effective media metamaterials) are not a due in metamaterial transmission lines. Indeed, some times, rather than tailoring the characteristic impedance or the phase of a transmission line, it might be simply necessary to use coupled resonators in order to achieve a transmission zero or to perturb somehow the line characteristics in the vicinity of particle resonance. As long as the considered resonators are electrically small and related to the SRR, these resonator-loaded lines are called transmission lines with metamaterial loading. This concept can be made extensive to other structures such as printed antennas, which is the case considered in this paper.

The paper is organized as follows. In Section 2, the metamaterial resonators considered in this paper are reviewed. Section 3 is focused on multiband printed dipole and monopole antennas loaded with open complementary split ring resonators (OCSRRs), and Section 4 is devoted to the implementation of dual-band UHF-RFID tags based on meander line and folded dipole antennas with metamaterial loading. Finally the main conclusions are highlighted in Section 5.

## 2. SRRs and Other Related Metamaterial Resonators

The typical topology of the SRR is depicted in Figure 1(a). It consists on a pair of coupled split rings with the apertures on opposite sides. The coupling between both rings drives the first resonance frequency to low values, as compared to that of the individual rings, and for this reason the SRR is electrically small. By virtue of the small electrical size of the particle, a quasistatic analysis can be applied to the SRR [4, 20], and the capacitance and inductance are given by the series connection of the distributed (edge) capacitances of both SRR halves and by the inductance of a single loop of identical width  $c$  and average radius  $r_0$ . Pairs of SRRs etched in the back substrate side of CPW transmission lines can be inductively driven by the magnetic field generated by the line, resulting in negative effective permeability metamaterial transmission lines [17, 18].

By applying duality, the complementary split ring resonator (CSRR) results [21, 22] (Figure 1(b)). This resonator exhibits roughly the same resonance frequency to that of the SRR (provided the same dimensions and substrate are considered) and is typically driven by an axial time-varying electric field. CSRRs have been used for the implementation of negative effective permittivity metamaterial transmission lines in microstrip technology, where the CSRRs are etched in the ground plane beneath the conductor strip (more details on the calculation of particle inductance and capacitance are given in [23]).

Let us now consider the open versions of the previous particles, that is, the open SRR (OSRR) [24] and the open CSRR (OCSRR) [25]. The typical topologies are depicted in Figures 1(c) and 1(d), respectively. Notice that as long

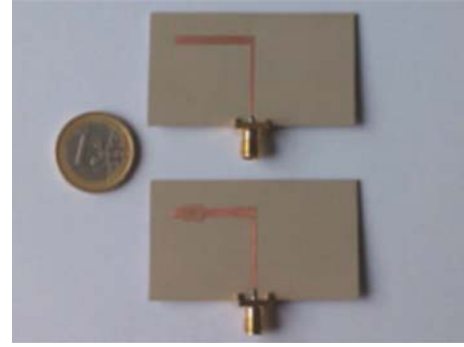


FIGURE 3: Picture of the fabricated prototypes. Top: unloaded printed dipole antenna. Bottom: proposed dual-band printed dipole antenna.

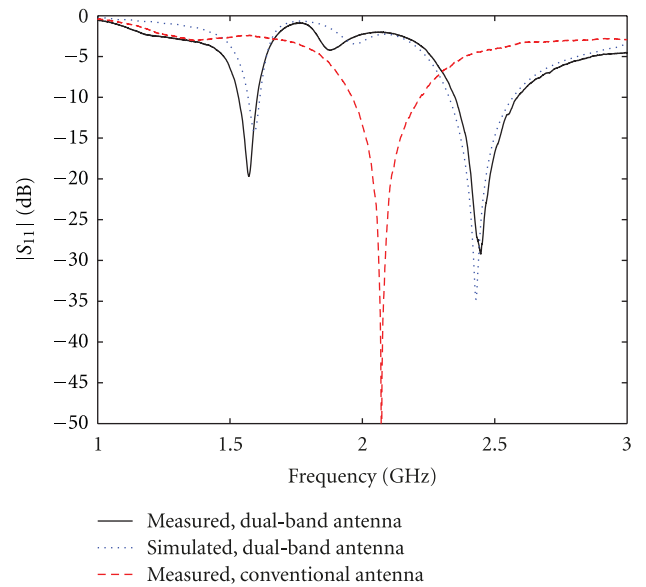


FIGURE 4: Measured and simulated reflection coefficient of the proposed dual-band antenna compared to the unloaded antenna. (—) measured dual-band printed dipole antenna; (· · ·) simulated dual-band printed dipole antenna; (— —) measured unloaded printed dipole antenna.

as these particles are open resonators (the connecting pins are indicated), they can be excited by means of a voltage or a current source. As compared to SRRs and CSRRs, OSRRs and OCSRRs are electrically smaller by a factor of two. The reason is simple: for the OSRR, the inductance is identical to that of the SRR, but the capacitance is the edge capacitance of the whole circumference, and hence it is 4 times higher than that of the SRR. This reduces the resonance frequency of the OSRR to half the resonance frequency of the SRR. For the OCSRR, the capacitance is identical to that of the CSRR, but the inductance is four times larger since in the CSRR there are two inductive paths (in parallel) between the inner region of the particle and the outside metallic region, whereas for the OCSRR there is a single inductive path corresponding to the whole circumference of the particle. As can be seen



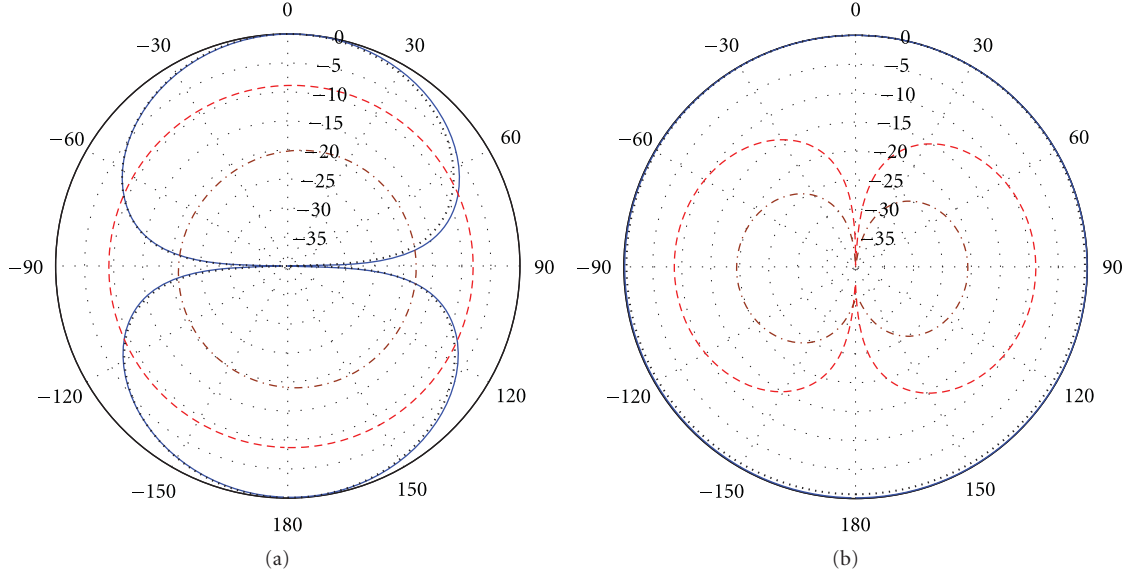


FIGURE 5: Simulated normalized radiation patterns for the dual-band dipole antenna. (a) XZ plane. (b) YZ plane. (—) 1.575 GHz (copolar component); (—) 1.575 GHz (cross-polar component); (- - -) 2.45 GHz (copolar component); (- - -) 2.45 GHz (cross-polar component).

in the circuit models depicted in Figure 1, the OSRR is an open series resonator, whereas the OCSRR is an open parallel resonator. It has been demonstrated that combined OSRRs and OCSRR in CPW and microstrip lines are useful for the implementation of metamaterial transmission lines (and many circuits based on them) and broadband bandpass filters [26].

By connecting the external pins of the OSRR, a 2-turn spiral resonator (2-SR) results [27, 28] (other multiple-turn spirals have been studied in the literature [29]). Therefore the 2-SR is a closed resonator that exhibits the same resonance frequency as that of the OSRR. It can also be concluded from duality arguments that the complementary counterpart of the 2-SR exhibits also this resonance frequency (which is also that of the OCSRR).

### 3. Multiband Printed Dipole and Monopole Antennas with Metamaterial Loading

Let us now focus on the design of antennas loaded with metamaterial resonators. Indeed, the improvement of antenna performance by means of metamaterials has been a subject of intensive research in recent years. Metamaterial substrates and superstrates to improve the antenna directivity in planar antennas, or leaky wave antennas with scanning capability based on metamaterial transmission lines, are two of the multiple applications of metamaterial technology in the field of antennas [1–5, 30–33] (an in-depth review of this topic is out of the scope of this paper).

In this section, the focus is on metamaterial-loaded printed antennas [34–36]. The idea of this technique is based on loading a conventional printed antenna with a set of resonant particles. For example, in [34], it is shown

that a dual-band antenna is achieved by coupling a set of SRRs to a printed dipole. Using this approach, the benefits of printed antennas are kept while dual-band antennas are achieved by using a simple design technique. The SRRs produce open circuits in their positions at the resonance frequencies. Hence the antenna resonance is achieved not only when the effective length of the dipole arms is  $\lambda/4$  ( $\lambda$  being the guided wavelength), but also when the different locations of the SRR are  $\lambda/4$  from the antenna feeding point (the SRRs must be tuned at these frequencies). By using SRRs, narrow bandwidths are reported in [34] for the bands associated with the SRR loading. Even the use of SRRs with different resonance frequencies leads to bandwidths smaller than 5% [35], which might not be useful for most applications. However, an open circuit in the dipole arms can also be obtained by means of OCSRRs. The advantage is that by series connecting OCSRRs within the dipole, broadband responses can be achieved (as compared to SRRs), due to the relative values of capacitance and inductance.

To illustrate the potential of OCSRR-loaded printed antennas, we report here a dual-band dipole [37] and a tri-band monopole [38]. The layout of the printed dipole (an antipodal structure) and the details of the OCSRR are depicted in Figure 2, whereas the photograph of the antenna is shown in Figure 3, and compared to the conventional monoband dipole. The parameters of each dipole strip are the length  $L$  and the width  $W$  (which must be engineered to optimize matching). This configuration has been chosen because it avoids the use of a balun to feed the antenna. This is possible because the antipodal printed dipole is fed through a paired strips transmission line with a SMA connector soldered to the end of the line. The dimensions of the feeding line are the length  $L_f$  and the width  $W_f$ . An OCSRR is connected in series to each dipole strip at

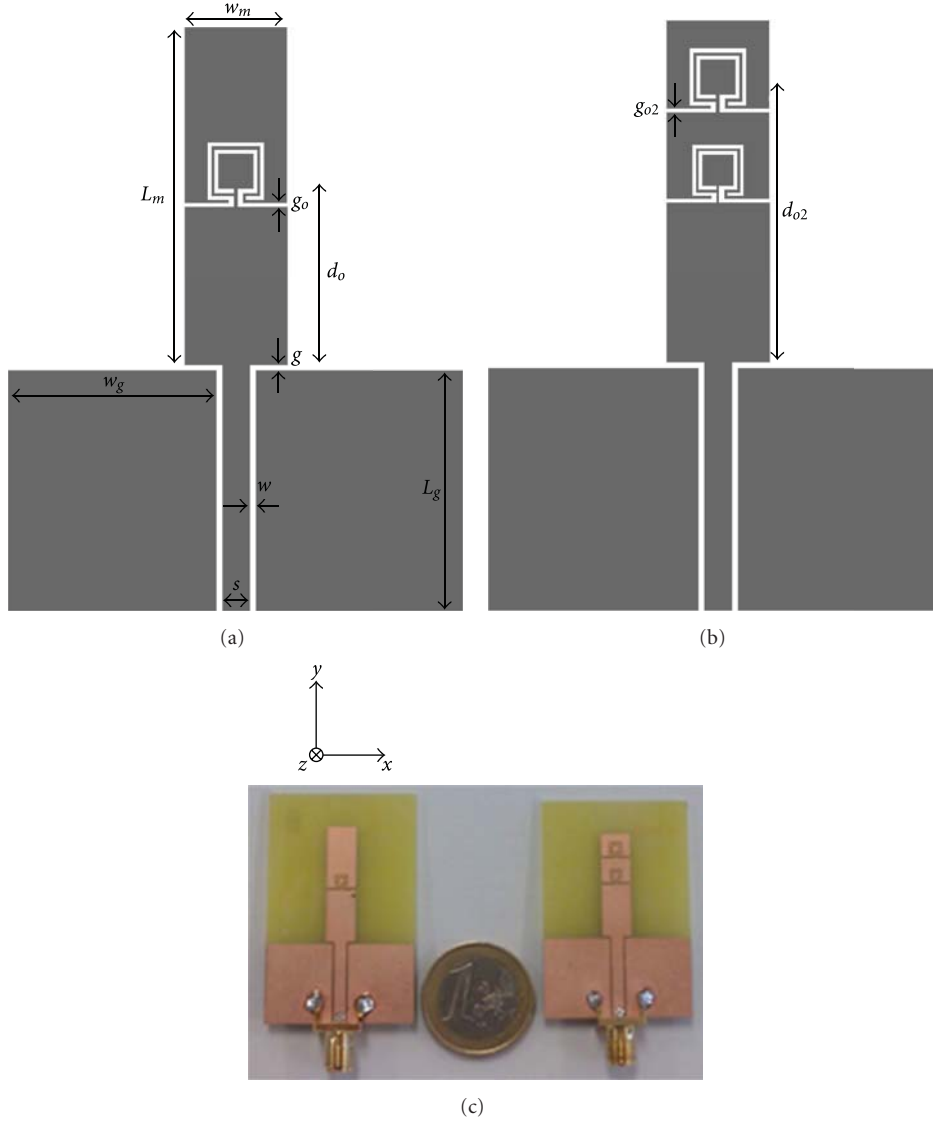


FIGURE 6: Sketch of the proposed dual-band (a), and triband (b) printed monopole antenna loaded with OCSRRs, and respective photographs (c).

a distance  $d_{\text{OCSRR}}$  from the center of the antenna. The different dimensions of the proposed antenna have been optimized to simultaneously operate at the L1-GPS frequency (1.575 GHz) and the WiFi band of 2.4–2.48 GHz. The final dimensions of the design are  $L = 22.00$  mm,  $W = 2.50$  mm,  $L_f = 25.00$  mm,  $W_f = 1.15$  mm,  $d_{\text{OCSRR}} = 17.00$  mm,  $l_{\text{ext}} = 4.00$  mm, and  $c = d = 0.30$  mm. The used substrate is the *Rogers RO3010* with  $\epsilon_r = 10.2$  and  $h = 1.27$  mm.

In the case of the conventional unloaded antenna, there is only one series resonance within the band of interest. This resonance frequency is 2.2 GHz. This resonance corresponds to the fundamental mode of the dipole antenna. Moreover, in the vicinity of the resonance, the value of the real part of the impedance is close to  $50 \Omega$  (not shown), which produces proper matching, as it can be observed in Figure 4. On the

other hand, the OCSRR loading introduces a parallel resonance in the proposed dual-band antenna input impedance. The addition of this parallel resonance has a double effect on the input impedance of the proposed dual-band antenna. The first one is a slight shift on the series resonance of the dipole antenna towards higher frequencies. In this case, this resonance is found at 2.45 GHz. The second effect is the appearance of an additional series resonance below the parallel resonance of the OCSRRs. This additional series resonance is found at 1.6 GHz. The real part of the input impedance is around  $50 \Omega$  in the vicinity of this additional series resonance. This allows achieving an additional band with proper matching in the proposed antenna (Figure 4). As it can be seen, this additional frequency is below the fundamental frequency of the unloaded dipole antenna, achieving some degree of miniaturization.

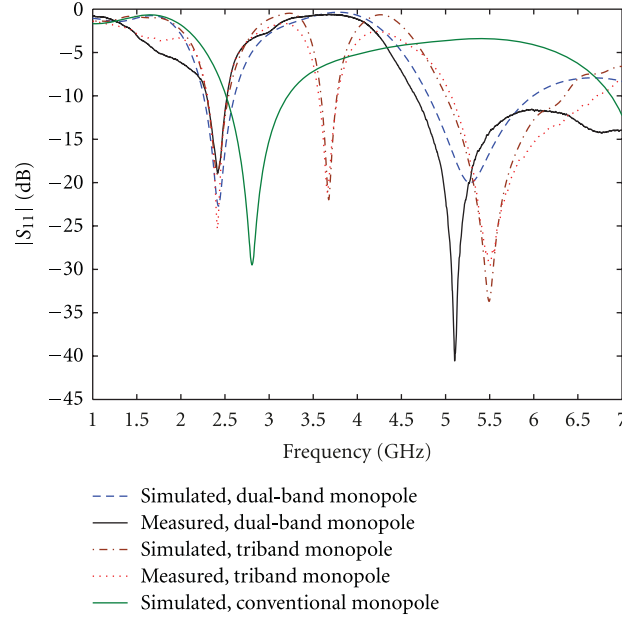


FIGURE 7: Simulated and measured reflection coefficient of the proposed dual-band and tri-band printed monopole antennas. The simulated reflection coefficient of the conventional monopole antenna is also plotted.

Considering  $|S_{11}|$  below  $-10$  dB, the first working band is centered at 1.56 GHz with 5% bandwidth and the second one is centered at 2.46 GHz with 9% bandwidth. It is important to note that this is a considerable improvement with respect to other works in which the bandwidth of one of the bands was always below 5% [34, 35]. The obtained results cover the bandwidth of the proposed applications (GPS and WiFi). The gain of the antenna has been estimated in a TEM cell from the power received by the antenna and the incident field measured by a probe [39]. The measured gain of the proposed antenna is 0.85 dB at the GPS band (1.575 GHz) and 2 dB at the WiFi band (2.45 GHz). These experimental results agree with the CST-simulated ones: 0.9 dB at the first band and 2.2 dB at the second one.

The CST-predicted radiation patterns for the proposed dual-band antenna are shown in Figure 5 for completeness. A dipolar-like radiation pattern is obtained at both working bands. The typical figure of eight is obtained in the XZ plane and an omnidirectional pattern is obtained in the YZ plane at both frequencies (1.575 and 2.45 GHz). The only difference between both working bands is the cross-polarization level, which is around  $-10$  dB in the first band while it is  $-20$  dB in the second one.

Following the ideas of the antipodal dipole antennas with metamaterial loading, we have also designed multiband printed monopole antennas. Figure 6 shows a photograph of two fabricated prototypes: a dual band and a tri-band printed monopole. The considered substrate in this case is the low-cost FR4 ( $\epsilon_r = 4.5$  and  $h = 1.5$  mm). The dual-band antenna covers the bands of 2.40–2.48 GHz (Bluetooth and WiFi) and 5.15–5.80 GHz (WiFi). The final dimensions of the monopole are  $L_m = 21$  mm,  $W_m = 5.85$  mm. The parameters of the feeding line are set to obtain a  $50 \Omega$  CPW.

Hence,  $S = 2.44$  mm and  $W = 0.30$  mm. The dimensions of each ground plane are  $L_g = 16$  mm and  $W_g = 13.48$  mm. The gap between the ground planes and the monopole is  $g = 0.30$  mm. The OCSRR is placed at a distance  $d_o = 12.50$  mm and its parameters are  $l_{\text{ext}} = 2.30$  mm,  $c = d = 0.25$  mm. The gap  $g_o$  is set to 0.50 mm.

The tri-band monopole antenna is an extension of the previous dual-band antenna and it covers the previous bands and the IEEE 802.11y band of 3.65–3.70 GHz. According to the layout of the tri-band monopole (Figure 6), the additional OCSRR is placed at a distance  $d_{o2} = 18.00$  mm. Its design parameters are  $l_{\text{ext}} = 2.70$  mm,  $c = d = 0.25$  mm. This corresponds to a resonance frequency of 3.65 GHz. The gap  $g_{o2}$  is set to 0.40 mm. These values have been optimized to only cover the desired bandwidth and not interfere with other systems. The other parameters of the antenna remain unchanged with respect to the dual-band design, except the length of the monopole which is reduced to  $L_m = 19.75$  mm to compensate the inductive behavior of the OCSRRs below their resonance frequencies.

The simulated and measured reflection coefficients of the dual-band and tri-band monopoles are depicted in Figure 7. The dual-band printed monopole antenna exhibits good matching ( $|S_{11}| < -10$  dB) from 2.29 GHz to 2.52 GHz at the lower frequency band. This corresponds to a 9.6% bandwidth. In the upper band, the antenna is well matched from 4.66 GHz to at least 7 GHz. Thus, the fabricated antenna satisfies the specifications of Bluetooth and WiFi (bands of 2.40–2.48 GHz and 5.15–5.80 GHz). The fabricated tri-band monopole antenna is well matched from 2.30 GHz to 2.52 GHz for the first band. Its reflection coefficient is below  $-10$  dB between 3.56 GHz and 3.78 GHz for the second band, and between 5.06 GHz and 6.71 GHz

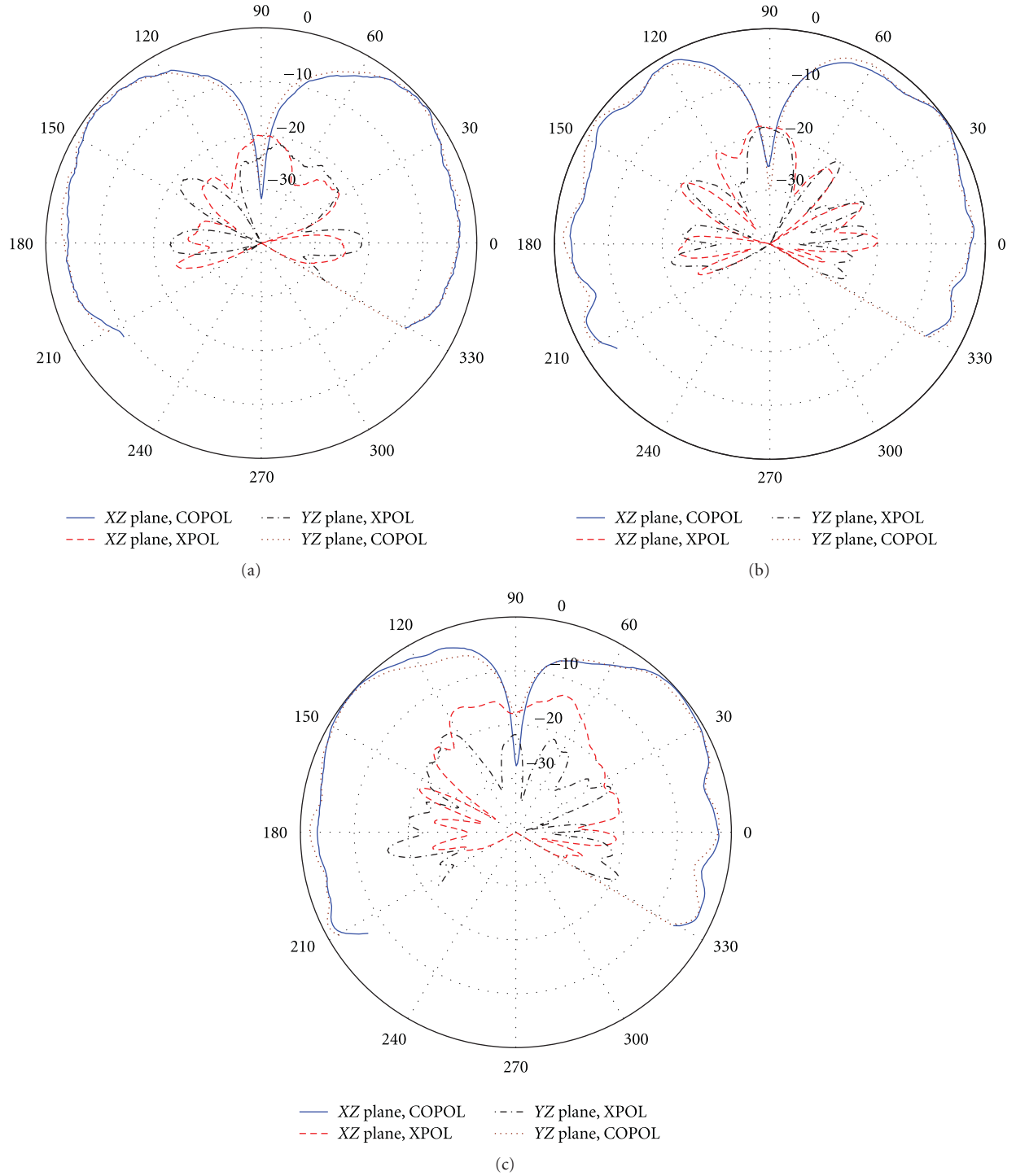


FIGURE 8: Measured radiation patterns of the tri-band printed monopole antenna. (a) 2.45 GHz, (b) 3.65 GHz, (c) 5.40 GHz.

for the third band. Hence, the fabricated prototype is well matched within the regulated bandwidths of Bluetooth and WiFi including IEEE 802.11y (3.65–3.70 GHz band).

The proposed antennas present monopolar radiation characteristics at all the bands. As an example, the normalized measured radiation patterns of the tri-band monopole

antenna are shown in Figure 8. A monopolar radiation pattern is obtained at the three frequencies. The cross-polar component (XPOL) has low values (below  $-20$  dB in all of the cases, except the XY plane of the third frequency which is below  $-15$  dB). The gains of this design are 1.4 dB, 1.2 dB, and 1.7 dB at the first, second, and third bands, respectively. These results are in good agreement with simulations, in

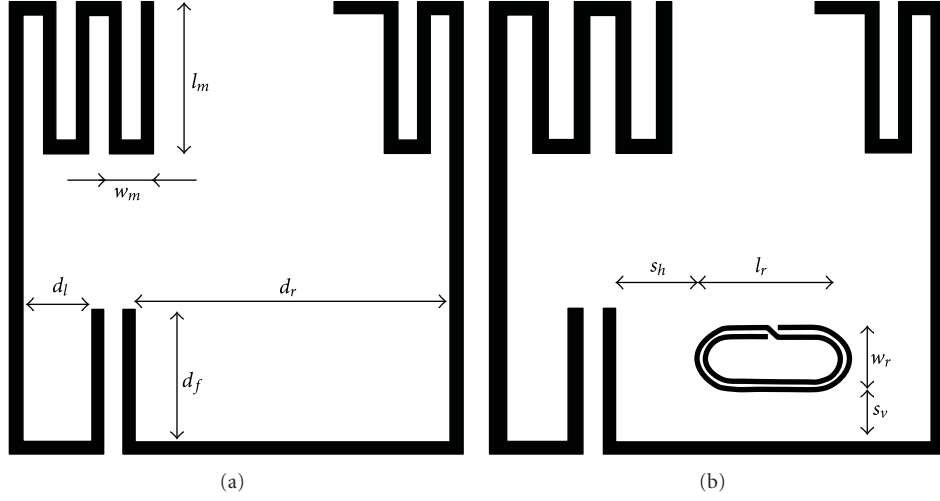


FIGURE 9: Layout of the meander line antenna considered for tag implementation (a) and layout of the MLA perturbed by the presence of a coupled two-turns spiral resonator, 2-SR (b). The strip width of the 2-SR is 0.5 mm, and the separation between strips is 0.3 mm.

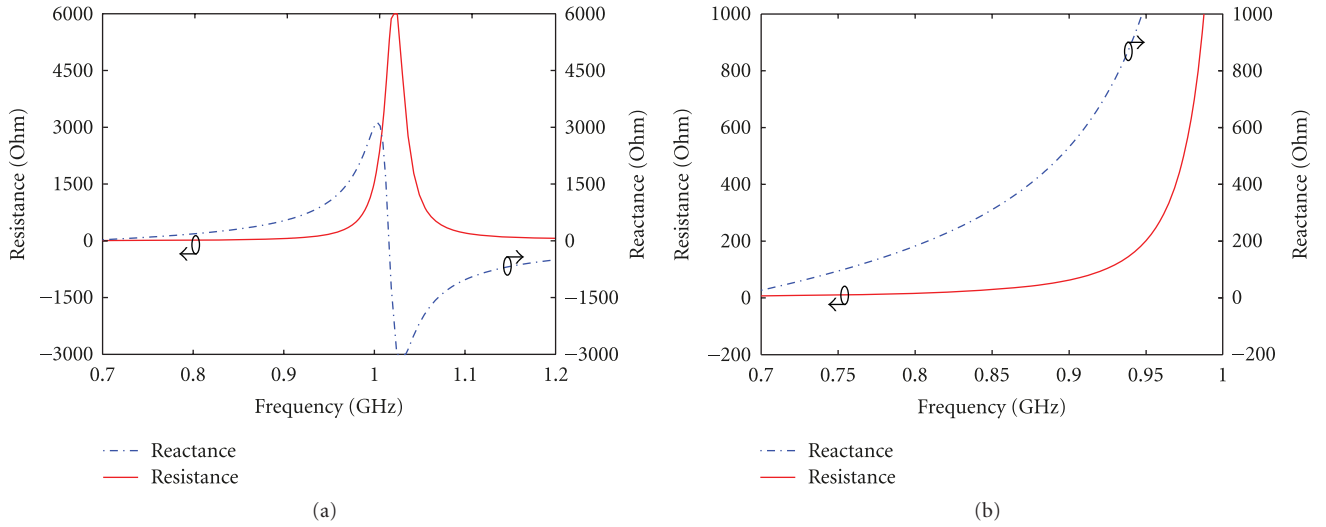


FIGURE 10: Input impedance of the MLA depicted in Figure 9(a) in a broader band (a) and input impedance of the MLA in the region of interest (b).

which the radiation efficiency is 92%, 83%, and 94% and the overall efficiency is 91%, 82%, and 93% at the central frequency of each band.

#### 4. Dual-Band UHF-RFID Tags

Metamaterial loading is also interesting for the implementation of dual-band antennas with closed frequency bands, as is the case of UHF-RFID, where the different regulated bands worldwide are contained in the spectral region between 860 MHz and 960 MHz. In this case, however, the approach is based on a perturbation method which was reported in [40]. The key aspect in the implementation of long read-range UHF-RFID tags is to achieve conjugate matching between the antenna and the integrated circuit (or chip). The input impedance of the chip is provided by the manufacturer

and varies with frequency. Therefore, the implementation of dual-band UHF-RFID tags means to design the antenna (and the matching network, if it is present) so that the chip “sees” its conjugate impedance at the required frequencies. This can be done by cascading a dual-band impedance matching network between the antenna and the chip, consisting on a transmission line loaded with a metamaterial resonator [40]. The resonator produces a perturbation in both the characteristic impedance and the phase constant of the transmission line, and conjugate matching at two frequencies can be obtained (the details are given in [40]). However, it is possible to directly actuate on the characteristic impedance of the antenna, by loading it with metamaterial resonant particles [41] (avoiding thus the matching circuitry). The principle is very similar to that reported in [40] for matching networks.



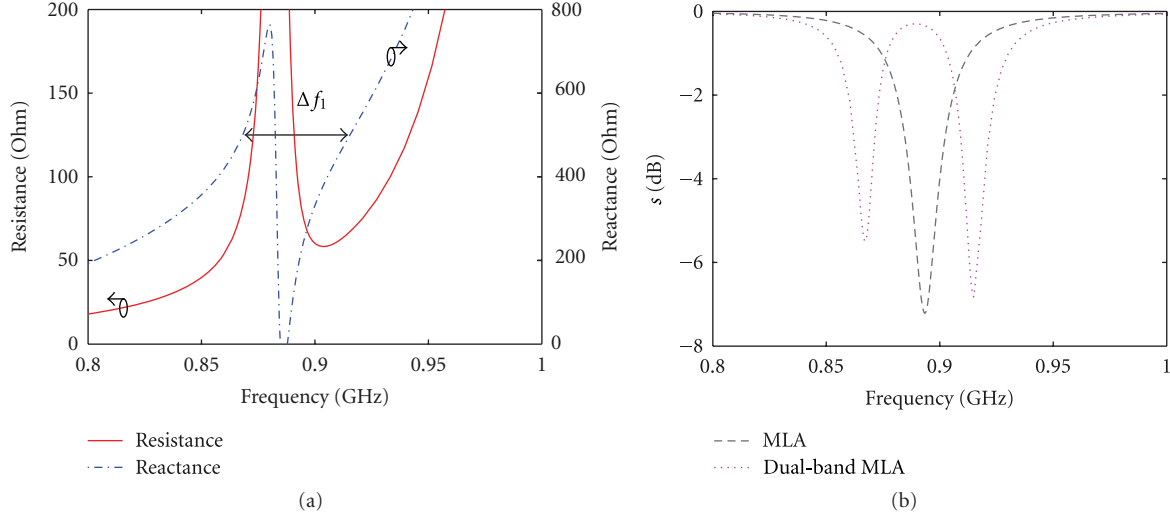


FIGURE 11: Input impedance of the dual-band MLA with coupled SR depicted in Figure 9(b) and power wave reflection coefficient of the monoband and dual-band meander line antenna. The frequencies where reactance matching is obtained, separated by  $\Delta f_1$ , are indicated and correspond to the resonance frequencies of the dual-band MLA.

Following the above-cited perturbation approach, several dual-band UHF-RFID tag antennas have been implemented. One prototype device consists on a meander line antenna (MLA) loaded with a spiral resonator (SR). The layout of the antenna, compared to the one without the SR, is depicted in Figure 9. The dual-band antenna has been designed to be operative at the European (867 MHz) and USA (915 MHz) UHF-RFID regulated bands. The antenna has been designed on the *Rogers RO3010* with dielectric constant  $\epsilon_r = 10.2$  and thickness  $h = 0.127$  mm. The considered RFID chip is the *SL31001* from *NXP semiconductors*. The impedance of the chip at the intermediate frequency is  $Z_{\text{chip}} = 20 - j485 \Omega$ . This impedance is considered as reference impedance so that the antenna is designed to roughly exhibit the conjugate impedance of the chip at this intermediate frequency, and then the perturbation (by means of the SR) is introduced in order to achieve conjugate matching at the required frequencies. The dimensions of the MLA are  $48 \text{ mm} \times 48 \text{ mm}$ , and the strip width is  $1.4 \text{ mm}$ . The other relevant dimensions are  $l_m = 16.3 \text{ mm}$ ,  $w_m = 4.8 \text{ mm}$ ,  $d_l = 7.3 \text{ mm}$ ,  $d_r = 33.9 \text{ mm}$ , and  $d_f = 14.2 \text{ mm}$ . The input impedance of the MLA is depicted in Figure 10, whereas Figure 11 depicts the input impedance and matching of the MLA loaded with the SR. As can be appreciated, the dual-band functionality in the SR-loaded MLA is achieved.

Both antennas have been fabricated, and the read range, given by

$$r = \frac{\lambda}{4\pi} \sqrt{\frac{\text{EIRP} G_r \tau}{P_{\text{chip}}}}, \quad (1)$$

has been measured through the experimental setup available in our laboratory (Figure 12). In (1),  $\lambda$  is the wavelength, EIRP, determined by local country regulations, is the product of  $P_t G_t$  which are the transmission power and the transmission gain, respectively,  $P_{\text{chip}}$  is the minimum threshold

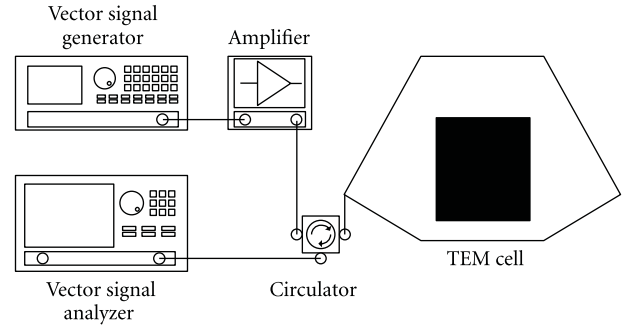


FIGURE 12: Bloch diagram of the experimental setup.

power necessary to activate the RFID chip,  $G_r$  is the gain of the receiving tag antenna, and  $\tau$  is the power transmission coefficient. The value of EIRP in European frequencies is  $3.3 \text{ W}$ ; whereas in American frequencies it is  $4 \text{ W}$ . The power transmission coefficient is inferred from the simulation of the return loss of the antenna, using as port impedance that of the chip. The tag gain is also obtained from simulation; hence the theoretical read range can be calculated.

The experimental setup consists of a *N5182A* vector signal generator which creates RFID frames. Such generator is connected to a TEM cell by means of a circulator. The tag under test is located inside the TEM cell and it is excited by the frame created by the generator. Then the tag sends a backscatter signal to a *N9020A* signal analyzer through the circulator. The RFID frame frequency is swept with a specific power. Once the operation frequencies are identified, the output power is decreased until the tag stops working. Finally, a probe is placed into the TEM cell in order to determine the incident electric field intensity  $E_0$  at each

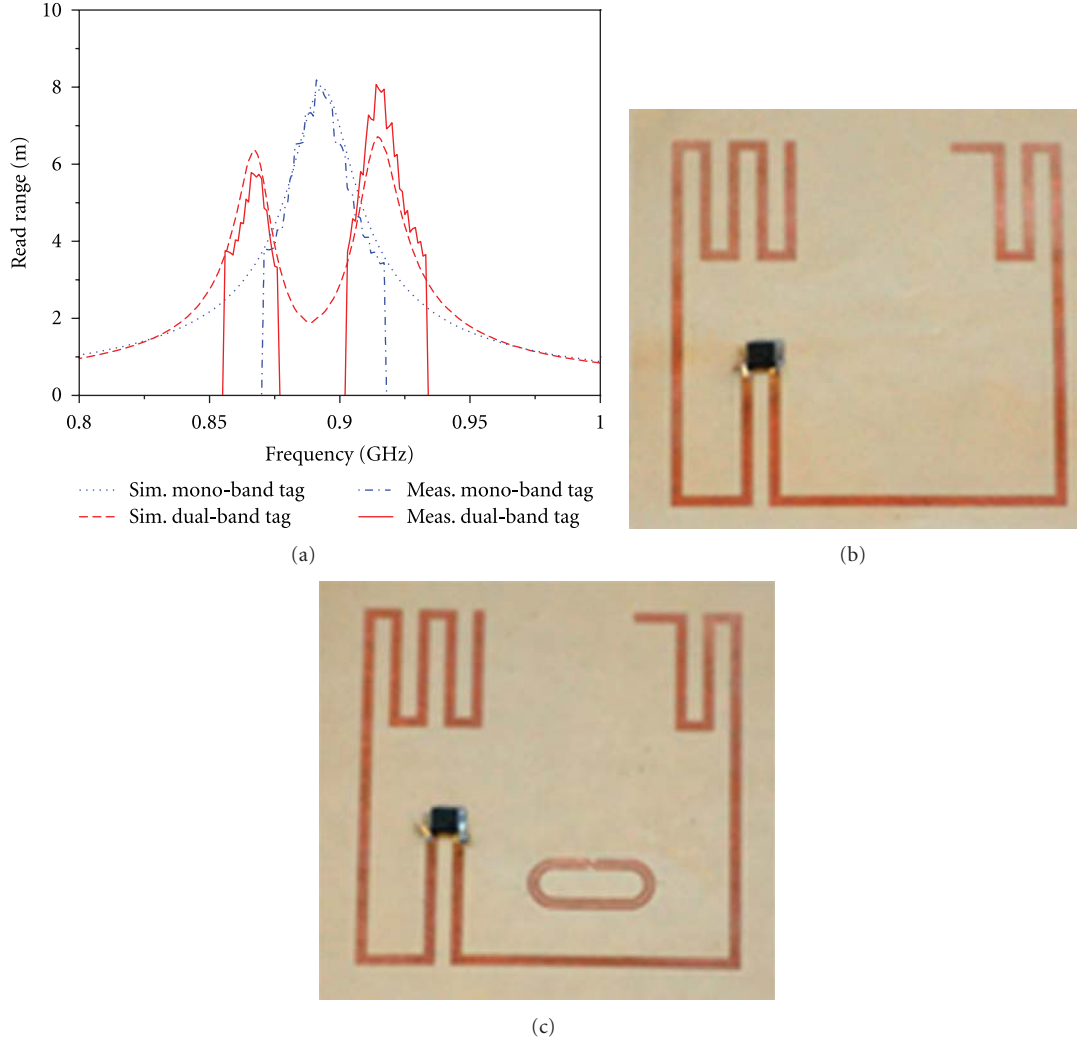


FIGURE 13: (a) Simulated and measured read ranges of the monoband and dual-band MLA RFID tags, and fabricated monoband (b) and dual-band (c) MLA RFID tags.

frequency, which is related to the received power by the chip according to

$$P_{\text{chip}} = S A_{\text{ef}} \tau = \frac{|E_0|^2}{2\eta} \frac{\lambda^2 G_r}{4\pi} \tau, \quad (2)$$

where  $S$  is the incident power density,  $A_{\text{ef}}$  is the effective area of the tag antenna, and  $\eta$  is the free-space wave impedance (which is equivalent to  $120\pi \Omega$ ). The measured read range can be inferred by introducing (2) in (1), resulting in

$$r = \frac{\sqrt{60 \text{EIRP}}}{E_0}. \quad (3)$$

As indicated before, the EIRP European value is lower than the USA counterpart, so the read range in Europe would be roughly reduced by a 0.9 factor for the same incident electric field intensity.

The fabricated tags, as well as the simulated and measured read ranges, are depicted in Figure 13, where it can

be seen that the read range obtained in the dual-band tags (at the frequencies of interest) is superior to that of the monoband tag. The read range of the monoband MLA tag is roughly 4 m at the frequencies of interest, whereas almost 6 m and 8 m at the European and USA frequency bands, respectively, are achieved by means of the designed dual-band MLA. This enhancement in the read range is due to an improved matching between the antenna and the integrated circuit, since it has been verified by simulation that the radiation efficiency of the monoband MLA is almost constant from 867 MHz to 950 MHz. In fact, if it was possible to achieve a perfect matching between the monoband antenna and the integrated circuit in all the band of interest, the obtained read range would be around 8 m at all frequencies. Nevertheless, this assumption is not possible due to the particularities of the chip impedance.

The perturbation method reported above can also be applied to folded dipole RFID tag antennas [42]. Figure 14 depicts a prototype, fabricated on the *Rogers RO3010* with



FIGURE 14: Photograph of the designed dual-band tag based on a folded dipole antenna.

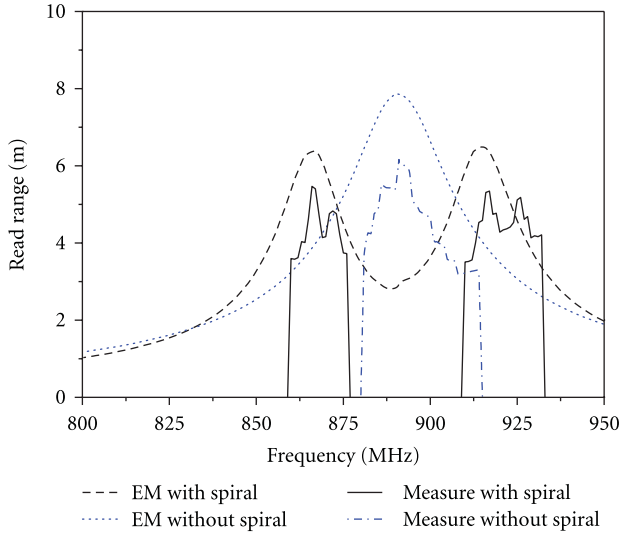


FIGURE 15: EM simulation and measurement of the read range of the tag shown in Figure 13, compared to that of the tag without SR.

dielectric constant  $\epsilon_r = 10.2$  and thickness  $h = 0.25$  mm. The dimensions are  $62.7 \text{ mm} \times 17.9 \text{ mm}$ . The simulated and measured read ranges are depicted in Figure 15 and compared to those of the tag without the presence of the SR. Again, the dual-band functionality at the regulated RFID European and USA frequency bands is achieved.

We would like to mention that in the designed RFID tags, the resonator frequency is set at the intermediate frequency (891 MHz), and as a consequence, the resonator impact on the antenna radiation efficiency can be neglected at the frequency bands of interest (867 MHz and 915 MHz).

## 5. Conclusions

In conclusion, two different approaches for the implementation of multiband printed antennas have been reviewed: one of them consisting on the introduction of series connected OCSRRs in the arms of printed dipole or printed monopole antennas; the other one based on a perturbation method achieved by loading printed antennas, such as meander line antennas (MLAs) or folded dipoles, with spiral resonators (SRs). The former approach has been revealed to be useful for personal area networks (PANs) and wireless local area networks (WLANS); the second one is of interest in the field of UHF-RFID. In both cases, the multiband functionality has

been demonstrated through the fabrication and characterization of several prototype devices.

## Acknowledgments

This work has been supported by Spain-MICIIN (Project contracts TEC2010-17512 METATRANSFER and CSD2008-00066) and Spain MITyC through the Projects TSI-020100-2009-778 and TSI-020100-2010-493. Thanks are also given to the Catalan Government for giving support through Project 2009SGR-421.

## References

- [1] G. V. Eleftheriades and K. G. Balmain, Eds., *Negative-Refractive Metamaterials: Fundamental Principles and Applications*, John Wiley & Sons, New York, NY, USA, 2005.
- [2] C. Caloz and T. Itoh, *Electromagnetic Metamaterials: Transmission Line Theory and Microwave Applications*, John Wiley & Sons, New York, NY, USA, 2006.
- [3] N. Engheta and R. W. Ziolkowski, *Metamaterials: Physics and Engineering Explorations*, John Wiley & Sons, New York, NY, USA, 2006.
- [4] R. Marques, F. Martín, and M. Sorolla, *Metamaterials with Negative Parameters: Theory, Design and Microwave Applications*, John Wiley & Sons, New York, NY, USA, 2008.
- [5] F. Capolino, Ed., *Metamaterials Handbook*, CRC Press, Boca Raton, Fla, USA, 2009.
- [6] L. Solymar and E. Shamonina, *Waves in Metamaterials*, Oxford University Press, Oxford, UK, 2009.
- [7] T. J. Cui, D. R. Smith, and R. Liu, Eds., *Metamaterials: Theory, Design and Applications*, Springer, New York, NY, USA, 2010.
- [8] W. Cai and V. Shalaev, *Optical Metamaterials: Fundamentals and Applications*, Springer, New York, NY, USA, 2010.
- [9] G. Shvets and I. Sukerman, Eds., *Plasmonics and Plasmonics Metamaterials: Analysis and Applications*, World Scientific, 2011.
- [10] Y. Hao and R. Mittra, *FDTD Modelling of Metamaterials: Modeling and Applications*, Artech House, 2009.
- [11] D. R. Smith, W. J. Padilla, D. C. Vier, S. C. Nemat-Nasser, and S. Schultz, "Composite medium with simultaneously negative permeability and permittivity," *Physical Review Letters*, vol. 84, no. 18, pp. 4184–4187, 2000.
- [12] J. B. Pendry, A. J. Holden, D. J. Robbins, and W. J. Stewart, "Magnetism from conductors and enhanced nonlinear phenomena," *IEEE Transactions on Microwave Theory and Techniques*, vol. 47, no. 11, pp. 2075–2084, 1999.
- [13] V. G. Veselago, "The electrodynamics of substances with simultaneously negative values of  $\epsilon$  and  $\mu$ ," *Soviet Physics Uspekhi*, vol. 10, pp. 509–514, 1968.
- [14] A. K. Iyer and G. V. Eleftheriades, "Negative refractive index metamaterials supporting 2-D waves," in *Proceedings of the IEEE MSS-S International Microwave Symposium Digest*, pp. 1067–1070, June 2002.
- [15] A. A. Oliner, "A periodic-structure negative-refractive-index medium without resonant elements," in *Proceedings of the IEEE-AP-S USNC/URSI National Radio Science Meeting: URSI Digest*, p. 41, San Antonio, Tex, USA, June 2002.
- [16] C. Caloz and T. Itoh, "Application of the transmission line theory of left-handed (LH) materials to the realization of a microstrip 'LH line,'" in *Proceedings of the IEEE Antennas and Propagation Society International Symposium*, pp. 412–415, Los Angeles, Calif, USA, June 2002.

- [17] F. Martín, J. Bonache, F. Falcone, M. Sorolla, and R. Marqués, "Split ring resonator-based left-handed coplanar waveguide," *Applied Physics Letters*, vol. 83, no. 22, pp. 4652–4654, 2003.
- [18] F. Falcone, F. Martín, J. Bonache, R. Marqués, and M. Sorolla, "Coplanar waveguide structures loaded with split-ring resonators," *Microwave and Optical Technology Letters*, vol. 40, no. 1, pp. 3–6, 2004.
- [19] M. Durán-Sindreu, A. Vélez, G. Sisó et al., "Recent advances in metamaterial transmission lines based on split rings," *Proceedings of the IEEE*, vol. 99, pp. 1701–1710, 2011.
- [20] R. Marqués, F. Medina, and R. Rafi-El-Idrissi, "Role of bianisotropy in negative, permeability and left-handed metamaterials," *Physical Review B*, vol. 65, no. 14, Article ID 144440, pp. 1–6, 2002.
- [21] F. Falcone, T. Lopetegi, J. D. Baena, R. Marqués, F. Martín, and M. Sorolla, "Effective negative- $\epsilon$  stopband microstrip lines based on complementary split ring resonators," *IEEE Microwave and Wireless Components Letters*, vol. 14, no. 6, pp. 280–282, 2004.
- [22] F. Falcone, T. Lopetegi, M. A. G. Laso et al., "Babinet principle applied to the design of metasurfaces and metamaterials," *Physical Review Letters*, vol. 93, no. 19, Article ID 197401, 2004.
- [23] J. D. Baena, J. Bonache, F. Martín et al., "Equivalent-circuit models for split-ring resonators and complementary split-ring resonators coupled to planar transmission lines," *IEEE Transactions on Microwave Theory and Techniques*, vol. 53, no. 4, pp. 1451–1460, 2005.
- [24] J. Martel, R. Marqués, F. Falcone et al., "A new LC series element for compact bandpass filter design," *IEEE Microwave and Wireless Components Letters*, vol. 14, no. 5, pp. 210–212, 2004.
- [25] A. Vélez, F. Aznar, J. Bonache, M. C. Velázquez-Ahumada, J. Martel, and F. Martín, "Open Complementary Split Ring Resonators (OCSRRs) and their application to wideband cwp band pass filters," *IEEE Microwave and Wireless Components Letters*, vol. 19, no. 4, pp. 197–199, 2009.
- [26] M. Durán-Sindreu, A. Vélez, F. Aznar, G. Sisó, J. Bonache, and F. Martín, "Applications of open split ring resonators and open complementary split ring resonators to the synthesis of artificial transmission lines and microwave passive components," *IEEE Transactions on Microwave Theory and Techniques*, vol. 57, no. 12, pp. 3395–3403, 2009.
- [27] J. D. Baena, R. Marqués, F. Medina, and J. Martel, "Artificial magnetic metamaterial design by using spiral resonators," *Physical Review B*, vol. 69, no. 1, Article ID 014402, pp. 1–5, 2004.
- [28] F. Falcone, F. Martín, J. Bonache et al., "Stop-band and band-pass characteristics in coplanar waveguides coupled to spiral resonators," *Microwave and Optical Technology Letters*, vol. 42, no. 5, pp. 386–388, 2004.
- [29] F. Bilotti, A. Toscano, and L. Vegni, "Design of spiral and multiple split-ring resonators for the realization of miniaturized metamaterial samples," *IEEE Transactions on Antennas and Propagation*, vol. 55, no. 8, pp. 2258–2267, 2007.
- [30] F. Bilotti, A. Alu, and L. Vegni, "Design of miniaturized metamaterial patch antennas with  $\mu$ -negative loading," *IEEE Transactions on Antennas and Propagation*, vol. 56, no. 6, pp. 1640–1647, 2008.
- [31] C. Caloz, T. Itoh, and A. Rennings, "CRLH metamaterial leaky-wave and resonant antennas," *IEEE Antennas and Propagation Magazine*, vol. 50, no. 5, pp. 25–39, 2008.
- [32] A. Erentok and R. W. Ziolkowski, "A dual-band efficient metamaterial-inspired electrically-small magnetic-based antenna," in *Proceedings of the IEEE Antennas and Propagation Society International Symposium (AP-S '07)*, pp. 1877–1880, Honolulu, Hawaii, USA, June 2007.
- [33] J. Zhu and G. V. Eleftheriades, "Dual-band metamaterial-inspired small monopole antenna for WiFi applications," *Electronics Letters*, vol. 45, no. 22, pp. 1104–1106, 2009.
- [34] F. J. Herraiz-Martínez, L. E. García-Muñoz, D. González-Ovejero, V. González-Posadas, and D. Segovia-Vargas, "Dual-frequency printed dipole loaded with split ring resonators," *IEEE Antennas and Wireless Propagation Letters*, vol. 8, pp. 137–140, 2009.
- [35] F. J. Herraiz-Martínez, L. E. García-Muñoz, D. González-Ovejero, V. González-Posadas, and D. Segovia-Vargas, "Dual-frequency printed dipole loaded with split ring resonators," *IEEE Antennas and Wireless Propagation Letters*, vol. 8, pp. 137–140, 2009.
- [36] J. Montero-de-Paz, E. Ugarte-Muñoz, F. J. Herraiz-Martínez, V. González-Posadas, L. E. García-Muñoz, and D. Segovia-Vargas, "Multifrequency self-diplexed single patch antennas loaded with split ring resonators," *Progress in Electromagnetics Research*, vol. 113, pp. 47–66, 2011.
- [37] F. J. Herraiz-Martínez, F. Paredes, G. Zamora, F. Martín, and J. Bonache, "Dual-band printed dipole antenna loaded with open complementary split-ring resonators (OCSRRs) for wireless applications," *Microwave and Optical Technology Letters*, vol. 54, no. 4, pp. 1014–1017, 2012.
- [38] F. J. Herraiz-Martínez, G. Zamora, F. Paredes, F. Martín, and J. Bonache, "Multiband printed monopole antennas loaded with open complementary split ring resonators for PANs and WLANs," *IEEE Antennas and Wireless Propagation Letters*, vol. 10, pp. 1528–1531, 2011.
- [39] Z. Živković and A. Šarolić, "Gain and antenna factor measurements of broadband biconical dipole in the GTEM cell," in *Proceedings of the 52nd International Symposium (ELMAR '10)*, pp. 297–300, Zadar, Croatia, September 2010.
- [40] F. Paredes, G. Zamora, J. Bonache, and F. Martín, "Dual-band impedance-matching networks based on split-ring resonators for applications in RF identification (RFID)," *IEEE Transactions on Microwave Theory and Techniques*, vol. 58, no. 5, pp. 1159–1166, 2010.
- [41] F. Paredes, G. Zamora, F. J. Herraiz-Martínez, F. Martín, and J. Bonache, "Dual-band UHF-RFID tags based on meander line antennas loaded with spiral resonators," *IEEE Antennas and Wireless Propagation Letters*, vol. 10, pp. 768–771, 2011.
- [42] F. Paredes, G. Zamora, F. Javier Herraiz-Martínez, F. Martín, and J. Bonache, "Dual-band RFID Tags based on Folded Dipole Antennas Loaded with Spiral Resonators," in *Proceedings of the IEEE International Workshop on Antenna Technology: Small Antennas and Unconventional Applications (IWAT '12)*, Tucson, Ariz, USA, March 2012.



## Review Article

# Nanocouplers for Infrared and Visible Light

**A. Andryieuski and A. V. Lavrinenko**

*DTU Fotonik, Technical University of Denmark, Ørstedss Plads 343, 2800 Kongens Lyngby, Denmark*

Correspondence should be addressed to A. Andryieuski, [andra@fotonik.dtu.dk](mailto:andra@fotonik.dtu.dk)

Received 14 June 2012; Accepted 6 September 2012

Academic Editor: Pavel A. Belov

Copyright © 2012 A. Andryieuski and A. V. Lavrinenko. This is an open access article distributed under the Creative Commons Attribution License, which permits unrestricted use, distribution, and reproduction in any medium, provided the original work is properly cited.

An efficient and compact coupler—a device that matches a microwaveguide and a nanowaveguide—is an essential component for practical applications of nanophotonic systems. The number of coupling approaches has been rapidly increasing in the past ten years with the help of plasmonic structures and metamaterials. In this paper we overview recent as well as common solutions for nanocoupling. More specifically we consider the physical principles of operation of the devices based on a tapered waveguide section, a direct coupler, a lens, and a scatterer and support them with a number of examples.

## 1. Introduction

Photonic components have advantages comparing to the electronic ones. Infrared and optical frequencies  $10^{14}$ – $10^{15}$  Hz provide much broader operational bandwidth than the fastest electronic circuits. The losses in optical waveguides are smaller than in metallic wires. This is why, as D. Miller wrote, “the optical interconnects are progressively replacing wires” [1]. To achieve larger functionality on an integrated optical chip the optical components have to be miniaturized. A natural limitation, however, comes into play: the diffraction limit claims that we cannot focus light in a spot less than a half of the wavelength. The transverse size of conventional dielectric waveguides (e.g., silicon waveguides) is also limited to a half of the wavelength. Only employment of metals allows to overcome the diffraction limit and to confine a wave to a smaller area, very often at the cost of increased propagation losses.

Nevertheless, the problem is not only to create efficient waveguides that provide subwavelength mode confinement, but also to make an efficient interface between free space or an optical fiber and a subwavelength nanowaveguide, that is, to focus light and launch it efficiently into the waveguide. The artistic view of the situation is depicted in Figure 1. Trying to pour water from a big bowl into a bottle with a narrow bottleneck, one would waste a lot. However, usage of a funnel

simplifies the task and increases the efficiency significantly. An optical coupler plays the role of a funnel for light.

The problem of optical coupling originates from the pronounced modal mismatch between an optical fiber (a conventional single-mode telecommunication fiber has the core of  $8\text{ }\mu\text{m}$  in diameter) and a nanosized waveguide, which has a core less than  $1\text{ }\mu\text{m}$ . They have a small overlap of modal fields that prevents from the efficient coupling. Long adiabatically tapered fibers can solve the coupling problem of a subwavelength waveguide, but for an efficient mode conversion the tapered region may reach the length of several millimeters that is totally incompatible with modern micro- and nanofabrication. The compact efficient subwavelength couplers require new approaches.

We are witnessing a real explosion of various metamaterial and plasmonic solutions for focusing and nanocoupling in recent years. The reasons for that are first of all the extraordinary optical properties the artificial metal-dielectric structures offer. Not only the proposed device geometries are different, but also the very physical principles they are based on vary significantly.

The goal of this paper is to give an overview of existing nanocoupling solutions for the visible and near-infrared (telecom) range and to reveal the most efficient ones. We wish to focus mostly on the physical effects employed for nanocoupling rather than on technical details of the devices.





FIGURE 1: An artistic view of the problem of coupling light from a wide microscopic fiber to a nanoscopic waveguide. Employment of a coupler, which is represented by a funnel on the figure, minimizes the losses and simplifies optical alignment.

We are not going to provide the complete set of references on nanocouplers, since with heaps of articles already published and being published every month it is almost impossible. The cited papers should be considered rather as valuable examples of each physical effect employment.

The paper is organized as follows. In Section 2 the definitions of a nanocoupler and a nanowaveguide are given as well as the basic information on the common waveguide properties. Various physical principles, on which the nanocoupler realization can be grounded, are listed in Section 3. The tapered waveguide-based nanocouplers are discussed in Section 4. Section 5 deals with the directional nanocouplers. The lenses-based and scatterer-based couplers are considered in Section 6 and Section 7 correspondingly. Other ideas are listed in Section 8. Conclusions summarize the paper.

## 2. Definitions

**2.1. Nanowaveguide.** We define a nanowaveguide as an electromagnetic waveguide that has lateral sizes in the “nano” range, that is, 1–1000 nm. Depending on the waveguide material and the wavelength of the light nanowaveguide can be subwavelength or not. The modal size of the subwavelength waveguide is smaller than the size of a focused light beam can be. The nanowaveguides can be divided in two groups: dielectric and plasmonic waveguides. Their combinations, the so-called hybrid waveguides, are also possible.

**2.2. Dielectric Waveguide.** The most common material for dielectric waveguides is silicon due to its high refractive index, transparency at the telecom wavelengths, and CMOS compatibility. Typically, silicon waveguides are rib, ridge, and photonic crystal waveguides. The high refractive index of

the silicon waveguide makes it possible to reduce the cross-section down to  $200 \times 500 \text{ nm}^2$ . The dielectric waveguide always has a cut-off size, below which the waveguide modes become leaky and the waveguide cannot transport light on reasonable distances.

Miniaturization of optoelectronic components requires decreasing the size of optical waveguides. However, the natural limitation comes into play. Due to diffraction the smallest size of an optical beam in a medium is on the order of the wavelength. If we consider a wave of the frequency  $\omega$  propagating in the medium with the refractive index  $n$ , the wavenumber is  $k = 2\pi n/\lambda$ . The transverse wavevector components, for example,  $k_x$  can take the values from  $-k$  to  $k$ , so its maximal uncertainty can be  $\Delta k_{x,\max} = 2k = 4\pi n/\lambda$ . Due to the uncertainty principle (or likewise Fourier transformations), the coordinate uncertainty  $\Delta x$  is connected to the wavevector uncertainty  $\Delta k_x$  [2] through

$$\Delta x \Delta k_x \geq 2\pi. \quad (1)$$

That limits the size of the light beam to

$$\Delta x = \frac{2\pi}{2k} = \frac{\lambda}{2n}. \quad (2)$$

Considering, for example, the telecom wavelength  $\lambda = 1.55 \mu\text{m}$  and silica refractive index  $n = 1.5$  we can estimate the smallest size of a light beam as  $\Delta x_{\min} = 517 \text{ nm}$ . Light can be confined to smaller spots only by using surface plasmons at an interface between metal and dielectric.

**2.3. Plasmonic Waveguide.** Plasmonic waveguides are by default metal-dielectric waveguides. They attract a lot of attention since in some configurations they can show the absence of the cut-off wavelength at any waveguide size. Therefore, the mode size can be reduced to extremely small values but at the cost of increased optical losses. Another advantage of the plasmonic waveguides is the presence of metal that can be used not only as a waveguiding element but also as an electric contact that allows using it for tuning the dielectric surrounding (e.g., due to the electrooptical or thermo-optical effects). Plasmonic waveguides are currently considered for the potential replacement of the electronic interconnects in the future generation integrated circuits.

Surface plasmon polaritons (SPPs) are the eigenmodes of a metal-dielectric interface. SPPs are combined light-electrons density waves. On a flat metal (permittivity  $\epsilon_1$ )-dielectric (permittivity  $\epsilon_2$ ) interface the SPPs are transverse waves with the magnetic field parallel to the interface. In the visible and near-infrared ranges the permittivity of metal is very dispersive. The propagating SPP solutions correspond to a case  $\text{Re}(\epsilon_1 + \epsilon_2) < 0$ . For a detailed background on plasmonics theory and applications we refer the reader to [3, 4].

Several types of plasmonic waveguiding structures were proposed, for example, metal-insulator-metal and insulator-metal-insulator multilayered structures [5], strip [6], trenches and V-grooves [7, 8], wedge [9], slot [10, 11], and nanoparticles chain [12] waveguides. A comprehensive overview of the plasmonic waveguides and nanoplasmonic systems can be found in [3, 4, 13–15].

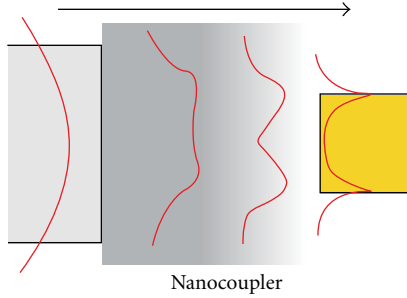


FIGURE 2: Nanocoupler concept: a focusing device or a mode convertor. As an example the mode of the dielectric waveguide (left) is gradually transformed into the mode of the plasmonic waveguide (right).

**2.4. Nanocoupler Definition.** A nanocoupler is a device that facilitates coupling of light from free space or a macroscopic optical fiber to a nanowaveguide. It can be understood as a focusing device, a sort of an optical funnel (see Figure 1) that squeezes light into a small spot. If we talk about matching a thick and a thin waveguides that have different modal distributions, the nanocoupler can be also understood as a mode convertor, a device that transforms a mode of the thick waveguide to a mode of the thin waveguide (see Figure 2).

**2.5. Requirements to a Nanocoupler.** We understand the nanocoupler as a focusing device or a mode convertor that gives a high coupling efficiency (CE) which is the ratio of the power loaded into the waveguide  $P_{WG}$  to the power incident on the nanocoupler from free space or power delivered by a thick waveguide  $P_{inc}$ :

$$CE = \frac{P_{WG}}{P_{inc}}. \quad (3)$$

High coupling efficiency automatically means low losses, including absorption  $A$ , reflection  $R$ , and scattering  $S$ . Additional requirements to the nanocoupler can be as follows.

- (1) Small size on the order of several micrometers. This is an important requirement for the integration of the nanocoupler within an optical integrated circuit.
- (2) Simplicity and small price of fabrication. This requirement is important for the mass production but not so important on the stage of the scientific development.
- (3) Spectral selectivity. The importance of this property depends on the application. In many cases a broad bandwidth is desirable. However, there are some applications, where a narrow bandwidth is preferable, for example, if the coupler is used at the same time for the wavelength demultiplexing.
- (4) Polarization sensitivity. The importance of this requirement depends on the application and on the selected nanowaveguide. If the nanowaveguide is polarization sensitive, the nanocoupler's working polarization should be matched with the polarization of the waveguide or it should be polarization insensitive.

We have to emphasize that the nanocoupler differs from a nanofocusing or a nanoimaging device. The goal of nanoimaging or nanofocusing is only to image a tiny light source or focus light into a small spot, respectively, no matter how large is the fraction of the transmitted power with respect to the incident power, while for the nanocoupler the coupling efficiency is the most crucial parameter. For example, the stimulated emission depletion technique [16, 17] allows for a fantastic resolution below 10 nm in the visible light imaging systems, but it can hardly be used for an efficient coupling.

### 3. Nanocouplers Classification

The role of the nanocoupler is to match the impedances (or wavevectors) and field profiles of an incident wave and a mode of the accepting nanowaveguide. Depending on the employed physical mechanisms several types of nanocouplers can be singled out.

- (1) Tapered waveguides (Figure 3(a)) which will be referred to as *tapered waveguide coupler*. In this case a waveguide with the gradually reduced core cross-section compresses a wave towards the matching parameters with the accepting nanowaveguide.
- (2) Light can be coupled first to a wide waveguide (e.g., a silicon or long-range surface plasmon-polariton waveguide) and then with the help of a directional coupler or a resonant stub coupled into a smaller nanowaveguide (Figure 3(b)). We will refer to this case as a *direct coupler*.
- (3) Light can be tightly focused with a lens (Figure 3(c)). This is what we are referring to as a *lens coupler*.
- (4) A single or multiple scatterers can be used for coupling (Figure 3(d)). Correspondingly, the device is called a *scatterer coupler*.
- (5) There are some other ideas that do not fall into the previously mentioned categories. We will refer to them under a unified shield as *other solutions*.

The nanocoupler can be arranged as a separate device (Figure 4(a)), as a device integrated with a waveguide on a chip (Figure 4(b)), or as a device integrated with an excitation fiber (Figure 4(c)). For the practical applications the integrated configurations (b) and (c) are preferable, since a lesser number of movable parts simplifies optical alignment.

Two main excitation configurations are important in the practical applications: lateral coupling (Figure 5(a)), when the incident wave direction coincides with the nanowaveguide, and vertical coupling (Figure 5(b)), when the light direction is perpendicular to the nanowaveguide. The second configuration can provide not only incoupling from free space, but also communication of the optical elements between two layers of an optical integrated circuit. Incident angles of light different from 0 and 90 degrees are also possible.

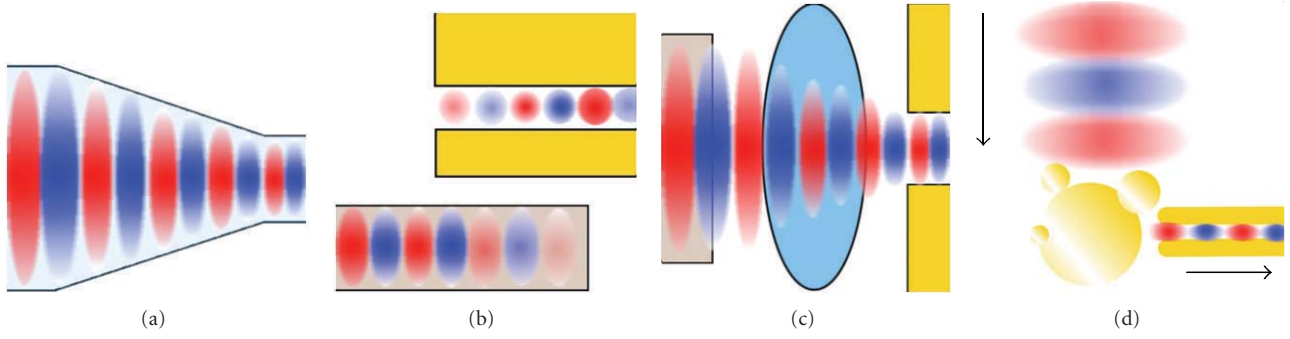


FIGURE 3: Types of the possible nanocouplers realizations: (a) tapered waveguide coupler, (b) direct coupler transferring the power from a wide waveguide to a narrow waveguide, (c) lens coupler, (d) scatterer coupler.

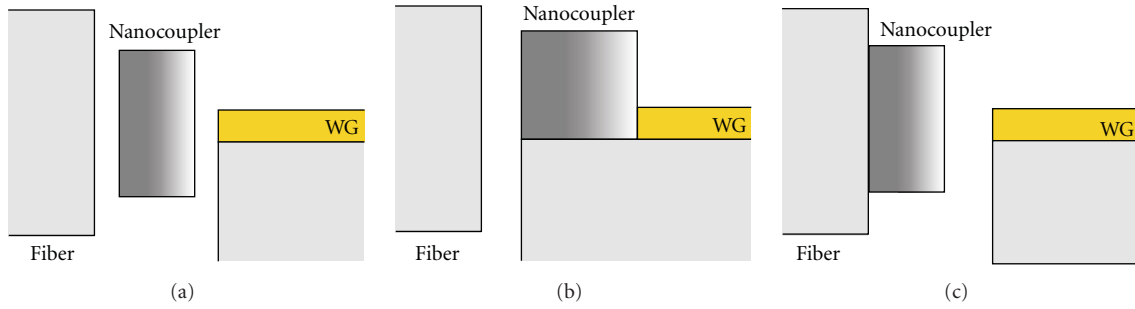


FIGURE 4: Possible geometrical configurations of the coupler: (a) a separate device, (b) integrated with a nanowaveguide (WG) on the same chip, (c) integrated with an excitation fiber.

#### 4. Tapered Waveguide Coupler

As we already mentioned the tapered waveguide coupler is nothing else but a waveguide with the gradually decreasing core. A mode of the waveguide is subjected to adiabatic compression, when propagating to the tip. Thus it reaches more favorable conditions for coupling to the nanowaveguide. The tapering angle and the rate of compression determine the coupling efficiency and depend on the properties of materials. Therefore, further classification of the tapered waveguides follows the material properties:

- (1) fully dielectric tapers having the dielectric core and the dielectric cladding (Figure 6(a)),
- (2) hybrid tapers having the metallic core and dielectric cladding or the dielectric core and metallic cladding (Figure 6(b)),
- (3) metamaterial tapers having the structured metal-dielectric composite core (Figure 6(c)).

**4.1. Dielectric Core and Cladding.** If one takes an optical fiber, heats it up, and then pulls, the diameters of the core and shell simultaneously decrease. So it is possible to draw the core down to a nanosize diameter. Low-loss tapered fibers were fabricated and measured [18]. The optical losses for a fiber of diameter  $d = 750$  nm at  $\lambda = 1.55$   $\mu$ m are 0.017 dB/mm. However, it was also theoretically shown [19] that even an ideal fiber does not allow the substantial core

thinning, since the propagating mode completely vanishes for the core size of one order of magnitude smaller than the wavelength. In the real fibers with imperfections this limitation is even tougher.

Nevertheless, the dielectric tapered waveguide coupler finds useful applications. As L. Zimmermann reported at the Silicon Photonics Workshop in 2011 [20], an inverted taper is commonly used for lateral coupling from a high numerical aperture lensed optical fibers with a spot size of 3  $\mu$ m to a  $200 \times 500$  nm<sup>2</sup> silicon waveguide. The inverted taper is also used for coupling to and from the slow light photonic crystal waveguide [21] reducing the insertion loss value to 10 dB. Tapering came out to be useful to outcoupling efficiency increase and far-field shaping of the nanopillar single photon sources [22, 23]. The coupling efficiency can be very large (80% and higher) for certain pairs waveguides, for example, for silicon ridge and silicon slot waveguides [24, 25].

**4.2. Metallic Core or Cladding.** Tapered fiber tips covered with metal are the essential part of the scanning near-field optical microscopy. It allows spatial compression of light below the diffraction limit by employment of SPPs [26]. Metal-dielectric-metal tapered plate waveguides were theoretically and experimentally demonstrated for the terahertz [27–30] and optical ranges [31–34] showing the ability of ultrahigh energy concentration. In the latter work [34] the maximal transmittivity of 8% was measured for the wavelength  $\lambda = 780$  nm in an adiabatically tapered metalized

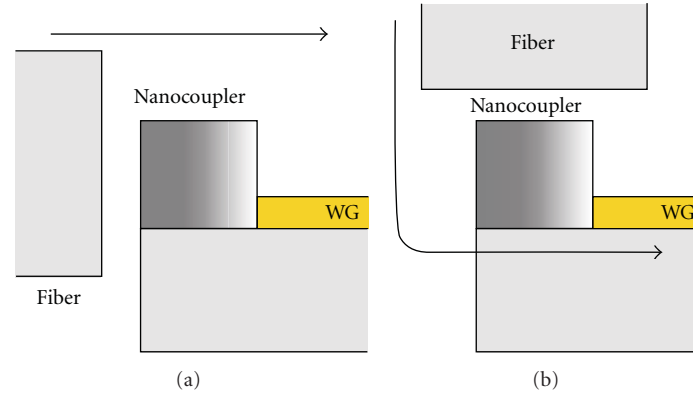


FIGURE 5: Two practically important coupling configurations: (a) lateral and (b) vertical. Black arrows show the direction of light propagation.

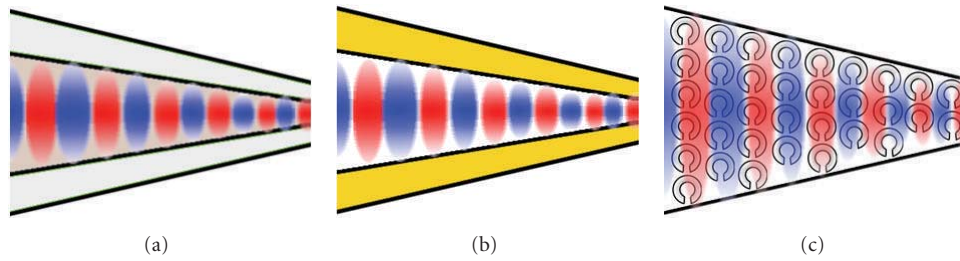


FIGURE 6: The types of taper couplers: (a) fully dielectric taper, (b) hybrid taper with metal core or cladding, (c) metamaterial taper.

fiber with the tip opening of about 150 nm. The prominent property of such system is that a metal-dielectric-metal waveguide does not have a cut-off, and only losses limit its performance. Nanofocusing with a V-shaped metallic groove, which is a similar system, was experimentally demonstrated [35]. A wave with  $\lambda = 1.5 \mu\text{m}$  wavelength was focused into a spot of  $\lambda/40$ . The reported energy efficiency was 50%. In 2004 M. Stockman predicted that a tapered metallic wire allows the giant energy accumulation and intensity enhancement at the tip of the metal taper [36]. The idea is applicable not only in the optical range but also in the terahertz range if the surface of the tapered wire is corrugated [37]. An experimental realization of the tapered wire structure was reported [38]. In this case light with  $\lambda = 1.55 \mu\text{m}$  was coupled to a 2000 nm wide wire and compressed down to 90 nm. The transmittivity of 20% was shown.

Another approach was proposed in [35]. A metallic funnel consisting of long metallic nanocylinders of the radii from 10 to 24 nm separated with a 2 nm thick dielectric was shown to focus a Gaussian beam of 200 nm full width into a spot of 20 nm with a power transmittivity of 80% [39]. However, a practical realization of such system is hardly possible at the moment.

**4.3. Metamaterial Core.** The idea behind this nanocoupler type is to use a metamaterial as the taper core. The advantage of utilization of metamaterials is that their properties are not

strictly limited to that we have from natural materials and can be designed to reach amazing diversity and values. An optical funnel containing a metal-dielectric photonic crystal was proposed in [40]. The field compression down to  $\lambda/30$  with a transmission of 13% was reported. The metamaterial-based nanotips for field enhancement were theoretically proposed [41, 42]. The nanotip consists of metallic nanospheres of a gradually changing density. They can be used for field concentration (200 times field enhancement was reported) and the light compression to a spot of 10 nm. In the work [41] it is stated that the power efficiency of such metamaterial tip is larger than of a metalized taper with the 10 nm output hole, but the exact values of the transmittivity are not mentioned.

**4.4. Summary.** A dielectric adiabatically tapered fiber is a well-known instrument of field concentration. However, it can provide either small spot size with low transmission or high transmission at the cost of large size of the light beam and the coupler itself. The metal- or metamaterial-based tapers can be of significantly smaller length. They can give field concentration and reasonable transmittivity (e.g., 20%). The difficulties in practical realization of effective design solutions are connected with the technological constraints; for example, fabrication of a regularly packed bundle of metallic cylinders of radius 10 nm separated with 2 nm of dielectric is currently out of reach.



## 5. Direct Coupler

Based on the geometrical position of one waveguide with respect to another, the direct couplers can be divided into the following classes:

- (1) one waveguide next to or inside another (Figure 7(a)),
- (2) end-fire direct connection of the waveguides (Figure 7(b)),
- (3) resonant stub between the waveguides (Figure 7(c)).

Direct couplers as we classified them are either directional couplers or schemes including end-fire coupling. Directional couplers are classical components of photonic integrated circuits. They are typically used for wavelength division or light switching. The principle of their operation is based on the coupling between parallel waveguides due to overlapping of their modes fields. The coupling leads to the hybrid modes (supermodes, compound modes) formation. The strength of the mode coupling can be controlled by the distance between the cores. Therefore, such couplers require preliminary feeding of a large waveguide at an intermediate step. Then disposing the first waveguide in a close proximity with a nanowaveguide we initiate their coupling with a consequent transit of the light energy in the second channel. Directional couplers are characterized by the coupling length, the distance, on which the maximal amount of the energy is transferred in the second channel and vice versa. The coupling length, in turn, is proportional to the wavenumbers mismatch. As a rule, directional couplers have a relatively large coupling length, what results in the total size of such systems about 10–20  $\mu\text{m}$ .

The end-fire coupling scheme also exploits the fields overlapping mechanism. Here the coupling appears as a result of the field profiles matching. The scheme does not require a lengthy coupling part; however, short sizes come at a price of lower coupling efficiency. To improve the efficiency a resonant stub is often placed between the input and nanosized waveguides.

**5.1. One Waveguide Next to or inside Another.** A typical scheme for direct coupling is to arrange one waveguide above another such that the eigenmodes of the waveguides hybridize, and the waveguides become coupled. In such case energy from the input mode is transferred from one waveguide to another and back. Making the overlap region equal to the coupling length it is possible to achieve the maximal energy transfer efficiency. Such systems were proposed, simulated, and experimentally realized for dielectric [43] and plasmonic long- and short-range waveguides [44–48]. The coupling length may vary from several micrometers [47, 49] to hundreds of micrometers [43]. For certain waveguides (dielectric to long-range surface plasmon polariton) the coupling efficiency can be extremely large. The theoretical prediction of coupling efficiency  $CE = 60\%$  from dielectric to plasmonic slot waveguide at  $\lambda = 1.55 \mu\text{m}$  was confirmed in measurements [47]. However, we should take into account that light should be first coupled from a fiber to an input

(silicon) waveguide and that the maximal coupling efficiency is in the order of 60–70%. That makes the total coupling efficiency of the system about 30–40%. It is possible to obtain light coupling by placing metal nanowires on top of the dielectric waveguide perpendicular to the latter [50]. In such arrangement the overlapping region is extremely small, and the coupling efficiency of such system is reported to be only 1%.

The configuration when one waveguide protrudes into another is possible to certain waveguide types only, since the bigger waveguide should contain empty space inside. For example, it is possible to insert a silicon waveguide inside a plasmonic slot waveguide, but not into another silicon waveguide. Several designs for telecom wavelengths were proposed [51–53] and experimentally realized, giving a theoretical coupling efficiency of 88% and measured coupling efficiency about 35% [53].

**5.2. End-Fire Coupling.** The end-fire coupling is the simplest case of the waveguides connections, and it is common in the optical communication systems. Nevertheless, the end-fire coupling from a dielectric to plasmonic slot waveguide or a nanowire is not usually very efficient due to the pronounced impedances mismatch. However, if the optimization of the geometry is conducted the coupling efficiency more than 70% [54, 55] and even 90% can be achieved [56, 57]. For example, at the wavelength of  $\lambda = 1.55 \mu\text{m}$  the coupling efficiency of 80% was measured for a long-range surface plasmon polaritons waveguide connected to a silicon waveguide [58]. In another work the coupling from a silicon to plasmonic slot waveguide with 30% efficiency at  $\lambda = 1.55 \mu\text{m}$  was experimentally demonstrated [59]. End-fire coupler based on optical tunneling can be used for identical waveguides separated with a small gap [60]. Varying the width of the gap one can tune the transmission and reflection in a wide range.

**5.3. Resonant Stub between the Waveguides.** The use of resonant stubs (e.g., a  $\lambda/4$ -transformer) for the efficient wave coupling is the well-known technique in the microwave waveguides engineering. It is based on the resonant transmission increase due to the constructive interference similarly to the antireflection coatings for lenses. The same concept can be used in the optical range, for the plasmonic waveguides of different cross-sections [11, 61–63] and for the silicon and plasmonic waveguides [64] matching. The coupling efficiency can be enhanced in comparison with the end-fire coupling. However, as based on the resonant phenomena the scheme has limited bandwidth and very individual application range.

The  $\lambda/4$ -transformer matching 500 nm and 50 nm wide plasmonic transmission lines with the coupling efficiency of 86% was shown numerically [61]. Matching of a 300 nm wide silicon waveguide with a 40 nm wide plasmonic slot waveguide with the coupling efficiency of 88% was also demonstrated [64].

**5.4. Summary.** While giving high values of the coupling efficiency (in case of a directional coupler up to 60%) and



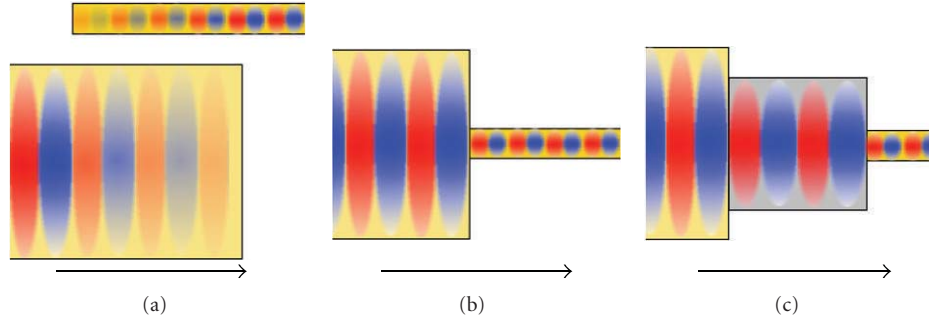


FIGURE 7: Types of the direct couplers: (a) one waveguide next to or inside another, (b) end-fire coupling, (c) resonant stub between waveguides.

being feasible for fabrication, the direct nanocouplers require additional structures such as an input silicon waveguide and a preliminary coupler to this silicon waveguide. That makes the total CE of up to 40% and extends the nanocoupler dimensions up to several dozens of micrometers. Moreover, additional structures (e.g., a preliminary coupler) may require additional processing steps during fabrication.

## 6. Lens Coupler

Lens is a well-known focusing device. However, we should emphasize that the requirements for a nanocoupler are stricter than to a focusing device, since nanocoupler should provide, apart from focusing, the high coupling efficiency. To be implemented as a nanocoupler a lens must have high transmission and execute matching of the focused beam to the nanowaveguide mode.

Based on the lens material and their functionality we divide lenses into the following categories:

- (1) dielectric lens (Figure 8(a)),
- (2) plasmonic lens (Figure 8(b)),
- (3) negative refractive index lens (Figure 8(c)),
- (4) photonic crystal lens (Figure 8(d)),
- (5) hyperlens (Figure 8(e)).

**6.1. Dielectric Lens.** A dielectric lens is a focusing device known for several centuries. It is well described in classical optical textbooks (see, e.g., [65]). The lens can provide the excellent light transmission, but its resolution is diffraction limited and for coherent light cannot be better than  $0.77\lambda/\text{NA}$ , where NA is a numerical aperture. The numerical aperture cannot exceed the refractive index  $n$  of a surrounding material. Even such resolution is hard to achieve in practice, as it requires a complex optical setup with a high numerical aperture objective; therefore, a conventional dielectric lens is not a suitable solution for nanocoupling.

Except a standard dielectric lens we should mention also two other focusing devices, namely, a Fresnel lens and a graded index (GRIN) lens. The Fresnel lens and zone plate are well described in optical textbooks [65]. The zone plate

consists of a set of concentric rings (Fresnel zones). Rings are transparent and nontransparent in the alternating order or have the  $180^\circ$  phase difference for the transmitted light. An important requirement is that the geometrical sizes of the zones impose the constructive interference conditions in the desired focal point. Being much lighter and much more compact than a bulk dielectric lens, the Fresnel lenses have worse resolution due to the diffraction at the zones' borders.

The GRIN lens was developed for photonics packaging [66]. It is called a lens even though its shape is far from being concave or convex (etymologically “lens” means to be of a double convex shape). It is usually a multilayer dielectric structure with a gradually changing refractive index. The refractive index gradient forces the wave propagating along the waveguide to refract and concentrate in a thin bottom layer, from where it is easier to launch it into a smaller waveguide. For example, a GRIN lens for silicon waveguides [67] allows for 45% coupling efficiency.

Very useful for practical purposes is a focusing optical fiber that combines mechanical flexibility of a fiber with the focusing effect of a lens. Commercial focusing fibers can provide a focal spot down to  $2\mu\text{m}$  in diameter [68]. The focusing effect of the fiber can be reached either by making a lensed output end or by the gradual index distribution within the fiber [69]. The extension of the latter approach is the nanoengineered fiber core [70] that uses complex refractive index distribution with the nanometric features to reach the desired functionalities. The disadvantage of the GRIN lens is that, being composed of dielectrics, it cannot overcome the diffraction limit.

**6.2. Plasmonic Lens.** Using plasmonic effects in metal-dielectric zone plates is quite new since fabrication of fine metallic structures has become possible only recently. The plasmons, excited in the concentric grating by an incident light wave, contribute to the energy transfer to the central ring. The wave constructive interference condition should be satisfied not only for the diffracted light waves but also for the plasmons. A comprehensive review of the plasmonic lenses can be found in [71]. An interesting property of the plasmonic Fresnel lens is that different wavelengths have different focal points. That gives opportunity to use such lenses for spectroscopy purposes.

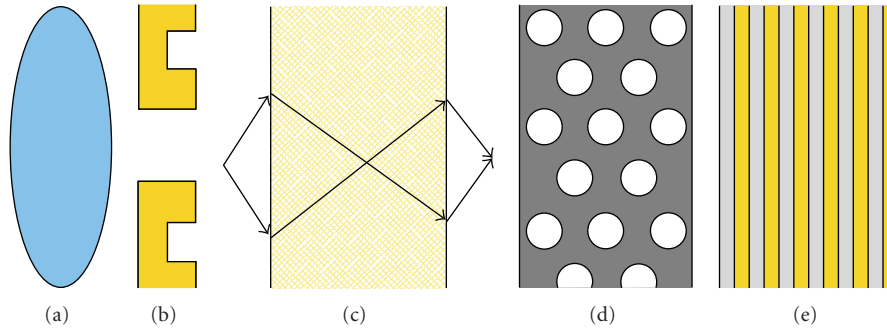


FIGURE 8: Types of lens couplers: (a) dielectric lens, (b) plasmonic lens, (c) negative index lens, (d) photonic crystal lens, (e) hyperlens.

The focusing effect of a plasmonic lens was experimentally shown in 2002 by Lezec et al. [72]. The theory and performance dependence on the geometry were discussed in the works [73–75]. A lens consisting of concentric rings of holes (the so-called nanopinhole lens) was numerically analyzed in [76]. Such lens allows for high transmission at  $\lambda = 550$  nm with focal spot of 250 nm, that is, just a bit less than a half of the wavelength. A subwavelength focusing of the  $\lambda = 532$  nm monochromatic light into the spot of  $\lambda/10$  with the transmittivity of 30% was numerically shown in [77]. Such high transmittivity is reached by adding a resonator to the entrance of the lens. Experimental investigation of the subwavelength focusing was also conducted [78]. Focusing of the visible light wave with  $\lambda = 633$  nm to a subwavelength spot with the diameter 468 nm was reported.

As can be seen from the previously mentioned results the plasmonic lens can provide the subwavelength focusing, but practically the focal spot is not much smaller comparing to a dielectric lens, while the transmittivity is lower due to the presence of metal elements.

**6.3. Negative Refractive Index Lens.** The seminal idea that a plane slab of a negative index material may focus light was mentioned by Veselago in 1968 [79]. However, the interest to the negative index material lenses exploded only at the beginning of the 21st century, when Pendry showed that a negative index slab not only focuses the propagating waves, but also enhances the evanescent waves, which contain the deep-subwavelength image details [80]. Such perfect lens works in the near-field regime and can provide the ideal image that repeats all small details of an original object. To function as a superresolution lens the negative index material should be isotropic. Some special cases of anisotropic materials without spatial dispersion may also be suitable [81].

The negative refractive index occurs as a rule in materials that simultaneously possess negative dielectric permittivity and magnetic permeability. A comprehensive overview of the negative index metamaterials can be found in [82, 83].

A negative index slab lens can be used not only for focusing and imaging but also as a coupler. The idea to use a flat negative index slab for coupling between two identical nanowaveguides was proposed by Degiron et al. [84]. By making a concave lens out of NIM, one can match two

waveguides with different cross-section. However, to be utilized for the nanocoupler construction the negative refractive index material must have bulk isotropic optical properties with small losses. The requirement for the bulk behavior means that the effective properties of the homogenized metamaterial should not depend on the slab thickness. It is usual situation that the properties of a metamaterial depend on the thickness (number of monolayer) due to the coupling between monolayers [85] with rare exceptions only [86].

In the most cases proposed metamaterials consist of planar layers, since their fabrication is based on the planar technology. That results in the optical anisotropy. To overcome such drawback several isotropic NIMs designs were proposed [87–93], but the material parameters needed to obtain the desired resonances in the optical regime can hardly be found in nature, thus limiting the application of such design to the microwave region. Moreover, the unit cell of most metamaterials is not very small comparing with the wavelength of light (usually it is in the order of  $\lambda/10 - \lambda/4$ ) that leads to spatial dispersion and hence deterioration of the effective properties introduction. So even the highest possible cubic symmetry of the unit cells and placement of unit cells in a cubic lattice do not ensure optical isotropy of negative index metamaterials [94].

The losses in a negative index metamaterial coupler are an important issue, since they reduce the coupling efficiency and decrease the spatial resolution. This is why a lot of efforts are applied at the moment to compensate the losses with gain material [95–97] or by switching for better plasmonic materials [98, 99]. Moreover, as it is shown in recent work [100], although the subwavelength resolution is possible in metamaterial-based lenses, practical focusing beyond the diffraction limit is challenging, and when designing such device one should consider “granularity, degree of isotropy and transverse size of the metamaterial lens.” Large losses, low coupling efficiency, anisotropy, and fabrication difficulties prevent a practical realization of the negative index metamaterial lens nanocoupler.

**6.4. Photonic Crystal Lens.** The negative refraction phenomenon may occur not only in negative index materials but also in photonic crystals typically at frequencies close to the bandgap edge [101]. This effect can be exploited to make a photonic crystal slab working for light focusing. For example,

in the theoretical work [102] there was reported that a photonic crystal in the so-called canalization regime provides the subwavelength focusing down to a spot of  $\lambda/6$ . To increase the transmission through a photonic crystal lens an antireflection coating can be applied [103]. Experimental realization of an *InGaAsP/InP* photonic crystal lens for  $\lambda = 1.5 \mu\text{m}$  was reported in the work [104]. They managed to obtain a focal spot of the area  $0.12\lambda^2$  that overcomes the diffraction limit. Similar results for  $\lambda = 1.55 \mu\text{m}$  in a *InP/InGaAsP/InP* photonic crystal lens were obtained in the work [105], where a focal spot of  $0.38\lambda$  size was demonstrated.

**6.5. Hyperlens.** Another solution for the subwavelength focusing involves a material with the hyperbolic dispersion, a so-called indefinite medium [106, 107] that simultaneously possesses positive and negative principle components of the permittivity tensor. This results in a hyperbolic isofrequency diagram, not circular or elliptical ones as in the case of conventional dielectric with positive permittivity. An important advantage of the hyperbolic material is that for a certain permittivity tensor it allows propagating waves with any values of the tangential component of the wavevector.

A medium with the hyperbolic dispersion is anisotropic by definition. To reach positive and negative permittivity for different directions one may use either metallic wires or a metal-dielectric multilayer stack. In case of wires the effective permittivity can be negative for electric field polarization along the wires, while for the polarization perpendicular to the wires the relevant principle value of the permittivity tensor is positive. In case of the metal-dielectric stack, the electric field polarized parallel to the metallic plates experiences negative dielectric response, while the permittivity associated with the perpendicular polarization is positive. A detailed theory of the multilayer and wire-medium hyperlens can be found in the works [108, 109].

The first theoretical work on a wire medium hyperlens [110] showed a subwavelength resolution  $\lambda/6$  for  $\lambda = 1.5 \mu\text{m}$ . In another theoretical work [109] the  $\lambda/10$  resolution was achieved in the infrared range. The same devices were successfully simulated and experimentally validated in the microwave range [111–113]. In the work [113] an impressive  $\lambda/15$  resolution was experimentally demonstrated.

Arranging metal wires in the tapering-up-like manner, not only the 1:1 image transfer but also the image magnification can be achieved. An analysis of the homogeneous medium approximation eligibility for the wire medium superlens was conducted in work [114]. In the work [115] a lens for color imaging in the visible range is proposed. The idea is to engineer the wavelength selective response introducing gaps in metallic nanowires. The experimental demonstration of a wire lens for the optical range [116] and for telecom  $\lambda = 1.55 \mu\text{m}$  has been recently shown [117]. The resolution measured with a scanning near-field optical microscope was about  $\lambda/4$ .

A flat metal-dielectric stack can transfer the subdiffraction image as a near-field lens. Using cylindrical or spherical multilayer system the image may be magnified up to above the diffraction limit. Such magnified image may be registered

with an optical microscope afterwards. So the hyperlens can serve as an addition to the standard optical microscope or photolithographic system improving the resolution below the diffraction limit. The first theoretical work [118] showed the resolution of  $\lambda/4.5$ . The hyperlens theory was described in paper [108]. The experimental realization of the lensing effect for the ultraviolet light  $\lambda = 365 \text{ nm}$ , which is a standard wavelength for the optical lithography, with the resolution less than  $\lambda/4$  was presented [119]. In theory the resolution was pushed further significantly. Ultraviolet light designs providing  $\lambda/18$  [120] and  $\lambda/60$  [121] resolution have been recently proposed.

Despite the fantastic resolution, the hyperlens typically has low transmission. Using the Fabry-Perot effect it is possible to increase the transmittivity values. For example, in the work [122] the three-layer thick hyperlens showed 50% transmission. However, the magnification of such hyperlens was very low due to the small ratio of the outer and inner radii—about 1.25. Making the thickness of the hyperlens thicker, one would lose a lot in transmission. So, when designing a hyperlens one should find a trade-off between tight focusing and high transmission.

**6.6. Summary.** An imaging device such as lens does not necessarily provide high coupling efficiency since the primary goal of imaging is focusing of light, regardless of the transmittivity. The dielectric lens can give high transmittivity (close to 100%) but the focal spot size is diffraction limited. A photonic crystal lens can indeed provide focusing at a specific frequency. However, the resolution of such lens is not much better than the diffraction limit allows. The plasmonic lens can provide a better spatial resolution with the cost of lower transmittivity. The negative index metamaterial lens is still far from the practical realization. From the resolution point of view, the hyperlens is the best. Theoretically it can provide the resolution as small as  $\lambda/60$ . However, the transmittivity through the hyperlens is not high due to the employment of a metal-dielectric multilayer stack or metallic nanowires, which hinder its coupling applicability.

## 7. Scatterer Coupler

The main idea behind the scatterer coupler is that there are single or multiple particles that first capture the radiation from the free space and then launch it into the waveguide. Based on the geometrical placement and material we singled out the following types:

- (1) antenna coupler (Figure 9(a)),
- (2) grating coupler (Figure 9(b)),
- (3) random scatterers (Figure 9(c)).

**7.1. Antenna Coupler.** According to the definition [123, 124], an antenna is a device that converts a free propagating radiation into the localized power and vice versa. For example, television antennas capture the waves propagating in air and transform them into an electrical current. In other words, an

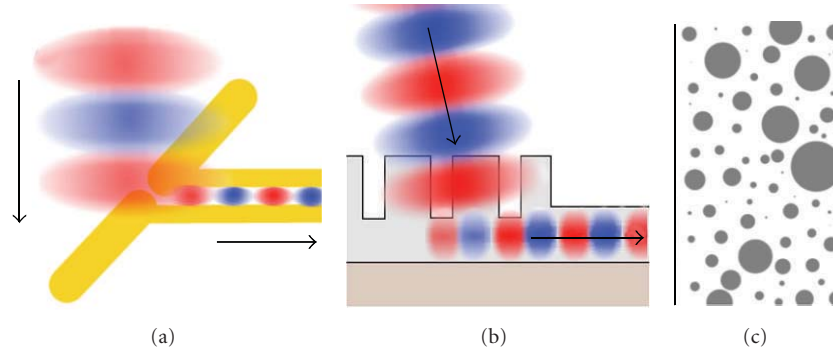


FIGURE 9: Types of scatterer couplers: (a) antenna, (b) grating, (c) random scatterers.

antenna is a coupler that matches together the impedances of free space and a waveguide. This application of antennas accounts for more than one hundred years, since Hertz, Popov, and Markoni invented the principles of the radio transmission. Now radio and microwave antennas are well-known engineering systems.

In principle, according to the definition, some nanocouplers of other types, for example, a lens coupler, can also be called antennas. In this section, however, we limit ourselves to the traditional geometrical antenna configurations, which consist of a single or multiple metallic particles, specially tuned for accepting electromagnetic radiation.

Optical nanoantennas drew the attention of many research groups [142–151]. Nanoantennas can be considered as the optical analogue of the microwave and radio antennas [142]. An incident electromagnetic wave excites charges oscillations along the metallic antenna, which are in the optical range nothing else than localized surface plasmons, and then couples to a mode of the connected waveguide.

Despite a lot of similarities, there are essential differences between radio and plasmonic antennas [152]

- (1) Metals are not such good conductors in the optical range as on the radio frequencies. Their permittivity is dispersive. It can be approximated by the Drude or more accurate Drude-Lorentz formulas [3] accounting for interband transitions in noble metals.
- (2) A typical penetrations depth is several dozens of nanometers [3], and that is very important for metallic nanostructures of comparable size.
- (3) The usual condition for the resonance of radiofrequency antennas is that the length of the antenna must be equal to the integer of a half of the wavelength. This condition is not satisfied for the optical antennas and should be corrected [145, 153, 154].

Plasmonic nanoantennas have attracted huge attention in the recent years because of their ability to concentrate light in the tiny gaps and significantly enhance light intensity [143, 144, 149, 154]. A comprehensive overview of the nanoantennas theory and applications can be found in [123, 152, 155].

Despite the fact that from the very beginning antennas served for coupling to a waveguide (transmission line), the application of an antenna for optical nanocoupling was

proposed only recently [125–127, 129–131]. The reasons for that are mainly the difficulties of ultrafine metallic structures fabrication (feature size on the order of 10–100 nm).

The advantage of the nanoantenna is that it is very compact. Moreover, the directivity of the antenna coupler can be tuned by design, thus enabling the maximal coupling efficiency at any desired angle of incidence. The first nanoantenna couplers analysis showed theoretically the coupling efficiency of 10% [125] for  $\lambda = 1.55 \mu\text{m}$  and 28% [126] for  $\lambda = 830 \text{ nm}$  for a focused Gaussian spot. Experimentally measured coupling efficiency of 15% for  $\lambda = 1.55 \mu\text{m}$  was demonstrated in the work [129]. It was shown that the coupling efficiency can be increased at least by two times by applying additional reflectors and arranging nanoantennas in a parallel or serial array [130].

**7.2. Grating Coupler.** An array of nanoantennas is closely related to the diffraction grating employment as a coupler. However, the difference is that each nanoantenna has a specific length designed to be in resonance with an incident electromagnetic wave, while in the diffraction grating each line can be very long. The lines of the diffraction grating lie on top of the waveguide and scatter light into the waveguide. It is of outmost importance that the scattered radiation from each line contributes constructively to the wave propagating in the waveguide. In other words, the role of the grating is to match the tangential wavevector component  $k_t$  of the incident wave with the waveguide propagation constant  $\beta$ . The grating with a specific period  $P$  allows light to diffract to a diffraction order  $m$  such that  $\beta = k_t + 2\pi m/P$ .

A diffraction grating is typically employed for coupling to a silicon waveguide in the vertical coupling configuration. The spot size from a single mode fiber is usually about  $10 \mu\text{m}$ . The wave should not be strictly perpendicular to the waveguide, but incident at a small angle (about 5 degrees) to provide the wavevector matching. The maximal coupling efficiency of 60–70% was reported [132, 133]. There was also claimed a high-efficiency (96%) vertical coupler based on the subwavelength grating [134]. Making the grating lines concentric and adding tapering it is possible to couple and focus light simultaneously. For example, a  $40 \mu\text{m}$  size focusing grating coupler with 25% coupling efficiency at  $\lambda = 2.75 \mu\text{m}$  was demonstrated in the work [135].



TABLE 1: Comparison of various nanocoupling approaches.

Approach	Coupling efficiency: low (<10%), medium (10–50%), high (>50%)	Size: compact (<10 $\mu\text{m}$ ) or large (>10 $\mu\text{m}$ )	Subwavelength coupling or focusing	Lateral or vertical coupling	References
4.1. Tapered dielectric	High	Both	No	Lateral	[18–25]
4.2. Tapered metal	Medium and large	Compact	Yes	Lateral	[26–39]
4.3. Tapered metamaterial	Low and medium	Compact	Yes	Lateral	[40–42]
5.1. Next to another	High	Both	Yes	Lateral	[43–53]
5.2. End-fire	High	Compact	No	Lateral	[54–60]
5.3. Resonant stub	High	Compact	Yes	Lateral	[11, 61–64]
6.1. Dielectric lens	High	Large	No	Lateral	[66, 67, 69, 70]
6.2. Plasmonic lens	Medium	Compact	Yes	Lateral	[71–78]
6.3. Negative index lens	N/a	N/a	Yes	Lateral	[79, 80, 84, 100]
6.4. Photonic crystal lens	N/a	Compact	Yes	Lateral	[101–105]
6.5. Hyperlens	Low or medium	Compact	Yes	Lateral	[107–122]
7.1. Antenna	Medium	Compact	Yes	Both	[125–131]
7.2. Grating	High	Large	No	Vertical	[132–140]
7.3. Random scatterers	Low	N/a	Yes	Both	[141]

A grating coupler can also be used for the surface plasmon polaritons waveguide excitation. The coupling efficiency up to 68% was theoretically shown [51, 136–138]. The grating can be designed to be polarization independent [139]. It can also combine the functions of a coupler and a nonlinear higher-order harmonics generator [140].

**7.3. Random Scatterers.** As we mentioned before the nanocoupler can be understood as a mode transforming device. In principle we can designate two extreme cases for mode conversion: evolution, that is, a careful adiabatic compression towards mode profile matching—this is realized by long tapered fibers—and revolution, that is, complete mode structure destruction and then construction of another mode in the same way as a new building can be built from the bricks of a ruined house. This analogy would mean introduction of a set of random scatterers. The photons coming from the first waveguide experience multiple scattering, and statistically some of them can couple to a mode of the second waveguide.

It is clear that the coupling efficiency of such random material coupler cannot be high due to the random nature of the photon scattering process. However, there was recently shown that under certain circumstances a disordered medium can work for light focusing [141].

**7.4. Summary.** The antenna nanocoupler is a natural transition of a standard microwave approach for coupling an electromagnetic wave to an optical (plasmonic) waveguide. There is a theoretical 50% limit of the coupling efficiency of the antenna systems [156] due to reradiation of the captured power back into free space. Practically, the nanoantennas

can exhibit the coupling efficiency close to the theoretical limit, being constrained only by optical losses and fabrication imperfections. Nevertheless, the main advantage of the nanoantenna coupler is that it is the most compact among all the nanocoupling solutions. Diffraction gratings are very efficient vertical coupling solutions providing the coupling efficiency up to 70%. Their disadvantage is relatively large size (more than 10  $\mu\text{m}$ ). The random scatterers have very low coupling efficiency due to stochastic scattering of light into the desired waveguide mode, so they are hardly suitable for the nanocoupling applications.

## 8. Other Solutions

In this section we included all other ideas that do not fall into the previously mentioned categories. Such coupling ideas are:

- (1) transformation optics coupler,
- (2) topology optimization designed coupler.

**8.1. Transformation Optics Coupler.** Inspired by the meta-materials possibilities of obtaining whatever permittivity and permeability values the field of transformation optics has recently emerged [157–159]. The transformation optics solves the problem of determination of the spatial permittivity and permeability distribution that provides a required wave propagation trajectory. For example, in case of invisibility cloaking engineering it is required that light rays pass around an object not interacting with it [160].

A problem of coupling can be expressed in the language of the transformation optics. To design a nanocoupler



is to determine such spatial distribution of permittivity and permeability that provides impedance matching and squeezing of the light from a thick waveguide to a thin one. In some sense the GRIN lens is also an example of the transformation optics application. Some designs for squeezing light [161] or light concentration [162, 163] were proposed.

Very often, however, the transformation optics designs require unusual values of permittivity and permeability that are not realistic even with the help of metamaterials (e.g., diverging permittivity and permeability values without losses or extremely large anisotropy).

**8.2. Topology Optimization.** Another approach to the coupler design is to select from the very beginning the realistic material properties (in the simplest case, of two materials) and to determine the spatial distribution (topology) of the materials that gives the largest coupling efficiency. With the efficient numerical algorithms one has no need to go deep into physical consideration when designing the nanocoupler. Such approach is called *topology optimization* [164]. The optimized structures usually have very weird shapes [165]. Setting some constraints on the geometrical size of the fine features one can design an efficient coupler that is reasonable for fabrication [166].

**8.3. Summary.** The transformation optics devices very often require unrealistic material properties. In contrary to the transformation optics the topology optimization starts from the realistic material properties and then finds the necessary geometry. We should admit that both of these approaches can be applied to almost any coupler in the Sections 4–7. Therefore we should better say that these are not independent physical approaches, but rather useful design methodologies.

## 9. Conclusions

In this paper we have analyzed various physical principles that can be used for coupling light from an optical fiber or free space to nanosized waveguides. The range of approaches is very broad, so we divided the subject into four classes (tapered waveguide coupler, direct coupler, lens coupler, and scatterer coupler). The most important features of each approach are summarized in Table 1.

The most compact solution for the nanocoupling is the antenna coupler. The most efficient are the tapered waveguide and the grating coupler combined with the directional coupler. The hyperlens gives a good trade-off between sub-diffraction imaging and transmission. The designs that use negative index materials are lossy and therefore can hardly be used for the nanocoupler at the moment. A discovery of new plasmonic materials with smaller losses or optical losses compensation with gain can probably make the latter approaches useful for light coupling.

We see the future of the nanocouplers mostly in their technical improvement. This includes a search for better

materials, optimization of the designs, and fabrication technologies. The previously mentioned coupling approaches can also be the building blocks of more advanced photonic devices. For example, tapering the directional slot waveguides coupler and filling the slots with a nonlinear material [167] give a new nanophotonic functionality and can be used for all-optical switching. Another direction is the transfer of the optical coupling approaches to other fields of physics, for example, to acoustics or surface waves.

## Acknowledgments

The authors acknowledge the members of the Metamaterials group at DTU Fotonik for useful discussions and the financial support from the Danish Council for Technical and Production Sciences through the projects GraTer (11-116991), NIMbus and THzCOW.

## References

- [1] D. A. B. Miller, "Optical interconnects to electronic chips," *Applied Optics*, vol. 49, no. 25, pp. F59–F70, 2010.
- [2] S. Kawata, M. Ohtsu, and M. Irie, *Nano-Optics*, vol. 84, Springer, 2002.
- [3] S. A. Maie, *Plasmonics: Fundamentals and Applications*, Springer, 2007.
- [4] S. I. Bozhevolnyi, *Plasmonic Nanoguides and Circuits*, Pan Stanford, 2008.
- [5] R. Zia, M. D. Selker, P. B. Catrysse, and M. L. Brongersma, "Geometries and materials for subwavelength surface plasmon modes," *Journal of the Optical Society of America A*, vol. 21, no. 12, pp. 2442–2446, 2004.
- [6] A. Boltasseva, T. Nikolajsen, K. Leosson, K. Kjaer, M. S. Larsen, and S. I. Bozhevolnyi, "Integrated optical components utilizing long-range surface plasmon polaritons," *Journal of Lightwave Technology*, vol. 23, no. 1, pp. 413–422, 2005.
- [7] S. I. Bozhevolnyi, "Effective-index modeling of channel plasmon polaritons," *Optics Express*, vol. 14, no. 20, pp. 9467–9476, 2006.
- [8] S. I. Bozhevolnyi, V. S. Volkov, E. Devaux, and T. W. Ebbesen, "Channel plasmon-polariton guiding by subwavelength metal grooves," *Physical Review Letters*, vol. 95, no. 4, Article ID 046802, 4 pages, 2005.
- [9] E. Moreno, S. G. Rodrigo, S. I. Bozhevolnyi, L. Martín-Moreno, and F. J. García-Vidal, "Guiding and focusing of electromagnetic fields with wedge plasmon polaritons," *Physical Review Letters*, vol. 100, no. 2, Article ID 023901, 4 pages, 2008.
- [10] L. Liu, Z. Han, and S. He, "Novel surface plasmon waveguide for high integration," *Optics Express*, vol. 13, no. 17, pp. 6645–6650, 2005.
- [11] G. Veronis and S. Fan, "Modes of subwavelength plasmonic slot waveguides," *Journal of Lightwave Technology*, vol. 25, no. 9, pp. 2511–2521, 2007.
- [12] S. A. Maier, P. G. Kik, and H. A. Atwater, "Observation of coupled plasmon-polariton modes in Au nanoparticle chain waveguides of different lengths: estimation of waveguide loss," *Applied Physics Letters*, vol. 81, no. 9, Article ID 1714, 3 pages, 2002.
- [13] M. L. Brongersma and P. G. Kik, *Surface Plasmon Nanophotonics*, vol. 131, Springer, 2007.

- [14] M. I. Stockman, "Nanoplasmonics: past, present, and glimpse into future," *Optics Express*, vol. 19, no. 22, pp. 22029–22106, 2011.
- [15] D. K. Gramotnev and S. I. Bozhevolnyi, "Plasmonics beyond the diffraction limit," *Nature Photonics*, vol. 4, no. 2, pp. 83–91, 2010.
- [16] S. W. Hell and J. Wichmann, "Breaking the diffraction resolution limit by stimulated emission: stimulated-emission-depletion fluorescence microscopy," *Optics Letters*, vol. 19, no. 11, pp. 780–782, 1994.
- [17] E. Rittweger, K. Y. Han, S. E. Irvine, C. Eggeling, and S. W. Hell, "STED microscopy reveals crystal colour centres with nanometric resolution," *Nature Photonics*, vol. 3, no. 3, pp. 144–147, 2009.
- [18] G. Brambilla, V. Finazzi, and D. J. Richardson, "Ultra-low-loss optical fiber nanotapers," *Optics Express*, vol. 12, no. 10, pp. 2258–2263, 2004.
- [19] M. Sumetsky, "How thin can a microfiber be and still guide light?" *Optics Letters*, vol. 31, no. 7, pp. 870–872, 2006.
- [20] L. Zimmermann, "State of the art and trends in silicon photonics packaging," 2011, <http://www.siliconphotonics.eu/workshop230511.slides.html>.
- [21] Q. V. Tran, S. Combri, P. Colman, and A. De Rossi, "Photonic crystal membrane waveguides with low insertion losses," *Applied Physics Letters*, vol. 95, no. 6, Article ID 061105, 3 pages, 2009.
- [22] N. Gregersen, T. R. Nielsen, J. Claudon, J. M. Gérard, and J. Mørk, "Controlling the emission profile of a nanowire with a conical taper," *Optics Letters*, vol. 33, no. 15, pp. 1693–1695, 2008.
- [23] J. Claudon, J. Bleuse, N. S. Malik et al., "A highly efficient single-photon source based on a quantum dot in a photonic nanowire," *Nature Photonics*, vol. 4, no. 3, pp. 174–177, 2010.
- [24] V. M. N. Passaro and M. la Notte, "Optimizing SOI slot waveguide fabrication tolerances and strip-slot coupling for very efficient optical sensing," *Sensors*, vol. 12, no. 3, pp. 2436–2455, 2012.
- [25] H. Zhang, J. Zhang, S. Chen et al., "CMOS-compatible fabrication of silicon-based sub-100-nm slot waveguide with efficient channel-slot coupler," *IEEE Photonics Technology Letters*, vol. 24, no. 1, pp. 10–12, 2012.
- [26] N. M. Arslanov and S. A. Moiseev, "Ultrahigh interference spatial compression of light inside the subwavelength aperture of a near-field optical probe," *Journal of the Optical Society of America A*, vol. 24, no. 3, pp. 831–838, 2007.
- [27] A. Rusina, M. Durach, K. A. Nelson, and M. I. Stockman, "Nanoconcentration of terahertz radiation in plasmonic waveguides," *Optics Express*, vol. 16, no. 23, pp. 18576–18589, 2008.
- [28] J. Liu, R. Mendis, and D. M. Mittleman, "The transition from a TEM-like mode to a plasmonic mode in parallel-plate waveguides," *Applied Physics Letters*, vol. 98, no. 23, Article ID 231113, 3 pages, 2011.
- [29] K. Iwaszczuk, A. Andryieuski, A. Lavrinenko, X.-C. Zhang, and P. U. Jepsen, "Non-invasive terahertz field imaging inside parallel plate waveguides," *Applied Physics Letters*, vol. 99, no. 7, Article ID 071113, 3 pages, 2011.
- [30] K. Iwaszczuk, A. Andryieuski, A. Lavrinenko, X.-C. Zhang, and P. U. Jepsen, "Terahertz field enhancement to the MV/cm regime in a tapered parallel plate waveguide," *Optics Express*, vol. 20, no. 8, pp. 8344–8355, 2012.
- [31] D. F. P. Pile and D. K. Gramotnev, "Adiabatic and nonadiabatic nanofocusing of plasmons by tapered gap plasmon waveguides," *Applied Physics Letters*, vol. 89, no. 4, Article ID 041111, 3 pages, 2006.
- [32] I.-Y. Park, S. Kim, J. Choi et al., "Plasmonic generation of ultrashort extreme-ultraviolet light pulses," *Nature Photonics*, vol. 5, no. 11, pp. 677–681, 2011.
- [33] S. Vedantam, H. Lee, J. Tang, J. Conway, M. Staffaroni, and E. Yablonovitch, "A plasmonic dimple lens for nanoscale focusing of light," *Nano Letters*, vol. 9, no. 10, pp. 3447–3452, 2009.
- [34] F. Renna, D. Cox, and G. Brambilla, "Efficient sub-wavelength light confinement using surface plasmon polaritons in tapered fibers," *Optics Express*, vol. 17, no. 9, pp. 7658–7663, 2009.
- [35] H. Choi, D. F. P. Pile, S. Nam, G. Bartal, and X. Zhang, "Compressing surface plasmons for nano-scale optical focusing," *Optics Express*, vol. 17, no. 9, pp. 7519–7524, 2009.
- [36] M. I. Stockman, "Nanofocusing of optical energy in tapered plasmonic waveguides," *Physical Review Letters*, vol. 93, no. 13, Article ID 137404, 4 pages, 2004.
- [37] S. A. Maier, S. R. Andrews, L. Martín-Moreno, and F. J. García-Vidal, "Terahertz surface plasmon-polariton propagation and focusing on periodically corrugated metal wires," *Physical Review Letters*, vol. 97, no. 17, Article ID 176805, 4 pages, 2006.
- [38] E. Verhagen, M. Spasenović, A. Polman, and L. Kuipers, "Nanowire plasmon excitation by adiabatic mode transformation," *Physical Review Letters*, vol. 102, no. 20, Article ID 203904, 4 pages, 2009.
- [39] X. L. Zhou, Y. Q. Fu, S. Y. Wang, A. J. Peng, and Z. H. Cai, "Funnel-shaped arrays of metal nano-cylinders for nano-focusing," *Chinese Physics Letters*, vol. 25, no. 9, pp. 3296–3299, 2008.
- [40] A. A. Govyadinov and V. A. Podolskiy, "Metamaterial photonic funnels for subdiffraction light compression and propagation," *Physical Review B*, vol. 73, no. 15, Article ID 155108, 5 pages, 2006.
- [41] S. Mühlig, C. Rockstuhl, J. Pniewski, C. R. Simovski, S. A. Tretyakov, and F. Lederer, "Three-dimensional metamaterial nanotips," *Physical Review B*, vol. 81, no. 7, Article ID 075317, 8 pages, 2010.
- [42] C. Rockstuhl, C. R. Simovski, S. A. Tretyakov, and F. Lederer, "Metamaterial nanotips," *Applied Physics Letters*, vol. 94, no. 11, Article ID 113110, 3 pages, 2009.
- [43] S. Dong, H. Ding, Y. Liu, and X. Qi, "Investigation of evanescent coupling between tapered fiber and a multimode slab waveguide," *Applied Optics*, vol. 51, no. 10, pp. C152–C157, 2012.
- [44] R. Yan, P. Pausauskie, J. Huang, and P. Yang, "Direct photonic—plasmonic coupling and routing in single nanowires," *Proceedings of the National Academy of Sciences of the United States of America*, vol. 106, no. 50, pp. 21045–21050, 2009.
- [45] Q. Li and M. Qiu, "Structurally-tolerant vertical directional coupling between metal-insulator-metal plasmonic waveguide and silicon dielectric waveguide," *Optics Express*, vol. 18, no. 15, pp. 15531–15543, 2010.
- [46] Q. Li, Y. Song, G. Zhou, Y. Su, and M. Qiu, "Asymmetric plasmonic-dielectric coupler with short coupling length, high extinction ratio, and low insertion loss," *Optics Letters*, vol. 35, no. 19, pp. 3153–3155, 2010.
- [47] C. Delacour, S. Blaize, P. Grosse et al., "Efficient directional coupling between silicon and copper plasmonic nanoslot waveguides: toward metal-oxide-silicon nanophotonics," *Nano Letters*, vol. 10, no. 8, pp. 2922–2926, 2010.
- [48] R. Wan, F. Liu, Y. Huang et al., "Excitation of short range surface plasmon polariton mode based on integrated hybrid

- coupler," *Applied Physics Letters*, vol. 97, no. 14, Article ID 141105, 3 pages, 2010.
- [49] Q. Li, S. Wang, Y. Chen, M. Yan, L. Tong, and M. Qiu, "Experimental demonstration of plasmon propagation, coupling, and splitting in silver nanowire at 1550-nm wavelength," *IEEE Journal on Selected Topics in Quantum Electronics*, vol. 17, no. 4, pp. 1107–1111, 2010.
  - [50] A. L. Pyayt, B. Wiley, Y. Xia, A. Chen, and L. Dalton, "Integration of photonic and silver nanowire plasmonic waveguides," *Nature Nanotechnology*, vol. 3, no. 11, pp. 660–665, 2008.
  - [51] Z. Wang, N. Zhu, Y. Tang, L. Wosinski, D. Dai, and S. He, "Ultracompact low-loss coupler between strip and slot waveguides," *Optics Letters*, vol. 34, no. 10, pp. 1498–1500, 2009.
  - [52] J. Gosciniaik, V. S. Volkov, S. I. Bozhevolnyi, L. Markey, S. Massenot, and A. Dereux, "Fiber-coupled dielectric-loaded plasmonic waveguides," *Optics Express*, vol. 18, no. 5, pp. 5314–5319, 2010.
  - [53] J. Tian, S. Yu, W. Yan, and M. Qiu, "Broadband high-efficiency surface-plasmon-polariton coupler with silicon-metal interface," *Applied Physics Letters*, vol. 95, no. 1, Article ID 013504, 3 pages, 2009.
  - [54] S. Y. Lee, J. Park, M. Kang, and B. Lee, "Highly efficient plasmonic interconnector based on the asymmetric junction between metal-dielectric-metal and dielectric slab waveguides," *Optics Express*, vol. 19, no. 10, pp. 9562–9574, 2011.
  - [55] Y. Song, J. Wang, Q. Li, M. Yan, and M. Qiu, "Broadband coupler between silicon waveguide and hybrid plasmonic waveguide," *Optics Express*, vol. 18, no. 12, pp. 13173–13179, 2010.
  - [56] X. W. Chen, V. Sandoghdar, and M. Agio, "Nanofocusing radially-polarized beams for high-throughput funneling of optical energy to the near field," *Optics Express*, vol. 18, no. 10, pp. 10878–10887, 2010.
  - [57] X. W. Chen, V. Sandoghdar, and M. Agio, "Highly efficient interfacing of guided plasmons and photons in nanowires," *Nano Letters*, vol. 9, no. 11, pp. 3756–3761, 2009.
  - [58] R. M. Briggs, J. Granddier, S. P. Burgos, E. Feigenbaum, and H. A. Atwater, "Efficient coupling between dielectric-loaded plasmonic and silicon photonic waveguides," *Nano Letters*, vol. 10, no. 12, pp. 4851–4857, 2010.
  - [59] Z. Han, A. Y. Elezzabi, and Van, "Experimental realization of subwavelength plasmonic slot waveguides on a silicon platform," *Optics Letters*, vol. 35, no. 4, pp. 502–504, 2010.
  - [60] D. L. MacFarlane, M. P. Christensen, K. Liu et al., "Four-port nanophotonic frustrated total internal reflection coupler," *IEEE Photonics Technology Letters*, vol. 24, no. 1, pp. 58–60, 2012.
  - [61] P. Ginzburg and M. Orenstein, "Plasmonic transmission lines: from micro to nano scale with  $\lambda/4$  impedance matching," *Optics Express*, vol. 15, no. 11, pp. 6762–6767, 2007.
  - [62] J. Liu, H. Zhao, Y. Zhang, and S. Liu, "Resonant cavity based antireflection structures for surface plasmon waveguides," *Applied Physics B*, vol. 98, no. 4, pp. 797–802, 2010.
  - [63] Ş. Kocabaş, G. Veronis, D. A. B. Miller, and S. Fan, "Modal analysis and coupling in metal-insulator-metal waveguides," *Physical Review B*, vol. 79, no. 3, Article ID 035120, 17 pages, 2009.
  - [64] A. Pannipitiya, I. D. Rukhlenko, M. Premaratne, H. T. Hattori, and G. P. Agrawal, "Improved transmission model for metal-dielectric-metal plasmonic waveguides with stub structure," *Optics Express*, vol. 18, no. 6, pp. 6191–6204, 2010.
  - [65] M. Born, E. Wolf, and A. B. Bhatia, *Principles of Optics*, vol. 10, Pergamon Pr, 1975.
  - [66] D. R. Beltrami, J. D. Love, A. Durandet et al., "Planar graded-index (GRIN) PECVD lens," *Electronics Letters*, vol. 32, no. 6, pp. 549–550, 1996.
  - [67] T. H. Loh, Q. Wang, J. Zhu et al., "Ultra-compact multilayer Si/SiO<sub>2</sub> GRIN lens mode-size converter for coupling single-mode fiber to Si-wire waveguide," *Optics Express*, vol. 18, no. 21, pp. 21519–21533, 2010.
  - [68] "OZ Optics Ltd," <http://ozoptics.com>.
  - [69] M. D. Feit and J. A. Fleck, "Light propagation in graded-index optical fibers," *Applied Optics*, vol. 17, no. 24, pp. 3990–3998, 1978.
  - [70] J. M. Nowosielski, R. Buczyński, F. Hudelist, A. J. Waddie, and M. R. Taghizadeh, "Nanostructured GRIN microlenses for Gaussian beam focusing," *Optics Communications*, vol. 283, no. 9, pp. 1938–1944, 2010.
  - [71] Y. Fu and X. Zhou, "Plasmonic lenses: a review," *Plasmonics*, vol. 5, no. 3, pp. 287–310, 2010.
  - [72] H. J. Lezec, A. Degiron, E. Devaux et al., "Beaming light from a subwavelength aperture," *Science*, vol. 297, no. 5582, pp. 820–822, 2002.
  - [73] A. G. Curto, A. Manjavacas, and F. J. G. De Abajo, "Near-field focusing with optical phase antennas," *Optics Express*, vol. 17, no. 20, pp. 17801–17811, 2009.
  - [74] D. R. Jackson, J. Chen, R. Qiang, F. Capolino, and A. A. Oliner, "The role of leaky plasmon waves in the directive beaming of light through a subwavelength aperture," *Optics Express*, vol. 16, no. 26, pp. 21271–21281, 2008.
  - [75] L. Martín-Moreno, F. J. García-Vidal, H. J. Lezec, A. Degiron, and T. W. Ebbesen, "Theory of highly directional emission from a single subwavelength aperture surrounded by surface corrugations," *Physical Review Letters*, vol. 90, no. 16, Article ID 167401, 4 pages, 2003.
  - [76] Y. Fu, C. Du, W. Zhou, and L. E. N. Lim, "Nanopinhole-based optical superlens," *Research Letters in Physics*, vol. 2008, Article ID 148505, 5 pages, 2008.
  - [77] M. Consonni, J. Hazart, G. Lronde, and A. Vial, "Nanometer scale light focusing with high cavity-enhanced output," *Journal of Applied Physics*, vol. 105, no. 8, Article ID 084308, 6 pages, 2009.
  - [78] J. Wang and W. Zhou, "Experimental investigation of focusing of gold planar plasmonic lenses," *Plasmonics*, vol. 5, no. 4, pp. 325–329, 2010.
  - [79] V. G. Veselago, "The electrodynamics of substances with simultaneously negative values of  $\epsilon$  and  $\mu$ ," *Soviet Physics Uspekhi*, vol. 10, no. 4, pp. 509–514, 1968.
  - [80] J. B. Pendry, "Negative refraction makes a perfect lens," *Physical Review Letters*, vol. 85, no. 18, pp. 3966–3969, 2000.
  - [81] N. H. Shen, S. Foteinopoulou, M. Kafesaki et al., "Compact planar far-field superlens based on anisotropic left-handed metamaterials," *Physical Review B*, vol. 80, no. 11, Article ID 115123, 9 pages, 2009.
  - [82] K. Busch, G. von Freymann, S. Linden, S. F. Mingaleev, L. Tkeshelashvili, and M. Wegener, "Periodic nanostructures for photonics," *Physics Reports*, vol. 444, no. 3–6, pp. 101–202, 2007.
  - [83] W. Cai and V. Shalaev, *Optical Metamaterials: Fundamentals and Applications*, Springer, 2009.
  - [84] A. Degiron, D. R. Smith, J. J. Mock, B. J. Justice, and J. Gollub, "Negative index and indefinite media waveguide couplers," *Applied Physics A*, vol. 87, no. 2, pp. 321–328, 2007.
  - [85] A. Andryieuski, C. Menzel, C. Rockstuhl, R. Malureanu, F. Lederer, and A. Lavrinenko, "Homogenization of resonant



- chiral metamaterials,” *Physical Review B*, vol. 82, no. 23, Article ID 235107, 7 pages, 2010.
- [86] A. Andryieuski, C. Menzel, C. Rockstuhl, R. Malureanu, and A. V. Lavrinenko, “The split cube in a cage: bulk negative-index material for infrared applications,” *Journal of Optics A*, vol. 11, no. 11, Article ID 114010, 2009.
- [87] A. K. Iyer and G. V. Eleftheriades, “A three-dimensional isotropic transmission-line metamaterial topology for free-space excitation,” *Applied Physics Letters*, vol. 92, no. 26, Article ID 261106, 3 pages, 2008.
- [88] C. Caloz and T. Itoh, *Electromagnetic Metamaterials: Transmission Line Theory and Microwave Applications: The Engineering Approach*, Wiley-IEEE Press, 2006.
- [89] T. Koschny, L. Zhang, and C. M. Soukoulis, “Isotropic three-dimensional left-handed metamaterials,” *Physical Review B*, vol. 71, no. 12, Article ID 121103, 4 pages, 2005.
- [90] V. Yannopapas and A. Moroz, “Negative refractive index metamaterials from inherently non-magnetic materials for deep infrared to terahertz frequency ranges,” *Journal of Physics Condensed Matter*, vol. 17, no. 25, pp. 3717–3734, 2005.
- [91] I. Vendik, O. Vendik, and M. Odit, “Isotropic artificial media with simultaneously negative permittivity and permeability,” *Microwave and Optical Technology Letters*, vol. 48, no. 12, pp. 2553–2556, 2006.
- [92] A. G. Kussow, A. Akyurtlu, and N. Angkawisittpan, “Optically isotropic negative index of refraction metamaterial,” *Physica Status Solidi (B)*, vol. 245, no. 5, pp. 992–997, 2008.
- [93] A. Alù and N. Engheta, “Three-dimensional nanotransmission lines at optical frequencies: a recipe for broadband negative-refraction optical metamaterials,” *Physical Review B*, vol. 75, no. 2, Article ID 024304, 20 pages, 2007.
- [94] C. Menzel, C. Rockstuhl, R. Iliew et al., “High symmetry versus optical isotropy of a negative-index metamaterial,” *Physical Review B*, vol. 81, no. 19, Article ID 195123, 6 pages, 2010.
- [95] Y. Sivan, S. Xiao, U. K. Chettiar, A. V. Kildishev, and V. M. Shalaev, “Frequency-domain simulations of a negative-index material with embedded gain,” *Optics Express*, vol. 17, no. 26, pp. 24060–24074, 2009.
- [96] A. N. Lagarkov, V. N. Kisel, and A. K. Sarychev, “Loss and gain in metamaterials,” *Journal of the Optical Society of America B*, vol. 27, no. 4, pp. 648–659, 2010.
- [97] A. Fang, T. Koschny, M. Wegener, and C. M. Soukoulis, “Self-consistent calculation of metamaterials with gain,” *Physical Review B*, vol. 79, no. 24, Article ID 241104, 4 pages, 2009.
- [98] A. Boltasseva and H. A. Atwater, “Low-loss plasmonic metamaterials,” *Science*, vol. 331, no. 6015, pp. 290–291, 2011.
- [99] P. R. West, S. Ishii, G. V. Naik, N. K. Emani, V. M. Shalaev, and A. Boltasseva, “Searching for better plasmonic materials,” *Laser and Photonics Reviews*, vol. 4, no. 6, pp. 795–808, 2010.
- [100] X.-X. Liu and A. Alù, “Limitations and potentials of metamaterial lenses,” *Journal of Nanophotonics*, vol. 5, no. 1, Article ID 053509, 2011.
- [101] M. Notomi, “Theory of light propagation in strongly modulated photonic crystals: refractionlike behavior in the vicinity of the photonic band gap,” *Physical Review B*, vol. 62, no. 16, pp. 10696–10705, 2000.
- [102] P. A. Belov, C. R. Simovski, and P. Ikonen, “Canalization of subwavelength images by electromagnetic crystals,” *Physical Review B*, vol. 71, no. 19, Article ID 193105, 4 pages, 2005.
- [103] W. Šmigaj, B. Gralak, R. Pierre, and G. Tayeb, “Antireflection gratings for a photonic-crystal flat lens,” *Optics Letters*, vol. 34, no. 22, pp. 3532–3534, 2009.
- [104] B. D. F. Casse, W. T. Lu, R. K. Banyal et al., “Imaging with sub-wavelength resolution by a generalized superlens at infrared wavelengths,” *Optics Letters*, vol. 34, no. 13, pp. 1994–1996, 2009.
- [105] M. Hofman, N. Fabre, X. Mélique, D. Lippens, and O. Vanbésien, “Defect assisted subwavelength resolution in III-V semiconductor photonic crystal flat lenses with  $n = -1$ ,” *Optics Communications*, vol. 283, no. 6, pp. 1169–1173, 2010.
- [106] D. R. Smith and D. Schurig, “Electromagnetic wave propagation in media with indefinite permittivity and permeability tensors,” *Physical Review Letters*, vol. 90, no. 7, Article ID 077405, 4 pages, 2003.
- [107] D. R. Smith, P. Kolinko, and D. Schurig, “Negative refraction in indefinite media,” *Journal of the Optical Society of America B*, vol. 21, no. 5, pp. 1032–1043, 2004.
- [108] Z. Jacob, L. V. Alekseyev, and E. Narimanov, “Semiclassical theory of the hyperlens,” *Journal of the Optical Society of America A*, vol. 24, no. 10, pp. A52–A59, 2007.
- [109] M. G. Silveirinha, P. A. Belov, and C. R. Simovski, “Sub-wavelength imaging at infrared frequencies using an array of metallic nanorods,” *Physical Review B*, vol. 75, no. 3, Article ID 035108, 12 pages, 2007.
- [110] J. Elser, R. Wangberg, V. A. Podolskiy, and E. E. Narimanov, “Nanowire metamaterials with extreme optical anisotropy,” *Applied Physics Letters*, vol. 89, no. 26, Article ID 261102, 3 pages, 2006.
- [111] P. A. Belov, P. Ikonen, C. R. Simovski, Y. Hao, and S. A. Tretyakov, “Magnification of subwavelength field distributions using a tapered array of wires operating in the canalization regime,” in *Proceedings of the IEEE International Symposium on Antennas and Propagation and USNC/URSI National Radio Science Meeting (APSURSI ’08)*, pp. 8–11, July 2008.
- [112] Y. Zhao, P. Belov, and Y. Hao, “Subwavelength internal imaging by means of a wire medium,” *Journal of Optics A*, vol. 11, no. 7, Article ID 075101, 2009.
- [113] P. A. Belov, Y. Hao, and S. Sudhakaran, “Subwavelength microwave imaging using an array of parallel conducting wires as a lens,” *Physical Review B*, vol. 73, no. 3, Article ID 033108, 4 pages, 2006.
- [114] A. Fang, T. Koschny, and C. M. Soukoulis, “Optical anisotropic metamaterials: negative refraction and focusing,” *Physical Review B*, vol. 79, no. 24, Article ID 245127, 7 pages, 2009.
- [115] S. Kawata, A. Ono, and P. Verma, “Subwavelength colour imaging with a metallic nanolens,” *Nature Photonics*, vol. 2, no. 7, pp. 438–442, 2008.
- [116] J. Yao, K. T. Tsai, Y. Wang et al., “Imaging visible light using anisotropic metamaterial slab lens,” *Optics Express*, vol. 17, no. 25, pp. 22380–22385, 2009.
- [117] B. D. F. Casse, W. T. Lu, Y. J. Huang, E. Gultepe, L. Menon, and S. Sridhar, “Super-resolution imaging using a three-dimensional metamaterials nanolens,” *Applied Physics Letters*, vol. 96, no. 2, Article ID 023114, 3 pages, 2010.
- [118] Z. Jacob, L. V. Alekseyev, and E. Narimanov, “Optical hyperlens: far-field imaging beyond the diffraction limit,” *Optics Express*, vol. 14, no. 18, pp. 8247–8256, 2006.
- [119] C. Jeppesen, R. B. Nielsen, A. Boltasseva, S. Xiao, N. A. Mortensen, and A. Kristensen, “Thin film Ag superlens

- towards lab-on-a-chip integration,” *Optics Express*, vol. 17, no. 25, pp. 22543–22552, 2009.
- [120] Y. Xiong, Z. Liu, and X. Zhang, “A simple design of flat hyperlens for lithography and imaging with half-pitch resolution down to 20 nm,” *Applied Physics Letters*, vol. 94, no. 20, Article ID 203108, 3 pages, 2009.
- [121] Q. Meng, X. Zhang, L. Cheng et al., “Deep subwavelength focusing of light by a trumpet hyperlens,” *Journal of Optics*, vol. 13, no. 7, Article ID 075102, 2011.
- [122] J. Kerbst, S. Schwaiger, A. Rottler et al., “Enhanced transmission in rolled-up hyperlenses utilizing Fabry-Pérot resonances,” *Applied Physics Letters*, vol. 99, no. 19, Article ID 191905, 3 pages, 2011.
- [123] P. Bharadwaj, B. Deutsch, and L. Novotny, “Optical antennas,” *Advances in Optics and Photonics*, vol. 1, no. 2, pp. 438–483, 2009.
- [124] C. A. Balanis, *Antenna Theory*, Wiley, New York, NY, USA, 1997.
- [125] J. Wen, S. Romanov, and U. Peschel, “Excitation of plasmonic gap waveguides by nanoantennas,” *Optics Express*, vol. 17, no. 8, pp. 5925–5932, 2009.
- [126] J. S. Huang, T. Feichtner, P. Biagioni, and B. Hecht, “Impedance matching and emission properties of nanoantennas in an optical nanocircuit,” *Nano Letters*, vol. 9, no. 5, pp. 1897–1902, 2009.
- [127] Z. Fang, Y. Lu, L. Fan, C. Lin, and X. Zhu, “Surface plasmon polariton enhancement in silver nanowire-nanoantenna structure,” *Plasmonics*, vol. 5, no. 1, pp. 57–62, 2010.
- [128] Z. Fang, L. Fan, C. Lin, D. Zhang, A. J. Meixner, and X. Zhu, “Plasmonic coupling of bow tie antennas with Ag nanowire,” *Nano Letters*, vol. 11, no. 4, pp. 1676–1680, 2011.
- [129] J. Wen, P. Banzer, A. Kriesch, D. Ploss, B. Schmauss, and U. Peschel, “Experimental cross-polarization detection of coupling far-field light to highly confined plasmonic gap modes via nanoantennas,” *Applied Physics Letters*, vol. 98, no. 10, Article ID 101109, 3 pages, 2011.
- [130] A. Andryieuski, R. Malureanu, G. Biagi, T. Holmgaard, and A. Lavrinenko, “Compact dipole nanoantenna coupler to plasmonic slot waveguide,” *Optics Letters*, vol. 37, no. 6, pp. 1124–1126, 2012.
- [131] A. Alù and N. Engheta, “Wireless at the nanoscale: optical interconnects using matched nanoantennas,” *Physical Review Letters*, vol. 104, no. 21, Article ID 213902, 4 pages, 2010.
- [132] Z. Xiao, F. Luan, T.-Y. Liow, J. Zhang, and P. Shum, “Design for broadband high-efficiency grating couplers,” *Optics Letters*, vol. 37, no. 4, pp. 530–532, 2012.
- [133] D. Vermeulen, S. Selvaraja, P. Verheyen et al., “High-efficiency fiber-to-chip grating couplers realized using an advanced CMOS-compatible Silicon-on-Insulator platform,” *Optics Express*, vol. 18, no. 17, pp. 18278–18283, 2010.
- [134] L. Zhu, V. Karagodsky, and C. Chang-Hasnain, “Novel high efficiency vertical to in-plane optical coupler,” in *High Contrast Metastructures*, vol. 8270 of *Proceedings of SPIE*, San Francisco, Calif, USA, 2012.
- [135] Z. Cheng, X. Chen, C. Y. Wong et al., “Focusing sub-wavelength grating coupler for mid-infrared suspended membrane waveguide,” *Optics Letters*, vol. 37, no. 7, pp. 1217–1219, 2012.
- [136] J. Andkjær, S. Nishiwaki, T. Nomura, and O. Sigmund, “Topology optimization of grating couplers for the efficient excitation of surface plasmons,” *Journal of the Optical Society of America B*, vol. 27, no. 9, pp. 1828–1832, 2010.
- [137] M. W. Maqsood, R. Mehfuz, and K. J. Chau, “High-throughput diffraction-assisted surface-plasmon-polariton coupling by a super-wavelength slit,” *Optics Express*, vol. 18, no. 21, pp. 21669–21677, 2010.
- [138] E. Verhagen, A. Polman, and L. Kuipers, “Nanofocusing in laterally tapered plasmonic waveguides,” *Optics Express*, vol. 16, no. 1, pp. 45–57, 2008.
- [139] X. Chen and H. K. Tsang, “Polarization-independent grating couplers for silicon-on-insulator nanophotonic waveguides,” *Optics Letters*, vol. 36, no. 6, pp. 796–798, 2011.
- [140] N. Talebi, M. Shahabadi, W. Khunsin, and R. Vogelgesang, “Plasmonic grating as a nonlinear converter-coupler,” *Optics Express*, vol. 20, no. 2, pp. 1392–1405, 2012.
- [141] I. M. Vellekoop, A. Lagendijk, and A. P. Mosk, “Exploiting disorder for perfect focusing,” *Nature Photonics*, 2010.
- [142] A. Alù and N. Engheta, “Input impedance, nanocircuit loading, and radiation tuning of optical nanoantennas,” *Physical Review Letters*, vol. 101, no. 4, Article ID 043901, 4 pages, 2008.
- [143] K. B. Crozier, A. Sundaramurthy, G. S. Kino, and C. F. Quate, “Optical antennas: resonators for local field enhancement,” *Journal of Applied Physics*, vol. 94, no. 7, Article ID 4632, 11 pages, 2003.
- [144] R. M. Bakker, A. Boltasseva, Z. Liu et al., “Near-field excitation of nanoantenna resonance,” *Optics Express*, vol. 15, no. 21, pp. 13682–13688, 2007.
- [145] L. Novotny, “Effective wavelength scaling for optical antennas,” *Physical Review Letters*, vol. 98, no. 26, Article ID 266802, 4 pages, 2007.
- [146] C. E. Talley, J. B. Jackson, C. Oubre et al., “Surface-enhanced Raman scattering from individual Au nanoparticles and nanoparticle dimer substrates,” *Nano Letters*, vol. 5, no. 8, pp. 1569–1574, 2005.
- [147] J. J. Greffet, “Nanoantennas for light emission,” *Science*, vol. 308, no. 5728, pp. 1561–1563, 2005.
- [148] M. Schnell, A. García-Etxarri, A. J. Huber, K. Crozier, J. Aizpurua, and R. Hillenbrand, “Controlling the near-field oscillations of loaded plasmonic nanoantennas,” *Nature Photonics*, vol. 3, no. 5, pp. 287–291, 2009.
- [149] J. A. Schuller, E. S. Barnard, W. Cai, Y. C. Jun, J. S. White, and M. L. Brongersma, “Plasmonics for extreme light concentration and manipulation,” *Nature Materials*, vol. 9, no. 3, pp. 193–204, 2010.
- [150] L. Novotny and N. Van Hulst, “Antennas for light,” *Nature Photonics*, vol. 5, no. 2, pp. 83–90, 2011.
- [151] M. Klemm, “Novel directional nanoantennas for single-emitter sources and wireless nano-links,” *International Journal of Optics*, vol. 2012, Article ID 348306, 7 pages, 2012.
- [152] Q. H. Park, “Optical antennas and plasmonics,” *Contemporary Physics*, vol. 50, no. 2, pp. 407–423, 2009.
- [153] E. Cubukcu and F. Capasso, “Optical nanorod antennas as dispersive one-dimensional Fabry-Pérot resonators for surface plasmons,” *Applied Physics Letters*, vol. 95, no. 20, Article ID 201101, 3 pages, 2009.
- [154] P. Mühlischlegel, H. J. Eisler, O. J. F. Martin, B. Hecht, and D. W. Pohl, “Applied physics: resonant optical antennas,” *Science*, vol. 308, no. 5728, pp. 1607–1609, 2005.
- [155] P. Biagioni and B. Hecht, “Nanoantennas for visible and infrared radiation,” *Reports on Progress in Physics*, vol. 57, no. 2, Article ID 024402, 2011.
- [156] C. Balanis, *Antenna Theory: Analysis and Design*, Wiley-Interscience, 3th edition, 2005.



- [157] A. J. Ward and J. B. Pendry, "Refraction and geometry in Maxwell's equations," *Journal of Modern Optics*, vol. 43, no. 4, pp. 773–793, 1996.
- [158] D. M. Shyroki, "Note on transformation to general curvilinear coordinates for Maxwell's curl equations (Is the magnetic field vector axial?)," <http://arxiv.org/abs/physics/0307029v2>.
- [159] U. Leonhardt and T. G. Philbin, "Chapter 2 transformation optics and the geometry of light," *Progress in Optics*, vol. 53, pp. 69–152, 2009.
- [160] J. B. Pendry, D. Schurig, and D. R. Smith, "Controlling electromagnetic fields," *Science*, vol. 312, no. 5781, pp. 1780–1782, 2006.
- [161] J. Zhang, Y. Luo, and N. A. Mortensen, "Transmission of electromagnetic waves through sub-wavelength channels," *Optics Express*, vol. 18, no. 4, pp. 3864–3870, 2010.
- [162] A. V. Kildishev and V. M. Shalaev, "Engineering space for light via transformation optics," *Optics Letters*, vol. 33, no. 1, pp. 43–45, 2008.
- [163] E. E. Narimanov and A. V. Kildishev, "Optical black hole: broadband omnidirectional light absorber," *Applied Physics Letters*, vol. 95, no. 4, Article ID 041106, 3 pages, 2009.
- [164] M. P. Bendsøe and O. Sigmund, *Topology Optimization: Theory, Methods, and Applications*, Springer, 2003.
- [165] J. S. Jensen and O. Sigmund, "Topology optimization for nano-photonics," *Laser and Photonics Reviews*, vol. 5, no. 2, pp. 308–321, 2011.
- [166] M. Pu, L. Yang, L. H. Frandsen et al., "Topology-optimized slow-light couplers for ring-shaped photonic crystal waveguide," in *Proceedings of the Conference on Optical Fiber Communication, Collocated National Fiber Optic Engineers Conference (OFC/NFOEC '10)*, San Diego, Calif, USA, March 2010.
- [167] R. Salgueiro and Y. S. Kivshar, "Nonlinear couplers with tapered plasmonic waveguides," *Optics Express*, vol. 20, no. 9, pp. 187–189, 2012.

## Research Article

# Metaoptics with Nonrelativistic Matter Waves

**T. Taillandier-Loize,<sup>1</sup> J. Baudon,<sup>1</sup> M. Hamamda,<sup>1</sup> G. Dutier,<sup>1</sup> V. Bocvarski,<sup>2</sup>  
 M. Boustimi,<sup>3</sup> F. Perales,<sup>1</sup> and M. Ducloy<sup>1</sup>**

<sup>1</sup> *Laboratoire de Physique des Lasers (CNRS-UMR 7538), Université Paris 13, 99 Av. J.B. Clément, 93430 Villetaneuse, France*

<sup>2</sup> *Atomic and Molecular Physics Group, Institute of Physics, Belgrade, Pregrevica, 11080 Zemun, Serbia*

<sup>3</sup> *Physics Department, Umm Al Qura University, P.O. Box 715, Mecca, Saudi Arabia*

Correspondence should be addressed to J. Baudon, jacques.baudon@univ-paris13.fr

Received 6 June 2012; Revised 22 August 2012; Accepted 24 August 2012

Academic Editor: Pavel A. Belov

Copyright © 2012 T. Taillandier-Loize et al. This is an open access article distributed under the Creative Commons Attribution License, which permits unrestricted use, distribution, and reproduction in any medium, provided the original work is properly cited.

The counterpart of metamaterials in light optics for nonrelativistic matter waves governed by the Schrödinger equation can be found by transiently reversing the group velocity using a so called comoving potential. Possible applications to wave-packet dynamics, atom interferometry, and atom deceleration are described.

## 1. Introduction

The genuine concept of “meta” materials for electromagnetic waves originates from the now famous Veselago’s paper published in 1967 [1]. The basic idea is that, in a material with negative electric permittivity ( $\epsilon < 0$ ) and negative magnetic permeability ( $\mu < 0$ ), Maxwell equations impose that the wave vector  $\mathbf{k}$  and the Poynting vector  $\mathbf{S}$  of a planar wave have opposite directions and, because of causality, the effective optical index is real negative:  $n = -(\epsilon\mu)^{1/2}$ . The realisation of such artificial or “meta” materials, also called left-handed materials (LHM), in a wide range of wavelengths, has been—and continues to be—the subject of considerable theoretical and experimental efforts [2–4]. Compared to an ordinary material with a positive index, a metamaterial has a similar group velocity, whereas its phase velocity is reversed. This gives rise to the negative refraction phenomenon, owing to which so-called “meta” lenses are conceivable. The concept is rather easily extended to matter waves, provided that the effective mass of the particle be zero or close to zero, as it is the case for electrons in graphene, governed by a (relativistic) Dirac equation [5].

Paradoxically the situation is much more intricate with nonrelativistic particles, as atoms having a thermal velocity (a few hundreds  $\text{ms}^{-1}$ ), the dynamics of which is governed by

the Schrödinger equation. The first obstacle is the inability of atoms to penetrate dense matter: hence a “material” should be replaced by a “medium”, namely, some external potential created in vacuum. A second difficulty comes from the fact that, in this situation, the phase velocity is an ambiguous concept since it is gauge dependent and its inversion appears to be problematic, if not meaningless. Nevertheless the key property of a metamedium lies in the opposite directions of phase and group velocities, a property which will be realised in our case by simply reversing the group velocity. Obviously, given a source of atoms, this property has necessarily a transient character since the group velocity is associated to the density of the probability flux which should finally be oriented outwards from the source. As a consequence, the external potential, assumed to depend on a single spatial coordinate ( $x$ ), must be also time dependent, of the type  $V(x, t)$ . In the following, the variation in  $x$  of this potential will be considered as being slow at the de Broglie wavelength ( $\lambda$ ) scale, allowing us to use “short wavelength approximations,” for example, WKB or iconal approximation. As shown in part 2, comoving potentials [6], of the general form

$$V(x, t) = V_0 s(t) \cos\left(2\pi \frac{x}{\Lambda}\right), \quad (1)$$

where  $V_0$  is a constant amplitude,  $s(t)$  is a normalized signal of finite duration, are able to cause the searched inversion of the group velocity and to induce a negative refraction upon the atomic trajectory [7]. The direct observation of this negative refraction on atomic trajectories implies a low velocity and/or a sufficiently high magnitude  $V_0$ , that is, in the case of a magnetic potential, a sufficiently intense magnetic field (typically a few hundreds Gauss at a velocity of a few  $\text{ms}^{-1}$ ). An atom interferometer as a Stern-Gerlach interferometer [8] is a much more sensitive tool to evidence the effect, in so far as it transforms a phase shift into a variation of intensity (part 3).

Two other consequences of the group-velocity inversion are worth to be noted: (i) primarily the negative refraction concerns the motion of a wave packet centre, but it affects also the shape of this wave packet, especially its width—which is *reduced*—, along the same general trend, namely, a transient time reversal [9]; (ii) for similar reasons, the fact that the potential is time dependent results into a nonconservation of energy and more precisely (in the case of negative refraction) into a decrease of the atom velocity. This phenomenon plays an important role in atom interferometry. It can be used to slow down atoms (part 4). As the total length of such a slower is an increasing function of the spatial period  $\Lambda$  of the potential, there is a great advantage to make use of a comoving *optical* potential for which  $\Lambda$  is of a few hundreds of nm [10].

Whilst they can give rise to similar effects (together with other specific effects), metamedia for atomic waves are basically different from metamaterials for light optics essentially because of the fundamental difference existing between the related wave equations (Schrödinger versus Maxwell or Dirac). To conclude (part 5), owing to the relative simplicity of their realisation as well as their large domain of applicability, metamedia are expected to play in the future a significant role in atom optics. Nevertheless note that a distinct approach to negative refraction for ultra-cold atoms, based upon “quantum simulators,” allows one to simulate condensed matter physics processes with cold atoms (For instance honeycomb optical lattices may be used to reproduce electron dynamics in grapheme [11, 12]. Also specific non-Abelian gauge potentials, simulated with light fields of given wave-vectors and frequencies allow one to assign a quasi-null effective mass to ultracold atoms ( $v < 1 \text{ cm/s}$ ) [13]. Thus, an adequate Klein potential barrier should induce negative refraction.) [11–13]. In the following of this paper we shall not consider this type of situations.

## 2. General Principle: Negative Index

The concept of comoving field of the form given previously, together with its generic property *to fashion the momentum ( $k$ )-dependence of the resulting phase shift*, have been introduced in 1997 [6]. Indeed it can be shown [10], using the WKB approximation, that for a field differing from zero within a given interval  $[0, \tau_1]$ , an incident plane wave  $\Psi_0(k, x, t)$  of specific momentum  $k$ , freely propagating along

the direction  $x$ , is altered by the comoving potential *via* a simple phase factor, becoming  $\Psi = \Psi_0 e^{i\varphi(k,t)}$  with

$$\begin{aligned} \varphi(k, t) = & -\hbar^{-1} \int_0^T dt' V_0 s(t') \cos\left(2\pi \frac{\hbar k}{m\Lambda} t'\right) \\ & - \hbar^{-1} V_0 s(\tau_1^-) \Theta(t - \tau_1) \cos\left(2\pi \frac{\hbar k}{m\Lambda} \tau_1\right) (t - \tau_1). \end{aligned} \quad (2)$$

In (2),  $T = \min[t, \tau_1]$ ,  $\tau_1^-$  is smaller than and arbitrarily close to  $\tau_1$ ,  $m$  is the atom mass and  $\Theta$  the Heaviside function. The second term in (2) results from the time-dependence of  $V$ , hence the nonconservation of energy. It warrants the continuity of  $\varphi$  and  $\Psi$  and their derivatives at  $t = \tau_1$ .

Let us now consider a wave packet, the momentum distribution of which,  $\rho(k)$ , is centred at  $k_0$ . Using the stationary-phase approximation, it is seen that the potential induces a spatial shift  $\delta x_c$  upon the motion  $x_{c0}(t)$  of the wave packet centre:

$$x_c = x_{c0} + \delta x_c = \frac{\hbar k_0}{m} t - [\partial_k \varphi]_{k_0} \quad (3)$$

which gives:

$$\begin{aligned} \delta x_c(t) = & -\frac{2\pi V_0}{m\Lambda} \\ & \times \left[ \int_0^T t' s(t') \sin\left(\frac{2\pi \hbar k_0 t'}{m\Lambda}\right) dt' + \tau_1 s(\tau_1) \Theta(t - \tau_1) \right. \\ & \left. \times \sin\left(\frac{2\pi \hbar k_0 \tau_1}{m\Lambda}\right) (t - \tau_1) \right]. \end{aligned} \quad (4)$$

For  $t > \tau_1$ , the integral part takes a finite limiting value, whereas the other term, linear in  $(t - \tau_1)$ , corresponds to a definite change

$$\delta v(\tau_1) = -\frac{2\pi V_0}{m\Lambda} \tau_1 s(\tau_1) \sin\left(\frac{2\pi \hbar k_0 \tau_1}{m\Lambda}\right) \quad (5)$$

of the final velocity. This change becomes negligible for comoving pulses of a sufficiently long duration, provided that the product  $\tau_1 s(\tau_1)$  tends to zero when  $\tau_1 \rightarrow \infty$ . The important point here is that, by a proper choice of  $s(t)$ , the  $k$ -dependence of  $\varphi$  can be made such that the group velocity (i.e., the velocity of the wave packet centre) be transiently negative. A trajectory initially in plane  $x, z$ , with initial velocity components  $v_{x0} > 0$ ,  $v_{z0} > 0$ , remains in this plane, exhibiting the negative refraction since  $v_x$  becomes transiently negative whereas the motion along  $z$  remains unaltered. For a sufficiently large value of  $\tau_1$ , the behaviour of the trajectory is similar to that of a ray traversing a negative-index flat plate with parallel surfaces. Figure 1(a) shows an example of such a trajectory for a metastable argon atom  $\text{Ar}^*(^3\text{P}_2)$ , spin polarized in Zeeman state  $M = +2$ , experiencing a magnetic comoving potential with  $V_0 = 2g\mu_B B_0$ ,  $g$  being the Landé factor,  $\mu_B$  the Bohr magneton and  $B_0 = 50 \text{ mT}$  the magnetic field intensity. In this example,

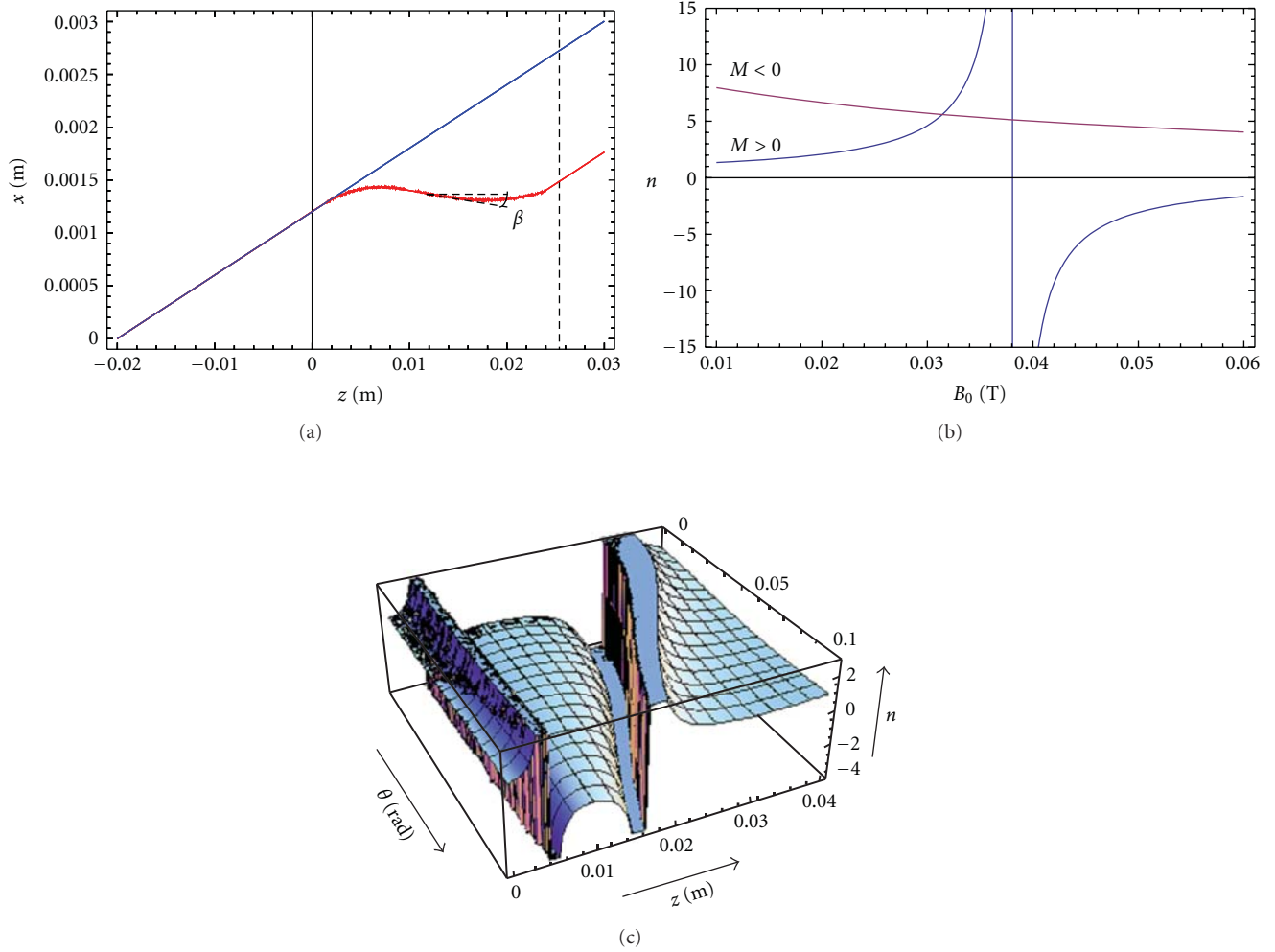


FIGURE 1: (a) Example of negative refraction of metastable argon atoms  $\text{Ar}^* (^3\text{P}_2)$  polarized in Zeeman state  $M = +2$ . Lower red curve: atomic trajectory in plane  $z, x$  under the action of a magnetic field comoving in the  $x$  direction. Blue straight line: free propagation. Parameters of the comoving field are as follows (see text): spatial period  $\Lambda = 5$  mm, magnitude of the magnetic field  $B_0 = 49$  mT, velocity components  $v_{0x} = 1.2 \text{ ms}^{-1}$ ,  $v_{0z} = 20 \text{ ms}^{-1}$ , time constant  $\tau = 0.37$  ms, duration  $\tau_1 = 4.0$  ms. The point-like source is on the  $z$  axis at  $z = -2$  cm. The angle  $\beta$  between the local velocity and the  $z$  axis (see text) is shown. (b) Effective constant index (see text, (6a)) as a function of  $B_0$ . Curve  $> 0$ : the index is negative for  $B_0 > 38$  mT. Curve  $M < 0$ : the index (multiplied by 10) is positive for any value of  $B_0$ . (c) Index  $n$  as a function of  $z$  and  $\theta$ , derived from an ensemble of trajectories similar to that shown in (a), but with different incidence angles. Positions in the  $(z, \theta)$  plane where  $n \rightarrow \pm\infty$  correspond to points where the atom velocity is parallel to the  $z$  axis. In between these two values,  $n$  is negative.

$\Lambda = 5$  mm,  $v_{x0} = 1.2 \text{ m s}^{-1}$ ,  $v_{z0} = 20 \text{ m s}^{-1}$ . The time-dependent signal is  $s(t) = \exp[-t/\tau]$  with  $\tau = 0.37$  ms and  $\tau_1 = 4$  ms. Note that, at these low velocities, the lateral shift of the trajectory is rather large (1.2 mm) in spite of the relatively modest value of the magnetic field. Other values of  $M(+1, 0, -1, -2)$  would lead to shifts proportional to  $M$ , which means that the comoving potential acts as an efficient beam splitter. More generally the comoving potential zone behaves as a multirefringent plate.

Assuming that deflection angles are small, by comparison with the light-optics counterpart under similar conditions, one can obtain an effective index  $n$  given, for  $\tau_1 \gg \tau$ , by [14]

$$n^{-1} \approx 1 - \frac{2\tau^3 M g \mu_B B_0}{m \tau_{\max}} \left( \frac{2\pi}{\Lambda} \right)^2, \quad (6a)$$

where  $\tau_{\max}$  is an estimate of the time at which  $\delta x_c$  reaches its asymptotic value ( $\tau_{\max} \approx 1.6\tau$ ). As it is seen in Figure 1(b), for  $M > 0$ , the effective index becomes negative for values of  $B_0$  larger than a critical value,  $B_c = 38$  mT in the present case. The fact that  $n \rightarrow \pm\infty$  at  $B_0 = B_c$  is not really a singularity since it simply means, in the light-optics analogy, that the ray inside the plate is normal to the plate's surfaces. On the other hand, for  $M < 0$ ,  $n$  is positive for any value of  $B_0$ , giving rise to ordinary positive refraction. The effective index given by (6a) is a constant related to a simplified trajectory consisting of three portions of straight lines. In the case of a comoving field, on the other hand, the index is  $z$ -dependent. It can be derived from the usual ray equation in an inhomogeneous medium:  $(n\mathbf{r}')' = \nabla n$ , where  $(\cdot)' = d/ds$ ,  $s$  being the curvilinear abscissa. As a function of the variable

$X(z) = (dx/dz)$ , the element of curvilinear abscissa is  $ds = dz\sqrt{1 + X^2}$ . Then the index is simply:

$$n = A \frac{\sqrt{X^2 + 1}}{X}, \quad (6b)$$

where  $A$  is a constant such that  $n(z = 0) = 1$ . This expression of  $n$  simply reflects the Snell-Descartes refraction law in a medium stratified by planes orthogonal to  $z$ , namely

$$n \sin \beta = \text{constant}, \quad (6c)$$

where  $\beta = \text{ArcTan}(v_x/v_{0z})$ . Finally, once modelled the trajectory, the index profile  $n(z)$  can be derived. Note that  $n$  has the sign of  $X$  and, as expected, it is infinite when  $X = 0$ . Actually especially at large values of  $z$ , the index profile derived from ((6b)-(6c)) depends on the angle of incidence  $\theta$  since the constant in (6c) is  $\sin \theta$ . On the other hand the medium is invariant in any translation along  $x$ . As a conclusion the metamedium is *anisotropic*. Figure 1(c) shows the 2D profile of the index  $n(z, \theta)$  derived from an ensemble of trajectories similar to that of Figure 1(a), but calculated with different incidence angles ranging from 0 to 0.1 rad.

### 3. Negative-Index Medium in a Stern-Gerlach Atom Interferometer

A standard Stern-Gerlach atom interferometer [8], also called some years later “spin-echo experiment,” in analogy to the well-known method of neutron spin-echo [15, 16], is a longitudinal polarisation interferometer in which an integrable static magnetic field profile  $B(x)$ , that is, a  $M$ -dependent magnetic potential  $W(x) = g\mu_B MB(x)$ , induces upon a planar wave (of momentum  $k$ ) describing the external motion along  $x$ , a phase shift of the form  $M\phi$ . In the following semiclassical approximation:

$$\phi \approx \frac{1}{\hbar v} \int_{-\infty}^{+\infty} W(x) dx, \quad (7)$$

where  $v \approx \hbar k/m$ . Starting from a given Zeeman state  $|M_0\rangle$  issued from a polarizer, for example, a Stern-Gerlach polarizer, one first prepares, using Majorana transitions (fast rotation of a tiny magnetic field) [17], a linear superposition of  $M$ -states

$$|\Psi_i\rangle = \sum_M a_{M_0M} |M\rangle, \quad (8)$$

where the  $a_{M_0M}$  are constant coefficients. Beyond the field profile  $B(x)$ , it becomes

$$|\Psi_f\rangle = \sum_M a_{M_0M} e^{iM\phi} |M\rangle. \quad (9)$$

Then a second Majorana zone generates the new combination (where the  $b_{MM'}$ -s are constant)

$$|\Psi_o\rangle = \sum_{M,M'} a_{M_0M} b_{MM'} e^{iM\phi} |M'\rangle. \quad (10)$$

Finally, an analyzer (similar to the polarizer) selects a specific Zeeman state  $|M_1\rangle$  and one measures the final intensity

$$I_1 = \left| \sum_M a_{M_0M} b_{MM_1} e^{iM\phi} \right|^2. \quad (11)$$

It contains interference terms in  $\phi$  which can be evidenced by varying the magnitude of the magnetic field or the velocity. In place of a static field profile, a comoving field can be used as well, as it has been demonstrated in [6] with a beam of fast ( $v = 10^4 \text{ ms}^{-1}$ ) metastable hydrogen atoms  $H^*(2^2S_{1/2}, F = 1)$ . Very recently, experiments dealing with similar questions have been realized by Sulyok et al. with a beam of neutrons at a velocity of  $2000 \text{ ms}^{-1}$ , in a so-called perfect crystal interferometer [18]. The magnetic potential they use is a sum of terms of the form  $C(x)V_k \cos(\omega_k t + \phi_k)$ , where  $C(x)$  is a square function of a definite width  $L$  and  $V_k$ ,  $\omega_k$ ,  $\phi_k$  are constants. It might seem different from our comoving potential. However it can be readily seen (by taking the Fourier transform of the spatial dependence) that this potential is actually a sum of comoving terms.

The main questions that arise about the use of comoving potentials as phase objects in an interferometer deal with similarities and differences they present with respect to static potentials. The first specificity of comoving potentials is that, because of the transient character of the effect, a treatment using wave packets is needed. Apart from the narrowing effect mentioned previously (difficult to observe except at low velocity), the first consequence of that is the *critical velocity dependence* of the interference effect, particularly when a purely sinusoidal signal of the type  $s(t) = \cos(2\pi\nu t)$  is used. Indeed in that case there exists a “resonant” atomic velocity coinciding with the field velocity  $u_{\text{com}} = v\Lambda$ . This resonant velocity can correspond to a bright fringe or a dark fringe, according to the value of the magnitude  $B_0$  of the magnetic field (which is generally low, less than 100 mG). This central fringe is surrounded by few other fringes within the envelope of the resonance. This phenomenon has been observed using a time-of-flight technique, with a single zone (see Figure 2, taken from [6]) or a double zone of comoving field.

Another manifestation, specific of comoving potentials, appears when a nonsinusoidal signal of a finite duration is used, for example,  $s(t) = e^{-t/\tau}$  for  $0 < t < \tau_1$ ,  $= 0$  elsewhere. When the value of the cut-off time  $\tau_1$  is large compared to  $\tau$ , final velocities  $v_+$  and  $v_-$  related to sublevels  $M > 0$  and  $M < 0$ , are almost equal to the initial velocity  $v_0$ . On the contrary, when  $\tau_1$  is comparable to or smaller than  $\tau$ , one gets  $v_+ < v_0$  (beginning of a negative refraction) and  $v_- > v_0$ . At  $\tau = \tau_1$ , the abscissas of the “+” and “−” wave packets are such that  $x_+ < x_-$ , then their mutual longitudinal separation  $\Delta_L x$  monotonously increases with  $t$  or  $x$ , which cancels any interference effect between them (once remixed), in other words a total loss of contrast as the distance to the detector is increased. Figure 3(a) shows  $\Delta_L x$  as a function of  $x$  in the realistic case of metastable argon atoms of initial velocity  $v_0 = 560 \text{ m s}^{-1}$ . Whilst the magnitude of  $\Delta_L x$  may seem small (a fraction of  $1 \mu\text{m}$ ), it is much larger than the wavelength ( $0.02 \text{ nm}$ ) and the effect on the interference is drastic.



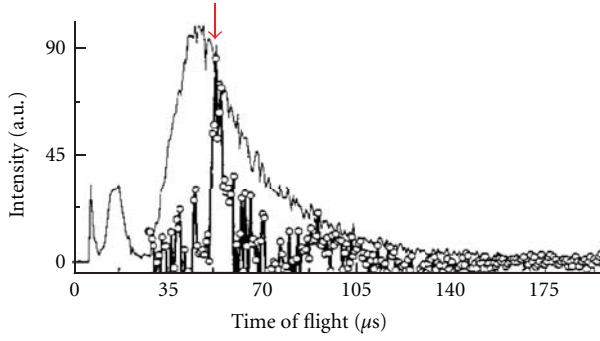


FIGURE 2: Time-of-flight spectrum over a distance of 49 cm, of hydrogen metastable atoms ( $H^*2s$ ,  $F = 1$ ) going out of a Stern-Gerlach atom interferometer (see text). The atom velocity is  $10 \text{ km s}^{-1}$ . Open circles: a comoving field is used as a phase object. The value  $B_0 = 6.5 \mu\text{T}$  is chosen to get a central bright fringe. The spatial period is  $\Lambda = 2 \text{ cm}$  and a unique frequency  $\nu = 440 \text{ kHz}$  is used. The field velocity is  $\Lambda\nu = 8.8 \text{ km s}^{-1}$ , which corresponds to the time of flight indicated by a vertical (red) arrow. Light line: time-of-flight spectrum without the interferometer.

A similar phenomenon is described in [18] for the case of neutron interferometry. In principle it is possible to recover the contrast *via* the action of a second reversed comoving pulse provided that the characteristics of this second pulse (especially its duration  $\tau_1$ ) are adjusted such that the final velocities are exactly equal to each other. Figure 3(b) shows an example of such compensation—over a distance of several centimetres—by means of a second reversed pulse similar to the first one but applied 2 ms later.

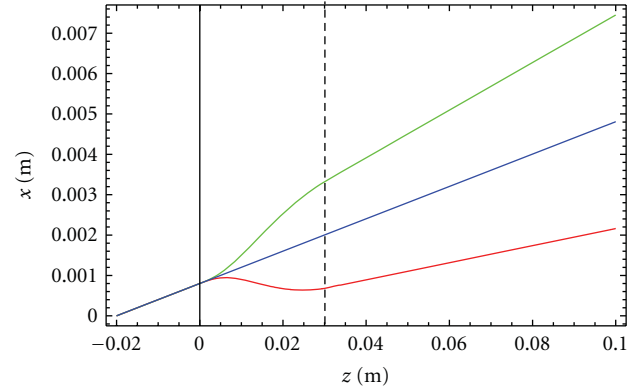
Figure 4 shows the high sensitivity of the interferometer operating with metastable argon atoms at thermal velocity ( $560 \text{ ms}^{-1}$ ). At such large velocity the inelastic effect induced by the potential pulse is small enough to make the contrast practically independent of the distance at which the detector is placed (from 0.1 to 1 m). On the other hand the contrast is reduced at “large” field magnitude, of the order of 0.1 mT or more, because of the increasing spatial separation between the two interfering wave packets and the related decrease of their overlap.

#### 4. Atom (or Molecule) Slower

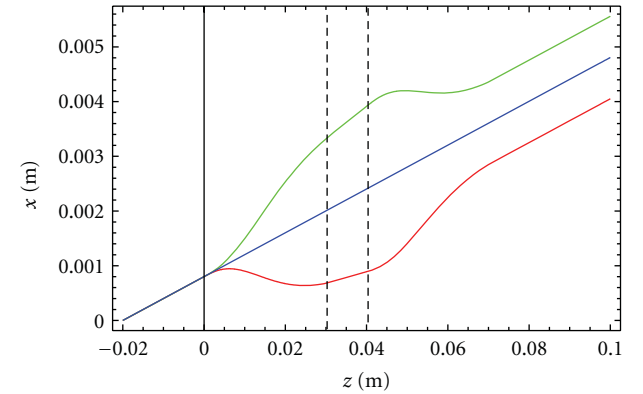
As explained in part 2, the primary effect of a potential pulse, comoving in the  $x$  direction, the sign of which is such that (for a sufficient magnitude) it results into a negative refraction, is to reduce the velocity component along  $x$  by an amount, derived from (3) (for  $t \leq \tau_1$ ):

$$\delta v(t) = \partial_t \delta x_c = -\frac{2\pi V_0}{m\Lambda} ts(t) \sin\left(\frac{2\pi \hbar k_0 t}{m\Lambda}\right). \quad (12)$$

In principle this effect can be used to slow down atoms or molecules. For neutrons this was shown to work [19]. However when the initial velocities are in the thermal range (e.g.,  $560 \text{ ms}^{-1}$  for  $\text{Ar}^*$  atoms) the predicted reduction of  $v$  is quite small, typically of a few  $\text{mm s}^{-1}$ , at least (in the case of a magnetic potential) for reasonable values of  $B_0$ , namely less than 0.1 T. As a consequence, to reduce the velocity down



(a)



(b)

FIGURE 3: (a) Effect of a *short* comoving pulse on the final velocities. The conditions are the same as in Figure 1(a) except the pulse duration,  $\tau_1 = 1.5 \text{ ms}$  (instead of 4 ms), indicated (converted in  $z$  value) by the broken vertical line. It is seen that the final velocity for atoms in state  $M = -2$  (upper green trajectory) is larger than for atoms in state  $M = +2$  (lower red trajectory). The two related wave packets fly apart from each other, cancelling the interference effect between them once they are remixed (see text). (b) Compensation of this effect by means of a second reversed comoving pulse. The first pulse is the same as in 3(a) (starting time  $t = 0$ , duration  $\tau_1 = 1.5 \text{ ms}$ ,  $B_0 = 49 \text{ mT}$ ). The second pulse starts at  $t = 2.0 \text{ ms}$  (second vertical broken line), its duration is also 1.5 ms and its amplitude is  $B_0 = 49 \text{ mT}$ . Resulting trajectories are shown as in (a). Final velocities become equal to the initial velocity.

to almost zero, a large number of successive pulses is needed. This is made possible by the fact that, immediately after the end of a pulse of duration  $\tau_1$  the velocity is practically equal to the reduced velocity obtained at time  $\tau_1$ . Then, when (after a short blank) the next pulse is applied, this latter velocity becomes the initial velocity, which is in turn reduced, and so forth. The best choice for the pulse duration  $\tau_1$  is such that  $|\delta v(\tau_1)|$  derived from (5) takes its first maximum value. For a signal of the form  $s(t) = \exp(-t/\tau)$  [6], there exists an optimum value of the time constant  $\tau$  leading to an absolute maximum of  $|\delta v(\tau_1)|$ . For  $v = 20 \text{ ms}^{-1}$ , the best values are obtained for  $\tau = 63.3 \mu\text{s}$  and  $\tau_1 = 62.6 \mu\text{s}$ . Actually they are almost equal to each other and their dependence on  $v$  is such that the product of the optimum value of  $\tau_1$  by  $v$  is a constant.

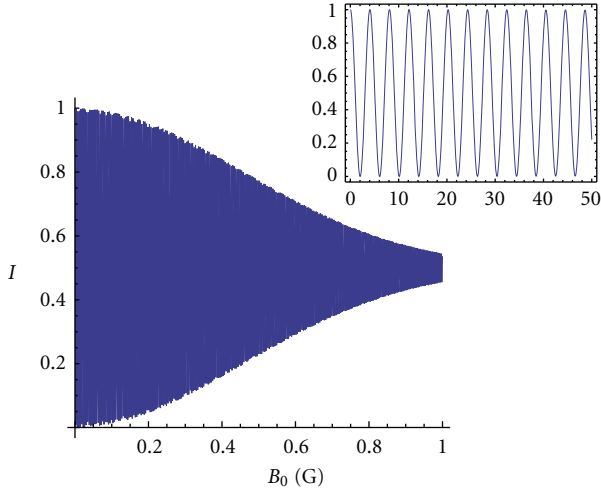


FIGURE 4: Calculated interference pattern of  $\text{Ar}^*(^3\text{P}_2)$  atoms passing through a Stern-Gerlach interferometer at  $560 \text{ ms}^{-1}$ . The phase object is a comoving potential pulse similar to that considered in Figure 1(a), except for the magnitude  $B_0$  of the field which is now the variable parameter. About 260 fringes are present within the interval  $[0, 0.1 \text{ mT} = 1 \text{ Gauss}]$  (see the inset for a zoom over an interval of  $5 \mu\text{T} = 50 \text{ milliGauss}$ ). The contrast decreases together with the overlap of the interfering wave packets (see text).

This means that the atomic path covered through successive pulses is almost a constant.

The present method bears some similarities with the so-called “adiabatic slowing” [20, 21]. This latter method has been applied to a wide variety of species, such as hydrogen atoms, polar and non polar molecules [22], Rydberg atoms and Rydberg molecules [23–25]. Low final velocities (a few  $10 \text{ ms}^{-1}$ ) are accessible, but at the price of rather strong fields (e.g.,  $B_0 = 5.2 \text{ T}$  in [23–25]). Here, the nature of the force is quite different, since it derives from a special potential depending on both space and time. In principle the method is applicable to the same species, with the advantage that it uses much lower fields.

As shown in [10] an atom slower using magnetic potential pulses ( $B_0 = 80 \text{ mT}$ ,  $\Lambda = 5 \text{ mm}$ ) is able to reduce the velocity of metastable argon atoms from  $560 \text{ m s}^{-1}$  to almost zero over a distance of  $2.2 \text{ m}$ , comparable to the total length of a standard Zeeman slower [26]. For a given magnitude of the potential, the length is governed by the spatial period  $\Lambda$ . In a simple magnetic version, it is almost impossible to reduce it below  $1 \text{ mm}$ , whereas the use of a dipolar *optical* potential obtained in a off-resonance standing wave provides us with a huge reduction of the period, which is half the optical wavelength  $\Lambda = \lambda_{\text{opt}}/2$  ( $\approx 0.4 \mu\text{m}$  in the case of metastable argon atoms). Far from resonance the general form of such a potential is [27]:

$$V(x, t) \approx \frac{\hbar\Omega^2}{\delta\omega} s(t) \cos^2\left(2\pi \frac{x}{\lambda_{\text{opt}}}\right), \quad (13)$$

where  $\Omega$  is the Rabi frequency and  $\delta\omega$  the detuning. To operate “far from resonance” (to avoid any spontaneous emission), the difference between the laser frequency and the

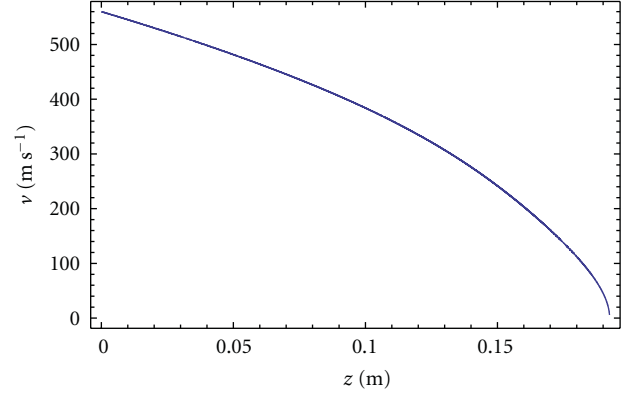


FIGURE 5: Calculated evolution of the velocity  $v$  along the slowing process using optical comoving pulses (see text), as a function of the abscissa  $z$ . An almost complete stopping is achieved at  $z = 19 \text{ cm}$ .

two resonances appearing in the standing wave, Doppler-shifted by  $\Delta\omega = \pm k_{\text{opt}}v$ , must be large compared to the power-broadened line width  $\gamma' = (1 + \Sigma)^{1/2}\gamma$ , where  $\gamma$  is the natural line width and  $\Sigma$  the saturation parameter. To get a magnitude of the potential sufficiently high to achieve the complete slowing over a distance shorter than say,  $20 \text{ cm}$ , using a reasonable laser power (e.g.,  $32 \text{ mW mm}^{-2}$ ), a moderately large (negative) detuning should be chosen, such as  $\delta\omega = -2\pi 3.45 \times 10^9 \text{ rad/s}$  ( $3.45 \text{ GHz}$ ). This leads to a ratio  $\delta\omega/\gamma' = 12.49$ , large compared to 1. As the velocity  $v$  is lowered,  $\Delta\omega$  decreases, tending to zero as  $v \rightarrow 0$ . Then either the detuning is kept constant and the condition  $R \gg 1$  is better and better verified, or  $\delta\omega$  is kept equal to  $5\Delta\omega(v)$ , allowing us to reduce the intensity (as  $v$ ) as well as  $\gamma'$  (as  $v^{1/2}$ ), but then the ratio  $R$  decreases as  $v^{1/2}$ , which implies a lower limit for  $v$  ( $R = 1$  at  $v = 3.59 \text{ m/s}$ ). As before a series of many pulses separated from each other by small blanks is applied, each of them (numbered  $n$ ) providing a small decrease  $|\delta v|$  of the velocity (a few  $\text{mm/s}$ ). The duration  $\tau_1(n)$  of each pulse is adjusted in such a way that the first maximum value of  $|\delta v|$  is reached at the end of the pulse. As previously the path  $v\tau_1$  covered by the atom during successive pulses is roughly a constant ( $\approx 0.12 \mu\text{m}$ ). Figure 5 shows how the velocity  $v$  decreases down to almost zero (with the restriction mentioned before) as a function of  $z$ . The total number of applied pulses is large (about  $2 \cdot 10^6$ ) but the total length is now  $19.2 \text{ cm}$ . Note that the method does not imply any permanent magnetic moment of the atom and is applicable for instance to  $\text{Ar}^*(^3\text{P}_0)$  metastable atoms.

In addition to the advantages of its short length and the absence of any random spreading of the velocity (at least if the spontaneous emission is negligible), the present decelerator is interesting from the point of view of the atomic density in the phase space. Indeed an important characteristic of comoving fields is their effect on the longitudinal spatial width of the atomic wave-packet. As mentioned previously [9], comoving potentials are able to transiently narrow wave packets, compensating for the free-propagation natural spreading. In the present case this effect

is very small at the beginning of the deceleration process but becomes more and more important as the velocity decreases. As a result the wave packet width  $\delta x$  progressively deviates from the free-propagation width  $\delta x_0(t)$  to rejoin its initial value  $\delta x_0(0)$ . On the other hand it can be verified, using the Wigner function, that the width  $\delta k$  of the momentum distribution remains unchanged, the reason being that the effect of the potential is a pure real phase shift. Consequently the density  $(\delta k \delta x)^{-1}$  in the phase space  $(x, k_x)$ , instead of continuously decreasing, recovers its initial value at the end of the slowing process.

## 5. Conclusion

In this paper comoving fields have been introduced in view of realizing negative-index media for matter waves in the nonrelativistic regime. Because of the fundamental difference between Schrödinger and Maxwell (or Dirac) equations, especially for what concerns the phase velocity, a method quite different from those used in light optics or ultrarelativistic particle optics is needed. The aim of our method is the transient inversion of the group velocity. Phenomena similar to those observed in metamaterials, as the negative refraction, metalens, etc.) are expected. Other properties are specific of our “meta-media.” In particular, the evolution of the wave-packet spatial width exhibits unusual features, as a transient narrowing, accompanying the negative refraction and related to time reversal, and also a velocity change in the case of short comoving potential pulses because of the nonconservation of energy.

All these effects, on atom trajectories or wave-packet width evolution, are directly observable provided that the atomic velocities are low, typically of a few  $\text{ms}^{-1}$ . At higher velocity, like a few hundreds of  $\text{ms}^{-1}$ , more sensitive techniques are necessary. Atom interferometers in general and Stern-Gerlach interferometers in particular, offer such sensitivity. We have shown that observable optical-index effects appear with magnetic fields as small as a few  $\mu\text{T}$ .

We have proposed an approach to atom beam deceleration based on dispersive optical forces. Atom stopping should be almost achieved on short distances using a moderate laser power, for example, less than  $50 \text{ mW/mm}^2$ . The absence of spontaneous emission processes should allow preservation of the transverse coherence properties of the initial beam. The technique is especially applicable to narrow supersonic beams, like metastable rare-gas atom beams, and it is able to provide us with ultra-low-velocity beams for coherent atom optics and atomic interferometry. It is also a promising technique applicable to slowing down not solely diamagnetic atoms (such as metastable argon atoms in the  $^3\text{P}_0$  state) but also molecules since any optical pumping toward molecular levels other than those interacting with light is absent. Slowing and trapping of molecules is a subject of a particular importance in the investigation of cold collisions (determination of intermolecular potentials at large distances, resonances of various kinds).

## Acknowledgments

The authors from Laboratoire de Physique des Lasers acknowledge the Institut Francilien de Recherche sur les Atomes Froids (IFRAF) for support.

## References

- [1] V. G. Veselago, “The electrodynamics of substances with simultaneously negative values of epsilon and  $\mu$ ,” *Soviet Physics Uspekhi*, vol. 10, no. 4, pp. 509–514, 1968.
- [2] J. Pendry, “Negative refraction makes a perfect lens,” *Physical Review Letters*, vol. 85, no. 18, pp. 3966–3969, 2000.
- [3] C. Foteinopoulou, E. N. Economou, and C. M. Soukoulis, “Refraction in media with a negative refractive index,” *Physical Review Letters*, vol. 90, Article ID 107401, 4 pages, 2003.
- [4] A. Sambale and D.-G. Welsch, “van der Waals interaction and spontaneous decay of an excited atom in a superlens-type geometry,” *Physical Review A*, vol. 78, Article ID 053828, 10 pages, 2008.
- [5] V. V. Klimov, J. Baudon, and M. Ducloy, “Comparative focusing of Maxwell and Dirac fields by negative-refraction half-space,” *Europhysics Letters*, vol. 94, no. 2, Article ID 20006, 2011.
- [6] R. Mathevet, K. Brodsky, B. J. Lawson-Daku, C. Miniatura, J. Robert, and J. Baudon, “Atomic interferences in a comoving magnetic field,” *Physical Review A*, vol. 56, no. 4, pp. 2954–2958, 1997.
- [7] J. Baudon, M. Hamamda, J. Grucker et al., “Negative-index media for matter-wave optics,” *Physical Review Letters*, vol. 102, no. 14, Article ID 140403, 2009.
- [8] C. Miniatura, J. Robert, O. Gorciceix et al., “Atomic interferences and the topological phase,” *Physical Review Letters*, vol. 69, no. 2, pp. 261–264, 1992.
- [9] M. Hamamda, F. Perales, G. Dutier et al., “Time reversal in matter-wave optics,” *European Physical Journal D*, vol. 61, no. 2, pp. 321–325, 2011.
- [10] M. Hamamda, M. Boustimi, F. Correia et al., “Atom slowing via dispersive optical interactions,” *Physical Review A*, vol. 85, no. 2, Article ID 023417, 5 pages, 2012.
- [11] S. L. Zhu, B. Wang, and L. M. Duan, “Simulation and detection of Dirac fermions with cold atoms in an optical lattice,” *Physical Review Letters*, vol. 98, no. 26, Article ID 260402, 4 pages, 2007.
- [12] K. L. Lee, B. Grémaud, R. Han, B. G. Englert, and C. Miniatura, “Ultracold fermions in a graphene-type optical lattice,” *Physical Review A*, vol. 80, no. 4, Article ID 043411, 2009.
- [13] G. Juzeliunas, J. Ruseckas, M. Lindberg, L. Santos, and P. Öhberg, “Quasirelativistic behavior of cold atoms in light fields,” *Physical Review A*, vol. 77, no. 1, Article ID 011802, 4 pages, 2008.
- [14] M. Hamamda, PhD thesis, University Paris 13.
- [15] F. Mezei, “Neutron spin echo: a new concept in polarized thermal neutron techniques,” *Physik*, vol. 255, no. 2, pp. 146–160, 1972.
- [16] M. De Kieviet, D. Dubbers, Ch. Schmidt, D. Scholz, and U. Spinola, “ $^3\text{He}$  spin echo: new atomic beam technique for probing phenomena in the new range,” *Physical Review Letters*, vol. 75, no. 10, pp. 1919–1922, 1995.
- [17] E. Majorana, “Atomi orientati in campo magnetico variabile,” *Nuovo Cimento*, vol. 9, no. 2, pp. 43–50, 1932.

- [18] G. Sulyok, H. Lemmel, and H. Rauch, "Neutrons in a time-dependent magnetic field: photon exchange and decoherence modeling," *Physical Review A*, vol. 85, no. 3, Article ID 033624, 7 pages, 2012.
- [19] L. Niel and H. Rauch, "Acceleration, deceleration and monochromatization of neutrons in time dependent magnetic fields," *Zeitschrift für Physik B*, vol. 74, no. 1, pp. 133–139, 1989.
- [20] H. L. Bethlem, F. M. H. Crompvoets, R. T. Jongma, S. Y. T. Van de Meerakker, and G. Meijer, "Deceleration and trapping of ammonia using time-varying electric fields," *Physical Review A*, vol. 65, no. 5, Article ID 053416, 20 pages, 2002.
- [21] H. L. Bethlem, G. Berden, and G. Meijer, "Decelerating neutral dipolar molecules," *Physical Review Letters*, vol. 83, no. 8, pp. 1558–1561, 1999.
- [22] E. Narevicius, A. Libson, C. G. Parthey et al., "Stopping supersonic beams with a series of pulsed electromagnetic coils: an atomic coilgun," *Physical Review Letters*, vol. 100, no. 9, Article ID 093003, 2008.
- [23] Y. Yamakita, S. R. Procter, A. L. Goodgame, T. P. Softley, and F. Merkt, "Deflection and deceleration of hydrogen Rydberg molecules in inhomogeneous electric fields," *Journal of Chemical Physics*, vol. 121, no. 3, p. 1419, 2004.
- [24] E. Vliegen, H. J. Wörner, T. P. Softley, and F. Merkt, "Non-hydrogenic effects in the deceleration of Rydberg atoms in inhomogeneous electric fields," *Physical Review Letters*, vol. 92, no. 3, Article ID 033005, 4 pages, 2004.
- [25] N. Vanhaecke, D. Comparat, and P. Pillet, "Rydberg decelerator using a travelling electric-field gradient," *Journal of Physics B*, vol. 38, no. 2, p. S409, 2005.
- [26] W. D. Phillips and H. J. Metcalf, "Laser deceleration of an atomic beam," *Physical Review Letters*, vol. 48, no. 9, pp. 596–599, 1982.
- [27] H. J. Metcalf and P. van der Straten, *Optical Cooling and Trapping*, Springer, New York, NY, USA, 2001.

## Research Article

# Homogeneous Hyperbolic Systems for Terahertz and Far-Infrared Frequencies

Leonid V. Alekseyev,<sup>1</sup> Viktor A. Podolskiy,<sup>2,3</sup> and Evgenii E. Narimanov<sup>1</sup>

<sup>1</sup>Electrical and Computer Engineering Department, Purdue University, West Lafayette, IN 47907, USA

<sup>2</sup>Department of Physics, Oregon State University, Corvallis, OR 97331, USA

<sup>3</sup>Department of Physics and Applied Physics, University of Massachusetts Lowell, Lowell, MA 01854, USA

Correspondence should be addressed to Evgenii E. Narimanov, [evgenii@purdue.edu](mailto:evgenii@purdue.edu)

Received 11 June 2012; Accepted 3 August 2012

Academic Editor: Pavel A. Belov

Copyright © 2012 Leonid V. Alekseyev et al. This is an open access article distributed under the Creative Commons Attribution License, which permits unrestricted use, distribution, and reproduction in any medium, provided the original work is properly cited.

We demonstrate that homogeneous naturally-occurring materials can form hyperbolic media, and can be used for nonmagnetic negative refractive index systems. We present specific realizations of the proposed approach for the THz and far-IR frequencies. The proposed structures operate away from resonance, thereby promising the capacity for low-loss devices.

Following the initial proposal by Veselago in 1968 [1], negative refraction materials spent over 30 years as a forlorn curiosity before being resurrected with renewed interest from both theoretical and experimental groups. Within the last decade it was realized that these materials (known also as left-handed materials), along with a broader classes of exotic media (known as epsilon near-zero materials, hyperbolic materials, etc.) possess unusual properties, some of which were not recognized at the time of their conceptions [2]. These properties include resonant enhancement of evanescent fields, strong suppression of diffraction, unusual modification to optical density of states, potentially enabling near-perfect imaging below the diffraction limit, and leading to a new class of optical devices [3], as well as nontrivial behavior in the nonlinear regime [4]. Despite initial controversy over the realizability of negative index materials (NIMs), successful proof of principle demonstrations have been accomplished [3, 5–8].

Existing designs for left-handed materials rely on achieving overlapping dipolar and magnetic resonances in sub-wavelength composites (metamaterials) [9, 10], or using photonic crystals near the bandgap [3, 11]. Both of these approaches necessitate complicated 3D patterning of the medium with microstructured periodic arrays. Fabrication of such structures presents significant challenges even for

GHz applications, while manufacturing metamaterials for higher frequencies becomes harder still [12]. Furthermore, near-resonant operational losses impose severe limitations on the imaging resolution [13].

As an alternative to periodic systems, a waveguide-based implementation of a NIM was proposed [14], which obviates the need for negative magnetic permeability and does not require periodic patterning. This approach circumvents major manufacturing obstacles to achieving NIM behavior at terahertz or optical frequencies, and simultaneously opens a new avenue in imaging, sensing, and light emission applications [15, 16].

To achieve this behavior, the waveguide material must possess characteristics of a uniaxial medium with a significant anisotropy. Furthermore, this anisotropy must ensure that  $\epsilon_x$  (the component of  $\epsilon$  transverse to the planar waveguide) is negative, while  $\epsilon_{\parallel} \equiv \epsilon_y (= \epsilon_z)$  (in-plane component) remains positive. TM modes in such waveguide undergo negative refraction in the waveguide plane, and propagate with negative phase velocity [14]. The materials with extremely strong anisotropy, hyperbolic materials, have since become a very active research area, enabling far-field imaging and focusing with subdiffraction resolution, broadband negative refraction, and superb control over light emission [17–22].



One of the key aspects in designing such a hyperbolic system is selecting the material for with strong underlying anisotropy. Several options have been proposed for the core material, in particular, nanostructured composites in a dielectric host and quantum well structures [14]. While being within the grasp of existing technology [23–25], the fabrication of such systems remains highly challenging.

In this work we present an alternative approach to hyperbolic media for THz and far-infrared domains based on naturally occurring materials with large dielectric anisotropy. In particular, we discuss the possibility of negative refraction in a system at approximately 20  $\mu\text{m}$ , 58  $\mu\text{m}$ , and 255  $\mu\text{m}$  using, respectively, sapphire, bismuth, or triglycine sulfate in the waveguide core. Similar results were recently demonstrated at UV frequencies in graphite [26]. We focus on monocrystalline bismuth as an attractive option for manufacturing the NIM waveguide core thanks to its large anisotropy and availability of samples with high purity. We illustrate the perspectives of natural hyperbolic metamaterials on example of negative refraction in planar waveguide geometry.

In a planar waveguide with anisotropic dielectric core the wave vector components  $k_z$  and  $k_y$  are governed by the dispersion relation

$$k_z^2 + k_y^2 = \epsilon \nu \frac{\omega^2}{c^2}, \quad (1)$$

with  $\nu = (1 - \kappa^2 c^2 / \epsilon_{\parallel} \omega^2)$ , where  $\omega$  is the frequency of light,  $\epsilon = \epsilon_x(\epsilon_{\parallel})$  for the TM(TE) modes,  $\kappa$  is the transverse mode parameter, and  $k_z$  and  $k_y$  lie in the waveguide plane. For perfectly conducting waveguide walls (a good approximation for silver and other metals at THz and far-IR frequencies [27]),  $\kappa = m\pi/d$ , where  $m$  is an integer and  $d$  is the thickness of the waveguide [14]. The effective refractive index for propagating waveguide modes in this system is given by  $n_{\text{eff}}^2 = \epsilon \nu$ . To support propagating modes,  $\epsilon$  and  $\nu$  must have the same sign. The case  $\epsilon > 0$ ,  $\nu > 0$  is typically realized in an isotropic planar waveguide operating above cut-off. However, in the case  $\epsilon < 0$ ,  $\nu < 0$  negative refraction occurs [14], with refractive index given by

$$n_{\text{eff}} = -\sqrt{\epsilon_x \nu}. \quad (2)$$

Note that if  $\kappa$  is regarded as the transverse wave vector component, (1) can be rewritten as a hyperbolic dispersion relation  $k_{\perp}^2 / \epsilon_{\parallel} - k_{\parallel}^2 / |\epsilon_x| = \omega^2 / c^2$ , identified in [28] with the onset of negative refraction.

As follows from the definition of  $\nu$ , the propagation with negative phase velocity occurs only for TM modes when  $\epsilon_{\parallel} > 0$ ,  $\epsilon_x < 0$ . This behavior is observed in a number of materials where structural anisotropy strongly affects the dielectric response.

One example of such materials is triglycine sulfate (TGS), a compound widely used in fabricating infrared photodetectors. Spectroscopic studies of the crystal at low temperature have shown that phonon modes polarized parallel to the crystal's monoclinic  $C_2$ -axis significantly differ in frequency from phonons transverse to the axis. This results in a large anisotropy in the dielectric tensor along these directions. In particular, dielectric response for the field polarized *along*

the  $C_2$ -axis features a resonance at 268  $\mu\text{m}$ , which is absent if the incident field is polarized *transverse* to the  $C_2$ -axis [29]. Dielectric function  $\epsilon_x$  in the vicinity of this resonance can be fitted with the Lorentz-Drude model [30], while  $\epsilon_{\parallel}$  in this region can be taken approximately constant [29, 31]. Lorentz-Drude model parameters from [30] were used to construct Figure 1(a). As is evident from the figure,  $\epsilon_x < 0$ , while  $\epsilon_{\parallel} > 0$  in the region  $250 \leq \lambda \leq 268 \mu\text{m}$ . Furthermore, the imaginary part of  $\epsilon$  becomes small away from the resonance, minimizing absorption. A TGS-filled waveguide with  $C_2$ -axis oriented perpendicular to the waveguide plane would support negative index propagation, while suffering from minimal propagation losses ( $\text{Im}[\epsilon] \sim 10^{-3}$  at 250  $\mu\text{m}$ ).

Whereas the phonon anisotropy of TGS exists in the low-THz domain, for other materials, it may occur in a different spectral band. In particular, the strong anisotropy of the dielectric response of sapphire ( $\text{Al}_2\text{O}_3$ ) is also due to excitation of different phonon modes (polarized either parallel or perpendicular to the  $c$ -axis of the rhombohedral structure), but occurs around 20  $\mu\text{m}$ . Figure 1(b) shows experimentally determined [32]  $\epsilon_{\parallel}$  and  $\epsilon_x$  as functions of frequency. As with TGS, a region of  $\epsilon_x < 0$ ,  $\epsilon_{\parallel} > 0$  is evident in the experimental data. This potentially enables a sapphire-based waveguide NIM (with the  $c$ -axis of sapphire core perpendicular to the waveguide plane). Note that the minimum of the material absorption occurs in the frequency range of interest.

Anisotropic phonon excitations are not the only mechanism that can lead to strong dielectric anisotropy. Bismuth, a Group V semimetal with rhombohedral lattice and trigonal symmetry, exhibits such anisotropy due to a substantial difference in its electron effective masses along different directions in the crystal.

In the frequency region of interest, the spectral dependence of the electric permittivity of Bismuth can be adequately described by the Drude model,

$$\epsilon = \epsilon_L \left( 1 - \frac{\omega_{\text{pl}}^2}{\omega^2 + i\omega\tau^{-1}} \right), \quad (3)$$

with  $\epsilon_L$  the lattice permittivity,  $\omega_{\text{pl}} = Ne^2/\epsilon_L m_{\text{eff}}$  the plasma frequency, and  $\tau$  the relaxation time. These parameters are known from interferometric and reflectance studies of Bi samples. In particular, plasma frequency of pure Bismuth at 4 K was measured to be 158  $\text{cm}^{-1}$  for the incident  $E$ -field polarized perpendicular to the trigonal axis, and 186  $\text{cm}^{-1}$  for the field polarized parallel to the axis [33]. These values are in agreement with other experiments [34, 35]. The lattice dielectric constant  $\epsilon_L$  for the field perpendicular to the trigonal axis was found to be  $110 \pm 10$  [35], in reasonable agreement with [34]. For polarization parallel to the trigonal axis,  $\epsilon_L = 76$  [36].

There can be substantial variation in the relaxation time  $\tau$  depending on the purity of the sample. We take  $\tau = 0.1 \text{ ns}$  [35], however, this is a conservative estimate; for low temperatures, relaxation times over an order of magnitude greater have been reported as far back as 1975 [36]. Even with  $\tau = 0.1 \text{ ns}$ , the typical ratio of imaginary and real parts of the dielectric function in Bi is on the order of 0.1% in

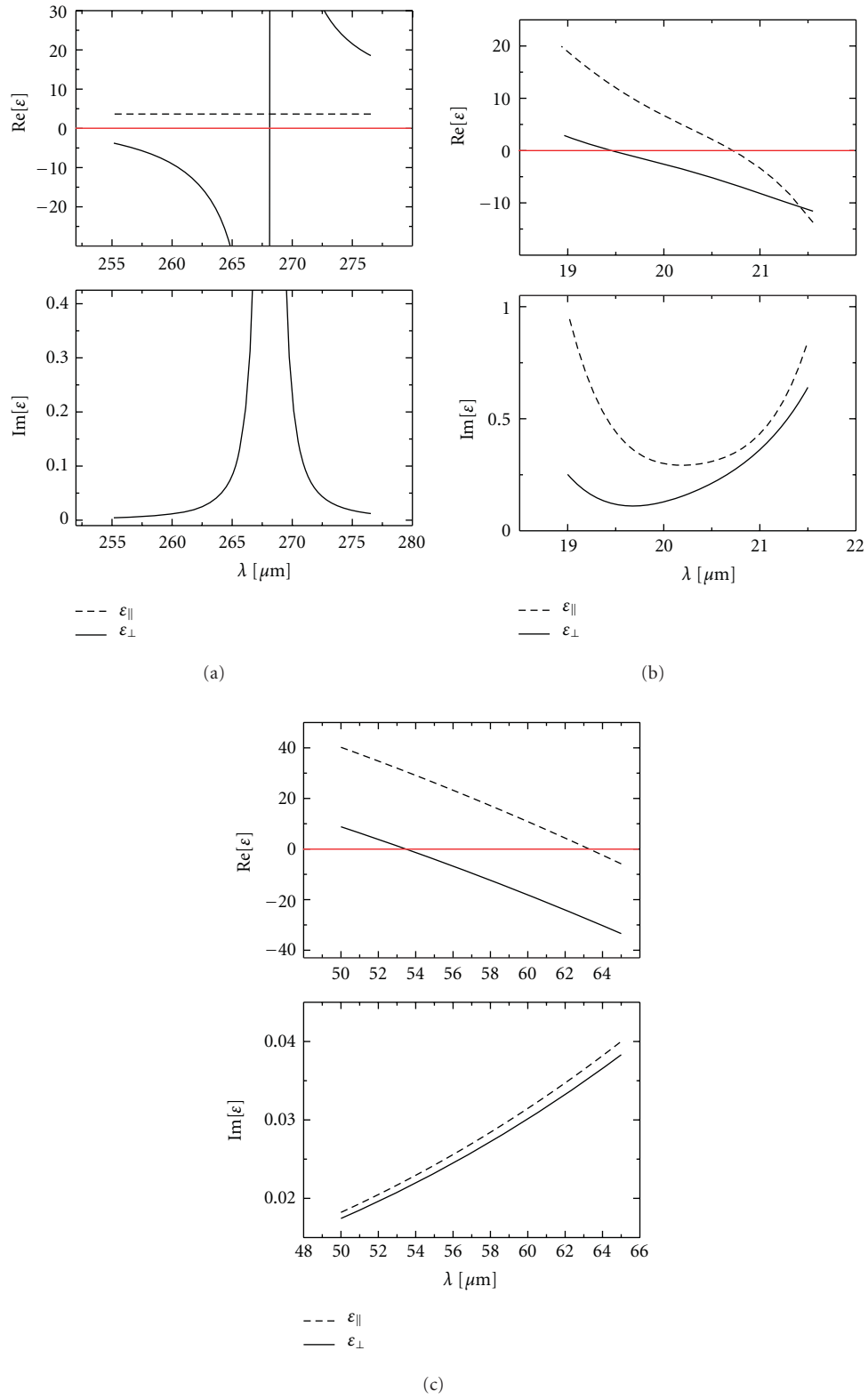


FIGURE 1: (a) The real (top panel) and the imaginary (bottom panel) parts of the dielectric function of TGS; the monoclinic  $C_2$ -axis is along the “perpendicular” ( $x$ ) direction. (b) Same for sapphire; the crystallographic  $c$ -axis is along the “perpendicular” ( $x$ ) direction. (c) Same for monocrystalline Bismuth.

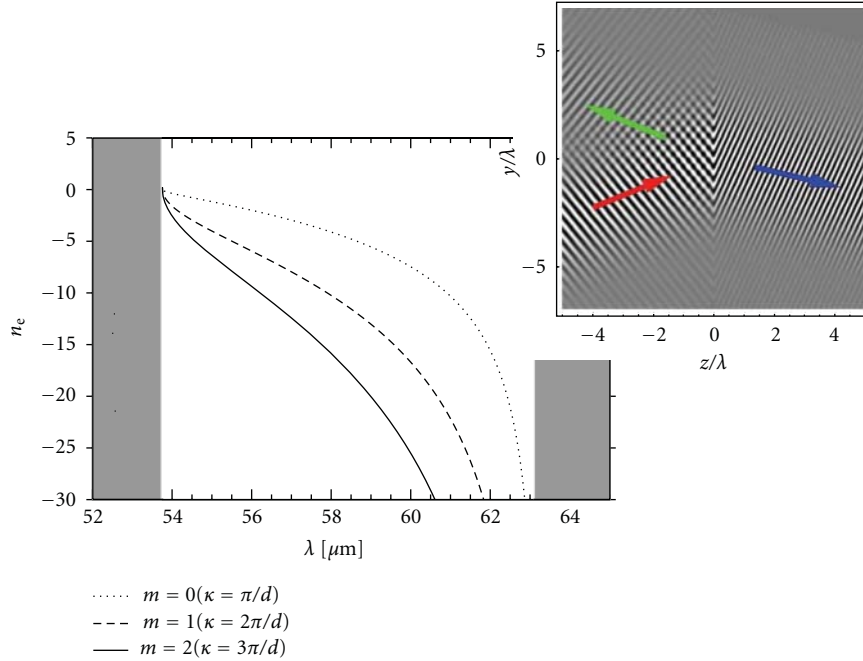


FIGURE 2: The effective refractive index of the three lowest order modes in a Bismuth waveguide. Inset: numerical simulation showing the refraction of a beam within a metallic waveguide (of thickness  $d = 4.5 \mu\text{m}$ ) at an interface between an isotropic dielectric with  $\epsilon = 55$  and monocrystalline Bismuth;  $\lambda = 61 \mu\text{m}$ .

the frequency interval of interest, which enables many imaging and transmission applications [13]. It should also be noted that high-quality single-crystal films as thin as  $1 \mu\text{m}$ , with the trigonal axis ( $C_3$ ) oriented perpendicular to the film plane, have been reported [37], thereby essentially solving the technological issues in fabricating the proposed negative index device.

Figure 1(c) shows the behavior of real and imaginary components of  $\epsilon$  for Bi based on (3). The most prominent feature of these plots, the transition from  $\epsilon > 0$  to  $\epsilon < 0$ , is determined by the highly anisotropic plasma frequency. This anisotropy creates a window between  $\lambda = 53.7 \mu\text{m}$  and  $63.2 \mu\text{m}$  where  $\epsilon < 0$  for the  $E$ -field along the  $C_3$ -axis, while  $\epsilon > 0$  for  $E$  transverse to  $C_3$ . The existence of such  $10 \mu\text{m}$  window was confirmed by direct measurement [38].

To allow for left-handed propagation in this frequency interval, Bi should be integrated into the core of a planar waveguide, with the  $C_3$ -axis oriented in the transverse direction. In Figure 2 we examine the behavior of the effective refractive index  $n_{\text{eff}}$  (2) for the proposed subcritical ( $d < \lambda/2$ ) waveguide structure with Bismuth core. Note that negative effective index is possible for all modes over the entire ( $\epsilon_x < 0$ ,  $\epsilon_{\parallel} > 0$ ) range. Negative refraction behavior of our system was further confirmed by a numerical calculation of the electric field incident on the Bi waveguide. The results of this calculation are presented in Figure 2 (inset). We assume a TM wave with a Gaussian profile, mode-matched into the Bi waveguide in the transverse direction by, for example, propagating the beam from a metallic waveguide of the same thickness, filled with a regular dielectric. One can clearly see

the negative refraction at the boundary. Furthermore, it is evident that attenuation of the transmitted wave is weak, as expected from low values of the imaginary part of the dielectric constant (Figure 1(c)).

In addition, this calculation shows that the NIM waveguide remains transparent despite the fact that transverse dimension of the waveguide is much smaller than the wavelength, which indicates strong confinement of the field within the core (since the cladding is assumed to be perfectly conducting). This behavior is not found in a subwavelength dielectric waveguide, where much of the field spreads into the cladding, or a subwavelength metallic waveguide, which does not support propagating modes. Such strong field confinement may find applications in photonic structures and nonlinear optics [39].

In conclusion, we have proposed a novel negative refraction system for several wavelengths from low-THz to far-IR. Our approach is nonmagnetic, avoids the use of periodic patterning, utilizes naturally occurring materials, and promises the capacity for low-loss devices.

## Acknowledgment

This work was partially supported by ARO-Multidisciplinary University Research Initiative Grant nos. 50342-PH-MUR and W911NF-09-1-0539, NSF Grant nos. DMR-0134736, ECS-0400615, and ECCS-1102183, the Princeton Institute for the Science and Technology of Materials (PRISM), GRF-OSU, and ACS-PRE.

## References

- [1] V. G. Veselago, "The electrodynamics of substances with simultaneously negative values of  $\epsilon$  and  $\mu$ ," *Soviet Physics Uspekhi*, vol. 10, no. 4, article 509, 1968.
- [2] M. Noginov and V. A. Podolskiy, Eds., *Tutorials in Metamaterials*, Taylor & Francis, Boca Raton, Fla, USA, 2012.
- [3] P. V. Parimi, W. T. Lu, P. Vodo, and S. Sridhar, "Imaging by flat lens using negative refraction," *Nature*, vol. 426, no. 6965, article 404, 2003.
- [4] I. R. Gabitov, R. A. Indik, N. M. Litchinitser, A. I. Maimistov, V. M. Shalaev, and J. E. Soneson, "Double-resonant optical materials with embedded metal nanostructures," *Journal of the Optical Society of America B*, vol. 23, no. 3, pp. 535–542, 2006.
- [5] R. A. Shelby, D. R. Smith, and S. Schultz, "Experimental verification of a negative index of refraction," *Science*, vol. 292, no. 5514, pp. 77–79, 2001.
- [6] V. M. Shalaev, W. Cai, U. K. Chettiar et al., "Negative index of refraction in optical metamaterials," *Optics Letters*, vol. 30, no. 24, pp. 3356–3358, 2005.
- [7] E. Schonbrun, T. Yamashita, W. Park, and C. J. Summers, "Negative-index imaging by an index-matched photonic crystal slab," *Physical Review B*, vol. 73, no. 19, Article ID 195117, 6 pages, 2006.
- [8] G. Dolling, C. Enkrich, M. Wegener, C. M. Soukoulis, and S. Linden, "Simultaneous negative phase and group velocity of light in a metamaterial," *Science*, vol. 312, no. 5775, pp. 892–894, 2006.
- [9] D. R. Smith, W. J. Padilla, D. C. Vier, S. C. Nemat-Nasser, and S. Schultz, "Composite medium with simultaneously negative permeability and permittivity," *Physical Review Letters*, vol. 84, no. 18, pp. 4184–4187, 2000.
- [10] C. G. Parazzoli, R. B. Greigor, K. Li, B. E. C. Koltenbah, and M. Tanielian, "Experimental verification and simulation of negative index of refraction using Snell's law," *Physical Review Letters*, vol. 90, no. 10, Article ID 107401, 4 pages, 2003.
- [11] M. Notomi, "Theory of light propagation in strongly modulated photonic crystals: refractionlike behavior in the vicinity of the photonic band gap," *Physical Review B*, vol. 62, no. 16, pp. 10696–10705, 2000.
- [12] A. Boltasseva, "Fabrication of optical metamaterials," in *Tutorials in Metamaterials*, M. Noginov and V. A. Podolskiy, Eds., Taylor & Francis, Boca Raton, Fla, USA, 2012.
- [13] V. A. Podolskiy and E. E. Narimanov, "Near-sighted superlens," *Optics Letters*, vol. 30, no. 1, pp. 75–77, 2005.
- [14] V. A. Podolskiy and E. E. Narimanov, "Strongly anisotropic waveguide as a nonmagnetic left-handed system," *Physical Review B*, vol. 71, no. 20, Article ID 201101(R), 4 pages, 2005.
- [15] V. A. Podolskiy, "Hyperbolic metamaterials," in *Tutorials in Metamaterials*, M. Noginov and V. A. Podolskiy, Eds., Taylor & Francis, Boca Raton, Fla, USA, 2012.
- [16] L. V. Alekseyev and E. E. Narimanov, "Radiative decay engineering in metamaterials," in *Tutorials in Metamaterials*, M. Noginov and V. A. Podolskiy, Eds., Taylor & Francis, Boca Raton, Fla, USA, 2012.
- [17] Z. Jacob, L. V. Alekseyev, and E. Narimanov, "Optical hyperlens: far-field imaging beyond the diffraction limit," *Optics Express*, vol. 14, no. 18, pp. 8247–8256, 2006.
- [18] S. Thongrattanasiri and V. A. Podolskiy, "Hypergratings: nanophotonics in planar anisotropic metamaterials," *Optics Letters*, vol. 34, no. 7, pp. 890–892, 2009.
- [19] A. Salandrino and N. Engheta, "Far-field subdiffraction optical microscopy using metamaterial crystals: theory and simulations," *Physical Review B*, vol. 74, no. 7, Article ID 075103, 2006.
- [20] Z. Liu, H. Lee, Y. Xiong, C. Sun, and X. Zhang, "Far-field optical hyperlens magnifying sub-diffraction-limited objects," *Science*, vol. 315, no. 5819, article 1686, 2007.
- [21] H. N. S. Krishnamoorthy, Z. Jacob, E. Narimanov, I. Kretzschmar, and V. M. Menon, "Topological transitions in metamaterials," *Science*, vol. 336, no. 6078, pp. 205–209, 2012.
- [22] E. E. Narimanov, H. Li, Y. A. Barnakov, and M. A. Noginov, "Darker than black: radiation-absorbing metamaterial," in *Proceedings of the Lasers and Electro-Optics/Quantum Electronics and Laser Science Conference: 2010 Laser Science to Photonic Applications (CLEO/QELS'10)*, Optical Society of America, San Jose, Calif, USA, May 2010, presentation #QPD6.
- [23] P. Evans, W. R. Hendren, R. Atkinson et al., "Growth and properties of gold and nickel nanorods in thin film alumina," *Nanotechnology*, vol. 17, no. 23, pp. 5746–5753, 2006.
- [24] J. Yao, Z. Liu, Y. Liu et al., "Optical negative refraction in bulk metamaterials of nanowires," *Science*, vol. 321, no. 5891, p. 930, 2008.
- [25] A. J. Hoffman, L. Alekseyev, S. S. Howard et al., "Negative refraction in semiconductor metamaterials," *Nature Materials*, vol. 6, no. 12, pp. 946–950, 2007.
- [26] J. Sun, J. Zhou, B. Li, and F. Kang, "Indefinite permittivity and negative refraction in natural material: graphite," *Applied Physics Letters*, vol. 98, no. 10, Article ID 101901, 3 pages, 2011.
- [27] R. Wangberg, J. Elser, E. E. Narimanov, and V. A. Podolskiy, "Nonmagnetic nanocomposites for optical and infrared negative-refractive-index media," *Journal of the Optical Society of America B*, vol. 23, no. 3, pp. 498–505, 2006.
- [28] C. Luo, S. G. Johnson, and J. D. Joannopoulos, "All-angle negative refraction without negative effective index," *Physical Review B*, vol. 65, no. 20, Article ID 201104(R), 4 pages, 2002.
- [29] A. Hadni and X. Gerbaux, "Far IR excitation of longitudinal optical phonons in triglycine sulphate," *Ferroelectrics*, vol. 248, no. 1, pp. 15–26, 2000.
- [30] X. Gerbaux, M. Tazawa, and A. Hadni, "Far IR transmission measurements on triglycine sulphate (TGS), at 5K," *Ferroelectrics*, vol. 215, no. 1, pp. 47–63, 1998.
- [31] T. Dumelow, J. A. P. da Costa, and V. N. Freire, "Slab lenses from simple anisotropic media," *Physical Review B*, vol. 72, no. 23, Article ID 235115, 8 pages, 2005.
- [32] M. Schubert, T. E. Tiwald, and C. M. Herzinger, "Infrared dielectric anisotropy and phonon modes of sapphire," *Physical Review B*, vol. 61, no. 12, pp. 8187–8201, 2000.
- [33] W. S. Boyle, A. D. Brailsford, and J. K. Galt, "Dielectric anomalies and cyclotron absorption in the infrared: observations on bismuth," *Physics Reviews*, vol. 109, no. 4, pp. 1396–1398, 1958.
- [34] W. S. Boyle and A. D. Brailsford, "Far infrared studies of bismuth," *Physics Reviews*, vol. 120, no. 6, pp. 1943–1949, 1960.
- [35] V. D. Kulakovskii and V. D. Egorov, "Plasma reflection in bismuth and bismuth-antimony alloys," *Soviet Physics—Solid State*, vol. 15, no. 7, p. 1368, 1974.
- [36] V. S. Edelman, "Electrons in bismuth," *Advances in Physics*, vol. 25, no. 6, pp. 555–613, 1976.
- [37] F. Y. Yang, K. Liu, K. Hong, D. H. Reich, P. C. Searson, and C. L. Chien, "Large magnetoresistance of electrodeposited single-crystal bismuth thin films," *Science*, vol. 284, no. 5418, pp. 1335–1337, 1999.

- [38] E. Gerlach, P. Grosse, M. Rautenberg, and W. Senske, “Dynamical conductivity and plasmon excitation in Bi,” *Physica Status Solidi (b)*, vol. 75, no. 2, pp. 553–558, 1976.
- [39] A. A. Goyyadinov and V. A. Podolskiy, “Metamaterial photonic funnels for subdiffraction light compression and propagation,” *Physical Review B*, vol. 73, no. 15, Article ID 155108, 5 pages, 2006.



## Research Article

# The Performance of Active Coated Nanoparticles Based on Quantum-Dot Gain Media

Sawyer D. Campbell<sup>1</sup> and Richard W. Ziolkowski<sup>1,2</sup>

<sup>1</sup> College of Optical Sciences, University of Arizona, Tucson, AZ 85721, USA

<sup>2</sup> Department of Electrical and Computer Engineering, University of Arizona, Tucson, AZ 85721, USA

Correspondence should be addressed to Richard W. Ziolkowski, ziolkowski@ece.arizona.edu

Received 25 June 2012; Revised 21 August 2012; Accepted 25 August 2012

Academic Editor: Pavel A. Belov

Copyright © 2012 S. D. Campbell and R. W. Ziolkowski. This is an open access article distributed under the Creative Commons Attribution License, which permits unrestricted use, distribution, and reproduction in any medium, provided the original work is properly cited.

Quantum-dots (QDs) provide an exciting option for the gain media incorporated in active coated nanoparticles (CNPs) because they possess large gain coefficients resulting from their extreme confinement effects. The optical properties of core/shell QDs can be tuned by changing the relative size of the core/shell, that is, by effectively changing its band gap structure. Similarly, the resonance of a CNP can be adjusted by changing the relative sizes of its layers. It is demonstrated here that by optimally locating the QDs inside a resonant CNP structure it is possible to greatly enhance the intrinsic amplifying behavior of the combined QD-CNP system.

## 1. Introduction

The active coated nanoparticle (CNP) designs studied previously considered active silica cores coated with either Ag or Au shells (depending on the wavelength region of interest) [1–3] or the corresponding “inside-out” (IO) designs, that is, metallic cores covered with active silica coatings [2, 4]. In general, these designs used a simple gain model that did not include the dispersion behavior typical of a physical, active medium. These nanoamplifier designs were predicted to require a gain value of  $10^4$ – $10^5$  cm<sup>-1</sup>. This is achievable with quantum dots (QDs); and, consequently, they have been a preferred choice for some discussions on the physical realizations of these nanoamplifiers [3]. QDs offer an alternative, more robust option to dye-based gain media, which are susceptible to bleaching. Nonetheless, the active IO-CNP has been experimentally verified with a dye impregnated silica coating [4]. Moreover, it and related studies [5, 6] suggest that the strong localized field and large cross-section effects associated with these plasmonic nanostructures reduce the model-based large gain values to more practical ones. We demonstrate here that QDs, which can be obtained commercially and could be integrated with the CNPs, do in fact represent an exciting practical option for a variety of active CNP designs. Moreover, it is established

that the number of QDs needed for a successful active CNP design is considerably smaller than anticipated.

## 2. Quantum-Dot Gain Model

The effective permittivity of a core-shell QD has been modeled by Holmström et al. and is applicable for core-shell QDs in the strong confinement regime [7]. This model is motivated by Maxwell-Garnett effective medium theory and is given by the following:

$$\epsilon_{\text{QD,Lor}}^{\text{CS}}(\omega) = \epsilon_b^{\text{CS}} + \frac{2}{V_{\text{QD}}^{\text{CS}}} (f_c - f_v) \frac{e^2 f / (m_0 \epsilon_0)}{\omega^2 - \omega_0^2 + i2\omega\gamma}, \quad (1)$$

where  $V_{\text{QD}}^{\text{CS}} = (4\pi/3)R_2^3$  is the volume of the entire core-shell structure;  $f$  is the oscillator strength;  $f_c$  and  $f_v$  are, respectively, the conduction and valence band carrier distribution functions;  $\gamma$  is a dampening term associated with the resonance width. The model assumes that a pump signal at a frequency higher than the resonance frequency,  $f_{\text{res}} = \omega_0/2\pi$ , creates the difference between the conduction- and valence-band populations:  $(f_c - f_v)$ . However, because this population difference term is effectively related to the pump strength, it takes on values between 0 and 1. It will be termed the gain scale. It supplies the model with the ability

to represent a desired gain value at the resonance frequency. The core-shell background dielectric constant  $\epsilon_b^{CS}$  is given by the following:

$$\epsilon_b^{CS} = \epsilon_s + 3f_{\text{core}}\epsilon_s \frac{\epsilon_c - \epsilon_s}{\epsilon_c + 2\epsilon_s - f_{\text{core}}(\epsilon_c - \epsilon_s)}, \quad (2)$$

where  $f_{\text{core}}$  is ratio of the core volume to the entire QD volume, and  $\epsilon_c$  and  $\epsilon_s$  are the bulk dielectric constants of the core and shell, respectively. The model was originally applied to an InAs/GaAs QD which operated at a bandgap energy of 0.8 eV ( $\lambda = 1550$  nm). Because of the desire to conduct prototype experiments to demonstrate their potential nanosensor applications, we have extended it here to commercially available QD structures.

Many different types of quantum dots are now available commercially in the frequency range of interest. For instance, Sigma-Aldrich produces a range of CdSe/ZnS core-shell quantum dots for use in the visible and near-infrared parts of the spectrum. The published properties of some of their CdSe/ZnS core-shell QDs are given in Table 1 [8]; they show a considerable range of available gain values and related optical extinction coefficients,  $g = -2 (\omega_0/c) \kappa$ ,  $c$  being the vacuum speed of light.

Their 560 nm emitting QD, whose diameter is 6.0 nm was chosen for our study; it has a gain value which is close to those used in our previous studies [6]. Moreover, its core-shell configuration conforms nicely to our analytical simulation approach. The indexes of refraction for CdSe and ZnS at visible wavelengths are approximately 2.5 and 2.41, respectively [9, 10]. These values, along with the published QD material properties, were used to calculate the wavelength-dependent effective permittivity and, hence, the index of refraction of a QD layer. Figure 1 depicts the wavelength dependence of the index of refraction for the commercially available Sigma-Aldrich 560 nm QD based on the theoretical model given by (1)-(2). It will be denoted as “SA-560 QD” in the following discussions. The oscillator strength  $f$  and the damping term  $\gamma$  were chosen, respectively, to be 1.9185 and 5.0 meV to match the corresponding peak gain value given in Table 1. Consequently, when the gain scale value equals one, the model recovers that peak gain value. As Table 1 shows, the observed QD resonance strength increases as the QD size becomes larger. As a consequence, its dispersion properties are quite large over the frequency band of interest. Moreover, the active CNP’s resonant linewidth, as would be expected for a core-shell amplifier, is quite narrow [1]. While the available gain bandwidth for these QDs is wider than the active CNP resonance, both of these properties nevertheless present added degrees of difficulty in the design and fabrication of any QD-CNP structure. The center frequency of the CNP resonance is rather sensitive to the material properties of its layers and to their respective radii. To achieve the desired enhanced responses, the final configuration must provide a significant overlap of the CNP and QD resonances.

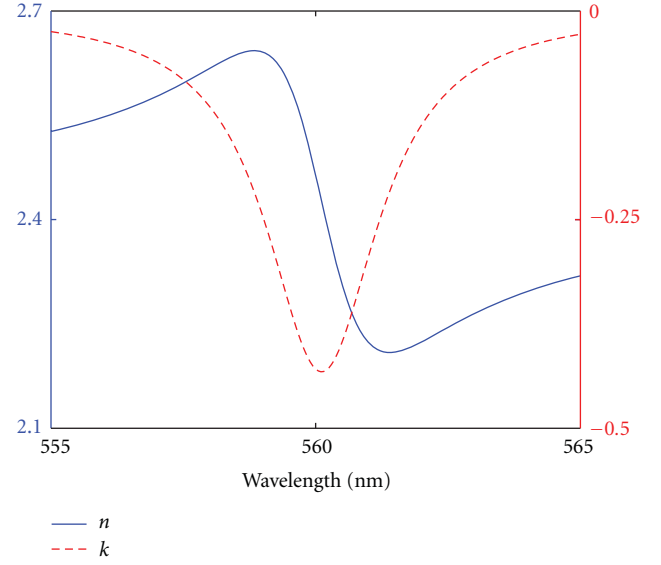


FIGURE 1: Behavior of the real,  $n$ , and imaginary,  $\kappa$ , parts of the index of refraction of the SA-560 QD as a function of the wavelength.

TABLE 1: Physical properties of commercially available Sigma-Aldrich core-shell quantum dots.

Emission wavelength (nm)	$g \times 10^5$ (cm <sup>-1</sup> )	$\kappa$	Core diameter (nm)	QD diameter (nm)
510	0.045	-0.018	3.0	4.9
530	0.065	-0.027	3.3	5.2
560	0.97	-0.432	3.4	6.0
590	1.6	-0.751	4.0	6.2
610	4.90	-2.379	5.2	7.7
640	5.90	-3.005	6.3	8.6

### 3. Active CNP Designs

The previously studied CNP and corresponding IO designs possess strong resonant behaviors [4, 6] and serve as the basis for the QD-augmented designs reported here. In particular, we replace the active silica region in the previous designs with an equivalent cluster of QDs, which we treat as a continuous region whose thickness is determined by the number of SA-560 QDs that could fit radially into the layer and whose permittivity is specified by (1) and (2). We used our previously-developed Mie theory CNP models [1, 3, 6, 11] to calculate the behavior of the proposed QD-augmented CNP designs. Silver was selected for the metal; it was modeled with a size- and wavelength-dependent permittivity [1] that recovers the known measured results [12]. As noted above, a background pump signal is assumed to create the necessary population difference to achieve the gain value specified by the manufacturer and recovered by the QD permittivity model, (1).

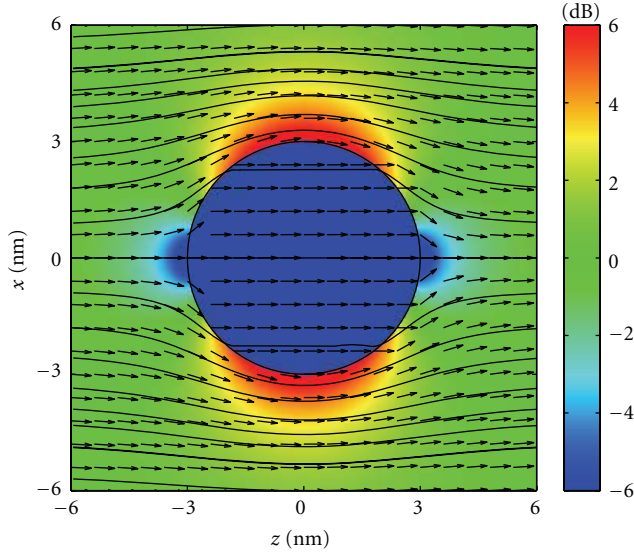


FIGURE 2: Contour plots of the electric field distribution along with the normalized total Poynting's vector field for a single SA-560 QD.

While a QD possesses amplifying behavior by itself, it only weakly couples to an incident field, which leads to a weak response. Figure 2 shows the electric field distribution and the corresponding Poynting's vector field for the SA-560 QD when it is excited by an incident plane wave at its resonance frequency. The streamlines of the Poynting's vector field flow around the QD, indicating a weak interaction of the incident field with it.

On the other hand, if the QD is simply coated with a metal, the coupling to and the localization of the incident field energy in the gain region can be improved substantially and the resulting resonant plasmonic behavior will significantly enhance its response. We have found that while a single SA-560 QD, when coated with an Ag shell, can be designed to have a strong resonance, it does not have enough gain to overcome the intrinsic losses associated with that shell. On the other hand, slightly larger CNPs that contain several QDs generally exhibit stronger light-matter interactions with (i.e., have a stronger coupling to) the incident field and, hence, have larger resonant responses. A multilayered cluster of QDs can be employed in the core and if the shell is properly designed, the resulting multilayer gain-augmented core-shell system will exhibit a super-resonance state [1] when its gain value is large enough to overcome its intrinsic losses. Figure 3 shows the electric field distribution for a core size equivalent to the radius of "two" QD layers (9 nm), that is, a QD in the center and one full layer of dots surrounding it, when coated with a 3 nm Ag shell. While the QD core region is treated as a continuous medium in the simulation, we have included circles that are overlaid in the core to represent the size of the individual QDs relative to the entire structure.

There is a significant enhancement in the electric field amplitude when compared to the single bare SA-560 QD seen in Figure 2. This enhancement effect can be increased with up to three layers of QDs. However, we found that it

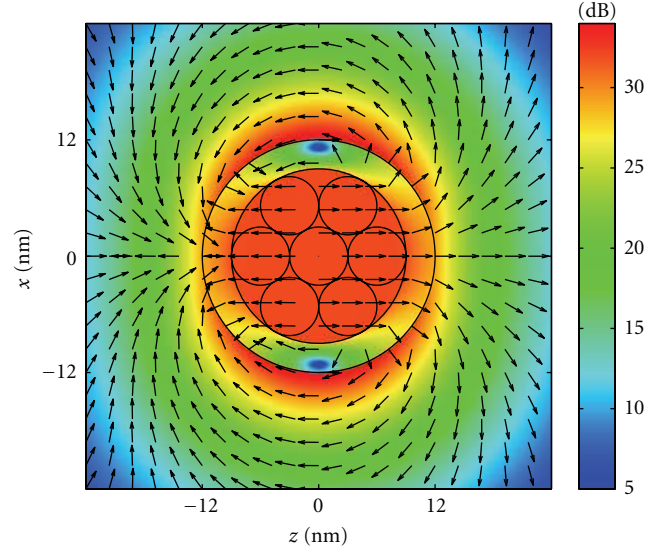


FIGURE 3: Contour plots of the electric field distribution along with the normalized total Poynting's vector field for a set of SA-560 QDs encapsulated in a 3.0 nm thick silver shell having a 12.0 nm exterior radius.

begins to fall off with four- and more layered cores because the gain is so large it significantly detunes the overlap of the QD and structural resonances. On the other hand, by placing the active region more strategically, as suggested by previous 3-layer designs [6], one can dramatically improve the active CNP performance while decreasing the number of QDs required.

The two designs whose performance characteristics are noticeably the best are the Ag/QD/SiO<sub>2</sub> (called the QD-CNP) and QD/Ag/SiO<sub>2</sub> (called the IO-CNP) configurations. Both are three-layer designs consisting of the same materials, but differ in the placement of the QD layer. The QD layer of the QD-CNP design lies between the Ag shell and the SiO<sub>2</sub> core, while the QD layer of the IO-CNP is the outermost layer. The core and shell sizes were adjustable parameters; the QD size was fixed by the manufacturer's specifications. Both of the resulting optimized designs feature a 17.5 nm radius core and a 6 nm thick QD layer. For both cases, a single layer of QDs is sufficient to achieve a very large resonant response. The optimized thickness of the Ag shell in the QD-CNP design was 6.2 nm (29.7 nm total radius); it was 6.3 nm thick (29.8 nm total radius) for the IO-CNP design. We note that other three layer designs featuring a single QD inside a metal coated dielectric core/shell structure have been proposed [13].

However, we have found that placing the active material near the shell boundary can greatly increase the performance of the active CNP. In fact, while we have studied designs with the active region near, but separated from the shell, we have seen that the optimal location of the active region is directly adjacent to the shell. While it is known that placing the active region next to a metal will enhance the nonradiative decay rate of the active material, that is, it will quench the emission rate, recent theoretical and experimental studies have shown

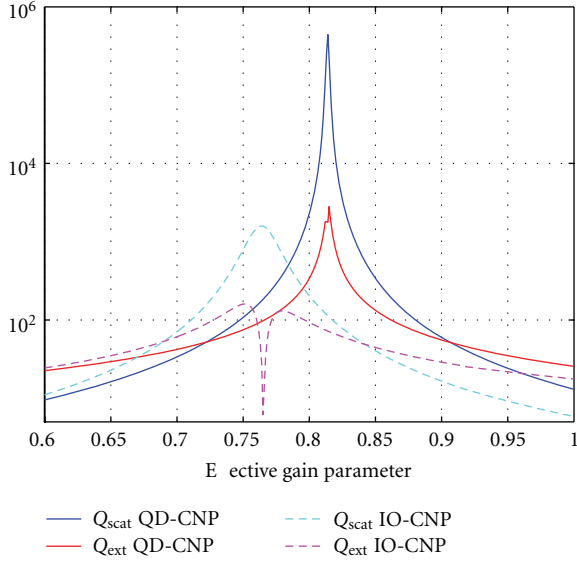


FIGURE 4: Scattering and extinction efficiencies for the optimized QD-CNP and the IO-CNP configurations.

that plasmonic-related effects can actually significantly enhance the radiative decay rates [14–20]. In particular, by properly designing a multi-layer structure to retain the unique optical and electronic properties of the QD and CNP and to provide a much larger density of radiating states to which the emissions can couple, one can produce active CNPs with very efficient fluorescence behaviors, especially for materials with high internal quantum efficiencies which QDs possess. Even though the metal layer is thin and the QDs are not, which would lead to lower quenching effects in any event, designs exhibiting the large radiated power enhancements associated with a super-resonance state [1] correspond to ones that foster enhanced radiative decays. Thus, the proposed optimized QD-CNP and IO-CNP designs avoid quenching and significantly outperform the single QD, two-layer version. The scattering efficiency and the absolute value of the extinction efficiency for these designs are plotted against the gain scale factor in Figure 4. We note that the optimized configurations require less than the peak gain value to achieve their resonant states, which would be quite advantageous in practice when fabrication and experimental tolerances tend to negatively impact the ideal component performance characteristics. Also note that the extinction efficiency achieves a negative value on the larger gain factor value (right) side of the resonant peaks of the scattering efficiency. (we note that this feature appears in the  $|Q_{\text{ext}}|$  curves as the sharp nulls since the absolute value is being plotted). Recall that when the extinction efficiency becomes negative, it means the losses are overcome and the incident field is amplified. One immediately observes that the scattering and extinction behaviors of the QD-CNP design are several orders of magnitude larger than those of the IO-CNP.

The resonant CNP-based designs have cross sections much larger than their physical size [6]; this behavior impacts the actual, rather than the model-based gain values needed for their operation. Figure 5 shows the power flow

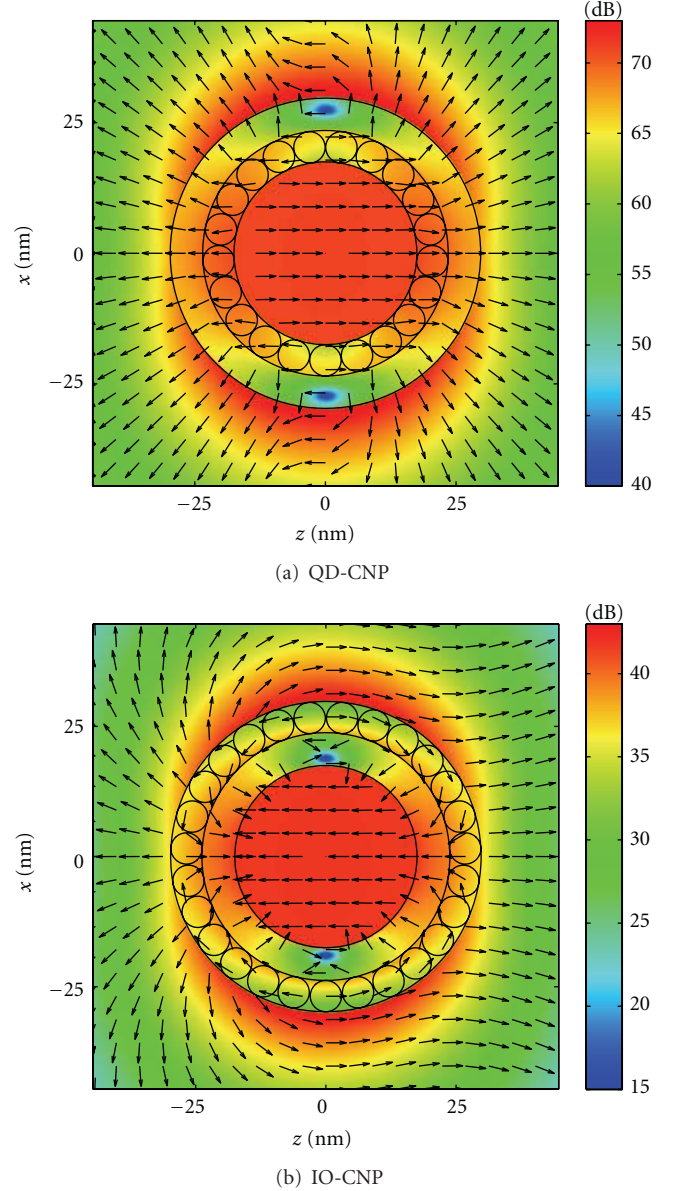


FIGURE 5: Contour plots of the electric field distribution along with the normalized total Poynting's vector field for the QD-CNP and IO-CNP designs.

behavior of the total Poynting's vector field for both designs when the incident plane wave has a 560 nm wavelength. The QDs are drawn as circles representing their actual size with respect to the size of the structure. In both the QD-CNP and IO-CNP cases, these structures produce a strong overall dipole resonance in their exteriors. However, it is clear that power is flowing more strongly outward from the QD layer in the QD-CNP structure than it is in the IO-CNP one (note that the minimum level in Figure 5(a) is the maximum one in Figure 5(b)), further emphasizing the large scattering cross section differences shown in Figure 4.

Although the gain region in the three-layer QD-CNP and IO-CNP designs is only a single layer of QDs, it has a volume equivalent to 282 and 481 individual dots, respectively.



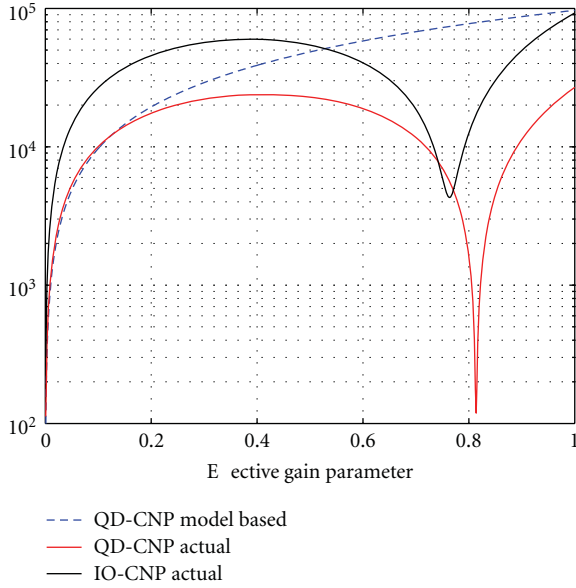


FIGURE 6: The core-shell model required gain values (blue) and the actual required gain values of the QD-CNP (red) and IO-CNP (black) designs (in  $\text{cm}^{-1}$ ).

However, the field overlap in the gain region is strong and is caused, in part, by an increase in the incident power flow into the gain region. This strong coupling of the incident field to the gain region leads to a large scattering cross-section  $Q_{\text{scat}}$ , which is in turn effectively related to the enhancement of the gain value by the amount  $\sqrt{Q_{\text{scat}}}$ , that is, the gain enhancement factor [6]. This enhanced coupling to the gain region thus leads to a reduction of the actual gain values required to achieve the results shown in Figure 4. They are given in Figure 6, where the model-based gain value (blue) and the actual gain values of the QD-CNP (red) and IO-CNP (black) designs are plotted versus the QD gain scale factor. The largest gain enhancement factor for the QD-CNP and IO-CNP configurations are, respectively,  $\approx 287$  and  $\approx 17$ . We again note that the optimized configurations require less than the peak gain value to achieve their resonant states. Moreover, the tolerance of the gain scale factor (i.e., the widths of the resonances in Figure 6) to achieve a significant, high gain enhancement factor provides further tolerances in practice to potential fabrication and experimental errors.

We note that the IO-CNP design has a similar, but weaker behavior. It simply does not possess as large a gain enhancement factor. This is due to the QD layer being the outermost one. In the QD-CNP case, the QD layer is within the cavity formed by the silica core and the metal shell. Thus, the coupling of the large fields in the core to the SPPs created in the Ag shell at the Ag-QD (i.e., an  $\epsilon < 0$ ,  $\epsilon > 0$ ) interface provides a much larger feedback mechanism through the QD gain layer. This feedback is much smaller in the IO-CNP case because it occurs between the outside vacuum region and the metal shell. These interpretations are supported by earlier 3-layer observations [6] that included an exterior metal coating to the basic IO-CNP configuration that substantially improved its performance.

## 4. Conclusions

With an enhancement factor of  $\approx 287$ , the actual required gain value in the QD-CNP configuration might be achieved with *only* 1 QD instead of the predicted 282 QDs that would make up an entire layer. In reality, the actual effectiveness of coupling energy into each QD would be lower than these ideal values. Nevertheless, the large enhancement factors observed indicate that designs using only a few QDs may be possible and that QD-QD coupling effects, while out of the scope of this study, can quite possibly be ignored due to the drastically reduced QD requirements. Also, the reduction of quenching effects seen with highly resonant plasmonic structures [14–20] suggests that QDs placed near the metal layer may not suffer from quenching effects, but rather could be further enhanced by the plasmonic resonance. These results further suggest that QDs may be a very realistic gain medium for active CNP designs and that QD-CNPs would be viable candidates for a variety of nanoamplifier applications. While the Mie theory analysis is limited in its scope, it has been used to describe the experimentally observed spectra of active NPs [4] and provides a good foundation for analyzing the effects of the resonant CNPs. The inclusion of off-the-shelf QD geometry and performance characteristics in this modeling added engineering realism to its outcomes. Future work includes experimentally encapsulating QDs in these CNP structures to measure the predicted enhancements in their emissions and, hence, to verify the theory and modeling.

## Acknowledgment

This work was supported in part by ONR Contract no. H940030920902 and NSF Contract no. ECCS-0823864.

## References

- [1] J. A. Gordon and R. W. Ziolkowski, "The design and simulated performance of a coated nano-particle laser," *Optics Express*, vol. 15, no. 5, pp. 2622–2653, 2007.
- [2] M. I. Stockman, "The spaser as a nanoscale quantum generator and ultrafast amplifier," *Journal of Optics A*, vol. 12, no. 2, Article ID 024004, 2010.
- [3] S. Arslanagić and R. W. Ziolkowski, "Active coated nano-particle excited by an arbitrarily located electric Hertzian dipole-resonance and transparency effects," *Journal of Optics A*, vol. 12, no. 2, Article ID 024014, 2010.
- [4] M. A. Noginov, G. Zhu, A. M. Belgrave et al., "Demonstration of a spaser-based nanolaser," *Nature*, vol. 460, no. 7259, pp. 1110–1112, 2009.
- [5] Y. Sivan, S. Xiao, U. K. Chettiar, A. V. Kildishev, and V. M. Shalaev, "Frequency-domain simulations of a negative-index material with embedded gain," *Optics Express*, vol. 17, no. 26, pp. 24060–24074, 2009.
- [6] S. D. Campbell and R. W. Ziolkowski, "Impact of strong localization of the incident power density on the nano-amplifier characteristics of active coated nano-particles," *Optics Communications*, vol. 285, no. 16, pp. 3341–3352, 2012.
- [7] P. Holmström, L. Thyñ, and A. Bratkovsky, "Dielectric function of quantum dots in the strong confinement regime,"



- Journal of Applied Physics*, vol. 107, no. 6, Article ID 064307, 2010.
- [8] <http://www.sigmaaldrich.com/materials-science/nanomaterials/lumidots.html>.
  - [9] B. Jensen and A. Torabi, "Refractive index of hexagonal II-VI compounds CdSe, CdS, and  $\text{CdSe}_x\text{S}_{1-x}$ ," *Journal of the Optical Society of America B*, vol. 3, pp. 857–863, 1986.
  - [10] [http://www.dow.com/assets/attachments/business/gt/infrared\\_materials/cleartran/tds/cleartran.pdf](http://www.dow.com/assets/attachments/business/gt/infrared_materials/cleartran/tds/cleartran.pdf).
  - [11] A. L. Aden and M. Kerker, "Scattering of electromagnetic waves from two concentric spheres," *Journal of Applied Physics*, vol. 22, no. 10, pp. 1242–1246, 1951.
  - [12] P. B. Johnson and R. W. Christy, "Optical constants of the noble metals," *Physical Review B*, vol. 6, no. 12, pp. 4370–4379, 1972.
  - [13] M. Klopfer and R. K. Jain, "Plasmonic quantum dots for nonlinear optical applications," *Optical Materials Express*, vol. 1, no. 7, pp. 1353–1366, 2011.
  - [14] W. C. H. Choy, X. W. Chen, S. L. He, and P. C. Chui, "The Purcell effect of silver nanoshell on the fluorescence of nanoparticles," in *Proceedings of the Asia Optical Fiber Communication and Optoelectronic Exposition and Conference (AOE '07)*, pp. 81–83, October 2007.
  - [15] A. Neogi, H. Morkoç, T. Kuroda, and A. Tackeuchi, "Coupling of spontaneous emission from GaN-AlN quantum dots into silver surface plasmons," *Optics Letters*, vol. 30, no. 1, pp. 93–95, 2005.
  - [16] J. H. Song, T. Atay, S. Shi, H. Urabe, and A. V. Nurmikko, "Large enhancement of fluorescence efficiency from CdSe/ZnS quantum dots induced by resonant coupling to spatially controlled surface plasmons," *Nano Letters*, vol. 5, no. 8, pp. 1557–1561, 2005.
  - [17] F. Tam, G. P. Goodrich, B. R. Johnson, and N. J. Halas, "Plasmonic enhancement of molecular fluorescence," *Nano Letters*, vol. 7, no. 2, pp. 496–501, 2007.
  - [18] Y. Jin and X. Gao, "Plasmonic fluorescent quantum dots," *Nature Nanotechnology*, vol. 4, no. 9, pp. 571–576, 2009.
  - [19] M. A. Noginov, H. Li, Y. A. Barnakov et al., "Controlling spontaneous emission with metamaterials," *Optics Letters*, vol. 35, no. 11, pp. 1863–1865, 2010.
  - [20] V. N. Pustovit and T. V. Shahbazyan, "Fluorescence quenching near small metal nanoparticles," *Journal of Chemical Physics*, vol. 136, no. 20, Article ID 204701, 2012.

## Research Article

# Nonlinear Scattering by Anisotropic Dielectric Periodic Structures

**O. V. Shramkova and A. G. Schuchinsky**

*School of Electronics, Electrical Engineering and Computer Science, Queen's University Belfast, Queen's Road, Queen's Island, Belfast BT3 9DT, UK*

Correspondence should be addressed to O. V. Shramkova, o.shramkova@qub.ac.uk

Received 28 June 2012; Accepted 24 July 2012

Academic Editor: Ivan D. Rukhlenko

Copyright © 2012 O. V. Shramkova and A. G. Schuchinsky. This is an open access article distributed under the Creative Commons Attribution License, which permits unrestricted use, distribution, and reproduction in any medium, provided the original work is properly cited.

The combinatorial frequency generation by the periodic stacks of binary layers of anisotropic nonlinear dielectrics is examined. The products of nonlinear scattering are characterised in terms of the three-wave mixing processes. It is shown that the intensity of the scattered waves of combinatorial frequencies is strongly influenced by the constitutive and geometrical parameters of the anisotropic layers, and the frequency ratio and angles of incidence of pump waves. The enhanced efficiency of the frequency conversion at Wolf-Bragg resonances has been demonstrated for the lossless and lossy-layered structures.

## 1. Introduction

A new generation of artificial electromagnetic materials has opened up new opportunities for engineering the media with the specified properties. The latest advancements in this field have prompted a surge of research in the new phenomenology, which could extend a range of functional capabilities and enable the development of innovative devices in the millimeter, terahertz (THz), and optical ranges.

Frequency conversion in dielectrics with nonlinearities of the second and third order has been investigated in optics, particularly, in the context of the second (SHG) and third (THG) harmonic generation. The recent studies have indicated that nonlinear photonic crystals (PhCs) and metamaterials (MMs) have significant potential for enhancement of the nonlinear activity associated with the mechanisms of field confinement, dispersion management and resonant intensification of the interacting waves. For example, it has been demonstrated in [1–5] that the PhCs dispersion can be tailored to facilitate the phase synchronism (The phase synchronism between pump wave and its harmonic is a prerequisite for efficient frequency conversion.) between the second harmonic and the pump wave of fundamental

frequency. The harmonic generation efficiency can be further increased when the pump wave frequencies are close to the PhC band edges [6–12] where the higher density of states provides favourable phase-matching conditions. The SHG efficiency also grows with the PhC thickness or the number of stacked layers [5].

Combinatorial frequency generation by mixing pump waves of two different frequencies provides alternative means for frequency conversion. The efficiency of mixing process can be dramatically increased in the layered structures, for example, at the higher order Wolf-Bragg resonances of the combinatorial frequencies generated in the anisotropic nonlinear dielectric slabs. As shown in [13], at the specific thickness of the layers illuminated by the plane waves of two tones, the mixing products reach their extremes and exhibit either giant growth of the peak intensity or full suppression. The global maxima and nulls at Wolf-Bragg resonances in the layer are achieved only at the particular combinations of the two frequencies  $\omega_{1,2}$  of pump waves and the layer parameters and anisotropy.

The aim of this paper is to explore the mechanisms of the combinatorial frequency generation in the PhC composed of a periodic stack of binary anisotropic nonlinear dielectric

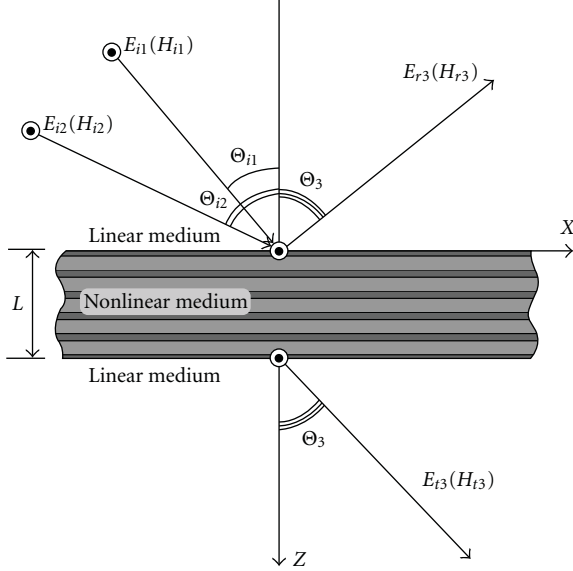


FIGURE 1: Geometry of the problem.

layers illuminated by two-tone pump waves that allows us to combine the effects of the resonance mixing with the dispersion control provided by the structure periodicity. Here the properties of the combinatorial frequencies generated by the nonlinear anisotropic dielectric PhC illuminated by plane waves of two tones are investigated. A generic approach, based on the transfer matrix method (TMM) [14], has been devised here to take into account nonlinear polarization of the constituent anisotropic layers and analyse frequency mixing of the two-tone plane waves obliquely incident on the PhC. The problem statement and the solution of the respective boundary value problem obtained in the three-wave approximation [15] are outlined in Section 2. The results of the numerical analysis and the properties of TM waves of combinatorial frequencies scattered by the nonlinear PhC are discussed in Section 3 and the main features of the three-wave mixing products generated by the anisotropic nonlinear PhCs are summarised in Conclusions.

## 2. Nonlinear Scattering in Three-Wave Mixing Process

Wave propagation and scattering in linear stratified media are usually modelled by TMM, which sequentially relates the fields at the layer interfaces, see, for example, [14, 16]. The TMM approach has also been applied to the study of optical harmonic generation and frequency mixing in 1D nonlinear-layered structures at normal incidence of the pump waves [17–20]. The nondepleted pump wave approximation has been usually employed taking into account multiple reflections from the layer interfaces and interference between all propagating waves, including the forward and backward propagating waves. A relatively simple approach based upon the TMM generalisation to a multiwavelength case has been proposed in [19] where interaction between the different

frequencies was described by the “effective” refractive index characteristic for each optical wave. The latter technique allows simulations of multiple optical wave interactions in the homogenised metamaterials as well as in PhCs.

In order to examine the three-wave mixing process in the 1D *anisotropic* PhC, it is necessary to generalise the TMM-based analysis for the case of two pump waves, incident at arbitrary angles. To elucidate the main features of the developed approach, we consider here a canonical PhC structure with the cross-section shown in Figure 1. It is composed of the periodic binary dielectric layers of thicknesses  $d_1$  and  $d_2$  and infinite extent in the  $x$  and  $y$  directions. The total thickness of the periodic stack is  $L = N \cdot (d_1 + d_2)$ , where  $N$  is the number of periods (unit cells). The PhC is surrounded by the linear homogeneous medium with the dielectric permittivity  $\epsilon_a$  at  $z \leq 0$  and  $z \geq L$ . It is illuminated by two plane waves of frequencies  $\omega_1$  and  $\omega_2$  incident at angles  $\Theta_{i1}$  and  $\Theta_{i2}$ , respectively, as shown in Figure 1.

Each layer has 6 mm class of anisotropy and is described by the linear dielectric permittivity tensor  $\hat{\epsilon} = (\epsilon_{xx}, \epsilon_{xx}, \epsilon_{zz})$  and the second-order nonlinear susceptibility tensor  $\hat{\chi}$ :

$$\hat{\chi} = \begin{pmatrix} 0 & 0 & 0 & 0 & \chi_{xxz} & 0 \\ 0 & 0 & 0 & \chi_{xxz} & 0 & 0 \\ \chi_{zxx} & \chi_{zxx} & \chi_{zzz} & 0 & 0 & 0 \end{pmatrix}. \quad (1)$$

Owing to the structure uniformity in the  $xOy$  plane and symmetry of the tensors  $\hat{\epsilon}$  and  $\hat{\chi}$ , we can assume without loss of generality that  $\partial/\partial y = 0$ . In this case, Maxwell's equations for TE and TM polarised waves are separated and can be treated independently. Only TM waves are considered in the rest of the paper (the analysis of TE waves is similar and somewhat simpler being unaffected by anisotropy of  $\hat{\chi}$  defined in (1)). The electric  $E_{x,z}$  and magnetic  $H_y$  field components of TM waves in each layer satisfy the following system of nonlinear equations:

$$\begin{aligned} \frac{\partial E_{xj}}{\partial z} - \frac{\partial E_{zj}}{\partial x} + \frac{1}{c} \frac{\partial H_{yj}}{\partial t} &= 0, \\ \frac{\partial H_{yj}}{\partial z} + \frac{\epsilon_{xxj}}{c} \frac{\partial E_{xj}}{\partial t} &= -\frac{4\pi}{c} \chi_{xxzj} \frac{\partial}{\partial t} (E_{xj} E_{zj}), \\ \frac{\partial H_{yj}}{\partial x} - \frac{\epsilon_{zzj}}{c} \frac{\partial E_{zj}}{\partial t} &= \frac{4\pi}{c} \left[ \chi_{zxxj} \frac{\partial}{\partial t} (E_{xj} E_{xj}) + \chi_{zzzj} \frac{\partial}{\partial t} (E_{zj} E_{zj}) \right], \end{aligned} \quad (2)$$

where  $j = 1, 2$  denotes the respective constituent nonlinear layer in the binary unit cell,  $c$  is the speed of light.

In the approximation of weak nonlinearity, the scattering characteristics of the TM waves can be obtained separately at each frequency by the harmonic balance method. Thus at the combinatorial frequency  $\omega_3 = \omega_1 + \omega_2$ , the system of nonlinear equations (2) can be reduced to inhomogeneous

Helmholtz equation for  $H_{yj}$  in each nonlinear anisotropic dielectric layer

$$\begin{aligned} & \frac{\partial^2 H_{yj}(\omega_3)}{\epsilon_{xxj} \partial z^2} + \left( k_3^2 - \frac{k_{x3}^2}{\epsilon_{zzj}} \right) H_{yj}(\omega_3) \\ &= 4\pi k_3 \left[ 2 \frac{\partial}{\partial x} \left( \frac{\chi_{zxxj}}{\epsilon_{zzj}} E_{xj}(\omega_1) E_{xj}(\omega_2) + \frac{\chi_{zzzj}}{\epsilon_{zzj}} E_{zj}(\omega_1) E_{zj}(\omega_2) \right) \right. \\ & \quad \left. - \frac{\chi_{xxzj}}{\epsilon_{xxj}} \frac{\partial}{\partial z} (E_{xj}(\omega_1) E_{zj}(\omega_2) + E_{xj}(\omega_2) E_{zj}(\omega_1)) \right], \end{aligned} \quad (3)$$

where  $k_p = \omega_p/c$ ,  $p = 1, 2, 3$  and  $k_{x3} = k_3 \sqrt{\epsilon_a} \sin \Theta_3$ . Since  $k_{x3}$  must obey the requirement of the waveform invariance along the layer interfaces, the phase synchronism condition in the three-wave mixing process [15] is enforced here in the following form:

$$k_{x3} = k_{x1} + k_{x2}, \quad (4)$$

where  $k_{x1,2} = k_{1,2} \sqrt{\epsilon_a} \sin \Theta_{i1,i2}$ . In order to make the solution procedure more transparent, we assume here that both incident pump waves of frequencies  $\omega_{1,2}$  have the same amplitudes equal to unity. Generalisation to the case of unequal pump wave amplitudes is straightforward but the resulting expressions are more cumbersome.

The full solution of inhomogeneous equation (3) is composed of the partial and general solutions which can be represented in the form

$$\begin{aligned} H_{yj}^{(n)}(\omega_3, x, z) &= \left( A_j^{n+} e^{ik_{zLj}^{(3)} z} + A_j^{n-} e^{-ik_{zLj}^{(3)} z} + D_{1j}^{n+} e^{ik_{zLj}^{(1)} z} \right. \\ & \quad \left. + D_{2j}^{n+} e^{-ik_{zLj}^{(2)} z} + D_{1j}^{n-} e^{ik_{zLj}^{(2)} z} + D_{2j}^{n-} e^{-ik_{zLj}^{(2)} z} \right) \\ & \quad \times e^{-i\omega_3 t + ik_{x3} x}. \end{aligned} \quad (5)$$

Here the amplitude coefficients  $A_j^{n\pm}$  are associated with the general solution of (3) and are determined by means of enforcing the continuity conditions for the tangential field components at the layer interfaces. The coefficients  $D_{1j,2j}^{n\pm}$  represent the partial solution of inhomogeneous equation (3) and are expressed in terms of the refracted field

amplitudes in each layer at the pump wave frequencies  $\omega_1$  and  $\omega_2$ :

$$\begin{aligned} D_{1j}^{n+} &= \alpha_j \beta_j \frac{B_j^{n+}(\omega_1) B_j^{n+}(\omega_2)}{(k_{zLj}^+)^2 - (k_{zLj}^{(3)})^2}, \\ D_{2j}^{n+} &= \alpha_j \beta_j \frac{B_j^{n-}(\omega_1) B_j^{n-}(\omega_2)}{(k_{zLj}^+)^2 - (k_{zLj}^{(3)})^2}, \\ D_{1j}^{n-} &= \alpha_j \gamma_j \frac{B_j^{n+}(\omega_1) B_j^{n-}(\omega_2)}{(k_{zLj}^-)^2 - (k_{zLj}^{(3)})^2}, \\ D_{2j}^{n-} &= \alpha_j \gamma_j \frac{B_j^{n-}(\omega_1) B_j^{n+}(\omega_2)}{(k_{zLj}^-)^2 - (k_{zLj}^{(3)})^2}, \\ \alpha_j &= \frac{4\pi}{\epsilon_{zzj}} \frac{k_3}{k_1 k_2}, \\ \beta_j &= -k_{zLj}^+ k_{x1} k_{zLj}^{(2)} \frac{\chi_{xxzj}}{\epsilon_{xxj}} \\ & \quad - k_{x3} \left( \frac{\chi_{zxxj}}{\epsilon_{xxj}} k_{zLj}^{(1)} k_{zLj}^{(2)} + \frac{\chi_{zzzj} \epsilon_{xxj}}{\epsilon_{zzj}^2} k_{x1} k_{x2} \right) \\ \gamma_j &= k_{zLj}^- k_{x1} k_{zLj}^{(2)} \frac{\chi_{xxzj}}{\epsilon_{xxj}} \\ & \quad + k_{x3} \left( \frac{\chi_{zxxj}}{\epsilon_{xxj}} k_{zLj}^{(1)} k_{zLj}^{(2)} - \frac{\chi_{zzzj} \epsilon_{xxj}}{\epsilon_{zzj}^2} k_{x1} k_{x2} \right), \\ k_{zLj}^{\pm} &= k_{zLj}^{(1)} \pm k_{zLj}^{(2)}, \quad k_{zLj}^{(p)} = \sqrt{\left( k_p^2 - \frac{k_{xp}^2}{\epsilon_{zzj}} \right) \epsilon_{xxj}}, \\ & \quad p = 1, 2, 3; \quad j = 1, 2. \end{aligned} \quad (6)$$

Here  $k_{zLj}^{(p)}$  are the  $z$  components of the wave vectors in  $j$ th layer at frequencies  $\omega_p$ , respectively; superscript  $n$  identifies the period number in the stack. The coefficients  $B_j^{n\pm}(\omega_{1,2})$  are the field amplitudes inside the  $j$ th layer of the  $n$ th period at the incident wave frequencies  $\omega_1$  and  $\omega_2$ . These coefficients are obtained by imposing the continuity conditions for the tangential field components of each pump wave of frequencies  $\omega = \omega_{1,2}$  independently at the layer interfaces and can be represented in the form:

$$\begin{aligned} & B_j^{n\pm}(\omega_p) \\ &= \left( s_{11j}^{(n)}(\omega_p) \pm \frac{k_p}{k_{zLj}^{(p)}} \epsilon_{xxj} s_{21j}^{(n)}(\omega_p) \right) (1 + R(\omega_p)) + \frac{k_{za}^{(p)}}{k_p \epsilon_a} \left( s_{12j}^{(n)}(\omega_p) \pm \frac{k_p}{k_{zLj}^{(p)}} \epsilon_{xxj} s_{22j}^{(n)}(\omega_p) \right) (1 - R(\omega_p)), \\ & R(\omega_p) \\ &= \frac{M_{11}(\omega_p) + (k_{za}^{(p)} / (\epsilon_a k_p)) M_{12}(\omega_p) - (\epsilon_a k_p / k_{za}^{(p)}) M_{21}(\omega_p) - M_{22}(\omega_p)}{M_{11}(\omega_p) + (k_{za}^{(p)} / (\epsilon_a k_p)) M_{12}(\omega_p) + (\epsilon_a k_p / k_{za}^{(p)}) M_{21}(\omega_p) + M_{22}(\omega_p)}; \quad p = 1, 2, \end{aligned} \quad (7)$$

where  $k_{za}^{(p)} = k_p \sqrt{\epsilon_a} \cos \Theta_{ip}$  is the longitudinal wavenumber in the surrounding medium and  $R(\omega_p)$  is the reflection coefficient at frequency  $\omega_p$ . The transfer matrix  $\widehat{M}(\omega_p)$  of the finite linear periodic structure containing  $N$  periods can be expressed in terms of the transfer matrix  $\widehat{m}(\omega_p) = \widehat{m}_{L1}(\omega_p) \widehat{m}_{L2}(\omega_p)$  of a single period using Abeles theorem [21]:  $\widehat{M}(\omega_p) = (\widehat{m}(\omega_p))^N$ , where  $\widehat{m}_{L1, L2}(\omega_p)$  are the transfer matrices of the constituent layers of the unit cell. The matrices  $\widehat{s}_j^{(n)}$  in (7) are defined as follows:  $\widehat{s}_1^{(n)}(\omega_p) = (\widehat{m}(\omega_p)^{n-1})^{-1}$  and  $\widehat{s}_2^{(n)}(\omega_p) = (\widehat{m}(\omega_p)^{n-1} \cdot \widehat{m}_{L1}(\omega_p))^{-1}$ .

To satisfy the boundary conditions at the interfaces of the nonlinear layers at the combinatorial frequency  $\omega_3$ , the TMM procedure has to be modified in order to take into account the contribution of the frequency mixing products generated in each layer and subsequently refracted through the periodic stack. Namely, the fields at interfaces of the first layer in the binary unit cell are related as follows:

$$\begin{pmatrix} H_{y1}^{(1)}(\omega_3, x, 0) \\ E_{x1}^{(1)}(\omega_3, x, 0) \end{pmatrix} = \widehat{m}_{L1}(\omega_3) \begin{pmatrix} H_{y1}^{(1)}(\omega_3, x, d_1) \\ E_{x1}^{(1)}(\omega_3, x, d_1) \end{pmatrix} + \widehat{m}_{L1}(\omega_3) \begin{pmatrix} \tau_{11}(d_1) \\ \xi_{11}(d_1) \end{pmatrix}. \quad (8)$$

Similarly, for the second layer we obtain

$$\begin{pmatrix} H_{y1}^{(1)}(\omega_3, x, d_1) \\ E_{x1}^{(1)}(\omega_3, x, d_1) \end{pmatrix} = \widehat{m}_{L2}(\omega_3) \begin{pmatrix} H_{y2}^{(1)}(\omega_3, x, d_1 + d_2) \\ E_{x2}^{(1)}(\omega_3, x, d_1 + d_2) \end{pmatrix} + \widehat{m}_{L2}(\omega_3) \begin{pmatrix} \tau_{21}(d_1 + d_2) \\ \xi_{21}(d_1 + d_2) \end{pmatrix}. \quad (9)$$

Thus, (8) and (9) define the interrelation between the fields at the external interfaces of the constituent unit cell. After applying the boundary conditions sequentially to all  $N$  unit cells, the fields at the stack outer interfaces can be represented in the form:

$$\begin{pmatrix} H_{y1}^{(1)}(\omega_3, x, 0) \\ E_{x1}^{(1)}(\omega_3, x, 0) \end{pmatrix} = \widehat{M}(\omega_3) \begin{pmatrix} H_{y2}^{(N)}(\omega_3, x, L) \\ E_{x2}^{(N)}(\omega_3, x, L) \end{pmatrix} + \widehat{m}_{L1}(\omega_3) \begin{pmatrix} \tau_{11}(d_1) \\ \xi_{11}(d_1) \end{pmatrix} + \widehat{m}_{L1}(\omega_3) \widehat{m}_{L2}(\omega_3) \begin{pmatrix} \tau_{21}(d_1 + d_2) \\ \xi_{21}(d_1 + d_2) \end{pmatrix} + \dots + \widehat{M}(\omega_3) \begin{pmatrix} \tau_{2N}(L) \\ \xi_{2N}(L) \end{pmatrix}. \quad (10)$$

Here  $\tau_{jn}$  and  $\xi_{jn}$  contain the terms proportional to coefficients  $D_{1j, 2j}^{n\pm}$ ,  $j = 1, 2$ :

$$\begin{aligned} \tau_{jn} &= D_{1j}^{n+} \sigma_{1j}^+ + D_{2j}^{n+} \sigma_{1j}^- + D_{1j}^{n-} \sigma_{2j}^+ + D_{2j}^{n-} \sigma_{2j}^-, \\ \xi_{jn} &= D_{1j}^{n+} \sigma_{3j}^+ + D_{2j}^{n+} \sigma_{3j}^- + D_{1j}^{n-} \sigma_{4j}^+ + D_{2j}^{n-} \sigma_{4j}^-, \\ \sigma_{1j}^\pm &= \cos k_{zLj}^{(3)} d_j \pm i \frac{k_{zLj}^+}{k_{zLj}^{(3)}} \sin k_{zLj}^{(3)} d_j - e^{\pm i k_{zLj}^+ d_j}, \\ \sigma_{2j}^\pm &= \cos k_{zLj}^{(3)} d_j \pm i \frac{k_{zLj}^-}{k_{zLj}^{(3)}} \sin k_{zLj}^{(3)} d_j - e^{\pm i k_{zLj}^- d_j}, \\ \sigma_{3j}^\pm &= \frac{c}{\omega_3} \frac{k_{zLj}^{(3)}}{\epsilon_{xxj}} \left( i \sin k_{zLj}^{(3)} d_j \pm \frac{k_{zLj}^+}{k_{zLj}^{(3)}} \cos k_{zLj}^{(3)} d_j \mp \frac{k_{zLj}^+}{k_{zLj}^{(3)}} e^{\pm i k_{zLj}^+ d_j} \right), \\ \sigma_{4j}^\pm &= \frac{c}{\omega_3} \frac{k_{zLj}^{(3)}}{\epsilon_{xxj}} \left( i \sin k_{zLj}^{(3)} d_j \pm \frac{k_{zLj}^-}{k_{zLj}^{(3)}} \cos k_{zLj}^{(3)} d_j \mp \frac{k_{zLj}^-}{k_{zLj}^{(3)}} e^{\pm i k_{zLj}^- d_j} \right). \end{aligned} \quad (11)$$

The magnetic field of frequency  $\omega_3$  emitted from the stack of nonlinear layers into the surrounding homogeneous medium has the form:

$$H_y^a(\omega_3) = e^{-i\omega_3 t + i k_{3z} x} \begin{cases} F_r e^{-i k_{za}^{(3)} z}, & z \leq 0, \\ F_t e^{i k_{za}^{(3)} z}, & z \geq L, \end{cases} \quad (12)$$

where  $k_{za}^{(3)} = \sqrt{k_3^2 \epsilon_a - k_{x3}^2}$  is the longitudinal wave number of the wave at frequency  $\omega_3$  in the homogeneous media and the nonlinear scattering coefficient  $F_r$  and  $F_t$  are determined by enforcing the interface boundary conditions at  $z = 0, L$ .

Finally, by combining (5), (10), and (12) we obtain the sought coefficients  $F_{r,t}$ :

$$\begin{aligned} F_r &= \left( \frac{k_3 \epsilon_a}{k_{za}^{(3)}} (\widehat{\eta}_N)_{21} + (\widehat{\eta}_N)_{22} \right) \lambda_1 - \left( \frac{k_3 \epsilon_a}{k_{za}^{(3)}} (\widehat{\eta}_N)_{11} + (\widehat{\eta}_N)_{12} \right) \lambda_2, \\ F_t &= - \left( \lambda_1 + \lambda_2 \frac{k_3 \epsilon_a}{k_{za}^{(3)}} \right), \end{aligned} \quad (13)$$

where

$$\lambda_p = \frac{1}{\Delta} \sum_{n=1}^N \left[ (\widehat{\eta}'_n)_{p1} \tau_{1n} + (\widehat{\eta}'_n)_{p2} \xi_{1n} + (\widehat{\eta}_n)_{p1} \tau_{2n} + (\widehat{\eta}_n)_{p2} \xi_{2n} \right], \quad p = 1, 2;$$

$$\begin{aligned} \Delta &= (\widehat{\eta}_N)_{11} + (\widehat{\eta}_N)_{22} + \frac{k_{za}^{(3)}}{k_3 \epsilon_a} (\widehat{\eta}_N)_{12} + \frac{k_3 \epsilon_a}{k_{za}^{(3)}} (\widehat{\eta}_N)_{21}; \\ \widehat{\eta}_n &= [\widehat{m}(\omega_3)]^n, \quad \widehat{\eta}'_n = \widehat{\eta}_{n-1} \widehat{m}_{L1}(\omega_3), \quad \widehat{\eta}_N = \widehat{M}(\omega_3). \end{aligned} \quad (14)$$

It is necessary to note that  $F_{r,t}$  in (13) always remain finite inspite of the fact that coefficients  $D_{1j, 2j}^{n\pm}$  have singularity at  $k_{zLj}^\pm = k_{zLj}^{(3)}$ . However, it can be shown that coefficients



$A_j^{\eta\pm}$  in (5) contain exactly the same pole as  $D_{1j,2j}^{\eta\pm}$  at  $\Theta_{i1} = \Theta_{i2}$ , and their combined contribution is finite at all frequencies and incidence angles.

Thus the modified TMM approach presented in this section gives the closed-form expressions for the nonlinear scattering coefficients of the finite PhC composed of the binary nonlinear layers. The obtained analytical formulations not only provide a qualitative insight in the formation of the nonlinear response and the properties of the scattered fields but also enable fast quantitative analysis of the specific PhC configurations.

The results of numerical simulations based upon the analytical solutions obtained here are presented in the next section to illustrate the effects of structure and materials parameters on the properties TM waves of combinatorial frequencies generated by nonlinear PhC in the three-wave mixing process.

### 3. Properties and Mechanisms of Nonlinear Scattering by Finite Periodic Stacks

The analytical solutions for the coefficients  $F_{r,t}$  obtained in the preceding section have allowed us to examine the mechanisms of nonlinear scattering in 1D anisotropic nonlinear PhCs. The effects of the constituent layer parameters, unit cell aspect ratio, and the pump wave frequencies  $\omega_{1,2}$  and incidence angles  $\Theta_{i1,2}$  on the properties of the waves of combinatorial frequency  $\omega_3 = \omega_1 + \omega_2$  generated in the three-wave mixing process have been analysed with the aim of increasing the efficiency of nonlinear processes in the artificial medium.

To illustrate the features of the frequency mixing in the 1D nonlinear anisotropic PhCs, the characteristics of the combinatorial frequency waves are discussed here with the examples of periodic stacks of binary anisotropic dielectric layers of CdS and ZnO described by the tensors  $\hat{\epsilon}$  and  $\hat{\chi}$  (1) with the following parameters [22]:

$$\text{CdS: } \epsilon_{xx1} = 5.382, \epsilon_{zz1} = 5.457 (\alpha_1 = \epsilon_{xx1}/\epsilon_{zz1} = 0.986), \chi_{xxz1} = 2.1 \times 10^{-7}, \chi_{zxx1} = 1.92 \times 10^{-7}, \chi_{zzz1} = 3.78 \times 10^{-7};$$

$$\text{ZnO: } \epsilon_{xx2} = 1.4, \epsilon_{zz2} = 2.6 (\alpha_2 = \epsilon_{xx2}/\epsilon_{zz2} = 0.538), \chi_{xxz2} = 2.82 \times 10^{-8}, \chi_{zxx2} = 2.58 \times 10^{-8}, \chi_{zzz2} = 8.58 \times 10^{-8}.$$

The constituent layer thicknesses are  $d_1 = 0.08$  mm and  $d_2 = 0.05$  mm, unless specifically defined. Exterior of the layer stack in Figure 1 is an air with permittivity  $\epsilon_a = 1$ .

**3.1. Spectral Efficiency of the Combinatorial Frequency Generation.** PhCs are known to be instrumental in enhancing the SHG and THG efficiency by choosing the pump wave frequency close to the PhC band edge. Therefore, it was interesting to explore whether similar facility could be exploited for the combinatorial frequencies generated in the three-wave mixing process. The spectral bands of a periodic stack of binary linear anisotropic dielectric layers have been inferred first from the reflectance  $|R(\omega)|$  of the pump waves. Figure 2 illustrates  $|R(\omega)|$  for the TM wave incident at angle

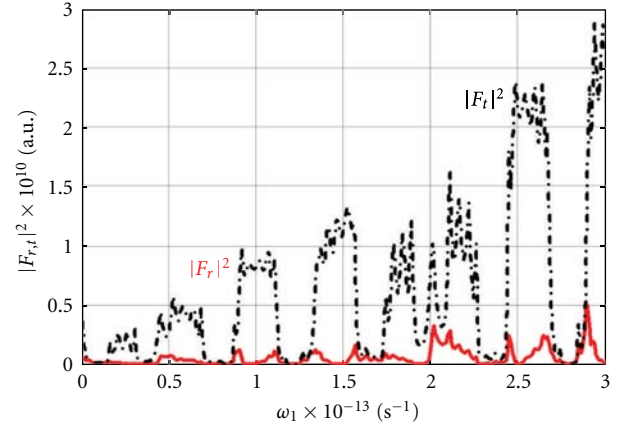


FIGURE 2: Reflectance of plane TM wave incident at  $\Theta_i = 30^\circ$  on the periodic stack of  $N = 7$  binary dielectric layers of thicknesses  $d_1 = 0.08$  mm and  $d_2 = 0.05$  mm.

$\Theta_{i1} = 30^\circ$  on the periodic stack containing  $N = 7$  unit cells. The bandgaps, corresponding to  $|R(\omega)| \approx 1$ , are clearly observable in Figure 2, but it is necessary to note that the respective frequency bands change with the incidence angle and layers' parameters.

The field intensities  $|F_{r,t}|^2$  at the combinatorial frequency  $\omega_3 = \omega_1 + \omega_2$  generated in the same structure are shown in Figure 3 for variable frequency  $\omega_1$  of a pump wave incident at  $\Theta_{i1} = 30^\circ$ , while the frequency  $\omega_2 = 1.135 \times 10^{13} \text{ s}^{-1}$  of the other pump wave, incident at  $\Theta_{i2} = 45^\circ$ , was fixed at the passband edge. Comparison of Figures 2 and 3 demonstrates strong correlation between  $|F_{r,t}|^2$  and  $|R(\omega)|$ . However, in contrast to SHG and THG, the band edges have little effect on the  $\omega_3$  generation efficiency, namely,  $|F_t|^2$  reaches its maxima inside the transparency bands, and only  $|F_r|^2$  exhibits small kinks at the band edges when frequency  $\omega_1$  of the first pump wave varies.

Figure 3 also shows that the peak intensity  $|F_t|^2$  grows with  $\omega_1$  and the efficiency of the frequency conversion is higher when the  $\omega_1$  remains inside the pump wave transparency bands. This effect can be attributed to the increase of the pump wave interaction length at the higher frequencies further assisted by the enhanced mixing efficiency at Wolf-Bragg resonances of Bloch waves in the finite PhCs. It is noteworthy that  $(N-1)$  resonances occur in each transparency band of the  $N$ -cell stack. At these resonances  $|R(\omega)| = 0$  as the stack overall thickness equals an integer number of Bloch half-waves with the wavenumbers  $\bar{k}(\omega)$ , that is,  $N\bar{k}(\omega)(d_1 + d_2) = \pi q$ ,  $q = 0, \pm 1, \pm 2, \dots$ , where  $\bar{k}(\omega)$  is defined by the relation  $\cos \bar{k}(d_1 + d_2) = (m_{11} + m_{22})/2$ ,  $m_{11}$  and  $m_{22}$  are elements of the unit cell transfer matrix  $\hat{m}(\omega)$  defined in connection with (7).

**3.2. Effect of the Stack Thickness.** As indicated in the preceding section, the number  $N$  of stacked unit cells and thickness of the whole stack may have strong impact on the efficiency of harmonic generation in nonlinear PhC. This effect has been predicted by the analytical formulations (13) and

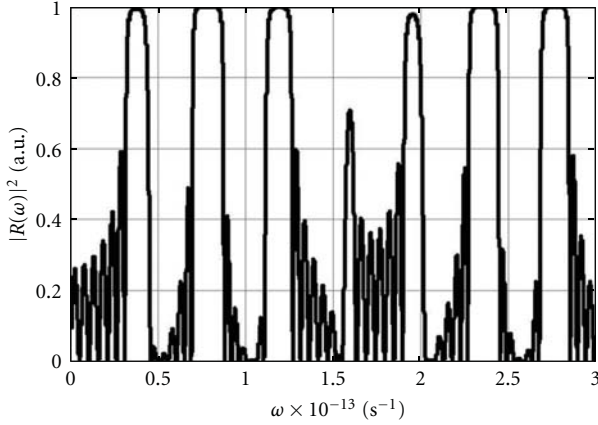


FIGURE 3: The field intensity at frequency  $\omega_3 = \omega_1 + \omega_2$  radiated in the reverse ( $|F_r|^2$ : red solid line) and forward ( $|F_t|^2$ : black dash-dot line) directions of the  $z$ -axis at  $\Theta_{i1} = 30^\circ$ ;  $\Theta_{i2} = 45^\circ$ ,  $N = 7$ ,  $d_1 = 0.08$  mm,  $d_2 = 0.05$  mm, and  $\omega_2 = 1.135 \times 10^{13}$  s $^{-1}$ .

confirmed by the numerical simulations in Figure 4. Indeed, the field intensity  $|F_{r,t}|^2$  exhibits nonmonotonic dependences on the number  $N$  of unit cells in the stack as illustrated by Figure 4 for two different combinatorial frequencies  $\omega_3 = \omega_1 + \omega_2$  (the pump wave frequencies  $\omega_1$  and  $\omega_2$  are close to the PhC band edges in both cases). Indeed, Figure 4(a) shows that  $|F_r|^2$  has maxima at  $N = 32, 57, 89, \dots$ , whereas  $|F_t|^2$  has a higher peak at  $N = 32$  and then follows almost the same pattern as  $|F_r|^2$ . However, at the higher frequency  $\omega_1$ , maxima of  $|F_{r,t}|^2$  occur at  $N = 108$  and  $N = 127$  as shown in Figure 4(b), where the peak values of  $|F_t|^2$  are about two orders of magnitude higher than those in Figure 4(a) and about 20 times larger than for  $|F_r|^2$ . The  $|F_{r,t}|^2$  can also exhibit giant growth and reach their extrema at Wolf-Bragg resonances of very high orders in rather thick stacks with the special combinations of the pump wave frequencies, incidence angles, and the layer parameters as suggested in [13].

**3.3. Effect of the Pump Wave Incidence Angles on the Frequency Mixing Efficiency.** Harmonic generation in 1D PhCs are usually analysed at normal incidence of pump wave on the stacked layers. In the case of combinatorial frequency generation by a pair of pump waves, incident at different angles, an additional degree of freedom exists in realising the phase synchronism and controlling the whole frequency mixing process. To gain insight in the effect of the incidence angle on the combinatorial frequency field intensities,  $|F_{r,t}|^2$  have been simulated at variable incidence angle  $\Theta_{i1}$  and fixed angle  $\Theta_{i2}$  of the respective pump waves and different number of the unit cells in the stack:  $N = 7, 15, 25$ .

Examination of  $|F_{r,t}(\Theta_{i1})|^2$  in Figure 5 shows that when the stack is relatively thin ( $N = 7$ ), both  $|F_r|^2$  and  $|F_t|^2$  exhibit similar behaviour and smoothly vary with  $\Theta_{i1}$ . However, additional resonances arise in the thicker stacks, and the  $|F_{r,t}(\Theta_{i1})|^2$  dependencies qualitatively change. Several factors are responsible for these alterations. At first,

dissimilar reflectance and transmittance of the individual pump waves have significant effect on the ratio of the pump wave amplitudes in the three-wave mixing process. Secondly, angular variations of the PhC transparency bands become more noticeable in the thicker stacks. Finally, the higher order spatial harmonics, which can resonate in thicker stacks, contribute to the combinatorial frequency generation.

Both the reflectance/transmittance of pump waves and the phase synchronism in the mixing process are essentially dependent on the permittivities and anisotropy of the constituent binary layers. Therefore the effect of the constituent layer parameters has been assessed first to discriminate contributions of the aforementioned mechanisms to the combinatorial frequency generation. In order to evaluate the effect of the layer anisotropy, the intensities  $|F_t(\Theta_{i1})|^2$  have been simulated at the modified permittivity ratios  $\epsilon_{xx1}/\epsilon_{zz1} = 2\alpha_1$ ,  $\epsilon_{xx2}/\epsilon_{zz2} = 2\alpha_2$ , and  $\epsilon_{xx1}/\epsilon_{zz1} = \alpha_1/2$ ,  $\epsilon_{xx2}/\epsilon_{zz2} = \alpha_2/2$  and are shown in Figure 6. Comparison of the plots in Figure 5(b) for  $\epsilon_{xx1}/\epsilon_{zz1} = \alpha_1$ ,  $\epsilon_{xx2}/\epsilon_{zz2} = \alpha_2$  with the respective plots in Figure 6 for the modified tensor  $\hat{\epsilon}$  demonstrates that variations of the layer anisotropy qualitatively alter the efficiency of the combinatorial frequency generation. Namely, we can observe that when the layer anisotropy deviates from the specified values of  $\alpha_{1,2}$  in either direction, the combinatorial frequency intensity considerably decreases, from a few times to several orders of magnitude. Furthermore, additional angular undulations of the field intensity occur at several incidence angles, Figure 6, being inflicted by the resonances of the higher order spatial harmonics.

**3.4. Effects of Constituent Layer Thicknesses and Resonance Enhancement of Frequency Conversion.** The stack overall thickness may have profound influence on the frequency mixing efficiency. This can be the result of the increased number of unit cells in the stack as illustrated in Figure 4 or variations in the thicknesses of the constituent layers. The earlier studies have demonstrated that the efficiency of combinatorial frequency generation can significantly vary with thickness of an individual nonlinear layer at the higher order Wolf-Bragg resonances [13]. This suggests that the aspect ratio of the binary layers in the unit cell as well as the unit cell size can provide independent controls of the dispersion and the pump wave reflectance/transmittance. In order to elucidate this effect, the intensities  $|F_{r,t}|^2$  at frequency  $\omega_3 = \omega_1 + \omega_2$  have been analysed at the variable thickness of one layer, while thickness of the other was fixed. Figure 7 displays  $|F_{r,t}|^2$  for a stack with  $N = 7$  unit cells illuminated by the pump waves incident at  $\Theta_{i1} = 38^\circ$  and  $\Theta_{i2} = 45^\circ$  corresponding to the maximal intensity of  $|F_{r,t}|^2$  for the reference unit cell with  $d_1 = 0.08$  mm and  $d_2 = 0.05$  mm in Figure 5. It can be seen that both  $|F_{r,t}|^2$  grow with thickness of the layers in the period, while  $|F_t|^2$  always remains greater than  $|F_r|^2$ . It is necessary to note that the growth rate of the  $|F_{r,t}|^2$  versus  $d_1$  (Figure 7(b)) is higher than that versus  $d_2$  (Figure 7(a)) for nearly an order of magnitude. This effect is directly related to the fact that the components of the nonlinear susceptibility tensor  $\hat{\chi}$  in

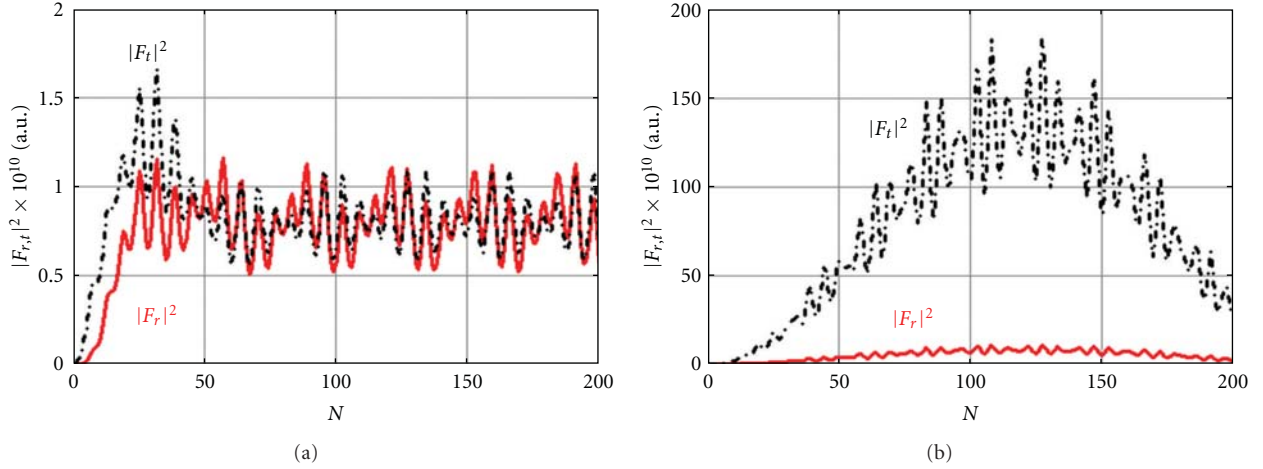


FIGURE 4: Intensities  $|F_{r,t}|^2$  of the field at frequency  $\omega_3 = \omega_1 + \omega_2$  radiated in the reverse ( $|F_r|^2$ : red solid line) and forward ( $|F_t|^2$ : black dash-dot line) directions of the  $z$ -axis at  $\Theta_{i1} = 30^\circ$ ,  $\Theta_{i2} = 45^\circ$ ,  $\omega_2 = 1.135 \times 10^{13} \text{ s}^{-1}$  and (a)  $\omega_1 = 0.4985 \times 10^{13} \text{ s}^{-1}$ ; (b)  $\omega_1 = 1.55 \times 10^{13} \text{ s}^{-1}$ .

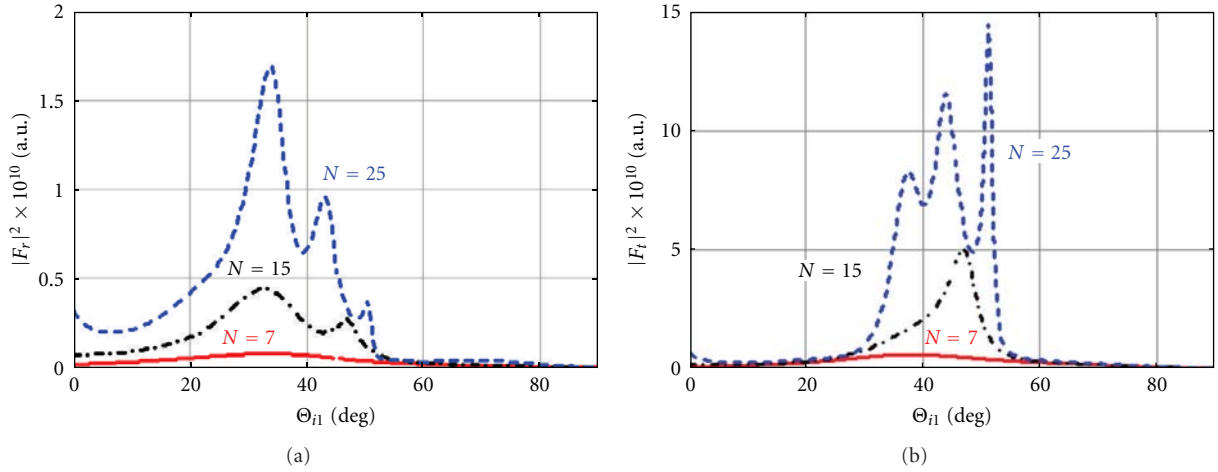


FIGURE 5: The field intensity at frequency  $\omega_3 = \omega_1 + \omega_2$  radiated in the reverse (a) and forward (b) directions of the  $z$ -axis; pump waves of frequencies  $\omega_1 = 0.4585 \times 10^{13} \text{ s}^{-1}$  and  $\omega_2 = 1.135 \times 10^{13} \text{ s}^{-1}$  are incident at  $\Theta_{i2} = 45^\circ$  and variable angle  $\Theta_{i1}$ .

the first layer are an order of magnitude greater than in the second one. Therefore when both layers are thin as compared with the wavelength,  $|F_{r,t}|^2$  are small at the low order Wolf-Bragg resonances. However, when thickness of one of the layers increases, this leads to considerable difference in the  $|F_{r,t}|^2$  undulation frequencies and the growth rates due to substantial dissimilarity of the constitutive parameters of the layers in the unit cell. The additional periodic undulations of  $|F_{r,t}|^2$  can also be attributed to unequal variations of the reflection coefficients  $R(\omega_{1,2})$  of the incident pump waves which cause the pump wave amplitude and phase disbalance in the mixing process.

The analytical study of nonlinear scattering by an isolated anisotropic dielectric slab in [13] has revealed that the efficiency of the combinatorial frequency generation can be increased for several orders of magnitude at the high-order

Wolf-Bragg resonances. In particular, in the CdS slab with the parameters  $\hat{\epsilon}_1$  and  $\hat{\chi}_1$  defined at the beginning of this section,  $|F_{r,t}|^2$  reaches the global maxima at the thickness  $d_1 = 1.695 \text{ mm}$ , frequency ratio  $\omega_1/\omega_2 = 1.911$ , the pump wave incidence angles  $\Theta_{i1} = 30^\circ$ ,  $\Theta_{i2} = 60^\circ$ . Similar analysis has been performed here for the periodic stacks containing  $N = 7$  unit cells with the thick binary layers of CdS and ZnO. The simulation results in Figure 8 shows that the higher order Wolf-Bragg resonances in individual layers create additional modulation of the  $|F_{r,t}|^2$  magnitude and the peak intensity is reached at  $d_2 = 1.35 \text{ mm}$ ,  $4.05 \text{ mm}$  and multiples of these thicknesses. In contrast to the case of an isolated layer, there is no full cancellation of the combinatorial frequency generation at the Wolf-Bragg resonances in the layer 2. Therefore when  $d_2$  changes,  $|F_{r,t}|^2$  vary about the same median level determined by the layer of thickness  $d_1$ .

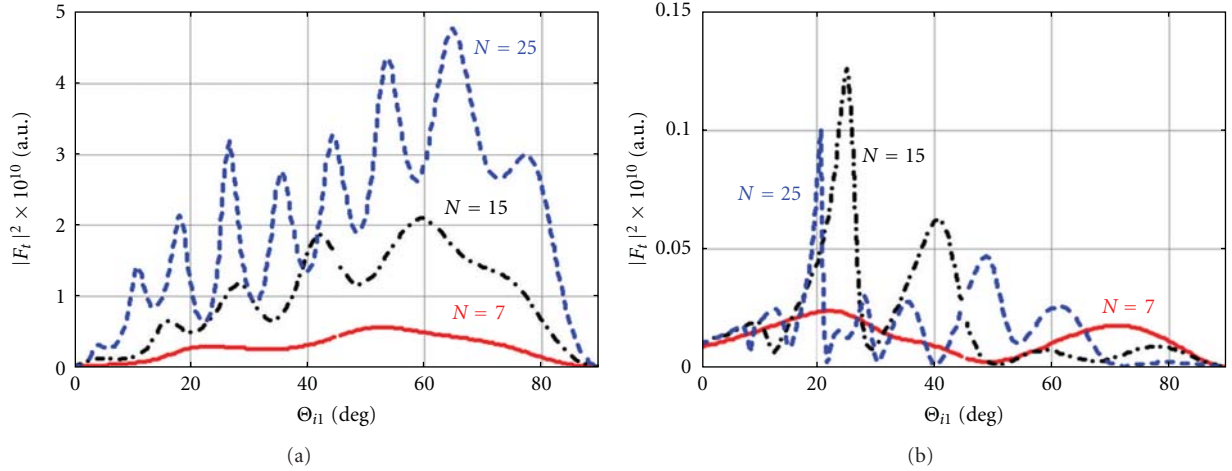


FIGURE 6: The field intensity at frequency  $\omega_3 = \omega_1 + \omega_2$  radiated in the forward direction of the  $z$ -axis; pump waves of frequencies  $\omega_1 = 0.4585 \times 10^{13} \text{ s}^{-1}$  and  $\omega_2 = 1.135 \times 10^{13} \text{ s}^{-1}$  are incident at  $\Theta_{i2} = 45^\circ$  and variable angle  $\Theta_{i1}$ ; the constituent binary layers have the modified anisotropy (a)  $\epsilon_{xx1}/\epsilon_{zz1} = 2\alpha_1$  and  $\epsilon_{xx2}/\epsilon_{zz2} = 2\alpha_2$ ; (b)  $\epsilon_{xx1}/\epsilon_{zz1} = \alpha_1/2$  and  $\epsilon_{xx2}/\epsilon_{zz2} = \alpha_2/2$ .

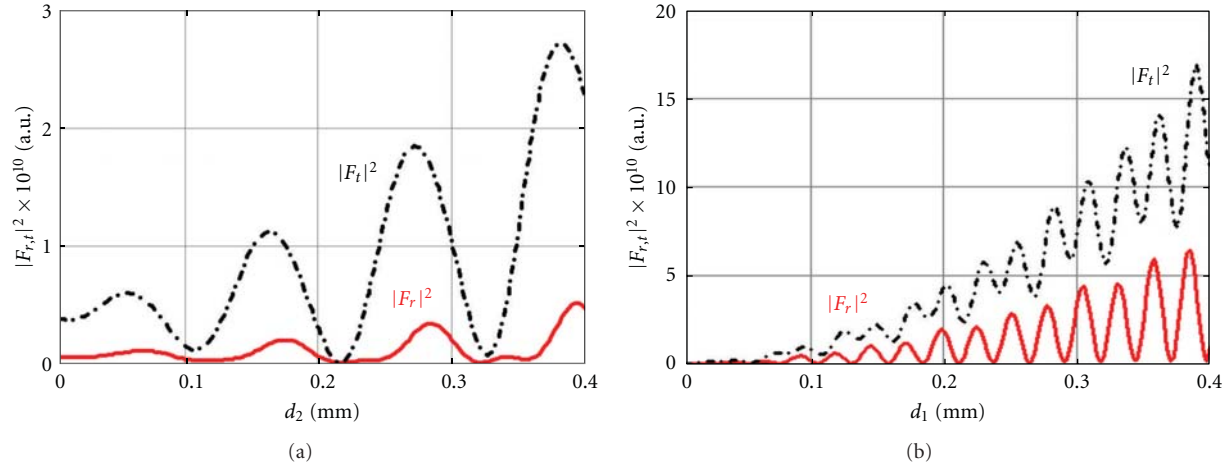


FIGURE 7: Intensities  $|F_{r,t}|^2$  of the field at frequency  $\omega_3 = \omega_1 + \omega_2$  and the pump waves of frequencies  $\omega_1 = 0.4585 \times 10^{13} \text{ s}^{-1}$  and  $\omega_2 = 1.135 \times 10^{13} \text{ s}^{-1}$ ;  $\Theta_{i1} = 38^\circ$ ,  $\Theta_{i2} = 45^\circ$ ,  $N = 7$ ; (a)  $d_1 = 0.08 \text{ mm}$ ; (b)  $d_2 = 0.05 \text{ mm}$ .

**3.5. Effect of Loss on the Three-Wave Mixing Process in the Periodic Stacks of Binary Layers.** The combinatorial frequency generation in the periodic stacks of binary layers discussed so far has been based upon the analysis of the lossless structures. To estimate the effect of dissipation on  $|F_{r,t}|^2$ , the structures with the same parameters as in Figures 2 and 3 have been simulated in the cases of imperfect layers with the loss tangents  $\text{tg}\delta_{xx,zz} = 0.01, 0.1$ . Comparison of the plots in Figures 9 and 10 with the respective results for the lossless cases in Figures 2 and 3 shows that dissipation strongly affects both the reflection coefficients  $R(\omega_{1,2})$  of the pump waves and the intensities of  $|F_{r,t}|^2$  of the generated combinatorial frequencies. First of all, this effect is caused by the lower reflection coefficients  $R(\omega_{1,2})$  of the pump waves (cf. Figures 2 and 9). In contrast to the lossless case in Figure 3, unequal dissipation of the pump waves in the nonlinear layers of the periodic structure entails an

additional disbalance in the three-wave mixing process which further reduces the efficiency of the combinatorial frequency generation, as seen in Figure 10. Moreover, in the case of higher losses ( $\text{tg}\delta_{xx,zz} = 0.1$ , Figure 10(b)), the combined effect of the pump wave dissipation and attenuation of the mixing products passing through the stack causes dramatic reduction of the  $|F_t|^2$  peak values, which become nearly an order of magnitude smaller than  $|F_r|^2$ .

The effect of loss on the intensity  $|F_{r,t}(\omega_3)|^2$  of the combinatorial frequency generation in the stack of thick layers with variable thickness is illustrated in Figure 11 for the structure with the same parameters as in Figure 8. Comparison of Figures 8 and 11 shows that in the presence of loss, both the median and the first peak levels of the  $|F_{r,t}(\omega_3)|^2$  decrease for about 3 times for  $|F_r|^2$  and 5 times for  $|F_t|^2$ . When thickness of the second layer increases the higher order resonance peaks of  $|F_t|^2$  progressively decay



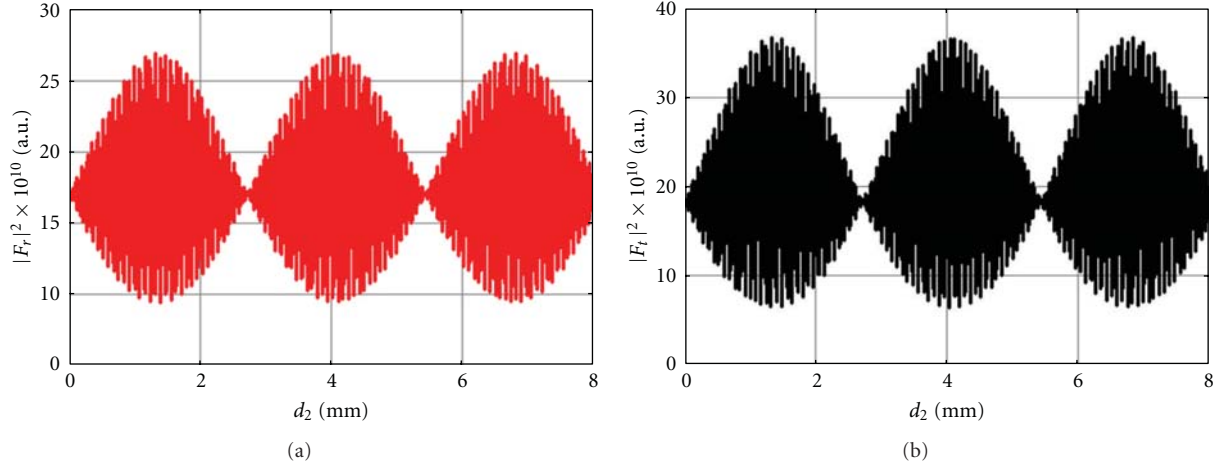


FIGURE 8: Intensities  $|F_{r,t}|^2$  of the field at frequency  $\omega_3 = \omega_1 + \omega_2$  radiated from the stack of the layers in the reverse (a) and forward (b) directions of the  $z$ -axis at  $N = 7$ ,  $d_1 = 1.695$  mm,  $\Theta_{i1} = 30^\circ$ ,  $\Theta_{i2} = 60^\circ$  and  $\omega_1 = 4.982 \times 10^{13} \text{ s}^{-1}$ ,  $\omega_2 = 2.607 \times 10^{13} \text{ s}^{-1}$ .

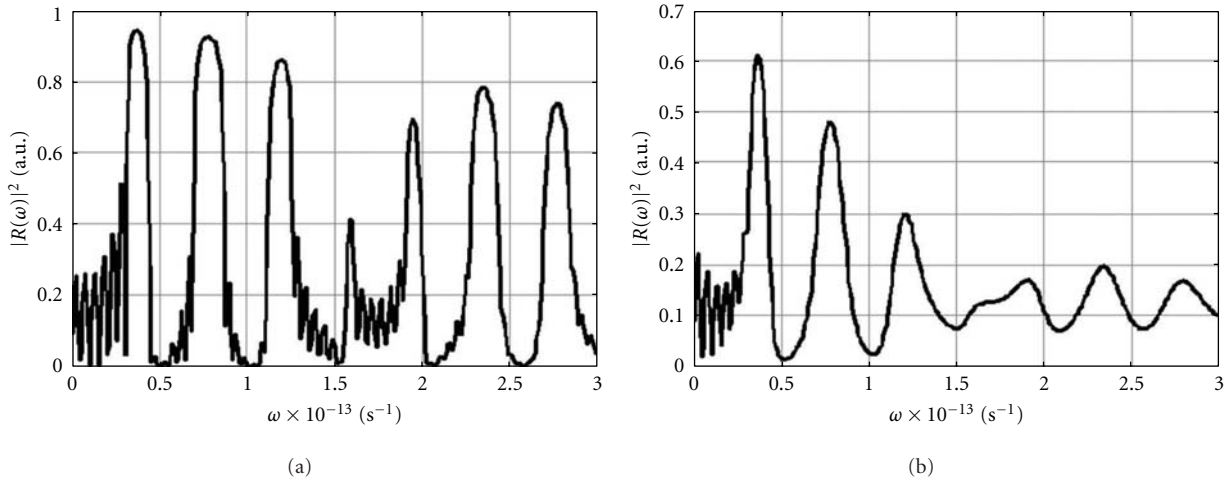


FIGURE 9: Reflectance of TM wave incident at  $\Theta_i = 30^\circ$  on the periodic stack containing  $N = 7$  unit cells with the dielectric layers of thicknesses  $d_1 = 0.08$  mm,  $d_2 = 0.05$  mm and (a)  $\text{tg}\delta_{xx,zz} = 0.01$ , (b)  $\text{tg}\delta_{xx,zz} = 0.1$ .

faster than the peak values of  $|F_r|^2$  as evidenced by Figure 11. These results show that the strong enhancement of the combinatorial frequency generation efficiency at the high order Wolf-Bragg resonances is feasible at the practical level of dissipation loss.

#### 4. Conclusions

The properties and mechanisms of the combinatorial frequency generation by periodic stacks of binary nonlinear anisotropic dielectric layers have been analysed. The closed-form solutions for the nonlinear scattering coefficients have been obtained in the approximation of the three-wave mixing process in the presence of weak polarisation nonlinearity. The effects of the structure parameters and the

incident pump wave characteristics on the efficiency of the combinatorial frequency generation have been investigated in detail. The performed parametric study has shown that in contrast to SHG and THG in the PhCs, the spectral band edges of the binary layer stacks do not improve the combinatorial frequency generation efficiency for the refracted waves. Alternatively, it is shown that the frequency conversion efficiency can be significantly enhanced at Wolf-Bragg resonances occurring at the appropriate combinations of the pump wave frequencies, incidence angles, and the layers' constitutive parameters. The effects of the individual parameters on the frequency mixing efficiency have been discussed in detail for the lossless and lossy constitutive layers in the periodic stacks. It has been demonstrated that the combinatorial frequency generation efficiency can be dramatically increased at the higher order Wolf-Bragg



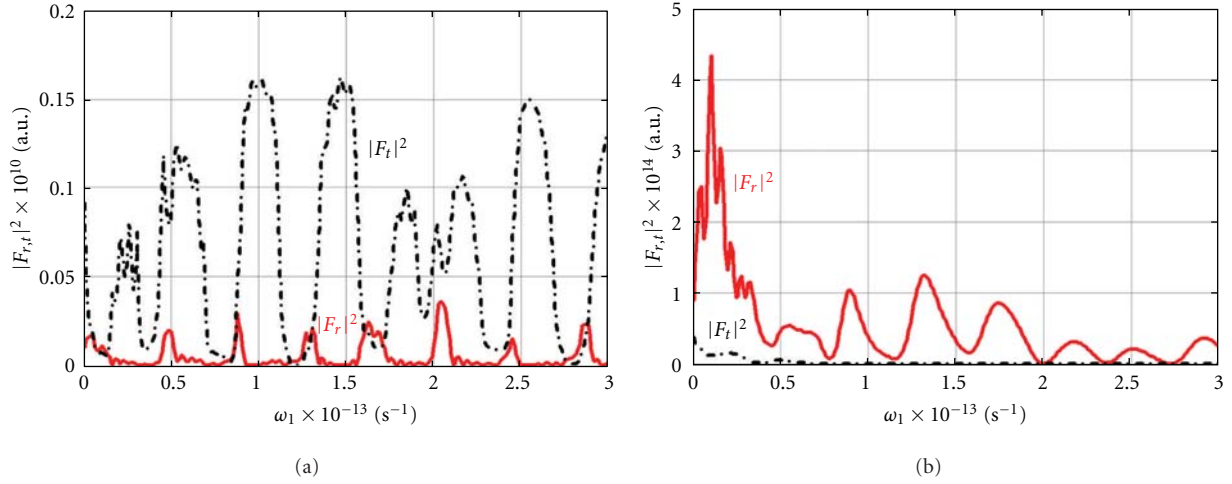


FIGURE 10: The field intensity at frequency  $\omega_3 = \omega_1 + \omega_2$  radiated in the reverse ( $|F_r|^2$ : red solid line) and forward ( $|F_t|^2$ : black dash-dot line) directions of the  $z$ -axis at  $\Theta_{i1} = 30^\circ$ ,  $\Theta_{i2} = 45^\circ$ ,  $N = 7$ ,  $d_1 = 0.08$  mm,  $d_2 = 0.05$  mm,  $\omega_2 = 1.135 \times 10^{13}$  s $^{-1}$  and (a)  $\text{tg}\delta_{xx,zz} = 0.01$ , (b)  $\text{tg}\delta_{xx,zz} = 0.1$ .

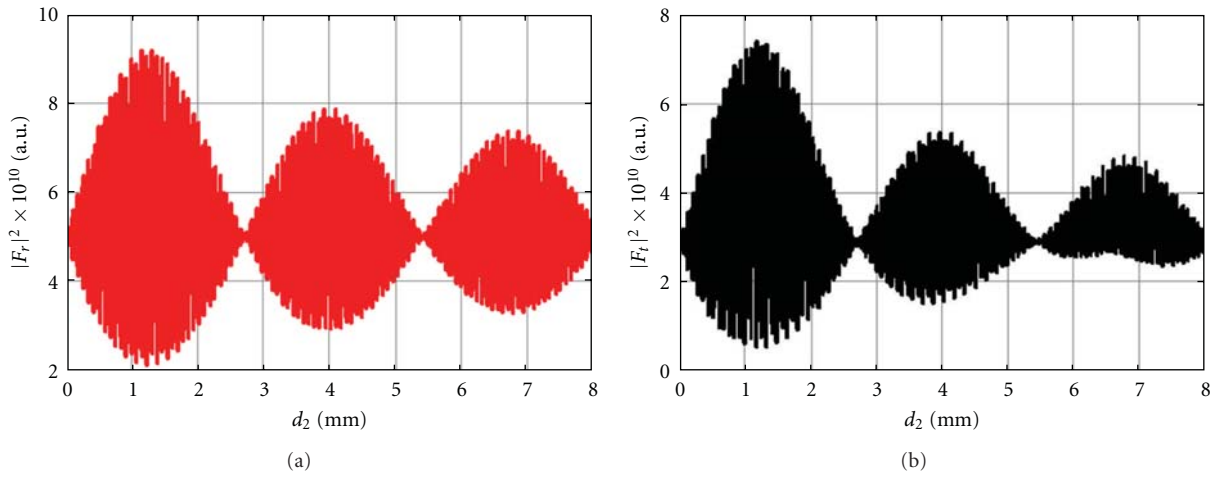


FIGURE 11: Intensities  $|F_{r,t}|^2$  of the field at frequency  $\omega_3 = \omega_1 + \omega_2$  radiated from the periodic stack with  $N = 7$  unit cells toward the reverse (a) and forward (b) directions of the  $z$ -axis at  $\Theta_{i1} = 30^\circ$ ,  $\Theta_{i2} = 60^\circ$  and  $\omega_1 = 4.982 \times 10^{13}$  s $^{-1}$ ,  $\omega_2 = 2.607 \times 10^{13}$  s $^{-1}$ ,  $\text{tg}\delta_{xx,zz} = 0.001$ .

resonances in the stacks with thick constitutive layers. The performed analysis provides insight in the main features of the combinatorial frequency generation by the periodic stacks of binary nonlinear anisotropic dielectric layers.

## Acknowledgment

This work has been performed in the framework of the Project PEARL supported by the FP7 Marie Curie IIF Grant 255110.

## References

- [1] M. Centini, C. Sibilia, M. Scalora et al., "Dispersive properties of finite, one-dimensional photonic band gap structures: applications to nonlinear quadratic interactions," *Physical Review E*, vol. 60, no. 4, pp. 4891–4898, 1999.
- [2] Y. Jeong and B. Lee, "Matrix analysis for layered quasi-phase-matched media considering multiple reflection and pump wave depletion," *IEEE Journal of Quantum Electronics*, vol. 35, no. 2, pp. 162–172, 1999.
- [3] X. Luo and T. Ishihara, "Mode-coexistent phase match condition for second harmonic generation in photonic crystal slabs consisting of centrosymmetric materials," *Optics Communications*, vol. 242, no. 1–3, pp. 147–154, 2004.
- [4] T. V. Murzina, F. Y. Sychev, E. M. Kim et al., "One-dimensional photonic crystals based on porous  $n$ -type silicon," *Journal of Applied Physics*, vol. 98, no. 12, Article ID 123702, pp. 1–4, 2005.
- [5] M.-L. Ren and Z. Y. Li, "Exact iterative solution of second harmonic generation in quasi-phase-matched structures," *Optics Express*, vol. 18, no. 7, pp. 7288–7299, 2010.
- [6] J.-J. Li, Z. Y. Li, and D. Z. Zhang, "Second harmonic generation in one-dimensional nonlinear photonic crystals solved by the transfer matrix method," *Physical Review E*, vol. 75, no. 5, Article ID 056606, 2007.

- [7] J. Yuan, "Computing for second harmonic generation in one-dimensional nonlinear photonic crystals," *Optics Communications*, vol. 282, no. 13, pp. 2628–2633, 2009.
- [8] J. W. Haus, R. Viswanathan, M. Scalora, A. G. Kalocsai, J. D. Cole, and J. Theimer, "Enhanced second-harmonic generation in media with a weak periodicity," *Physical Review A*, vol. 57, no. 3, pp. 2120–2128, 1998.
- [9] Y. Dumeige, P. Vidakovic, S. Sauvage et al., "Enhancement of second-harmonic generation in a one-dimensional semiconductor photonic band gap," *Applied Physics Letters*, vol. 78, no. 20, pp. 3021–3023, 2001.
- [10] G. D'Aguanno, M. Centini, M. Scalora et al., "Photonic band edge effects in finite structures and applications to X(2) interactions," *Physical Review E*, vol. 64, no. 1, pp. 016609/1–016609/9, 2001.
- [11] J. Li, Z. Li, Y. Sheng, and D. Zhang, "Giant enhancement of second harmonic generation in poled ferroelectric crystals," *Applied Physics Letters*, vol. 91, no. 2, Article ID 022903, pp. 1–3, 2007.
- [12] Y. Dumeige, I. Sagnes, P. Monnier et al., "Phase-matched frequency doubling at photonic band edges: efficiency scaling as the fifth power of the length," *Physical Review Letters*, vol. 89, no. 4, pp. 043901/1–043901/4, 2002.
- [13] O. V. Shramkova and A. G. Schuchinsky, "Resonant three-wave interaction in the nonlinear anisotropic dielectric slabs," in *Proceedings of the 5th International Congress on Advanced Electromagnetic Materials in Microwaves and Optics (Metamaterials '11)*, pp. 757–759, Barcelona, Spain, October 2011.
- [14] M. Born and E. Wolf, *Principles of Optics*, Pergamon Press, Oxford, UK, 1968.
- [15] N. Blombergen, *Nonlinear Optics: A Lecture Note*, Benjamin, New York, NY, USA, 1965.
- [16] J. M. Bendickson, J. P. Dowling, and M. Scalora, "Analytic expressions for the electromagnetic mode density infinite, one-dimensional, photonic band-gap structures," *Physical Review E*, vol. 53, no. 4, pp. 4107–4121, 1996.
- [17] Y. Jeong and B. Lee, "Matrix analysis for layered quasi-phase-matched media considering multiple reflection and pump wave depletion," *IEEE Journal of Quantum Electronics*, vol. 35, no. 2, pp. 162–172, 1999.
- [18] J.-J. Li, Z. Y. Li, and D. Z. Zhang, "Second harmonic generation in one-dimensional nonlinear photonic crystals solved by the transfer matrix method," *Physical Review E*, vol. 75, no. 5, Article ID 056606, pp. 1–7, 2007.
- [19] P. Szczepanski, T. Osuch, and Z. Jaroszewicz, "Modeling of amplification and light generation in one-dimensional photonic crystal using a multiwavelength transfer matrix approach," *Applied Optics*, vol. 48, no. 28, pp. 5401–5406, 2009.
- [20] J.-J. Li, Z. Y. Li, and D. Z. Zhang, "Nonlinear frequency conversion in two-dimensional nonlinear photonic crystals solved by a plane-wave-based transfer-matrix method," *Physical Review B*, vol. 77, no. 19, Article ID 195127, pp. 1–5, 2008.
- [21] F. G. Bass and A. A. Bulgakov, *Kinetic and Electrodynamical Phenomena in Classical and Quantum Semiconductor Superlattices*, Nova Science, New York, NY, USA, 1997.
- [22] A. Yariv and P. Yeh, *Waves in Crystals: Propagation and Control of Laser Radiation*, Wiley, New York, NY, USA, 1984.

## Research Article

# Laser Writing of Multiscale Chiral Polymer Metamaterials

**E. P. Furlani,<sup>1,2,3</sup> H. S. Jee,<sup>2,3</sup> H. S. Oh,<sup>3</sup> A. Baev,<sup>3</sup> and P. N. Prasad<sup>2,3,4</sup>**

<sup>1</sup> Department of Chemical and Biological Engineering, University at Buffalo SUNY, Buffalo, NY 14260, USA

<sup>2</sup> Department of Electrical Engineering, University at Buffalo SUNY, Buffalo, NY 14260, USA

<sup>3</sup> Institute for Lasers, Photonics and Biophotonics, University at Buffalo SUNY, Buffalo, NY 14260, USA

<sup>4</sup> Department of Chemistry, University at Buffalo SUNY, Buffalo, NY 14260, USA

Correspondence should be addressed to E. P. Furlani, efurlani@buffalo.edu

Received 1 July 2012; Revised 31 July 2012; Accepted 31 July 2012

Academic Editor: Ivan D. Rukhlenko

Copyright © 2012 E. P. Furlani et al. This is an open access article distributed under the Creative Commons Attribution License, which permits unrestricted use, distribution, and reproduction in any medium, provided the original work is properly cited.

A new approach to metamaterials is presented that involves laser-based patterning of novel chiral polymer media, wherein chirality is realized at two distinct length scales, intrinsically at the molecular level and geometrically at a length scale on the order of the wavelength of the incident field. In this approach, femtosecond-pulsed laser-induced two-photon lithography (TPL) is used to pattern a photoresist-chiral polymer mixture into planar chiral shapes. Enhanced bulk chirality can be realized by tuning the wavelength-dependent chiral response at both the molecular and geometric level to ensure an overlap of their respective spectra. The approach is demonstrated via the fabrication of a metamaterial consisting of a two-dimensional array of chiral polymer-based L-structures. The fabrication process is described and modeling is performed to demonstrate the distinction between molecular and planar geometric-based chirality and the effects of the enhanced multiscale chirality on the optical response of such media. This new approach to metamaterials holds promise for the development of tunable, polymer-based optical metamaterials with low loss.

## 1. Introduction

Metamaterials are artificial electromagnetic materials with constituent elements that are subwavelength in size relative to the incident field and engineered to produce bulk electromagnetic properties not readily found in nature. The interest in these materials has grown steadily since the seminal theoretical work by Pendry [1] and subsequent experimental work by Shelby et al. [2]. Various interesting and exotic phenomena can be realized using metamaterials including the reverse Vavilov-Cherenkov effect [3], negative refraction [1, 2], sub-diffraction-limit imaging [1, 4–6], the reverse Doppler effect, slow light [7–9], and cloaking [10–12]. Applications of metamaterials span the electromagnetic (EM) spectrum with potential transformative impact in fields such as imaging (superlens) [1, 13], data storage [14], optical switching [15], electromagnetic shielding, and stealth technology [16–18].

To date, the majority of research on metamaterials has focused on developing negative index materials (NIMs) as first proposed by Veselago [3]. Initially, these were designed

to have simultaneous negative values of permittivity,  $\epsilon$ , and permeability,  $\mu$ . To achieve this, many of the early NIMs operating at GHz and THz frequencies made use of an electromagnetic resonance involving subwavelength metallic structures such as split-ring resonators (SRR) [19] and pairs of cut wires (PCW) [20, 21]. However, it was found that this approach has drawbacks. The reliance on resonance leads to NIM behavior with limited bandwidth, and the use of metallic structures results in relatively high loss. As the field advanced, other metamaterial constructs such as fishnet structures [22, 23] emerged and were shown to be superior to SRR and PCW designs in terms of a lower loss and ease in achieving overlap between electric and magnetic resonances. Nevertheless, the desire for practical metamaterials with wide bandwidth and low loss persists. In addition to performance limitations, there are issues associated with the fabrication of metamaterials, especially for use at optical frequencies. To date, the majority of such materials for THz applications have been fabricated using “top-down” techniques such as electron-beam lithography (EBL) or focused-ion beam (FIB) milling [23]. While these methods provide an

adequate nanometer resolution for tailoring subwavelength constituent elements, they tend to be limited to the fabrication of 2D planar materials on rigid substrates at low throughput and with high cost. Currently, there is intense interest and effort towards the development of fabrication methods and materials that overcome the aforementioned limitations.

In this paper, we introduce a new laser-based chiral chemical approach to metamaterials that overcomes some of the limitations of more conventional approaches. Our approach involves the use of a pulsed laser to pattern novel chiral polymer materials that exhibit chirality at two distinct length scales, intrinsically at the molecular level and geometrically at a length scale on the order of the wavelength of the incident field. Specifically, we use femtosecond-pulsed laser-induced two-photon initiated polymerization of a photoresist, which is premixed with a chiral polymer, to write patterned arrays of chiral polymer-based 2D planar chiral structures. Thus, this fabricated metamaterial exhibits chirality due to both its molecular structure and geometric shape. The idea is to obtain enhanced bulk chirality by tuning the wavelength-dependent chiral response at both the molecular and geometric level so as to ensure an overlap in their respective spectra.

Chiral metamaterials offer an alternate route to NIMs as compared to the more conventional metallic-structure-based resonance approach. The chirality of a material can be characterized in terms of a chirality parameter  $\kappa$ . If  $\kappa$  is sufficiently large, a bulk negative index can be realized within the material. Specifically, in a chiral material, negative refraction will occur at one of the eigen (circular) polarization states of the incident field if  $\kappa$  is larger than the square root of the product of real parts of permittivity and permeability, that is, when

$$\kappa > \sqrt{\epsilon' \cdot \mu'}, \quad (1)$$

where the refractive index is given by

$$n = \sqrt{\epsilon' \cdot \mu'} - \kappa \quad (2)$$

and  $\epsilon'$  and  $\mu'$  are the relative values of the real parts of the permittivity and permeability, respectively. Thus, in the chiral approach to NIMs, a negative index can potentially be achieved with a wider bandwidth and lower loss as there is no need to introduce lossy resonant metallic constituents. Our strategy is to use a laser to fabricate materials with enhanced multiscale chirality (sufficiently large  $\kappa$ ) in order to obtain polymer-based NIMs without resorting to top-down fabrication or resonant metallic structures as is common in conventional approaches to metamaterials. In the following, we report of the progress towards this end by describing the synthesis and demonstrating the fabrication of novel 2D planar media possessing multiscale chirality. We also present modeling results that demonstrate the effects of multiscale chirality on the optical response (optical rotation) of such media.

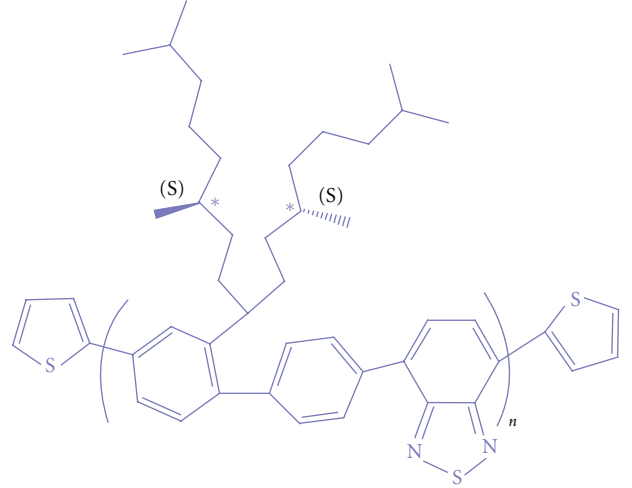


FIGURE 1: Chemical structure of PFBT polymer.

## 2. Fabrication

The fabrication of our multiscale chiral media begins with the formation of a photoresist-chiral polymer mixture consisting of SU-8 2025 from Microchem and Chiral Poly(fluorene-alt-benzothiadiazole) (PFBT) in a mixture ratio of 35 : 1. The PFBT was synthesized using palladium-catalyzed Suzuki polycondensation as the final step and purified with a Soxhlet extraction. We introduced chirality in PFBT of the fluorene-based monomer modified with (S)-3,7-dimethyloctyl substituents at the 9 positions as shown in Figure 1 and described in [24]. The photoresist-chiral polymer mixture is stirred for 24 hours and then spin-coated at 1000 rpm on a glass substrate. After spin coating, the sample is baked for 30 min at 95°C to evaporate the solvent before performing lithograph patterning. The circular dichroism (CD) (differential absorption of left and right circularly polarized light) and absorption spectra of both the pure PFBT polymer and SU-8/PFBT blend are shown in Figure 2. Note that the SU-8/PFBT exhibits a 68-fold increase in optical activity at  $\lambda = 500$  nm. Presently, the reason for the enhanced optical activity is not fully understood and is the subject of continued investigation by our group. The chirality parameters for the PFBT polymer and the SU-8/PFBT are on the order of  $\kappa \sim 10^{-5}$  and  $2 \times 10^{-3}$ , respectively.

In order to obtain multiscale chirality, we pattern the chiral SU-8/PFBT film into a planar array of L-structures using two-photon photolithography (TPL). We use a near-IR (800 nm) writing wavelength and a schematic of the writing set up is shown in Figure 3(a). In this system, a piezo stage moves the sample relative to a fixed laser beam and a desired pattern is produced within the sample by controlling the motion of the stage while exposing the sample. Once the sample is patterned, it is developed with Propylene Glycol Methyl Ether Acetate for 3 hours, which removes the unexposed material leaving only the patterned media. We have recently reported the use of this method for writing novel subwavelength polymer-based planar plasmonic metamaterials, which were prepared using SU-8 with a high gold

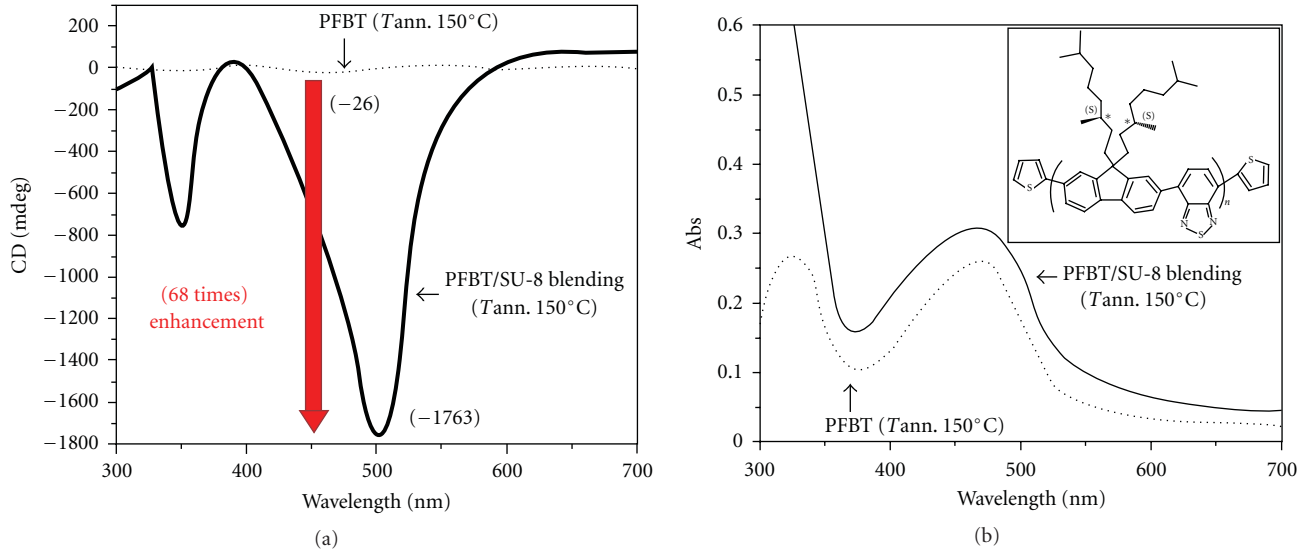


FIGURE 2: CD (a) and UV-vis absorption (b) spectra of (dots) annealed pure PFBT film; (solid) PFBT/SU-8 blending, 1/30 mass ratio film spin-coated from 20% solid content solution, after prebaking and annealing.

precursor (metallic salt) loading [25, 26]. Specifically, we used a femtosecond-pulsed laser to induce two-photon initiated *in situ* reduction of the metal salt and simultaneous polymerization of the SU8. Gold nanoparticles are formed during the writing process, which renders a plasmonic functionality in the written structures [26]. Figure 3(b) shows examples of different written structures, which demonstrate the versatility of the writing process. The present effort on patterning chiral SU-8/PFBT film is an extension of this prior work on plasmonic structures.

A 2D array of planar L-structures fabricated using this method is shown in Figure 4. Note that while the L geometry is not chiral in a 3D sense, it is considered chiral in a 2D planar sense because it cannot be mapped onto its mirror image using a sequence of rotations or translations confined to the plane; that is, it needs to be lifted out of the plane and rotated to achieve this. Thus, based on geometric considerations alone, that is, ignoring the chirality of the SU-8/PFBT, the fabricated material is not chiral in 3D; for example, it would not rotate polarization of waves propagating in the plane of L-structures, rather it is bianisotropic. However, in addition to the planar geometric chirality, the L-structures possess intrinsic chirality due to the constituent SU-8/PFBT. Thus, the material shown in Figure 4 represents a 2D planar metamaterial with multiscale chirality. In principle, this process can be used to fabricate bulk enhanced 3D chiral metamaterials layer-by-layer, wherein a stacked sequence of carefully chosen 2D patterns combine to produce a 3D unit cell chiral geometry, an approach that we are currently pursuing.

### 3. Theory and Simulation

From a theoretical perspective, a periodic array of planar chiral L-structure elements, such as shown in Figure 4, will exhibit circular birefringence in the visible and near-infrared

regions of the spectrum when their linear dimensions are close to these wavelengths [27, 28]. In principle, the molecular chirality of the constituent polymer can be tuned to occur at these wavelengths as well, allowing for the development of materials with enhanced multiscale chirality as described above.

We use computational electrodynamics to model the electromagnetic response of chiral polymer-based chiral L-structures as shown in Figure 4. However, to facilitate the computational analysis, we use submicron geometric dimensions, that is, slightly smaller than those shown in Figure 4. In order to take into account the overlap of 2D geometric chirality with molecular chirality [24, 29] we modify Maxwell's equations to include natural optical activity. This emerges when the spatial dispersion of a medium is considered along with the time dispersion in the linear relation between the applied electric field and the medium's displacement vector [30]. In case of relatively weak spatial dispersion, the dielectric permittivity tensor,  $\epsilon_{ij}(\omega, \mathbf{k})$ , can be expanded in a series over powers of the wave vector. The coefficient of the first-order term can be related to the macroscopic chirality parameter of the medium after some algebraic operations. The 0th-order term represents the usual local dielectric permittivity tensor. In the case of an isotropic medium, consisting of a randomly oriented collection of chiral molecules, both the 0th- and 1st-order coefficients become averaged.

To compute the rotation of polarization of an incident field we employed the Finite-Element-(FE) based COMSOL multiphysics RF solver using a time-harmonic approximation (<http://www.comsol.com/>). The computational domain for the L-Structure is shown in Figure 5. In this model, the polymeric L-structure resides on a glass substrate with a refractive index of 1.6. The base of the unit cell is 1050 nm by 750 nm, and its height is 2 microns. The dimensions of the L-shape are as follows: 750 nm in length, 450 nm at the base, the width of both branches is 150 nm, and the thickness



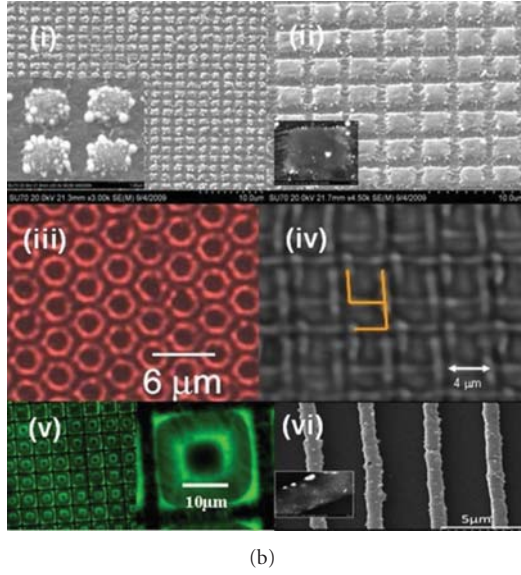
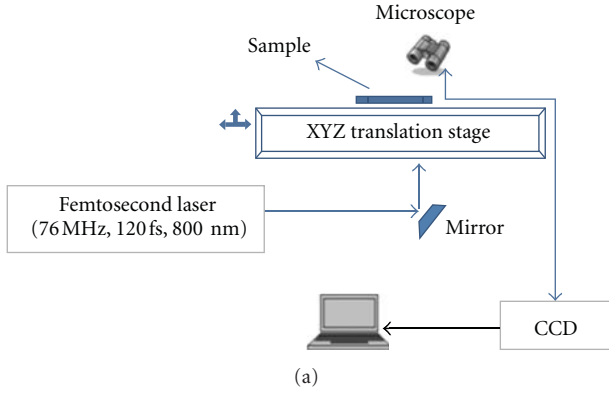


FIGURE 3: Laser-based TPL fabrication of metamaterials: (a) schematic of the TPL laser writing system, (b) SEM images of fabricated polymer-based plasmonic structures (i) cauliflowers; (ii) blocks; confocal microscope image of (iii) hexagonal ring structures; (iv) planar chiral Y structures with highlighted geometry; (v) donuts; SEM image of (vi) grating structure (adapted from [25]).

is 500 nm. Note that while these dimensions are slightly smaller than the fabricated structures shown in Figure 4, the analysis presented here is scalable as long as the molecular chirality can be tuned to overlap the structural chirality. The isotropic refractive index of the modeled L-structure is 1.4. Scattering (low reflection) boundary conditions with Perfectly Matching Layers (PML) are applied at the top and bottom of the solution space as described in [31, 32]. Double periodic boundaries are imposed on the side boundaries to account for the fact that this structure is one element of a 2D array, that is, the periodic conditions account for the presence of the other elements, even though they do not appear in the model. The incident (input) field is generated by a time-harmonic surface current source positioned in the  $x$ - $y$  plane [31, 32]. The magnitude of the surface current is chosen to provide an  $x$ -polarized plane wave with a field magnitude of  $E_x = 2 \times 10^6$  V/m [31–33].

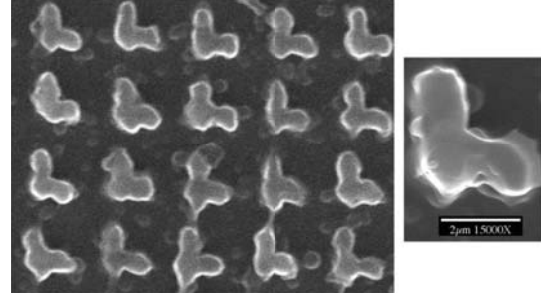


FIGURE 4: SEM of fabricated chiral polymer-based L-structures.

The intrinsic chirality of the L-structure is introduced via the bulk chirality parameter,  $\kappa$ , which is related to macroscopic optical rotation of the medium. Here, we are not concerned with the microscopic origin of chirality [29]. Instead, we model the frequency dispersion of chirality parameter with a damped Lorentzian centered at a certain resonant wavelength. Specifically, the permittivity tensor for our analysis is of the following diagonal form:

$$\epsilon_{ii}(\omega) = n^2 + \kappa'(\omega) \sqrt{\frac{\mu_0}{\epsilon_0}} \frac{H_{ii}}{E_{ii}}, \quad (3)$$

where

$$\kappa'(\omega) = \frac{\kappa_0}{(\omega - \omega_0) + i\Gamma}, \quad (4)$$

and  $n$  is homogeneous refractive index,  $\omega_0$  is the resonant frequency of molecular optical activity, and  $\Gamma$  is the damping rate of corresponding molecular resonance. In our simulations the damping rate is set to  $10^{13} \text{ sec}^{-1}$  and  $\kappa_0$  to  $10^{12} \text{ sec}^{-1}$ . It should be noted that the specific form of permittivity tensor (3) results in the corresponding dispersion relation and an equation for the square of the effective refractive index of the medium. Equation (2) is then derived via Taylor expansion over the small parameter, assuming the smallness of chirality parameter,  $\kappa'(\omega)$ . Therefore  $\kappa$  of (2) and  $\kappa'(\omega)$  of (3) are related through a simple formula:  $\kappa'(\omega) = 2 * n * \kappa$ .

It is instructive to note that the resonance is a molecular resonance and basically determined by the microscopic electronic structure of constituent chiral molecules. Significantly, the resonance can be tuned in a relatively broad range from UV to near IR for a class of  $\pi$ -conjugated donor-acceptor molecules depending on the donor and acceptor strength and conjugation length. For example, the first absorption band of the PFBT molecule was tuned to approximately 500 nm to overlap with the plasmon resonance of gold nanoparticles in our previous work [30]. Shifting the molecular resonance to the infrared region, with a simultaneous decrease of the linear dimensions of the L-structure, results in an overlap of resonant features and an effective increase of the degree of optical rotation. The peak absolute value of chirality parameter,  $|\kappa'_{\max}|$ , was set to 0.1 in our simulations. This value is a projected maximum that can be readily achieved with combined plasmonic [24], excitonic [34], and structural

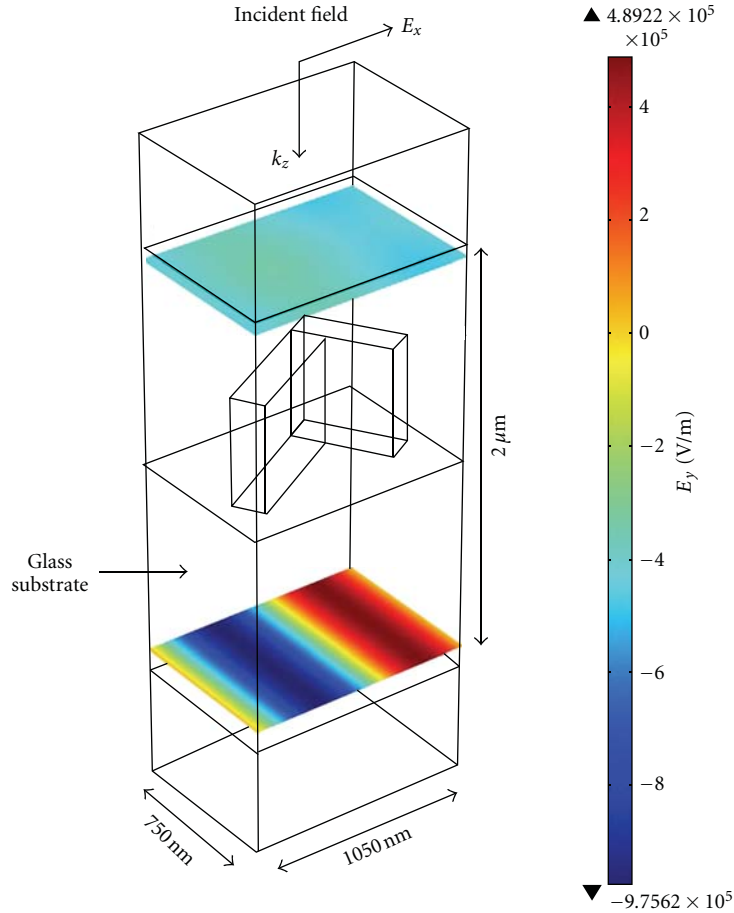


FIGURE 5: Computational domain for the planar chiral L-structure EM analysis.

enhancement [35] of chirality. Even higher values of chirality parameter can be expected from combinations of natural optical activity with (i) a magneto-optical effect enhanced by magnetoplasmonic nanoparticles, (ii) further modifications of chiral molecular building blocks, and/or (iii) chiral aggregation in thick films. The optical rotation of an L-structure with molecular chirality is compared to one with just spatial chirality in Figure 5 and the discussion thereof.

To make sure the observed optical rotation is due to actual chirality of the L-shapes and not a computational artifact or accidental diffraction pattern we compared the EM transmission of a dielectric sphere to that of sphere made from chiral material (Figure 6). The dielectric sphere should show no optical activity as the geometry it is not chiral. As shown in Figure 7, and discussed below, the polarization state of the incident light was preserved in the former case as expected. However, the sphere consisting of chiral molecules, and therefore possessing a bulk chirality parameter, showed a chiral signature.

The results of our simulations of optical rotation are presented in Figure 7. The angle is computed with respect to the initial polarization of the incoming field. First, note that the L-structure without molecular chirality rotates the

polarization in a broad range. Rotation in this case is solely determined by the shape and dimensions of the scattering object and is not resonant in nature. However, the L-structure made of chiral material shows a narrow resonance on top of the broad rotation curve. Similarly, in the case of the spherical geometry one can see that there is no rotation of polarization in the case of the dielectric sphere. However, the chiral sphere reveals rotation due to the chiral nature of its material: the chiral signature is centered at the wavelength of the molecular resonance. This analysis demonstrates the distinction between molecular and geometric-based chirality and the effects of the enhanced multiscale chirality on the optical response of the media.

#### 4. Conclusions

We have introduced a novel approach to metamaterials that combines the use of ultrafast pulsed laser-based fabrication with chiral chemistry to produce a new class of polymeric metamaterials that have enhanced bulk chirality. The enhanced chirality is achieved by tuning the wavelength-dependent chiral response of the media at both the molecular and geometric level so as to ensure an overlap of

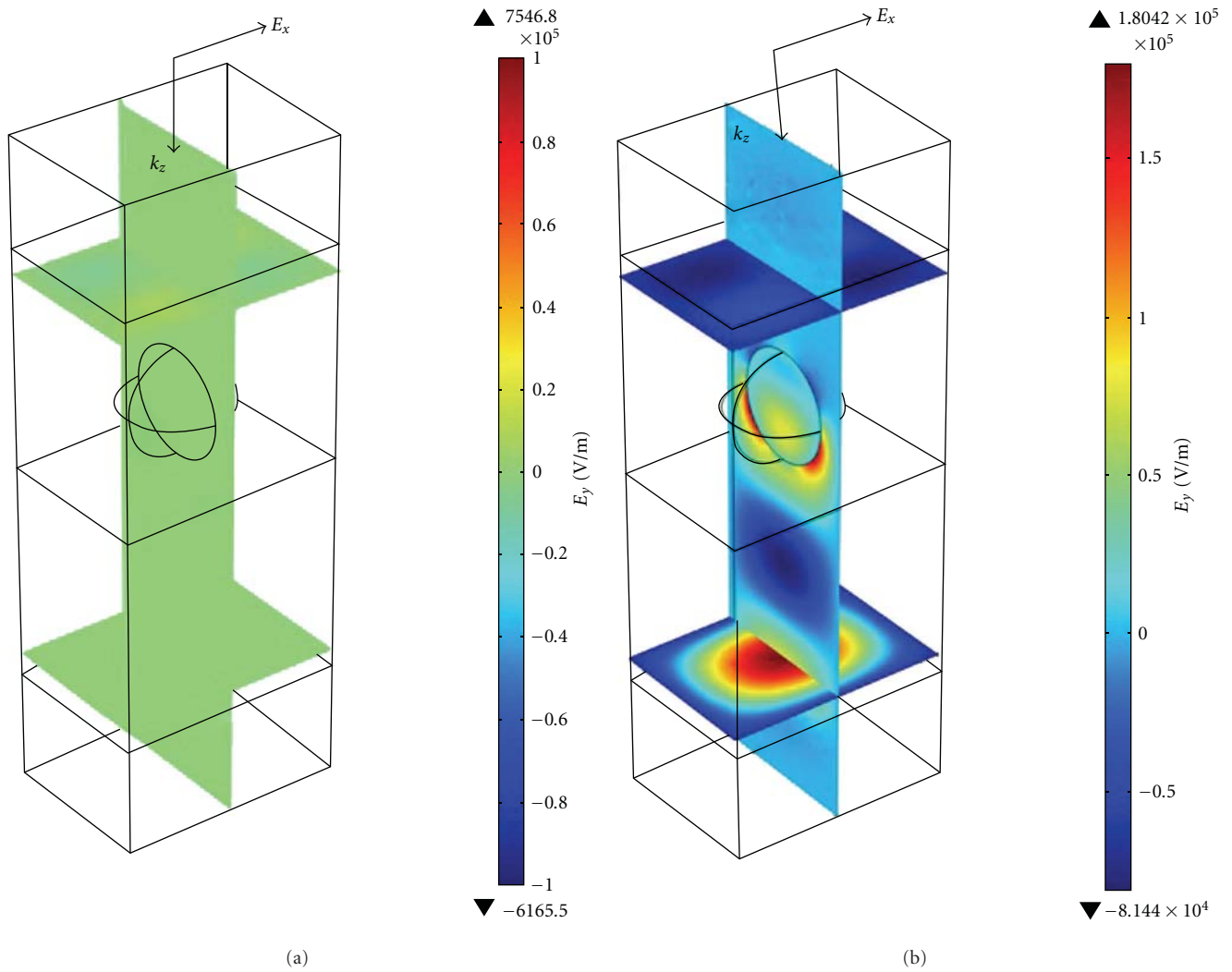


FIGURE 6: Simulated EM transmission (y-component of the  $E$ -field is plotted): (a) dielectric sphere without intrinsic molecular chirality; (b) sphere with intrinsic molecular chirality.

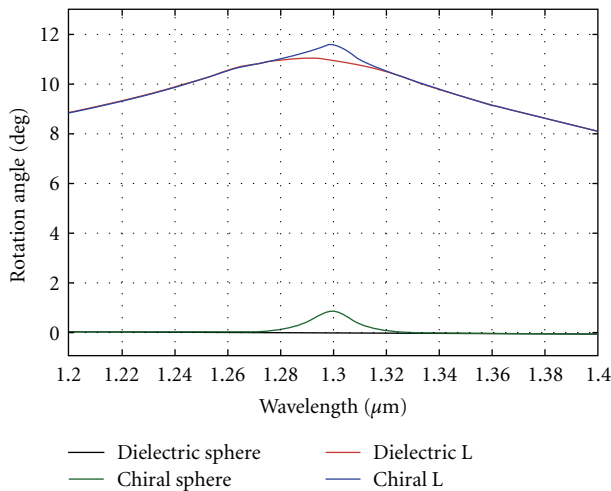


FIGURE 7: Predictions of the optical rotation angle for structures with and without molecular chirality.

their respective spectra. This approach is demonstrated via the fabrication of a metamaterial consisting of a two-dimensional array of chiral polymer-based planar chiral L-structures. The fabrication process is described and modeling is performed to demonstrate the effects of multiscale chirality of the optical response (optical rotation) of such media. This new approach to metamaterials holds promise for the development of tunable, polymer-based negative index optical metamaterials with low loss.

## References

- [1] J. B. Pendry, "Negative refraction makes a perfect lens," *Physical Review Letters*, vol. 85, no. 18, pp. 3966–3969, 2000.
- [2] R. A. Shelby, D. R. Smith, and S. Schultz, "Experimental verification of a negative index of refraction," *Science*, vol. 292, no. 5514, pp. 77–79, 2001.
- [3] V. G. Veselago, "The electrodynamics of substance with simultaneously negative values of  $\epsilon$  and  $\mu$ ," *Soviet Physics Uspekhi*, vol. 10, pp. 509–514, 1968.

- [4] Z. Jacob, L. V. Alekseyev, and E. Narimanov, "Optical hyperlens: far-field imaging beyond the diffraction limit," *Optics Express*, vol. 14, no. 18, pp. 8247–8256, 2006.
- [5] Z. Liu, H. Lee, Y. Xiong, C. Sun, and X. Zhang, "Far-field optical hyperlens magnifying sub-diffraction-limited objects," *Science*, vol. 315, no. 5819, p. 1686, 2007.
- [6] I. I. Smolyaninov, Y. J. Hung, and C. C. Davis, "Magnifying superlens in the visible frequency range," *Science*, vol. 315, no. 5819, pp. 1699–1701, 2007.
- [7] Q. Bai, C. Liu, J. Chen, C. Cheng, M. Kang, and H. T. Wang, "Tunable slow light in semiconductor metamaterial in a broad terahertz regime," *Journal of Applied Physics*, vol. 107, no. 9, Article ID 093104, 8 pages, 2010.
- [8] R. Singh, C. Rockstuhl, F. Lederer, and W. Zhang, "Coupling between a dark and a bright eigenmode in a terahertz metamaterial," *Physical Review B*, vol. 79, no. 8, Article ID 085111, 4 pages, 2009.
- [9] S. Y. Chiam, R. Singh, C. Rockstuhl, F. Lederer, W. Zhang, and A. A. Bettiol, "Analogue of electromagnetically induced transparency in a terahertz metamaterial," *Physical Review B*, vol. 80, no. 15, Article ID 153103, 4 pages, 2009.
- [10] J. B. Pendry, D. Schurig, and D. R. Smith, "Controlling electromagnetic fields," *Science*, vol. 312, no. 5781, pp. 1780–1782, 2006.
- [11] D. Schurig, J. J. Mock, B. J. Justice et al., "Metamaterial electromagnetic cloak at microwave frequencies," *Science*, vol. 314, no. 5801, pp. 977–980, 2006.
- [12] W. Cai, U. K. Chettiar, A. V. Kildishev, and V. M. Shalaev, "Optical cloaking with metamaterials," *Nature Photonics*, vol. 1, no. 4, pp. 224–227, 2007.
- [13] N. Fang, H. Lee, C. Sun, and X. Zhang, "Sub-diffraction-limited optical imaging with a silver superlens," *Science*, vol. 308, no. 5721, pp. 534–537, 2005.
- [14] M. Wuttig and N. Yamada, "Phase-change materials for rewriteable data storage," *Nature Materials*, vol. 6, no. 11, pp. 824–832, 2007.
- [15] H. Kind, H. Yan, B. Messer, M. Law, and P. Yang, "Nanowire ultraviolet photodetectors and optical switches," *Advanced Materials*, vol. 14, pp. 158–160, 2002.
- [16] W. M. Zhu, A. Q. Liu, X. M. Zhang et al., "Switchable magnetic metamaterials using micromachining processes," *Advanced Materials*, vol. 23, no. 15, pp. 1792–1796, 2011.
- [17] N. Liu, H. Guo, L. Fu, S. Kaiser, H. Schweizer, and H. Giessen, "Three-dimensional photonic metamaterials at optical frequencies," *Nature Materials*, vol. 7, no. 1, pp. 31–37, 2008.
- [18] J. Valentine, S. Zhang, T. Zentgraf et al., "Three-dimensional optical metamaterial with a negative refractive index," *Nature*, vol. 455, no. 7211, pp. 376–379, 2008.
- [19] V. M. Shalaev, W. Cai, U. K. Chettiar et al., "Negative index of refraction in optical metamaterials," *Optics Letters*, vol. 30, no. 24, pp. 3356–3358, 2005.
- [20] A. N. Grigorenko, A. K. Geim, H. F. Gleeson et al., "Nanofabricated media with negative permeability at visible frequencies," *Nature*, vol. 438, no. 7066, pp. 335–338, 2005.
- [21] G. Dolling, C. Enkrich, M. Wegener, C. M. Soukoulis, and S. Linden, "Low-loss negative-index metamaterial at telecommunication wavelengths," *Optics Letters*, vol. 31, no. 12, pp. 1800–1802, 2006.
- [22] G. Dolling, C. Enkrich, M. Wegener, C. M. Soukoulis, and S. Linden, "Simultaneous negative phase and group velocity of light in a metamaterial," *Science*, vol. 312, no. 5775, pp. 892–894, 2006.
- [23] A. Boltasseva and V. M. Shalaev, "Fabrication of optical negative-index metamaterials: recent advances and outlook," *Metamaterials*, vol. 2, no. 1, pp. 1–17, 2008.
- [24] H. S. Oh, S. Liu, H. S. Jee, A. Baev, M. T. Swihart, and P. N. Prasad, "Chiral poly(fluorene-alt-benzothiadiazole) (PFBT) and nanocomposites with gold nanoparticles: plasmonically and structurally enhanced chirality," *Journal of the American Chemical Society*, vol. 132, no. 49, pp. 17346–17348, 2010.
- [25] S. Shukla, E. P. Furlani, X. Vidal, M. T. Swihart, and P. N. Prasad, "Subwavelength direct laser patterning of conductive gold nanostructures by simultaneous photopolymerization and photoreduction," *ACS Nano*, vol. 5, no. 3, pp. 1947–1957, 2011.
- [26] S. Shukla, E. P. Furlani, X. Vidal, M. T. Swihart, and P. N. Prasad, "Two-photon lithography of sub-wavelength metallic structures in a polymer matrix," *Advanced Materials*, vol. 22, no. 33, pp. 3695–3699, 2010.
- [27] A. Papakostas, A. Potts, D. M. Bagnall, S. L. Prosvirnin, H. J. Coles, and N. I. Zheludev, "Optical manifestations of planar chirality," *Physical Review Letters*, vol. 90, no. 10, Article ID 107404, 4 pages, 2003.
- [28] M. Kuwata-Gonokami, N. Saito, Y. Ino et al., "Giant optical activity in quasi-two-dimensional planar nanostructures," *Physical Review Letters*, vol. 95, no. 22, Article ID 227401, 4 pages, 2005.
- [29] A. Baev, M. Samoc, P. N. Prasad, M. Krykunov, and J. Autschbach, "A quantum chemical approach to the design of chiral negative index materials," *Optics Express*, vol. 15, no. 9, pp. 5730–5741, 2007.
- [30] L. D. Landau, E. M. Lifshitz, and L. P. Pitaevskii, *Electrodynamics of Continuous Media*, Pergamon Press.
- [31] E. P. Furlani and A. Baev, "Optical nanotrapping using cloaking metamaterial," *Physical Review E*, vol. 79, no. 2, Article ID 026607, 6 pages, 2009.
- [32] E. P. Furlani and A. Baev, "Free-space excitation of resonant cavities formed from cloaking metamaterial," *Journal of Modern Optics*, vol. 56, no. 4, pp. 523–529, 2009.
- [33] E. P. Furlani, R. Biswas, A. N. Cartwright, and N. M. Litvinchits, "Antiresonant guiding optofluidic biosensor," *Optics Communications*, vol. 284, no. 16–17, pp. 4094–4098, 2011.
- [34] H. S. Oh, W.-Ch. Law, A. Baev et al., "A new twist on optical metamaterials: resonantly coupled hybrid chiral nanocomposites for metaphotonics," *Nature Photonics*. In press.
- [35] H. S. Oh, H. S. Jee, A. Baev, M. T. Swihart, and P. N. Prasad, "Dramatic structural enhancement of chirality in photopatternable nanocomposites of chiral poly(fluorene-alt-benzothiadiazole) (PFBT) in achiral SU-8 photoresist," *Advanced Functional Materials*. In press.



## Research Article

# 3D Photonic Nanostructures via Diffusion-Assisted Direct fs Laser Writing

**Gabija Bickauskaite,<sup>1,2</sup> Maria Manousidaki,<sup>2,3</sup> Konstantina Terzaki,<sup>2,4</sup> Elmina Kambouraki,<sup>2,4</sup> Ioanna Sakellari,<sup>2,3</sup> Nikos Vasilantonakis,<sup>2,4</sup> David Gray,<sup>2</sup> Costas M. Soukoulis,<sup>2,5</sup> Costas Fotakis,<sup>2,3</sup> Maria Vamvakaki,<sup>2,4</sup> Maria Kafesaki,<sup>2,4</sup> Maria Farsari,<sup>2</sup> Alexander Pikulin,<sup>6</sup> and Nikita Bityurin<sup>6</sup>**

<sup>1</sup> Department of Quantum Electronics, Vilnius University, 02300 Vilnius, Lithuania

<sup>2</sup> IESL-FORTH, N. Plastira 100, Heraklion, 70013 Crete, Greece

<sup>3</sup> Department of Physics, University of Crete, Heraklion, 71003 Crete, Greece

<sup>4</sup> Department of Materials Science and Technology, University of Crete, Heraklion, 71003 Crete, Greece

<sup>5</sup> Ames Laboratory, Department of Physics and Astronomy, Iowa State University, Ames, IA 50011-2011, USA

<sup>6</sup> Institute of Applied Physics, Russian Academy of Sciences, Nizhny Novgorod, Russia

Correspondence should be addressed to Maria Farsari, mfarsari@iesl.forth.gr

Received 28 May 2012; Revised 24 July 2012; Accepted 24 July 2012

Academic Editor: Natalia M. Litchinitser

Copyright © 2012 Gabija Bickauskaite et al. This is an open access article distributed under the Creative Commons Attribution License, which permits unrestricted use, distribution, and reproduction in any medium, provided the original work is properly cited.

We present our research into the fabrication of fully three-dimensional metallic nanostructures using diffusion-assisted direct laser writing, a technique which employs quencher diffusion to fabricate structures with resolution beyond the diffraction limit. We have made dielectric 3D nanostructures by multiphoton polymerization using a metal-binding organic-inorganic hybrid material, and we covered them with silver using selective electroless plating. We have used this method to make spirals and woodpiles with 600 nm intralayer periodicity. The resulting photonic nanostructures have a smooth metallic surface and exhibit well-defined diffraction spectra, indicating good fabrication quality and internal periodicity. In addition, we have made dielectric woodpile structures decorated with gold nanoparticles. Our results show that diffusion-assisted direct laser writing and selective electroless plating can be combined to form a viable route for the fabrication of 3D dielectric and metallic photonic nanostructures.

## 1. Introduction

Direct fs laser writing is a technique that allows the construction of three-dimensional micro- and nanostructures [1]. It is based on the phenomenon of multiphoton absorption and subsequent polymerization; the beam of an ultrafast laser is tightly focused into the volume of a photosensitive material, initiating multiphoton polymerization within the focused beam voxel. By moving the beam three-dimensionally, arbitrary 3D, high-resolution structures can be written. By simply immersing the sample in an appropriate solvent, the unscanned, unpolymerized area can be removed, allowing the 3D structure to reveal. A variety of applications have been proposed including microfluidics [2], micro-optics [3, 4],

scaffolds for biomolecules and cells [5–7], and photonics and metamaterials [8–10].

There has been a lot of research efforts to improve the resolution of DLW technology, which for a long time has been in the range of 100 nm. The method which most successfully and substantially has increased the resolution not only of single lines but also of 3D structures is DLW inspired by stimulated-emission-depletion (STED) fluorescence microscopy [11, 12]. In STED-DLW, two laser beams are used; one is used to generate the radicals, and the second beam to deactivate them. Several schemes have been proposed including single-photon (rather than multiphoton) excitation [13], a one-color scheme [14] and multiphoton two-color scheme [15, 16]. Structures with



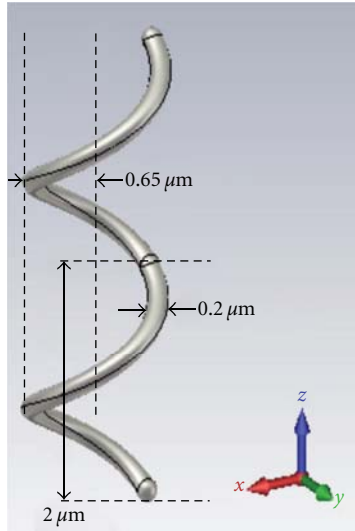


FIGURE 1: The design of the 3D spirals.

very high resolution and very small intralayer distances have been fabricated using this approach. However, the implementation of DLW-STED is complicated, requiring very fine beam control and specialized photoinitiators which not only have high two-photon cross-section, but also high fluorescence quantum efficiency [15, 17]. Consequently, only geometrically simple structures have been fabricated to-date.

Our team has shown recently that it is possible to increase the writing resolution of multiphoton polymerization by employing diffusion-assisted DLW (DA-DLW), a scheme based on quencher diffusion, in a chemical equivalent of STED [18]. This is based on the combination of a mobile quenching molecule with a slow laser scanning speed, allowing the diffusion of the quencher in the scanned area, the depletion of the generated radicals, and the regeneration of the consumed quencher. The material used as quencher is 2-(dimethylamino) ethyl methacrylate (DMAEMA), an organic monomer which is also part of the polymer structure. Due to its amine moieties, this is the same monomer we have employed in the past as a metal ligand, to enable the selective metallization of 3D photonic crystals [19]. In general, metallic nanostructures are very interesting due to their potential electromagnetic functionalities, which are not observed in bulk materials [20–23]. Metallic periodic nanostructures can significantly modify the properties of light with wavelength close to their periodicity, resulting in potential applications in scientific and technical areas such as filters, optical switches, sensing, imaging, energy harvesting and photovoltaics, cavities, and efficient laser design [24]. Several fabrication techniques have been employed for the fabrication of such structures, including colloidal lithography, [25] focused ion beam drilling [26], photopolymerization and photoreduction [27], and others [28]. Our approach was to fabricate 3D dielectric nanostructures containing the metal binding material DMAEMA and subsequently selectively metallize them with silver using electroless plating (EP). EP is a fairly simple process that does not require

any specialized equipment, and the metal deposition can be done without using any electrical potential [29, 30]. In general, it is characterized by the selective reduction of metal ions at the surface of a catalytic substrate immersed into an aqueous solution of metal ions, with continued deposition on the substrate through the catalytic action of the deposit itself. Using DLW and selective EP, we successfully fabricated 3D metallic photonic crystals with bandgaps at optical wavelengths [31].

In this paper, we combine these two methodologies to fabricate 3D metallic and structures with complex geometries and subdiffraction limit resolution. We fabricate woodpile and spiral photonic crystals, and we show that they have well-defined diffraction patterns, indicating the quality of their fabrication and their internal periodicity. In addition, we have fabricated 3D structures decorated with gold nanoparticles. Such structures can be useful in applications such as biosensing.

## 2. Design

In this paper, we present three kinds of nanostructures.

- (i) Silver-coated woodpile structures with a period of 600 nm: these type of structures were investigated theoretically and experimentally in [31], and they were found to have bandgaps at optical wavelengths.
- (ii) Dielectric woodpile structures, also with period 600 nm, decorated with gold nanoparticles: these can be useful in applications such as biosensing, where thiol chemistry can be employed for biomolecule immobilization [32].
- (iii) Spiral photonic structures: these were modeled on the structures presented in [33] by Ganzel and colleagues from KIT, Germany (Figure 1). In the KIT study, voids were fabricated into a positive photoresist using DLW, which were subsequently filled with gold using electroplating. Their structures were used as broadband polarizers. In our study, we have copied the spiral design and used a metal-binding negative photopolymer to recreate these spiral structures. As these spirals have high aspect ratio and it is difficult for them to remain free standing during the sample development process, support structures were added to the design, as it will be shown in the Results section.

## 3. Fabrication

The materials investigation, synthesis, and metallization protocols employed have been described in detail previously in [18, 19, 31]. The silver-coated structures were fabricated using 30% DMAEMA [19], while the gold-nanoparticle-covered ones 10% DMAEMA [18]. The gold nanoparticles were prepared following the metallization process described in [19], omitting the last plating step.

For the fabrication of the 3D nanostructures, a Ti:Sapphire femtosecond laser (800 nm, 75 MHz, <20 fs) was

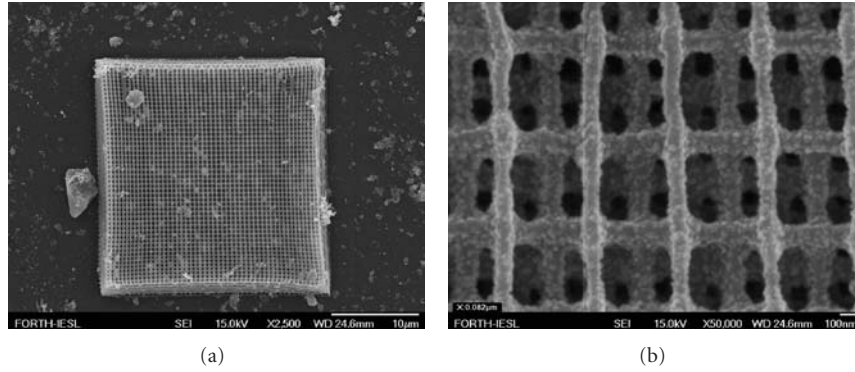


FIGURE 2: Woodpile photonic crystals: (a) the whole structure, (b) detail.

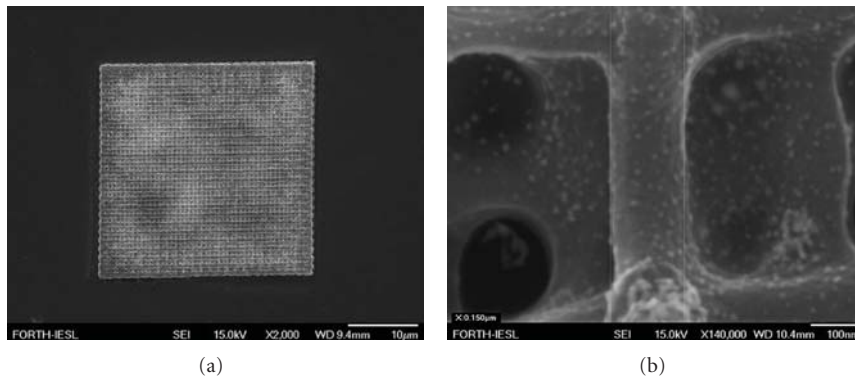


FIGURE 3: Woodpiles decorated with gold nanoparticles (a) the whole structure, (b) detail.

focused into the photopolymerisable composite using a high numerical aperture focusing microscope objective lens (100x, N.A. = 1.4, Zeiss, Plan Apochromat). Sample movement was achieved using piezoelectric and linear stages, for accurate and step movement, respectively (PI). The whole DLW setup, which is described in detail in [34], was computer controlled using the 3DPoli software. Here, the average laser power used for the fabrication of the high-resolution woodpile structures was 1.85 mW, measured before the objective, while the average transmission to the sample was 20%. For the spiral structures, the average power was increased to 5.5 mW, scanning the beam at  $10 \mu/s$  and  $20 \mu/s$  to write the spirals and the supports, respectively. To avoid contact with the lens immersion oil, all structures were fabricated upside down with the glass substrate in contact with the oil. They were built in a layer-by-layer fashion starting from the top with the last layer adhering to the substrate. This way, the laser beam did not cross an already polymerized layer, causing second polymerization or beam distortion.

#### 4. Diffraction Spectra

To check the quality of the structures, we used the diffraction pattern in the transmitted waves produced by the structure when illuminated using a white light beam. In general, diffraction patterns reveal structural characteristics

as well as sample quality [35]. For this, a home-built setup was employed, built according to [36, 37]. Light from a Ti:Sapphire laser (800 nm, 180 fs, 1 mJ/pulse, 1 KHz repetition rate) was focused using an  $f = 3$  cm lens into a 3 cm long cell filled with distilled water, in order to produce white light continuum, providing a useful broad spectral range of 450 nm to 1000 nm wavelength. The light was collimated and then focused on the sample. The sample was mounted to have accurate 3D and rotational control. The half-opening angle of the incident light was reduced to  $5^\circ$ , assured by iris diaphragms.

#### 5. Results and Discussion

Figure 2(a) shows a scanning electron microscopy (SEM) image of a woodpile structure with 600 nm period fabricated and metallized using the procedure described earlier. Figure 2(b) shows a detail of such a structure. It can be seen that the resolution achieved is in the order of 100 nm.

Figure 3 shows SEM images of woodpile structures decorated with gold nanoparticles. Figure 3(a) shows the whole structure, while Figure 3(b) shows a detail of such a structure, where the nanoparticles are clearly visible. The density of these nanoparticles can increase or decrease by increasing or decreasing the percentage of DMAEMA, respectively [19]. The size of the nanoparticles can be modified by altering the growing conditions [19].

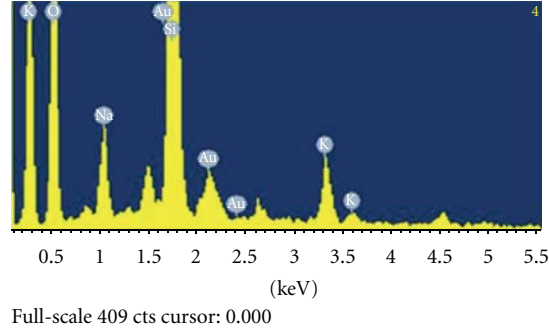


FIGURE 4: EDX spectrogram of the woodpile structures. The gold (Au) peaks are clearly visible.

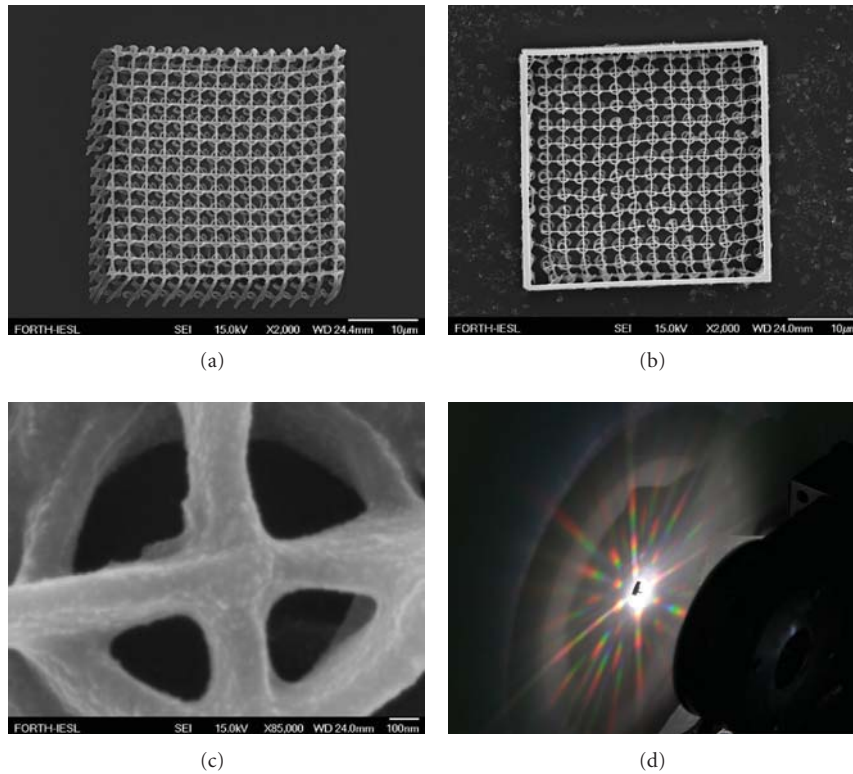


FIGURE 5: Spiral photonic crystal structures. (a) An array of dielectric spirals. (b) An array of metalized spirals. (c) Detail of a spiral with lateral resolution is in the order of 100 nm. (d) The diffraction pattern generated when the structure is illuminated with white light.

Figure 4 shows the energy-dispersive X-ray (EDX) spectrogram of the woodpile structures, where the gold (Au) peaks are clearly visible.

Figure 5 shows a series of dielectric and silver-coated spiral structures fabricated as described earlier. Figures 3(a) and 3(b) show  $14 \times 14$  arrays of spirals before silver coating, respectively. Support lines between the spirals are clearly visible. It is also clear that even though there is some debris on the glass substrate, the silver metallization is selective. Figure 3(c) shows a close SEM image of a spiral; the resolution achieved is in the order of 100 nm. In addition, the silver coating is fairly uniform, with no visible large silver grains. Figure 3(d) shows the diffraction pattern produced when the spirals were illuminated with white light. As it can

be seen, the pattern is regular, symmetric, and having well-defined colours, indicating the periodicity of the structures. This periodicity is not disturbed by the support structures.

## 6. Conclusions

To conclude, we have employed DA-DLW and EP of a metal-binding hybrid material to make helical spirals and woodpile structures with 600 nm intralayer periodicity. The fabricated nanostructures have a smooth surface and exhibit well-defined diffraction spectra, indicating their good fabrication quality and internal periodicity. We have shown that this methodology combination can be employed as a viable route

for the fabrication of 3D dielectric, nanoparticle-coated, and metallic photonic nanostructures.

## Acknowledgments

This work was partly funded by the ITN TOPBIO (PITN-GA-2010-264362). G.Bickaускаite was supported by the EU Marie Curie Fellowship Program: FASTQUAST (PITN-GA-2008-214962). A. Pikulin and N. Bityurin were supported in part by Federal Targeted Program “Scientific and scientific-pedagogical personnel of the innovative Russia” under Contract nos. 16.740.11.0656 and 16.740.11.0018, RFBR under Grant nos. 09-02-00665-a and 11-02-97053-r\_povoljie\_a, and by the Program of presidium of the Russian Academy of Sciences “Extreme light fields and applications.” It was also supported by Dr. Athanasios Gavrielides from the AFOSR/EORD London Office via the Grant FA8655-11-1-3090. The authors would like to thank Mrs. Aleka Manousaki for expert technical assistance with SEM.

## References

- [1] S. Juodkazis, V. Mizeikis, and H. Misawa, “Three-dimensional microfabrication of materials by femtosecond lasers for photonics applications,” *Journal of Applied Physics*, vol. 106, no. 5, Article ID 051101, 2009.
- [2] L. Amato, Y. Gu, N. Bellini et al., “Integrated three-dimensional filter separates nanoscale from microscale elements in a microfluidic chip,” *Lab on a Chip*, vol. 12, no. 6, pp. 1135–1142, 2012.
- [3] M. Malinauskas, A. Zukauskas, K. Belazaras et al., “Laser fabrication of various polymer micro-optical components,” *The European Physical Journal Applied Physics*, vol. 58, Article ID 20501, 8 pages, 2012.
- [4] E. Brasselet, M. Malinauskas, A. Žukauskas, and S. Juodkazis, “Photopolymerized microscopic vortex beam generators: precise delivery of optical orbital angular momentum,” *Applied Physics Letters*, vol. 97, no. 21, Article ID 211108, 2010.
- [5] T. S. Drakakis, G. Papadakis, K. Sambani et al., “Construction of three-dimensional biomolecule structures employing femtosecond lasers,” *Applied Physics Letters*, vol. 89, no. 14, Article ID 144108, 2006.
- [6] V. Melissinaki, A. A. Gill, I. Ortega et al., “Direct laser writing of 3D scaffolds for neural tissue engineering applications,” *Biofabrication*, vol. 3, Article ID 045005, 2011.
- [7] S. Engelhardt, E. Hoch, and K. Borchers, “Fabrication of 2D protein microstructures and 3D polymer-protein hybrid microstructures by two-photon polymerization,” *Biofabrication*, vol. 3, Article ID 3025003, 2011.
- [8] V. Mizeikis, S. Juodkazis, R. Tarozaite, J. Juodkazyte, K. Juodkazis, and H. Misawa, “Fabrication and properties of metalodielectric photonic crystal structures for infrared spectral region,” *Optics Express*, vol. 15, no. 13, pp. 8454–8464, 2007.
- [9] A. Radke, T. Gissibl, T. Klotzbücher, P. V. Braun, and H. Giessen, “Three-dimensional bichiral plasmonic crystals fabricated by direct laser writing and electroless silver plating,” *Advanced Materials*, vol. 23, no. 27, pp. 3018–3021, 2011.
- [10] M. D. Turner, G. E. Schröder-Turk, and M. Gu, “Fabrication and characterization of three-dimensional biomimetic chiral composites,” *Optics Express*, vol. 19, no. 10, pp. 10001–10008, 2011.
- [11] S. W. Hell and J. Wichmann, “Breaking the diffraction resolution limit by stimulated emission: stimulated-emission-depletion fluorescence microscopy,” *Optics Letters*, vol. 19, no. 11, pp. 780–782, 1994.
- [12] T. A. Klar, S. Jakobs, M. Dyba, A. Egner, and S. W. Hell, “Fluorescence microscopy with diffraction resolution barrier broken by stimulated emission,” *Proceedings of the National Academy of Sciences of the United States of America*, vol. 97, no. 15, pp. 8206–8210, 2000.
- [13] T. F. Scott, B. A. Kowalski, A. C. Sullivan, C. N. Bowman, and R. R. McLeod, “Two-color single-photon photoinitiation and photoinhibition for subdiffraction photolithography,” *Science*, vol. 324, no. 5929, pp. 913–917, 2009.
- [14] N. Li, R. R. Gattass, E. Gershgoren, H. Hwang, and J. T. Fourkas, “Achieving  $\lambda/20$  resolution by one-color initiation and deactivation of polymerization,” *Science*, vol. 324, no. 5929, pp. 910–913, 2009.
- [15] J. Fischer and M. Wegener, “Three-dimensional direct laser writing inspired by stimulated-emission-depletion microscopy,” *Optical Materials Express*, vol. 1, pp. 614–624, 2011.
- [16] Y. Cao, Z. Gan, and B. Jia, “High-photosensitive resin for super-resolution direct-laser-writing based on photoinhibited polymerization,” *Optics Express*, vol. 19, pp. 19486–19494, 2011.
- [17] T. J. A. Wolf, J. Fischer, and M. Wegener, “Pump-probe spectroscopy on photoinitiators for stimulated-emission-depletion optical lithography,” *Optics Letters*, vol. 36, pp. 3188–3190, 2011.
- [18] I. Sakellari, E. Kabouraki, D. Gray et al., “Diffusion-assisted high resolution direct femtosecond laser writing,” *ACS Nano*, vol. 6, no. 3, pp. 2302–2311, 2012.
- [19] K. Terzaki, N. Vasilantonakis, A. Gaidukeviciute et al., “3D conducting nanostructures fabricated using direct laser writing,” *Optical Materials Express*, vol. 1, pp. 586–597, 2011.
- [20] S. John, “Strong localization of photons in certain disordered dielectric superlattices,” *Physical Review Letters*, vol. 58, no. 23, pp. 2486–2489, 1987.
- [21] E. Yablonovitch, “Inhibited spontaneous emission in solid-state physics and electronics,” *Physical Review Letters*, vol. 58, no. 20, pp. 2059–2062, 1987.
- [22] K. M. Ho, C. T. Chan, and C. M. Soukoulis, “Existence of a photonic gap in periodic dielectric structures,” *Physical Review Letters*, vol. 65, no. 25, pp. 3152–3155, 1990.
- [23] C. M. Soukoulis and M. Wegener, “Past achievements and future challenges in the development of three-dimensional photonic metamaterials,” *Nature Photonics*, vol. 5, no. 9, pp. 523–530, 2011.
- [24] J. M. Lourtioz, H. Benisty, V. Berger et al., “Photonic crystals: towards nanoscale photonic devices,” *Physics Today*, vol. 59, no. 8, pp. 54–55, 2006.
- [25] F. A. Denis, P. Hanarp, D. S. Sutherland, and Y. F. Dufrène, “Nanoscale chemical patterns fabricated by using colloidal lithography and self-assembled monolayers,” *Langmuir*, vol. 20, no. 21, pp. 9335–9339, 2004.
- [26] C. García-Meca, J. Hurtado, J. Martí, A. Martínez, W. Dickson, and A. V. Zayats, “Low-loss multilayered metamaterial exhibiting a negative index of refraction at visible wavelengths,” *Physical Review Letters*, vol. 106, no. 6, Article ID 067402, 2011.
- [27] S. Shukla, X. Vidal, E. P. Furlani et al., “Subwavelength direct laser patterning of conductive gold nanostructures by



- simultaneous photopolymerization and photoreduction,” *ACS Nano*, vol. 5, no. 3, pp. 1947–1957, 2011.
- [28] G. J. Leggett, “Direct writing of metal nanostructures: lithographic tools for nanoplasmonics research,” *ACS Nano*, vol. 5, no. 3, pp. 1575–1579, 2011.
  - [29] G. O. Mallory and J. B. Hajdu, *Electroless Plating: Fundamentals and Applications*, chapter 1, American Electroplaters and Surface Finishers Society, Orlando, Fla, USA, 1990.
  - [30] S. Hrapovic, Y. Liu, G. Enright, F. Bensebaa, and J. H. T. Luong, “New strategy for preparing thin gold films on modified glass surfaces by electroless deposition,” *Langmuir*, vol. 19, no. 9, pp. 3958–3965, 2003.
  - [31] N. Vasilantonakis, K. Terzaki, I. Sakellari et al., “Three-dimensional metallic photonic crystals with optical bandgaps,” *Advanced Materials*, vol. 24, pp. 1101–1105, 2012.
  - [32] A. V. Kabashin, P. Evans, S. Pastkovsky et al., “Plasmonic nanorod metamaterials for biosensing,” *Nature Materials*, vol. 8, no. 11, pp. 867–871, 2009.
  - [33] J. K. Gansel, M. Thiel, M. S. Rill et al., “Gold helix photonic metamaterial as broadband circular polarizer,” *Science*, vol. 325, no. 5947, pp. 1513–1515, 2009.
  - [34] S. Turunen, E. Käpylä, K. Terzaki et al., “Pico- and femtosecond laser-induced crosslinking of protein microstructures: evaluation of processability and bioactivity,” *Biofabrication*, vol. 3, Article ID 045002, 2011.
  - [35] D. Roundy and J. Joannopoulos, “Photonic crystal structure with square symmetry within each layer and a three-dimensional band gap,” *Applied Physics Letters*, vol. 82, no. 22, pp. 3835–3837, 2003.
  - [36] M. Deubel, *Three-dimensional photonic crystals via direct laser writing: fabrication and characterization [Doctoral thesis]*, Universitat Karlsruhe, 2006.
  - [37] M. Deubel, M. Wegener, S. Linden, and G. Von Freymann, “Angle-resolved transmission spectroscopy of three-dimensional photonic crystals fabricated by direct laser writing,” *Applied Physics Letters*, vol. 87, no. 22, Article ID 221104, pp. 1–3, 2005.



## Research Article

# Design of Matched Absorbing Layers for Surface Plasmon-Polaritons

**Sergio de la Cruz,<sup>1</sup> Eugenio R. Méndez,<sup>1</sup> and Alexei A. Maradudin<sup>2</sup>**

<sup>1</sup> *División de Física Aplicada, Centro de Investigación Científica y de Educación Superior de Ensenada, Carretera Ensenada-Tijuana No. 3918, 22860 Ensenada, BC, Mexico*

<sup>2</sup> *Department of Physics and Astronomy and Institute for Surface and Interface Science, University of California, Irvine, CA 92697, USA*

Correspondence should be addressed to Eugenio R. Méndez, emendez@cicese.mx

Received 29 June 2012; Accepted 23 July 2012

Academic Editor: Natalia M. Litchinitser

Copyright © 2012 Sergio de la Cruz et al. This is an open access article distributed under the Creative Commons Attribution License, which permits unrestricted use, distribution, and reproduction in any medium, provided the original work is properly cited.

We describe a procedure for designing metal-metal boundaries for the strong attenuation of surface plasmon-polaritons without the introduction of reflections or scattering effects. Solutions associated with different sets of matching materials are found. To illustrate the results and the consequences of adopting different solutions, we present calculations based on an integral equation formulation for the scattering problem and the use of a nonlocal impedance boundary condition.

## 1. Introduction

In the numerical solution of spatially unbounded electromagnetic problems it is often necessary to truncate the computational domain. The use of a region of finite spatial size can introduce reflections and other spurious effects in the calculations. Several techniques have been proposed to overcome this problem. An established one, used commonly in finite-difference time-domain (FDTD) calculations [1], is the perfectly matched layer (PML) technique proposed by Berenger [2]. Such a layer can absorb electromagnetic waves without reflections at the vacuum-PML interfaces. Methods of calculation based on Green's theorem (see, e.g., [3]) do not present such complications with volume waves, but the truncation of the interfaces can produce spurious effects in the presence of surface waves, like surface plasmon-polaritons (SPPs).

The basic properties of SPPs have been known for some time, but their importance for nanophotonic applications has produced a renewed interest on the subject [4, 5]. In studies of the interactions of SPPs with objects or surface structures, the computational problem grows as a function of the physical size of the sample and, thus, it is desirable to reduce the computational domain as much as possible. The

PML techniques known to us were not designed to handle truncation effects involving SPPs, and are not well-adapted for situations involving metallic structures and evanescent waves [6].

In this paper, we present a procedure for determining the optical constants of absorbing materials for the attenuation of SPPs without introducing, or minimizing at least, spurious reflections and/or radiative scattering effects. Although SPPs are already lossy traveling waves, a reduction of their propagation length in the matched medium permits an important reduction in the dimensions of the region over which the computational domain extends. Although our approach is related in spirit to the usual PML techniques, we point out that it addresses a different problem, namely, the termination of surfaces over which surface waves propagate without the introduction of artificial scattering or reflection effects.

The absorbing materials that we propose are homogeneous and isotropic. The flexibility for choosing their optical properties permits the selection of materials that are appropriate for the use of impedance boundary conditions. All these facts simplify considerably the electromagnetic problem. The results presented here can be applied not only for electromagnetic calculations based on integral equations,

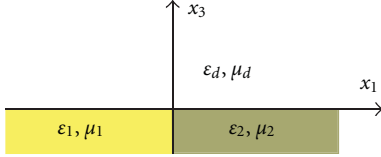


FIGURE 1: Schematic diagram of the three media considered. The upper medium is a dielectric, characterized by its electric permittivity  $\epsilon_d$  and magnetic permeability  $\mu_d$  in the frequency region of interest. Similarly, the metals 1 and 2 are characterized by  $\epsilon_1, \mu_1$  and  $\epsilon_2, \mu_2$ , respectively.

like the one used for our examples, but also for those based on differential equations, like the FDTD.

## 2. Theory

To describe the technique, let us consider the generic geometry illustrated in Figure 1. The figure shows a flat interface involving three media: a semi-infinite dielectric and two metals, defined through their permittivities and permeabilities, with a vertical boundary. We assume that SPPs traveling from left to right, impinge on the vertical boundary between media 1 and 2. The optical properties of medium 2 are to be chosen in such a way that the SPPs are strongly attenuated without the introduction of significant reflections or coupling into radiative modes.

Let us consider the magnetic field associated with an SPP traveling on the flat surface of medium 2, in the direction  $+x_1$ . This field may be conveniently written in terms of the magnetic field along the  $x_2$ -direction. We write

$$H_2^>(x_1, x_3) = H_0 e^{ik_{sp}^{(2)} x_1 + i\alpha_d(k_{sp}^{(2)}) x_3} \quad x_3 \geq 0, \quad (1a)$$

$$H_2^<(x_1, x_3) = H_0 e^{ik_{sp}^{(2)} x_1 - i\alpha_2(k_{sp}^{(2)}) x_3} \quad x_3 \leq 0, \quad (1b)$$

where  $H_0$  is a constant,

$$\begin{aligned} k_{sp}^{(2)} &= \frac{\omega}{c} \sqrt{\frac{\epsilon_d \epsilon_2 (\epsilon_2 \mu_d - \epsilon_d \mu_2)}{\epsilon_2^2 - \epsilon_d^2}}, \\ \alpha_d(k_{sp}^{(2)}) &= \sqrt{\epsilon_d \mu_d \left( \frac{\omega}{c} \right)^2 - (k_{sp}^{(2)})^2}, \\ \alpha_2(k_{sp}^{(2)}) &= \sqrt{\epsilon_2 \mu_2 \left( \frac{\omega}{c} \right)^2 - (k_{sp}^{(2)})^2}. \end{aligned} \quad (2)$$

The signs of the square roots are taken in such a way that the imaginary parts of  $k_{sp}^{(2)}$ ,  $\alpha_d(k_{sp}^{(2)})$ , and  $\alpha_2(k_{sp}^{(2)})$ , are positive. In the dielectric, the attenuation constant along  $x_3$  is given by

$$\kappa_2^> = \Im \{ \alpha_d(k_{sp}^{(2)}) \} = \frac{\omega}{c} \Im \left\{ \sqrt{\frac{\epsilon_d^2 (\epsilon_2 \mu_2 - \epsilon_d \mu_d)}{\epsilon_2^2 - \epsilon_d^2}} \right\}. \quad (3)$$

Similar expressions can be written for the interface between the dielectric and medium 1.

To minimize the scattering losses due to the vertical metallic interface of Figure 1, the transverse profile of the SPP wave must be the same on the two sides of the interface [7–9]. That is, one must have that  $\kappa_1^> = \kappa_2^>$ . On the other hand, the reflection of the SPP at the boundary should be minimized when  $\Re \{ k_{sp}^{(2)} \} = \Re \{ k_{sp}^{(1)} \}$ . We will refer to these conditions as the no scattering and no reflection conditions.

At this stage, we focus our attention on the case in which  $\epsilon_d = 1, \mu_d = 1$ , and assume that the metal on the left is nonmagnetic at optical frequencies (i.e.,  $\mu_1 = 1$ ), while that on the right has arbitrary properties. As a particular example, we consider the design of absorbing layers that match the properties of gold at the vacuum wavelength  $\lambda = 980$  nm. Then,  $\epsilon_1 = -40.44 + i2.97$  [10] and  $\mu_1 = 1.0$ . Since  $\epsilon_2$  and  $\mu_2$  are complex quantities, one must seek solutions in a four-dimensional space. To simplify matters, we have decided to fix the imaginary parts of  $\epsilon_2$  and  $\mu_2$ , and explore the space  $(\Re \{ \epsilon_2 \} - \Re \{ \mu_2 \})$ .

For physical reasons, we choose  $\Im \{ \epsilon_2 \} > 0$ . Although there seems to be no problem with the choice of a negative  $\Im \{ \mu_2 \}$  [11], we also took it as positive. With these choices, the search space is restricted to the quadrant defined by the conditions  $\Re \{ \epsilon_2 \} < 0$  and  $\Re \{ \mu_2 \} > 0$ .

For our first example we have set  $\Im \{ \epsilon_2 \} = 3.0$  and  $\Im \{ \mu_2 \} = 0.0$ . The solutions to the equations for no scattering and no reflection are shown in Figure 2(a). We observe that the two curves practically coincide when  $\Re \{ \epsilon_2 \} < -10$  and that they gradually separate as  $\Re \{ \epsilon_2 \}$  approaches zero. It is thus advisable to seek solutions in the region  $\Re \{ \epsilon_2 \} \leq -10$ .

One can see in Figure 2(a) that the pair of  $x, y$  values  $(-40.44, 1)$ , which corresponds to the properties of medium 1, lie on the solution curve. This is due to the closeness between the chosen value of  $\Im \{ \epsilon_2 \}$  and that of  $\Im \{ \epsilon_1 \}$ .

As one moves along these solution curves from left to right, the absorption coefficient of the SPPs,  $\Im \{ k_{sp}^{(2)} \}$ , increases. The behavior is illustrated in Figure 2(b). On the basis of these results, and since we are looking for solutions with a strong attenuation coefficient, we have chosen a value of  $\Re \{ \epsilon_2 \} = -10.0$ , which leads to  $\Re \{ \mu_2 \} = 0.19$  and an attenuation constant  $\Im \{ k_{sp}^{(2)} \} = 0.033 \mu\text{m}^{-1}$ . We will refer to this example as case I.

Values of the real parts of  $\epsilon_2$  and  $\mu_2$  that result in higher attenuation coefficients are not appropriate for our purposes, as they produce a mismatch between the no scattering and no reflection conditions. Moreover, as can be inferred from the discussion in the following section, they lead to solutions that are more difficult to handle computationally.

For our second example, we chose  $\Im \{ \epsilon_2 \} = 3.0$  and  $\Im \{ \mu_2 \} = 10.0$ . The solution map is shown in Figure 3(a), and the attenuation coefficient for SPPs is shown in Figure 3(b). We see that, with these parameters, the curves corresponding to the no scattering and no reflection conditions are fairly close, but differ by an increasing amount as the magnitude of  $\Re \{ \epsilon_2 \}$  decreases. The attenuation coefficient curves, on the other hand, are practically indistinguishable in this case. For this second example, we choose  $\Re \{ \epsilon_2 \} = -531.62$ , and based on

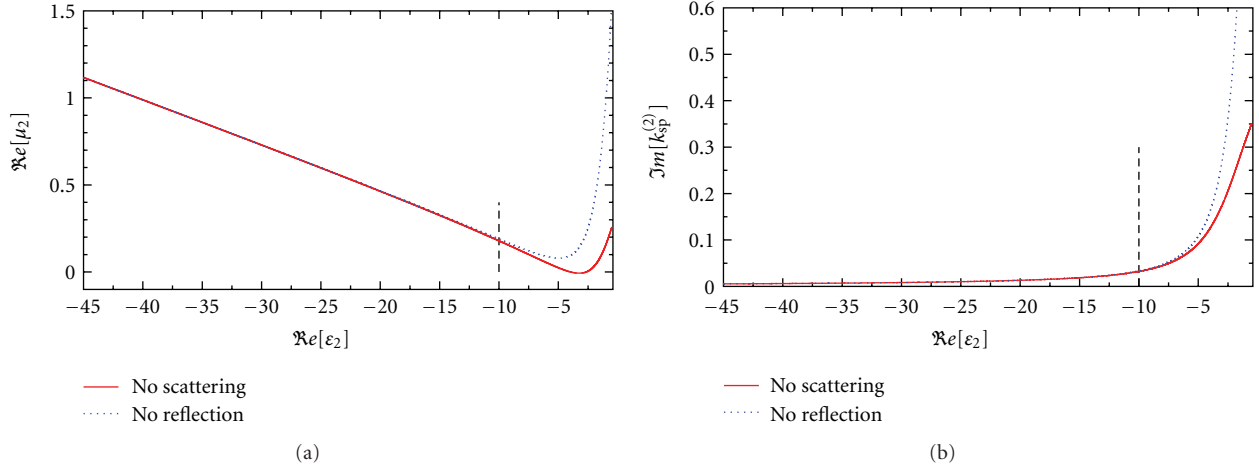


FIGURE 2: (a) Solution curves corresponding to the no reflection and no scattering conditions assuming  $\Im m\{\epsilon_2\} = 3.0$  and  $\Im m\{\mu_2\} = 0.0$ . (b) Behavior of  $\Im m\{k_{sp}^{(2)}\}$  along the solution curves. The value of  $\Re\{\epsilon_2\}$  chosen for the example is denoted by the vertical dashed line.

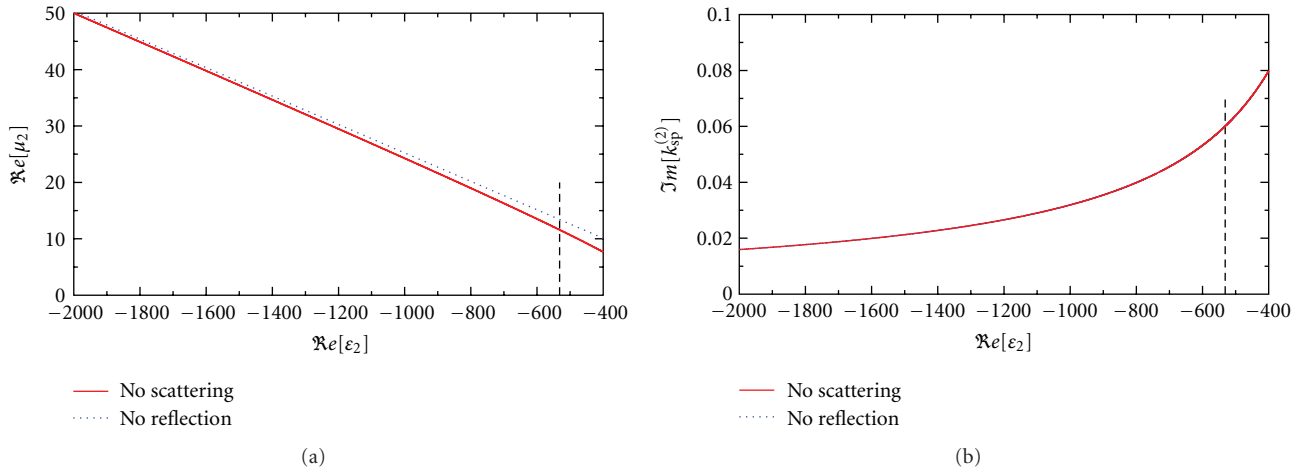


FIGURE 3: (a) Solution curves corresponding to the no reflection and no scattering conditions assuming  $\Im m\{\epsilon_2\} = 3.0$  and  $\Im m\{\mu_2\} = 10.0$ . (b) Behavior of  $\Im m\{k_{sp}^{(2)}\}$  along the solution curves. The value of  $\Re\{\epsilon_2\}$  chosen for the example is denoted by the vertical dashed line.

the no-scattering-condition curve, one has that  $\Re\{\mu_2\} = 13.44$  and  $\Im m\{k_{sp}^{(2)}\} = 0.06 \mu\text{m}^{-1}$ . We will refer to this example as case II. It is worth mentioning that the results obtained with these parameters are practically the same as those obtained with the parameters corresponding to the no reflection curve.

Scattering calculations involving gold and the materials proposed in this section will be presented and discussed in Section 4.

### 3. A Nonlocal Impedance Boundary Condition

The attenuation of SPPs in the proposed matching media can be visualized through rigorous electromagnetic simulations of the problem. We base our calculations on an integral

equation formulation that has been used for rough-surface-scattering studies [3]. Geometries like the one depicted in Figure 1 pose some difficulties for this kind of approach, but the problem can be simplified with the use of an impedance boundary condition [12–14]. The use of an impedance boundary condition in the present problem leads to a formulation of the scattering problem that does not require knowledge of the field below the interface.

Impedance boundary conditions have been used in the past for scattering calculations and are known to provide accurate results for good conductors, like gold and silver, in the near infrared [15]. We shall see however that, due to the rapid decay of the SPPs in the absorbing region, a local impedance boundary condition is insufficient to deal with some of the media considered here. So, before discussing the scattering calculations, we present a brief derivation of

the impedance boundary condition for flat surfaces, which includes the first nonlocal term.

With reference to Figure 1, we consider the field below a flat interface, inside a medium with the properties of medium 2. It can be written in the form

$$H_2^<(x_1, x_3) = \int_{-\infty}^{\infty} \frac{dq}{2\pi} A(q) e^{iqx_1 - i\alpha_2(q)x_3}, \quad (4)$$

where  $A(q)$  is the scattering amplitude, or angular spectrum of the field below the interface.

Here,  $\alpha_2(q) = \sqrt{\epsilon_2 \mu_2 (\omega/c)^2 - q^2}$ , with  $\Im\{\alpha_2(q)\} > 0$ . Since

$$A(q) = \int_{-\infty}^{\infty} dx'_1 H_2^<(x'_1, 0) e^{-iqx'_1}, \quad (5)$$

one can write

$$H_2^<(x_1, x_3) = \int_{-\infty}^{\infty} \frac{dq}{2\pi} \int_{-\infty}^{\infty} dx'_1 \times H_2^<(x'_1, 0) e^{iq(x_1 - x'_1) - i\alpha_2(q)x_3}. \quad (6)$$

From this expression, one can establish the following integral equation involving the field and its normal derivative on the interface:

$$\left. \frac{\partial H_2^<(x_1, x_3)}{\partial x_3} \right|_{x_3=0} = \int_{-\infty}^{\infty} dx'_1 K(x_1, x'_1) H_2^<(x'_1, 0), \quad (7)$$

where

$$K(x_1, x'_1) = \frac{1}{i} \int_{-\infty}^{\infty} \frac{dq}{2\pi} \alpha_2(q) e^{iq(x_1 - x'_1)}. \quad (8)$$

We now seek the solution of (7) by expanding  $\alpha_2(q)$  as follows:

$$\alpha_2(q) \approx \sqrt{\epsilon_2 \mu_2} \left( \frac{\omega}{c} \right) \left[ 1 - \frac{q^2}{2\epsilon_2 \mu_2 (\omega/c)^2} + \dots \right], \quad (9)$$

which leads to

$$K(x_1, x'_1) = \frac{1}{i} \sqrt{\epsilon_2 \mu_2} \left( \frac{\omega}{c} \right) \delta(x_1 - x'_1) + \frac{1}{2i(\omega/c) \sqrt{\epsilon_2 \mu_2}} \delta''(x_1 - x'_1) + \dots \quad (10)$$

In this expression,  $\delta(x_1)$  is a delta function and  $\delta''(x_1)$  its second derivative.

Keeping only the first two terms, we find the relation

$$\left. \frac{\partial H_2^<(x_1, x_3)}{\partial x_3} \right|_{x_3=0} = \frac{1}{i} \sqrt{\epsilon_2 \mu_2} \left( \frac{\omega}{c} \right) H_2^<(x_1, x_3) \Big|_{x_3=0} + \frac{1}{2i \sqrt{\epsilon_2 \mu_2} (\omega/c)} \left. \frac{\partial^2 H_2^<(x_1, x_3)}{\partial x_1^2} \right|_{x_3=0}, \quad (11)$$

and using the continuity of the tangential components of the fields across the interface we find that

$$\frac{1}{\epsilon_d} L^>(x_1) = \frac{1}{\epsilon_2} \left[ \frac{1}{i} \sqrt{\epsilon_2 \mu_2} \left( \frac{\omega}{c} \right) H^>(x_1) + \frac{1}{2i \sqrt{\epsilon_2 \mu_2} (\omega/c)} \frac{d^2 H^>(x_1)}{dx_1^2} \right], \quad (12)$$

where

$$H^>(x_1) = H_2^>(x_1, x_3) \Big|_{x_3=0}, \quad (13)$$

$$L^>(x_1) = \left. \frac{\partial H_2^>(x_1, x_3)}{\partial x_3} \right|_{x_3=0}.$$

Finally, we write (12) in the form

$$L^>(x_1) = K_p^{(0)} H^>(x_1) + K_p^{(2)} \frac{d^2 H^>(x_1)}{dx_1^2}, \quad (14)$$

where

$$K_p^{(0)} = \frac{\omega}{ic} \epsilon_d \sqrt{\frac{\mu_2}{\epsilon_2}}, \quad (15)$$

$$K_p^{(2)} = \frac{\epsilon_d / \epsilon_2}{2i \sqrt{\epsilon_2 \mu_2} (\omega/c)}.$$

The first term in the impedance expansion (14) represents a local relation between  $L^>(x_1)$  and  $H^>(x_1)$  (or between the  $E$  and  $H$  fields). The second term, represents the first nonlocal correction.

We see that as the attenuation of the SPPs becomes stronger, the second derivative of the field appearing in (14) becomes larger. Looking at the quantities entering the expression for  $K_p^{(2)}$ , we conclude that it is desirable to have media with a high refractive index  $n_2 = \sqrt{\epsilon_2 \mu_2}$ . For a more quantitative evaluation of this issue, we consider the ratio between the first two terms of the expansion. This ratio  $\mathcal{R}$  constitutes an incomplete but, nevertheless, essential knowledge for establishing the validity of the local relation and the convergence of the expansion. Using the general form of the field associated with an SPP on a flat surface given by (1a), we find that

$$\mathcal{R} = \left| \frac{K_p^{(2)} (d^2 H^>(x_1) / dx_1^2)}{K_p^{(0)} H^>(x_1)} \right| = \frac{1}{2} \left| \frac{k_{sp}^{(2)}}{n_2 (\omega/c)} \right|^2, \quad (16)$$

where  $n_2$  is the complex refractive index of medium 2.

In normal circumstances (i.e., when  $\mu_2 = 1$ ), for a good conductor one has that  $n_2$  is large and that  $|k_{sp}^{(2)}| \approx (\omega/c)$ . Thus,  $\mathcal{R}$  is small, and the nonlocal term can be neglected. For instance, for a gold-vacuum interface and the wavelength considered, this ratio is  $\mathcal{R} = 0.0125$ .

Turning our attention to the absorbing materials proposed in Section 2, for our first example (case I) this ratio turns out to be  $\mathcal{R} = 0.258$ . It is clear that a local impedance boundary condition would not be accurate on the absorbing side of the boundary and that nonlocal correction terms are needed. This conclusion is supported by the numerical calculations presented in Section 4.

For case II, the ratio between the first two terms of expansion (14) is  $\mathcal{R} = 1.67 \times 10^{-5}$ . Not surprisingly, the local impedance boundary condition is very accurate in this case. This case leads to parameters that are more convenient for our type of calculation.

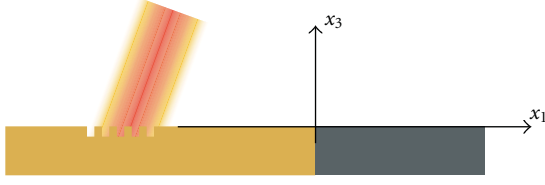


FIGURE 4: Schematic diagram of the scattering geometry considered for the calculations. A Gaussian beam illuminates a short gold grating that couples a fraction of the incident light to SPPs traveling to the right. The absorbing material is represented by the darker region.

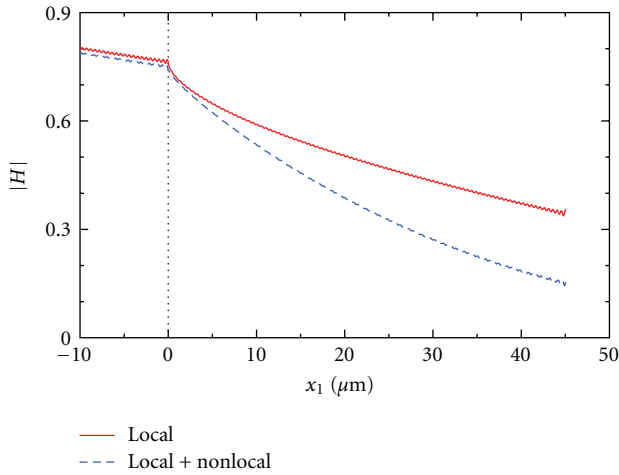


FIGURE 5: Magnitude of the surface field calculated using the local impedance boundary condition and the first nonlocal correction for case I. The boundary between the two metals is at  $x_1 = 0$  and, to facilitate the visualization of the interaction of the SPP with the metal-metal boundary, the region of the grating is not shown.

#### 4. Results and Discussion

In this section, we present scattering calculations corresponding to the two examples of matching media proposed in Section 2, starting with a summary of their properties: For case I we have  $\epsilon_2 = -10.0 + 3.0i$  and  $\mu_2 = 0.19$ , while for case II,  $\epsilon_2 = -531.62 + 3.0i$  and  $\mu_2 = 13.44 + 10.0i$ . In the first case, the attenuation constant for SPPs is  $\Im m\{k_{sp}^{(2)}\} = 0.033 \mu\text{m}^{-1}$ , while for the second  $\Im m\{k_{sp}^{(2)}\} = 0.06 \mu\text{m}^{-1}$ .

The geometry employed for the scattering calculations is shown in Figure 4. Based on previous results [16], to excite SPPs traveling to the right, we use an array of 5 rectangular grooves of period  $T = 0.863\lambda$ , illuminated by a Gaussian beam of width  $g = 2\lambda$  with an angle of incidence  $\theta_0 \approx -6.5^\circ$ . The coupling efficiency for the SPPs travelling to the right is about 45%. The distance between the start of the buffer material and the end of the surface is  $45 \mu\text{m}$ .

The magnitude of the surface field associated with the SPP propagating along the surface for case I is shown in Figure 5. To simplify the visualization of the region of interest, the section with the grating was omitted from the figure. The curve shown with a continuous line was calculated with a local impedance boundary condition,

while for the dashed-line curve we included also the first nonlocal term. One observes that the attenuation constant of SPP changes as the wave enters the absorbing material. As expected, the nonlocal correction does make a substantial difference in the calculations. The small ripples observed in the upper curve are due to standing waves caused by the reflection of the SPP at the end of the surface. With this material it is important to use at least the first nonlocal correction in expansion (14).

In Figure 6, we show the calculated magnetic near-field intensity map (i.e.,  $|H|^2$ ) for case I. As in the previous figure, only the rightmost section of the sample is shown. It can be observed that the SPP arrives from the left and decays quite steeply as it enters the absorbing medium. The results are encouraging. The incident SPP is not perturbed much by the interface, and it is clear that the reflection and scattering effects are low.

The near-field intensity map corresponding to case II is shown in Figure 7. The attenuation of the SPP is stronger in this case, and the local impedance boundary condition gives accurate results. As desired, the SPP wave practically vanishes after only a few microns. As in case I, the incident SPP does not appear to be perturbed much by the interface.

To investigate the possible leakage of the SPPs guided waves due to the absorbing boundary, we present, in Figure 8, far-field calculations corresponding to a complete gold sample and to samples terminated with the absorbing materials that we have called cases I and II (see Figure 4).

The scattering curves show that there is a relatively strong reflected beam in the specular direction ( $\theta_s \approx -6.5^\circ$ ) as well as a broad, grazing diffraction order. The rapid oscillations observed in the diffraction order for the case of the gold surface are due to the leakage of the SPP at the end of the surface, which interfere with the grazing order. Moreover, the SPP reflected at this end propagate back and leak into the specular direction upon interaction with the grating. This gives rise to the small-scale oscillations over the whole curve.

The differential reflection coefficient curves corresponding to cases I and II are much cleaner. In particular, the fine-scale oscillations that can be observed over the whole curve associated with the gold surface have disappeared. Also, the strong and rapid oscillations in the region of the diffraction order have been replaced by smoother and less important oscillations that seem to be due to residual scattering at the metal-metal interface.

#### 5. Summary and Conclusions

In this paper, we have presented a procedure for designing metal-metal boundaries for the strong attenuation of surface plasmon-polaritons, minimizing the introduction of reflections or scattering effects.

We have illustrated the results by means of computer simulations based on an integral equation formulation of the scattering problem and an impedance boundary condition. Depending on the parameters chosen for the matching medium, nonlocal corrections might be needed for the calculations.



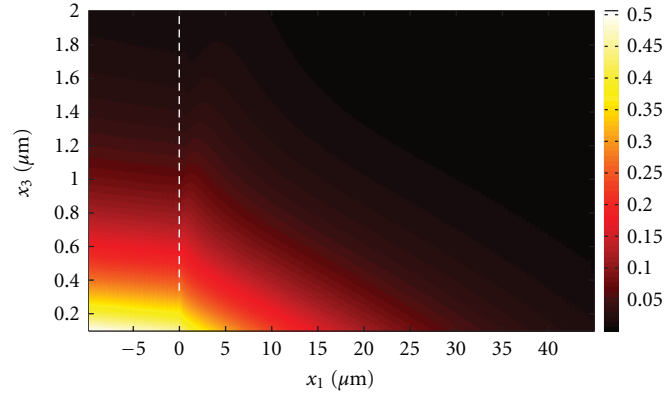


FIGURE 6: Squared modulus of the magnetic field in the vacuum region, above the flat metallic surfaces for case I. The position of the vertical border between the two metals at  $x_1 = 0$  is denoted by the vertical dashed white line.

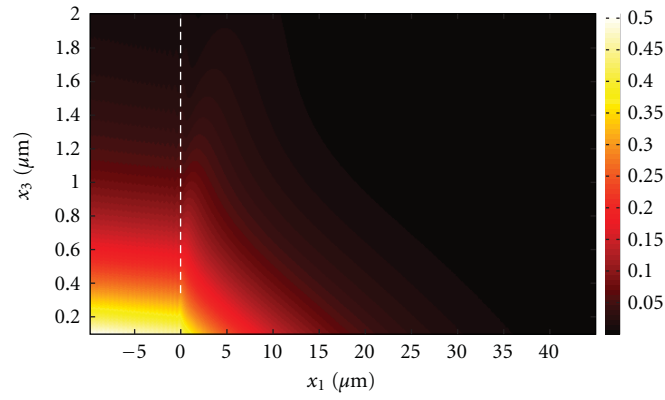


FIGURE 7: Squared modulus of the magnetic field in the vacuum region, above the flat metallic surfaces for case II. The position of the vertical border between the two metals at  $x_1 = 0$  is denoted by the vertical dashed white line.

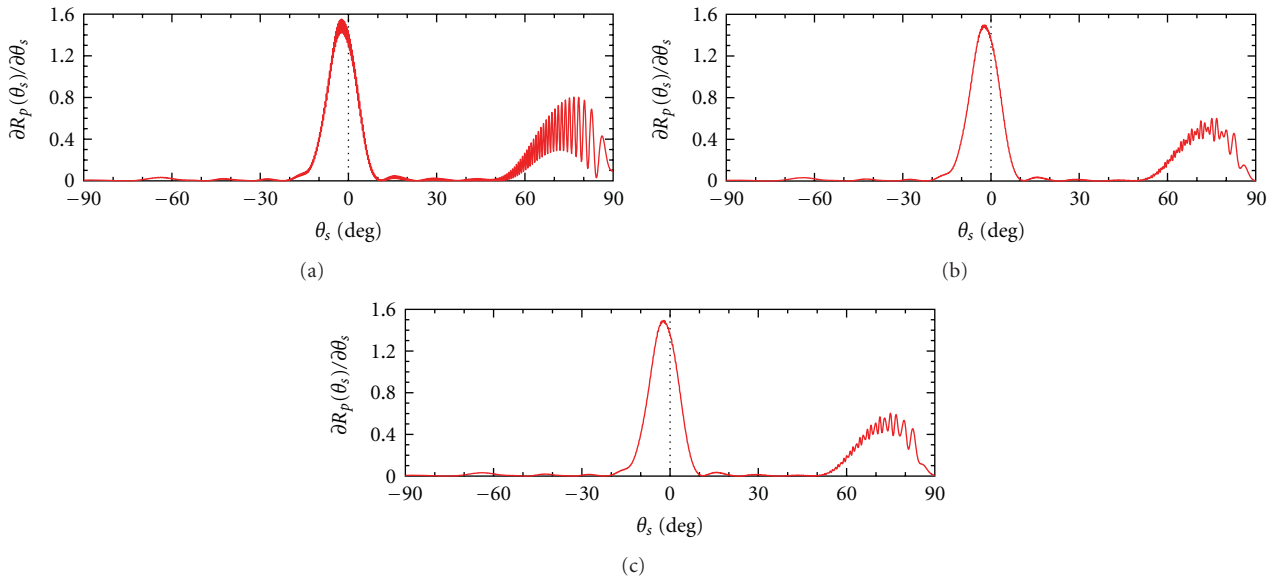


FIGURE 8: The differential reflection coefficient for a gold surface (a), a gold surface terminated with the material of case I (b), and a gold surface terminated with the material of case II (c).

The results show that with the method described here, SPPs can be attenuated strongly without introducing significant effects in near field calculations. The propagation of the SPP is practically unperturbed along the original interface and spurious reflection and scattering effects are minimal. The implementation of the technique is fairly simple and can be used effectively in plasmonic and nanophotonic calculations by different methods.

The far-field results, however, seem to indicate the presence of some residual scattering originating from the metal-metal boundary. It is worth pointing out that this leakage is not due to the use of an impedance boundary condition or to the small difference between the values of the dielectric constants corresponding to the no-scattering and no-reflection conditions.

## Acknowledgments

S. de la Cruz is grateful to the Consejo Nacional de Ciencia y Tecnología (CONACYT) for the award of a scholarship. The work of E. R. Méndez was supported in part by CONACYT, under Grant numbers 150466 and 180654. The research of A. A. Maradudin was supported in part by AFRL contract FA9453-08-C-0230.

## References

- [1] A. Taflové, *Computational Electrodynamics: The Finite-Difference Time-Domain Method*, Artech House, Boston, Mass, USA, 1995.
- [2] J. P. Berenger, "A perfectly matched layer for the absorption of electromagnetic waves," *Journal of Computational Physics*, vol. 114, no. 2, pp. 185–200, 1994.
- [3] A. A. Maradudin, T. Michel, A. R. McGurn, and E. R. Méndez, "Enhanced backscattering of light from a random grating," *Annals of Physics*, vol. 203, no. 2, pp. 255–307, 1990.
- [4] A. V. Zayats, I. I. Smolyaninov, and A. A. Maradudin, "Nano-optics of surface plasmon polaritons," *Physics Reports*, vol. 408, no. 3–4, pp. 131–314, 2005.
- [5] S. A. Maier, *Plasmonics: Fundamentals and Applications*, Springer, New York, NY, USA, 2007.
- [6] C. C. Chao, S. H. Tu, C. M. Wang, H. I. Huang, C. C. Chen, and J. Y. Chang, "Impedance-matching surface plasmon absorber for FDTD simulations," *Plasmonics*, vol. 5, no. 1, pp. 51–55, 2010.
- [7] R. F. Oulton, D. F. P. Pile, Y. Liu, and X. Zhang, "Scattering of surface plasmon polaritons at abrupt surface interfaces: implications for nanoscale cavities," *Physical Review B*, vol. 76, no. 3, Article ID 035408, 12 pages, 2007.
- [8] J. Elser and V. A. Podolskiy, "Scattering-free plasmonic optics with anisotropic metamaterials," *Physical Review Letters*, vol. 100, no. 6, Article ID 066402, 4 pages, 2008.
- [9] N. Zavareian and R. Massudi, "Study on scattering coefficient of surface plasmon polariton waves at interface of two metal-dielectric waveguides by using G-GFSIEM method," *Optics Express*, vol. 18, no. 8, pp. 8574–8586, 2010.
- [10] P. B. Johnson and R. W. Christy, "Optical constants of the noble metals," *Physical Review B*, vol. 6, no. 12, pp. 4370–4379, 1972.
- [11] V. A. Markel, "Can the imaginary part of permeability be negative?" *Physical Review E*, vol. 78, no. 2, Article ID 026608, 5 pages, 2008.
- [12] R. A. Depine and J. M. Simon, "Surface impedance boundary condition for metallic diffraction gratings in the optical and infrared range," *Optica Acta*, vol. 30, no. 3, pp. 313–322, 1983.
- [13] R. García-Molina, A. A. Maradudin, and T. A. Leskova, "The impedance boundary condition for a curved surface," *Physics Report*, vol. 194, no. 5–6, pp. 351–359, 1990.
- [14] A. A. Maradudin and E. R. Méndez, "Theoretical studies of the enhanced backscattering of light from one-dimensional randomly rough metal surfaces by the use of a nonlocal impedance boundary condition," *Physica A*, vol. 207, no. 1–3, pp. 302–314, 1994.
- [15] M. E. Knotts, T. R. Michel, and K. A. O'Donnell, "Comparisons of theory and experiment in light scattering from a randomly rough surface," *Journal of the Optical Society of America A*, vol. 10, no. 5, pp. 928–941, 1993.
- [16] S. de la Cruz, E. R. Méndez, D. Macías, R. Salas-Montiel, and P. M. Adam, "Compact surface structures for the efficient excitation of surface plasmon-polaritons," *Physica Status Solidi B*, vol. 249, no. 6, pp. 1178–1187, 2012.

## Research Article

# Optical Manipulation with Plasmonic Beam Shaping Antenna Structures

Young Chul Jun<sup>1,2</sup> and Igal Brener<sup>1,2</sup>

<sup>1</sup> Center for Integrated Nanotechnologies (CINT), Sandia National Laboratories, Albuquerque, NM 87185, USA

<sup>2</sup> Sandia National Laboratories, Albuquerque, NM 87185, USA

Correspondence should be addressed to Young Chul Jun, youngchul.jun@sandia.gov

Received 6 June 2012; Accepted 16 July 2012

Academic Editor: Alexandra E. Boltasseva

Copyright © 2012 Y. C. Jun and I. Brener. This is an open access article distributed under the Creative Commons Attribution License, which permits unrestricted use, distribution, and reproduction in any medium, provided the original work is properly cited.

Near-field optical trapping of objects using plasmonic antenna structures has recently attracted great attention. However, metal nanostructures also provide a compact platform for general wavefront engineering of intermediate and far-field beams. Here, we analyze optical forces generated by plasmonic beam shaping antenna structures and show that they can be used for general optical manipulation such as guiding of a dielectric particle along a linear or curved trajectory. This removes the need for bulky diffractive optical components and facilitates the integration of optical force manipulation into a highly functional, compact system.

## 1. Introduction

Optical forces can be exerted on objects by transferring light momentum. A tightly focused optical field can produce a stable trapping force around its focus and is highly useful for trapping particles or biological molecules; this effect is known as “optical tweezers” [1–3]. More generally, carefully tailored wavefronts of light can be utilized for various types of optical manipulation such as particle guiding and rotation [4–6]. Recently, plasmonic nanostructures have attracted attention for this application [7–9]. A variety of nanopatterns such as metallic nanoparticles [10] and sharp tips [11] have been considered for plasmonic optical tweezers. Those structures have tighter light confinement and greater field gradient than conventional optical tweezers and thus produce a larger trapping force and smaller trapping volume.

However, plasmonic antenna structures are also useful for shaping intermediate and far-field beam patterns. Metal nanostructures provide a general platform for wavefront engineering [12, 13]. Metal slitgroove or hole-groove structures were shown to be useful for collimating/directing light [14–16]. Metal nanoslit or nanohole arrays were used for focusing a beam into a small spot [17–19]. Metal nanostructures were also studied for angular momentum control of light [20–22]. Previously, such beam shaping has been

achieved with elaborate wavefront and beam control (such as Bessel, Airy, or Laguerre-Gaussian beams) involving bulky diffractive or holographic components [5]. Nanostructured metal films provide an alternative, compact way for tailoring wavefronts without such bulky and complicated elements.

In this paper, we analyze optical forces caused by nanostructured metal films and show that they can be used for general optical manipulation. The force magnitude is comparable to that achieved with conventional diffractive optics, but the plasmonic nanostructures have larger design and patterning flexibility. Moreover, the planar geometry facilitates integration with other components, such as lasers [23] and optical fibers [24]. They can be integrated with microfluidics or micromechanical systems too. Thus, we expect that plasmonic beam shaping will give another interesting venue for optical manipulation studies, especially promising for compact integrated systems.

## 2. Guiding along a Linear Trajectory

We first consider optical forces using symmetric metal slit-groove structures. Lezec et al. demonstrated narrow angle ( $\pm 3^\circ$ ) light collimation using such structures [14]. Light still diverges, but it can be collimated tightly over a nonnegligible

distance (more than tens of micrometers for visible light). Figure 1(a) shows a plasmonic beaming structure exhibiting such light collimation in water. A metal slit is surrounded by 6 side grooves on each side. The optimal groove parameters for beaming were chosen using numerical simulations (Figure 1(a) caption). Laser light ( $\lambda_0 = 633$  nm) is incident from the left and collimated after passing the slitgroove.

An incident plane wave excites surface plasmon waves in the slit, and those surface plasmons are scattered into far-field light again at the exit slit. The properly designed sidegrooves produce the constructive interference of scattered light and a collimated, narrow-angle beam as shown in Figure 1(b) [25]. The incident side of the metal film can be also patterned to increase the optical power throughput by orders of magnitude [26]. This will reduce the required incident laser power for optical manipulation. However, it is well known that the beaming pattern is determined solely by the groove pattern on the output side.

We now calculate the optical forces and show that this beaming structure can be used for dielectric particle guiding. A dielectric sphere (diameter  $D = 1 \mu\text{m}$ ,  $n = 1.59$ ) is placed around the collimated beam, and we perform numerical simulations (3-dimensional finite difference time domain, FDTD) [27] to obtain the total electromagnetic fields (including both incident and scattered fields). Then, we evaluate the optical force on a particle by calculating and integrating Maxwell's stress tensor over a surface surrounding the particle. The time-averaged optical force is

$$\langle \mathbf{F} \rangle = \int \langle \mathbf{T} \rangle \cdot \mathbf{n} da, \quad (1)$$

where  $\mathbf{n}$  is the unit vector normal to the surface, and  $\mathbf{T}$  is the Maxwell's stress tensor [28] given by

$$\mathbf{T} = \epsilon\epsilon_0 \mathbf{E}\mathbf{E} + \mu\mu_0 \mathbf{H}\mathbf{H} - \frac{\mathbf{I}}{2} (\epsilon\epsilon_0 |\mathbf{E}|^2 + \mu\mu_0 |\mathbf{H}|^2). \quad (2)$$

Figure 1(c) shows optical forces for a particle located  $12 \mu\text{m}$  away from the film. The force in the  $Y$ -direction ( $F_Y$ ) has a negative slope around the beam center (which means the particle is attracted toward the beam center), and the force in the  $X$ -direction ( $F_X$ ) is positive (which means the particle is pushed forward). We calculate the pushing force  $F_X$  as a function of the particle diameter and find it increasing rapidly with size in the considered range (Figure 1(d)). We gradually move a particle (within the dotted region in Figure 1(b)) and obtain the force vector map (Figure 1(e)). The arrows indicate the direction and magnitude of optical forces at a corresponding position. A particle is trapped into the center of the collimated beam due to the gradient force and is pushed forward along a linear trajectory due to the scattering force.

Such optical guiding has been achieved with nondiffractive or propagation-invariant laser modes (such as Bessel beams) which are generated by diffractive or holographic optical elements [5, 29]. The origin of nondiffracting beams can be explained by the decomposition of a field into plane waves. Each plane wave component acquires an equal phase shift as the field propagates in such beams. This makes the

sum of plane waves invariant, generating diffraction-free behavior over a limited distance range. The nanopatterned metal films provide a simple, alternative way for particle guiding over a nonnegligible distance.

### 3. Guiding along a Tilted or Curved Trajectory

We can also guide a particle at a predefined direction with a slightly modified structure. An asymmetric slitgroove structure shown in Figure 2(a) generates a collimated beam at an angle (Figure 2(b)). The different groove periods on either side generate constructive interference in the off-axis direction. As in the previous section, we optimize the asymmetric groove parameters through numerical simulations. The calculated force vector map for this structure (Figure 2(c)) shows that a particle is trapped and guided into the off-axis direction; the trajectory is also curved. The slitgroove structures in Figures 1 and 2 extend in the  $Z$ -direction. Thus, the collimated beam also extends in the  $Z$ -direction and this is good for manipulating elongated particles or molecules. Moreover, we could also use a holegroove or bull's eye structure [14] to get 2-dimensional collimation. Then, a particle will be trapped and guided along an axial beam. With shifted hole/groove positions, the axial beam can be also directed off-axis [30], similar to Figure 2(b).

Such curved optical guiding can also be achieved using sophisticated optical beam modes. For example, Airy beams were recently used to guide a dielectric particle along a curved trajectory over  $75 \mu\text{m}$ , termed "optical snowblowing" [31]. Airy beams do not propagate along straight lines but instead follow parabolic trajectories. Such beams can be used to transfer particles and cells between microfluidic chambers or remove particles from a region of space. Plasmonic antenna structures provide a simple, alternative way for such optical manipulation.

Similar guiding of a particle has been demonstrated using waveguide structures too [32–35]. A dielectric particle can be trapped by the evanescent field of waveguide modes and pushed along the waveguide toward the light propagation direction. In contrary to this waveguide method, the plasmonic beam shaping enables such guiding even in regions beyond the extent of evanescent fields (intermediate to far field). Furthermore, plasmonic beam shaping has larger design flexibility and tunability.

It is possible to obtain dynamic tuning in our beaming and optical manipulation system. Figure 3 shows the simulated field intensities for two incident light wavelengths ( $\lambda_0 = 560$  nm and  $700$  nm). The pattern geometry is the same as Figure 2(a) (i.e., asymmetric slitgroove). We notice that the shorter wavelength light ( $\lambda_0 = 560$  nm) is directed along the center line (Figure 3(a)), while the long wavelength light ( $\lambda_0 = 700$  nm) is directed upward ( $Y > 0$ , Figure 3(b)). Different wavelengths result in different interference conditions and beaming directions. This also implies that a particle will be pushed into different directions depending on the incident laser wavelength. If we use two different wavelength laser sources or a tunable laser, we can change the optical force directions. Moreover, light diffraction in these slitgroove

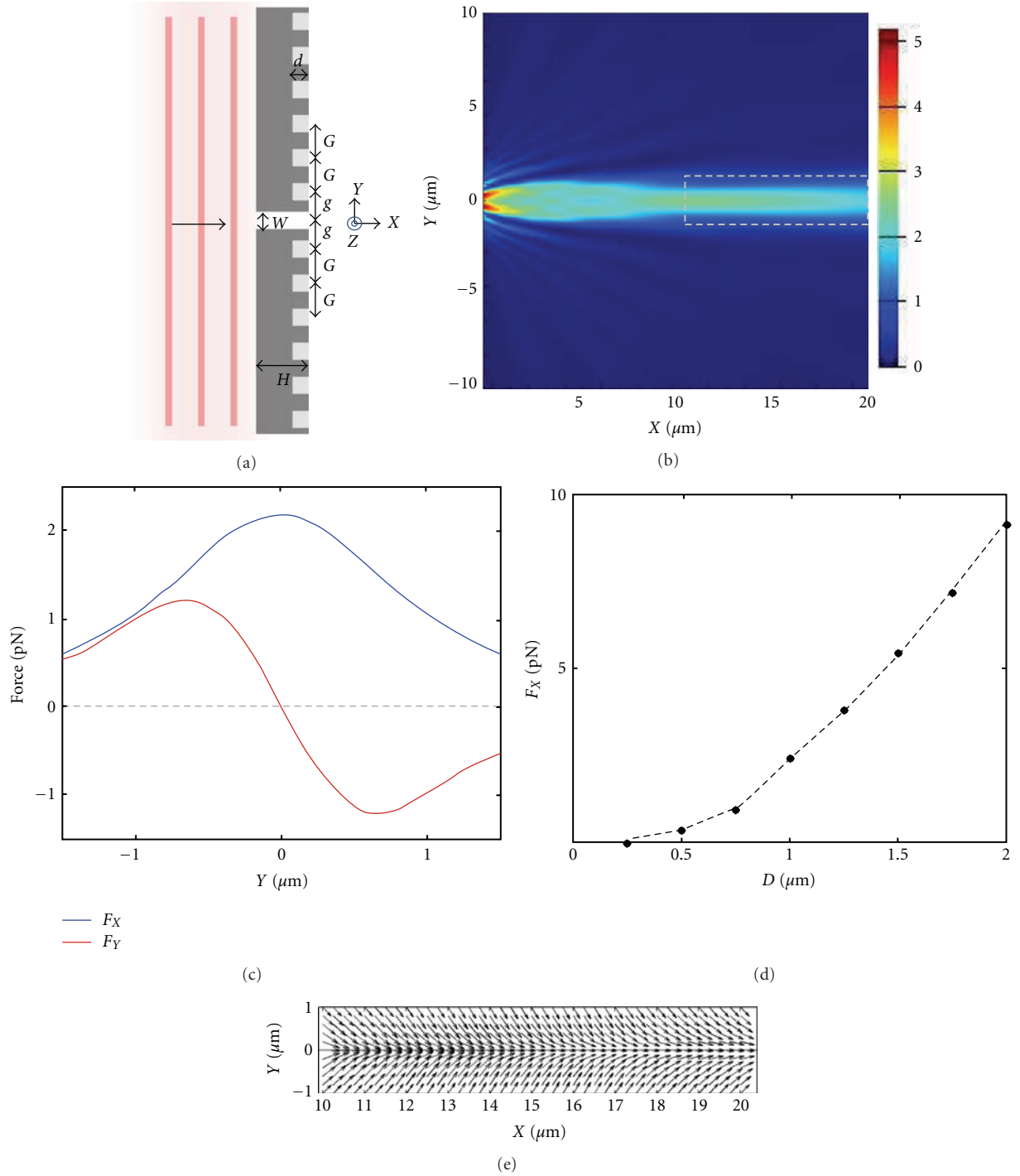


FIGURE 1: (Color online) Optical guiding with a symmetric slitgroove along a linear trajectory. (a) Schematic of the silver slitgroove.  $W = 80$  nm,  $G = g = 415$  nm,  $d = 40$  nm, and  $H = 300$  nm. The film is immersed in water ( $n = 1.33$ ). The structure is extended in the  $Z$ -direction. The optimal geometry for beaming was determined by numerical simulations. (b) Electric field intensity obtained from a numerical simulation. (c) Optical force for a dielectric particle ( $D = 1 \mu\text{m}$ ,  $n = 1.59$ ) located at  $X = 12 \mu\text{m}$ . The force magnitude is normalized to the transmitted power (through the slit) of  $10 \text{ mW}/\mu\text{m}$  in the  $Z$ -direction. (d) Optical force  $F_X$  as a function of the particle diameter. The particle is located at  $X = 12 \mu\text{m}$ ,  $Y = 0 \mu\text{m}$ . (e) Optical force vector map.



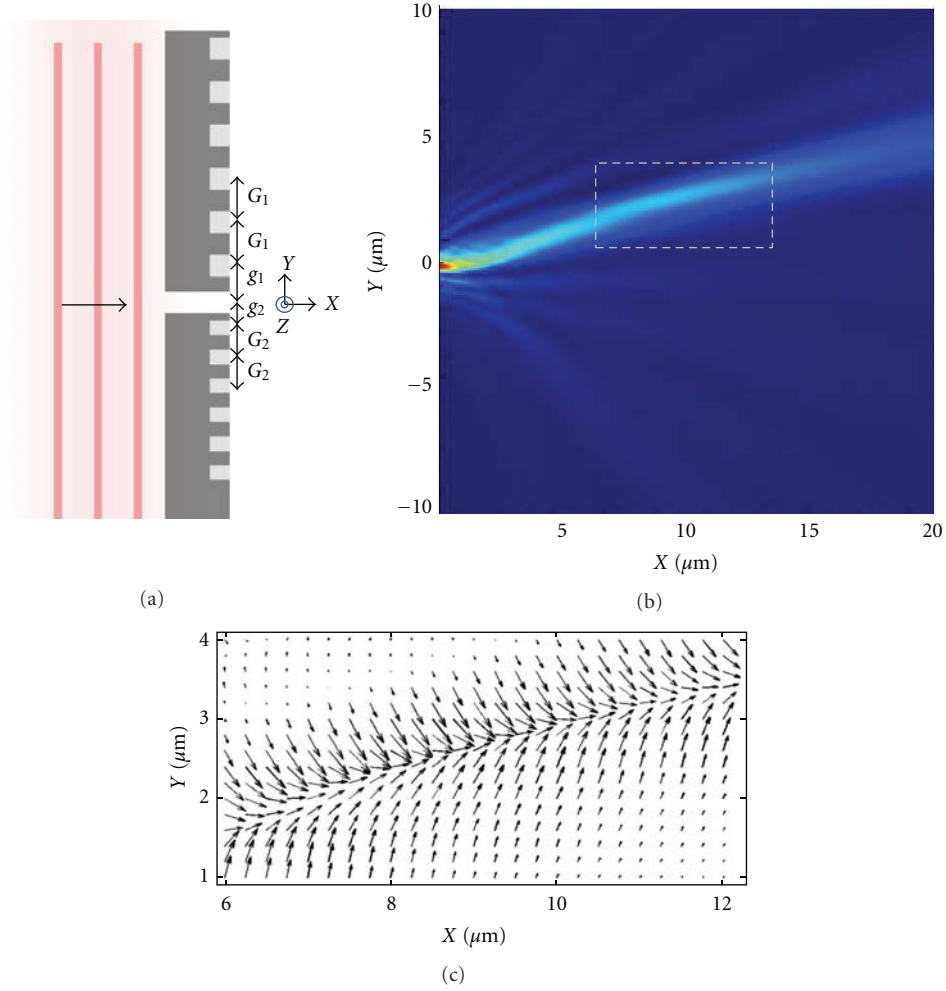


FIGURE 2: (Color online) Optical guiding with an asymmetric slitgroove. (a) Schematic of the silver slitgroove.  $G_1 = g_1 = 500$  nm,  $G_2 = g_2 = 320$  nm,  $W = 80$  nm,  $d = 40$  nm, and  $H = 300$  nm. (immersed in water). (b) Electric field intensity showing the plasmonic beaming at off-axis. (c) Optical force vector map for the dotted region in (b).

systems is sensitive to the refractive index of a medium inside the slit or on the grooves. There have been studies for dynamic control of metal slit transmission using nonlinear optical medium [36] or optical interference with a control beam [37]. Thus, if we dynamically tune the refractive index either optically or electrically, we can actively control optical force directions without using any moving parts.

#### 4. “On-Chip” Optical Rotation

Light also possesses angular momentum, and the transfer of angular momentum can lead to rotational motion of a particle (by exerting optical torques on the object). For a monochromatic field, the time-averaged optical torque [8] can be obtained as

$$\langle \mathbf{N} \rangle = - \int \langle \mathbf{T}(\mathbf{r}, t) \times \mathbf{r} \rangle \cdot \mathbf{n}(\mathbf{r}) da, \quad (3)$$

where  $\mathbf{n}$  is the unit vector normal to a surface surrounding the particle, and  $\mathbf{T}$  is the Maxwell’s stress tensor.

Nanopatterned metal films have also been used for angular momentum control of light. Linearly polarized light can be converted into circularly polarized one (that possesses the spin angular momentum of  $\hbar/2\pi$  per photon), for example, by passing through an elliptical metal hole-groove structure (Figure 4(a)) [20] or coupled orthogonal metal slits [21]. These structures effectively work as a plasmonic quarter waveplate. Recently, a plasmonic spiral waveplate was demonstrated, consisting of arrays of rotated V-shaped plasmonic antennas [22, 38]. This structure generates a helical wavefront that possesses the orbital angular momentum of  $l\hbar/2\pi$  per photon (where  $l$  is an integer). V-shaped plasmonic antennas impart abrupt phase shifts to propagating light. By arranging continuously rotated V-shaped antennas (Figure 4(b)) on a transparent substrate, we can implement a plasmonic spiral waveplate. Laguerre-Gaussian laser modes are typically used to generate such a helical wavefront [3]. But metal nanostructures provide an alternative, compact way to produce it without bulky diffractive optical components. We can potentially combine these plasmonic structures with a

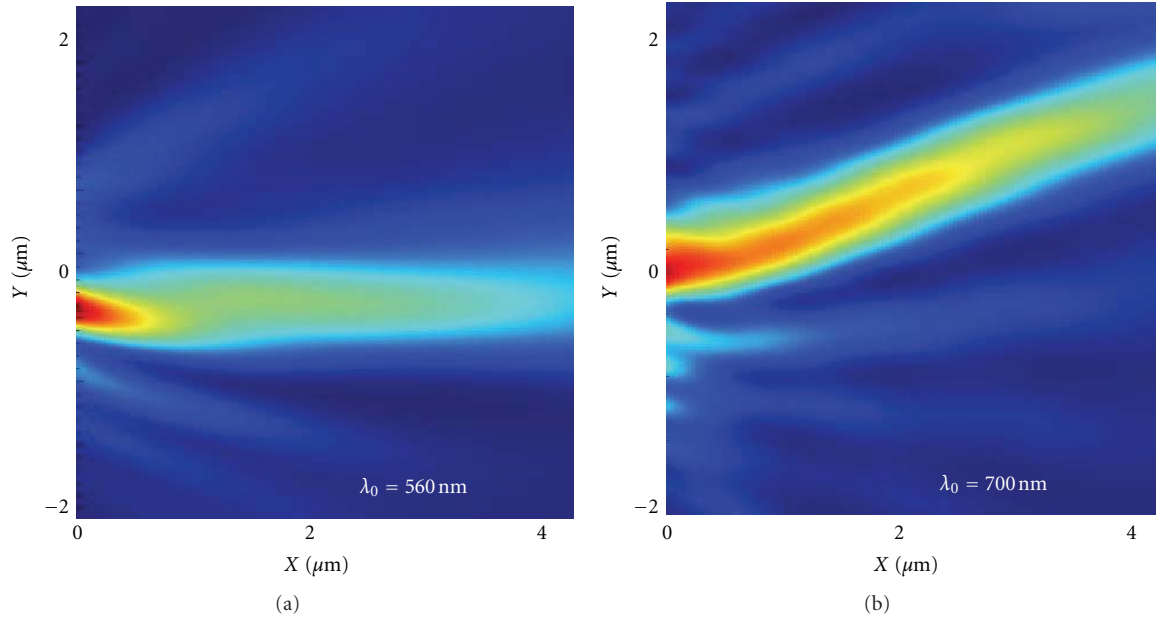


FIGURE 3: (Color online) Wavelength-dependent beam steering from an asymmetric slitgroove. Electric field intensities of the transmitted light are shown at two different wavelengths.

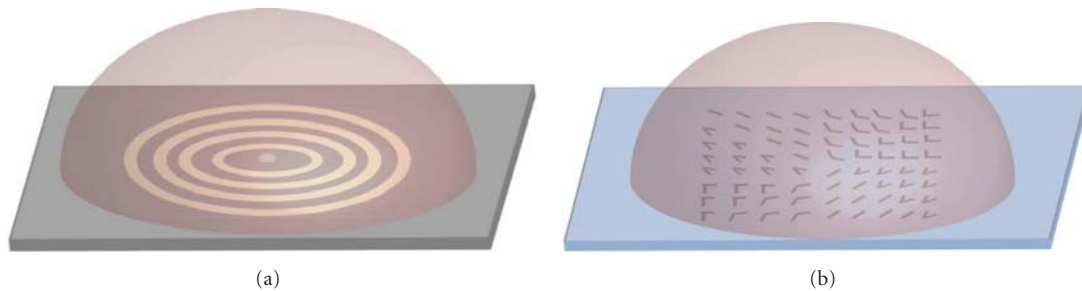


FIGURE 4: (Color online) Schematics for the "on-chip" optical rotation. A dielectric microlens is integrated with (a) a plasmonic quarter waveplate (milled on a metal film) or (b) a plasmonic spiral waveplate (consisting of V-antenna arrays on a transparent substrate). Linearly polarized light is incident from below and focused on top passing through the microlens. Objects can be trapped at the focus and be rotated on a chip.

dielectric microlens to achieve optical trapping and rotation simultaneously (Figure 4). This will be an interesting topic of future investigation.

## 5. Conclusion

In summary, we have studied optical forces generated by plasmonic beam shaping antenna structures and find that they are suitable for general optical manipulation, such as guiding of a dielectric particle along a linear or curved trajectory. The planar geometry and design flexibility make them ideal for large array fabrication. This could enable a multitude of new opportunities for integrating optical manipulation into compact, chip-scale systems.

## Acknowledgments

This work was performed, in part, at the Center for Integrated Nanotechnologies, a U.S. Department of Energy,

Office of Basic Energy Sciences user facility. Sandia National Laboratories is a multiprogram laboratory managed and operated by Sandia Corporation, a wholly owned subsidiary of Lockheed Martin Corporation, for the U.S. Department of Energy's National Nuclear Security Administration under Contract DE-AC04-94AL85000.

## References

- [1] A. Ashkin, J. M. Dziedzic, J. E. Bjorkholm, and S. Chu, "Observation of a single-beam gradient force optical trap for dielectric particles," *Optics Letters*, vol. 11, no. 5, pp. 288–290, 1986.
- [2] A. Ashkin, "History of optical trapping and manipulation of small-neutral particle, atoms, and molecules," *IEEE Journal on Selected Topics in Quantum Electronics*, vol. 6, no. 6, pp. 841–856, 2000.
- [3] K. C. Neuman and S. M. Block, "Optical trapping," *Review of Scientific Instruments*, vol. 75, no. 9, pp. 2787–2809, 2004.
- [4] D. G. Grier, "A revolution in optical manipulation," *Nature*, vol. 424, no. 6950, pp. 810–816, 2003.

- [5] K. Dholakia and T. Čižmár, "Shaping the future of manipulation," *Nature Photonics*, vol. 5, no. 6, pp. 335–342, 2011.
- [6] M. Padgett and R. Bowman, "Tweezers with a twist," *Nature Photonics*, vol. 5, no. 6, pp. 343–348, 2011.
- [7] M. L. Juan, M. Righini, and R. Quidant, "Plasmon nano-optical tweezers," *Nature Photonics*, vol. 5, no. 6, pp. 349–356, 2011.
- [8] L. Novotny and B. Hecht, *Principles of Nano-Optics*, chapter 13, Cambridge University Press, 2006.
- [9] X. Yang, Y. Liu, R. F. Oulton, X. Yin, and X. Zhang, "Optical forces in hybrid plasmonic waveguides," *Nano Letters*, vol. 11, no. 2, pp. 321–328, 2011.
- [10] R. Quidant, D. Petrov, and G. Badenes, "Radiation forces on a Rayleigh dielectric sphere in a patterned optical near field," *Optics Letters*, vol. 30, no. 9, pp. 1009–1011, 2005.
- [11] L. Novotny, R. X. Bian, and X. Sunney Xie, "Theory of Nanometric optical tweezers," *Physical Review Letters*, vol. 79, no. 4, pp. 645–648, 1997.
- [12] L. Verslegers, P. B. Catrysse, Z. Yu, W. Shin, Z. Ruan, and S. Fan, "Phase front design with metallic pillar arrays," *Optics Letters*, vol. 35, no. 6, pp. 844–846, 2010.
- [13] N. Yu and F. Capasso, "Wavefront engineering for mid-infrared and terahertz quantum cascade lasers," *Journal of the Optical Society of America B*, vol. 27, no. 11, pp. B18–B35, 2010.
- [14] H. J. Lezec, A. Degiron, E. Devaux et al., "Beaming light from a subwavelength aperture," *Science*, vol. 297, no. 5582, pp. 820–822, 2002.
- [15] S. Kim, H. Kim, Y. Lim, and B. Lee, "Off-axis directional beaming of optical field diffracted by a single subwavelength metal slit with asymmetric dielectric surface gratings," *Applied Physics Letters*, vol. 90, no. 5, Article ID 051113, 4 pages, 2007.
- [16] Y. C. Jun, K. C. Y. Huang, and M. L. Brongersma, "Plasmonic beaming and active control over fluorescent emission," *Nature Communications*, vol. 2, no. 1, Article ID 283, 2011.
- [17] Z. Sun and H. K. Kim, "Refractive transmission of light and beam shaping with metallic nano-optic lenses," *Applied Physics Letters*, vol. 85, no. 4, pp. 642–644, 2004.
- [18] L. Verslegers, P. B. Catrysse, Z. Yu et al., "Planar lenses based on nanoscale slit arrays in a metallic film," *Nano Letters*, vol. 9, no. 1, pp. 235–238, 2009.
- [19] H. Gao, J. K. Hyun, M. H. Lee, J. C. Yang, L. J. Lauhon, and T. W. Odom, "Broadband plasmonic microlenses based on patches of nanoholes," *Nano Letters*, vol. 10, no. 10, pp. 4111–4116, 2010.
- [20] A. Drezet, C. Genet, and T. W. Ebbesen, "Miniature plasmonic wave plates," *Physical Review Letters*, vol. 101, no. 4, Article ID 043902, 4 pages, 2008.
- [21] E. H. Khoo, E. P. Li, and K. B. Crozier, "Plasmonic wave plate based on subwavelength nanoslits," *Optics Letters*, vol. 36, no. 13, pp. 2498–2500, 2011.
- [22] N. Yu, P. Genevet, M. A. Kats et al., "Light propagation with phase discontinuities: generalized laws of reflection and refraction," *Science*, vol. 334, no. 6054, pp. 333–337, 2011.
- [23] N. Yu, J. Fan, Q. J. Wang et al., "Small-divergence semiconductor lasers by plasmonic collimation," *Nature Photonics*, vol. 2, no. 9, pp. 564–570, 2008.
- [24] S. Kang, H. E. Joe, J. Kim, Y. Jeong, B. K. Min, and K. Oh, "Subwavelength plasmonic lens patterned on a composite optical fiber facet for quasi-one-dimensional Bessel beam generation," *Applied Physics Letters*, vol. 98, no. 24, Article ID 241103, 3 pages, 2011.
- [25] L. B. Yu, D. Z. Lin, Y. C. Chen et al., "Physical origin of directional beaming emitted from a subwavelength slit," *Physical Review B*, vol. 71, no. 4, Article ID 041405, 4 pages, 2005.
- [26] F. J. García-Vidal, H. J. Lezec, T. W. Ebbesen, and L. Martín-Moreno, "Multiple paths to enhance optical transmission through a single subwavelength slit," *Physical Review Letters*, vol. 90, no. 21, Article ID 213901, 4 pages, 2003.
- [27] Lumerical solutions, <http://www.lumerical.com/>.
- [28] J. D. Jackson, *Classical Electrodynamics*, Wiley, 3rd edition, 1998.
- [29] V. Garcés-Chávez, D. McGloin, H. Melville, W. Sibbett, and K. Dholakia, "Simultaneous micromanipulation in multiple planes using a self-reconstructing light beam," *Nature*, vol. 419, no. 6903, pp. 145–147, 2002.
- [30] J. P. Tetienne, R. Blanchard, N. Yu et al., "Dipolar modeling and experimental demonstration of multi-beam plasmonic collimators," *New Journal of Physics*, vol. 13, Article ID 053057, 2011.
- [31] J. Baumgartl, M. Mazilu, and K. Dholakia, "Optically mediated particle clearing using Airy wavepackets," *Nature Photonics*, vol. 2, no. 11, pp. 675–678, 2008.
- [32] S. Kawata and T. Sugiura, "Movement of micrometer-sized particles in the evanescent field of a laser beam," *Optics Letters*, vol. 17, no. 11, pp. 772–774, 1992.
- [33] S. Kawata and T. Tani, "Optically driven Mie particles in an evanescent field along a channeled waveguide," *Optics Letters*, vol. 21, no. 21, pp. 1768–1770, 1996.
- [34] A. H. J. Yang, S. D. Moore, B. S. Schmidt, M. Klug, M. Lipson, and D. Erickson, "Optical manipulation of nanoparticles and biomolecules in sub-wavelength slot waveguides," *Nature*, vol. 457, no. 7225, pp. 71–75, 2009.
- [35] D. Erickson, X. Serey, Y. F. Chen, and S. Mandal, "Nanomanipulation using near field photonics," *Lab on a Chip*, vol. 11, no. 6, pp. 995–1009, 2011.
- [36] C. Min, P. Wang, X. Jiao, Y. Deng, and H. Ming, "Beam manipulating by metallic nano-optic lens containing nonlinear media," *Optics Express*, vol. 15, no. 15, pp. 9541–9546, 2007.
- [37] A. E. Çetin, K. Güven, and Ö. E. Müstecaplıoğlu, "Active control of focal length and beam deflection in a metallic nanoslit array lens with multiple sources," *Optics Letters*, vol. 35, no. 12, pp. 1980–1982, 2010.
- [38] X. Ni, N. K. Emani, A. V. Kildishev, A. Boltasseva, and V. M. Shalaev, "Broadband light bending with plasmonic nanoantennas," *Science*, vol. 335, no. 6067, article 427, 427.

## Research Article

# Plasmonic Modes of Metamaterial-Based Slot Waveguides

Ivan D. Rukhlenko,<sup>1</sup> Malin Premaratne,<sup>1</sup> and Govind P. Agrawal<sup>2</sup>

<sup>1</sup> Advanced Computing and Simulation Laboratory (AxL), Department of Electrical and Computer Systems Engineering, Monash University, Clayton, VIC 3800, Australia

<sup>2</sup> Institute of Optics, University of Rochester, Rochester, NY 14627, USA

Correspondence should be addressed to Ivan D. Rukhlenko, ivan.rukhlenko@monash.edu

Received 13 April 2012; Accepted 3 July 2012

Academic Editor: Alexandra E. Boltasseva

Copyright © 2012 Ivan D. Rukhlenko et al. This is an open access article distributed under the Creative Commons Attribution License, which permits unrestricted use, distribution, and reproduction in any medium, provided the original work is properly cited.

Most metamaterials exhibit pronounced anisotropic properties that are crucial for the understanding of their superior optical behavior, especially when they are integrated into the structure of a plasmonic waveguide. In this paper, we analytically solve the dispersion relation for a slot plasmonic waveguide filled with an anisotropic-stratified metamaterial and reveal that it supports two modes featuring relatively long propagation lengths in the limit of vanishing slot thickness. We classify these modes according to their physical origin and study the variation of their dispersion properties with material parameters.

## 1. Introduction

The ultimate goal of optics is to enable a perfect control of the interaction between light and matter. This goal has been brought closer by the recent advances in nanotechnology that have made possible the fabrication of optical metamaterials [1, 2]. The unusual electromagnetic properties of metamaterials are expected to enable a new generation of optical devices. In developing design strategies and new concepts for such devices, it is paramount that anisotropic properties of metamaterials are considered along with their other material features. Moreover, even the ways in which common devices operate require revisions when ordinary materials in their design are replaced by anisotropic metamaterials. A considerable amount of theoretical effort has been recently devoted to the analysis of optical propagation through different types of metamaterial structures, including uniaxial dielectrics [3] and indefinite media [4, 5], metal–dielectric heterostructures [6] and superlattices [7], and strongly anisotropic waveguides [8]. In this paper, we reexamine the guiding properties of slot plasmonic waveguides filled with an anisotropic medium. Our work is intended to demonstrate that integration of plasmonic waveguides with anisotropic optical metamaterials not only brings additional freedom to their design, but can also lead to new physical phenomena that may benefit the waveguide performance.

The plasmonic waveguide discussed here consists of an anisotropic medium of thickness  $2h$  embedded between two metals of permittivity  $\epsilon_m$ . We assume that the medium's permittivity is described by a constant, diagonal tensor  $\epsilon = \text{diag}(\epsilon_{xx}, \epsilon_{yy}, \epsilon_{zz})$  with its principle axes parallel to the waveguide's edges. Even though the permeability has similar anisotropic properties, only one component of its tensor affects the transverse magnetic (TM) modes, which are of primary interest for plasmonic waveguides. This allows us to describe the permeability using a single parameter  $\mu$ . As is well known, the evolution of the electric field  $\mathbf{E} = (E_x, 0, E_z)$  and the magnetic field  $\mathbf{H} = (0, H_y, 0)$  of a TM mode is governed by the propagation constant  $\beta$ . In the case of an anisotropic core layer,  $\beta$  obeys the dispersion relation

$$\tanh(qh) = - \left[ \left( \frac{k_m}{q} \right) \left( \frac{\epsilon_{zz}}{\epsilon_m} \right) \right]^{\pm 1}, \quad (1)$$

where  $q = \sqrt{(\epsilon_{zz}/\epsilon_{xx})\beta^2 - \epsilon_{zz}\mu k^2}$ ,  $k_m = \sqrt{\beta^2 - \epsilon_m k^2}$ ,  $k = \omega/c$ ,  $\omega$  is the frequency of the surface plasmon polariton (SPP),  $c$  is the speed of light in vacuum, and the  $\pm$  signs correspond to the symmetric and antisymmetric modes, respectively.

Equation (1) is applicable to a broad range of metamaterial-based plasmonic waveguides and requires the specification of metamaterial design for further analysis. We restrict



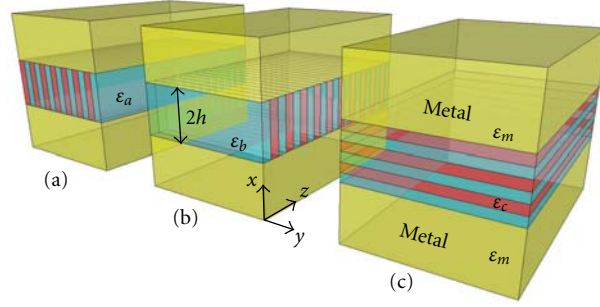


FIGURE 1: (Color online) Three types of plasmonic waveguides made using a stratified metamaterial. In all cases, SPP modes propagate in the  $z$  direction and the waveguide extends to infinity in the  $y$  direction.

ourselves to the simplest scenario in which the metamaterial is created via stacking layers of isotropic materials into a periodic heterostructure. If the layers' thicknesses are much smaller than the optical wavelength, then the permittivity tensor of the heterostructure has only two different diagonal components given by [9]

$$\varepsilon_{\parallel} = \sum_{j=1}^n f_j \varepsilon_j, \quad \frac{1}{\varepsilon_{\perp}} = \sum_{j=1}^n \frac{f_j}{\varepsilon_j}, \quad (2)$$

where the subscripts  $\parallel$  and  $\perp$  designate directions parallel and perpendicular to the layers,  $n$  is the number of layers within one heterostructure period, and  $f_j$  is the filling factor for the  $j$ th layer of permittivity  $\varepsilon_j$  (all filling factors must add up to unity). Such a stratified metamaterial offers fabrication of the three types of plasmonic waveguides shown in Figure 1. Their permittivities are  $\varepsilon_a = \text{diag}(\varepsilon_{\parallel}, \varepsilon_{\perp}, \varepsilon_{\parallel})$ ,  $\varepsilon_b = \text{diag}(\varepsilon_{\parallel}, \varepsilon_{\parallel}, \varepsilon_{\perp})$ , and  $\varepsilon_c = \text{diag}(\varepsilon_{\perp}, \varepsilon_{\parallel}, \varepsilon_{\parallel})$ . Although all of them can, in principle, be created using modern fabrication techniques, we focus here on the last structure that is relatively easy to fabricate.

Apart from the ease of fabrication, the third type of plasmonic waveguide in Figure 1 is the only one that supports symmetric TM modes with complex  $\beta$  values in the limit of vanishing  $\varepsilon_{\parallel}$ , which can be realized by properly matching metamaterial constituents and compensating for the absorption losses inside them (note that the condition  $\varepsilon_{\parallel} = 0$  is not equivalent to an epsilon-near-zero (ENZ) regime [10], because the permittivity is a complex tensor). Within the slot region, these modes are characterized by the components  $E_x$  and  $H_y$  that are independent of  $x$ , and by  $E_z \propto x$ . Solving (1) in the limit  $\varepsilon_{\parallel} \rightarrow 0$  yields the following four values of  $\beta$ :

$$\beta = \pm \left( \frac{1 + 2r\mu K \pm \sqrt{1 + 4r(\mu - r)K}}{2r^2 h^2} \right)^{1/2}, \quad (3)$$

where  $K = \varepsilon_m(kh)^2$  and  $r = \varepsilon_m/\varepsilon_{\perp}$  is the ratio of the dielectric constants. Since both of these parameters are generally complex,  $\beta = \beta' + i\beta''$  is also complex, and its real and imaginary parts provide the phase velocity and energy loss of various SPP modes. Because  $\beta$  in (3) satisfies (1) approximately in the limit of small  $h$  (when  $|q|h \ll 1$ ) even

when  $\varepsilon_{\parallel} \neq 0$ , the following analysis allows us to elucidate some general features of the SPP behavior in metamaterial-based plasmonic waveguides.

For simplicity, we focus on the stratified heterostructure composed of two different nonmagnetic ( $\mu = 1$ ) materials, one of which is the metal used for waveguide cladding. The permittivity of the second material is then fixed by the condition  $\varepsilon_{\parallel} = 0$  (this material should provide gain, since metals are essentially lossy). It then follows that the ratio  $r$  depends solely on the filling factor  $f$  of the metal;  $r = 2 - 1/f$ . We use silver as a metal in our simulations, take its permittivity in the form of a seven-pole Drude-Lorentz formula given in the work by Pannipitiya et al. [11], and introduce an absorption parameter  $\gamma$ , such that  $\varepsilon_m(\gamma) = \varepsilon' + i\gamma\varepsilon''$ . For definiteness, we also choose  $\beta' > 0$  and refer to  $\beta''$  as the “damping factor,” thus implying that our waveguides do not amplify SPPs.

According to (3), the waveguide in Figure 1(c) supports a maximum of two SPP modes regardless of slot's thickness, provided that  $\varepsilon_{\parallel} = 0$ . The dispersion curves of these two modes are plotted in Figure 2 for three values of  $\gamma$  and two sets of material parameters  $f$  and  $h$ . In the lossless case ( $\gamma = 0$ , green curves), the modes can be grouped into three distinct classes: (i) propagating modes with  $\beta'' = 0$  and  $\beta' \neq 0$ ; (ii) complex modes with  $\beta'' \neq 0$  and  $\beta' \neq 0$ ; (iii) evanescent modes with  $\beta'' \neq 0$  and  $\beta' = 0$ . The first two types of modes may travel either forward or backward, except for certain “degenerate” frequencies for which the group velocity and total energy flow of SPPs vanish. In our example, the degenerate frequencies correspond to the points A, B, and C of the energy spectrum. The degeneracy of waves traveling in the opposite directions is removed by absorption (see pink curves for  $\gamma = 0.2$ ) since the two modes develop a slightly different lateral confinement.

The complex modes of a lossy waveguide arise through quasimixing of the three types of modes as  $\gamma$  is gradually varied from 0 to 1. Such transformation of the propagating, complex, and/or evanescent modes is accompanied by their degeneracy removal, which is also the scenario followed by the quadrupole modes of plasmonic nanowires [12]. Indeed, the twofold degenerate propagating mode at point B and the twofold degenerate evanescent mode at point C split into two nondegenerate complex modes for  $\gamma = 1$  (see Figure 2). The process of modes transformation allows one to track their



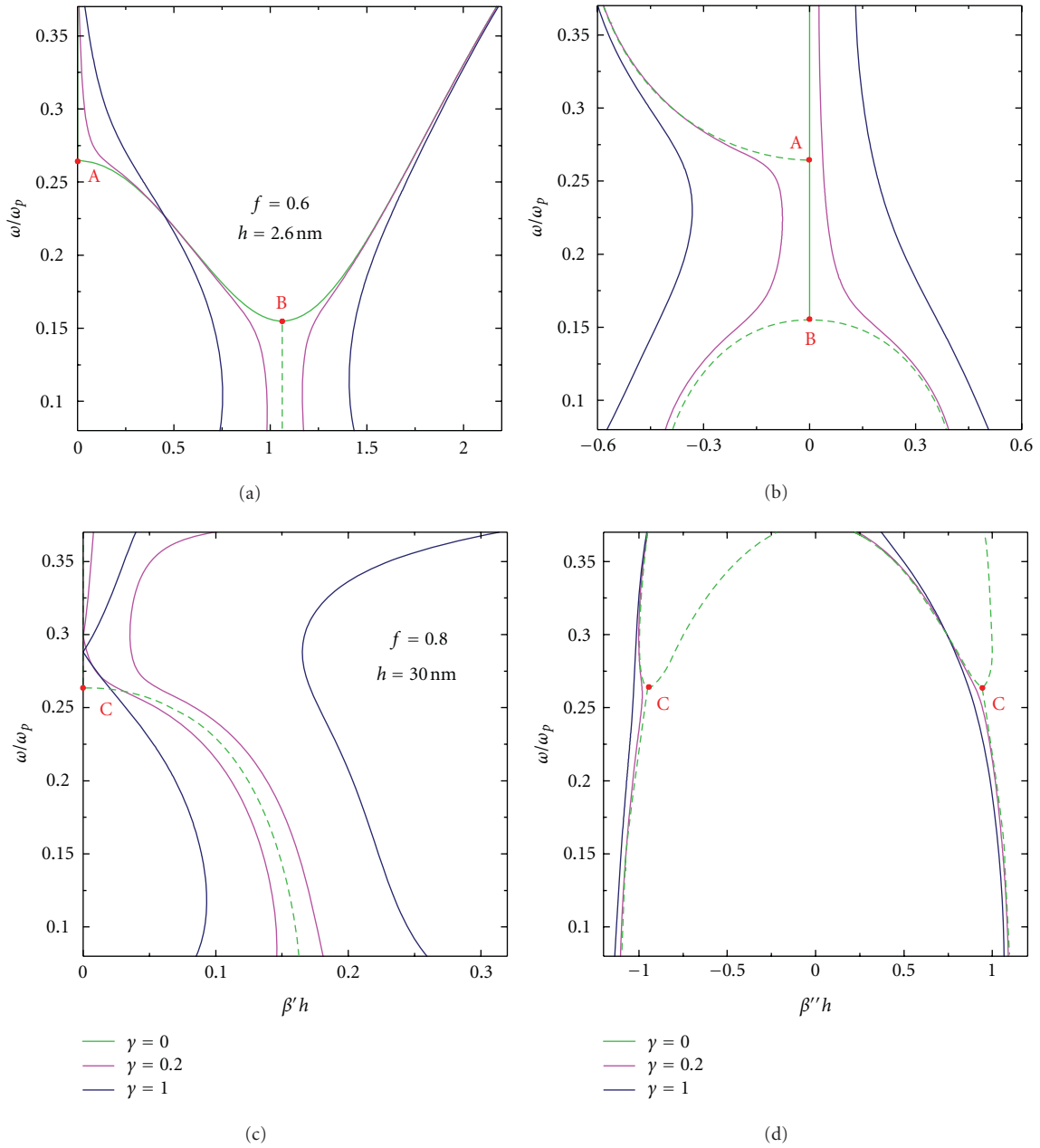


FIGURE 2: (Color online) Transformation of [(a) and (c)] SPP energy spectrum and [(b) and (d)] damping-factor dispersion with changing absorption parameter  $\gamma$ . The SPP frequency is normalized to the plasma frequency  $\omega_p$  of silver. Solid green curves show propagating modes, whereas dashed curves show complex and evanescent modes.

origin and better understand waveguide performance. For example, because of the strong damping intrinsic to evanescent modes, one can expect that the segments of spectra  $\beta''(\omega)$  emerging from them in the case of real losses will be lesser affected by the dispersion properties of  $\epsilon''(\omega)$  than the segments that stem from undamped propagating modes. This conclusion is confirmed by Figures 2(b) and 2(d), where the damping factors are separately shown for the forward (right curves) and backward (left curves) propagating SPP modes. Notice that the spectra in Figure 2 are congregate of

the results valid for different plasmonic waveguides, rather than spectra corresponding to a specific structure.

As we have seen, dispersions of the real and imaginary parts of  $\beta$  drastically depend on the filling factor of metal and slot thickness. To study this dependance, we set  $\omega = 0.2\omega_p$ , where  $\omega_p$  is the plasma frequency of silver, and plot in Figure 3  $\beta'$  and  $\beta''$  as functions of slot thickness for five values of  $f$ . By looking at this figure from left to right, one can draw up the following picture of SPP behavior. When the filling factor of metal is small, two SPP modes of different

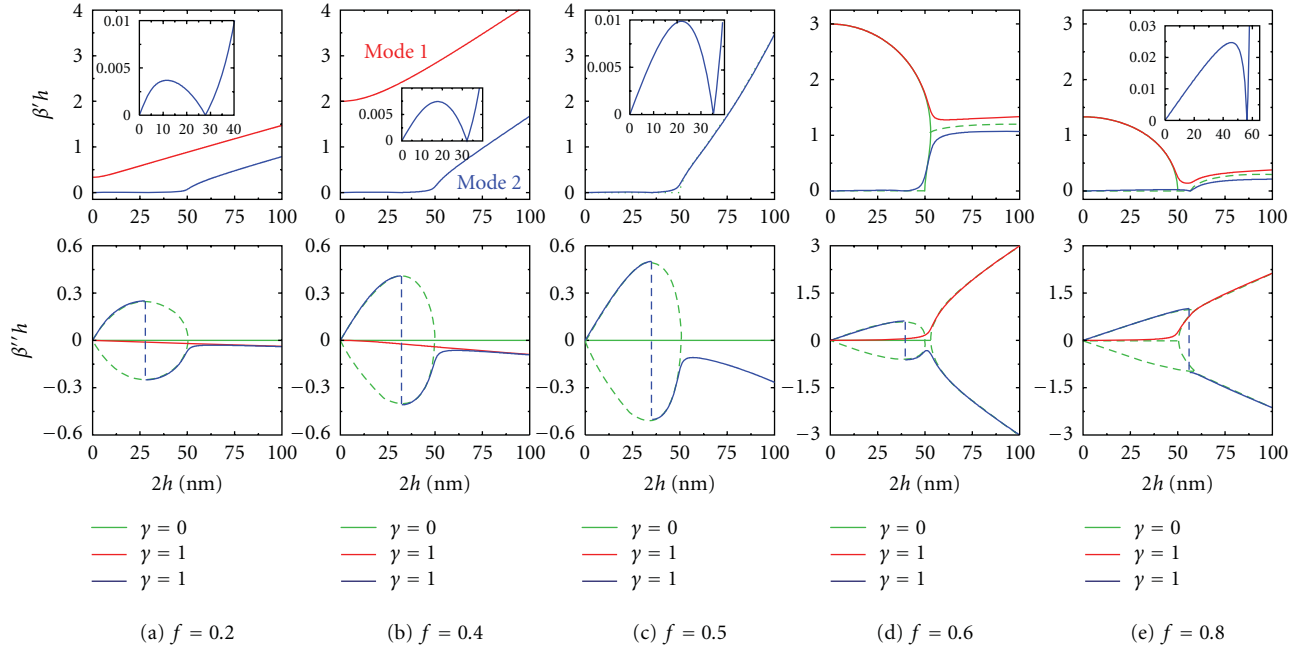


FIGURE 3: (Color and multimedia online) Transformation of the real (upper panels) and imaginary (lower panels) parts of  $\beta$  at a specific frequency  $\omega = 0.2\omega_p$  as the filling factor  $f$  of the metal is increased from 0.2 to 0.8. Insets show a magnified view of mode 2.

origins are supported by the waveguide. One of them—mode 1 shown by red curves—springs from the propagating mode of a lossless waveguide and, therefore, exhibits small damping. The other—mode 2 plotted in blue—arises from the evanescent mode when  $h < h_0 = k^{-1}|\epsilon_m|^{-1/2} \approx 25$  nm and from the propagating mode when  $h > h_0$  ( $h_0$  is the skin depth of a metal in the limit  $f \rightarrow 0$ ). The first mode propagates backward regardless of  $h$ , whereas the second one changes its traveling direction from forward to backward around  $h = h_0/2$ . Because modes 1 and 2 originate from the propagating modes for  $h > h_0$  and  $f < 0.5$ , their damping rates are almost the same for this range of parameters  $h$  and  $f$ . When  $f = 0.5$ , the ratio  $r = 0$  since the transverse component of the permittivity tensor becomes infinite, and only mode 2 with  $\beta = \pm k\sqrt{\epsilon_m(1+K)}$  survives. For  $f > 0.5$ , mode 1 becomes forward propagating, while mode 2 gets strongly attenuated for all  $h$ . The overall dynamics of such changes with  $f$  is illustrated in the supplementary animation. It should be emphasized that these results are based on the effective-medium theory and approximate. For a more accurate treatment, the inclusion of nonlocality effects is required [13, 14].

An important feature of the modes given in (3) is that they can exhibit relatively small damping depending on the values of the parameters  $f$  and  $h$ . For example, low damping occurs for both modes for  $f < 0.2$  and  $h > h_0$ . Moreover, the damping of mode 1 vanishes in the limit of small  $h$  for all values of  $f \neq 0.5$ . This behavior is opposite to that of SPPs in ordinary (isotropic) metal-dielectric-metal waveguides, whose attenuation rate diverges as  $1/h$  [15]. Also noteworthy is that the confinement of mode 1, determined by the evanescent decay length scaling like  $\delta_1 \propto h \text{Re} \sqrt{r^2}$  when  $h \rightarrow 0$ ,

improves with the reduction of the waveguide thickness, whereas the confinement of mode 2 worsens in the limit of small  $h$ , due to the divergence of the decay length  $\delta_2 \propto (hk_0^2 \text{Re} \sqrt{\epsilon_m^2(1-r)^2})^{-1}$ . Hence, we expect that metamaterial-based plasmonic waveguides may enable strong localization of optical energy in an SPP mode that can propagate over relatively long lengths.

In conclusion, we have found that a maximum of two symmetric TM modes with essentially different propagation properties are supported by plasmonic slot waveguides filled with a stratified metamaterial exhibiting a relatively small permittivity in the plane of the layers.

## Acknowledgments

This work was supported by the Australian Research Council, through its Discovery Grant scheme under Grant DP110100713 and by the Discovery Early Career Researcher Award DE120100055.

## References

- [1] W. Cai and V. Shalaev, *Optical Metamaterials: Fundamentals and Applications*, Springer, New York, NY, USA, 2010.
- [2] V. G. Veselago and E. E. Narimanov, “The left hand of brightness: past, present and future of negative index materials,” *Nature Materials*, vol. 5, no. 10, pp. 759–762, 2006.
- [3] P. A. Belov, “Backward waves and negative refraction in uniaxial dielectrics with negative dielectric permittivity along the anisotropy axis,” *Microwave and Optical Technology Letters*, vol. 37, no. 4, pp. 259–263, 2003.

- [4] D. R. Smith, D. Schurig, J. J. Mock, P. Kolinko, and P. Rye, "Partial focusing of radiation by a slab of indefinite media," *Applied Physics Letters*, vol. 84, no. 13, pp. 2244–2246, 2004.
- [5] D. R. Smith and D. Schurig, "Electromagnetic wave propagation in media with indefinite permittivity and permeability tensors," *Physical Review Letters*, vol. 90, no. 7, Article ID 077405, pp. 1–4, 2003.
- [6] J. Elser, V. A. Podolskiy, I. Salakhutdinov, and I. Avrutsky, "Nonlocal effects in effective-medium response of nanolayered metamaterials," *Applied Physics Letters*, vol. 90, no. 19, Article ID 191109, 2007.
- [7] S. M. Vukovic, I. V. Shadrivov, and Y. S. Kivshar, "Surface bloch waves in metamaterial and metal-dielectric superlattices," *Applied Physics Letters*, vol. 95, no. 4, Article ID 041902, 2009.
- [8] V. A. Podolskiy and E. E. Narimanov, "Strongly anisotropic waveguide as a nonmagnetic left-handed system," *Physical Review B*, vol. 71, no. 20, Article ID 201101, 4 pages, 2005.
- [9] I. D. Rukhlenko, M. Premaratne, and G. P. Agrawal, "Theory of negative refraction in periodic stratified metamaterials," *Optics Express*, vol. 18, no. 26, pp. 27916–27929, 2010.
- [10] A. Alù, M. G. Silveirinha, A. Salandrino, and N. Engheta, "Epsilon-near-zero metamaterials and electromagnetic sources: tailoring the radiation phase pattern," *Physical Review B*, vol. 75, no. 15, Article ID 155410, 2007.
- [11] A. Pannipitiya, I. D. Rukhlenko, M. Premaratne, H. T. Hattori, and G. P. Agrawal, "Improved transmission model for metal-dielectric-metal plasmonic waveguides with stub structure," *Optics Express*, vol. 18, no. 6, pp. 6191–6204, 2010.
- [12] A. R. Davoyan, W. Liu, A. E. Miroshnichenko, I. V. Shadrivov, Y. S. Kivshar, and S. I. Bozhevolnyi, "Mode transformation in waveguiding plasmonic structures," *Photonics and Nanostructures*, vol. 9, no. 3, pp. 207–212, 2011.
- [13] A. A. Orlov, P. M. Voroshilov, P. A. Belov, and Y. S. Kivshar, "Engineered optical nonlocality in nanostructured metamaterials," *Physical Review B*, vol. 84, no. 4, Article ID 045424, 2011.
- [14] A. V. Chebykin, A. A. Orlov, A. V. Vozianova, S. I. Maslovski, S. Yu. Kivshar, and P. A. Belov, "Nonlocal effective medium model for multilayered metal-dielectric metamaterials," *Physical Review B*, vol. 2011, Article ID 115438, 2011.
- [15] I. D. Rukhlenko, M. Premaratne, and G. P. Agrawal, "Nonlinear propagation in silicon-based plasmonic waveguides from the standpoint of applications," *Optics Express*, vol. 19, no. 1, pp. 206–217, 2011.

## Research Article

# Magnetic Plasmon Sensing in Twisted Split-Ring Resonators

J. X. Cao, H. Liu, S. M. Wang, Y. J. Zheng, C. Zhu, Y. Wang, and S. N. Zhu

Department of Physics and National Laboratory of Solid State Microstructures, Nanjing University, Nanjing 210093, China

Correspondence should be addressed to H. Liu, liuhui@nju.edu.cn and S. N. Zhu, zhushn@nju.edu.cn

Received 10 February 2012; Accepted 31 March 2012

Academic Editor: Ivan D. Rukhlenko

Copyright © 2012 J. X. Cao et al. This is an open access article distributed under the Creative Commons Attribution License, which permits unrestricted use, distribution, and reproduction in any medium, provided the original work is properly cited.

We studied the sensing properties of stereo-SRRs metamaterials composed from two twisted split-ring resonators (SRRs). Due to the strong hybridization effect in the system, the polarization state of the transmitted wave is greatly changed at resonances. Since the stereo-SRRs structure is strongly coupled to the surrounding medium, the polarization change of the transmitted waves is quite sensitive to the refractive index change of the environment medium. The polarization ratio  $PR_{\text{tran}} = T_y/T_x$  is used as sensing parameter and its figure of merit can reach 22.3 at the hybridized magnetic plasmon resonance. The results showed that the stereo-SRRs metamaterial can be applied to optical sensors and other related field.

## 1. Introduction

Recently, a new concept in nanophotonics named as stereometamaterial was proposed [1]. This indicated that the electromagnetic properties of plasmonic metamaterials are determined not only by the geometry structure of elements but also by the spatial arrangement of these elements. Up to now, some different stereometamaterials are reported, such as gammadions [2], spirals [3], crosses [4], and stacked wires [5]. Among them, the twisted-SRRs system, also named as stereo-SRRs, is an interesting example for investigation. According to the previous studies, the electromagnetic responses could be tuned through changing the orientation angle of the SRRs [6]; a Lagrange model was introduced to demonstrate the chiral optical properties [7] and give a good description for the polarization change of the electromagnetic wave passing through the twisted-SRRs metamaterials [8, 9].

As is well known, surface plasmon resonance and localized surface plasmon resonance based on metal structures can be used as optical sensors because the resonance modes shift with the refractive index change of the surrounding medium [10, 11]. Since the magnetic plasmon resonance had a stronger field localization and narrower response linewidth, it could also be used as sensors [12, 13]. In this work, we will show that polarization change induced by magnetic plasmon resonances in the stereo-SRRs could be strongly

coupled to the environment and is sensitive to the refractive index fluctuation of the surrounding medium. Stereo-SRRs structure could possibly work as a new kind of optical sensor.

## 2. Design of Numerical Models

Figure 1 presents one unit cell of the stereo-SRRs metamaterial with its geometry parameters. The structure is composed of two stacked SRRs, between which there is a twisted angle  $90^\circ$ . The period of the unit cell is  $p = 700$  nm. The incident electromagnetic wave propagates in the  $z$  direction. Periodic boundary condition is used in the  $x$  and  $y$  direction, and the open boundary condition is used in the  $z$  direction. The substrate and the middle layer between the two SRRs are  $\text{MgF}_2$ , whose permittivity is taken as  $\epsilon = 1.9$ .

To study the electromagnetic response of the twisted-SRRs metamaterial, a commercial software package CST Microwave Studio (Computer Simulation Technology GmbH, Darmstadt, Germany) is employed to investigate the transmission properties. The permittivity of metal is defined by the Drude model,  $\epsilon(\omega) = 1 - \omega_p^2/(\omega^2 + i\omega\tau)$ , where  $\omega_p$  and  $\omega_\tau$  are the bulk plasma frequency and the relaxation rate, respectively. For gold, the characteristic frequencies fitted to experimental data are  $\omega_p = 2\pi \times 2.175 \times 10^{15} \text{ s}^{-1}$  and  $\omega_\tau = 2\pi \times 6.5 \times 10^{12} \text{ s}^{-1}$  [14].

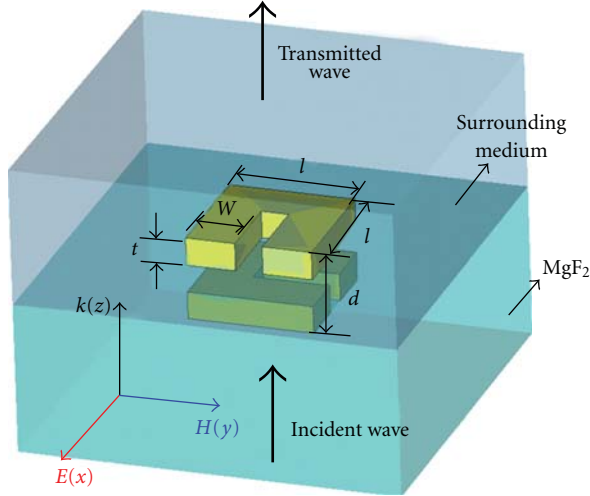


FIGURE 1: Schematics of unit cell of the stereo-SRRs metamaterial, together with the direction of the incident wave. The geometry parameters were  $l = 230$  nm,  $w = 90$  nm,  $t = 50$  nm, and  $d = 50$  nm. The periods in both of the  $x$  and  $y$  directions were  $p = 700$  nm.

### 3. Results and Discussions

In the simulations, the incident linearly polarized plane wave shined on the structure along the  $z$  direction with its electric field in the  $x$  direction (see Figure 1). As reported in [6–9], there are two magnetic plasmon modes induced in the twisted-SRRs system due to the hybridization effect. For the mode at the shorter resonance wavelength, the magnetic fields in two SRRs are in the opposite direction along the  $z$  axis (this mode is named as mode 1); while for the mode at the longer resonance wavelength, the magnetic fields in two SRRs are in the same direction along the  $z$  axis (this mode is named as mode 2). Like the electromagnetic properties of localized surface plasmon resonance, the electromagnetic field is strongly localized around the twisted SRRs at these two resonance wavelengths. This makes the structure couple with the environment strongly. The fluctuation of the refractive index of the surrounding medium will change the magnetic plasmon resonances of the structure greatly. Thus, the two hybrid magnetic plasmon modes could also be possibly applied in sensing.

Due to the chirality of this structure, the polarization state of the transmission wave will be changed at two resonance wavelengths [7]. Generally, the transmitted wave is not linearly  $x$ -polarized state. It includes the electric field components in both the  $x$  and  $y$  direction:  $E_x^{\text{tran}}$  and  $E_y^{\text{tran}}$ . Figures 2(a) and 2(b) give the transmitted energy of the two electric components  $T_x = |E_x^{\text{tran}}|^2 / |E_x^{\text{in}}|^2$  and  $T_y = |E_y^{\text{tran}}|^2 / |E_x^{\text{in}}|^2$  of the transmitted wave through the twisted-SRRs metamaterials. Here, the input signal of the excited plane wave is normalized. The two hybridized magnetic plasmon modes correspond to two absorption ditches in the transmission curves of  $T_x$ , while for the transmission curves of  $T_y$ , they correspond to two peaks. This means that

part of the energy of the incident wave  $E_x^{\text{in}}$  is transferred into the transmitted wave  $E_y^{\text{tran}}$ . Here, we could define the polarization ratio (PR)  $\text{PR} = T_y / T_x$  to characterize the polarization change between the incident wave and the transmitted one. Obviously, for the  $x$  polarized incident wave,  $\text{PR}_{\text{in}} = 0$ . For the transmitted wave,  $\text{PR}_{\text{tran}}$  results can be determined through the simulation data, which are given in Figure 2(c). Compared with the curves of  $T_x$  and  $T_y$ , it can be obviously found that the  $\text{PR}_{\text{tran}}$  curves have narrower linewidth. This makes  $\text{PR}_{\text{tran}}$  a better sensing parameter.

In order to investigate the sensing properties of the twisted-SRRs system, we change the refractive index of the surrounding medium to see what happens to the magnetic plasmon response of the structure. In our simulations, when the refractive index of the surrounding medium is increased from 1.312 to 1.352 with step being 0.01, different transmission curves are obtained, and the resonance wavelengths will shift to longer wavelengths (see Figure 2). For mode 1, the resonance wavelength changes from  $1.859 \mu\text{m}$  to  $1.877 \mu\text{m}$ . For mode 2, the resonance wavelength changes from  $2.083 \mu\text{m}$  to  $2.107 \mu\text{m}$ . Under the different refractive indices of the surrounding medium, the resonance wavelengths of the two magnetic plasmon modes show good linear relationship. As is well known to all, the slope of the wavelength shift via the refractive index change represents the sensitivity as sensing element. That is to say, the sensitivity  $m$  here is defined as the wavelength shift over one refractive index unit change of the surrounding medium. So, for the case of our proposed twisted-SRRs system, the sensitivities for mode 1 and mode 2 are equal to  $461 \text{ nm}/\text{RIU}$  (refractive index unit) and  $581 \text{ nm}/\text{RIU}$ , respectively.

To understand the sensing performance of the two hybridized magnetic plasmon modes in the twisted-SRRs metamaterials, the general concept “figure of merit” (FOM) is introduced as follows [15]:

$$\text{FOM} = \frac{m (\text{nm}/\text{RIU})}{\text{FWHM} (\text{nm})}. \quad (1)$$

Here,  $m$  and FWHM are the sensitivity of the two hybridized magnetic plasmon modes and the full width at half maximum of the obtained curves ( $T_x$ ,  $T_y$ , or  $\text{PR}_{\text{tran}}$ ). Due to including the information of the sensitivity  $m$  and the linewidth of the signals, the parameter FOM represents the overall sensing performance of the twisted-SRRs metamaterials. Table 1 shows the calculated linewidth and FOM at the two resonance modes. In Table 1, when  $T_x$  is chosen as the sensing parameter, the FOM for mode 1 and mode 2 is 9.1 and 12.5, respectively, both of which are larger than that of the single-SRR structures being 8.73. While  $T_y$  is used for the sensing parameter, the FOM for mode 1 and mode 2 is 8.0 and 10.6. Obviously,  $T_x$  is better than  $T_y$ . For the  $\text{PR}_{\text{tran}}$  curves, it can be clearly found that the FOM parameters for mode 1 and mode 2 are 14.0 and 22.3, respectively. Both of them are larger not only than the FOM of the single SRR structures, but also than  $T_x$  and  $T_y$  of the stereo-SRRs system. Especially, the FOM at mode 2 is even much larger than mode 1. Thus,  $\text{PR}_{\text{tran}}$  is the best choice of sensing parameter.

As we reported before, when two SRRs compose one magnetic dimer, the coupling between the two SRRs leads to



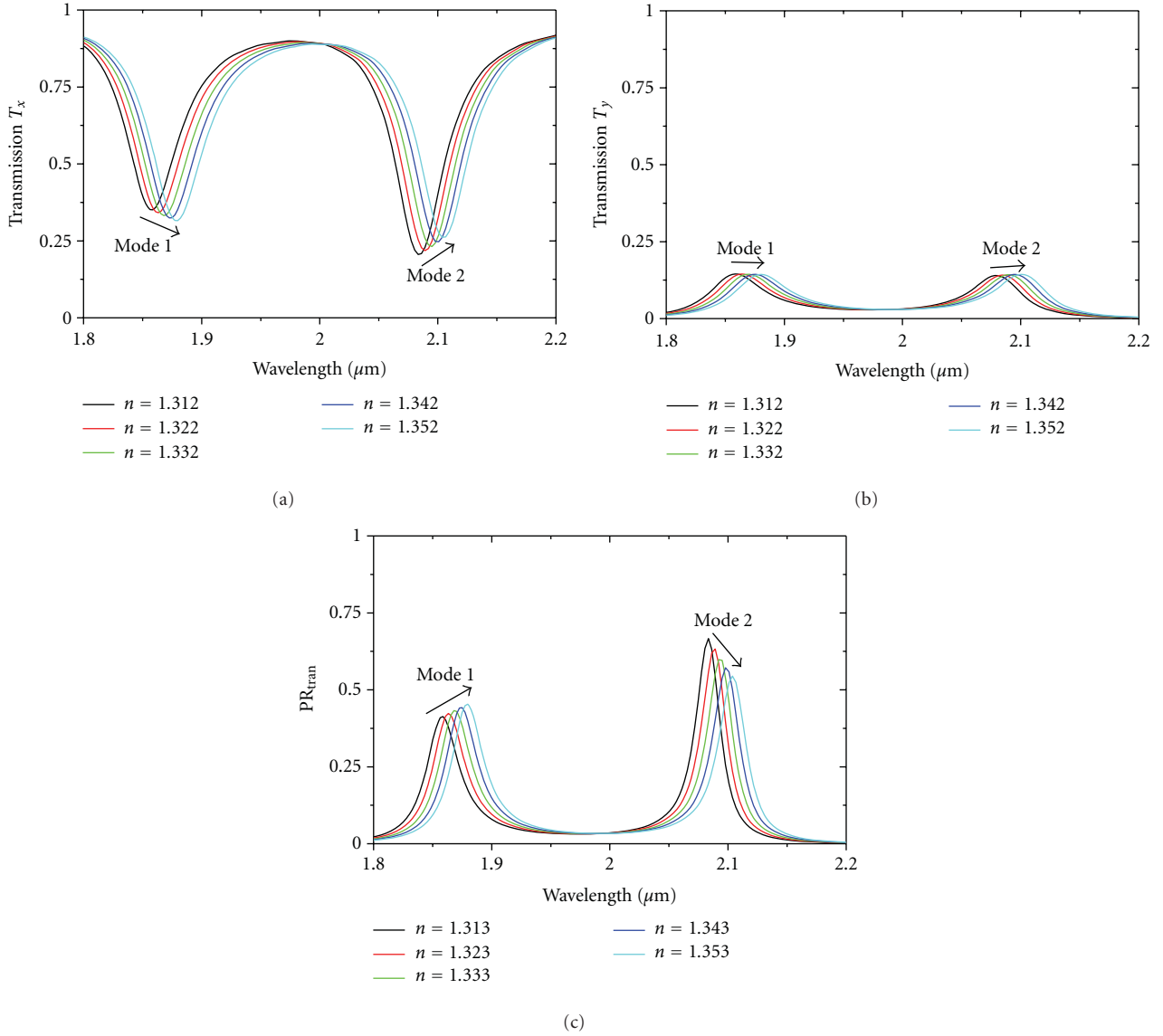


FIGURE 2: The calculated transmission spectrums for (a)  $T_x$ , (b)  $T_y$ , together with (c)  $\text{PR}_{\text{tran}}$  curves obtained by the simulated transmission data. The arrows in Figure 2 denoted that the resonance wavelengths shifted to longer wavelength when the refractive index of the surrounding medium was increased from 1.312 to 1.352.

TABLE 1: The FOM for the two hybridized magnetic plasmon modes of the stereo-SRRs metamaterials, and the parameters FWHM. Obviously, when the  $\text{PR}_{\text{tran}}$  result was used as sensing signal, the sensing performance of the two modes was best.

Eigenmode	FWHM (nm)	FOM
Mode 1 ( $T_x$ )	50.7	9.1
Mode 2 ( $T_x$ )	46.3	12.5
Mode 1 ( $T_y$ )	57.8	8.0
Mode 2 ( $T_y$ )	54.6	10.6
Mode 1 ( $\text{PR}_{\text{tran}}$ )	33.0	14.0
Mode 2 ( $\text{PR}_{\text{tran}}$ )	26.0	22.3

the hybridization of the magnetic response in the magnetic dimer, and two magnetic plasmon modes could be excited

[8, 9, 16]. That is to say, the two magnetic plasmon resonance modes of the twisted SRRs come from the coupling between the two SRRs. Then their sensing properties are dependent on the coupling process. In the simulation, we change coupling strength through changing the distance between two SRRs. The dependence of sensitivity  $m$ , FWHM, and FOM of  $\text{PR}_{\text{tran}}$  at the two modes on the distance between two SRRs is calculated and given in Figures 3–5. The results show that, for both two modes, when the distance between two SRRs is reduced, the sensitivity  $m$  is increased (see Figure 3). Simultaneously, their FWHM is decreased (see Figure 4). As a result, FOM of the two modes will be increased when the distance between the two SRRs is decreased (see Figure 5). This means that stronger coupling will improve the sensing performance.

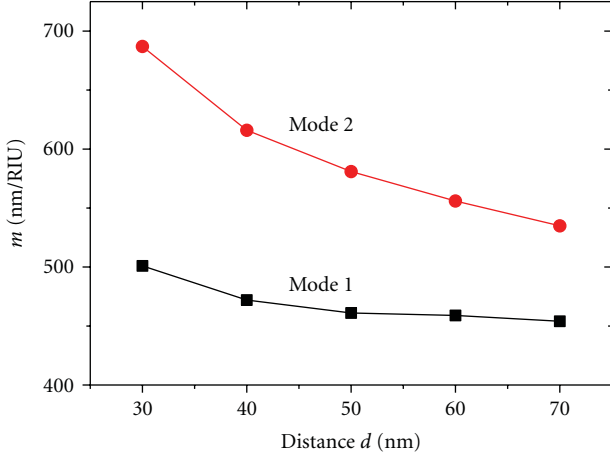


FIGURE 3: Sensitivity  $m$  for the two magnetic plasmon modes with different distances of the two SRRs when choosing the  $PR_{\text{tran}}$  curves as sensing signal.

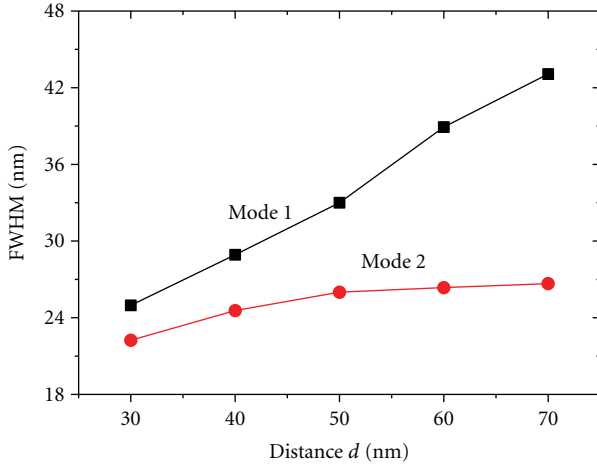


FIGURE 4: FWHM for the two magnetic plasmon modes with different distances of the two SRRs when choosing the  $PR_{\text{tran}}$  curves as sensing signal.

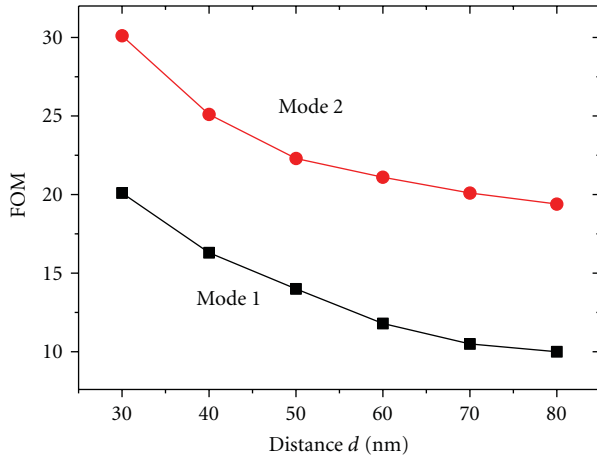


FIGURE 5: FOM for the two magnetic plasmon modes with different distances of the two SRRs when choosing the  $PR_{\text{tran}}$  curves as sensing signal.

According to our former work, the chirality of stereo-SRRs metamaterial comes from the magnetic coupling between two SRRs. Due to this coupling effect, the part of energy of the  $x$ -component of the incident wave can be converted to the  $y$ -component of the transmitted wave. The polarization conversion efficiency is determined by the coupling process. When we decrease the distance between two SRRs, the coupling effect becomes stronger. Then we can obtain larger FOM and better sensing performance.

## 4. Conclusion

In conclusion, the sensing properties of the stereo-SRRs metamaterials are investigated in this work. Based on the hybridization effect of the twisted SRRs, the polarization state of the transmitted wave is changed and great polarization ratio  $PR_{\text{tran}}$  is obtained at resonances. Compared with the transmission curves of  $T_x$  and  $T_y$ ,  $PR_{\text{tran}}$  has narrower linewidth and larger FOM and is a better sensing parameter. Our work shows that stereo-SRRs metamaterials can be possibly applied in optical sensors and other related techniques.

## Acknowledgments

This work was supported by the National Natural Science Foundation of China (Grants no. 11104138, 11074119, 10704036, 10874081, 60907009, 10904012, 10974090, and 60990320) and by the National Key Projects for Basic Research of China (Grants no. 2009CB930501 and 2010CB630703).

## References

- [1] O. Graydon, "A clever twist," *Nature Photonics*, vol. 3, no. 3, p. 176, 2009.
- [2] A. V. Rogacheva, V. A. Fedotov, A. S. Schwanecke, and N. I. Zheludev, "Giant gyrotropy due to electromagnetic-field coupling in a bilayered chiral structure," *Physical Review Letters*, vol. 97, no. 17, pp. 177401–1774014, 2006.
- [3] J. K. Gansel, M. Thiel, M. S. Rill et al., "Gold helix photonic metamaterial as broadband circular polarizer," *Science*, vol. 325, no. 5947, pp. 1513–1515, 2009.
- [4] M. Decker, M. Ruther, C. E. Kriegler et al., "Strong optical activity from twisted-cross photonic metamaterials," *Optics Letters*, vol. 34, no. 16, pp. 2501–2503, 2009.
- [5] N. Liu, L. Langguth, T. Weiss et al., "Plasmonic analogue of electromagnetically induced transparency at the Drude damping limit," *Nature Materials*, vol. 8, no. 9, pp. 758–762, 2009.
- [6] N. Liu, H. Liu, S. Zhu, and H. Giessen, "Stereometamaterials," *Nature Photonics*, vol. 3, no. 3, pp. 157–162, 2009.
- [7] H. Liu, J. X. Cao, S. N. Zhu, N. Liu, R. Ameling, and H. Giessen, "Lagrange model for the chiral optical properties of stereometamaterials," *Physical Review B*, vol. 81, no. 24, pp. R2414031–R2414034, 2010.
- [8] H. Liu, D. A. Genov, D. M. Wu et al., "Magnetic plasmon hybridization and optical activity at optical frequencies in metallic nanostructures," *Physical Review B*, vol. 76, no. 7, pp. 0731011–0731014, 2007.

- [9] T. Q. Li, H. Liu, T. Li et al., "Magnetic resonance hybridization and optical activity of microwaves in a chiral metamaterial," *Applied Physics Letters*, vol. 92, no. 13, pp. 131111–131113, 2008.
- [10] J. Homola, "Surface plasmon resonance sensors for detection of chemical and biological species," *Chemical Reviews*, vol. 108, no. 2, pp. 462–493, 2008.
- [11] J. N. Anker, W. P. Hall, O. Lyandres, N. C. Shah, J. Zhao, and R. P. Van Duyne, "Biosensing with plasmonic nanosensors," *Nature Materials*, vol. 7, no. 6, pp. 442–453, 2008.
- [12] T. Driscoll, G. O. Andreev, D. N. Basov et al., "Tuned permeability in terahertz split-ring resonators for devices and sensors," *Applied Physics Letters*, vol. 91, no. 6, pp. 062511–062513, 2007.
- [13] J. X. Cao, H. Liu, T. Li, S. M. Wang, Z. G. Dong, and S. N. Zhu, "High sensing properties of magnetic plasmon resonance in the double-rod and tri-rod structures," *Applied Physics Letters*, vol. 97, no. 7, pp. 071905–071905, 2010.
- [14] M. A. Ordal, L. L. Long, R. J. Bell et al., "Optical properties of the metals Al, Co, Cu, Au, Fe, Pb, Ni, Pd, Pt, Ag, Ti, and W in the infrared and far infrared," *Applied Optics*, vol. 22, no. 7, pp. 1099–1119, 1983.
- [15] L. J. Sherry, S. H. Chang, G. C. Schatz, R. P. Van Duyne, B. J. Wiley, and Y. Xia, "Localized surface plasmon resonance spectroscopy of single silver nanocubes," *Nano Letters*, vol. 5, no. 10, pp. 2034–2038, 2005.
- [16] N. Liu and H. Giessen, "Coupling effects in optical metamaterials," *Angewandte Chemie*, vol. 49, no. 51, pp. 9838–9852, 2010.